EDITOR'S PICK 2021: HIGHLIGHTS IN CELL ADHESION AND MIGRATION

EDITED BY: Claudia Tanja Mierke and Akihiko Ito
PUBLISHED IN: Frontiers in Cell and Developmental Biology

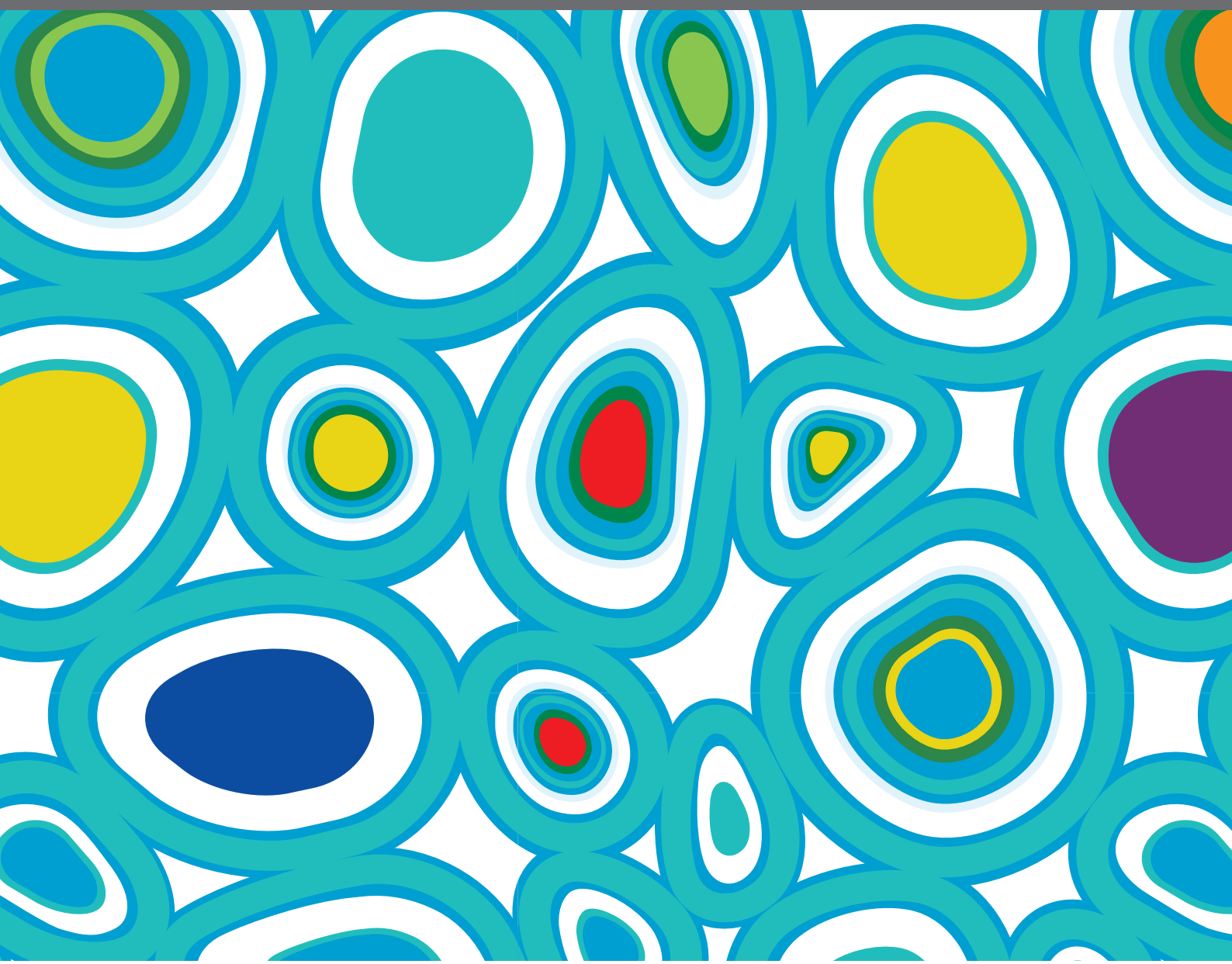

frontiers Research Topics

ISSN 1664-8714
ISBN 978-2-88974-782-5
DOI 10.3389/978-2-88974-782-5

About Frontiers

Frontiers is more than just an open-access publisher of scholarly articles: it is a pioneering approach to the world of academia, radically improving the way scholarly research is managed. The grand vision of Frontiers is a world where all people have an equal opportunity to seek, share and generate knowledge. Frontiers provides immediate and permanent online open access to all its publications, but this alone is not enough to realize our grand goals.

Frontiers Journal Series

The Frontiers Journal Series is a multi-tier and interdisciplinary set of open-access, online journals, promising a paradigm shift from the current review, selection and dissemination processes in academic publishing. All Frontiers journals are driven by researchers for researchers; therefore, they constitute a service to the scholarly community. At the same time, the Frontiers Journal Series operates on a revolutionary invention, the tiered publishing system, initially addressing specific communities of scholars, and gradually climbing up to broader public understanding, thus serving the interests of the lay society, too.

Dedication to Quality

Each Frontiers article is a landmark of the highest quality, thanks to genuinely collaborative interactions between authors and review editors, who include some of the world's best academicians. Research must be certified by peers before entering a stream of knowledge that may eventually reach the public - and shape society; therefore, Frontiers only applies the most rigorous and unbiased reviews.
Frontiers revolutionizes research publishing by freely delivering the most outstanding research, evaluated with no bias from both the academic and social point of view. By applying the most advanced information technologies, Frontiers is catapulting scholarly publishing into a new generation.

What are Frontiers Research Topics?

Frontiers Research Topics are very popular trademarks of the Frontiers Journals Series: they are collections of at least ten articles, all centered on a particular subject. With their unique mix of varied contributions from Original Research to Review Articles, Frontiers Research Topics unify the most influential researchers, the latest key findings and historical advances in a hot research area! Find out more on how to host your own Frontiers Research Topic or contribute to one as an author by contacting the Frontiers Editorial Office: frontiersin.org/about/contact

EDITOR'S PICK 2021: HIGHLIGHTS IN CELL ADHESION AND MIGRATION

Topic Editors:
Claudia Tanja Mierke, Leipzig University, Germany
Akihiko Ito, Kindai University, Japan

Citation: Mierke, C. T., Ito, A., eds. (2022). Editor's Pick 2021: Highlights in Cell Adhesion and Migration. Lausanne: Frontiers Media SA.
doi: 10.3389/978-2-88974-782-5

Table of Contents

frontiers in Cell and Developmental Biology

EDITORIAL
published: 07 March 2022
doi: 10.3389/fcell.2022.852781

Editorial: Editor's Pick 2021: Highlights in Cell Adhesion and Migration

*Claudia Tanja Mierke**

Faculty of Physics and Earth Science, Peter Debye Institute of Soft Matter Physics, Biological Physics Division, University of Leipzig, Leipzig, Germany

Keywords: cell and matrix mechanics, focal adhesion proteins, actin and actin binding proteins, mechanosignaling, migrasome, microtubules, integrins, individual and collective migration

Editorial on the Research Topic

Editorial: Editor's Pick 2021: Highlights in Cell Adhesion and Migration

The Editor's Picks are not a standard Frontiers in Cell and Developmental Biology Research topic in Cell Adhesion and Migration, as it focuses on outstanding high-impact manuscripts that are of interest to a broad group of scientists and were not already assigned to a specific Research topic. The migration and invasion of cells can be sculpted in various model systems, encompassing human (Cuenca et al., 2020; Hayn et al.; Paradžik et al., 2020; Zhang et al., 2020; Liu et al., 2021; Zhou et al., 2021) and murine cell cultures (Becsky et al.; Cheong et al.; Jiang et al.) or animals, such as zebrafish (Van der Meulen et al.; Dries et al.) and mouse models (Burr et al.; Garcia-Guillin et al.). In this regard, it is crucial to choose an appropriate microenvironment for the analysis of cell adhesion and migration, as there is an interaction between the phenotype of the cytoskeleton, the nuclear or organelle phenotype of the cells and their extracellular matrix environment (Mierke, 2020). This particular research theme of Frontiers in Cell and Developmental Biology Section Cell Adhesion and Migration includes eleven original research articles, one methods article and two reviews.

Burr et al. investigated how the AGE/RAGE signaling pathway alters the migration of two kinds of cardiac fibroblasts, such as non-diabetic and diabetic cardiac fibroblasts (Burr et al.). Notably, the AGE/RAGE signaling pathway has been altered by the supplementation of ERK1/2 and PKC-ζ inhibitors, and by exogenous AGEs treatment. Since the small GTPase Rap1 has been identified to fulfill fundamental cellular tasks, such as cell-cell and cell-matrix adhesion, proliferation and polarity governance (Chrzanowska-Wodnicka et al., 2015), it seems to be likely that it acts in the Age/RAGE signaling cascade. In fact, Burr et al. found that the small GTPase Rap1a functions as a coupler between the extracellular cues to intracellular events.

In 2018, novel adhesive structures referred to as reticular adhesions (RAs) have been detected. They are abundant in integrin αvβ5, while lacking most of the characteristic cytoskeletal moieties seen in other integrin adhesion complexes (IACs), and are interconnected in their place with the clathrin system (Lock et al., 2018). In addition, reduced motility and heightened susceptibility to microtubule toxins (MT), paclitaxel, and vincristine, following transfection with integrin-αV-specific siRNA, has been identified in the melanoma cell line MDA-MB-435S, implying an association between adhesion and medication susceptibility (Stojanović et al., 2018). Paradžik et al. addressed the clarification of the enabling mechanism and identified αV-dependent modifications in the assortment of IACs that compose the adhesome (Paradžik et al., 2020). Mass spectrometry proteomics yielded, that cells preferably exploit integrin αVβ5 for the assembly of IACs. Due to knockdown of the αV-integrin subunit, reduced levels of specific elements of the cortical microtubule stabilization complex that align MTs to adhesion sites can be detected, including the proteins KN motif and ankyrin repeat domain-containing 1 (KANK1) and KANK2. Moreover, the knockdown of KANK2 in human MDA-MB-435S melanoma cells can replicate the phenotype of the integrin-αV

Edited and reviewed by:
Florian Rehfeldt,
University of Bayreuth, Germany

***Correspondence:**
Claudia Tanja Mierke
claudia.mierke@uni-leipzig.de
orcid.org/0000-0002-6622-335X

Specialty section:
This article was submitted to Cell Adhesion and Migration, a section of the journal Frontiers in Cell and Developmental Biology

Received: *11 January 2022*
Accepted: *16 February 2022*
Published: *07 March 2022*

Citation:
Mierke CT (2022) Editorial: Editor's Pick 2021: Highlights in Cell Adhesion and Migration. Front. Cell Dev. Biol. 10:852781. doi: 10.3389/fcell.2022.852781

knockdown and induce enhanced susceptibility to MT toxicants and diminished migration (Paradžik et al., 2020). Finally, they pointed out that KANK2 is a critical factor that joins integrin-αVβ5 adhesion complexes to MTs and facilitates actin-MT interactions that are vital for both susceptibility to MT toxins and migration of cells.

Besides the adhesome, a new migration-dependent organelle referred to as the migrasome has been identified to facilitate the liberation of cytoplasmic constituents; this cellular process has been termed migracytosis (Ma et al., 2015). Thereafter, the migrasomes can be taken up by adjacent cells. Thus, Zhang et al. reviewed timely the impact of the migrasome in a cardiovascular system and pointed out that the generation of the migrasome is tightly governed through tetraspanins (TSPANs), cholesterol, and integrins. Their review focuses on TSPANs, migrasomes, and migracytosis, which perform critical functions in the coordination of vascular homeostasis. Moreover, the differences between migrasomes and exosomes are pointed out (Zhang et al., 2020).

In a zebrafish model, Van der Meulen et al. intended to analyze the performance of the periocular mesenchyme (POM) and identify transcriptional activities during the early development of the zebrafish anterior segment (AS) of the eye (Van der Meulen et al.). Disruption of AS might be the reason for congenital blindness and disposition to glaucoma. Analysis of the performance of POM cells at fixed time points and in real time has been arranged in a capacious model for the settlement of the AS of the zebrafish. In doing so, they generated transcriptomic single cell microprofiles (scRNA) from the POM-generated reporter lines and mapped unique expression patterns of distinct subpopulations. Subsequently, they noted that AS-associated POM or anterior segment mesenchyme is not uniform, but consists of multiple subpopulations with diverse colonization profiles, migratory habits, and transcriptomic patterns (Van der Meulen et al.).

Efficient cell locomotion demands the polarization of cells, which is well-known to entail the generation of leading and trailing ends, adequate placement of the nucleus, and realignment of the Golgi apparatus and centrosomes with respect to the leading edge (Vicente-Manzanares et al., 2005; Keller-Pinter et al., 2010). Asymmetric calcium gradient (Ca^{2+}) evolution from anterior to posterior is also prerequisite for focal adhesion assemblage and actomyosin-driven contractility to govern migration. Becsky et al. identified that knockdown of syndecan-4 results in nanoscale changes in the architecture of lamellipodial actin fibers of motile myoblasts (Becsky et al.). They subsequently revealed that syndecan-4 spreads asymmetrically throughout cell migration and dictates cellular polarity through affecting centrosome location and anterior-posterior Ca^{2+} gradient evolution. Despite several earlier published articles detailing a function of syndecan-4 in cell migration by triggering EMT (Toba-Ichihashi et al., 2016) and subsequently fostering the persistence of locomotion (Becsky et al.), in their original article they provide a super-resolved structural view of the actin cytoskeleton of syndecam-4 knock-out cells. In addition, this is the initial record delineating the involvement of syndecan-4 in the deployment of the Ca^{2+} gradient and the placement of the centrosome in a wandering cell.

The polarization of cells is also important in cellular assemblies, as it affects the morphology of tissues and supports repair mechanisms. Specifically, there is a phenomenon known as planar cell polarity (PCP), which is part of the non-canonical Wnt signaling pathway and governs the group polarization of cells at the level of a cell layer. Even though PCP modulates actin cytoskeleton rearrangements through its downstream effector RhoA (Henderson et al., 2018), suggesting a function of the PCP pathway in mechanotransduction processes where mechanical signaling sensing quickly elicits signaling mechanisms that result in cytoskeleton rearrangement and alteration of cell shape or movement, which had not yet been established. Mechanical stress triggers activation of RhoA, which encourages actin stress fiber generation and promotes phosphorylation of myosin light chain 2 through Rho-associated kinase (Sun et al., 2016). Cheong et al. hypothesized that VANGL2 may serve a key purpose in mechanosignaling, which they set out to test in a mouse model (Cheong et al.). The hypothesis is based on a prior investigation that demonstrated a connection between the PCP/WNT5A-Frizzled DVL pathway and YAP (Park et al., 2015). Yap is a well-known mechanotransducer that translates mechanical inputs into biochemical responses through the regulation of gene expression (Jaalouk and Lammerding, 2009). Because YAP and the looptail mouse mutant (Vangl2Lp) deficiency result in similar defects in lung branching (Lin et al., 2017), it seems probable that Vangl2 may act in cellular mechanotransduction. In particular, the Vangl2Lp has the missense mutation S464N in the Vangl2 gene. Vangl2Lp represents a dominant-negative type of mutation affecting not just the trafficking of mutant VANGL2 from the endoplasmic reticulum to the Golgi apparatus, but also blocking the trafficking of wild-type VANGL2 protein to the plasma membrane, causing a complete loss of function (Kibar et al., 2001). Using Vangl2Lp, Cheong et al. therefore investigated whether VANGL2 malfunction alters cellular mechanics and mechanotransduction processes. They established that VANGL2 is necessary for normal alveologenesis and wound healing mediated through its involvement in directional cell migration. They mechanistically demonstrated that disruption of VANGL2 impairs focal adhesion complexes, stress fiber generation, and activation of MLC2, which results in impaired intracellular contractility through the RhoA signal pathway. These abnormalities lead to disturbed generation of traction forces and a lack of the mechanotransducer YAP (Cheong et al.).

In a zebrafish model, Dries et al. explored the collective migration of cells (Dries et al.). Specifically, the zebrafish is a singular model for the analysis of collective cell migration, axonal growth, and route-finding mechanisms. It is recognized that the posterior lateral line system (pLLS) of these aquatic species consists of small clustered mechanosensory organs located longitudinally down the side of the animal, which evolve from proneuromasts (Metcalfe et al., 1985). Dries et al. revealed that the neuronal cell adhesion molecule Ncam1b forms an integral element of the pathways that induce and govern the evolution of pLLS in zebrafish. Specifically, they inferred that morpholino

knockdowns of Ncam1b firstly, decrease cell proliferation inside the primordium, secondly, decrease Fgf target gene Erm expression, thirdly, profoundly impair proneuromast assembly, and fourthly, interfere with primordium migration. Their findings aimed in the following model: Firstly, Ncam1b becomes expressed at the trailing zone of the posterior lateral line primordium. Thereby, it directly interferes with Fgfr1a to trigger the transcription factor Erm expression. Consequently, Erm fosters the proliferation of cells within the trailing zone. However, the proliferation within the leading zone is guided through the Wnt pathway by the transcription factor Lef1. Second, Ncam1b elicits expression of the chemokine receptor Cxcr7b. This could be attributable to direct Fgfr1a signaling on the one hand or to Fgfr1a-dependent inhibition of Wnt signaling on the other hand, which ends up blocking the expression of Cxcr7b. Cxcr7b labels the trailing zone where proneuromasts decelerate to be ultimately segregated. Thirdly, homophilic binding of Ncam1b between adjacent cells effectively steadies the newly established proneuromasts. Ncam1a, on the contrary, is not decisive for the development of pLLS. This argues for a kind of sub-functionalization of the two Ncam1 paralogs in zebrafish, as suspected previously (Langhauser et al., 2012). Finally, Ncam1b acts as a new type of actor in the intricate loopback network that governs pLLS assembly (Dries et al.). Subsequently, it influences several cellular tasks, including primordial cell proliferation, the locomotion of a collective of cells and the abundance of sensory proneuromasts.

Concentrating on the mechanical features of cell migration and invasion and depicting the heterogeneity of extracellular matrices, Mierke's review discusses that there are three different directions of cell motility centered on the mechanical facets (Mierke, 2020). In the first place, the generally deployed invasion assays are discussed where structural and structure-based environmental mechanical stimuli are exploited; in the second place, the mechano-invasion assay is presented where cells are examined to be influenced by mechanical forces to cause migration and invasion; and in the third place, the impact of cell mechanics, comprising cytoskeletal and nuclear mechanics, is mentioned to interfere with motile and invasive cells. Apart from that, what also arises is the interplay between the cytoskeleton of the cell and its constituent compartments, for example, the cell nucleus. Specifically, a ternary approach is outlined to examine the effects of mechanics on cell migration and invasion by incorporating the impacts of the mechano-phenotype of the cytoskeleton, nucleus, and the microenvironment of the cell throughout the spectrum of analysis (Mierke, 2020). The final target still appears to rely on tunable mechanical excitations delivered to 3D matrices with diverse biochemical and embedded cellular assemblies. Future research will also emphasize co-culture efforts in which surrounding cells, such as cancer-associated fibroblasts or macrophages and cancer-associated endothelial cells, can promote or interfere with cancer cell migration and invasion by perhaps modifying the mechano-phenotype of cancer cells, comprising the cytoskeleton as well as the mechano-phenotype of the nucleus and other organelles, or the extracellular matrix's mechano-phenotype.

There is a major commitment of cell motility research toward three-dimensional (3D) cell migration. However, 3D motility has been preferably examined using biomimetic extracellular matrix models. Hayn et al. pointed out that in most of these investigations, *in vitro* collagen scaffolds are presumed to be homogeneous because they are usually composed of a particular type of collagen, e.g., type I collagen that has been isolated from a single species (Hayn et al.). The impact of any local changes in extracellular matrix microstructure on matrix mechanics and migration of cells is poorly understood. Hayn et al. postulate that there are local inhomogeneities that alter cell migration because of changes in matrix mechanics, which are common in *in vivo* tissue scaffolds and have even been implicated in abnormal tissues, such as cancer. To dissect the implications of structural inhomogeneities on cell locomotion, Hayn et al. utilized a blend of rat tail and bovine skin type I collagen, along with pure rat and bovine collagens at various concentrations to evaluate 3D inhomogeneities of the architecture. Actually, the invasiveness of three breast cancer cell types is modified by the type and concentration of the matrix, indicating that these two determinants are decisive for the invasiveness of the cells (Hayn et al.). Their outcomes demonstrated that the local inhomogeneity of the matrix framework is one more critical factor to account for the disparities in cell migration, which is not solely a function of the pore size and the stiffness of the collagen matrices. Consequently, these three different biophysical constraints permit us to accurately define the structure and mechanics of the collagen matrix-based migration model schemes.

The interpeduncular nucleus is a hindbrain structural component consisting of three main areas: the prodromal area (Pro), situated at the isthmus (Ist), and the rostral and caudal interpeduncular domains (IPR, IPC) in rhombomere 1 (r1). Garcia-Guillin et al. investigated the impact of the netrin-1/DCC signaling pathway on these migrations, as it is widely acknowledged to govern distinct processes of neuronal migration across the brain (Garcia-Guillin et al.). Specifically, Garcia-Guillin et al. studied the evolution of the interpeduncular nucleus in wild-type and Deleted in Colorectal Cancer (DCC)−/− mice during late gestational ages. *In situ* hybridizations were primarily performed to pinpoint cells expressing each of the listed genes above, these genes comprise the following transcription factors: Nkx6.1, Otp, Otx2, Pax7, and/or Irx2. Garcia-Guillin et al. discovered that the migration of $Nkx6.1^+$ and $Irx2^+$ cells into the Pro domain suffered severe impairment by the loss of DCC, as during the process of locomotion of $Pax7^+$, $Irx2^+$, and Otp^+ cells that usually dominate the IPR. They also found a slight interference with the migration of the $Pax7^+$ and $Otx2^+$ cells that build the IPC. Subsequently, they concluded that their findings are not only relevant for developing knowledge of this structure, but also provide a foundation for exploring the potential neuroembryological etiology of brain dysfunctions associated with the habenulo-interpeduncular system.

In their methods article, Cuenca et al. presented a single-cell movement in a modular scaffold that can be employed to model the collective response of glioblastoma cells, the most common and virulent primary brain cancer (Cuenca et al., 2020). Cuenca et al. utilized the human primary glioblastoma cell line U87, that can be cultured as monolayers or tightly spatially grouped and

arranged in 3D structures, for example spheroids. Their inclusive model takes into account the main mechanisms implicated in cell migration: chemotaxis of attractants, mechanical perceptual exchanges, and incidental movement. Moreover, their simulations matched and replicated the evolving behavior of the spheroids in a series of migration tests that monitored the trajectories of single cells. From both physiological, e.g., the generation of organs, tissue regeneration, and others, and pathological viewpoints, it is necessary to provide a multifaceted tool that can predict the individual and collective behavior of U87 cells (Cuenca et al., 2020), but it can also anticipated to be adaptable to a variety of settings, e.g., different cell types and culture conditions.

Zhou et al. endeavor to investigate diversely expressed long noncoding RNAs (lncRNAs) and mRNAs involved in atherosclerosis (Zhou et al., 2021). They then evidenced the expression of lncRNAs employing quantitative real-time polymerase chain reaction and coexpressed targeting genes in established proliferation and migration model systems of human coronary artery smooth muscle cells (HCASMCs). Specifically, oxidized low-density lipoprotein (ox-LDL) has been added to the culture medium of HCASMCs in order to trigger their proliferation and migration. 68 lncRNAs and 222 mRNAs have been identified that are differentially expressed in atherosclerosis and act as candidates that play critical roles in atherosclerosis (Zhou et al., 2021). Database analysis revealed that the Fanconi anemia signaling pathway could potentially be implicated in atherosclerosis. A sum of six coexpressed mRNAs have been found to be grossly upregulated in HCASMCs. Zhou et al. hypothesized that the variously expressed lncRNAs detected through RNA sequencing and confirmed in smooth muscle cells could serve as a regulatory therapeutic target for HCASMC proliferation and migration in atherosclerosis, thereby representing a new diagnostic ground and a therapeutic objective for the cardiovascular disease setting. Finally, their work appears to offer a new perspective on ox-LDL-induced HCASMC dysfunction in atherosclerosis and potentially proposes a promising coronary artery disease therapeutic strategy, encompassing a new diagnostic rationale and therapeutic objective.

Activin A belongs to the transforming growth factor-beta (TGF-β) superfamily and operates in the process of tissue healing and fibrosis. The cytokine signaling transduction cascades are governed by activin A supporting the inflammatory reaction (Jones et al., 2007). Moreover, activin A controls the activation of M2 macrophage to interfere with the wound healing process after tissue injury and fibrosis during the late inflammatory stage (Morianos et al., 2019). Jiang et al. examined the effect of activin A on adhesion and migration employing the human L929 fibroblast cell line. They found that activin A promotes fibroblast migration using transwell chambers and microfluidics (Jiang et al.). In addition, activin A causes the expression of α-SMA and liberates TGF-β1, factors intimately associated with tissue fibrosis. Activin A increased calcium content in L929 cells and p-ERK protein activity. As a consequence, their outcome data implied that activin A, as a new kind of chemokine, triggers chemotactic migration of L929 cells using ERK signaling and subsequently contributes to fibrosis (Jiang et al.).

The dynamic actin cytoskeleton governs the process of cell locomotion in a spatial and temporal manner (Tang and Gerlach, 2017). Cell migration is preceded by the establishment of actin-based plasma membrane protuberances at the front line of migrating cells (Lauffenburger and Horwitz, 1996). There, a dynamic conversion of the branched actin filament reticulum into lamellipodia takes place, which is accompanied by multiple actin regulators, such as actin-related protein 2/3 (Arp2/3), and filamins, including filamin A (Skau and Waterman, 2015). Liu et al. examined the regulation of filamin A stability (Liu et al., 2021). In the filamentous fungus Aspergillus nidulans, the developmentally conserved nuclear distribution gene C (NudC) has been revealed to be an upstream element of NudF, a key dynein regulator that affects nuclear locomotion (Jheng et al., 2018). It is possible to propose that NudC could improve the folding of its candidate proteins through its proprietary chaperone activity or its function as an Hsp90 cochaperone through volatile modification of Hsp90 ATPase activity (Dean and Johnson, 2021). Liu et al. further identified that NudC-L279P, a conserved mutation of human NudC to Leu146, resulting in reduced NudF in Aspergillus, compromises NudC function and affects Hsp90 chaperone activity (Zhu et al., 2010). Overexpression of NudC-L279P reduces LIS1, a major effector of cell migration, on a Hsp90-driven basis (Zhu et al., 2010). Nevertheless, the undergirding mechanism of NudC in modulating mammalian cell migration remarkably stays obscure. Liu et al. have demonstrated that NudC can stabilize filamin A due to their interplay. NudC L279P overexpression disturbs filamin A and inhibits cell locomotion. In summary, ectopic expression of Hsp90 reverts filamin A fragility and phenotype aberrations conferred upon by overexpression of NudC-L279P. Therefore, Liu et al. propose that the NudC-L279P mutation works to destabilize filamin A via inhibiting the Hsp90-facilitated chaperoning route, which is a yet to be delineated mechanism that is pivotal in governing filamin A stability.

All articles show the complexity of different cell adhesion and migration research approaches, whereby vastly different model systems have been employed to reveal the biochemical and mechanical characteristics of cells, spheroids, tissues and entire organisms. There are still many more interesting facts to explore, such as whether there is a unique mechanical phenotype of cells, tissues and their microenvironment independent of the model organism that fosters the motility of cells or collections of cells. The broad variety of techniques and methods employed in the different investigations indicates that this is highly needed to generate a comprehensive view on cell adhesion and migration.

AUTHOR CONTRIBUTIONS

CM designed, discussed and wrote the Editorial herself. She was a topic editor of the Research Topic: Editor's Pick 2021: Highlights in Cell Adhesion and Migration.

REFERENCES

Chrzanowska-Wodnicka, M., White, G. C., Quilliam, L. A., and Whitehead, K. J. (2015). Small GTPase Rap1 Is Essential for Mouse Development and Formation of Functional Vasculature. *PLoS ONE* 10, e0145689. doi:10.1371/journal.pone.0145689

Dean, M. E., and Johnson, J. L. (2021). Human Hsp90 Cochaperones: Perspectives on Tissue-specific Expression and Identification of Cochaperones with Similar *In Vivo* Functions. *Cell Stress and Chaperones* 26, 3–13. doi:10.1007/s12192-020-01167-0

Henderson, D. J., Long, D. A., and Dean, C. H. (2018). Planar Cell Polarity in Organ Formation. *Curr. Opin. Cel Biol.* 55, 96–103. doi:10.1016/j.ceb.2018.06.011

Jaalouk, D. E., and Lammerding, J. (2009). Mechanotransduction Gone Awry. *Nat. Rev. Mol. Cel Biol* 10, 63–73. doi:10.1038/nrm2597

Jheng, G.-W., Hur, S. S., Chang, C.-M., Wu, C.-C., Cheng, J.-S., Lee, H.-H., et al. (2018). Lis1 Dysfunction Leads to Traction Force Reduction and Cytoskeletal Disorganization during Cell Migration. *Biochem. Biophysical Res. Commun.* 497, 869–875. doi:10.1016/j.bbrc.2018.02.151

Jones, K. L., Mansell, A., Patella, S., Scott, B. J., Hedger, M. P., de Kretser, D. M., et al. (2007). Activin A Is a Critical Component of the Inflammatory Response, and its Binding Protein, Follistatin, Reduces Mortality in Endotoxemia. *Proc. Natl. Acad. Sci.* 104, 16239–16244. doi:10.1073/pnas.0705971104

Keller-Pinter, A., Bottka, S., Timar, J., Kulka, J., Katona, R., Dux, L., et al. (2010). Syndecan-4 Promotes Cytokinesis in a Phosphorylation-dependent Manner. *Cell. Mol. Life Sci.* 67, 1881–1894. doi:10.1007/s00018-010-0298-6

Kibar, Z., Vogan, K. J., Groulx, N., Justice, M. J., Underhill, D. A., and Gros, P. (2001). Ltap, a Mammalian Homolog of Drosophila Strabismus/Van Gogh, Is Altered in the Mouse Neural Tube Mutant Loop-Tail. *Nat. Genet.* 28, 251–255. doi:10.1038/90081

Langhauser, M., Ustinova, J., Rivera-Milla, E., Ivannikov, D., Seidl, C., Slomka, C., et al. (2012). Ncam1a and Ncam1b: Two Carriers of Polysialic Acid with Different Functions in the Developing Zebrafish Nervous System. *Glycobiology* 22, 196–209. doi:10.1093/glycob/cwr129

Lauffenburger, D. A., and Horwitz, A. F. (1996). Cell Migration: A Physically Integrated Molecular Process. *Cell* 84, 359–369. doi:10.1016/S0092-8674(00)81280-5

Lin, C., Yao, E., Zhang, K., Jiang, X., Croll, S., Thompson-Peer, K., et al. (2017). YAP Is Essential for Mechanical Force Production and Epithelial Cell Proliferation during Lung Branching Morphogenesis. *eLife* 6, e21130. doi:10.7554/eLife.21130

Lock, J. G., Jones, M. C., Askari, J. A., Gong, X., Oddone, A., Olofsson, H., et al. (2018). Reticular Adhesions Are a Distinct Class of Cell-Matrix Adhesions that Mediate Attachment during Mitosis. *Nat. Cel Biol* 20, 1290–1302. doi:10.1038/s41556-018-0220-2

Ma, L., Li, Y., Peng, J., Wu, D., Zhao, X., Cui, Y., et al. (2015). Discovery of the Migrasome, an Organelle Mediating Release of Cytoplasmic Contents during Cell Migration. *Cell Res* 25, 24–38. doi:10.1038/cr.2014.135

Metcalfe, W. K., Kimmel, C. B., and Schabtach, E. (1985). Anatomy of the Posterior Lateral Line System in Young Larvae of the Zebrafish. *J. Comp. Neurol.* 233, 377–389. doi:10.1002/cne.902330307

Morianos, I., Papadopoulou, G., Semitekolou, M., and Xanthou, G. (2019). Activin-A in the Regulation of Immunity in Health and Disease. *J. Autoimmun.* 104, 102314. doi:10.1016/j.jaut.2019.102314

Park, H. W., Kim, Y. C., Yu, B., Moroishi, T., Mo, J.-S., Plouffe, S. W., et al. (2015). Alternative Wnt Signaling Activates YAP/TAZ. *Cell* 162, 780–794. doi:10.1016/j.cell.2015.07.013

Skau, C. T., and Waterman, C. M. (2015). Specification of Architecture and Function of Actin Structures by Actin Nucleation Factors. *Annu. Rev. Biophys.* 44, 285–310. doi:10.1146/annurev-biophys-060414-034308

Stojanović, N., Dekanić, A., Paradžik, M., Majhen, D., Ferenčak, K., Ruščić, J., et al. (2018). Differential Effects of Integrin αv Knockdown and Cilengitide on Sensitization of Triple-Negative Breast Cancer and Melanoma Cells to Microtubule Poisons. *Mol. Pharmacol.* 94, 1334–1351. doi:10.1124/mol.118.113027

Sun, Z., Guo, S. S., and Fässler, R. (2016). Integrin-mediated Mechanotransduction. *J. Cel Biol.* 215, 445–456. doi:10.1083/jcb.201609037

Tang, D. D., and Gerlach, B. D. (2017). The Roles and Regulation of the Actin Cytoskeleton, Intermediate Filaments and Microtubules in Smooth Muscle Cell Migration. *Respir. Res.* 18, 54. doi:10.1186/s12931-017-0544-7

Toba-Ichihashi, Y., Yamaoka, T., Ohmori, T., and Ohba, M. (2016). Up-regulation of Syndecan-4 Contributes to TGF-B1-Induced Epithelial to Mesenchymal Transition in Lung Adenocarcinoma A549 Cells. *Biochem. Biophys. Rep.* 5, 1–7. doi:10.1016/j.bbrep.2015.11.021

Vicente-Manzanares, M., Webb, D. J., and Horwitz, A. R. (2005). Cell Migration at a Glance. *J. Cel Sci.* 118, 4917–4919. doi:10.1242/jcs.02662

Zhu, X J., Liu, X. Y., Jin, Q., Cai, Y. Q., Yang, Y. H., and Zhou, T. H. (2010). The L279P Mutation of Nuclear Distribution Gene C (n.d.) Influences Its Chaperone Activity and Lissencephaly Protein 1 (LIS1) Stability. *J. Biol. Chem.* 285, 29903–29910. doi:10.1074/jbc.m110.105494

Conflict of Interest: The author declares that the research was conducted in the absence of any commercial or financial relationships that could be construed as a potential conflict of interest.

Publisher's Note: All claims expressed in this article are solely those of the authors and do not necessarily represent those of their affiliated organizations, or those of the publisher, the editors and the reviewers. Any product that may be evaluated in this article, or claim that may be made by its manufacturer, is not guaranteed or endorsed by the publisher.

frontiers in Cell and Developmental Biology

ORIGINAL RESEARCH
published: 25 February 2020
doi: 10.3389/fcell.2020.00112

The Impact of Diabetic Conditions and AGE/RAGE Signaling on Cardiac Fibroblast Migration

Stephanie D. Burr, Mallory B. Harmon and James A. Stewart Jr.*

Department of BioMolecular Sciences, School of Pharmacy, The University of Mississippi, Oxford, MS, United States

Diabetic individuals have an increased risk for developing cardiovascular disease due to stiffening of the left ventricle (LV), which is thought to occur, in part, by increased AGE/RAGE signaling inducing fibroblast differentiation. Advanced glycated end-products (AGEs) accumulate within the body over time, and under hyperglycemic conditions, the formation and accumulation of AGEs is accelerated. AGEs exert their effect by binding to their receptor (RAGE) and can induce myofibroblast differentiation, leading to increased cell migration. Previous studies have focused on fibroblast migration during wound healing, in which diabetics have impaired fibroblast migration compared to healthy individuals. However, the impact of diabetic conditions as well as AGE/RAGE signaling has not been extensively studied in cardiac fibroblasts. Therefore, the goal of this study was to determine how the AGE/RAGE signaling pathway impacts cell migration in non-diabetic and diabetic cardiac fibroblasts. Cardiac fibroblasts were isolated from non-diabetic and diabetic mice with and without functional RAGE and used to perform a migration assay. Cardiac fibroblasts were plated on plastic, non-diabetic, or diabetic collagen, and when confluency was reached, a line of migration was generated by scratching the plate and followed by treatment with pharmacological agents that modify AGE/RAGE signaling. Modification of the AGE/RAGE signaling cascade was done with ERK1/2 and PKC-ζ inhibitors as well as treatment with exogenous AGEs. Diabetic fibroblasts displayed an increase in migration compared to non-diabetic fibroblasts whereas inhibiting the AGE/RAGE signaling pathway resulted in a significant increase in migration. The results indicate that the AGE/RAGE signaling cascade causes a decrease in cardiac fibroblast migration and altering the pathway will produce alterations in cardiac fibroblast migration.

Keywords: AGE/RAGE signaling, cardiac fibroblasts, fibroblast migration, diabetes, Rap1a

OPEN ACCESS

Edited by:
Claudia Tanja Mierke,
Leipzig University, Germany

Reviewed by:
Elia Ranzato,
University of Eastern Piedmont, Italy
Judyta Juranek,
New York University, United States

****Correspondence:***
Stephanie D. Burr
sburr@go.olemiss.edu

Specialty section:
This article was submitted to Cell Adhesion and Migration, a section of the journal Frontiers in Cell and Developmental Biology

Received: *10 December 2019*
Accepted: *10 February 2020*
Published: *25 February 2020*

Citation:
Burr SD, Harmon MB and Stewart JA Jr (2020) The Impact of Diabetic Conditions and AGE/RAGE Signaling on Cardiac Fibroblast Migration. Front. Cell Dev. Biol. 8:112. doi: 10.3389/fcell.2020.00112

INTRODUCTION

Individuals with diabetes mellitus, both type I and type II, are at an increased risk of developing complications as a result of hyperglycemia, such as cardiovascular disease (American Diabetes Association, 2018). A common form of cardiovascular disease associated with diabetics is left ventricle (LV) hypertrophy, which contributes to poor heart function (Fowlkes et al., 2013; Shang et al., 2018). Studies have indicated that myocardial remodeling and fibrosis could be a possible mechanism leading to LV hypertrophy due to cardiac cell-mediated remodeling of the extracellular

matrix (ECM) composition (Shang et al., 2018). Fibrosis is a common complication of diabetes, and cardiac tissues from type II diabetics, with no other disease risk factors, have an increased amount of interstitial ECM accumulation (Fowlkes et al., 2013). The increase in fibrosis can be attributed to an increasing number of fibroblasts differentiating into myofibroblasts (Fowlkes et al., 2013).

Cardiac fibroblasts orchestrate the maintenance, synthesis, and degradation of the ECM and can be influenced by both extracellular and intracellular signaling (Lerman et al., 2003; Hutchinson et al., 2013). Among the mechanisms shown to induce myofibroblast transition are matrix metalloproteases (MMPs) and tissue inhibitors of matrix metalloprotease (TIMPS), which collectively can modify the ECM in response to extracellular stimuli (Yabluchanskiy et al., 2013; Caley et al., 2015). These signaling cues can activate neighboring fibroblast cells to differentiate into myofibroblasts to migrate and actively remodel the ECM by increasing matrix protein synthesis and secretion production resulting in fibrosis (Lerman et al., 2003; Darby et al., 2014). In addition, it has been shown that a greater number of myofibroblasts can be detected, via increased levels of α-smooth muscle action (α-SMA), increased cell migration, and increased ECM production, in the heart of diabetic individuals (Shamhart et al., 2014). While we know external circumstances and extracellular signaling can induce myofibroblast differentiation, the mechanism by which these events are triggered is still unclear. One possible mechanism triggering myofibroblast transition could be the AGE/RAGE signaling cascade.

Advanced glycated end-products (AGEs) are formed through a non-enzymatic reaction in which sugar molecules and proteins are combined (Hegab et al., 2012). Accumulation of AGEs occurs naturally in the body and are usually present to a lesser degree in healthy individuals (Simm et al., 2007). AGE accumulation occurs at a higher rate and are more abundant in individuals suffering from elevated glucose levels, such as seen in diabetics (Hegab et al., 2012). The accumulation of AGEs can lead to an increase in crosslinking of matrix proteins, such as collagen, to contribute to the rigidity of the ECM (Ramasamy et al., 2011). In addition, AGEs can elicit an intracellular signaling cascade by activating their receptor (RAGE; receptor for AGEs) (Bierhaus et al., 2005). When activated, the AGE/RAGE cascade stimulates growth factor secretion and increased collagen production along with upregulation of RAGE expression on the cellular membrane (Suchal et al., 2017). A loss of cellular elasticity due in activation of AGE/RAGE signaling affects the physiological function of many tissues and organs. For example, studies have shown that AGE/RAGE signaling can produce endothelial dysfunction by impacting vasodilation in coronary arterioles in type II diabetic mice (Gao et al., 2008). When activated, the AGE/RAGE cascade subsequently stimulates the cardiac fibroblast to myofibroblast transition resulting in increased ECM production or fibrosis leading to the development of cardiovascular disease such as LV stiffness commonly observed in diabetic patients (Suchal et al., 2017). An additional protein thought to impact AGE/RAGE signaling is Rap1a, a small GTPase, which may contribute to activation of cardiac fibroblasts.

The repressor/activator protein 1a (Rap1a) homolog is associated with different organ systems and multiple signaling pathways. Focusing on the cardiovascular system, Rap1a is involved in the development and functionality of the heart (Dong et al., 2012). Rap1a is a member of the Ras superfamily which is composed of small GTPases (Dong et al., 2012). Due to its ability to act as a molecular switch, Rap1a is able to act as a connector to transmit extracellular signaling to intracellular signals (Yan et al., 2008). Rap1a is able to bind and activate an assortment of proteins including cardiovascular effector proteins (Roberts et al., 2013). These effector proteins can regulate mechanisms like cell proliferation, cell adhesion, and cell migration within the cardiovascular tissue (Jeyaraj et al., 2011). Under hyperglycemic conditions, Rap1a has been shown to activate downstream signaling pathways, such as extracellular signal-regulated kinase 1/2 (ERK1/2) (Asif et al., 2002; Yan et al., 2008). Activation of ERK1/2 pathway stimulates ECM fibrosis, which contributes to cardiovascular disorders (Asif et al., 2002). Based off initial studies, Rap1a appears to intersect the AGE/RAGE cascade to promote activation of cardiac fibroblasts, leading to ECM remodeling and consequently fibrosis within the heart.

Migration of cells is an integral part in the structure and function of body systems. Stimuli such as cytokines and growth factors have been shown to induce cardiac fibroblast differentiation into myofibroblasts, which is characterized by increased motility (Li et al., 2004; Velnar et al., 2009; Fowlkes et al., 2013). Currently, there are conflicting research regarding diabetic fibroblast migration. Previous studies have demonstrated an impaired migration in diabetic dermal fibroblasts; however, other studies have reported that hyperglycemic conditions increased rat cardiac fibroblast migration (Chen et al., 1996; Lerman et al., 2003; Straino et al., 2008; Velnar et al., 2009). This project aims to fill in the gaps in knowledge regarding cardiac fibroblast migration in diabetics. More specially, our laboratory aims to examine the effects of the AGE/RAGE signaling cascade on cardiac fibroblast migration in diabetes. Therefore, we hypothesized activation of the RAGE cascade alters cardiac fibroblast migration in type II diabetic mice. Using genotypically different cardiac fibroblasts on collagen matrices from diabetic and non-diabetic mice, we were able to observe changes in cell mobility to determine a mechanistic role for RAGE signaling and Rap1a in diabetes-induced fibroblast migration. The results of this study determined that diabetic fibroblasts exhibited a higher degree of migration compared to non-diabetic fibroblasts. Examination of AGE/RAGE signaling on cardiac fibroblast migration determined that AGE/RAGE signaling lowered the amount of fibroblast migration. Overall, this reduction in migration can be alleviated with prevention or reduction of AGE/RAGE signaling.

MATERIALS AND METHODS

Animal Models

Male *Lepr^{db}* (db/db model, referred to as diabetic*)* type II diabetes mellitus mice (BKS.Cg-*Dock7^{m}*+/+ *Lepr^{db}*/J, Jackson Labs) were

used for this study. The db/db mouse model has a point mutation in the leptin receptor leading to a nonfunctional leptin receptor. This mutation results in obesity and insulin resistance leading to the development of hyperglycemia by 8 weeks of age and overt diabetes by 12 weeks of age. Heterozygous mice (non-diabetic) were used as lean controls.

Male RAGE knockout mice (RAGE RKO) were used for this study. A Tie2 Cre mouse line was generated by flanking the extracellular domain of the receptor with two *loxP* sites in the same orientation. Additionally, a reversely oriented transcriptional EGFP reporter gene was inserted into intron 1, and a neomycin cassette and a thymidine kinase promoter were inserted into intron 7. EGFP PCR genotyping reactions are performed as a positive control for RAGE knockout mice (Constien et al., 2001; Liliensiek et al., 2004; Brodeur et al., 2014). After exposure to Cre recombinase (*Cre*), the *loxP* flanked sequences were deleted, resulting in the global loss of RAGE mRNA expression and loss of RAGE signaling. RAGE knockout mice were crossbred with heterozygous (non-diabetic) mice to generate RAGE knockout diabetic (diabetic RKO) and non-diabetic (non-diabetic RKO) mice (Constien et al., 2001; Liliensiek et al., 2004). Breeder mice were a generous gift from Dr. Pamela Lucchesi and Dr. Angelika Bierhaus.

Male Rap1a knockout mice (Rap1a KO) and wild-type (Rap1a WT) were used for this study. This mouse model was generated by inserting a neomycin resistant gene downstream of exon 4 of RAP1A in the opposite (3′–5′) orientation. A targeting vector (a 0.95 kb *PvuII-NdeI* fragment) was used to insert the resistance gene in order to disrupt Rap1a mRNA expression (Li et al., 2007). Breeder mice were a generous gift from Dr. Maqsood Chotani and Dr. Lawerence Quilliam.

Animal Care

All experiments were performed using adult male mice at 16 weeks of age. The mice were housed under standard environmental conditions and maintained on commercial mouse chow and tap water *ad libitum*. All studies conformed with the principles of the National Institutes of Health "Guide for the Care and Use of Laboratory Animals," (NIH publication No. 85-12, revised 1996), and the protocol was approved by the University of Mississippi Institutional Animal Care and Use Committee (protocol #17-024). Anesthesia for euthanasia at the experimental endpoint was caused by carbon dioxide inhalation followed by cervical dislocation, which served as a second mechanism for euthanasia. At this time, the chest was opened, and the heart was quickly excised for further cellular, histological, and biochemical experiments.

Fibroblast Isolation and Cell Culture

Mice were weighed and non-fasting blood glucose levels were measured via tail cut (**Table 1**: glucometer; OneTouch Ultra®, LifeScan, Inc., Johnson & Johnson). Hearts were then removed from the chest cavity, the atria dissected away, and ventricles weighed (**Table 1**). Three hearts of each genotype were used for a single fibroblast isolation. In a sterile, cell culture hood, the hearts were cut into ∼5 mm small pieces and placed a

TABLE 1 | Physiological measurements of mice.

	Body weight (g)	Blood glucose (mg/dL)	Heart weight (g)
Non-diabetic (n = 47)	29.05 ± 0.37	204.7 ± 7.30	0.1173 ± 0.005
Diabetic (n = 28)	51.09 ± 1.26****	525.0 ± 22.67****	0.1106 ± 0.002
Non-diabetic RKO (n = 41)	32.32 ± 0.43***	213.3 ± 4.58	0.1184 ± 0.002
Diabetic RKO (n = 12)	56.61 ± 0.70****	412.7 ± 29.44****	0.1216 ± 0.002
Rap1a WT (n = 34)	27.72 ± 0.35	217.2 ± 6.32	0.1106 ± 0.002
Rap1a KO (n = 16)	27.61 ± 0.74	172.1 ± 6.73	0.1085 ± 0.005

*Data represents average values from mice used for cardiac fibroblast isolation with an average of three hearts per isolation. A one-way ANOVA was conducted followed by a Tukey's post hoc test to determine significant difference between non-diabetic mice and the other genotype groups (***$p < 0.001$, ****$p < 0.0001$).*

10 mL of collagenase-trypsin enzymatic solution (0.1% Trypsin, Gibco; 100 U/mL collagenase II, Worthington Biochemical). Fibroblasts were continually mixed in the tissue-enzymatic mixture using water-jacketed spinner flasks maintained at 37°C until hearts were broken down into a single cell suspension. The single cell suspension was centrifuged (250 x *g* at room temperature for 10 min) and resuspended in high glucose Dulbecco's Modified Eagles Medium (DMEM) [high glucose media; DMEM containing 4.5 g/L glucose, sodium pyruvate, L-glutamine, and supplemented with 14.2 mM $NaHCO_3$, 14.9 mM HEPES, 30% heat-inactivated fetal bovine serum (FBS), 1% L-glutamine, and 0.02% Primocin (Thermo Fisher)] for 24 h in an incubator buffered with 5% CO_2 kept at 37°C. After 24 h, the cardiac fibroblasts were washed with their appropriate media three times and then incubated at 37°C in their appropriate media [non-diabetic and Rap1a fibroblasts: low glucose (1 g glucose/L) and diabetic fibroblasts (these are fibroblasts removed from diabetic mouse hearts): high glucose (4.5 g glucose/L)]. All experiments were performed using cells at P1, in order to ensure the cell *in vivo* phenotype was maintained. Cells were passaged just prior to reaching 95% confluency using a 0.25% trypsin and 0.1% ethylenediaminetetraacetic acid (trypsin/EDTA) solution (Life Technology). Both cell culture and migration plates were kept in a CO_2 incubator at 37°C.

Collagen Extraction

Tails from non-diabetic and diabetic mice were collected and stored at −20°C. After roughly 20 tails had been collected, the four major tail tendons were removed, minced, washed in dH_2O, and placed in 150 mL acetic acid (1:1000 dilution in dH_2O). The tendons were continually mixed for 3 days at 4°C (Rajan et al., 2007). All steps, hereinafter, were conducted in sterile conditions in a cell culture hood. After 3 days, the tendon-acetic acid solution was centrifuged at 3000 x *g* for 30 min at 4°C. The supernatant, containing the collagen, was removed to a new container and centrifuged again under the same conditions. The collagen solution was stored at 4°C, and concentration was estimated using Sircol™ Soluble Collagen Assay Kit (BioColor Ltd.) as per manufacturer's directions.

Western Blot Analysis

Protein was isolated from cells cultured in 60 mm dish using modified Hunter's buffer [MHB; 1% Triton X-100, 75 mM NaCl, 5 mM tris pH 7.4, 0.5 mM orthovanadate, 0.5 mM ECTA, 0.5 mM EGTA, 0.25% NP-40, and freshly added Halt Protease Inhibitor Cocktail (100×; Thermo Fisher)]. Plates were incubated on ice with MHB for 10 min then a cell scrapper was used to dislodge cells from plate. Cell lysate was removed and placed into 1.5 mL tube followed by probe-sonication. Samples were centrifuged for 15 min at 32,000 x *g* at 4°C and supernatant was removed and stored at −80°C. Protein concentration was determined using a bicinchoninic acid assay (BCA; Pierce Biotechnology) according to manufacturer's instructions. Twelve micrograms of protein was used per sample for western blot analysis. Antibodies used were as follow: monoclonal α-smooth muscle actin [α-SMA (1:400); Sigma Aldrich 2547], RAGE [(1:400) Santa Cruz sc-365154], and β-tubulin [(1:400) Santa Cruz sc-398937] were used as a loading control. Western blots were visualized using an iBRIGHT imaging system.

Migration Assay

Migration assay plates consisted of a 48-well culture plate with a line and hash marks drawn on the bottom of each well for image orientation. Before plating cells, 50 μL non-diabetic and diabetic collagen were added to wells and incubated for 1 h at 37°C (Lerman et al., 2003). Excess collagen was removed with 1× sterile PBS wash. Next, fibroblasts at P1 were plated and grown to 95% confluency. The experimental design for assessing migration used two replicates per treatment. Once reaching confluency, the media was suctioned off and each well was scratched with the tip of a 200 μL pipet tip along the previously marked line through the center of each well on the bottom of the plate (Xuan et al., 2014). After scratching, the plates were rinsed with the appropriate media containing 1.5% FBS. Initial experiments conducted indicated a concentration of 1.5% FBS promoted cell migration and at the same time prevent cell division. 500 μL of the appropriate 1.5% FBS media was added to each well. At this time, AGE-BSA (glycated albumin 0.5 mg/mL), U0126 (5 μm; inhibitor of ERK), and PKC-ζ pseudosubstrate (1 μg/mL; ps-PKC-ζ) were added. U0126 and PKC-ζ pseudosubstrate were selected as inhibitors for the AGE/RAGE cascade due to previous studies indicating these proteins are involved in the AGE/RAGE cascade (Wu et al., 2003; Adamopoulos et al., 2016; Evankovich et al., 2017). The cells were allowed to incubate for 24°h after scratching. Images of cells were taken at 0 and 24°h post scratching.

Immunohistology

Morphological evaluation of collagen content was performed on hearts from age-matched Rap1a WT and KO mice as previously described (Stewart et al., 2003). Briefly, hearts were fixed in histology grade 4% paraformaldehyde and embedded in paraffin blocks. Blocks were sectioned at 5-μm thickness from the equator of the heart and stained with Picric Acid Sirius Red F3BA. Estimates of the fractions of thick and thin collagen fibrils were obtained by using polarized light. Due to the birefringent quality of the stain, collagen refracted a distinct color based upon the size of the collagen fibrils: red and yellow (thick filaments) and green (thin filaments). Quantitative analysis is accomplished by light microscopy with a video-based image-analyzer system. Color thresholds were set for biphasic analysis to capture and generate a percent collagen content per 40× field within the specified RGB wavelength ranges separate from the background: Phase 1 represents collagen capture Red (0–40) Green (0–80) Blue (0–255) and Phase 2 represents background capture: Red (20–255) Green (40–255) Blue (35–255). Results are presented as the mean ± SEM values computed from the average of n = 25–35 individual measurements obtained from each heart. Cardiac vasculature, epicardium, and endocardium were avoided due to high levels of collagen content and do not accurately reflect myocardial interstitial collagen.

Non-diabetic and diabetic collagen were fixed with histology grade 4% paraformaldehyde for 10 min at room temperature. Collagen was then incubated with blocking solution (3% donkey serum, 2% BSA, and 0.01% Triton X-100 in 1× PBS) overnight at 4°C. After 24 h, primary antibody was added and incubated overnight at 4°C. AGE antibody (1:50; Abcam) and carboxymethyl lysine (CML) antibody (1:50; Abcam) were added to collagen. Slides were mounted using Vectashield hard set mounting media.

Cell Migration Imaging and Analysis

At the 0 h time point, pictures were taken to document the position of cells prior to migration using a Zeiss Primovert microscope with camera (Zen Blue 2.3 edition, Zeiss). Hashmarks along the scratch line were used to align the plate to determine areas of interest for imaging as well as were used to prevent imaging of overlapping regions. At the 24 h time point, the plate was removed from the incubator and fixed with 4% paraformaldehyde fixative for 10 min at room temperature. After 10 min, the fixative was removed, and the cells were washed with 1× PBS. Next, cells were incubated in 1× PBS with 0.1% Trition-100 for 30 min at room temperature with continuous rocking motion to permeabilize the fixed cells. Cells were stained with 1% Brilliant Blue Coomassie stain (3% Coomassie Brilliant Blue, 10% acetic acid, 45% methanol, and 45% dH_2O) for 10 min at room temperature with continual rocking. Finally, 24 h post-scratched pictures of the cells were taken using the 0 h time point images as templates for the correct position of the areas of interest.

Adobe Photoshop Elements 2018 was used to draw lines on 0 h images to denote the scratched area. The scratched areas were determined by denoting the linear area that lacked fibroblasts. Areas that lacked fibroblasts, but where not in line with the orientation of the scratch, were not included in the calculation as these areas may contain cells which detached from the culture dish for reasons other than the physical scratch. The 0 h image was superimposed on the 24 h image in order to indicate the scratch area (i.e. line of migration) on the 24 h image. Next, the number of cells that had migrated across the lines drawn were counted and recorded for each well. The area of the scratch was calculated using Image J, and the number of migrated cells was normalized to calculated area of the scratch by dividing the number of migrated cells by the area. This process was

completed twice for two separate images which together showed approximately the total cell migration of one well.

Statistical Analysis

Differences in non-diabetic and diabetic, non-diabetic RKO and diabetic RKO, and Rap1a WT and Rap1a KO migration on different collagens were determined by performing a Student's *t*-test. Differences associated with inhibition of RAGE signaling were assessed by one-way analysis of variance (ANOVA). After one-way ANOVA analysis, a Dunnett's *post hoc* test was conducted in order to determine differences between control and treatment groups. Comparisons between genotypes and AGE-treated fibroblasts were determined by performing two-way ANOVA. A Sidak's *post hoc* test was conducted in order to assess differences between different genotypes on the same type of collagen as well as differences between the control and AGE-treated fibroblasts of the same genotype. GraphPad Prism 8 was used for all statistical analysis. Significance was defined as $p < 0.05$. Error bars represent ±standard error of the mean (SEM).

RESULTS

The Presence of RAGE Signaling Negatively Impacts Cardiac Fibroblast Migration

Isolated cardiac fibroblasts were used to assess the impact of RAGE signaling on cell migration (**Figure 1**). Prevention of RAGE signaling by genetically altering RAGE to a non-functioning receptor (RAGE knockout, RKO) resulted in increased non-diabetic RKO fibroblast (3.31 #migrated cells/% area) migration over that of non-diabetic fibroblasts (1.66 #migrated cells/% area) (**Figures 1A,B**; Student's *t*-test $p = 0.0076$). Diabetic RKO fibroblasts (7.04 #migrated cells/% area) migrated significantly more than diabetic fibroblasts (3.19 #migrated cells/% area) (**Figures 1C,D**; Student's *t*-test $p = 0.0002$). Diabetic fibroblasts, regardless of the presence or absence of RAGE, migrated significantly more than non-diabetic fibroblasts with percent differences ranging from 63% between non-diabetic and diabetic to 73% for RKO non-diabetic versus RKO diabetic fibroblasts. Further studies were then performed to determine the role of Rap1a in AGE/RAGE signaling and fibroblast migration.

Knockout of Rap1a Results in Decreased Collagen Expression in the Heart as Well as Reduced Protein Expression of Specific AGE/RAGE Markers

Previous studies by our laboratory have revealed that silencing Rap1a in diabetic cells altered RAGE protein expression (Zhao et al., 2014). By manipulating Rap1a, we could amplify or reduce the RAGE signaling pathway to modify signaling outcomes, accordingly. We further examined total collagen expression, an outcome of the AGE/RAGE cascade, in hearts from Rap1a wild-type (Rap1a WT) and Rap1a knockout (Rap1a KO) mice (**Figures 2A–C**). Rap1a KO hearts had significantly less total collagen compared to Rap1a WT hearts (**Figure 2C**, Student's *t*-test $p = 0.0103$). Further examination of AGE/RAGE signaling outcomes in cardiac fibroblasts isolated from Rap1a WT and KO hearts indicated a decrease in α-SMA and RAGE protein expression, indicative of reduced AGE/RAGE signaling (**Figure 2D**). Due to Rap1a impact on AGE/RAGE signaling outcomes *in vivo* and *in vitro*, we examined the impact of Rap1a on cardiac fibroblast migration.

To further investigate this idea, cardiac fibroblasts from Rap1a KO and Rap1a WT mice were used to determine if changes in Rap1a expression effected changes in the RAGE signaling cascade to impact fibroblast migration. Rap1a KO fibroblasts (4.62 #migrated cells/% area) tended to have more migration when compared to Rap1a WT fibroblasts; even though, results were not significant (2.09 #migrated cells/% area) (**Figures 3A,B**; Student's *t*-test $p = 0.0677$). Rap1a WT fibroblasts (2.09 #migrated cells/% area) had similar migration rates compared to non-diabetic fibroblasts (1.66 #migrated cells/% area). Whereas Rap1a KO fibroblast migration was similar to that of non-diabetic RKO fibroblasts. The percent difference between Rap1a KO and WT fibroblasts was 76% which is comparable to RKO fibroblasts. These results indicate that with reduced RAGE signaling or elimination of RAGE, cardiac fibroblast migration was shown to be increased.

The Elevated Levels of AGEs in Diabetic Collagen Did Not Cause a Significant Impact on Fibroblast Migration

In an *in vivo* setting, cardiac fibroblasts undergoing migration will continuously interact with the ECM, and the composition of the matrix will conversely impact cell behavior. In order to replicate this environment, specially focusing on RAGE signaling, collagen from diabetic and non-diabetic mice was used as a scaffold for migration assays. Extracted tail collagen from diabetic mice had higher accumulation of CMLs and AGEs compared to non-diabetic collagen (**Figure 4A**). Based off these findings, collagen could be used to assess changes in fibroblast migration. Cells were plated on plastic, which had no AGEs, on non-diabetic collagen, which had a very low presence of AGEs, and diabetic collagen, which had high levels of AGEs, to determine the impact of AGE accumulation and presence on fibroblast migration.

The difference in the amount of AGEs in collagen did not significantly impact the number of migrated fibroblasts. Non-diabetic fibroblast migration slightly increased as the levels of AGEs rose from no AGEs on plastic, to low AGE levels on non-diabetic collagen, and to high concentrations of AGEs on diabetic collagen. In contrast, diabetic fibroblast migration did not change between plastic, non-diabetic collagen, and diabetic collagen (**Figure 4C**; two-way ANOVA, genotype $p = 0.0094$). In contrast, non-diabetic RKO and diabetic RKO fibroblasts displayed similar amounts of migration with increasing accumulation of AGEs from plastic to diabetic collagen (**Figure 4D**; two-way ANOVA, genotype $p < 0.0001$). Rap1a WT and Rap1a KO fibroblasts

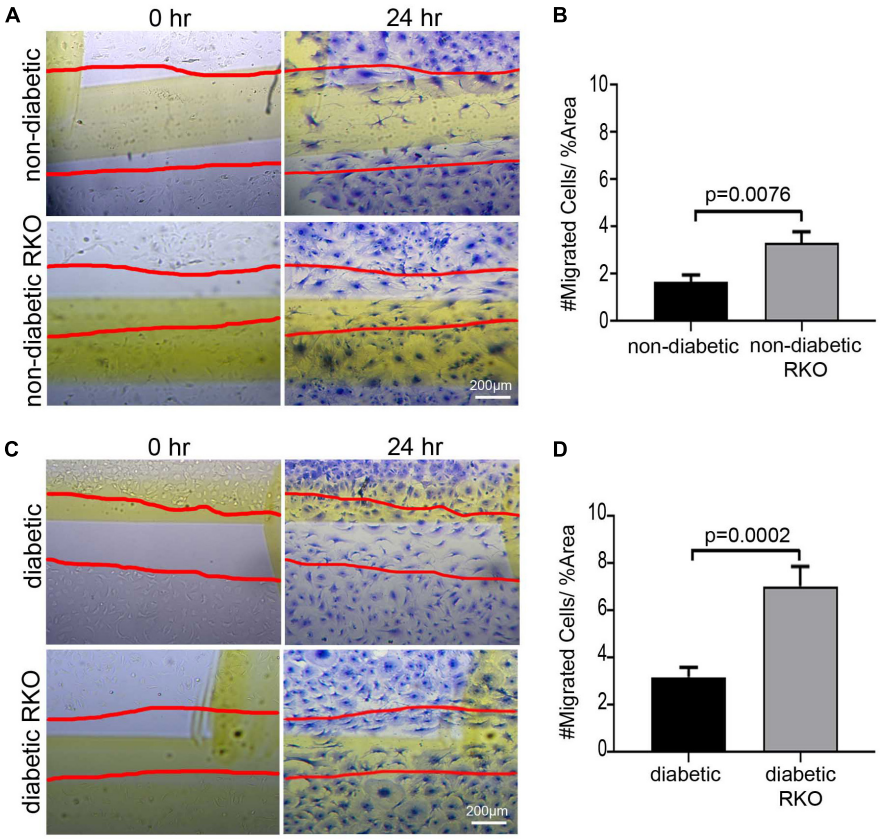

FIGURE 1 | The presence of RAGE signaling negatively impacts cardiac fibroblast migration. Cardiac fibroblasts were isolated from **(A,B)** non-diabetic with and without RAGE mice as well as **(C,D)** diabetic with and without RAGE mice. Fibroblasts were plated onto plastic cell culture dishes, scratched (0 h: **A,C**), and assessed for cell migration after 24 h **(B,D)**. Cells were stained with Coomassie for visualization with the red lines depicting scratched area (40× and scale bar = 200 μm). Number of migrated cells were normalized to percent scratched area and plotted as mean ± SEM (n = 7–13). Student's t-test used to determine significance, which is depicted on graph.

displayed similar migration when plated on plastic, non-diabetic, and diabetic collagen (**Figure 4E**; two-way ANOVA, genotype $p = 0.0005$).

Cardiac Fibroblasts Display Increased Migration With Attenuated RAGE Signaling on Diabetic Collagen

In order to further demonstrate the impact of AGE/RAGE signaling on migration, U0126 (ERK inhibitor, 5 μM) and pseudosubstrate PKC-ζ (ps PKC-ζ, PKC-ζ inhibitor, 1 μg/mL) were used to dampen RAGE signaling in cardiac fibroblasts. Fibroblast migration on diabetic collagen was used, as diabetic collagen contained the higher prevalence of AGEs and would allow for the best insight into the impact of AGE/RAGE signaling on migration (**Figure 5**). Non-diabetic fibroblasts migrated significantly more when treated with U0126 and ps PKC-ζ (**Figure 5A**; one-way ANOVA $p = 0.0004$) when compared to untreated non-diabetic cells. Similar increased levels of migration occurred with treated diabetic fibroblasts (**Figure 5B**; one-way ANOVA $p = 0.0058$). In contrast, fibroblasts lacking functional RAGE (RKO fibroblasts) did not exhibit altered cell migration when treated with either U0126 or ps PKC-ζ (**Figures 5C,D**; one-way ANOVA, non-diabetic RKO $p = 0.8595$, diabetic RKO $p = 0.9927$).

Rap1a WT cardiac fibroblasts displayed a significant increase in migration with U0126 and ps PKC-ζ treatment (**Figure 5E**; one-way ANOVA $p = 0.0033$). Although Rap1a KO fibroblasts had increased migration with U0126 and ps PKC-ζ treatment, only ps PKC-ζ was significant (**Figure 5F**; one-way ANOVA $p = 0.0303$).

Increased Exogenous AGEs in Diabetic Collagen Led to Increased Fibroblast Migration

While AGEs in the ECM can induce AGE/RAGE signaling, they can also increase stiffness of ECM due to formation of crosslinks between collagen fibers. In order to determine the impact of AGEs on fibroblast migration, additional exogenous AGEs (glycated albumin; 0.5 mg/mL) were added to fibroblasts plated on diabetic collagen (**Figure 6**). Non-diabetic and diabetic fibroblasts migrated significantly more with treatment of AGEs, compared to untreated control (**Figure 6A**; two-way ANOVA

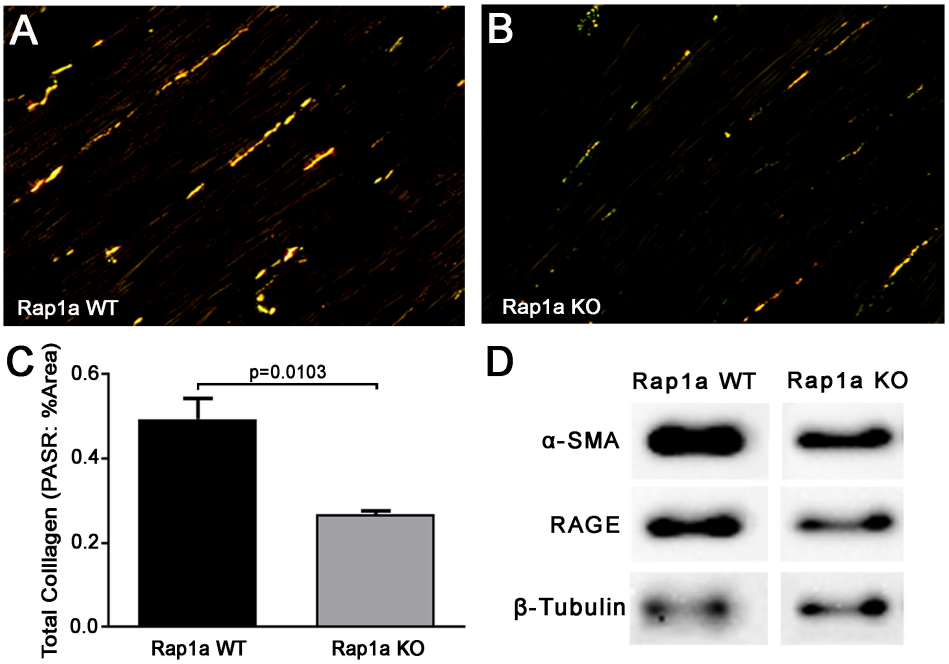

FIGURE 2 | Knockout of Rap1a resulted in decreased collgen expression in hearts (*in vivo*) and reduced protein expression of specific AGE/RAGE signaling markers in *cardiac fibroblasts* (*in vitro*). Hearts from Rap1a wild-type (WT; **A**) and knockout (KO; **B**) mice were sectioned and stained with picric acid sirius red (PASR) which fluorescences with exposure to polaized light. Total collagen was determined by normalizing the amount of PASR fluorescence to the percent area and graphed as mean ± SEM **(C)**. Student's *t*-test was preformed to assess significance with a sample size of three to four hearts. Protein expression for specific AGE/RAGE signaling cascade indicators was assessed in cardiac fibroblasts isolated from Rap1a WT and KO hearts **(D)**. Alpha smooth muscle actin (α-SMA) was used to indicate the presence of differentiated fibroblasts (myofibroblasts) and RAGE indicated expression of the receptor for AGE (RAGE). β-Tubulin was used as a loading control. Western blot images shown are not displayed as a continuous blot due to running on different membranes.

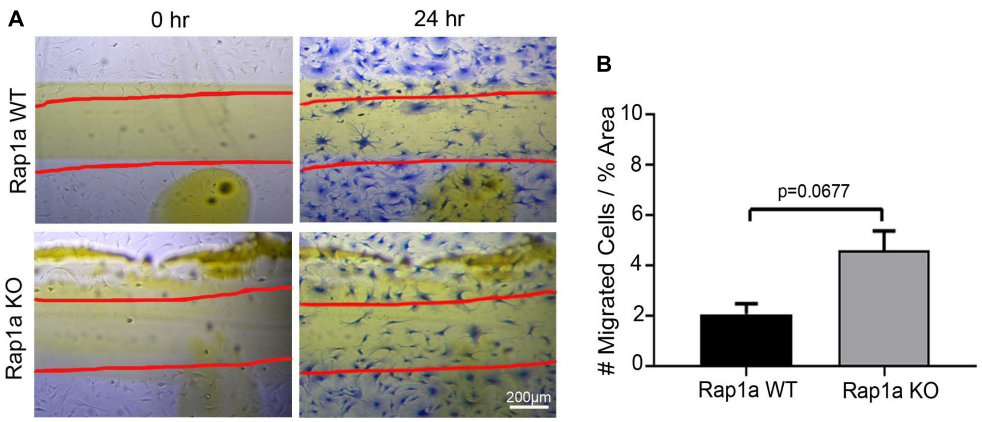

FIGURE 3 | Knockout of Rap1a led to an increase in cardiac fibroblast migraiton. Cardiac fibroblasts were isolated from Rap1a WT and KO hearts, cultured on plastic cell culture dish, scratched (0 h) and assessed for migration after 24 h **(A)**. Scratched lines were depicted with red lines and cells were stained with Coomassie blue for visualization (40× and scale bar = 200 μm). Number of migrated cells were normalized to percent scratched area and graphed as mean ± SEM (**B**; n = 6–10). Statistical anayslsis consisted of Student's *t*-test.

treatment $p < 0.0001$, Sidak's *post hoc* test $p = 0.0061$ non-diabetic and $p = 0.0085$ diabetic). Exogenous AGE treatment of RKO fibroblasts did not induce a change in migration (**Figure 6B**: two-way ANOVA treatment $p = 0.8549$).

Rap1a WT and KO fibroblast migrations were more significantly impacted with AGE treatment (**Figure 6C**; two-way ANOVA, treatment $p = 0.0490$). These results indicated that AGEs present in the diabetic matrix when combined with the treatment of exogenous AGEs resulted in a shift in fibroblast phenotype to that of a diabetic cell. Diabetic cardiac fibroblasts exhibit significantly more migration compared to their non-diabetic counterparts.

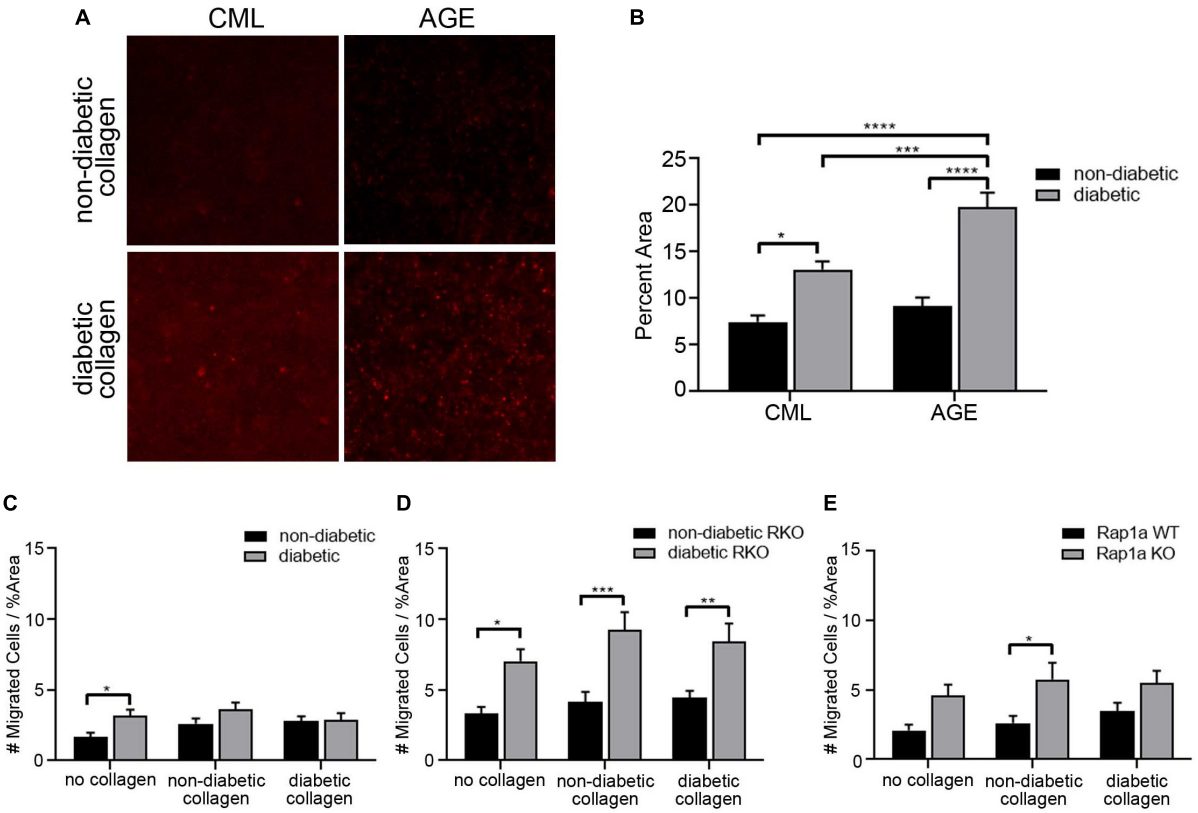

FIGURE 4 | The elevated levels of AGEs in diabetic collagen did not significantly impact fibroblast migration. **(A)** Immunofluorescence (100×; scale bar = 50 μm) images for carboxymethyl lysine (CML) and advanced glycated end-products (AGEs) in non-diabetic collagen and diabetic collagen. **(B)** Graph depicting semi-quantification of CML and AGEs present in non-diabetic and diabetic collagen. Cardiac fibroblasts isolated from **(C)** non-diabetic and diabetic, **(D)** non-diabetic and diabetic RAGE knockout, and **(E)** Rap1a WT and KO mice were plated on either no collagen (results shown in **Figure 1**) non-diabetic collagen, or diabetic collagen. The number of migrated cells were normalized to percent scratch area. Data are mean ± SEM with a two-way ANOVA and a Sidak's *post hoc* test, $n = 10–13$. A red line was set at $y = 1$ Migrated Cells/%Area and was used for comparison across cardiac fibroblast genotypes (*$p < 0.05$, **$p < 0.01$, ***$p < 0.001$, ****$p < 0.0001$).

DISCUSSION

The aim of this study was to assess the role of AGE/RAGE signaling on cardiac fibroblast migration in diabetic conditions. While fibroblast migration, specifically epithelial fibroblast migration, has been widely studied in conjunction with impaired diabetic skin wound healing (Stewart et al., 2010; Darby et al., 2014; Tracy et al., 2014). The mechanism of fibroblast migration in other organ systems under diabetic conditions is still relatively uncertain. The results presented in this study demonstrated diabetic cardiac fibroblasts migrated significantly more than non-diabetic cardiac fibroblasts. By altering either (1) RAGE expression using RKO fibroblasts, (2) suppressing key components of the AGE/RAGE cascade using pharmacological inhibitors, or (3) downregulating RAGE signaling in Rap1a KO cells, we observed an increase in fibroblast migration over that of non-diabetic and diabetic fibroblasts with functional RAGE. These findings contrast those observed in skin fibroblast studies, in that, diabetic cardiac fibroblasts have a higher migration phenotype than non-diabetic cardiac fibroblasts, and by impeding the RAGE signaling cascade, fibroblast migration greatly improved cell migration (Almeida et al., 2016). Thus, providing evidence that decreasing RAGE signaling could potentially improve wound healing in the heart; however, further experiments will need to be performed to determine if this response exists *in vivo*. The AGE/RAGE signaling pathway has been shown to increase ECM deposition; therefore, it could be proposed that the AGE/RAGE signaling cascade may impact cell migration via ECM remodeling (Asif et al., 2002; Yan et al., 2008).

The cardiac ECM is composed of a variety of biological molecules capable of altering cell-matrix interactions resulting in changes in migration phenotype (Charras and Sahai, 2014). It has been demonstrated that diabetics have increased AGE accumulation in their cells as well as in their extracellular compartments (Hartog et al., 2007). AGEs will form crosslinks with one another, which can contribute to a stiffer collagen matrix (Verzijl et al., 2002). Therefore, this study also aimed to determine if collagen isolated from non-diabetic mice with low amounts of AGEs and collagen from diabetic mice with high amounts of AGEs could alter cardiac fibroblast migration. Our results showed that non-diabetic cardiac fibroblasts migrated slightly more as the prevalence of AGEs climbed. These data

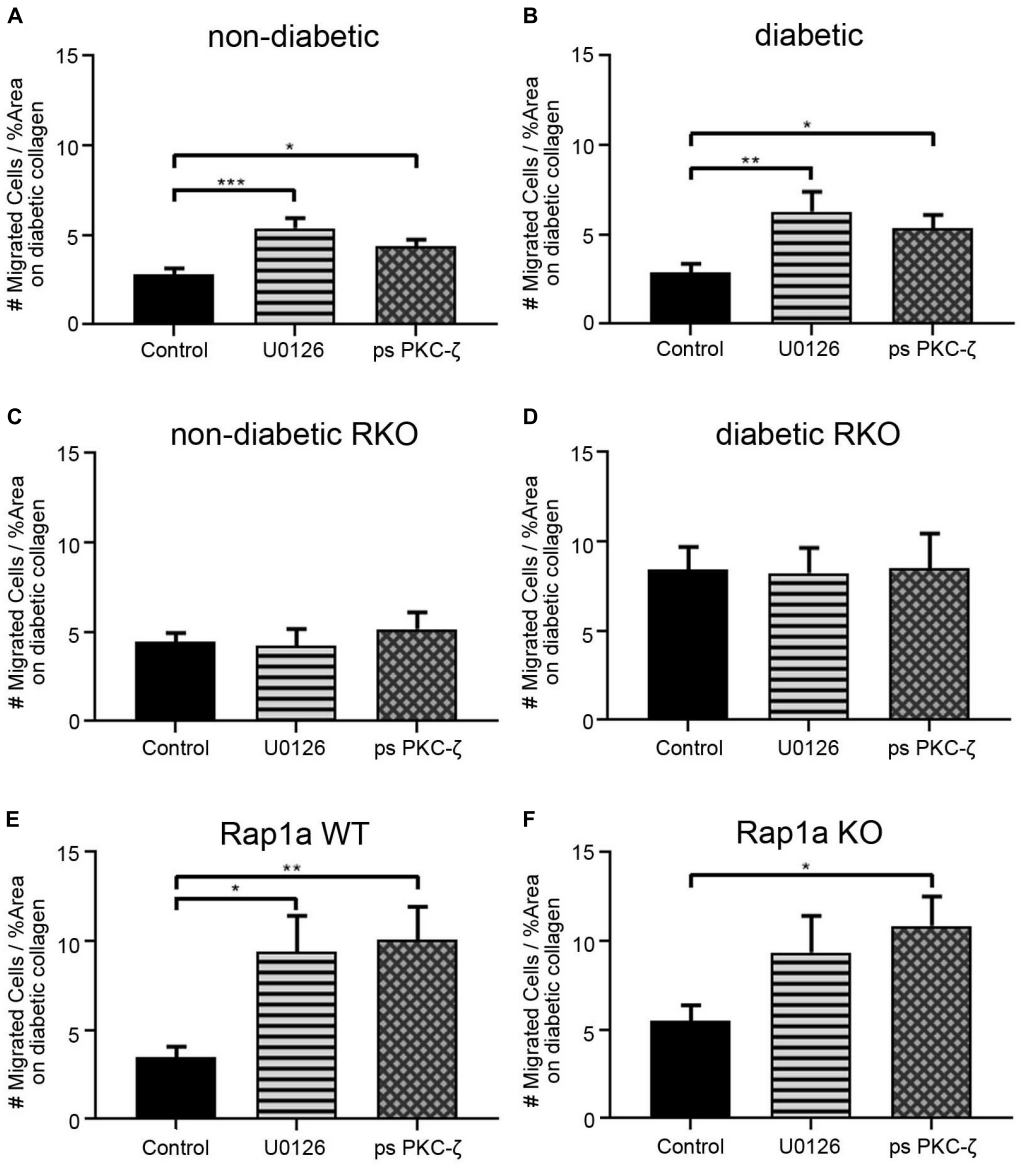

FIGURE 5 | Cardiac fibroblasts display increased migration with decreased RAGE signaling on diabetic collagen. **(A)** Non-diabetic, **(B)** diabetic, **(C)** non-diabetic RKO, **(D)** diabetic RKO, **(E)** Rap1a WT, and **(F)** Rap1a KO cardiac fibroblasts plated on diabetic collagen were treated with U0126 (ERK inhibitor; 5 μM) and ps PKC-ζ (pseudosubstrate PKC-ζ inhibitor; 1 μg/mL). Data represent mean ± SEM with a $n = 10–13$ for control and $n = 3–9$ for treatments. A one-way ANOVA and a Dunnett's *post hoc* test determined significance (*$p < 0.05$, **$p < 0.01$, ***$p < 0.001$).

suggested the composition of the ECM along with the escalating levels of ECM AGEs were a contributing factor impacting cardiac fibroblast migration.

Elevated diabetic cardiac fibroblast migration, as presented in this work, in comparison to other studies, could be attributed to the heterogeneity of fibroblasts. Cells isolated from differing tissue sources will retain their *in vivo* characteristics while in culture, and would thus yield different phenotypic responses to similar stimuli (Sorrell and Caplan, 2004; Driskell and Watt, 2015; Sriram et al., 2015). Hyperglycemic conditions could possibly contribute to changes noted in previous studies in which diabetic cardiac fibroblast migration was examined. Findings have shown that culturing cells in high glucose media can result in changes in cardiac fibroblast migration (Kanazawa et al., 2010; Xuan et al., 2014). Hyperglycemic conditions have also been demonstrated to cause AGE accumulation. While AGEs accumulate naturally within the body over time, the formation and accumulation of AGEs is accelerated under diabetic conditions (Hegab et al., 2012). It has also been noted that AGE serum levels in diabetics are almost double of that of healthy individuals (Hegab et al., 2012). Therefore, it is a strong possibility that fibroblasts residing in distinct tissues could respond differently under diabetic conditions.

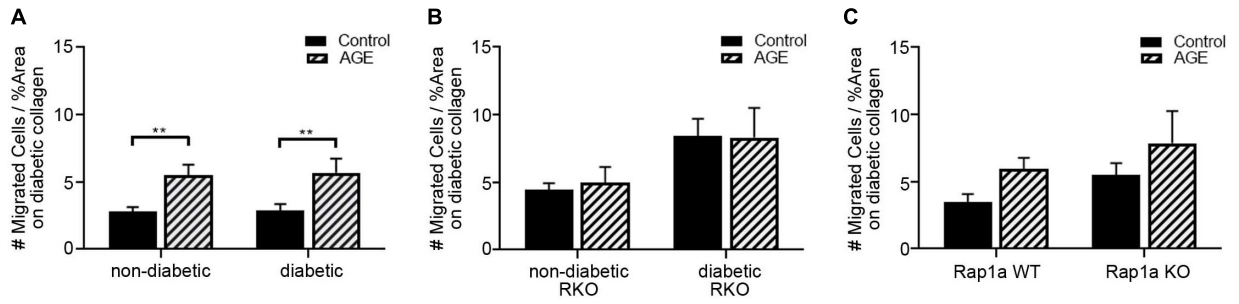

FIGURE 6 | Increased exogenous AGEs in diabetic collagen led to increased fibroblast migration. Cardiac fibroblasts from **(A)** non-diabetic and diabetic, **(B)** RAGE knockout, and **(C)** Rap1a mice were plated on diabetic collagen. Fibroblasts were either untreated (control) or treated with AGEs (0.5 mg/mL). Cell migration was normalized to percent scratch area with mean ± SEM being depicted on graph. Two-way ANOVA with Sidak's *post hoc* test determined significance (**$p < 0.01$, $n = 5–10$).

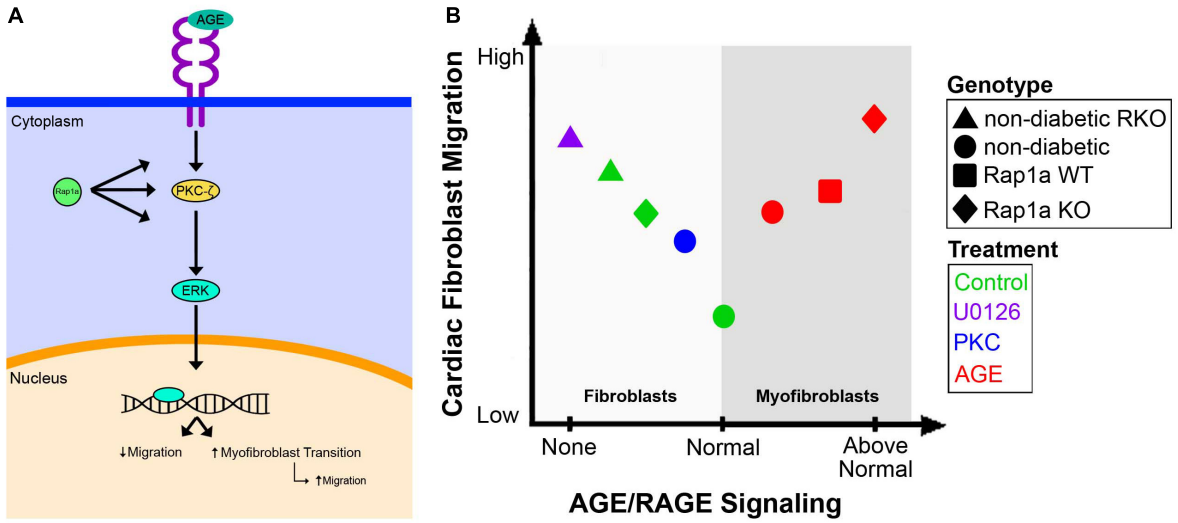

FIGURE 7 | Overview of the AGE/RAGE signaling cascade and its impact on cardiac fibroblast migration. A diagram depicted the proposed signaling network of AGE/RAGE that impacts cardiac fibroblast migration **(A)**. The impact of varying levels of AGE/RAGE signaling on cardiac fibroblast migration and possible differentiation **(B)**.

By studying the effects of the AGE/RAGE signaling pathway on cardiac fibroblast migration, we were able to determine that activation of the signaling cascade altered cardiac fibroblast migration. Fibroblast migration was elevated in diabetic hearts compared to that of cells from non-diabetic hearts. In addition, it was found that cardiac fibroblasts lacking functional RAGE (RKO; RAGE knockout mice) had higher migration levels in both non-diabetic RKO and diabetic RKO fibroblasts when compared to cardiac fibroblasts with intact RAGE. Our results showed when RAGE was eliminated, migration levels were significantly elevated allowing for a more motile cell phenotype, as seen in **Figure 7**. Additionally, pharmacological inhibition of key signaling proteins within the RAGE cascade, such as ERK1/2 and PKC-ζ, resulted in increased migration (**Figure 7A**). Migration was not altered by ERK1/2 or PKC-ζ inhibition in RKO fibroblasts, which stands to reason, as the RAGE receptor has been rendered ineffective by genetic ablation. Therefore, downregulating the RAGE cascade allowed for increased cell migration. Due to the extensive impact of ERK1/2 activation in cell signaling, it could be argued that increased migration though inhibition of ERK1/2 was a result of impacting additional pathways other than AGE/RAGE. To counter this argument, an independent study found that inhibition of ERK1/2 activation downstream of MAP kinase signaling resulted in decreased migration (Mitchell et al., 2006). Therefore, if ERK1/2 was influencing migration via a pathway separate from AGE/RAGE, a decrease in migration would be expected. Our results showed increased migration with inhibition of active ERK1/2 to suggest inhibition of AGE/RAGE signaling in cardiac fibroblasts can increase and improve cell migration within the heart.

At basal levels non-diabetic cardiac fibroblasts displayed a lowered migration ability; however, when AGE/RAGE signaling was increased, as in diabetic fibroblasts, there was a concomitant increase in cardiac fibroblast migration. Our study found

that treatment with exogenous AGEs also caused an increase in cardiac fibroblast migration much like that observed in diabetic cells, but the level of migration never superseded the migration noted in RKO cardiac fibroblasts. The increase in migration with AGE treatment is most likely due to the cardiac fibroblasts differentiating into myofibroblasts, which can indirectly impact cell migration (Suchal et al., 2017; **Figure 7B**). Prior research by our lab and others have shown that increases in α-SMA expression, a marker for myofibroblasts, in lung fibroblasts was linked to increased migration (Kawamoto et al., 1997). In addition, in cardiac fibroblasts a decrease in α-SMA expression was correlated with decreased fibroblast migration (Shi et al., 2011). These results support the idea that RAGE signaling above "normal" levels results in increased migration due to these cells transitioning into myofibroblasts, and therefore characterized by elevated migration (**Figure 7**); however, further studies will need to be performed to determine if AGE can directly induce fibroblast to myofibroblast conversion. Another factor our lab has found to impact RAGE signaling and in turn cardiac fibroblast migration is the small GTPase, Rap1a.

Rap1a acts as a linker molecule connecting extracellular stimuli to intracellular effects. Based off previous findings, we proposed that Rap1a intersects the AGE/RAGE pathway and modifies the signal transduction strength (Yan et al., 2008; Zhao et al., 2014). Our results also demonstrated decreased collagen levels in Rap1a KO hearts as well as reduced protein expression of specific RAGE cascade markers in cardiac fibroblasts. In terms of the role Rap1a plays in fibroblast migration, previously conducted studies showed conflicting results. In colonic epithelial cells decreased Rap1a expression resulted in decreased migration, whereas in macrophages a loss of Rap1a produced increased migration (Li et al., 2007; Severson et al., 2009). Another study by Yan et al. (2008) found that depletion of Rap1a via silencing RNA reduced migration in human microvascular endothelial cells during angiogenesis (Yan et al., 2008). These conflicting studies suggest that the impact Rap1a on cell migration is tissue and/or cell specific. Our study found cardiac fibroblasts without Rap1a (Rap1a KO) had more migration than fibroblasts with Rap1a (Rap1a WT). Comparing this to fibroblasts with functional RAGE and those without RAGE, Rap1a KO cardiac fibroblasts exhibited an intermediate migratory ability. The intermediate migration exhibited in Rap1a KO suggested that Rap1a may contribute to further exacerbation of downstream outcomes of AGE/RAGE signaling to impact cardiac fibroblast migration. Further studies will need to be performed to understand the role of Rap1a in fibroblast function.

The findings of this study suggested that cardiac fibroblast migration is differentially regulated by a number of factors. We found that diabetic fibroblasts have a higher migration level than non-diabetic cells. In addition, the RAGE signaling cascade leads to reduced migration compared to higher migration observed in RKO fibroblasts. Reduction of AGE/RAGE signaling with U0126 and ps-PKC resulted in increased cardiac fibroblast migration. With the addition of AGEs, cell migration was elevated due, most likely, to myofibroblast differentiation brought on by higher concentration of AGEs and increased AGE/RAGE signaling. Decreased RAGE signaling via knocking out Rap1a GTPase resulted in an increase in cardiac migration, but not to the level noted in RKO fibroblasts. Therefore, changes in fibroblast migration and factors that influence this behavior can have the potential to alter organ performance. For example, increased LV collagen deposition by myofibroblasts can impact ventricular remodeling, heart function, and contribute to cardiovascular disease (Zhang et al., 2007; Dludla et al., 2017). As scratch assays may mimic an injury to confound experimental conditions, future studies will need to be performed using a more specific migration, such as Boyden chamber assays, to confirm results. Examination of changes in migration protein markers in the future will provide further evidence to the role of RAGE signaling has on fibroblast migration. In addition to these studies, experiments that assess the impact of diabetic conditions and the link with RAGE signaling can be done to determine the influence of diabetes on cardiac fibroblast migration. While there is still more to investigate regarding AGE/RAGE signaling on cardiac fibroblast migration, our study provides convincing results demonstrating that diabetes-related hyperglycemia will increase AGE levels and active RAGE signaling to alter migration contributing to the progression of LV remodeling. By generating therapeutics against modulators of the RAGE signaling pathway, such as Rap1a, there is the potential to lessen diabetic complications.

DATA AVAILABILITY STATEMENT

All relevant data are included within the manuscript. Supplemental and original blot images are available: 10.6084/m9.figshare.10248983.

ETHICS STATEMENT

The animal study was reviewed and approved by the University of Mississippi Institutional Animal Care and Use Committee.

AUTHOR CONTRIBUTIONS

All authors contributed to the experimental design, data analysis, and manuscript preparation. SB and MH conducted the experiments. JS obtained the funding.

FUNDING

This work was supported by the US Army Medical Research Award #81XWH-16-1-0710, University of Mississippi School of Pharmacy, and the Department of BioMolecular Sciences.

ACKNOWLEDGMENTS

We would like to thank the University of Mississippi School of Pharmacy and the Department of BioMolecular Sciences for their support.

REFERENCES

Adamopoulos, C., Piperi, C., Gargalionis, A. N., Dalagiorgou, G., Spilioti, E., Korkolopoulou, P., et al. (2016). Advanced glycation end products upregulate lysyl oxidase and endothelin-1 in human aortic endothelial cells via parallel activation of ERK1/2-NF-??B and JNK-AP-1 signaling pathways. *Cell Mol. Life Sci.* 73, 1685–1698. doi: 10.1007/s00018-015-2091-z

Almeida, M. E. S., Monteiro, K. S., Kato, E. E., Sampaio, S. C., Braga, T. T., Câmara, N. O. S., et al. (2016). Hyperglycemia reduces integrin subunits alpha v and alpha 5 on the surface of dermal fibroblasts contributing to deficient migration. *Mol. Cell. Biochem.* 421, 19–28. doi: 10.1007/s11010-016-2780-2784

American Diabetes Association, (2018). *Statistics About Diabetes*. Arlington County: American Diabetes Association.

Asif, M., Egan, J., Vasan, S., Jyothirmayi, G. N., Masurekar, M. R., Lopez, S., et al. (2002). An advanced glycation endproduct cross-link breaker can reverse age-related increases in myocardial stiffness. *Proc. Natl. Acad. Sci. U.S.A.* 97, 2809–2813. doi: 10.1073/pnas.040558497

Bierhaus, A., Humpert, P. M., Morcos, M., Wendt, T., Chavakis, T., Arnold, B., et al. (2005). Understanding RAGE, the receptor for advanced glycation end products. *J. Mol. Med.* 83, 876–886. doi: 10.1007/s00109-005-0688-7

Brodeur, M. R., Bouvet, C., Bouchard, S., Moreau, S., and Leblond, J. (2014). Reduction of advanced-Glycation end products levels and inhibition of RAGE signaling decreases rat vascular calcification induced by diabetes. *PLoS One* 9:85922. doi: 10.1371/journal.pone.0085922

Caley, M. P., Martins, V. L. C., and O'Toole, E. A. (2015). Metalloproteinases and wound healing. *Adv. Wound Care* 4, 225–234. doi: 10.1089/wound.2014.0581

Charras, G., and Sahai, E. (2014). Physical influences of the extracellular environment on cell migration. *Nat. Rev. Mol. Cell Biol.* 15, 813–824. doi: 10.1038/nrm3897

Chen, H., Charlat, O., Tartaglia, L. A., Woolf, E. A., Weng, X., Ellis, S. J., et al. (1996). Evidence that the diabetes gene encodes the leptin receptor: identification of a mutation in the leptin receptor gene in db/db mice. *Cell* 84, 491–495. doi: 10.1016/S0092-8674(00)81294-81295

Constien, R., Forde, A., Liliensiek, B., Gröne, H. J., Nawroth, P., Hämmerling, G., et al. (2001). Characterization of a novel EGFP reporter mouse to monitor Cre recombination as demonstrated by a Tie2 Cre mouse line. *Genesis* 30, 36–44.

Darby, I. A., Laverdet, B., Bonté, F., and Desmoulière, A. (2014). Fibroblasts and myofibroblasts in wound healing. *Clin. Cosmet. Investig. Dermatol.* 7, 301–311. doi: 10.2147/CCID.S50046

Dludla, P. V., Essop, M. F., Gabuza, K. B., Muller, C. J. F., Louw, J., and Johnson, R. (2017). Age-dependent development of left ventricular wall thickness in type 2 diabetic (db/db) mice is associated with elevated low-density lipoprotein and triglyceride serum levels. *Heart Vessels* 32, 1025–1031. doi: 10.1007/s00380-017-0978-973

Dong, W., Yang, Z., Yang, F., Wang, J., Zhuang, Y., Xu, C., et al. (2012). Suppression of Rap1 Impairs cardiac myofibrils and conduction system in zebrafish. *PLoS One* 7:e0050960. doi: 10.1371/journal.pone.0050960

Driskell, R. R., and Watt, F. M. (2015). Understanding fibroblast heterogeneity in the skin. *Trends Cell Biol.* 25, 92–99.

Evankovich, J., Lear, T., McKelvey, A., Dunn, S., Londino, J., Liu, Y., et al. (2017). Receptor for advanced glycation end products is targeted by FBXO10 for ubiquitination and degradation. *FASEB J.* 31, 3894–3903. doi: 10.1096/fj.201700031R

Fowlkes, V., Clark, J., Fix, C., Law, B. A., Morales, M. O., Qiao, X., et al. (2013). Type II diabetes promotes a myofibroblast phenotype in cardiac fibroblasts. *Life Sci.* 92, 669–676. doi: 10.1016/j.lfs.2013.01.003

Gao, X., Zhang, H., Schmidt, A. M., and Zhang, C. (2008). AGE/RAGE produces endothelial dysfunction in coronary arterioles in Type 2 diabetic mice. *Am. J. Physiol. Circ. Physiol.* 295, H491–H498. doi: 10.1152/ajpheart.00464.2008

Hartog, J. W. L., Voors, A. A., Bakker, S. J. L., Smit, A. J., and van Veldhuisen, D. J. (2007). Advanced glycation end-products (AGEs) and heart failure: pathophysiology and clinical implications. *Eur. J. Heart Fail.* 9, 1146–1155. doi: 10.1016/j.ejheart.2007.09.009

Hegab, Z., Gibbons, S., Neyses, L., and Mamas, M. A. (2012). Role of advanced glycation end products in cardiovascular disease. *World J. Cardiol.* 4, 90–102. doi: 10.4330/wjc.v4.i4.90

Hutchinson, K. R., Lord, C. K., West, T. A., and Stewart, J. A. (2013). Cardiac fibroblast-dependent extracellular matrix accumulation is associated with diastolic stiffness in Type 2 diabetes. *PLoS One* 8:e0072080. doi: 10.1371/journal.pone.0072080

Jeyaraj, S. C., Unger, N. T., and Chotani, M. A. (2011). Rap1 GTPases: an emerging role in the cardiovasculature. *Life Sci.* 88, 645–652. doi: 10.1016/j.lfs.2011.01.023

Kanazawa, S., Fujiwara, T., Matsuzaki, S., Shingaki, K., Taniguchi, M., Miyata, S., et al. (2010). bFGF regulates PI3-Kinase-Rac1-JNK pathway and promotes fibroblast migration in wound healing. *PLoS One* 5:e0012228. doi: 10.1371/journal.pone.0012228

Kawamoto, M., Matsunami, T., Ertl, R. F., Fukuda, Y. U. H., Ogawa, M., Spurzem, J. R., et al. (1997). Selective migration of α-smooth muscle actin-positive myofibroblasts toward fibronectin in the Boyden's blindwell chamber. *Clin. Sci.* 93, 355–362.

Lerman, O. Z., Galiano, R. D., Armour, M., Levine, J. P., and Gurtner, G. C. (2003). Cellular dysfunction in the diabetic fibroblast: impairment in migration, vascular endothelial growth factor production, and response to hypoxia. *Am. J. Pathol.* 162, 303–312. doi: 10.1016/S0002-9440(10)63821-63827

Li, W., Fan, J., Chen, M., Guan, S., Sawcer, D., Bokoch, G. M., et al. (2004). Mechanism of human dermal fibroblast migration driven by type I collagen and platelet-derived growth factor-BB. *Mol. Biol. Cell* 15, 294–309.

Li, Y., Yan, J., De, P., Chang, H.-C., Yamauchi, A., Christopherson, K. W., et al. (2007). Rap1a null mice have altered myeloid cell functions suggesting distinct roles for the closely related Rap1a and 1b proteins. *J. Immunol.* 179, 8322–8331. doi: 10.4049/jimmunol.179.12.8322

Liliensiek, B., Nawroth, P. P., Arnold, B., Liliensiek, B., Weigand, M. A., Bierhaus, A., et al. (2004). Receptor for advanced glycation end products (RAGE) regulates sepsis but not the adaptive immune response Find the latest version?: receptor for advanced glycation end products (RAGE) regulates sepsis but not the adaptive immune response. *J. Clin. Invest.* 113, 1641–1650. doi: 10.1172/JCI200418704

Mitchell, M. D., Laird, R. E., Brown, R. D., and Long, C. S. (2006). IL-1β stimulates rat cardiac fibroblast migration via MAP kinase pathways. *Am. J. Physiol. Circ. Physiol.* 292, H1139–H1147. doi: 10.1152/ajpheart.00881.2005

Rajan, N., Habermehl, J., Coté, M.-F., Doillon, C. J., and Mantovani, D. (2007). Preparation of ready-to-use, storable and reconstituted type I collagen from rat tail tendon for tissue engineering applications. *Nat. Protoc.* 1:2753. doi: 10.1038/nprot.2006.430

Ramasamy, R., Yan, S. F., and Schmidt, A. M. (2011). Receptor for AGE (RAGE): signaling mechanisms in the pathogenesis of diabetes and its complications. *Ann. N. Y. Acad. Sci.* 1243, 88–102. doi: 10.1111/j.1749-6632.2011.06320.x

Roberts, O. L., Kamishima, T., Barrett-Jolley, R., Quayle, J. M., and Dart, C. (2013). Exchange protein activated by cAMP (Epac) induces vascular relaxation by activating Ca2+-sensitive K+ channels in rat mesenteric artery. *J. Physiol.* 591, 5107–5123. doi: 10.1113/jphysiol.2013.262006

Severson, E. A., Lee, W. Y., Capaldo, C. T., Nusrat, A., and Parkos, C. A. (2009). Junctional adhesion molecule A interacts with Afadin and PDZ-GEF2 to activate Rap1A, regulate β1 integrin levels, and enhance cell migration. *Mol. Biol. Cell* 20, 1916–1925. doi: 10.1091/mbc.E08-10-1014

Shamhart, P., Luther, D., Adapala, R., Bryant, J., Petersen, K., Meszaros, J., et al. (2014). Hyperglycemia enhances function and differentiation of adult rat cardiac fibroblasts. *Can J. Physiol. Pharmacol.* 92, 598–604. doi: 10.1126/science.1249098.Sleep

Shang, Y., Zhang, X., Leng, W., Lei, X., Chen, L., Zhou, X., et al. (2018). Increased fractal dimension of left ventricular trabeculations is associated with subclinical diastolic dysfunction in patients with type-2 diabetes mellitus. *Int. J. Cardiovasc. Imaging* 35, 665–673. doi: 10.1007/s10554-018-1492-1490

Shi, Q., Liu, X., Bai, Y., Cui, C., Li, J., Li, Y., et al. (2011). In vitro effects of pirfenidone on cardiac fibroblasts: proliferation, myofibroblast differentiation, migration and cytokine secretion. *PLoS One* 6:e0028134. doi: 10.1371/journal.pone.0028134

Simm, A., Wagner, J., Gursinsky, T., Nass, N., Friedrich, I., Schinzel, R., et al. (2007). Advanced glycation endproducts: a biomarker for age as an outcome predictor after cardiac surgery? *Exp. Gerontol.* 42, 668–675. doi: 10.1016/j.exger.2007.03.006

Sorrell, J. M., and Caplan, A. I. (2004). Fibroblast heterogeneity: more than skin deep. *J. Cell Sci.* 117, 667–675. doi: 10.1242/jcs.01005

Sriram, G., Bigliardi, P. L., and Bigliardi-Qi, M. (2015). Fibroblast heterogeneity and its implications for engineering organotypic skin models in vitro. *Eur. J. Cell Biol.* 94, 483–512. doi: 10.1016/j.ejcb.2015.08.001

Stewart, J. A., Massey, E. P., Fix, C., Zhu, J., Goldsmith, E. C., and Carver, W. (2010). Temporal alterations in cardiac fibroblast function following induction of pressure overload. *Cell Tissue Res.* 340, 117–126. doi: 10.1007/s00441-010-0943-2

Stewart, J. A., Wei, C.-C., Brower, G. L., Rynders, P. E., Hankes, G. H., Dillon, A. R., et al. (2003). *Cardiac Mast Cell-and Chymase-Mediated Matrix Metalloproteinase Activity and Left Ventricular Remodeling in Mitral Regurgitation in the Dog*. Available at: www.elsevier.com/locate/yjmcc (Accessed July 11, 2019).

Straino, S., Di Carlo, A., Mangoni, A., De Mori, R., Guerra, L., Maurelli, R., et al. (2008). High-mobility group box 1 protein in human and murine skin: involvement in wound healing. *J. Invest. Dermatol.* 128, 1545–1553. doi: 10.1038/sj.jid.5701212

Suchal, K., Malik, S., Khan, S. I., Malhotra, R. K., Goyal, S. N., Bhatia, J., et al. (2017). Protective effect of mangiferin on myocardial ischemia-reperfusion injury in streptozotocin-induced diabetic rats: role of AGE-RAGE/MAPK pathways. *Sci. Rep.* 7:42027. doi: 10.1038/srep42027

Tracy, L. E., Minasian, R. A., and Caterson, E. J. (2014). Extracellular matrix and dermal fibroblast function in the healing wound. *Adv. Wound Care* 5, 119–136. doi: 10.1089/wound.2014.0561

Velnar, T., Bailey, T., and Smrkolj, V. (2009). The wound healing process: an overview of the cellular and molecular mechanisms. *J. Int. Med. Res.* 37, 1528–1542.

Verzijl, N., DeGroot, J., Zaken, C. B., Braun-Benjamin, O., Bank, R. A., Mizrahi, J., et al. (2002). Crosslinking by advanced glycation end products increases the stiffness of the Collagen network in human articular cartilage. *Arthritis Rheum.* 46, 114–123. doi: 10.1002/art.10025

Wu, C. H., Chang, C. H., Lin, H. C., Chen, C. M., Lin, C. H., and Lee, H. M. (2003). Role of protein kinase C in BSA-AGE-mediated inducible nitric oxide synthase expression in RAW 264.7 macrophages. *Biochem. Pharmacol.* 66, 203–212. doi: 10.1016/S0006-2952(03)00249-241

Xuan, Y. H., Huang, B. Bin, Tian, H. S., Chi, L. S., Duan, Y. M., Wang, X., et al. (2014). High-glucose inhibits human fibroblast cell migration in wound healing via repression of bFGF-regulating JNK phosphorylation. *PLoS One* 9:e0108182. doi: 10.1371/journal.pone.0108182

Yabluchanskiy, A., Ma, Y., Iyer, R. P., Hall, M. E., and Lindsey, M. L. (2013). Matrix metalloproteinase-9: many shades of function in cardiovascular disease. *Physiology* 28, 391–403. doi: 10.1152/physiol.00029.2013

Yan, J., Li, F., Ingram, D. A., and Quilliam, L. A. (2008). Rap1a is a key regulator of Fibroblast growth factor 2-induced angiogenesis and together with Rap1b controls human endothelial cell functions. *Mol. Cell. Biol.* 28, 5803–5810. doi: 10.1128/mcb.00393-398

Zhang, X., Stewart, J. A., Kane, I. D., Massey, E. P., Cashatt, D. O., and Carver, W. E. (2007). Effects of elevated glucose levels on interactions of cardiac fibroblasts with the extracellular matrix. *Vitr. Cell. Dev. Biol. Anim.* 43, 297–305. doi: 10.1007/s11626-007-9052-9052

Zhao, J., Randive, R., and Stewart, J. A. (2014). Molecular mechanisms of AGE/RAGE-mediated fibrosis in the diabetic heart. *World J. Diabetes* 5, 860–867. doi: 10.4239/wjd.v5.i6.860

Conflict of Interest: The authors declare that the research was conducted in the absence of any commercial or financial relationships that could be construed as a potential conflict of interest.

frontiers in Cell and Developmental Biology

ORIGINAL RESEARCH
published: 03 March 2020
doi: 10.3389/fcell.2020.00125

KANK2 Links αVβ5 Focal Adhesions to Microtubules and Regulates Sensitivity to Microtubule Poisons and Cell Migration

*Mladen Paradžik[1], Jonathan D. Humphries[2], Nikolina Stojanović[1], Davor Nestić[1], Dragomira Majhen[1], Ana Dekanić[1], Ivana Samaržija[1], Delphine Sedda[1], Igor Weber[3], Martin J. Humphries[2] and Andreja Ambriović-Ristov[1]**

[1] Laboratory for Cell Biology and Signalling, Division of Molecular Biology, Ruđer Bošković Institute, Zagreb, Croatia, [2] Wellcome Centre for Cell-Matrix Research, Faculty of Biology, Medicine and Health, University of Manchester, Manchester, United Kingdom, [3] Laboratory of Cell Biophysics, Division of Molecular Biology, Ruđer Bošković Institute, Zagreb, Croatia

OPEN ACCESS

Edited by:
Claudia Tanja Mierke,
Leipzig University, Germany

Reviewed by:
Benjamin Thomas Goult,
University of Kent, United Kingdom
Srikala Raghavan,
Institute for Stem Cell Biology and Regenerative Medicine, India

***Correspondence:**
Andreja Ambriović-Ristov
Andreja.Ambriovic.Ristov@irb.hr

Specialty section:
This article was submitted to Cell Adhesion and Migration, a section of the journal Frontiers in Cell and Developmental Biology

Received: 16 December 2019
Accepted: 13 February 2020
Published: 03 March 2020

Citation:
Paradžik M, Humphries JD, Stojanović N, Nestić D, Majhen D, Dekanić A, Samaržija I, Sedda D, Weber I, Humphries MJ and Ambriović-Ristov A (2020) KANK2 Links αVβ5 Focal Adhesions to Microtubules and Regulates Sensitivity to Microtubule Poisons and Cell Migration. Front. Cell Dev. Biol. 8:125. doi: 10.3389/fcell.2020.00125

Integrins are heterodimeric glycoproteins that bind cells to extracellular matrix. Upon integrin clustering, multimolecular integrin adhesion complexes (IACs) are formed, creating links to the cell cytoskeleton. We have previously observed decreased cell migration and increased sensitivity to microtubule (MT) poisons, paclitaxel and vincristine, in the melanoma cell line MDA-MB-435S upon transfection with integrin αV-specific siRNA, suggesting a link between adhesion and drug sensitivity. To elucidate the underlying mechanism, we determined αV-dependent changes in IAC composition. Using mass spectrometry (MS)-based proteomics, we analyzed the components of isolated IACs of MDA-MB-435S cells and two MDA-MB-435S-derived integrin αV-specific shRNA-expressing cell clones with decreased expression of integrin αV. MS analysis showed that cells preferentially use integrin αVβ5 for the formation of IACs. The differential analysis between MDA-MB-435S cells and clones with decreased expression of integrin αV identified key components of integrin αVβ5 adhesion complexes as talins 1 and 2, α-actinins 1 and 4, filamins A and B, plectin and vinculin. The data also revealed decreased levels of several components of the cortical microtubule stabilization complex, which recruits MTs to adhesion sites (notably liprins α and β, ELKS, LL5β, MACF1, KANK1, and KANK2), following αV knockdown. KANK2 knockdown in MDA-MB-435S cells mimicked the effect of integrin αV knockdown and resulted in increased sensitivity to MT poisons and decreased migration. Taken together, we conclude that KANK2 is a key molecule linking integrin αVβ5 IACs to MTs, and enabling the actin-MT crosstalk that is important for both sensitivity to MT poisons and cell migration.

Keywords: adhesome, integrin αVβ5, antitumor drug resistance, cell migration, cortical microtubule stabilizing complex, KANK2

INTRODUCTION

Integrins are cell-surface adhesion molecules that connect cells to other cells and components of the ECM. Integrins are heterodimers composed of α and β subunits. A set of 18 α and 8 β subunits that associate to form 24 different αβ heterodimers have thus far been identified. Integrins are involved in signaling pathways that regulate many essential cellular functions including survival, proliferation and migration (Desgrosellier and Cheresh, 2010; Cooper and Giancotti, 2019). Upon clustering of integrins, other proteins are recruited to their cytoplasmic tails to form multimolecular IACs which establish the linkage between integrins and the cell cytoskeleton (Winograd-Katz et al., 2014). Integrins together with their associated IAC components have been termed the adhesome (Zaidel-Bar et al., 2007; Kuo et al., 2011; Schiller et al., 2011; Byron et al., 2015; Jones et al., 2015). The fate of such a complex depends on cell type, composition of ECM, matrix stiffness, integrin subtype, etc. ultimately leading to formation of a variety of IAC-induced structures including nascent adhesions, FAs, fibrillar adhesions, podosomes and invadopodia (Klapholz and Brown, 2017; Gough and Goult, 2018). Novel adhesive structures termed reticular adhesions (RAs) were identified in 2018, which are rich in integrin αvβ5 but devoid of most of the typical cytoskeletal components found in other IACs, and, instead, are connected to the clathrin machinery (Lock et al., 2018). The association between integrins and F-actin occurs through proteins such as talin and vinculin (Atherton et al., 2015). Talin also coordinates the microtubule (MT) cytoskeleton at adhesion sites through the interaction with KN motif and ankyrin repeat domain-containing (KANK) proteins (Bouchet et al., 2016; Sun et al., 2016), which stimulates FA turnover (Stehbens and Wittmann, 2012).

Several protocols have been developed to purify ventral IACs from 2D cell cultures (Humphries et al., 2009; Kuo et al., 2011; Schiller et al., 2011; Jones et al., 2015). A variety of cell types have been investigated using these methods. However, most IAC preparations have been isolated from cells seeded on fibronectin. Seven of these datasets have been analyzed together which led to the definition of a fibronectin-induced "meta adhesome" composed of over 2400 proteins. The meta adhesome was further reduced to 60 core proteins, termed as the "consensus adhesome" i.e., proteins that are most frequently identified in IACs (Winograd-Katz et al., 2014; Horton et al., 2015). The consensus adhesome was obtained from cells seeded on fibronectin, and therefore its composition reflects components of integrin heterodimers α5β1 and αVβ3 (Horton et al., 2016). It was also shown to be centered around potential axes that link integrins to actin, namely ILK-PINCH-parvin-kindlin, FAK-paxillin, talin-vinculin and α-actinin-zyxin-VASP axis (Humphries et al., 2019).

The repertoire of integrins in tumor cells and the composition of ECM, deposited by tumor and stromal cells, both contribute to integrin signaling in promoting invasive growth and metastasis (Cooper and Giancotti, 2019). Integrin signaling confers resistance of cancer cells to chemotherapy (Stojanovic et al., 2016) and radiotherapy (Eke et al., 2018). Conversely, knockdown of integrins may sensitize tumor cells to both chemo- and radiotherapy (Stojanovic et al., 2018; Wang et al., 2019). Therefore, integrins are promising targets to be combined with classical therapy, especially αV integrins which play non-essential roles in development but are involved in tumor growth and angiogenesis (Seguin et al., 2015). The integrin αV subunit is known to form heterodimers with one of five different β subunits (β1, β3, β5, β6, and β8) (Hynes, 2002). Among these integrins, αVβ3 and αVβ5 have been extensively studied. Integrin αVβ3, highly expressed in melanoma (Nip et al., 1992; Danen et al., 1995), has a pivotal role in melanoma growth (Mitjans et al., 2000), initiates the transition from the benign radial growth phase to the malignant vertical growth phase (Albelda et al., 1990), and its expression is increased in brain metastases compared to primary melanoma (Vogetseder et al., 2013). The importance of integrin αVβ5 was also demonstrated in melanoma, showing its involvement in the highly aggressive phenotype of melanoma cells expressing neuropilin 1 (Ruffini et al., 2015). Integrin αVβ5 has been shown to trigger formation of FAs (De Deyne et al., 1998). Moreover, it has been recently shown that integrin αVβ5 is the predominant integrin used by cells in long term culture, not only in FAs but also in RAs. RAs are morphologically and dynamically distinct from classical FAs, formed during interphase and preserved at cell-ECM attachment sites throughout cell division (Lock et al., 2018, 2019).

Using the melanoma cell line MDA-MB-435S, which expresses only integrins β3 and β5 as αV integrins binding partners, we showed that αV knockdown increases sensitivity to antitumor drugs that target MTs, paclitaxel (PTX) and vincristine (VCR). We also identified integrin αVβ5 as a key integrin in this process. Concomitantly, we demonstrated that integrin αV knockdown decreases migration and invasion, a process in which both integrins αVβ3 and αVβ5 are involved (Stojanovic et al., 2018). Here, we aimed to identify the integrin(s) used by MDA-MB-435S cells in cell culture and to catalog changes in IAC composition upon integrin αV knockdown. We report that integrin αVβ5 is the predominant integrin used by MDA-MB-435S cells in long term culture and reveal the composition of integrin αVβ5 adhesion complexes. We show that one of the identified components is KANK2, whose knockdown in MDA-MB-435S cells mimics increased sensitivity to MT poisons and decreased migration upon

Abbreviations: AHNAK, neuroblast differentiation-associated protein; ANOVA, related-measure two-way analysis of variance; cDDP, cisplatin; CLASP, cytoplasmic linker-associated proteins; CMSC, cortical microtubule stabilizing complex; DMEM, Dulbecco's modified Eagle's medium; DMSO, dimethyl sulfoxide; DTBP, dimethyl 3,3′-dithiobispropionimidate, Wang and Richard's reagent; ECM, extracellular matrix; EDTA, ethylenediaminetetraacetic acid; EdU, 5-ethynyl-2′-deoxyuridine; ELKS, ELKS/RAB6-interacting/CAST family member 1; FA, focal adhesion; FAK, focal adhesion kinase; FBS, fetal bovine serum; FN, fibronectin; HEPES, hydroxyethyl piperazineethanesulfonic acid; IAC, integrin adhesion complex; IF, immunofluorescence; ILK, integrin linked kinase; IRM, interference reflection microscopy; KANK, KN motif and ankyrin repeat domain-containing proteins; KIF21A, kinesin family member 21A; LL5β, pleckstrin homology (PH)–like domain, family B, member 2 (PHLDB2); MACF1, MT-actin cross-linking factor 1; MS, mass spectrometry; MT, microtubule; MTT, 3-((4,5-dimethylthiazol-2-yl)-2,5-diphenyltetrazolium bromide); PBS, phosphate-buffered saline; PINCH, particularly interesting new cys-his protein 1; PTX, paclitaxel; RA, reticular adhesion; Src, non-receptor tyrosin kinase Src; VASP, vasodilator-stimulated phosphoprotein; VCR, vincristine; WB, western blot WB.

integrin αV knockdown. Therefore, KANK2 is crucial for the functional connection of integrin αVβ5-containing FAs with MTs and represents a potential target for improvement of melanoma therapy.

MATERIALS AND METHODS

Cells and Isolation of Stable Cell Clones

Human melanoma cell line MDA-MB-435S (a spindle-shaped variant of the parental MDA-MB-435) was obtained from the American Type Culture Collection (ATCC, United States). Cells were grown in DMEM (Invitrogen, United States), and supplemented with 10% (v/v) FBS (Invitrogen, United States) at 37°C with 5% CO_2 (v/v) in a humidified atmosphere. To construct MDA-MB-435S clones with decreased expression of integrin αV subunit, pSUPER vector system for the expression of shRNA was used (OligoEngine, United States). Briefly, oligonucleotides were constructed according to the sequence of siRNA specific for integrin subunit αV (s7568- Ambion, United States), previously used in transient transfection in the same cell model (Stojanovic et al., 2018). Oligonucleotides P1 – GATCCCCGAATATCGGTTGGATTATATTCAAGAGA TATAATCCAACCGATATTCTTTTTA and P2 – AGCTTAAA AAGAATATCGGTTGGATTATATCTCTTGAATATAATCCAA CCGATATTCGGG were annealed and cloned into *Hin*dIII (NEB, United Kingdom) and *Bgl*II (Thermo Fisher Scientific, United States) digested vector. Resulting plasmid pSuper shαV was purified using Miniprep columns (Qiagen, Germany) and transfected into MDA-MB-435S cells using Lipofectamine (Thermo Fisher Scientific, United States). Clones 2αV and 3αV were selected using puromycin (0.2 μg/ml, Sigma-Aldrich, United States) according to expression of integrin αV measured by flow cytometry.

Drugs, Chemicals, Determination of Cell Survival, and Transient siRNA Transfection

Cis-diamminedichloroplatinum (cisplatin, CDDP) was dissolved in water and stored at −20°C. Vincristine and paclitaxel (all Sigma-Aldrich, United States) were dissolved in phosphate-buffered saline (PBS) and DMSO, respectively, and stored at −20°C. The 3-((4,5-dimethylthiazol-2-yl)-2,5-diphenyltetrazolium bromide) (MTT) (Millipore, United States) was dissolved in PBS and stored at 4°C. The sensitivity of cells to antitumor drugs was determined using MTT assay. Briefly, 24 h after seeding in 96-well tissue culture plates (1–1.2 × 10^4 cells/well) cells were treated with different concentrations of antitumor drugs. Seventy-two hours later, the absorbance of MTT-formazan product dissolved in DMSO was measured with a microplate reader (Awareness Technology, Inc., United States) at 600 nm. Single siRNA specific for KANK2 (target sequence ATGTCAACGTGCAAGATGA; Sigma-Aldrich) was used at 20 nM, validated by western blot analysis (WB) and immunofluorescence (IF) using KANK2 specific antibody as previously described (Bouchet et al., 2016) (**Supplementary Table S1**). Twenty-four hours after KANK2 knockdown cells were used in MTT or migration assays.

Determination of Cell Migration

For monitoring cell migration, serum-starved (24 h) cells [8 × 10^4 cells in 0.5 mL of DMEM containing 0.1% (w/v) BSA] were placed in the Transwell Cell Culture Inserts (pore size, 8 μm) (Corning, United States) and left to migrate for 22 h toward 10% (v/v) FBS in DMEM as a chemoattractant. Cells on the upper side of the filters were removed with cotton-tipped swabs, the filters were fixed in paraformaldehyde for 15 min and stained with 1% (w/v) crystal violet in PBS for 90 min. Cells on the underside of the filters were photographed using Olympus BX51TF microscope (five images/sample). The number of cells was determined using ImageJ (NIH, United States) software.

Determination of Integrin αVβ3, αVβ5, αV, and β1 Expression by Flow Cytometry

Flow cytometry to analyze the expression of αVβ3, αVβ5, αV, and β1 was performed using integrin subunit- or heterodimer-specific monoclonal antibodies (MAb). Briefly, adherent cells were grown in tissue culture dishes, detached by EDTA (Invitrogen, United States) and washed twice with PBS. Membrane fluorescence staining was performed using unlabeled primary antibodies (1 h, 4°C) while its binding was revealed by incubation (30 min, 4°C) of FITC-conjugated anti-mouse antibody. Isotype control samples were incubated with mouse IgG1 followed by FITC-conjugated anti-mouse antibody. Flow cytometry experiments were performed using FACSCalibur, while cell acquisition was made using BD CellQuest software package (all BD Biosciences, United States). Data were analyzed using FCS Express 3 (*De Novo* Software, United States) software. All antibodies are listed in **Supplementary Table S1**.

Assessment of Apoptosis and Cell Proliferation

The induction of apoptosis in MDA-MB-435S, 2αV, and 3αV cells was determined by the Annexin V-FITC (BD Pharmingen, Germany)/PI double-staining. Cells were treated for 72 h with PTX (0.004 μg/mL) and apoptosis was measured by flow cytometry. To monitor cell proliferation, Click-iT® assay was used according to the manufacturer's instructions (Thermo Fisher Scientific, United States). Briefly, 2.75 × 10^5 cells/well were seeded on 6-well plate and grown for 72 h in DMEM supplemented with 10% (v/v) FBS. Two hours before harvesting, modified thymidine analog EdU (5-ethynyl-2′-deoxyuridine, final concentration 10 μM) was added. Cells were collected, fixed with 4% (w/v) paraformaldehyde, permeabilized with saponin, stained with AF 488 azide (in the presence of $CuSO_4$) and analyzed by flow cytometry. To determine the proliferation rate, the frequencies of the proliferative (EdU +) cells were compared.

Confocal Microscopy and Live Cell Imaging

For confocal microscopy, 48 h after being seeded on coverslips, cells were fixed with 2% (w/v) paraformaldehyde (methanol was

used only when staining of α-tubulin/KANK2 was performed), permeabilized with 0.1% (v/v) Triton X-100, incubated with the appropriate antibodies for 1 h, followed by incubation with the appropriate secondary antibody for 1 h. F-actin fibers were stained with rhodamine phalloidin (Sigma-Aldrich, United States) while MTs were stained with antibody against α-tubulin (Sigma-Aldrich, United States), and slides mounted in DAPI Fluoromount-G (SouthernBiotech, United States) (all antibodies are listed in **Supplementary Table S1**). Fluorescence and respective IRM images were acquired using HC PL APOCS2 63 × /1.40 oil-immersion objective on an inverted confocal microscope (Leica TCS SP8 X, Leica Microsystems, Germany), with the focus adjusted to the adhesion sites of cells at the upper surface of glass coverslip (Weber, 2003). Images were analyzed using LAS X (Leica Microsystems, Germany) and ImageJ (NIH, United States) software. For quantification of FA proteins/KANK2, images were processed using ImageJ and threshold was set to restrict analysis to sites where the signals from the protein staining overlaps with the F-actin/MT staining at the tip of the actin stress fibers/MT fibers. For the stress fiber quantification, only those fibers that end with FAs, marked by paxillin staining, were identified as stress fibers and quantified using ImageJ. For time-lapse live cell imaging, cells were seeded on 35 mm glass bottom dishes (Ibidi, Martinsried, Germany) and 2–3 fields containing cells were imaged every 44 s for 18–20 h using HC PL APOCS2 40 × /1.30 oil-immersion objective on the Leica TCS SP8 X microscope equipped with a top stage incubator at 37°C. Images were analyzed using LAS X. EVOS cell imaging system (Thermo Fisher Scientific, United States) was used to obtain cell morphology images of cells seeded in 6-well plates, every 24 h for a 72 h period. Images were analyzed using ImageJ (NIH, United States) software.

Isolation of IACs, Sample Preparation for Mass Spectrometry, and Data Analysis

Integrin adhesion complexes were isolated as previously described (Jones et al., 2015). In short, cells (2–2.5 × 10^6, depending on cell clone, to obtain similar cell number 48 h later) were plated on 10 cm diameter cell culture dishes (at least six dishes per cell line) and grown in DMEM supplemented with 10% (v/v) FBS. After 48 h, the medium was removed, cells were washed with DMEM-HEPES and incubated with Wang and Richard's reagent for 5 min (6 mM DTBP, Thermo Fisher Scientific, United States). At the same time, cells in an additional plate were counted to ensure equal cell number per sample. DTBP was quenched by 0.03M Tris-HCl (pH 8) and cells were lysed using modified RIPA buffer. Cell bodies were removed by high-pressure washing and remaining adhesions were collected by scraping. Samples containing isolated IACs were acetone precipitated, dissolved in Laemmli buffer and further processed either for MS or WB analysis.

Samples were prepared as previously described (Humphries et al., 2009), using a slightly modified procedure. Briefly, samples were loaded onto gradient gels (NuPage 4–12% Bis-Tris protein gels, Thermo Fisher Scientific, United Kingdom) and electrophoresis was performed for 3 min (200V). Protein bands were stained with InstantBlue (Expedeon, United Kingdom), followed by excision and destaining using series of alternate washing steps with ammonium bicarbonate (Fluka, United States) and acetonitrile (Thermo Fisher Scientific, United Kingdom). Washing and drying steps were made in 96-well perforated plates (GlySci, United States). Gel pieces were dried with acetonitrile and additional drying was performed using vacuum centrifuge. Samples were reduced with dithiothreitol (DTT, 1 h at 56°C) and alkylated using 55 mM iodoacetamide (37°C, 45 min, dark) (both Sigma-Aldrich, United States). After series of washing and drying steps, gel pieces were incubated with trypsin (1.25 ng/μL, Promega, United States) and incubated for 45 min at 4°C, followed by an overnight incubation at 37°C. Peptides were collected and extracted using acetonitrile supplemented with formic acid (Sigma-Aldrich, United States), then dried and resuspended in a solution of 5% (v/v) acetonitrile plus 0.1% (v/v) formic acid. Peptides were desalted using OLIGO R3 beads (Life technologies, United States) using 96-well plates with PVDF membranes (Corning, United States). Desalting was performed with a 0.1% formic acid wash steps before being eluted twice with 50% acetonitrile in 0.1% formic acid. Peptides were subsequently dried and resuspended in a solution of 5% (v/v) acetonitrile plus 0.1% (v/v) formic acid for LC-MS/MS analysis.

Samples were analyzed using a modified version of the LC-MS/MS method previously described (Horton et al., 2015). Briefly, an UltiMate® 3000 Rapid Separation LC (RSLC, United States) coupled to an Orbitrap Elite mass detector (Thermo Fisher Scientific, United States) with electrospray ionization. Peptide mixtures were eluted for 44 min using a gradient containing 92% of solution A (0.1% formic acid in water) and 8% up to 33% of solution B (0.1% formic acid in acetonitrile). Solvent flow was set to 300 nL per minute. To identify proteins, data were searched against the human Swissprot database (version 2018_01) using Mascot (Matrix science, version 2.5.1). Fragment ion tolerance was set to 0.50 Da, while parent ion tolerance was 5 PPM. Protein identifications were further refined using Scaffold (Proteome software). Protein (99.9%) and peptide (95%) probabilities were assigned using the Protein Prophet algorithm (Nesvizhskii et al., 2003) as incorporated by Scaffold including a minimum of four unique peptides per each protein.

PPI Network Formation, Functional Enrichment, Gene Ontology Analysis, and MS Data Visualization

Human protein–protein interactions were loaded from STRING database, using stringApp (confidence score cut-off = 0.40, maximum additional interactors = 0) (Doncheva et al., 2019) for Cytoscape software (version 3.7.1) (Shannon et al., 2003). Functional annotation was performed using the Database for annotation, visualization and integrated discovery (DAVID), version 6.8 (Huang da et al., 2009a) and Panther GO database (Thomas et al., 2003), while the literature search was performed in case of cortical stabilization microtubule complex (Lansbergen et al., 2006; Astro et al., 2014; Bouchet et al., 2016; Noordstra and Akhmanova, 2017).

Functional enrichment was performed using DAVID_CC subontology list (Benjamini–Hochberg corrected P-value < 0.05, EASE score < 0.1, at least four identified proteins). To summarize the gene ontology terms and place them in similarity-based space, REViGO tool, with the following setup (comparison of corrected P-values related to GO terms were used, allowed similarity: small (0.5), semantic similarity measure to use: Resnik-normalized) was used (Supek et al., 2011). QSpec Spectral counter tool was used to provide the statistical measure of differentially expressed proteins in MDA-MB-435S versus 2αV datasets and MDA-MB-435S versus 3αV datasets (Choi et al., 2008). For visualization of differentially expressed proteins, volcano plot (GraphPad Prism) with the following setup was created: fold change > 1.5 (MDA MB 435S/2αV and MDA MB 435S/3αV, respectively), $-\log(\text{FDR}) > 1$. Fold change was calculated according to Qspec output values.

Western Blot Analysis

Isolated IACs from at least six 10 cm diameter culture dishes were mixed with 2x loading buffer and heated for 20 min at 70°C. Proteins were loaded onto gradient pre-cast gels (Biorad, United States), separated with SDS-PAGE and transferred to a nitrocellulose membrane (Amersham, Germany). For assessment of successful KANK2 knockdown cells were lysed using RIPA buffer, mixed with 5x loading buffer, separated by SDS-PAGE and transferred to nitrocellulose membrane (Amersham, Germany). The membrane was blocked in 5% (w/v) non-fat dry milk, and incubated with the appropriate antibodies, followed by incubation with horseradish peroxidase-coupled secondary antibody (GE Healthcare, United States, Invitrogen, United States) (**Supplementary Table S1**). Detection was performed using chemiluminescence (GE Healthcare) and visualized using iBright CL1000 (Thermo Fisher Scientific, United States).

Statistical Analysis

Each experiment was repeated at least three times, and GraphPad Prism v5.0 (GraphPad Software, United States) was used to analyze the data. All data from MTT experiments were analyzed by unpaired Student's t-test, and expressed as mean ± standard deviation (SD). ns, not significant; $^{*}P < 0.05$; $^{**}P < 0.01$; $^{***}P < 0.001$. Data obtained from migration and IF were analyzed by related measure one-way ANOVA with Dunnett's multiple comparison: $^{*}P < 0.05$, $^{**}P < 0.01$, $^{***}P < 0.001$.

RESULTS

MDA-MB-435S Clones With Stable Knockdown of Integrin αV Subunit Display Increased Sensitivity to Microtubule Poisons and Decreased Cell Migration

We have recently shown that knockdown of integrin subunit αV, via transient transfection of integrin αV-specific siRNA, increased sensitivity of MDA-MB-435S cells to PTX and VCR and decreased migration. In a series of experiments, the effect on sensitivity to MT poisons was ascribed to integrin αVβ5 but not to integrin αVβ3. On the other hand, both αV integrins, αVβ3 and αVβ5, were implicated in the regulation of cell migration (Stojanovic et al., 2018). In the present work, our aim was to unravel a possible link between these alterations in sensitivity to MT poisons and migration and the adhesome composition. When β5 was knocked down, we observed upregulation of integrin αVβ3, and vice versa. We named this phenomenon the integrin balance effect (Stojanovic et al., 2018). For this reason, we cataloged the adhesome of MDA-MB-435S cells and compared it to the adhesome of cells upon integrin αV knockdown. We isolated two MDA-MB-435S clones stably transfected with a plasmid expressing shRNA specific for integrin αV: clones 2αV and 3αV. The surface expression of integrin subunit αV and integrin heterodimers αVβ3 and αVβ5 in both clones was substantially decreased, as measured by flow cytometry. Additionally, we observed slightly lower expression of these integrins in 3αV compared to 2αV. Since the MDA-MB-435S cell line does not express integrin αVβ1 (Taherian et al., 2011), the knockdown of integrin αV did not affect the expression of integrin β1 heterodimers (**Figure 1**). Both clones showed increased sensitivity to PTX and VCR and decreased sensitivity to cDDP (**Figure 2A**), which is in line with our previous results using transient transfection of integrin αV- or β5-specific siRNA (Stojanovic et al., 2018). In addition, 72 h after PTX treatment a greater number of apoptotic cells was found in the cultures of both clones 2αV and 3αV as compared to parental MDA-MB-435S cells (30 and 32% compared to 17%, respectively) (**Figure 2B**). Decreased expression of integrins αVβ3 and αVβ5 in clones 2αV and 3αV did not affect cell proliferation (**Figure 2C**). However, when cells were cultivated for 72 h, starting with the same number of plated cells, we observed decreased number of 2αV cells and particularly 3αV cells, showing a dose response relationship with integrin αV knockdown (**Figure 2D**). In addition, when culturing cells for 48 h to perform IF staining (**Figure 3**), we observed that clones 2αV and 3αV were smaller than MDA-MB-435S cells. We assumed that delayed adhesion to ECM proteins, due to integrin αV knockdown, was the main reason for this effect. In order to test this hypothesis, we visualized cell attachment and spreading using live cell microscopy for 12 h following plating (**Figure 2E**), monitored cell spreading within 72 h of growth (**Supplementary Figure S1A**), and analyzed cell surface area (**Supplementary Figure S1B**), size and granularity of cells in suspension using flow cytometry (**Supplementary Figure S1C**). Results showed that although all cells have similar initial rounded sizes in suspension, clones 2αV and 3αV have significantly impaired attachment and spreading when plated on culture dishes compared to parental cells. Finally, decreased migration of both clones compared to MDA-MB-435S cells was observed (**Figure 2F**), which is also in line with our previous results following transient transfection with integrin αV-specific siRNA (Stojanovic et al., 2018). The degree of inhibition of migration correlated with the extent of integrin αV knockdown (**Figures 1**, **2F**).

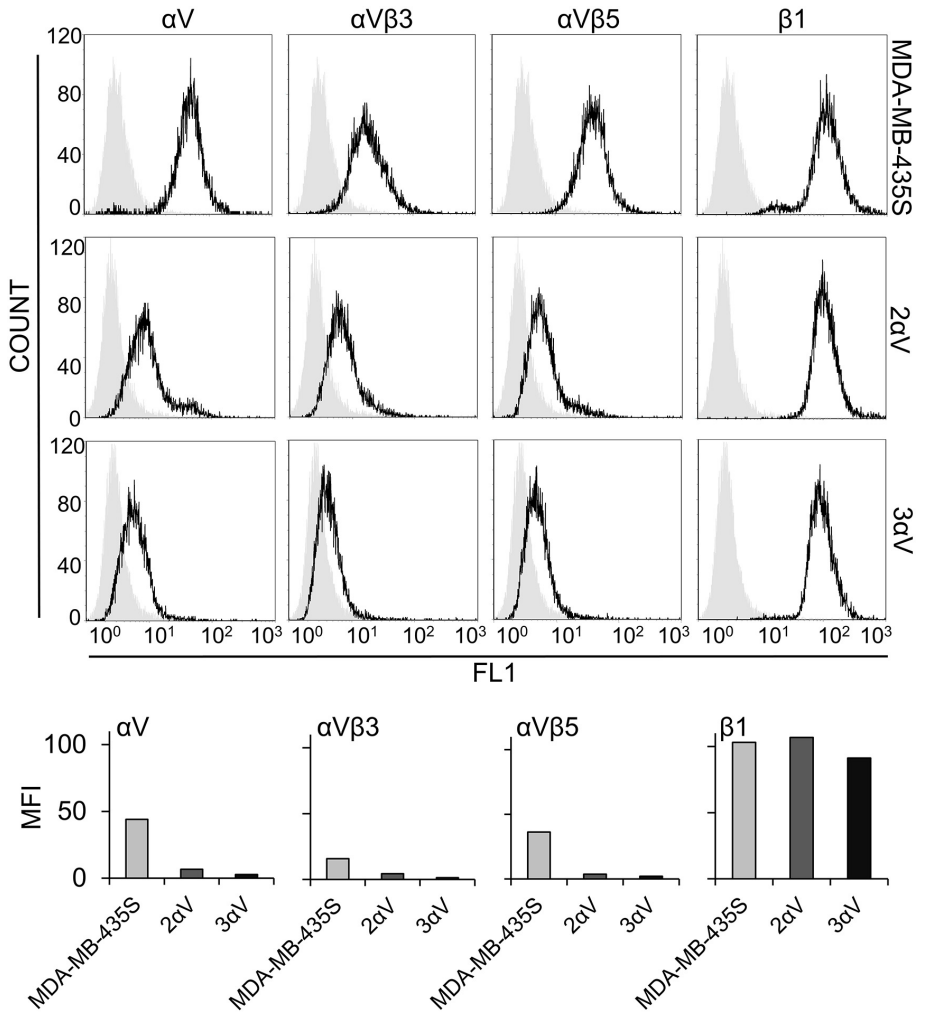

FIGURE 1 | Characterization of the MDA-MB-435S cell model. Surface expression of integrin subunit αV, integrin heterodimers αVβ3 and αVβ5, and integrin subunit β1 in melanoma cell line MDA-MB-435S and clones 2αV and 3αV obtained by stable transfection with integrin αV-specific shRNA. Cells were detached by EDTA and analyzed by flow cytometry upon incubation with antibodies against integrin subunit αV, β1, or integrin heterodimers αVβ3 or αVβ5 (black histogram), and isotype-matched antibody as a negative control (gray histogram), followed by rabbit FITC-conjugated-anti-mouse antibody (upper panel). Results from upper panel were presented as comparisons of MFIs within the cell model (lower panel). Representative data of three independent experiments yielding similar results are shown.

Our recently published data have shown that upon transient knockdown of integrin subunit αV in MDA-MB-435S, the cells showed disorganization of actin with loss of stress fibers and significant loss of paxillin staining at the tips of stress fibers, indicating a reduction in the number of FAs (Stojanovic et al., 2018). We therefore tested whether clones 2αV and 3αV show similar features. IF staining of MDA-MB-435S cells confirmed the formation of well-defined adhesion structures containing integrin αV and paxillin while in clones 2αV and 3αV their number was reduced (**Figure 3A**). Furthermore, both clones had a decreased number of FAs per cell analyzed by counting either integrin αV- or paxillin-positive puncta, as well as a decreased amount of actin stress fibers per cell (**Figure 3B**). In conclusion, the model of MDA-MB-435S-derived stably transfected clones 2αV and 3αV fully mimics the effects of transient transfection with integrin αV-specific siRNA.

Melanoma Cell Line MDA-MB-435S Primarily Utilizes Integrin αVβ5 for Adhesion

To better understand the observed changes in cell migration and sensitivity to microtubule poisons, PTX and VCR, the adhesome of MDA-MB-435S and clones 2αV and 3αV was analyzed. Since cytotoxicity assays (**Figures 2A,B**), as well as IF analysis (**Figure 3**), were performed in cell culture without prior coating with ECM proteins, we analyzed IACs in the same manner. This approach also enabled cell-secreted ECM proteins to be analyzed. We performed MS analysis of isolated IACs from MDA-MB-435S cells and clones 2αV and 3αV following 48 h of growth. IACs were isolated as previously described (Jones et al., 2015). The duration of crosslinking (see section "Materials and Methods") was chosen based on the

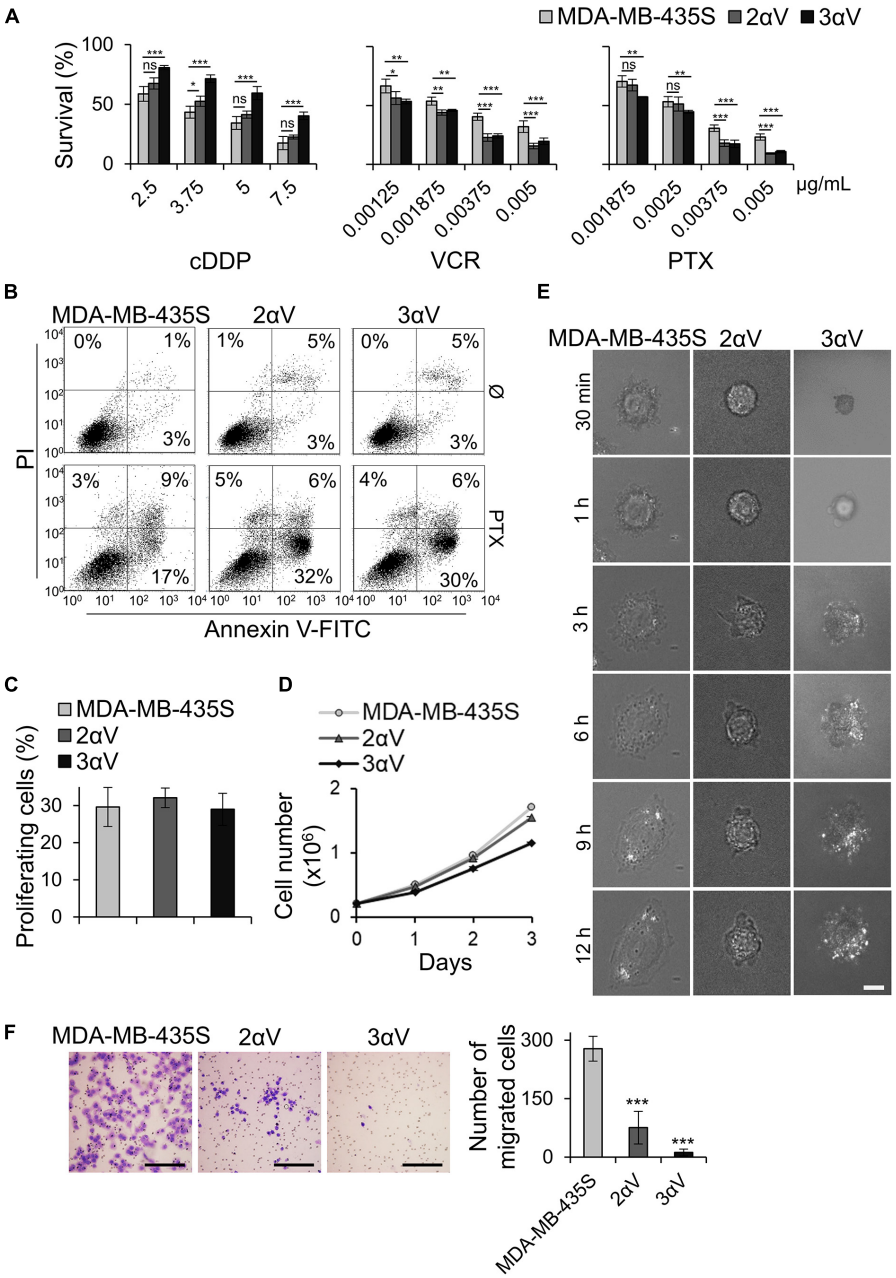

FIGURE 2 | Effect of integrin αV knockdown on cell sensitivity to antitumor drugs, PTX-induced apoptosis, cell proliferation, growth, spreading and migration. **(A)** Clones 2αV and 3αV demonstrate decreased sensitivity to cDDP and increased sensitivity to VCR and PTX as compared to parental MDA-MB-435S cells. Cells were seeded in 96-well plates and 24 h later treated with different concentrations of cDDP, VCR, and PTX. Cytotoxicity was measured by MTT assay. Results presented are representative of three independent experiments with similar results ± SD. Data were analyzed by unpaired Student's *t*-test. ns, not significant; $^{*}P < 0.05$; $^{**}P < 0.01$; $^{***}P < 0.001$. **(B)** Clones 2αV and 3αV upon PTX treatment demonstrate increased apoptosis as compared to MDA-MB-435S cells. Cells were treated with 0.004 μg/mL of PTX for 72 h, harvested for Annexin V/PI staining and analyzed by flow cytometry to discriminate between live (lower left quadrant), apoptotic and/or necrotic cells (right quadrants). The representative data of three independent experiments yielding similar results are shown. **(C)** Cell proliferation in MDA-MB-435S cells and clones 2αV and 3αV. Cell proliferation was measured using ClickIT EdU assay. DNA synthesis was measured upon 2 h cell growth in medium supplemented with EdU and the amount of incorporated EdU was measured by flow cytometry. Comparison of average percentage of EdU + cells from three different experiments are shown. **(D)** Growth curve of MDA-MB-435S cells and clones 2αV and 3αV. Cells were seeded in 10 cm culture plates and counted on days 1, 2, and 3. The results presented are representative of three independent experiments with similar results. **(E)** Cell spreading of MDA-MB-435S cells and clones 2αV and 3αV. Live cell imaging was performed during 18–20 h upon seeding and cell spreading was compared using time lapse IRM images (30 min–12 h). Scale bar = 10 μm. **(F)** Decreased migration of clones 2αV and 3αV as compared to MDA-MB-435S cells. Serum starved (24 h) cells were seeded in Transwell cell culture inserts and left to migrate for 22 h toward serum. Cells on the underside of the inserts were stained with crystal violet, photographed, and counted. Scale bar = 100 μm. Averages of five microscope fields of three independently performed experiments ± SD are shown ($n = 3$). Data were analyzed by one-way ANOVA with Dunnett's multiple Comparison. $^{***}P < 0.001$.

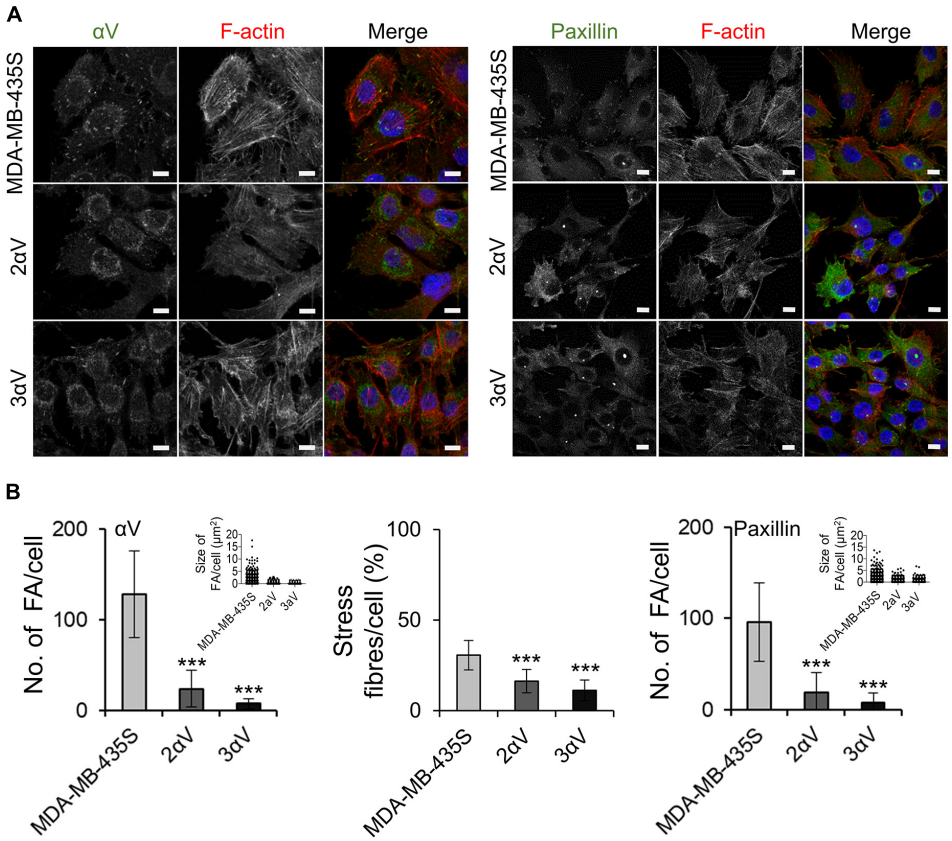

FIGURE 3 | Clones 2αV and 3αV have decreased number and size of FAs and decreased amount of stress fibers per cell as compared to MDA-MB-435S cells. **(A)** Clones 2αV and 3αV show decreased expression of the integrin subunit αV and the FA marker, paxillin. Forty-eight hours after seeding on coverslips, cells were fixed, permeabilized and stained with antibody against integrin αV or paxillin followed by Alexa-Fluor 488-conjugated antibody (green). F-actin staining (red) was performed in all samples, and nuclei were stained with DAPI (blue). Analysis was performed using TCS SP8 Leica. Scale bar = 10 μm. **(B)** Quantification of αV and paxillin, FA size and % of stress fibers per cell. Data presented as histograms or scatter plots (FA size) represent measurements of > 50 cells and are plotted as mean ± SD (n = 3). Data were analyzed by one-way ANOVA with Dunnett's multiple comparison. ***$P < 0.001$.

WB analysis of isolated IACs using antibodies against well-defined adhesion complex components, such as paxillin and non-receptor tyrosine kinase Src [pSrc (Y418)] (data not shown). IACs were then isolated from MDA-MB-435S and clones 2αV and 3αV and the isolation procedure performed in triplicate for MDA-MB-435S and 3αV and in duplicate for 2αV. Samples were analyzed by LC-MS/MS and spectral counts used as a measure of protein abundance. These analyses detected 153 proteins with at least 99% confidence from IACs isolated from MDA-MB-435S cells (**Supplementary Table S2.1**), including 120 proteins that were termed as meta-adhesome proteins (Horton et al., 2015). Label-free quantification demonstrated good reproducibility between data either from technical or biological replicates.

To provide an overall view of both components of the isolated IACs in MDA-MB-435S cells and of components of the ECM, a protein–protein interaction network was constructed (**Figure 4A** and **Supplementary Table S2.2**). The most surprising finding was that the only integrin receptor subunits identified in MDA-MB-435S cells were αV and β5, indicating that these cells primarily utilize integrin αVβ5 for adhesion in long term 2D culture (48 h). The majority of identified proteins were actin-binding and ECM proteins. We also identified proteins reported to bind MT and intermediate filaments, several GTPases and kinases, together with components of the CMSC (Noordstra and Akhmanova, 2017; Chen et al., 2018).

To further analyze the dataset, Gene Ontology (GO) enrichment analysis was performed on proteins identified in IACs isolated from MDA-MB-435S cells, using the online bioinformatics tools available via the Database for Annotation, Visualization and Integrated Discovery (DAVID[1]) (Huang da et al., 2009b), and GO terms were visualized using REViGO tool (Supek et al., 2011). Analysis confirmed a significant enrichment of GO terms related to ECM, extracellular exosome, FA and actin cytoskeleton (**Figure 4B** and **Supplementary Table S2.3**).

Integrin αVβ5-Induced Interaction Networks

A volcano plot was constructed displaying proteins whose abundance was different in clones 2αV (red dots) or 3αV (black

[1]http://david.abcc.ncifcrf.gov/home.jsp

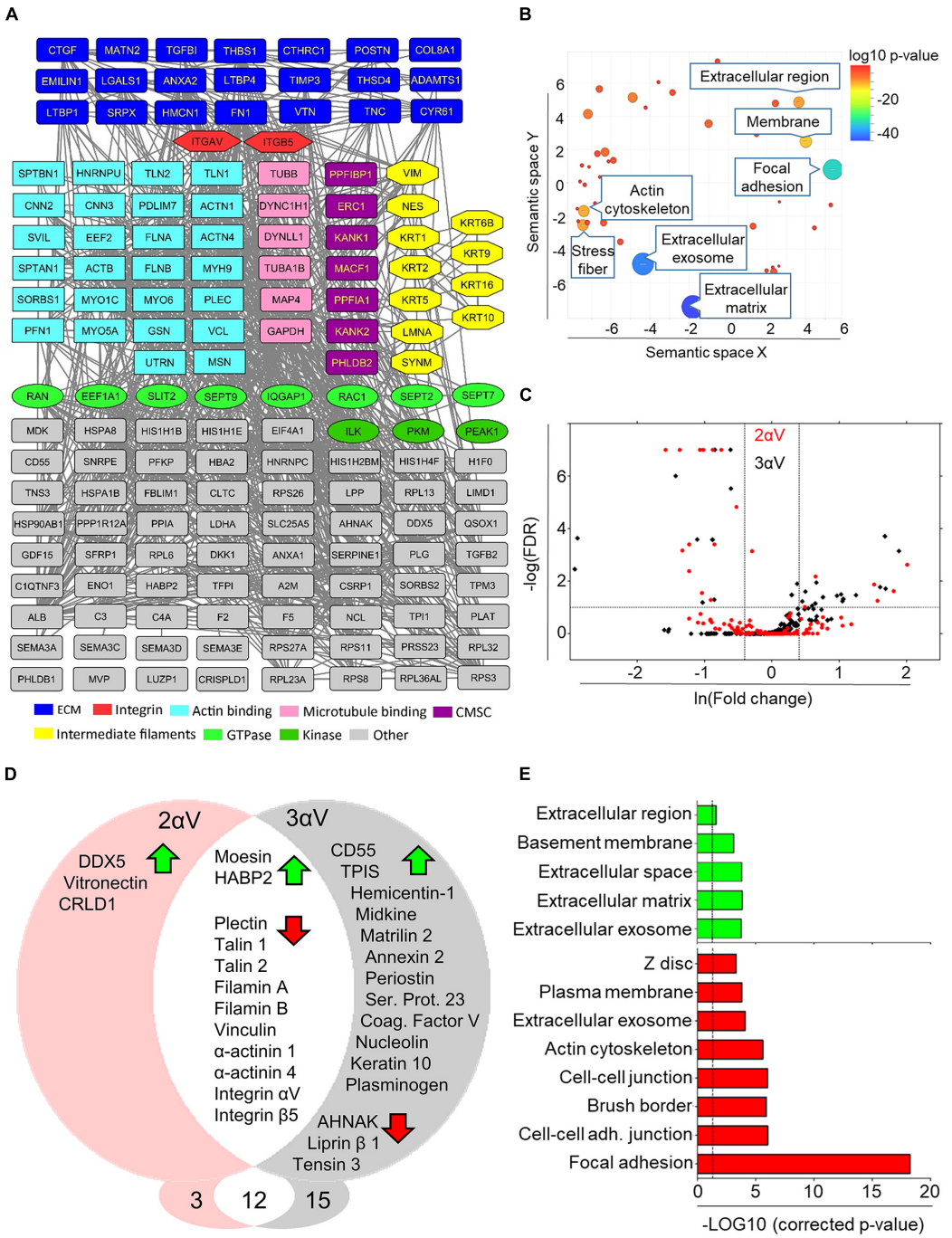

FIGURE 4 | Mass spectrometry analysis of IACs isolated from MDA-MB-435S cells and clones 2αV and 3αV. **(A)** Protein–protein interaction network of components identified by MS in IACs isolated form MDA-MB-435S cells. Shapes represent identified proteins and are labeled with gene symbols, arranged and colored according to their functional group as indicated (CMSC). In case of multiple functional terms assigned for each protein, the molecular function assigned by both databases has been chosen for interpretation of results. **(B)** Total identified IAC proteins in MDA-MB-435S cells (number of spectral counts ≥ 4, FDR < 5%, probability for protein identification ≥ 99.9%) were annotated using David GO database. To determine the sample enrichment, *P*-values related to GO terms of cellular components (GOTERM_CC_DIRECT), were used. Analysis of gene ontology terms was performed using REViGO tool. Statistically significant GO terms ($P = 0.05$) were presented from highest *P*-value (bottom) to the lowest (top). **(C)** Volcano plot of MDA-MB-435S versus 2αV (red) and 3αV (black). To determine the significantly changed proteins −Log (FDR) ≥ 1 and fold change ≥ 1.5 were used. Upper left quadrant – proteins detected at lower level of spectra, upper right quadrant – proteins detected at higher level of spectra. **(D)** Venn diagram – proteins with higher (green arrow) and lower (red arrow) level of spectra detected in clones 2αV and 3αV versus MDA-MB-435S cells. Proteins found in both clones with changed abundances were showed in the intersected white area of the diagram. **(E)** DAVID GO analysis of proteins detected with higher (green arrow) and lower (red arrow) abundances. Statistically significant GO terms ($P = 0.05$; dashed line) were presented from highest *P*-value (bottom) to the lowest (top).

dots) compared to parental cells (**Figure 4C**). The differences observed in clones 2αV and 3αV, compared to MDA-MB-435S cells, were summarized using a Venn diagram (**Figure 4D**). As expected, both clones showed reduced levels of integrins αV and β5 compared to control cells. IAC proteins detected at lower levels in clones 2αV and 3αV are in the category of proteins detected by high number of spectra (**Supplementary Table S2**), and they belong mostly to the actin binding subgroup of the adhesome: plectin, talin 1 and 2, filamin A and B, α-actinin 1 and 4, and vinculin. Additionally, lower levels of three adhesome proteins, liprin β1, AHNAK and tensin 3, were found only in clone 3αV. We also observed higher levels of 17 proteins upon integrin αV knockdown in either 2αV (5), 3αV (14), or both (2) (**Figure 4D**), all belonging to the group of proteins identified by lower number of spectra (**Supplementary Table S2.4**). DAVID GO analysis of IAC proteins with lower abundance in clones 2αV or 3αV, compared to MDA-MB-435S cells, suggested that they are mostly components of FAs. Conversely, proteins present in higher levels in clones 2αV or 3αV as compared to MDA-MB-435S cells were classified as ECM or extracellular exosome proteins (**Figure 4E** and **Supplementary Table S2.4**).

We compared our adhesome protein dataset with those previously reported in the literature (Winograd-Katz et al., 2014; Horton et al., 2015). However, it should be noted that this adhesome dataset differed in that it was not obtained from cells seeded on fibronectin, but upon cultivation of cells for 48 h without prior coating with any ECM component. Therefore, it was not surprising that, unlike other reported adhesomes, we detected many ECM proteins secreted by the cells themselves. More specifically, from 153 proteins that we identified in our adhesome, 120 were reported in earlier studies (**Supplementary Table S2.1**). DAVID GO analysis of the remaining 33 proteins showed that they were mostly related with extracellular proteins (exosome and ECM proteins; **Supplementary Table S2.5**). In addition, we investigated whether any proteins were differentially expressed in our cell model which might indicate that they are specific for either the integrin αV adhesome or matrisome. We identified only one, i.e., Hyaluronan Binding Protein 2 (HABP2) for which the increased abundance had been observed in cell clones with decreased expression of integrin αV. Interestingly, we have observed the increased abundance of HABP2 in another melanoma cell line RPMI-7951 cell model upon transient knockdown of integrin αV (data not shown, manuscript in preparation). HABP2 is the extracellular serine protease which play a role in non-small lung cancer progression (Mirzapoiazova et al., 2015) but its role in melanoma is unknown.

Next we validated data from MS using IF and WB. We selected two proteins in clone 2αV with the largest decrease, vinculin and talin, and one protein with a low but still significant decrease, α-actinin 1 (**Supplementary Table S2**). IF analysis showed a lower number of FAs per cell according to vinculin or talin 1/2 labeling, as well as a reduced area of α-actinin 1 labeling in both clones compared to MDA-MB-435S cells (**Figures 5A,B**). Of note, although they were not identified by MS, we analyzed the expression of pFAK (Y397) and pSrc (Y418) using IF and found changes in their expression, which is in line with the decreased number of FAs (**Supplementary Figure S2**). Finally, WB was performed on IAC isolates, which confirmed decreased levels of filamin A, talin 1/2, vinculin, α-actinin 1, α-actinin 4, liprin β1, and FA marker protein paxillin (**Figure 5C** and **Supplementary Figure S5**).

Integrin αVβ5 Adhesion Complexes Are Composed of Focal and Reticular Adhesions

Our results have shown that integrin αVβ5 is the preferential integrin used in cell culture by melanoma cell line MDA-MB-435S (**Figure 4**). Stable knockdown of integrin αV in clones 2αV and 3αV decreased the number of integrin αV and β5 peptides detected by MS (**Figure 6A**), which correlated with the results of measurement of integrin αVβ5 surface expression by flow cytometry (**Figure 1**). We have also quantified the number of FAs per cell according to integrin αVβ5 heterodimer-specific antibody staining (**Figures 6B,C**) and observed a similar dose-response relationship as already observed for integrin αV and paxillin (**Figures 3A,B**) or talin 1/2 or vinculin (**Figures 5A,B**). Interestingly, IF analysis has shown that integrin αVβ5 in MDA-MB-435S was also localized further from the cell periphery, forming ring-like or reticular structures, but without recruiting vinculin (**Figure 6D**, left panel). These structures resembled recently described RAs shown to maintain cell–ECM attachment during mitotic rounding and division (Lock et al., 2018). The FAs and RAs were shown to colocalize with dark areas in IRM, indicating their presence at the cell-substrate adhesion sites. Reticular adhesions were also present in cell clone 2αV and also colocalized with dark IRM areas (**Figure 6D**, right panel). Lock et al. (2018) observed a range of defects in β5 depleted cells, including the failure of cytokinesis which resulted in binucleate daughter cells. Indeed, in MDA-MB-435S cells upon integrin αV knockdown we observed more multinucleated cells (**Supplementary Figure S3**).

KANK2 Is a Potential Key Target for Increasing Sensitivity to Microtubule Poisons and Decreasing Migration

A recent report (Bouchet et al., 2016) demonstrated the existence of CMSC in the vicinity of mature FAs that capture MTs, containing CLASPs, kinesin family member 21A (KIF21A), LL5β [also known as pleckstrin homology (PH)–like domain, family B, member 2 (PHLDB2)], liprin α1 and β1, as well as paralogs of KANK. They showed that the CMSC is recruited to FAs by KANK1, which directly interacts with the major FA component, talin. On the other hand, KANK2 was also found adjacent to FAs in regions enriched in liprin β1 and ELKS (known as ERC1 for ELKS/RAB6-interacting/CAST family member 1), and was shown to bind talin directly to MTs (Sun et al., 2016).

As described above, in one of the clones (3αV), we observed a reduced abundance of liprin β1 in IACs (**Figure 4D**), which is a key component of CMSC (Bouchet et al., 2016). However, assessment of MS data (**Supplementary Table S2.1**, marked as YES in CMSC column) showed that liprin β1, although not statistically significant, was also present at a lower abundance in cell clone 2αV. The reduced abundance of liprin β1 was

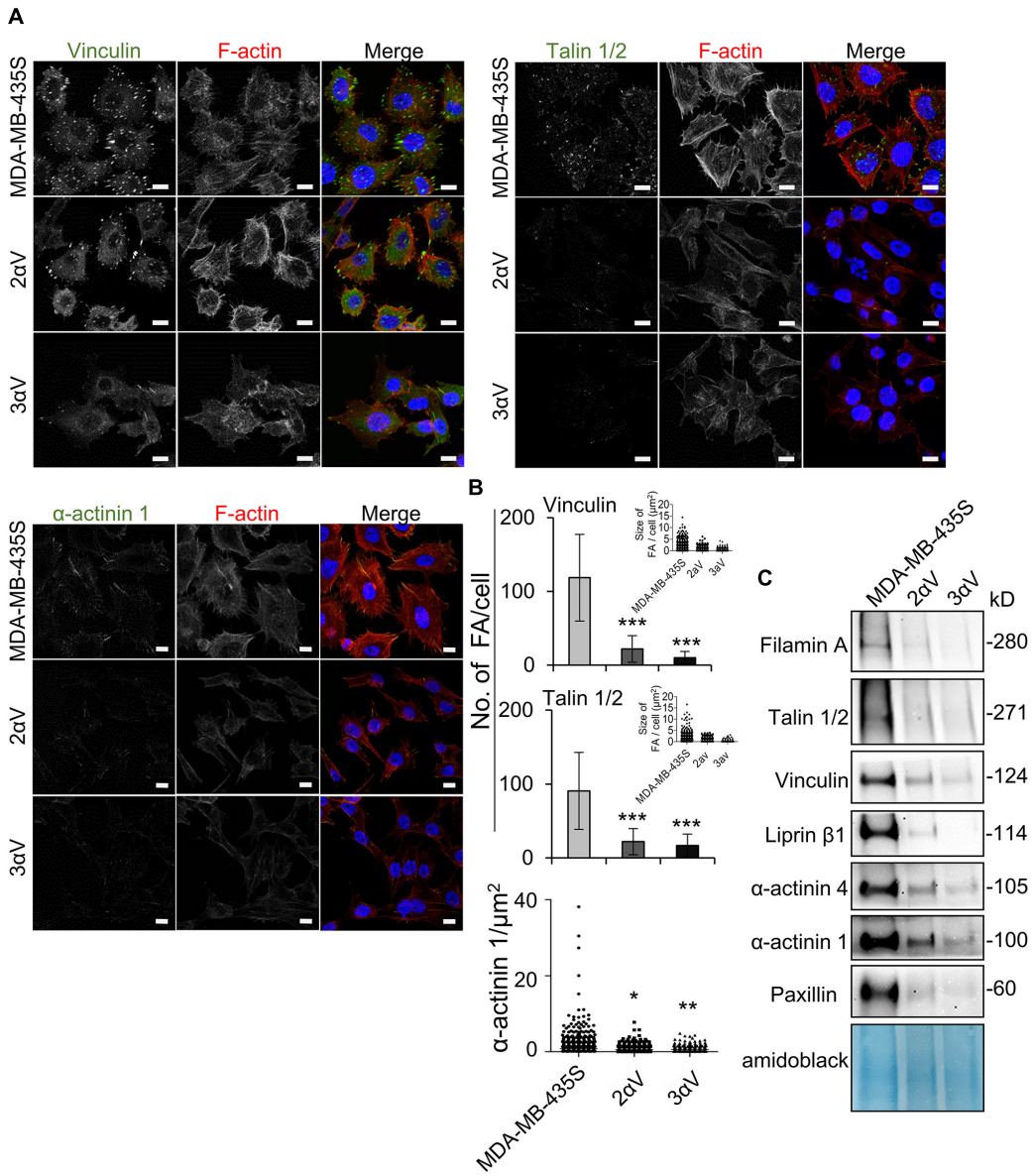

FIGURE 5 | MS data validation in MDA-MB-435S cells and clones 2αV and 3αV. **(A)** Clones 2αV and 3αV show decreased expression of vinculin, talin 1/2 and α-actinin 1 as compared to MDA-MB-435S cells. Forty-eight hours after seeding on coverslips, cells were fixed, permeabilized, incubated with antibodies against vinculin, talin 1/2 or α-actinin 1 antibody, followed by Alexa-Fluor 488-conjugated antibody (green). F-actin staining (red) was performed in all samples, and nuclei were stained with DAPI (blue). Analysis was performed using TCS SP8 Leica. Scale bar = 10 μm. **(B)** Quantification data of results in **(A)** presented as histograms (FA number) and scatter plots (FA or α-actinin 1 size) represent measurements of > 50 cells and are plotted as mean ± SD (n = 3). Data were analyzed by one-way ANOVA with Dunnett's multiple comparison. *$P < 0.05$; **$P < 0.01$; ***$P < 0.001$. **(C)** WB analysis of IAC proteins from clones 2αV and 3αV and MDA-MB-435S cells. Forty-eight hours after seeding, IACs were isolated and WB analysis was performed. The results presented are representative of three independent experiments yielding similar results.

confirmed in both clones using WB analysis (**Figure 5C**). Further inspection of the MS data identified several other CMSC proteins in MDA-MB-435S and clones 2αV and 3αV, although represented at a lower abundance. These were liprin α1, ELKS, LL5β, MT-actin cross-linking factor 1 (MACF1), and KANK1 and 2 (**Supplementary Table S2.1**, marked as YES in CMSC column). Since KANK proteins recently emerged as key regulators of adhesion dynamics (Chen et al., 2018), we selected KANK2 for further investigation. We observed lower number of average spectra for KANK2 in clones 2αV and 3αV compared to MDA-MB-435S cells (**Figure 7A**), and confirmed lower expression by WB in samples of isolated IACs (**Figure 7B** and **Supplementary Figure S6**).

In order to analyze the role of KANK2 in sensitivity to MT poisons, we measured sensitivity to PTX and VCR upon transient transfection of MDA-MB-435S cells with control

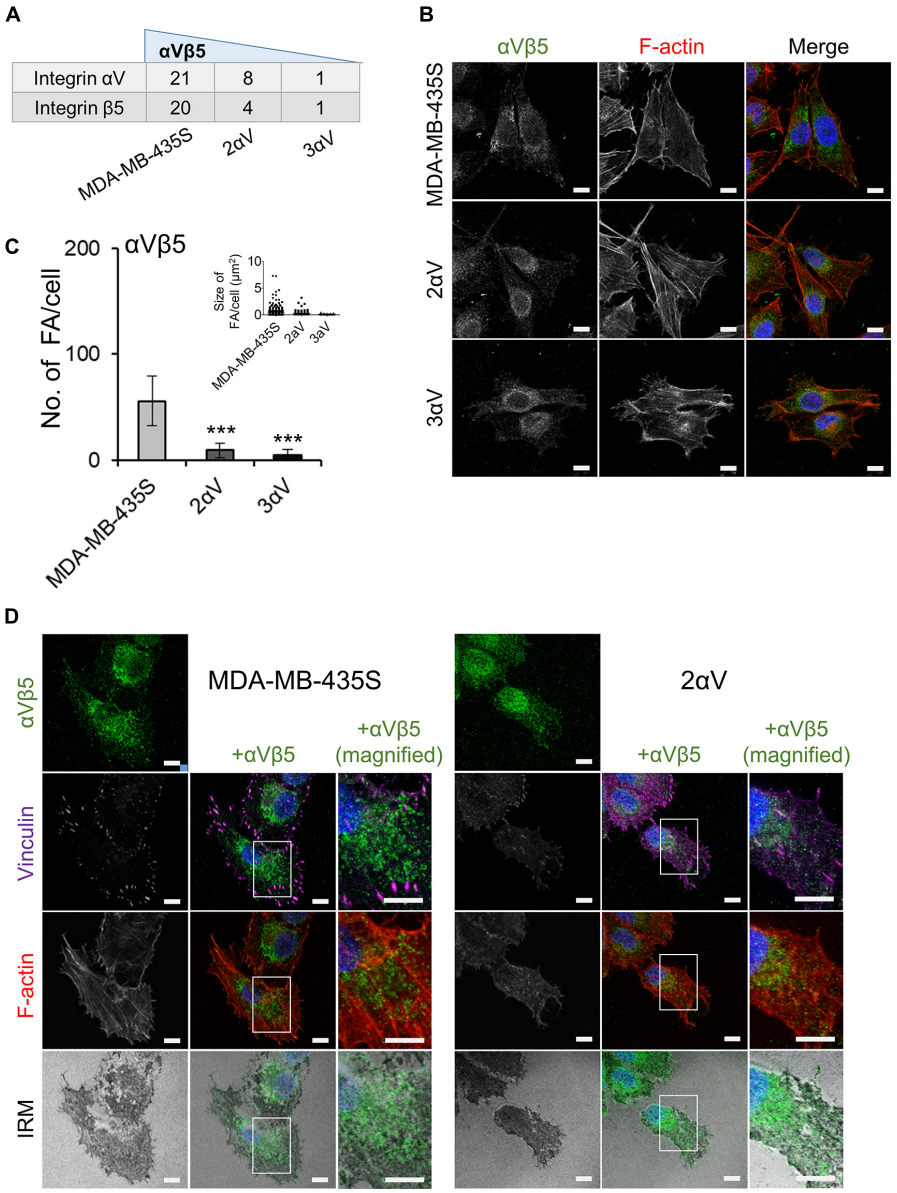

FIGURE 6 | Characterization of αVβ5-associated adhesion complexes. **(A)** The most abundant integrin subunits found in IACs. Dataset consists of at least two different experiments. Average spectral count number shown. **(B)** Clones with integrin subunit αV knockdown show decreased expression of integrin αVβ5. Forty-eight hours after seeding on coverslips, cells were fixed, permeabilized, and stained with anti-αVβ5 antibody, followed by Alexa-Fluor 488-conjugated antibody (green). F-actin staining (red) was performed, and nuclei were stained with DAPI (blue). Analysis was performed using TCS SP8 Leica. Scale bar = 10 μm. **(C)** Quantification data of results in **(B)** presented as histogram (FA number) and scatter plot (FA size) represent measurements of > 50 cells and are plotted as mean ± SD (n = 2). Data were analyzed by one-way ANOVA with Dunnett's multiple comparison. ***$P < 0.001$. **(D)** Identification of reticular adhesion structures in MDA-MB-435S cells and clone 2αV. Forty-eight hours after seeding on coverslips, cells were fixed, permeabilized, and stained for anti-αVβ5 followed by Alexa-Fluor 488-conjugated antibody (green), and anti-vinculin followed by Alexa-Fluor 647-conjugated antibody (purple). F-actin staining (red) was performed, nuclei were stained with DAPI (blue) and IRM images were taken. Analysis was performed using TCS SP8 Leica. Scale bar = 10 μm.

vs. KANK2-specific siRNA. Knockdown of KANK2 in MDA-MB-435S cells was successful (**Figure 7C** and **Supplementary Figure S6**), and resulted in increased sensitivity to VCR and PTX (**Figure 7D**). Finally, we demonstrated that migration of MDA-MB-435S cells transfected transiently with KANK2-specific siRNA was reduced in comparison to cells transfected with control siRNA (**Figure 7E**). We conclude that KANK2 is a potential target IAC protein for increasing sensitivity to MT poisons and decreasing migration.

Crosstalk between actin and MT dynamics is mediated through a number of proteins (Garcin and Straube, 2019). Among them is the KANK family of proteins, which play important roles in regulating MT dynamics around FAs (Bouchet et al., 2016; Chen et al., 2018). KANK2, MTs and the actin

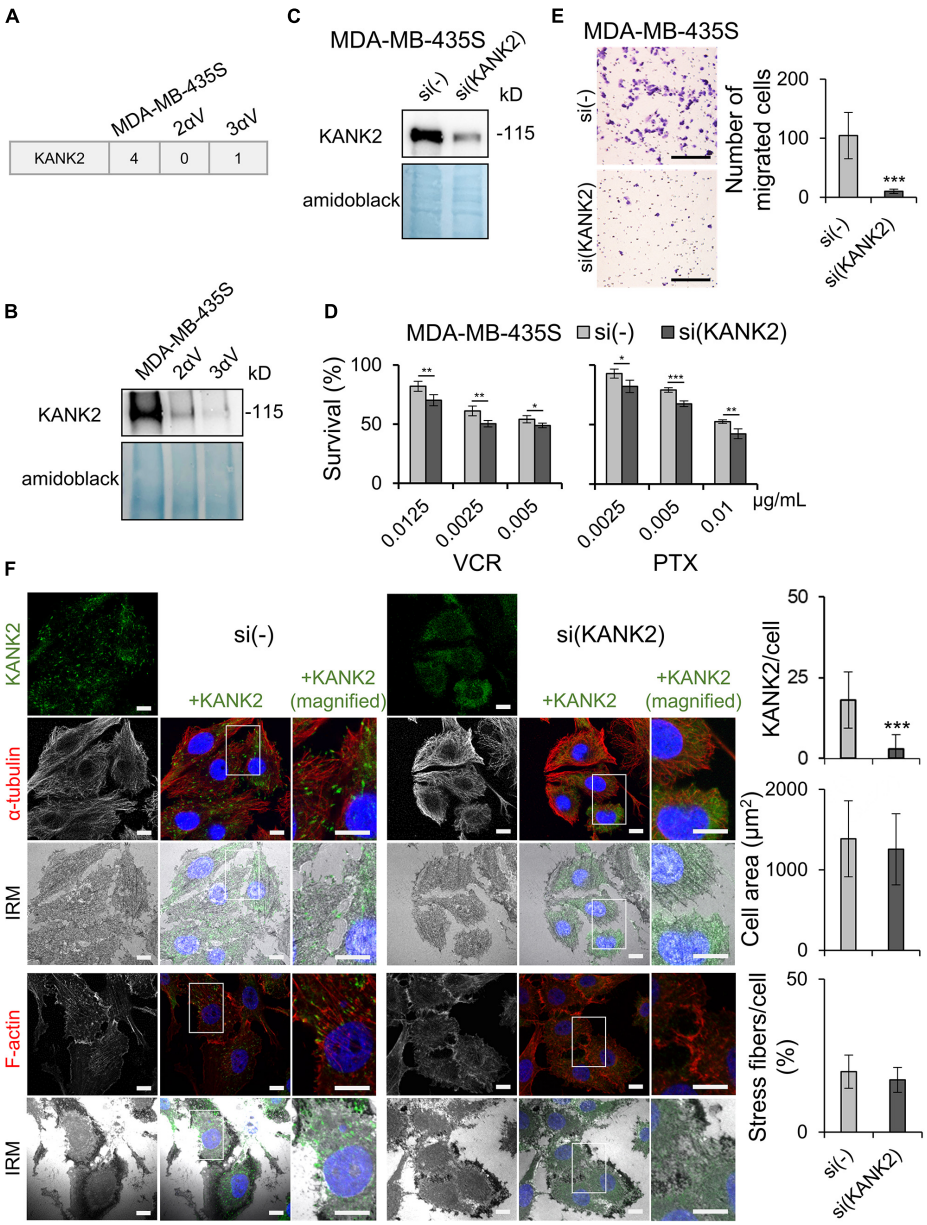

FIGURE 7 | KANK2 knockdown in MDA-MB-435S cells increases sensitivity to MT poisons and decreases migration mimicking integrin αV knockdown. **(A)** Average MS data of number of spectra specific for KANK2 in MDA-MB-435S cell model. Dataset consists of at least two different experiments. **(B)** KANK2 is present in lower amount in IACs of clones 2αV and 3αV. WB analysis of KANK2 in isolated IAC proteins from clones 2αV and 3αV and MDA-MB-435S cells. Forty-eight hours after seeding, IACs were isolated and WB analysis was performed. The results presented are representative of two independent experiments yielding similar results. **(C)** Knockdown of KANK2 in MDA-MB-435S cells. WB analysis of KANK2 from MDA-MB-435S cells transfected with either control (si(-)) or KANK2-specific siRNA (si(KANK2)). Forty-eight hours after transfection total cell lysates were collected and WB analysis was performed. The results presented are representative of two independent experiments yielding similar results. **(D)** MDA-MB-435S cells upon KANK2 knockdown demonstrate increased sensitivity to VCR and PTX as compared to MDA-MB-435S cells transfected with control siRNA. Twenty-four hours upon transfection, cells were seeded in 96-well plates and 24 h later treated with different concentrations of VCR and PTX. Cytotoxicity was measured by MTT assay. Results presented are representative of three independent experiments with similar results ± SD. Data were analyzed by unpaired Student's *t*-test. $^{*}P < 0.05$; $^{**}P < 0.01$; $^{***}P < 0.001$. **(E)** KANK2 knockdown decreases migration in MDA-MB-435S cells. Serum starved (24 h) cells, transfected previously with either control or KANK2-specific siRNA were seeded in Transwell cell culture inserts and left to migrate for 22 h toward serum. Cells on the underside of the inserts were stained with crystal violet, photographed, and counted. Scale bar = 100 μm. Averages of five microscope fields of three independently performed experiments ± SD are shown ($n = 3$). Data were analyzed by one-way ANOVA with Dunnett's multiple Comparison. $^{***}P < 0.001$. **(F)** KANK2 knockdown in MDA-MB-435S cells does not alter cell size or amount of stress fibers but slightly alters appearance of MTs. Forty-eight hours after transfection of MDA-MB-435S cells with KANK2-specific or control siRNA cells were fixed, permeabilized, and stained with anti-KANK2 antibody, followed by Alexa-Fluor 488-conjugated antibody (green). The α-tubulin or F-actin staining (red) was performed, nuclei were stained with DAPI (blue) and IRM images were taken. Analysis was performed using TCS SP8 Leica. Scale bar = 10 μm. Quantification data of results are presented as histograms represent measurements of > 50 cells and are plotted as mean ± SD ($n = 2$). Data were analyzed by one-way ANOVA with Dunnett's multiple comparison. $^{***}P < 0.001$.

cytoskeleton were therefore visualized in MDA-MB-435S cells with and without KANK2 knockdown. Simultaneously, IRM was used to visualize FAs. In control cells, we found KANK2 at the tips of MT fibers that overlapped with FAs. Although the cell size did not change upon KANK2 knockdown, the MTs did appear more condensed. Visualization of actin upon KANK2 knockdown showed that the amount of stress fibers did not change (**Figure 7F**).

Finally, to test whether KANK2 is predominantly linked to integrin αVβ5, we analyzed KANK2 localization upon integrin β5 knockdown (**Supplementary Figure S4A**). Results showed strongly reduced levels of KANK2-positive puncta, reduced amount of stress fibers and reduced cell size (**Supplementary Figures S4B,C**). We conclude that KANK2 is a key molecule linking integrin αVβ5 FAs to MTs, thus enabling actin-MT crosstalk that is important for both sensitivity to MT poisons and cell migration.

DISCUSSION

αV integrins, which have been implicated in tumor growth and angiogenesis, as well as in sensitivity to chemo- and radiotherapy, have long been recognized as therapeutic targets. However, there are several factors that complicate the development of integrin-based therapeutics for cancer, and deepening the basic knowledge about integrin αV-adhesion complexes is thus necessary. Recent advances in proteomics have enabled researchers to study IAC composition (adhesome) in detail (Humphries et al., 2019). Here, we assessed αV-dependent changes in the adhesome of MDA-MB-435S cells to understand better the increased sensitivity to PTX and VCR and decreased migration observed in this cell line upon integrin αV knockdown. Our major finding is that KANK2 provides a link between IACs and MTs that determines sensitivity to MT poisons.

Analysis of the MDA-MB-435S adhesome detected only αV and β5 integrin subunits, thus showing that in long term culture these cells use preferentially integrin αVβ5 for adhesion. This result is in accordance with recently published results by Lock et al. (2018), who found predominantly αV and β5 subunits in the adhesome of human osteosarcoma U2OS, lung carcinoma A549 and melanoma A375 cells in long term culture, whereas other integrin α and β subunits were present at much lower levels. Although we did not detect other integrin subunits, we do not exclude the possibility that MDA-MB-435S cells use integrin αVβ3 or small amounts of other integrin heterodimers in adhesion.

Among the ECM proteins detected, vitronectin (Takada et al., 2007) and periostin (Gillan et al., 2002) are able to bind integrin αVβ5. Major group of cytoskeletal proteins detected in the adhesome were actin-binding proteins, together with several MT-binding and intermediate filament proteins. However, the striking characteristic of MDA-MB-435S adhesome was detection of several proteins from the CMSC (liprin α1 and β1, ELKS, LL5β, MACF1, KANK1 and 2), the punctate structures behind the lamellipodium that cluster in the vicinity of mature FAs (Bouchet et al., 2016; Chen et al., 2018).

Statistical comparison of adhesomes from clones 2αV and 3αV to MDA-MB-435S adhesome showed reduced abundance of liprin β1 in clone 3αV. In addition, WB analysis of isolated IAC proteins confirmed reduced abundance of liprin β1 in both 2αV and 3αV clones, compared to MDA-MB-345S cells. In melanoma, liprin β1 was found to be overexpressed and its expression strongly correlated with the expression of KANK1 and KANK2 (Luo et al., 2016). Talin 1 and liprin β1, both showing reduced abundance in clones 2αV and 3αV, were identified as binding partners of KANK2 (Sun et al., 2016; Weng et al., 2018). Inspection of MS data revealed that, despite a lower number of spectra for CMSC proteins in our cell model, clones 2αV and 3αV show slightly reduced abundance compared to MDA-MB-435S cells, especially for KANK2. By combining these results with literature data on the role of KANK2 as a linker between talin and MTs (Bouchet et al., 2016; Chen et al., 2018), we hypothesized that KANK2 is the key protein involved in increased sensitivity to MT poisons and decreased cell migration. Indeed, KANK2 knockdown in MDA-MB-435S cells mimics increased sensitivity to MT poisons and decreased migration previously shown in αV knockdowns. Our MS data demonstrated small but similar number of spectra for KANK1 and KANK2, thus indicating their similar expression. Therefore, reduced expression of KANK1 as well as similar role of KANK1 in sensitivity to MT poisons cannot be excluded. It is well-known that three out of four KANK family members contribute to microtubule targeting (Chen et al., 2018) and addressing the issue of isoform-specific roles will be the subject of a further study.

IF analysis did not show striking changes in actin and MT cytoskeleton upon KANK2 knockdown in MDA-MB-435S cells, unlike integrin αV knockdown, which led to disorganization of actin with loss of stress fibers. This indicates that KANK2 knockdown in MDA-MB-435S cells did not disrupt FAs nor significantly changed the appearance of the MT cytoskeleton. This conclusion is supported by unchanged cell spreading area upon KANK2 knockdown, whereas knockdown of integrin αV decreased the cell spreading area. This is in line with depletion of KANK2 in fibroblasts or KANK1 in HeLa cells, which both did not result in any obvious alteration of FAs size or disassembly (Bouchet et al., 2016; Sun et al., 2016). We tested the effect of two antitumor drugs with the opposite mechanism of action, PTX which stabilizes and VCR which destabilize microtubules. The increased sensitivity of MDA-MB-435S cells to both MT poisons upon integrin αV or KANK2 knockdown points to altered MT dynamics in these cells. Consistently, recent data in other cell models have shown that KANK proteins mediate crosstalk between actin and MT cytoskeletons at FAs (Bouchet et al., 2016; Sun et al., 2016; Chen et al., 2018; Rafiq et al., 2019).

The question that arises is whether integrin αVβ5 FAs in MDA-MB-435S cells are the only ones linked to CMSCs through KANK2. Since the KANK localization to adhesions is primarily through talin (Gough and Goult, 2018) it is very likely that integrin αVβ3 FAs contain KANK2 as well. Our previously published results have shown that knockdown of either integrin

β5 or β3 did not change cell migration, while knockdown using integrin αV-specific siRNA of both heterodimers αVβ3 and αVβ5, the only integrins containing αV expressed in MDA-MB-435S cells, dramatically inhibited migration. Additionally, integrin β5 knockdown increased sensitivity of MDA-MB-435S cells to MT poisons, but not as efficiently as integrin αV knockdown, while integrin β3 knockdown had an opposite effect. We explained these results by a balance effect in MDA-MB-435S cell line in which integrin β5 knockdown increased the expression of integrin αVβ3 heterodimer on the cell surface and vice versa, and concluded that integrin αVβ5 is the one responsible for sensitivity to MT poisons while both integrins αV (αVβ3 and αVβ5) are implicated in cell migration (Stojanovic et al., 2018). KANK2 knockdown would knockdown microtubule localization to all integrin adhesions, whereas β5 knockdown would knock it down only to β5 integrins, so it is not surprising that the effect on cell migration is more pronounced. In conclusion, our results indicate that targeting KANK2 might simultaneously increase sensitivity to MT poisons therapy and decrease migration. Cell-specific effects of KANK 1 or 2 knockdown have been reported: in HeLa cells and podocytes KANK1 knockdown was shown to reduce motility (Li et al., 2011; Gee et al., 2015), while KANK2 knockdown in mice kidney fibroblasts increased migration (Sun et al., 2016).

In summary, the data presented here identify αVβ5 as the main integrin used by MDA-MB-435S cells to make both FAs and RAs. MS analysis revealed many proteins associated with integrin αVβ5 and represents the first published adhesome of this integrin heterodimer. KANK2 was shown to be associated with integrin αVβ5 since its knockdown mimicked initially observed integrin αV knockdown effects. Therefore, we propose KANK2 as a potential target for increasing sensitivity of melanoma cells to MT poisons and decreasing migration. These data will enable follow-up analyses of signaling mediated by integrin αVβ5 and therefore represent a valuable resource to improve our understanding of the mechanisms involved in the adhesion control of melanoma cell sensitivity to MT poisons and cell migration.

DATA AVAILABILITY STATEMENT

The mass spectrometry proteomics data have been deposited to the ProteomeXchange repository with the dataset identifier PXD016837. Other raw data supporting the conclusions of this article will be made available by the authors, without undue reservation, to any qualified researcher.

AUTHOR CONTRIBUTIONS

AA-R and MP contributed to the study conception and design. MP, JH, NS, DN, DM, AD, IS, DS, IW, MH, and AA-R performed research by material preparation, data collection and analysis. The first draft of the manuscript was written by AA-R while MP, MH, NS, and JH commented on previous versions of the manuscript. All authors read and approved the final manuscript.

FUNDING

This work was supported by the Croatian Science Foundation Project (Grant IP-2013-11-2465 to AA-R) and (Grant IP-2019-04-1577 to AA-R), Cancer Research UK (Grant C13329/A21671 to MH) and the EuroCellNet COST Action CA15214 [Short Term Scientific Mission (STSM) of MP].

ACKNOWLEDGMENTS

We thank the Biological Mass Spectrometry Facility at The University of Manchester for assistance with MS sample analysis.

SUPPLEMENTARY MATERIAL

The Supplementary Material for this article can be found online at: https://www.frontiersin.org/articles/10.3389/fcell.2020.00125/full#supplementary-material

REFERENCES

Albelda, S. M., Mette, S. A., Elder, D. E., Stewart, R., Damjanovich, L., Herlyn, M., et al. (1990). Integrin distribution in malignant melanoma: association of the beta 3 subunit with tumor progression. *Cancer Res.* 50, 6757–6764.

Astro, V., Chiaretti, S., Magistrati, E., Fivaz, M., and de Curtis, I. (2014). Liprin-alpha1, ERC1 and LL5 define polarized and dynamic structures that are implicated in cell migration. *J. Cell Sci.* 127(Pt 17), 3862–3876. doi: 10.1242/jcs.155663

Atherton, P., Stutchbury, B., Wang, D. Y., Jethwa, D., Tsang, R., Meiler-Rodriguez, E., et al. (2015). Vinculin controls talin engagement with the actomyosin machinery. *Nat. Commun* 6:10038. doi: 10.1038/ncomms10038

Bouchet, B. P., Gough, R. E., Ammon, Y. C., van de Willige, D., Post, H., Jacquemet, G., et al. (2016). Talin-KANK1 interaction controls the recruitment of cortical microtubule stabilizing complexes to focal adhesions. *Elife* 5:e18124. doi: 10.7554/eLife.18124

Byron, A., Askari, J. A., Humphries, J. D., Jacquemet, G., Koper, E. J., Warwood, S., et al. (2015). A proteomic approach reveals integrin activation state-dependent control of microtubule cortical targeting. *Nat. Commun.* 6:6135. doi: 10.1038/ncomms7135

Chen, N. P., Sun, Z., and Fassler, R. (2018). The Kank family proteins in adhesion dynamics. *Curr. Opin. Cell Biol.* 54, 130–136. doi: 10.1016/j.ceb.2018.05.015

Choi, H., Fermin, D., and Nesvizhskii, A. I. (2008). Significance analysis of spectral count data in label-free shotgun proteomics. *Mol. Cell. Proteomics* 7, 2373–2385. doi: 10.1074/mcp.M800203-MCP200

Cooper, J., and Giancotti, F. G. (2019). Integrin signaling in cancer: mechanotransduction, stemness, epithelial plasticity, and therapeutic resistance. *Cancer Cell* 35, 347–367. doi: 10.1016/j.ccell.2019.01.007

Danen, E. H., Jansen, K. F., Van Kraats, A. A., Cornelissen, I. M., Ruiter, D. J., and Van Muijen, G. N. (1995). Alpha v-integrins in human melanoma: gain of alpha v beta 3 and loss of alpha v beta 5 are related to tumor progression in situ but not to metastatic capacity of cell lines in nude mice. *Int. J. Cancer* 61, 491–496. doi: 10.1002/ijc.2910610411

De Deyne, P. G., O'Neill, A., Resneck, W. G., Dmytrenko, G. M., Pumplin, D. W., and Bloch, R. J. (1998). The vitronectin receptor associates with clathrin-coated membrane domains via the cytoplasmic domain of its beta5 subunit. *J. Cell Sci.* 111(Pt 18), 2729–2740.

Desgrosellier, J. S., and Cheresh, D. A. (2010). Integrins in cancer: biological implications and therapeutic opportunities. *Nat. Rev. Cancer* 10, 9–22. doi: 10.1038/nrc2748

Doncheva, N. T., Morris, J. H., Gorodkin, J., and Jensen, L. J. (2019). Cytoscape stringapp: network analysis and visualization of proteomics data. *J. Proteome Res.* 18, 623–632. doi: 10.1021/acs.jproteome.8b00702

Eke, I., Makinde, A. Y., Aryankalayil, M. J., Reedy, J. L., Citrin, D. E., Chopra, S., et al. (2018). Long-term tumor adaptation after radiotherapy: therapeutic implications for targeting integrins in prostate cancer. *Mol. Cancer Res.* 16, 1855–1864. doi: 10.1158/1541-7786.MCR-18-0232

Garcin, C., and Straube, A. (2019). Microtubules in cell migration. *Essays Biochem.* 29, 471–499. doi: 10.1042/EBC20190016

Gee, H. Y., Zhang, F., Ashraf, S., Kohl, S., Sadowski, C. E., Vega-Warner, V., et al. (2015). KANK deficiency leads to podocyte dysfunction and nephrotic syndrome. *J. Clin. Invest.* 125, 2375–2384. doi: 10.1172/JCI79504

Gillan, L., Matei, D., Fishman, D. A., Gerbin, C. S., Karlan, B. Y., and Chang, D. D. (2002). Periostin secreted by epithelial ovarian carcinoma is a ligand for alpha(V)beta(3) and alpha(V)beta(5) integrins and promotes cell motility. *Cancer Res.* 62, 5358–5364.

Gough, R. E., and Goult, B. T. (2018). The tale of two talins - two isoforms to fine-tune integrin signalling. *FEBS Lett.* 592, 2108–2125. doi: 10.1002/1873-3468.13081

Horton, E. R., Byron, A., Askari, J. A., Ng, D. H. J., Millon-Fremillon, A., Robertson, J., et al. (2015). Definition of a consensus integrin adhesome and its dynamics during adhesion complex assembly and disassembly. *Nat. Cell Biol.* 17, 1577–1587. doi: 10.1038/ncb3257

Horton, E. R., Humphries, J. D., James, J., Jones, M. C., Askari, J. A., and Humphries, M. J. (2016). The integrin adhesome network at a glance. *J. Cell Sci.* 129, 4159–4163. doi: 10.1242/jcs.192054

Huang da, W., Sherman, B. T., and Lempicki, R. A. (2009a). Bioinformatics enrichment tools: paths toward the comprehensive functional analysis of large gene lists. *Nucleic Acids Res.* 37, 1–13. doi: 10.1093/nar/gkn923

Huang da, W., Sherman, B. T., and Lempicki, R. A. (2009b). Systematic and integrative analysis of large gene lists using DAVID bioinformatics resources. *Nat. Protoc.* 4, 44–57. doi: 10.1038/nprot.2008.211

Humphries, J. D., Byron, A., Bass, M. D., Craig, S. E., Pinney, J. W., Knight, D., et al. (2009). Proteomic analysis of integrin-associated complexes identifies RCC2 as a dual regulator of Rac1 and Arf6. *Sci. Signal.* 2:ra51. doi: 10.1126/scisignal.2000396

Humphries, J. D., Chastney, M. R., Askari, J. A., and Humphries, M. J. (2019). Signal transduction via integrin adhesion complexes. *Curr. Opin. Cell Biol.* 56, 14–21. doi: 10.1016/j.ceb.2018.08.004

Hynes, R. O. (2002). Integrins: bidirectional, allosteric signaling machines. *Cell* 110, 673–687. doi: 10.1016/S0092-8674(02)00971-6

Jones, M. C., Humphries, J. D., Byron, A., Millon-Fremillon, A., Robertson, J., Paul, N. R., et al. (2015). Isolation of integrin-based adhesion complexes. *Curr. Protoc. Cell Biol.* 66 9, 1–15. doi: 10.1002/0471143030.cb0908s66

Klapholz, B., and Brown, N. H. (2017). Talin - the master of integrin adhesions. *J. Cell Sci.* 130, 2435–2446. doi: 10.1242/jcs.190991

Kuo, J. C., Han, X., Hsiao, C. T., Yates, J. R. III, and Waterman, C. M. (2011). Analysis of the myosin-II-responsive focal adhesion proteome reveals a role for beta-Pix in negative regulation of focal adhesion maturation. *Nat. Cell Biol.* 13, 383–393. doi: 10.1038/ncb2216

Lansbergen, G., Grigoriev, I., Mimori-Kiyosue, Y., Ohtsuka, T., Higa, S., Kitajima, I., et al. (2006). CLASPs attach microtubule plus ends to the cell cortex through a complex with LL5beta. *Dev. Cell* 11, 21–32. doi: 10.1016/j.devcel.2006.05.012

Li, C. C., Kuo, J. C., Waterman, C. M., Kiyama, R., Moss, J., and Vaughan, M. (2011). Effects of brefeldin A-inhibited guanine nucleotide-exchange (BIG) 1 and KANK1 proteins on cell polarity and directed migration during wound healing. *Proc. Natl. Acad. Sci. U.S.A.* 108, 19228–19233. doi: 10.1073/pnas.1117011108

Lock, J. G., Baschieri, F., Jones, M. C., Humphries, J. D., Montagnac, G., Stromblad, S., et al. (2019). Clathrin-containing adhesion complexes. *J. Cell Biol.* 218, 2086–2095. doi: 10.1083/jcb.201811160

Lock, J. G., Jones, M. C., Askari, J. A., Gong, X., Oddone, A., Olofsson, H., et al. (2018). Reticular adhesions are a distinct class of cell-matrix adhesions that mediate attachment during mitosis. *Nat. Cell Biol.* 20, 1290–1302. doi: 10.1038/s41556-018-0220-2

Luo, M., Mengos, A. E., Mandarino, L. J., and Sekulic, A. (2016). Association of liprin beta-1 with kank proteins in melanoma. *Exp. Dermatol.* 25, 321–323. doi: 10.1111/exd.12933

Mirzapoiazova, T., Mambetsariev, N., Lennon, F. E., Mambetsariev, B., Berlind, J. E., Salgia, R., et al. (2015). HABP2 is a novel regulator of hyaluronan-mediated human lung cancer progression. *Front. Oncol.* 5:164. doi: 10.3389/fonc.2015.00164

Mitjans, F., Meyer, T., Fittschen, C., Goodman, S., Jonczyk, A., Marshall, J. F., et al. (2000). In vivo therapy of malignant melanoma by means of antagonists of alphav integrins. *Int. J. Cancer* 87, 716–723. doi: 10.1002/1097-0215(20000901)87:5<716::aid-ijc14>3.0.co;2-r

Nesvizhskii, A. I., Keller, A., Kolker, E., and Aebersold, R. (2003). A statistical model for identifying proteins by tandem mass spectrometry. *Anal. Chem.* 75, 4646–4658. doi: 10.1021/ac0341261

Nip, J., Shibata, H., Loskutoff, D. J., Cheresh, D. A., and Brodt, P. (1992). Human melanoma cells derived from lymphatic metastases use integrin alpha v beta 3 to adhere to lymph node vitronectin. *J. Clin. Invest.* 90, 1406–1413. doi: 10.1172/JCI116007

Noordstra, I., and Akhmanova, A. (2017). Linking cortical microtubule attachment and exocytosis. *F1000Res.* 6:469. doi: 10.12688/f1000research.10729.1

Rafiq, N. B. M., Nishimura, Y., Plotnikov, S. V., Thiagarajan, V., Zhang, Z., Shi, S., et al. (2019). A mechano-signalling network linking microtubules, myosin IIA filaments and integrin-based adhesions. *Nat. Mater.* 18, 638–649. doi: 10.1038/s41563-019-0371-y

Ruffini, F., Graziani, G., Levati, L., Tentori, L., D'Atri, S., and Lacal, P. M. (2015). Cilengitide downmodulates invasiveness and vasculogenic mimicry of neuropilin 1 expressing melanoma cells through the inhibition of alphavbeta5 integrin. *Int. J. Cancer* 136, E545–E558. doi: 10.1002/ijc.29252

Schiller, H. B., Friedel, C. C., Boulegue, C., and Fassler, R. (2011). Quantitative proteomics of the integrin adhesome show a myosin II-dependent recruitment of LIM domain proteins. *EMBO Rep.* 12, 259–266. doi: 10.1038/embor.2011.5

Seguin, L., Desgrosellier, J. S., Weis, S. M., and Cheresh, D. A. (2015). Integrins and cancer: regulators of cancer stemness, metastasis, and drug resistance. *Trends Cell Biol.* 25, 234–240. doi: 10.1016/j.tcb.2014.12.006

Shannon, P., Markiel, A., Ozier, O., Baliga, N. S., Wang, J. T., Ramage, D., et al. (2003). Cytoscape: a software environment for integrated models of biomolecular interaction networks. *Genome Res.* 13, 2498–2504. doi: 10.1101/gr.1239303

Stehbens, S., and Wittmann, T. (2012). Targeting and transport: how microtubules control focal adhesion dynamics. *J. Cell Biol.* 198, 481–489. doi: 10.1083/jcb.201206050

Stojanovic, N., Brozovic, A., Majhen, D., Bosnar, M. H., Fritz, G., Osmak, M., et al. (2016). Integrin alphavbeta3 expression in tongue squamous carcinoma cells Cal27 confers anticancer drug resistance through loss of pSrc(Y418). *Biochim. Biophys. Acta* 1863, 1969–1978. doi: 10.1016/j.bbamcr.2016.04.019

Stojanovic, N., Dekanic, A., Paradzik, M., Majhen, D., Ferencak, K., Ruscic, J., et al. (2018). Differential effects of integrin alphav knockdown and cilengitide on sensitization of triple-negative breast cancer and melanoma cells to microtubule poisons. *Mol. Pharmacol.* 94, 1334–1351. doi: 10.1124/mol.118.113027

Sun, Z., Tseng, H. Y., Tan, S., Senger, F., Kurzawa, L., Dedden, D., et al. (2016). Kank2 activates talin, reduces force transduction across integrins and induces central adhesion formation. *Nat. Cell Biol.* 18, 941–953. doi: 10.1038/ncb3402

Supek, F., Bosnjak, M., Skunca, N., and Smuc, T. (2011). REVIGO summarizes and visualizes long lists of gene ontology terms. *PLoS One* 6:e21800. doi: 10.1371/journal.pone.0021800

Taherian, A., Li, X., Liu, Y., and Haas, T. A. (2011). Differences in integrin expression and signaling within human breast cancer cells. *BMC Cancer* 11:293. doi: 10.1186/1471-2407-11-293

Takada, Y., Ye, X., and Simon, S. (2007). The integrins. *Genome Biol.* 8:215. doi: 10.1186/gb-2007-8-5-215

Thomas, P. D., Campbell, M. J., Kejariwal, A., Mi, H. Y., Karlak, B., Daverman, R., et al. (2003). PANTHER: a library of protein families and subfamilies indexed by function. *Genome Res.* 13, 2129–2141. doi: 10.1101/gr.772403

Vogetseder, A., Thies, S., Ingold, B., Roth, P., Weller, M., Schraml, P., et al. (2013). alphav-Integrin isoform expression in primary human tumors and brain metastases. *Int. J. Cancer* 133, 2362–2371. doi: 10.1002/ijc.28267

Wang, T., Huang, J., Vue, M., Alavian, M. R., Goel, H. L., Altieri, D. C., et al. (2019). alphavbeta3 integrin mediates radioresistance of prostate cancer cells through regulation of survivin. *Mol. Cancer Res.* 17, 398–408. doi: 10.1158/1541-7786.MCR-18-0544

Weber, I. (2003). Reflection interference contrast microscopy. *Methods Enzymol.* 361, 34–47. doi: 10.1016/s0076-6879(03)61004-9

Weng, Z., Shang, Y., Yao, D., Zhu, J., and Zhang, R. (2018). Structural analyses of key features in the KANK1.K*IF*21A complex yield mechanistic insights into the cross-talk between microtubules and the cell cortex. *J. Biol. Chem.* 293, 215–225. doi: 10.1074/jbc.M117.816017

Winograd-Katz, S. E., Fassler, R., Geiger, B., and Legate, K. R. (2014). The integrin adhesome: from genes and proteins to human disease. *Nat. Rev. Mol. Cell Biol.* 15, 273–288. doi: 10.1038/nrm3769

Zaidel-Bar, R., Itzkovitz, S., Ma'ayan, A., Iyengar, R., and Geiger, B. (2007). Functional atlas of the integrin adhesome. *Nat. Cell Biol.* 9, 858–867. doi: 10.1038/ncb0807-858

Conflict of Interest: The authors declare that the research was conducted in the absence of any commercial or financial relationships that could be construed as a potential conflict of interest.

frontiers in Cell and Developmental Biology

ORIGINAL RESEARCH
published: 27 May 2020
doi: 10.3389/fcell.2020.00379

Spatiotemporal Characterization of Anterior Segment Mesenchyme Heterogeneity During Zebrafish Ocular Anterior Segment Development

*Kristyn L. Van Der Meulen, Oliver Vöcking, Megan L. Weaver, Nishita N. Meshram and Jakub K. Famulski**

Department of Biology, University of Kentucky, Lexington, KY, United States

OPEN ACCESS

Edited by:
Claudia Tanja Mierke, Leipzig University, Germany

Reviewed by:
Min Zhang, Shanghai Children's Medical Center, China
Diego Franco, University of Jaén, Spain
Kristin Artinger, University of Colorado Denver, United States

***Correspondence:**
Jakub K. Famulski
jkfa226@uky.edu

Specialty section:
This article was submitted to Cell Adhesion and Migration, a section of the journal Frontiers in Cell and Developmental Biology

Received: *02 March 2020*
Accepted: *27 April 2020*
Published: *27 May 2020*

Citation:
Van Der Meulen KL, Vöcking O, Weaver ML, Meshram NN and Famulski JK (2020) Spatiotemporal Characterization of Anterior Segment Mesenchyme Heterogeneity During Zebrafish Ocular Anterior Segment Development. Front. Cell Dev. Biol. 8:379. doi: 10.3389/fcell.2020.00379

Assembly of the ocular anterior segment (AS) is a critical event during development of the vertebrate visual system. Failure in this process leads to anterior segment dysgenesis (ASD), which is characterized by congenital blindness and predisposition to glaucoma. The anterior segment is largely formed via a neural crest-derived population, the Periocular Mesenchyme (POM). In this study, we aimed to characterize POM behaviors and transcriptional identities during early establishment of the zebrafish AS. Two-color fluorescent *in situ* hybridization suggested that early AS associated POM comprise of a heterogenous population. *In vivo* and time-course imaging analysis of POM distribution and migratory dynamics analyzed using transgenic zebrafish embryos (Tg[*foxc1b:*GFP], Tg[*foxd3:*GFP], Tg[*pitx2:*GFP], Tg[*lmx1b.1:*GFP], and Tg[*sox10:*GFP]) revealed unique AS distribution and migratory behavior among the reporter lines. Based on fixed timepoint and real-time analysis of POM cell behavior a comprehensive model for colonization of the zebrafish AS was assembled. Furthermore, we generated single cell transcriptomic profiles (scRNA) from our POM reporter lines and characterized unique subpopulation expression patterns. Based on scRNA clustering analysis we observed cluster overlap between neural crest associated (*sox10*/*foxd3*), POM (*pitx2*) and finally AS specified cells (*lmx1b*, and *foxc1b*). scRNA clustering also revealed several novel markers potentially associated with AS development and/or function including *lum*, *fmoda*, *adcyap1b*, *tgfbi*, and *hmng2*. Taken together, our data indicates that AS-associated POM, or Anterior Segment Mesenchyme (ASM), is not homogeneous but rather comprised of several subpopulations with differing colonization patterns, migration behavior, and transcriptomic profiles.

Keywords: periocular mesenchyme, anterior segment, anterior segment dysgenesis, neural crest, *pitx2*, *foxc1*

INTRODUCTION

Vertebrate cranial development has benefitted significantly from the evolutionary addition of the multipotent neural crest cells (NCC). Originating in the dorsal neural ectoderm of the folding neural tube, neural crest cells (NCC) undergo an epithelial-to-mesenchymal transition, detaching themselves from the epithelial sheet and migrating in distinct streams to invade regions all over

the developing embryo. NCCs ultimately go on to form diverse mesodermal derivatives including cartilage, myofibroblasts, neurons, and glial cells (Trainor and Tam, 1995; Langenberg et al., 2008; Williams and Bohnsack, 2015). In the developing cranial region, migrating NCCs come together with lateral plate mesoderm to surround the developing optic cup and form the Periocular Mesenchyme (POM) (Trainor and Tam, 1995; Langenberg et al., 2008; Williams and Bohnsack, 2015). POM subsequently contribute to the development of the ocular anterior segment (AS) (**Supplementary Figure S1**) (Fuhrmann et al., 2000; Creuzet et al., 2005; Williams and Bohnsack, 2015; Akula et al., 2018). The AS, comprising of the cornea, lens, iris, ciliary body, and drainage structures of the iridocorneal angle, is essential for the function of the visual system. The AS focuses light onto the retina while maintaining intraocular homeostasis.

Anterior segment development begins after the establishment of the optic cup, when POM cells migrate into the periocular space between the retina and the newly established corneal epithelium (Creuzet et al., 2005; Cavodeassi, 2018). These mesenchymal cells will eventually differentiate into the corneal stroma and endothelium, iris and ciliary body stroma, and the iridocorneal angle, amongst others. Mis-regulation of POM migration or function has been associated with congenital blinding disorders under the term anterior segment dysgenesis (ASD). ASD includes, alone or in combination, corneal opacity, iris hypoplasia, polycoria, corectopia, posterior embryotoxon, juvenile glaucoma, and disorders including Peter's Anomaly and Axenfeld-Rieger Syndrome (Gould et al., 2004; Volkmann et al., 2011; Akula et al., 2018). These rare autosomal dominant disorders, in addition to ASD phenotypes, also often exhibit systemic issues including dental malformations and craniofacial defects (Volkmann et al., 2011; Bohnsack et al., 2012; Ji et al., 2016). In addition to congenital diagnoses, failure of proper AS formation may also result in a predisposition to ASD later in life. Despite its fundamental role in the establishment of the AS, little is understood about the mechanisms governing POM specification, migration or differentiation.

The most common mutations seen in ASD patients involve the transcription factor *pitx2* (Paired-like homeodomain) (Ji et al., 2016), as well as *foxc1* (Forkhead Box c1) (Berry et al., 2006; Bohnsack et al., 2012; Reis et al., 2012; Chen and Gage, 2016; Seo et al., 2017). Loss of function of either *pitx2* or *foxc1* has been shown to result in ASD phenotypes in mice and zebrafish (Berry et al., 2006; Liu and Semina, 2012; Reis et al., 2012; Chen and Gage, 2016; Ji et al., 2016; Seo et al., 2017; Hendee et al., 2018). *Pitx2* in particular has been associated with the survival and migration of NCCs, as well as the development of the optic stalk, establishment of angiogenic privilege within the cornea, and craniofacial development (Evans and Gage, 2005; Bohnsack et al., 2012; Liu and Semina, 2012; Gage et al., 2014; Chawla et al., 2016; Chen and Gage, 2016; Ji et al., 2016; Hendee et al., 2018). *Foxc1* and *pitx2* are also known to interact with one another, and their expression is regulated by retinoic acid signaling (Matt et al., 2005; Chawla et al., 2018). Not surprisingly, mutations in NCC regulatory genes have also been associated with ASD. *Foxd3* (Forkhead Box d3) has been implicated in ASD (Volkmann Kloss et al., 2012) and is known to regulate early NCC specification, migration and long-term cell survival (Lister et al., 2006; Stewart et al., 2006; Drerup et al., 2009; Wang et al., 2011). *Sox10* (SRY-Box 10), another key regulator of the NCC population (Dutton et al., 2001; Creuzet et al., 2005; Langenberg et al., 2008; Drerup et al., 2009; Williams and Bohnsack, 2015), is critical for NCC migration and viability during early development (Dutton et al., 2001). Finally, *lmx1b* (LIM homeobox Transcription Factor 1 beta) is associated with Nail-Patella syndrome and glaucoma predisposition (McMahon et al., 2009; Liu and Johnson, 2010). *Lmx1b* is expressed within the developing cornea, iris, ciliary bodies, and trabecular meshwork of the iridocorneal angle in mice (McMahon et al., 2009; Liu and Johnson, 2010) and is essential for POM migration in zebrafish (McMahon et al., 2009). While several genes have been linked to POM or ASD, few studies to date have shed light on how POM cells, migrate to and participate in AS formation.

One signaling molecule that is known to be involved in cranial neural crest cell migration and anterior segment specification is Retinoic Acid (RA). RA, a metabolite of vitamin A, is instrumental for the overall development of the eye. RALDHs (RA-synthesizing enzyme retinaldehyde dehydrogenases) are expressed in a gradient through the eye, specifically in the retina, cornea, RPE, and lens (Matt et al., 2005, 2008; Lupo et al., 2011). RA produced in these areas diffuses out toward the anterior space of the developing eye, which will be populated by the POM. RA signaling is activated through the heterodimer receptors RARα/RARβ and RARα/RARγ expressed within the POM (Matt et al., 2005, 2008; Lupo et al., 2011). This signal is a vital determinate in eye morphogenesis. Activation of these receptors helps to control *eya2* dependent apoptosis in the POM as well as control the expression levels of *foxc1* and *pitx2* and therefore anterior segment development (Matt et al., 2005, 2008). NCC-specific deactivation of RARα, RARβ, and RARγ results in a complete loss of *pitx2* in the POM and AS, while increased RA signaling leads to an increase in *pitx2*, *foxc1a*, and *lmx1b.1* (Matt et al., 2008; Lupo et al., 2011). Though not explicitly explored in this study, RA signaling is a crucial component of cell migration and overall eye morphogenesis.

Although information about the anatomy of the anterior segment in vertebrates and anatomical consequences of POM regulatory gene mutations has been well documented, few studies have investigated the mechanism of development for AS structures overall. Specifically, little is known about when or how POM cells acquire their AS targeting, behave during migration, interact with one another, and finally, specify into various AS structures. Within this study, we aimed to characterize the developmental underpinnings that drive the formation of the AS. Using zebrafish embryos, we characterized the precise migration patterns and transcriptional profiles of AS associated POM cells (ASM). We specifically examined ASM gene expression as well as cellular distribution by taking advantage of POM-associated transgenic lines; Tg[*foxc1b*:GFP], Tg[*foxd3*:GFP], Tg[*pitx2*:GFP], Tg[*lmx1b.1*:GFP], and Tg[*sox10*:GFP]. In doing so, we have cataloged distribution, migratory dynamics, and population size of ASM during early AS development. Furthermore, single cell transcriptomic comparison of isolated ASM cells revealed

four specific clusters, each associated with potentially novel AS regulatory genes. Our findings indicate that AS-associated POM is composed of several subpopulations, each identifiable by their own distributions, migratory patterns, and gene expression profile.

RESULTS

POM-Associated Genes Exhibit Unique Expression Patterns During Early Establishment of the Anterior Segment

With several genes being implicated in regulating POM migration and identity, we first chose to carefully characterize patterns of their expression during zebrafish ocular morphogenesis (12–72 hpf). Whole Mount *In Situ* Hybridization (WISH) using embryos aged 12, 18, 24, 32, 48, and 72 hpf revealed that POM-related genes *foxc1a*, *foxc1b*, *eya2*, *foxd3*, *pitx2*, *sox10*, *lmx1b.1* and *2*, display both overlapping and individualized expression patterns within their originating neural crest streams and surrounding the AS (**Figure 1**). Several POM-related genes showed expression at 12 hpf, the earliest time point we assayed, suggesting that POM acquire their identity early, perhaps immediately following their delamination from the neural tube. As the optic cup begins to take shape (18 hpf), *foxc1a*, *foxc1b*, and *sox10* expressing POM cells are already visible within the craniofacial space. At the same time, *pitx2* expression is absent from periocular regions and presents primarily in the lens. By 24 hpf we observed various degrees of periocular expression of all the aforementioned POM-associated genes. *Foxc1a* displays the prototypical POM expression pattern with signal extending from the forebrain and into the surrounding periphery, and on top of, the retina by 32 hpf (**Figure 1A** and **Supplementary Figure S1**). Similar, albeit much weaker expression of *foxc1b* and *eya2* can be observed at 24 and 32 hpf (**Figures 1B,H**). Both *foxd3* and *sox10* display partial periocular patterns of expression, predominantly in the temporal regions at 24 hpf and more homogenously by 32 hpf (**Figures 1C,G**). *Pitx2* also displays strong periocular expression staining at 32 hpf but is also uniquely expressed in the lens (**Figure 1D**). Periocular-like expression patterns become clearest by 48 hpf for *foxc1a*, *foxc1b*, *eya2*, *pitx2*, and *sox10*. *Foxd3* periocular expression is significantly diminished by 48 hpf. By 72 hpf only *foxc1a*, *pitx2*, *sox10*, and *eya2* still exhibit strong periocular expression. In spite of the implicated role of *lmx1b* genes in pathogenic features of the Nail-Patella Syndrome (McMahon et al., 2009; Liu and Johnson, 2010), both *lmx1b.1* and *lmx1b.2* genes did not display classical AS expression patterns in our WISH assay at early timepoints, 12–48 hpf, but are detected in the AS at later stages, 72 hpf+ (**Figures 1E,F**). Taken together, we observe that POM-associated genes are not uniformly co-expressed in POM cells during early AS formation. Early POM, 12–24 hpf, express high levels of *foxc1a*, and only at later stages of AS colonization, 24–32 hpf, do they initiate high levels of expression for *foxc1b*, *eya2,* and *pitx2*. POM cells which express *sox10/foxd3* display periocular patterns only after 24 hpf, suggesting they may arrive as a second wave. At late stages of AS colonization, 48–72 hpf, we observe the persistence of strong *foxc1a* expression and an upregulation of *foxc1b*, *pitx2*, and *eya2*. Between 48 and 72 hpf, *sox10* expression is detected throughout the AS but does not appear to increase significantly while *foxd3* expression is no longer detected in the AS after 48 hpf. Based on our WISH observations, we therefore hypothesized that AS colonizing POM populations are likely heterogenous.

Co-expression Analysis Confirms Anterior Segment Mesenchyme Heterogeneity

Based on our WISH study, we next sought to determine the extent of co-expression between the POM associated genes. To study these relationships, we performed two-color fluorescent whole mount *in situ* hybridization (FWISH) at 32 and 48 hpf. These timepoints represent early and intermediate steps of POM AS colonization. We focused our attention on the expression of *foxc1*, *foxd3*, *sox10*, and *pitx2* as they represent the best studied AS-associated POM marker genes. 3D confocal imaging qualitatively indicated that all these POM markers clearly exhibit both overlapping and individualized expression patterns at 32 hpf (**Figures 2A–F**). All of our described results are based on reproducible patterns observed in 12 hpf+ embryos from two independent experiments. At 32 hpf, *foxc1* expression appears restricted largely to the periphery of the AS while *sox10*, *foxd3*, and *pitx2* display varying degrees of expression throughout the dorsal, ventral, nasal, and temporal quadrants. *Pitx2* exhibited broad expression throughout the AS and a high degree of co-expression with *foxc1*, primarily in the dorsal quadrant, and *sox10*, throughout the entire AS, at 32 hpf (**Figures 2C,D**). *Foxc1* exhibited a high degree of co-expression with *pitx2* in the dorsal and ventro-temporal AS and partial co-expression with *foxd3* and *sox10* (**Figures 2A,B,D**). The expression of *sox10* was most pronounced in the dorsal AS and had the highest degree of co-expression with *foxd3* (**Figures 2B,C,F**). *Foxd3* expression was detected throughout the AS, albeit in fewer cells than the other markers, and exhibited a co-expression primarily with *sox10* and *pitx2* throughout the entire AS (**Figures 2A,E,F**). By 48 hpf, noticeably pronounced individualized expression patterns emerged (**Figures 2G–L**). *Pitx2* expression became restricted to the dorsal and ventral quadrants of the AS, while *foxc1* expression expanded into the entire AS (**Figures 2G–K**). Co-expression was still evident between *pitx2* and *foxc1*, but primarily in the dorsal and ventral quadrants. *Foxd3* and *sox10* maintained the same spatial pattern of expression as observed at 32 hpf and continued to have a high degree of co-expression, particularly surrounding the lens (**Figure 2L**). *Foxd3* and *sox10* continued to have only minor co-expression with *pitx2* or *foxc1* throughout the AS. We also analyzed expression of *eya2* and observed a high degree of co-expression with *pitx2* throughout the entire AS, and slight co-expression with all the other markers (**Supplementary Figure S2**). Taken together, we show that already at 32 hpf AS-associated POM do not exhibit a homogenous expression pattern of POM-associated regulatory genes. This suggest that the AS is colonized as an

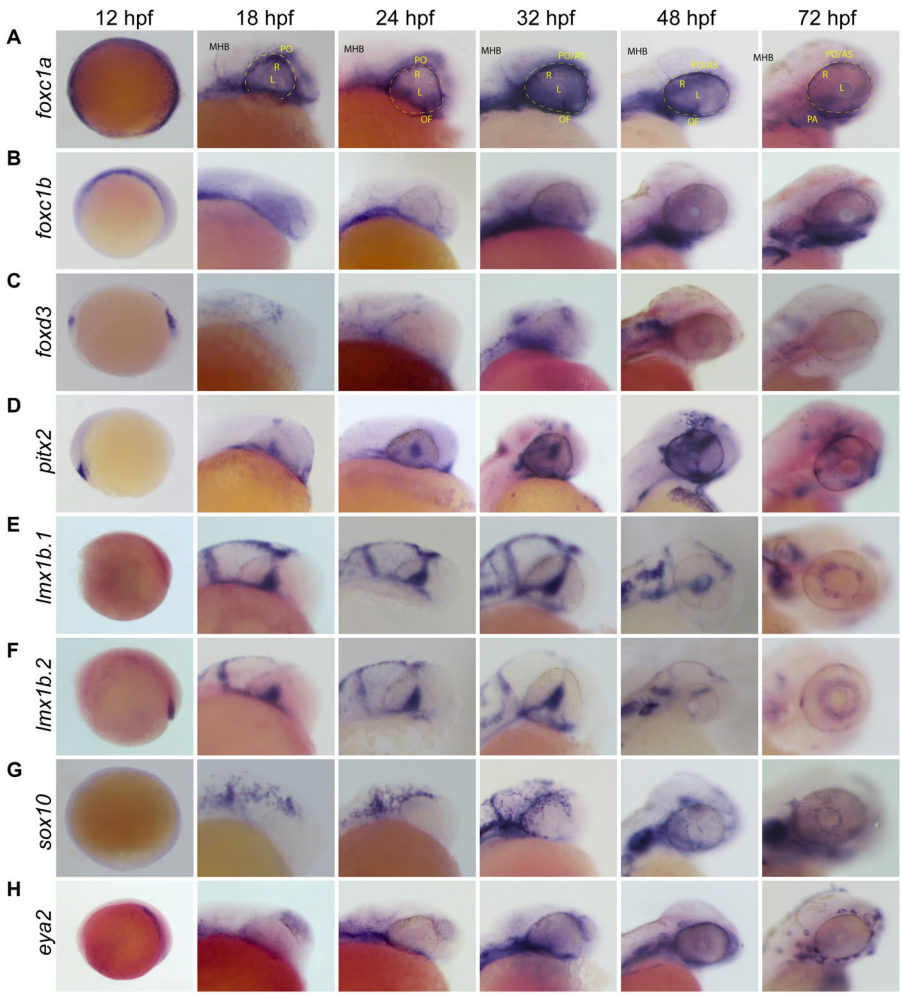

FIGURE 1 | Whole Mount *In Situ* Hybridization (WISH) of known POM and neural crest-related marker genes. Whole-mount *in situ* hybridization for POM marker gene mRNA expression patterns were observed during early to late stage eye development in the lateral view. POM genes examined were **(A)** *foxc1a*, **(B)** *foxc1b*, **(C)** *foxd3*, **(D)** *pitx2*, **(E)** *lmx1b.1*, **(F)** *lmx1b.2*, **(G)** *sox10*, and **(H)** *eya2. Foxc1a*, *foxc1b*, *pitx2*, *eya2*, and *sox10* in particular show strong expression surrounding the optic cup and on the surface of the anterior segment from 24 to 72 hpf. *Lmx1b.1* and *lmx1b.2* expression is detected within the anterior segment, surrounding the lens by 48–72 hpf. MHB, midbrain-hindbrain boundary; R, retina; L, lens; OV, optic vesicle; PO, periocular space (outlined with dashed line); OF, optic fissure; AS, anterior segment.

already heterogenous population rather than undergoing later diversification from a common progenitor.

POM Cells Display Distinct Targeting Patterns During Early AS Colonization

Based on our FWISH results we hypothesized that the heterogenous population of AS progenitors may display unique migration patterns and behavior. Furthermore, key to our understanding of AS formation will be the awareness of when and how the POM colonize. To begin characterizing this process, we first took advantage of available transgenic lines known to label POM: Tg[*foxc1b*:GFP], Tg[*pitx2*:GFP], Tg[*lmx1b.1*:GFP], or NCC: Tg[*foxd3*:GFP], Tg[*sox10*:GFP] (Matt et al., 2005, 2008; McMahon et al., 2009; Volkmann et al., 2011). These reporter lines enable single cell distribution analysis while also delineating lineage specification. Due to persistence of GFP protein, these lines do not necessarily represent active expression of their reporter driven promoter but do mark the lineage of POM/NCCs that have, at some point, expressed the respective POM-associated gene. To analyze AS colonization, transgenic embryos were fixed at key AS developmental stages (24, 26, 28, 30, 48, 56, and 72 hpf) and immunohistochemistry (IHC) was used to detect GFP. 3D confocal images of the AS were collected for each transgenic line at each timepoint and were employed to subsequently quantify distribution of the cells within the AS (**Figure 3A**). In particular, 3D rendered images of the AS were subdivided into four quadrants (**Figure 3A**, top left panel) and cells found in each were quantified at each timepoint.

Our assay revealed that initial colonization of the AS begins at approximately 22 hpf (data not shown) with GFP+ cells of the *pitx2*-derived population occupying the temporal AS regions

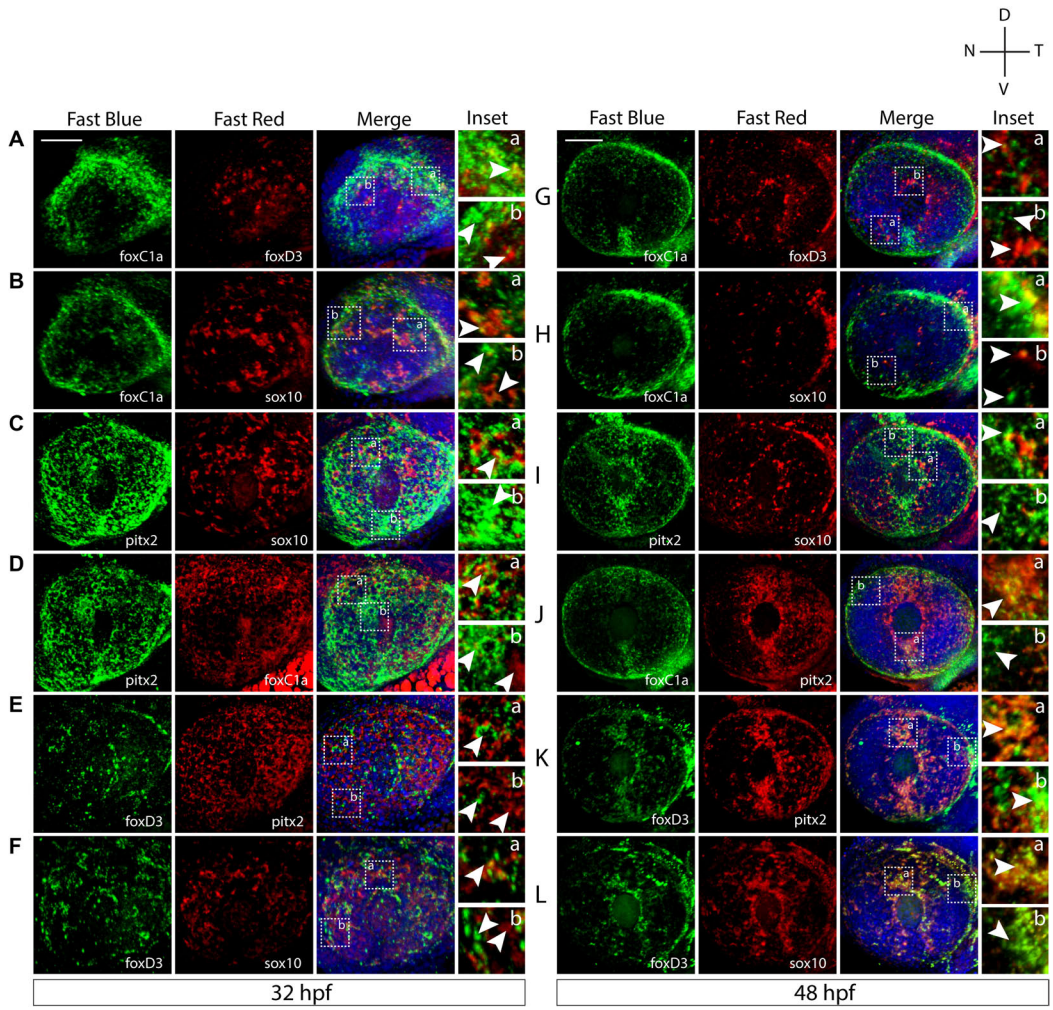

FIGURE 2 | Two-color fluorescent *in situ* hybridization supports ASM heterogeneity. Two-color fluorescent WISH (FWISH) performed for all possible combinations of *foxc1a*, *foxd3*, *pitx2*, and *sox10* at 32 **(A–F)** and 48 hpf **(G–L).** DAPI is in blue. Lateral images of 3D reconstructions are displayed. White arrows within inset panels (dashed squares) display instances of individual **(b)** and co-expression **(a)**. Scale bar = 50 μm.

(**Figure 3A**). At 24 hpf *foxc1b*, *foxd3*, and *lmx1b.1* derived GFP+ cells have begun to enter the AS across the dorsal most periocular regions, while *sox10*-derived cells begin to occupy all four regions. By 28 hpf all of the reporter lines, with the exception of *pitx2*, exhibit GFP+ cells primarily in the dorsal half of the AS. Tg[*foxc1b*:GFP] signal is also observed in the developing lens region up to 32 hpf, but was not considered for our analysis. Similarly, up to 32 hpf Tg[*lmx1b.1*:GFP] non-AS signal is observed in the dorsal-nasal region but is not considered in our analysis because it does not contribute to the AS. *Foxc1b*, *foxd3*, and *sox10* derived cells continue to spread to the ventral regions with roughly equal distribution throughout the AS by 48 hpf. Conversely, *pitx2*-derived cells remain exclusively associated with the temporal half of the AS while *lmx1b.1*-derived cells gradually re-distribute to occupy the nasal half of the AS. Starting at 54 hpf and continuing to 72 hpf, Tg[*pitx2*:GFP] expression turns off in POM cells and initiates in what is likely photoreceptor progenitor cells. Of note, our Tg[*pitx2*:GFP] transgenic line did not exhibit GFP signal in all regions of AS that were found to be positive for *pitx2* mRNA using FWISH (**Figures 2**, **3A**). We hypothesize this discrepancy arises from the fact that ASM progenitor cells induce *pitx2* expression upon arrival at the AS, while the GFP+ cells are a lineage mark of the early *pitx2*+ progenitors. The enhancer element driving the Tg[*pitx2*:GFP] line, C4, may be no longer responsive in ASM cells at the later time points and therefore explain the lack of GFP signal in all of the *pitx2* expressing cells.

All of our observations were subsequently validated by quantification of each GFP+ population (**Figure 3B**). At 24 hpf the majority of POM cells are located within the dorsal half of the AS, with the exception of *pitx2*-derived cells. By 30 hpf we note a significant reduction in the proportion of *foxc1b*, *foxd3*, and *lmx1b.1*-derived cells in the dorsal half combined with significant increase of these cells in the ventral half. At 48 hpf, we found equal distribution of *foxc1b*, *foxd3*, and *sox10* derived cells within all regions of the AS, while

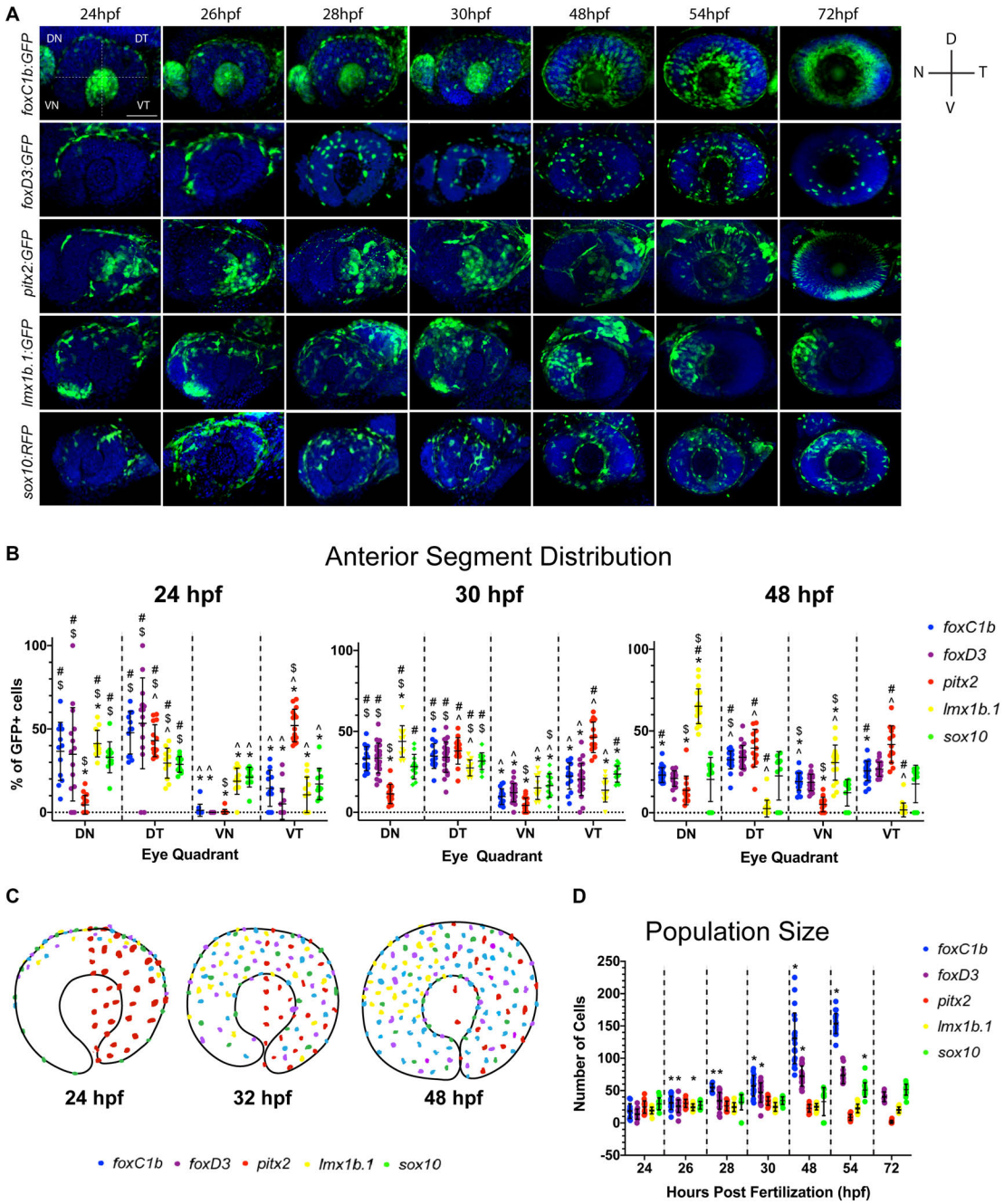

FIGURE 3 | Periocular mesenchyme subpopulation distribution analysis. **(A)** 3D rendering of confocal stacks encompassing the AS in POM transgenic lines between 24 and 72 hpf. GFP+ cells are green, DNA was stained with DAPI (blue). DN, dorsal-nasal; DT, dorsal-temporal; VN, ventral-nasal; VT, ventral-temporal. Scale bar = 50 μm. **(B)** Distribution of quantified GFP+ cells within each AS quadrant (DN, DT, VN, and VT) at 24, 30, and 48 hpf. Distribution is represented as an average percentage of the total number of GFP+ in each quadrant of the AS for each transgenic line. Statistically significant difference ($p < 0.05$): * vs. DT, # vs. VN, $ vs. VT and ^ vs. DN. **(C)** Model of POM colonization at 24, 30, and 48 hpf. **(D)** Average AS cell population size for each transgenic line at 24–72 hpf. * indicates statistically significant ($p < 0.05$) change from previous time point.

lmx1b.1-derived cells become predominantly associated with the nasal half of the AS.

Overall, we observe an ordered pattern of AS colonization, as summarized in **Figure 3C**. The majority of POM cells, *foxc1b*, *foxd3*, and *sox10:*GFP-derived cells, enter the AS along the dorsal retina and progress ventrally, while the *pitx2:*GFP sub-lineage enters the AS temporally and remains exclusively within the temporal AS. *lmx1b.1:*GFP cells enter the AS dorsally and initially migrate ventrally but by 48 hpf become restricted to the nasal regions of the AS.

Cell Proliferation Does Not Drive ASM Population Growth During AS Colonization

A distinct fluctuation in the total number of GFP+ cells within each transgenic line examined throughout the time course was also noted. While *lmx1b.1*, *pitx2*, and *sox10*-derived populations maintained a relatively consistent total number of cells, f*oxc1b* and *foxd3*-derived populations increased in size over time (**Figure 3D**). This is particularly evident in the *foxc1b*-population which increased size so significantly by 72 hpf that it was no longer quantifiable by our assay. Having documented the increase in population size of some ASM subpopulations, we next sought to understand the mechanisms responsible for this change. Specifically, we wanted to investigate whether the increase in population size of the *foxc1b:GFP* and *foxd3:GFP* subpopulations was the result of a continued influx of migratory cells into the AS or proliferation of cells already in the AS. Transgenic embryos were fixed at 32 and 48 hpf as this window in development sees the largest increase in population size. Proliferating cells were identified using pH3 antibody staining. 3D images of the AS were collected using a confocal microscope. Cells positive for both the GFP and the pH3 signal were quantified (**Supplementary Figure S3**). Little to no pH3 signal at either 32 or 48 hpf in *foxd3*:GFP or *foxc1b*:GFP embryos, or any of our transgenic lines, indicates that ASM cells are not actively dividing while migrating within the AS. Based on these data, we suggest that the increase in *foxc1b*:GFP and *foxd3*:GFP cell populations is the sole result of rapid and continuous migration of cells to the AS between 32 and 48 hpf.

ASM Subpopulations Exhibit Unique Migratory Behavior

In addition to cellular distribution over time, we also sought to catalog the migratory behavior of ASM cells. Specifically, we aimed to determine if they behaved in a similar fashion to cranial NCCs. Hence, we tracked their migration within the AS using *in vivo* 4D imaging. Using this approach we documented migration of *foxc1b:*GFP, *foxd3:*GFP, *pitx2:*GFP, *lmx1b.1:*GFP, and *sox10:*GFP-derived cells (**Figure 4A**). Qualitative examination of our data indicated that in all the transgenic lines, ASM cells migrated in a stochastic manner. This suggests that similar to cranial NCCs, ASM cells lack leader/follower cell identities or chain migration behavior (**Figure 4A** and **Supplementary Movies S1–S5**). The 4D data sets mirrored the cellular distribution trends we quantified in our previous time course assay (**Figure 3**). As expected based on our distribution studies, both *pitx2* and *lmx1b.1*:GFP cells displayed very specific distributions within the AS (**Figure 4B**), while *foxc1b*, *foxd3*, and *sox10:*GFP had more homogenous distribution patterns.

To analyze individual migratory behavior, we performed individual cell tracking. As expected, *foxc1b:*GFP, *foxd3:*GFP, *lmx1b.1:*GFP and *sox10:*GFP-derived cells migrated in a general dorsal to ventral pattern (**Figure 4B** and **Supplementary Movies S6–S10**). *Pitx2:*GFP cells migrated in a generally temporal to nasal direction (**Figure 4B**). Tracked cells were analyzed for their total distance traveled, directed migration, and velocity. *Foxc1b*-derived ASM had the highest velocities (0.115 ± 0.048 μm/min) while the cells of the *pitx2*-derived subpopulation were the slowest (0.049 ± 0.023 μm/min) (**Figure 4C**). *Foxd3*, *lmx1b.1*, and *sox10*-derived ASM cells had similar velocities (0.095 ± 0.042; 0.091 ± 0.050; and 0.079 ± 0.033 μm/min). When examining total distance traveled, *foxc1b*-derived cells displayed the farthest distances overall (44.667 ± 18.531 μm), while *pitx2*-derived cells exhibited the shortest (20.719 ± 9.936 μm) (**Figure 4D**). *Foxd3*, *lmx1b.1*, and *sox10*-derived ASM all exhibited similar overall distances traveled (37.339 ± 16.769; 33.267 ± 15.869; and 31.688 ± 13.289 μm). Differences in total migratory distance and velocity based on the AS quadrant of entry were also compared. Only *foxc1b*-dervied cells originating in the dorsal temporal quadrant showed differences in migration displaying shorter total distance traveled and slower velocity (data not shown). Based on analysis of migration velocity and distance traveled we conclude that ASM exhibit of a mixture of migration patterns and behaviors. This further supports our hypothesis that during colonization of the AS, the ASM are a heterogenous population.

Lastly, we measured the degree of directed migration by examining individual cell displacement within the AS (**Figure 4E**). Displacement was used as a measure of purposeful, or targeted, migration. We saw that cells within the *sox10* subpopulation showed the highest overall displacement (136.885 ± 63.327 pixels), followed by cells in the *foxd3* subpopulation (109.70 ± 75.434 pixels). Displacement of *foxc1b* and *lmx1b.1* was found to be 84.632 ± 49.223 and 95.559 ± 61.285 pixels, respectively. Similar to our previous observations for velocity and distance, the *pitx2* subpopulation exhibited the least amount of displacement (44.698 ± 33.008 pixels). Our data indicate that all ASM cells are highly migratory, but that as observed for POM marker gene expression, there is heterogeneity when comparing the various reporter lines.

ASM Subpopulations Cluster According to Developmental Transcriptomic Profiles

Having observed the AS-associated POM subdivide into several ASM subpopulations, based on distribution and migratory behavior, our final goal was to analyze single cell transcriptomic profiles of ASM cells during AS colonization. To do so, we dissected the eyes off of our transgenic embryos at 48 hpf, isolated GFP+ cells via FACS, and subsequently employed the Chromium 10X genomics platform to generate single cell transcriptomes (scRNA). Resulting transcriptomes were sequenced using Illumina technology and analyzed using Cell Ranger3.1 and Loupe software. In total we sequenced 2,460 individual cells with per cell reads of greater than 100,000 (**Supplementary Table S2**).

K-means clustering (t-SNE) of all five data sets resulted in four distinct clusters (**Figure 5A** and **Supplementary Figure S4**). We identified one predominantly NCC-like cluster

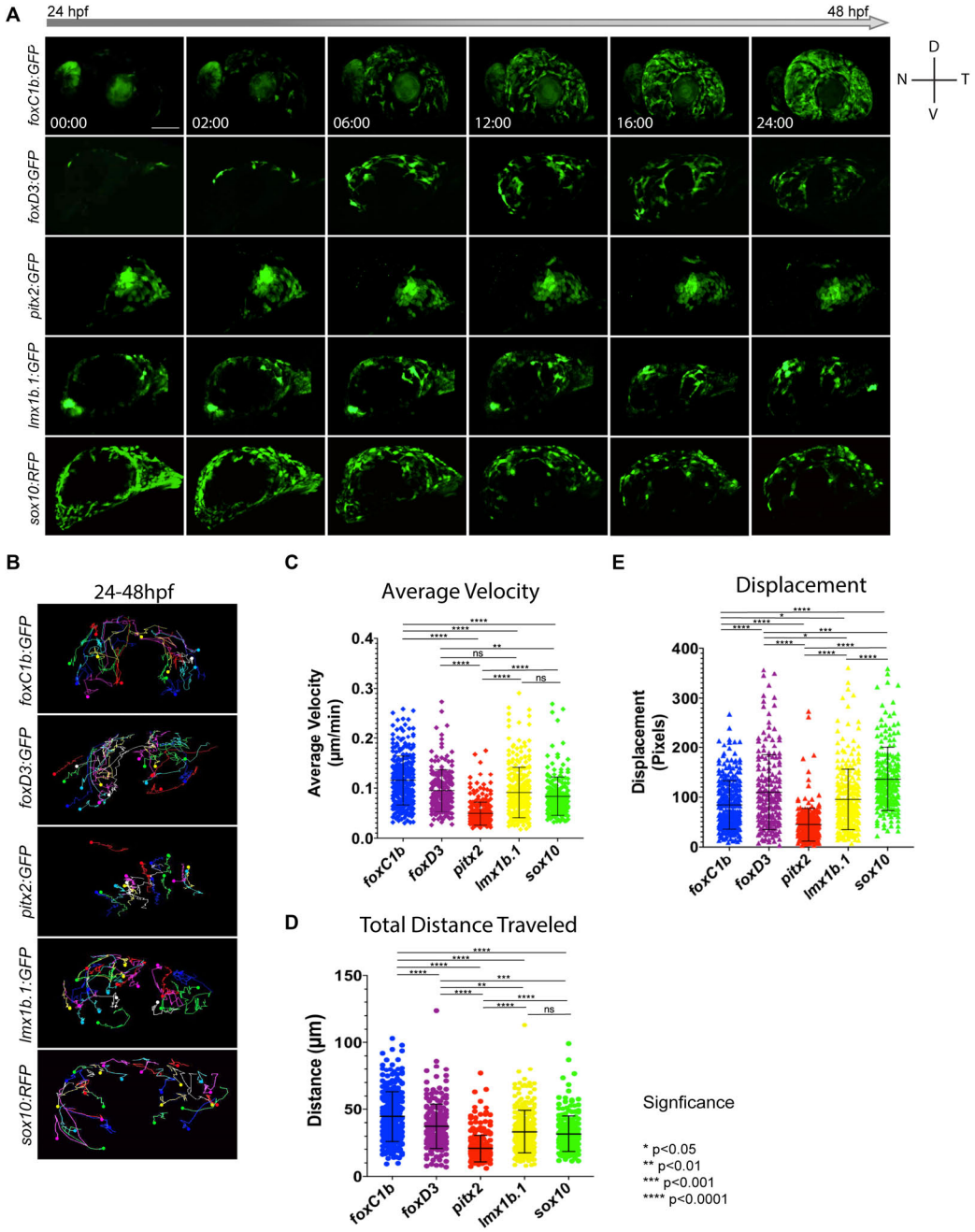

FIGURE 4 | *In vivo* 4D imaging of POM anterior segment colonization. **(A)** 4D *in vivo* imaging of the AS conducted between 24–48 hpf using POM transgenic lines. Time stamp hours:minutes. Scale bar = 50 μm. **(B)** Individual cell tracking for each POM transgenic line reveals migratory patterns during early AS colonization. Solid spheres indicate terminal end of track. **(C–E)** Cell tracking measurements of average migratory velocity (ANOVA $p < 0.0001$), total migration distance (ANOVA $p < 0.0001$), and migratory displacement within the AS (ANOVA $p < 0.0001$).

(Cluster 1) with cells largely originating from the *foxd3* and *sox10* transgenic lines (**Figure 5B**). 85.6% of *sox10*:GFP and 84.3% of *foxd3*:GFP cells were found in cluster 1. *Sox10*:GFP and *foxd3*:GFP cells were also found in cluster 3 with 11.5 and 15% of their total distribution, respectively. A majority of cells isolated from the *foxc1b*:GFP line were found in Cluster 2, 70.1%, with a small proportion also present in cluster 3, 10.2%, and cluster 4, 15.8% (**Figure 5B**). *Pitx2:GFP* isolated cells were predominantly found in cluster 3, 83.9%, and cluster 2, 7.1%, with a low proportion found in clusters 1 and 4, 5.3% and 3.6% distribution, respectively. *Lmx1b*:GFP derived cells have the unique classification of being almost equally represented throughout all 4 clusters, 24.3% in cluster 1, 15.7% in cluster 2, 29% in cluster 3

and 31% in cluster 4 (**Figure 5B**). When comparing spatially, UMAP-based plotting of the clusters indicated a continuous or connected expression profile suggestive of interaction or progression between the clusters (**Figure 5A** and **Supplementary Figure S4**). The placement of the clusters within the UMAP graph predicts interaction between *sox10/foxd3* with *pitx2*, *pitx2* and *lmx1b/foxc1b* and finally *lmx1b/foxc1b* with *foxc1b*-derived cells (**Figure 5C**). Interestingly, cluster 4 appears to represent a transition stage where multiple AS cell fates are possible. Taken together, we observed that none of the clusters are made up solely of cells originating from one individual transgenic line. This observation is supported by our two-color fluorescent *in situ* expression analysis (**Figure 2**) and is particularly relevant in terms of the relationships amongst POM associated genes, particularly *pitx2* and *foxc1* whose products are actually known to physically interact (Matt et al., 2005; Chawla et al., 2018). Finding four distinct subpopulations of ASM cells further supports our previous findings that suggest ASM are a developmentally heterogenous population during colonization of the AS.

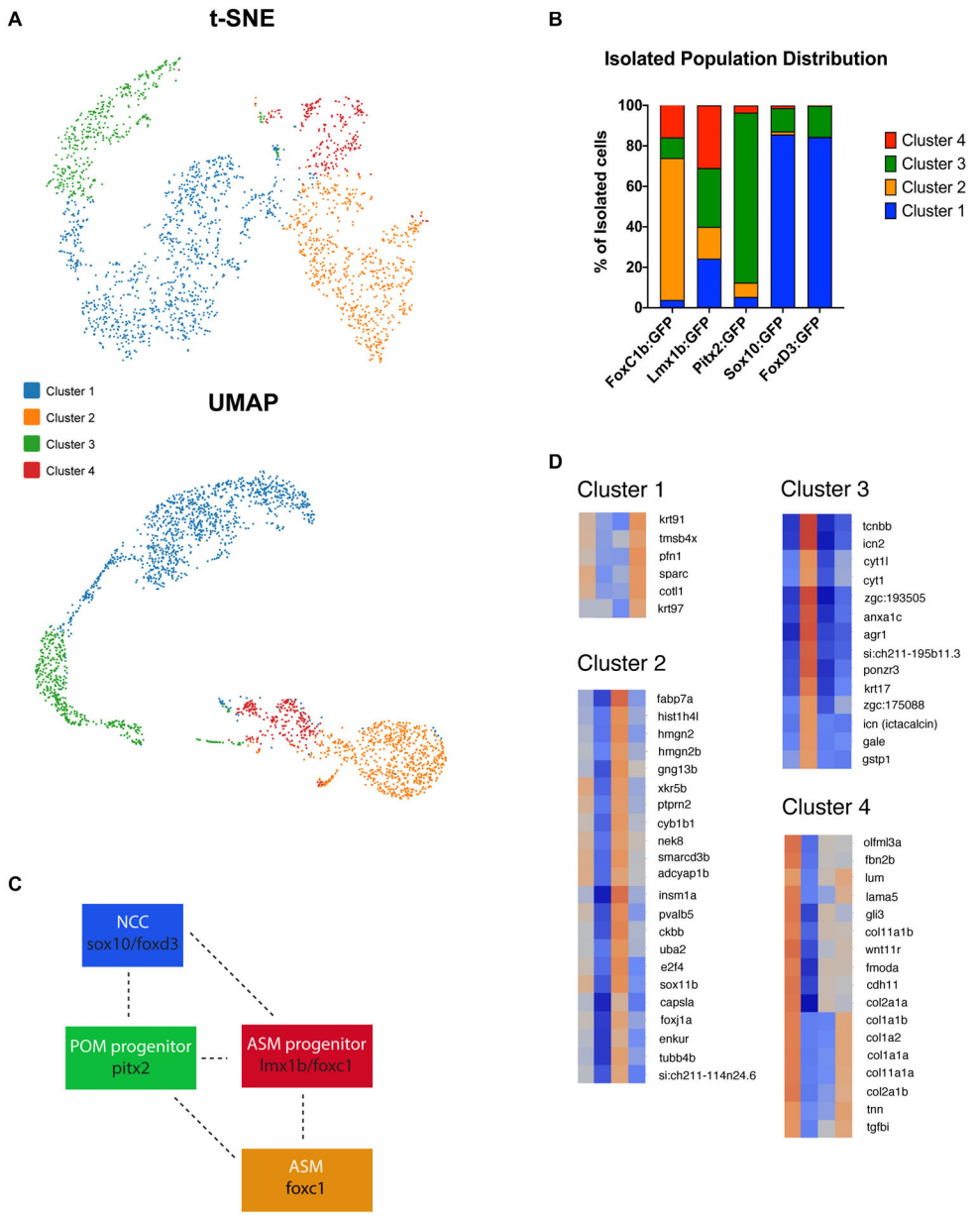

FIGURE 5 | Anterior segment mesenchyme single cell clustering analysis at 48 hpf. **(A)** *K*-means clustering of scRNA sequencing of isolated 48 hpf *foxc1b*:GFP, *lmx1b*:GFP, *sox10*:GFP, *foxd3*:GFP, and *pitx2*:GFP ASM cells in both tSNE and UMAP readouts. Both plots identified four general clusters. **(B)** Distribution of isolated ASM cells within each of the clusters generated by the Cell Ranger3.1 software. **(C)** Model of identified cluster interactions. Interaction and overlap is indicated by dashed lines. **(D)** Heat maps of cluster specific gene expression patterns.

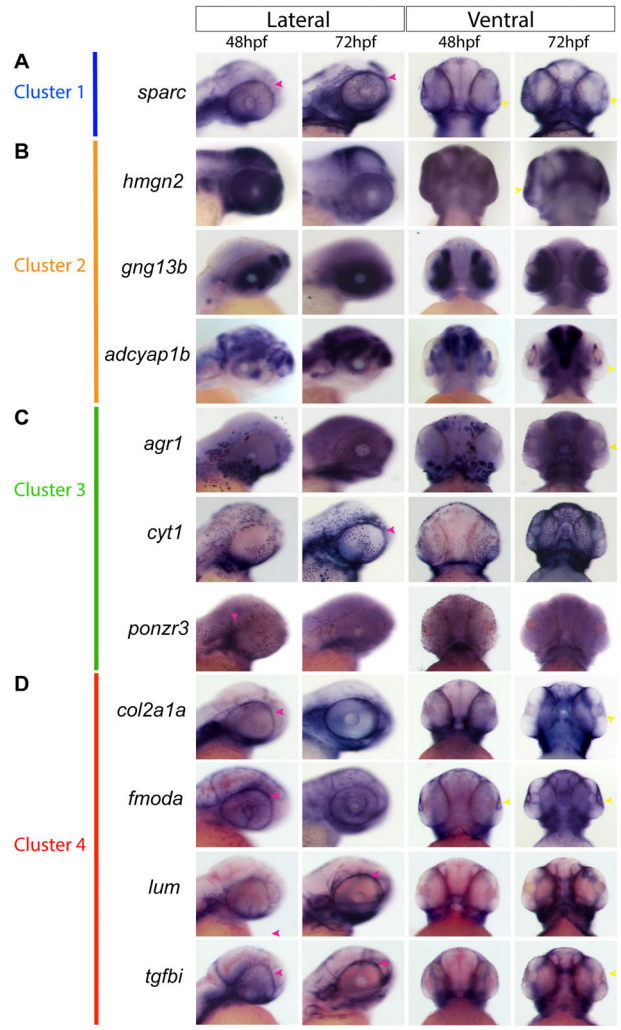

FIGURE 6 | Gene expression of sequencing-derived genes. Whole-mount *in situ* hybridization for novel ASM marker gene mRNA expression patterns was performed during early (48 hpf) and intermediate stages (72 hpf) of AS development and observed in lateral and ventral views. **(A)**, *Sparc* expression representing cluster 1. **(B)** *gng13b*, *hmgn2*, and *adcyap1b* expression representing cluster 2. **(C)** *cyt1*, *agr1*, and *ponzr3* expression representing cluster 3. **(D)** *lum*, *fmoda*, *col2a1a*, and *tgfbi* expression representing cluster 4. Yellow arrowheads indicate AS expression, magenta arrowheads indicate periocular expression.

scRNA Analysis of ASM Uncovers Novel AS Markers

Based on the clustering analysis we generated heatmaps and gene ontology analysis of the most representative expression patterns for each cluster (**Figure 5D** and **Supplementary Figure S5**). Within some of the clusters, genes with possible links to one or more AS structures were identified based on association with ASD-related disorders or potential similarities to POM/NCC-like expression patterns. For example, *cyp1b1*, known to be associated with glaucoma predisposition (Zhao et al., 2015), was identified in cluster 2, while *tgfbi*, isolated in cluster 4, is associated with corneal dystrophy (Poulaki and Colby, 2008). We also noted expression of several collagen (*col2a1a*, *1a1b*, *1a2*, *1a1a*, *2a1b*, *11a1a*, and *11a1b*) and laminin (*lama5*) genes, known to be associated with extracellular matrix properties of AS trabecular meshwork cells (Abu-Hassan et al., 2014), in cluster 4 (**Figure 5D**). Importantly, our analysis also identified novel candidate genes potentially associated with AS specification and development. We therefore analyzed expression of several potential novel target genes to assess their contribution to AS development at 48 and 72 hpf. Our expression analysis included *sparc* (cluster 1); *gng13b*, *hmgn2* and *adcyap1b* (cluster 2); *cyt1*, *arg1*, *ponzr3*, and *si:ch211-195b11.3* (cluster 3); and *lum*, *fmoda*, *tgfbi*, and *col2a1a* (cluster 4) (**Figure 6**). Examining expression of cluster 1 associated gene *sparc* revealed that at 48 and 72 hpf *sparc* mRNA was associated with the developing AS, in particular the periphery of the lens and iris regions (**Figure 6A**). From cluster 2, we examined expression of *hmgn2*, *gng13b*, and *adcyap1b*. We observed strong expression of *hmgn2* throughout the AS by 72 hpf, and strong expression of *adcyap1b* in the lens periphery and future iris region (**Figure 6B**). Cluster 3 targets included *agr1*, *cyt1*, *ponzr3*, and the currently uncharacterized *si:ch211-195b11.3*. Both *cyt1* and *agr1* appear to label dermal cells in the periocular and AS regions (**Figure 6C**). *Ponzr3* did not display AS associated expression patterns (**Figure 6C**), while *si:ch211-195b11.3* does not appear to be related to the AS development (data not shown). Lastly, from cluster 4 we examined *col2a1a*, *fmoda*, *lum,* and *tgfbi* expression. By 72 hpf, we observed strong expression of *fmoda* in the AS as well as some overlapping expression of *tgfbi* and *col2a1a* (**Figure 6D**). Several genes in our list including *sparc*, *col2a1a*, *lum*, and *tgfbi* also demonstrated periocular expression patterns similar to other known ASM genes at 48 hpf. In particular, *sparc* expression was reminiscent of *sox10*, *lum* expression was reminiscent of *foxc1a* while *tgfbi*, *col2a1a,* and *fmoda* expression were reminiscent of *foxc1b* and *eya2* (**Figures 1**, **6**). In summary, our single cell transcriptomic analysis of ASM cells identified several novel markers associated with early AS formation which may represent uncharacterized regulators of AS development and/or function.

CONCLUSION

In the literature, POM has become an umbrella term associated with a host of developmental events including cranial-facial, vascular, retinal as well as anterior segment development. In order to provide some much-needed clarity, our study aimed to characterize specifically the AS associated subset of POM cells, which we term the ASM. As such, our focus was strictly on POM cells that have entered the AS and ultimately contributed to its formation. We used a combination of *in situ* hybridization, real-time imaging of transgenic reporter lines and single cell transcriptomic analysis. Based on our results of ASM distribution, migration dynamics and lastly single cell transcriptional profiles, we conclude that AS colonization employs several distinct, yet developmentally connected, subpopulations of ASM. Overall, our work is the first comprehensive examination of ASM during AS development in

zebrafish which we believe will serve as a starting point for future studies of novel regulators of this critical developmental event.

Observing a lack of total co-expression for POM marker genes in ASM cells suggested to us a lack of uniformity within the population. Furthermore, when co-expression of POM markers occurred, the degree and localization within the AS varied between genes examined (**Figures 1**, **2**). *Sox10* and *foxd3*, both NCC markers, appear to be co-expressed in ASM cells distributed over the entire AS at 32 hpf (**Figures 2A–C,E,F**). Co-expression of *pitx2* and *foxc1* was limited to the periphery of the AS while co-expression of *pitx2* and *eya2* was detected throughout the AS (**Figure 2D** and **Supplementary Figure S2**). *Pitx2* displayed a high degree of co-expression with all other POM and NCC markers which likely coincides with its predicted wide-reaching role during AS development. Although we do see some degree of co-localization amongst all POM marker genes, the distinction between each gene's expression pattern remains evident. Individual ASM cells therefore exhibit a range of POM marker expression patterns which supports our hypothesis that the ASM is heterogenous during AS development. Our findings also speak for the fact that when deciding on a marker for analysis of ASM, not all of the classical POM marker genes may be representative of the entire population and this should be taken into consideration during experimental design.

Utilizing transgenic lines: *foxc1b*:GFP, *foxd3*:GFP, *pitx2*:GFP, *lmx1b.1*:GFP, and *sox10*:GFP we examined the dispersal and distribution of ASM cells during the critical window of POM AS colonization (24–72 hpf). Our detailed imaging studies indicated that the first POM cells arrive on the AS between 22–24 hpf (**Figure 3A**). GFP+ cells of the *pitx2* subpopulation appear to arrive the earliest of all observed ASM populations, entering the AS as early as 22 hpf, and specifically from the temporal quadrant. When examined as a whole, ASM colonization is, however, primarily dorsal in origin and ASM cells proceed to spread throughout the AS as development proceeds. This pattern was observed for *foxc1b*:GFP, *foxd3*:GFP, *sox10*:GFP, and *lmx1b*:GFP ASM cells. In addition to several differing entry points, we also observed varying targeting behavior of ASM cells. By 48 hpf homogenous AS distribution was observed for *foxc1b*:GFP, *foxd3*:GFP, and *sox10*:GFP cells. Conversely, *lmx1b.1*:GFP and *pitx2*:GFP cells remained strictly restricted to the nasal and temporal quadrants of the AS, respectively. This is a clear indication that heterogeneity during AS colonization is also a potential mechanism for specific targeting within the AS. Lastly, we observed that migratory ASM are not actively undergoing cellular division. The rapid increase in ASM cell number between 24–48 hpf within some subpopulations, in particular *foxc1b*:GFP and *foxd3*:GFP, may therefore be primarily attributed to the continual arrival of migratory cells to the AS. This notion is supported by the fact that cranial NCCs, the main source of POM/ASM, originate dorsal to the AS and that we observe *foxd3*:GFP and *foxc1b*:GFP cells entering the AS predominantly within the dorsal quadrant. Alternatively, it remains possible that GFP+ cells represent a non-proliferative pool of ASM. Analyzing co-expression of ASM markers and cell cycle transcripts will be necessary to test this alternative. When combining all of our ASM distribution data, we propose a progressive colonization model outlined in **Figure 3C**.

The ability to migrate long distances and respond to specific cues is a crucial and well documented behavior of NCCs. Cranial NCCs migrate without designated leader or follower identities, instead maintaining a large homogenous population wherein each member exhibits the same migratory capabilities as its neighbors (Clay and Halloran, 2010; Kulesa et al., 2010; Richardson et al., 2016). 4D live imaging of *foxc1b*:GFP, *foxd3*:GFP, *sox10*:GFP, *pitx2*:GFP, and *lmx1b.1*:GFP transgenic embryos aged 24–48 hpf showed a uniform migration behavior pattern in ASM subpopulations indicative of cranial neural crest-like migration (**Supplementary Movies S1–S5**). Tracking analyses indicated cells had stochastic and independent migratory capabilities, frequently pausing during migration, altering directionality, and extending filipodia to communicate with one another (**Supplementary Movies S6–S10**). Quantification of total distance and average velocity indicated that *foxc1b*:GFP ASM cells traveled the farthest distance and with the highest velocity (**Figures 4C,D**). Conversely, *pitx2*:GFP ASM cells traveled the shortest distances and with the slowest velocities, but also with the least amount of stochastic movement (**Figures 4B–D**). Interestingly, since *pitx2*:GFP+ cells are the first POM cells to colonize the AS, we hypothesize that they may serve as sentinels to mark the AS for later arriving POM. Their need for timely arrival at the AS may explain their unique, highly targeted, migratory behavior. Displacement, also referred to as directed migration, was measured as a way to characterize the purposeful migration of ASM cells. We wanted to quantify whether certain ASM cells migrated with more directionality than their counterparts. Interestingly, our data indicates that cells in the *sox10*:GFP and *foxd3*:GFP subpopulation, associated with NCC identity (Stewart et al., 2006; Drerup et al., 2009; Wang et al., 2011), engage the most in directed migration (**Figure 4E**). These likely pluripotent, NCC-like cells may be directly targeting to specific regions of the AS in order to ensure equal distribution. Cells likely associated with a more traditional POM identity, *foxc1b*:GFP and *pitx2*:GFP (Liu and Semina, 2012; Reis et al., 2012), appear to have more stochastic migration paths (**Figure 4E**). A more stochastic migration pattern may be indicative of ASM cells further along the differentiation spectrum and no longer needing to target to specific AS regions. Similar to our observations of ASM expression patterns and distribution (**Figures 1–3**), migratory behavior is also clearly variable amongst ASM cells which further supports the notion of a heterogenous population.

Lastly, we investigated the transcriptomic differences amongst the ASM. Utilizing the 10× Genomics process of scRNA sequencing, we isolated 48 hpf eyes from transgenic embryos (*foxc1b*:GFP, *foxd3*:GFP, *lmx1b*:GFP, *sox10*:GFP, and *pitx2*:GFP) and used FACS to isolate our GFP+ ASM cells. This approach aimed to ensure only AS associated cells were included in our analysis. ASM specific single cell cDNA libraries were generated, sequenced, and based on transcriptomic profiles, grouped into four distinct clusters (**Figures 5A,B**). We classified these clusters into a NCC-like cluster (*sox10*/*foxd3*), POM progenitor cluster

(*pitx2*), a ASM progenitor cluster (*lmx1b/foxc1b*) and finally a specified ASM cluster (*foxc1b*) (**Figures 5B,C**). UMAP analysis of the data indicates a connection between clusters suggesting that ASM cells may be found along a heterogenous, but connected, spectrum during AS colonization. This connection is also apparent when examining the cluster associated percentage distribution of our isolated cells. The four clusters all appear to be connected along a plausible trajectory of AS development starting with the NCC-like cluster (cluster 1), then the POM progenitor cluster (cluster 3) followed by the ASM progenitor cluster (cluster 4) and finally an ASM-like cluster (cluster 2). We predict that early AS is therefore likely colonized by a heterogenous population of ASM that may represent different stages of differentiation along the path to an AS cell fate. This combination could ensure that while some ASM enter already poised to begin differentiation and assembly of functional AS structures, such as the *pitx2*, *foxc1b*, or *lmx1b* driven subpopulations, others that are likely more pluripotent, *foxd3/sox10* driven, serve to ensure that proper numbers of ASM arrive at all points along the AS and then further differentiate in response to local signaling cues. It is therefore not surprising that distributions, migratory patterns and transcriptomic profiles of *sox10*:GFP and *foxd3*:GFP cells are highly similar when compared to *foxc1b*:GFP, *lmx1b.1*:GFP, or *pitx2*:GFP. Finally, while transcriptomic differences observed in our data support the notion of a heterogenous ASM population, they do not infer lineage marking. Future fate mapping experiments will need to be performed to determine whether specific transcriptomic differences directly determine cell fate or simply represent transitional states along the ASM differentiation pathway.

Expression analysis of cluster specific targets identified by our scRNA assay revealed a number of genes of particular interest including *sparc*, *hmgn2*, *adcyap1b*, *agr1*, *col2a1a tgfbi*, and *fmoda* (**Figure 6**). Several of these genes are associated with regulation and function of the extracellular matrix including *sparc*, *col2a1a*, and *fmoda*, indicating a possible relationship with the drainage systems of the iridocorneal angle (Abu-Hassan et al., 2014). While the drainage networks are the last to fully differentiate in the AS, their importance to the function of the eye cannot be understated. *Tgfbi* is associated with head mesenchyme and neural crest and is also predicted to be localized to the extracellular matrix (Chakravarthi et al., 2005; Kannabiran and Klintworth, 2006). Interestingly, the t*gfbi* gene is associated with a subset of familial corneal dystrophies (Nielsen et al., 2020). *Hmgn2* is a non-histone component of nucleosomal DNA and is associated with transcriptionally active chromatin, especially in cells that remain undifferentiated, and is involved in DNA replication, transcription, and repair (Lucey et al., 2008; Furusawa and Cherukuri, 2010). Although not yet associated with AS development or ASD pathology, *hmgn2* is abundantly expressed throughout the ocular structures of the AS and retina in mice, especially in the lens fibers and epithelium layer of the cornea (Lucey et al., 2008). *Adcyap1b* is a neuropeptide also known as PACAP associated with brain and camera-type eye development, meaning that it plays a role in the development of the lens and retina of the eye (Wu et al., 2006; Denes et al., 2019). PACAP also appears to have retinoprotective attributes (Shioda et al., 2016). The mechanisms of *adcyap1b* function during AS development is unclear at this time. Finally, *agr1* is associated with the negative regulation of cell death, regenerative abilities of fish and frogs and is strongly associated with liver function (Ivanova et al., 2015, 2018). While it's function within the eye remains unclear at this time, *agr1* does show expression in the corneal region (**Figure 6**) (Ivanova et al., 2015). Future studies will focus on examining the functional roles of the aforementioned AS associated target genes as well as others from our transcriptomic screen (**Figure 5D**). We will also seek to determine whether the identified clusters also represent lineages of specific AS structures, such as the cornea, iridocorneal angle (annular element in zebrafish) or iris.

Heterogeneity within the early colonizing POM and subsequent ASM poses an important question: what is the functional interplay between such subpopulations? Previous studies of AS development in several models suggest that there are in fact "master regulators" of this process, in particular *foxc1* and *pitx2*. Loss of function of either has significant consequences on AS formation and function. However, the status of other POM/ASM markers, or subpopulations, in these circumstances has not been thoroughly examined. It therefore remains unknown whether all ASM subpopulations are affected and to what degree. We know even less about the consequences of other POM/ASM regulators, such as *eya2*, *foxd3*, or *lmx1b*, in this context. Future work will need to concentrate on carefully teasing out how individual regulators of POM influence the entire process of AS colonization, rather than simply observing for physiological consequences in juvenile or adult AS tissues.

In conclusion, our findings, based on distribution, migration and transcriptomic profiles, indicate that POM cells targeted to the anterior segment, which we have termed the Anterior Segment Mesenchyme (ASM), are not homogenous. Rather, the ASM simultaneously comprises of several subpopulations likely divided along the ASM differentiation pathway. Our findings open a wide range of possible new investigative paths in the area of AS development and ASD disorders. Future examination of the interplay between these subpopulations will be prudent to further our understanding of eye development and ultimately predisposition to ASD associated blinding disorders.

MATERIALS AND METHODS

Zebrafish Maintenance

Zebrafish lines were bred and maintained in accordance with IACUC regulations (IACUC protocol 2015-1380) at the University of Kentucky. AB strain was used as wildtype. Transgenic lines used were: Tg[*foxc1b:GFP]* (Dr. Bryan Link), Tg[*foxd3:GFP]* (Dr. Lister), Tg[*pitx2C4:GFP]* (Dr. Elena Semina), and Tg[*lmx1b.1:GFP]* (Dr. Brian Link), Tg[*sox10:RFP]* (Dr. Lister). All embryos were raised for the first 24 h post fertilization in embryo media (E3) at 28°C. After 24 h, E3 media was replaced with embryo media containing 1-phenyl 2-thiourea (PTU) every 24 h to maintain embryo transparency.

Whole-Mount *in situ* Hybridization (WISH)

Whole-mount *in situ* hybridizations were performed using a minimum of 20–25 embryos for each time point (12, 18, 24, 32, 48, and 72). DIG and FITC labeled RNA probes were created using PCR incorporating T7 promoters in the primers and transcribed with T7 polymerase (Roche). Forward and Reverse primer sequences are listed in **Supplementary Table S1**. WISH protocol was performed as previously described (Holly et al., 2014). Dorsal, lateral, and ventral images of embryos were captured using a Nikon Digital Sight DS-U3 camera and Elements software. Images were adjusted for brightness using Adobe Photoshop and assembled into figures using Adobe Illustrator.

Immunohistochemistry (IHC) for Distribution and Proliferation Analysis

Approximately 30 embryos were imaged for each transgenic line at each of the given time points (24, 26, 28, 30, 48, 54, and 72 hpf). Embryos were fixed overnight at 4°C using 4% PFA. PFA was washed out with PBST 4 times for 5 min each. Embryos were permeabilized with Proteinase K (10 μg/ml) at the following times (24 hpf = 5 min; 26 hpf = 6 min; 28 hpf = 7 min; 30 hpf = 9 min; 48 hpf = 20 min; 54 hpf = 25 min; 72 hpf = 40 min), washed with PBST and then blocked with 5% goat serum (1 g/100 ml), 1% BSA in a solution of 1x PBST for at least 2 h at room temperature. Primary antibody (Rockland rabbit anti-GFP) was diluted at 1/200 in blocking buffer and incubated overnight at 4°C on rotation. The following day, the primary antibody solution was washed out with PBST 5 times for 15 min each. Secondary antibody (Alexa Fluor 488 anti rabbit, 1/1000) and DAPI (1/2500) were diluted in blocking buffer and incubated for 1 h on rotation in the dark at room temperature. Embryos were washed 2× for 15 min with PBST in the dark.

After staining, embryos were embedded in a 1.2% Low-gelling agarose in a 1-inch glass bottom cell culture dish (Fluorodish, World Precision Instruments) and visualized using a Nikon C2+ confocal microscope with a 20× (0.95 NA) oil immersion objective. The anterior segment of the eye was imaged in 3D in the lateral position as a 100 μm z-stack using 3.50 μm steps. All images were captured using Nikon Elements software, adjusted for contrast and brightness using Adobe Photoshop and assembled into figures using Adobe Illustrator. Images generated from IHC analysis were rendered in 3D using Nikon Elements Viewer software. Eyes were divided into 4 quadrants: dorsal nasal, dorsal temporal, ventral nasal, and ventral temporal. Nasal and temporal regions were divided by a vertical straight line through the center of the lens, while dorsal and ventral were divided by a horizontal straight line through the center of the lens. For distribution analysis, GFP+ cells were manually counted based on their position within one of the four quadrants of a 3D constructed anterior segment. For each timepoint 25+ embryos from three independent trials were imaged for quantification.

Two-Color Fluorescent WISH

RNA probes were generated using the MEGAscript T7 transcription Kit (Ambion) in combination with RNA labeling mixes for both DIG and FITC (Roche). Double *in situ* hybridization was performed according to the protocol by Lauter et al. (2011). This included exposing embryos to acidified methanol and adding Dextran Sulfate into the hybridization reaction. Staining was done by combining Fast Blue and Fast Red dyes (Sigma) (50 μg/ml). After successful *in situ* double staining, embryos were additionally stained using DAPI and imaged using a NIKON C2+ confocal microscope. Images were adjusted for brightness and contrast using Adobe Photoshop and assembled into figures using Adobe Illustrator. 15–20 embryos were analyzed for each probe combination.

Time-Lapse Confocal *in vivo* Imaging

Embryos from each of the previously mentioned transgenic lines were collected and raised in E3 media at 28°C. Fluorescent embryos were placed in E3 PTU media including 3-amino benzoic acid ethyl ester (Tricaine) to prevent pigmentation and to anesthetize them, respectively. They were then dechorionated and embedded laterally in 1% low-gelling agarose in a 35 mm glass bottom cell culture dish (Fluordish, World Precision instruments). Real-time imaging was conducted at 28°C using a Nikon C2+ confocal microscope and a 20× (0.95 NA) oil immersion objective. 3D *z*-stacks over a 75 μm thickness with a slice size of 3.5 μm were collected to encompass the entire developing anterior segment. *Z*-stack images were taken at 10 min intervals over a 24 h period (embryos imaged: n = 12 *foxc1b:GFP*, n = 9 *foxd3:GFP*, n = 13 *pitx2:GFP*, n = 10 *lmx1b.1:GFP*, n = 7 *sox10:RFP*). Data were collected and rendered using Nikon Elements software. Images were adjusted for brightness using Adobe Photoshop and assembled into figures using Adobe Illustrator.

Cell Migration Tracking and Displacement Analysis

Completed 4D live imaging files were uploaded into FIJI software for analysis. Approximately 25 cells were manually tracked per video file using manual tracking tools. Tracked cells were measured for total distance traveled (μm), average velocity (μm/min), and total displacement (pixels). Tracked cells were randomly selected from all four eye quadrants to ensure all eye regions were represented, as well as all time frames. After tracking, data were exported to Microsoft Excel for statistical analysis. Displacement was measured using the line measurement tool in FIJI software. Previously tracked lines were identified as "completed" tracks in one of two ways: (1) at the end of the migration video or (2) the track was seen in the last frames of video before the specific track disappeared. Once the completed track was identified, the line measurement tool was used to measure the straight-line distance (in pixels) from the first point of the track to the last point of the track. Stats were analyzed in Microsoft Excel and Graphpad Prism8.

Single Cell Transcriptomic Analysis

Embryos from each of the POM subpopulation transgenic lines were dechorionated and incubated in E3 media at 28°C until 48 hpf. At this time, embryos were anesthetized using 3-amino benzoic acid ethyl ester (Tricaine) and their eyes dissected and collected on ice. Eyes were incubated for 2 min in 0.25% Trypsin + EDTA at 37°C. After incubation, a 20G needle and syringe were used to dissociate the tissue before the tube was placed back at 37°C for 2 min. This process was repeated four times. After incubation, the dissociated cells were strained using a 40 μm filter (VWR) and spun down for 10 min at 3,500 rpm at 4°C. The supernatant was removed and the pellet resuspended in 1x PBS + 2 mM EDTA and goat serum. Cells were sorted for GFP+ identity at the University of Kentucky Flow Cytometry and Immune Monitoring Core at the Markey Cancer Center. After sorting, cells were spun down and resuspended using PBS and goat serum. Approximately 1,000 cells from each transgenic line were then loaded onto the Chromium 10× V3 chip (10× genomics) and processed in the University of Kentucky Department of Biology Imaging Core to generate single cell barcoded cDNA. Sequencing was performed using NovaSeq SP, 2 × 150 bp paired ends to achieve 100,000 reads per cell at University of Illinois at Urbana-Champaign Roy J. Carver Biotechnology Center. Sequencing results were processed and subsequently aggregated (incorporating mapped normalization), using the Cell Ranger3.1 pipeline and results analyzed using Loupe Cell Browser 3.1.1 software (10× genomics).

Statistics

One-way ANOVA analysis (multiple point analysis) and unpaired *t*-tests (individual comparison analysis) were performed using Microsoft Excel and GraphPad Prism8 software. All graphs are shown with their respective means and standard deviations. Values were considered significant by the conventional standard: *P*-value of 0.05 or less.

DATA AVAILABILITY STATEMENT

The raw data supporting the conclusions of this article will be made available by the authors, without undue reservation, to any qualified researcher.

ETHICS STATEMENT

The use of zebrafish in this study was approved by the University of Kentucky IACUC committee, Institutional PHS Assurance #D16-00217 (A3336-01) with a protocol number: 2015-1370. All experimental protocols were approved by the University of Kentucky Institutional Biosafety Committee, registration number B18-3186-M.

AUTHOR CONTRIBUTIONS

JF and KV wrote the manuscript. KV, OV, MW, and NM performed the experiments and analysis. JF oversaw the project secured funding. JF and KV contributed to conception and design of the study. All authors contributed to manuscript revision, read and approved the submitted version.

FUNDING

This work was supported by the NIH-NEI grant EY027805-01. MW was supported by the Lyman T. Johnson Scholarship from the University of Kentucky. OV was supported by the Knights Templar Eye Foundation Career Starter Grant.

ACKNOWLEDGMENTS

We thank Dr. Link, Dr. Semina, and Dr. Lister for providing transgenic zebrafish lines. We thank members of the Famulski lab for helpful discussions. We also thank Dr. Jeramiah Smith for assistance with single cell sequencing analysis. This manuscript has been released as a pre-print at Biorxiv (Van Der Meulen et al., 2019).

SUPPLEMENTARY MATERIAL

The Supplementary Material for this article can be found online at: https://www.frontiersin.org/articles/10.3389/fcell.2020.00379/full#supplementary-material

FIGURE S1 | Schematic representation of AS colonization in a zebrafish embryo. Upon closure of the neural tube (NT) neural crest cells (NCC) delaminate and begin to migrate throughout the embryo (12–18 hpf), including the cranial NCC within the developing head (pictured as black outline; OV, optic vesicle). Upon retinal morphogenesis and lens (L) induction (18–28 hpf), NCC begin to surround the retina (R) in anticipation of AS colonization and become periocular mesenchyme (POM). POM targeted to the AS subsequently migrate onto the surface of the retina and occupy the future AS (28–48 hpf).

FIGURE S2 | Anterior segment ASM heterogeneity for *eya2* expression. **(A–D)** Two-color fluorescent WISH (FWISH) performed for all possible combinations of *eya2* vs. *foxc1a*, *foxd3*, *pitx2*, and *sox10* at 32 and 48 hpf. DAPI is in blue. White arrows within inset panels (dashed squares) display instances of individual **(b)** and co-expression **(a)**. Scale bar = 50 μm.

FIGURE S3 | PH3 proliferation staining assay. 3D rendering of confocal stacks of the AS at 32 and 48 hpf. GFP+ cells (green) are the result of transgenic lines, pH3+ cells (red) indicate active cell division, and DAPI (blue) stains the nucleus. **(A)** Few pH3+ cells can be seen on the surface of the AS at 32 hpf, indicating little to no cell division is taking place. No co-expression was seen between the GFP+ cells and pH3+ cells in any of the POM subpopulations. **(B)** Similarly, the AS at 48 hpf also lacked pH3+ cells and had little to no co-expression with the various POM subpopulations.

FIGURE S4 | cDNA library-based t-SNE and UMAP clusters. *K*-means clustering of scRNA sequencing of isolated 48 hpf *foxc1b:*GFP (pink), *lmx1b.1:*GFP (green), *sox10:*GFP (blue), *foxd3:*GFP (mustard) and *pitx2*:GFP (teal) ASM cells in both tSNE and UMAP readouts.

FIGURE S5 | PANTHER Gene Ontology for 48 hpf ASM clusters. Protein function Gene Ontology was applied to gene lists from clusters 1–4. Pie graphs display the distribution of each GO term applied.

TABLE S1 | *WISH* Primer Sequences. mRNA forward and reverse primer sequences for all POM and NCC-related genes.

TABLE S2 | scRNA sequencing aggregation gene list. Distribution of all gene expression analyzed during aggregation analysis.

MOVIE S1 | *Foxc1b:GFP* 4D imaging (24–28 hpf).

MOVIE S2 | *Foxd3:GFP* 4D imaging (24–48 hpf).

MOVIE S3 | *Pitx2:GFP* 4D imaging (22–46 hpf).

MOVIE S4 | *Lmx1b.1:GFP* 4D imaging (24–48 hpf).

MOVIE S5 | *Sox10:RFP* 4D imaging (23–47 hpf).

MOVIE S6 | *Foxc1b:GFP* Tracking analysis.

MOVIE S7 | *Foxd3:GFP* Tracking analysis.

MOVIE S8 | *Pitx2:GFP* Tracking analysis.

MOVIE S9 | *Lmx1b.1* Tracking analysis.

MOVIE S10 | *Sox10:RFP* Tracking analysis.

REFERENCES

Abu-Hassan, D. W., Acott, T. S., and Kelley, M. J. (2014). The trabecular meshwork: a basic review of form and function. *J. Ocul. Biol.* 2, 1–9.

Akula, M., Park, J. W., and West-Mays, J. (2018). Relationship between neural crest cell specification and rare ocular diseases. *J. Neurosci. Res.* 97, 7–15. doi: 10.1002/jnr.24245

Berry, F., Lines, M., Oas, J., Footz, T., Underhill, D., Gage, P., et al. (2006). Functional interactions between foxc1 and pitx2 underlie the sensitivity to foxc1 gene dose in axenfeld-rieger syndrome and anterior segment dysgenesis. *Hum. Mol. Genet.* 15, 905–919. doi: 10.1093/hmg/ddl008

Bohnsack, B., Kasprick, D., Kish, P., Goldman, D., and Kahana, A. (2012). A zebrafish model of axenfeld-rieger syndrome reveals that pitx2 reglation by retinoic acid is essential for cular and craniofacial development. *Invest. Ophthalmol. Vis. Sci.* 53, 7–22. doi: 10.1167/iovs.11-8494

Cavodeassi, F. (2018). Dynamic tissue rearrangments during vertebrate eye morphogenesis: insights from fish models. *J. Dev. Biol.* 6:4. doi: 10.3390/jdb6010004

Chakravarthi, S. V., Kannabiran, C., Sridhar, M. S., and Vemuganti, G. K. (2005). TGFBI gene mutations causing lattice and granular corneal dystrophies in Indian patients. *Invest, Ophthalmol. Vis. Sci.* 46, 121–125. doi: 10.1167/iovs.04-0440

Chawla, B., Schley, E., Williams, A., and Bohnsack, B. (2016). Retinoic acid and pitx2 regulate early neural crest survival and migration in craniofacial and ocular development. *Birth Defect Res. Part B* 107, 126–135. doi: 10.1002/bdrb.21177

Chawla, B., Swain, W., Williams, A., and Bohnsack, B. (2018). Retinoic acid maintains function of neural crest-derived ocular and craniofacial structures in adult zebrafish. *Invest. Ophthalmol. Vis. Sci.* 59, 1924–1935. doi: 10.1167/iovs.17-22845

Chen, L., and Gage, P. (2016). Heterozygous Pitx2 null mice accurately recapitulate the ocular features of axenfeld-rieger syndrome and congenital glaucoma. *Investig. Ophthalmol. Vis. Sci.* 57, 5023–5030. doi: 10.1167/iovs.16-19700

Clay, M., and Halloran, M. (2010). Control of neural crest cell behavior and migration. *Cell Adh. Mig.* 4, 586–594. doi: 10.4161/cam.4.4.12902

Creuzet, S., Vincent, C., and Couly, G. (2005). Neural crest derivatives in ocular and periocular structures. *Int. J. Dev. Biol.* 49, 161–171. doi: 10.1387/ijdb.041937sc

Denes, V., Hideg, O., Nyisztor, Z., Lakk, M., Godri, Z., Berta, G., et al. (2019). The neuroprotective peptide PACAP1-38 Contributes to horizontal cell development in postnatal rat retina. *Invest. Ophthalmol. Vis. Sci.* 60, 770–778. doi: 10.1167/iovs.18-25719

Drerup, C., Wiora, H., Topczewski, J., and Morris, J. (2009). Disc1 regulates foxd3 and sox10 expression, affecting neural crest migration and differentiation. *Development* 136, 2623–2632. doi: 10.1242/dev.030577

Dutton, K., Pauliny, A., Lopes, S., Elworthy, S., Carney, T., Rauch, J., et al. (2001). Zebrafish colourless encodes sox10 and specifies non-ectomesenchymal neural crest fates. *Development* 128, 4113–4125.

Evans, A., and Gage, P. (2005). Expression of the homeobox gene Pitx2 in neural crest is required for optic stalk and ocular anterior segment development. *Hum. Mol. Genet.* 14, 3347–3359. doi: 10.1093/hmg/ddi365

Fuhrmann, S., Levine, E., and Reh, T. (2000). Extraocular mesenchyme patterns the optic vesicle during early eye development in the embryonic chick. *Development* 127, 4599–4609.

Furusawa, T., and Cherukuri, S. (2010). Developmental function of HMGN proteins. *Biochim. Biophys. Acta* 1799, 69–73. doi: 10.1016/j.bbagrm.2009.11.011

Gage, P., Kaung, C., and Zacharias, A. (2014). The homeodomain transcription factor pitx2 is required for specifying correct cell fates and establishing angiogenic privilege in the developing cornea. *Dev. Dyn.* 243, 1391–1400. doi: 10.1002/dvdy.24165

Gould, D., Smith, R., and John, S. (2004). Anterior segment development relevent to glaucoma. *Int. J. Dev. Biol.* 48, 1015–1029.

Hendee, K., Sorokina, E., Muheisen, S., Reis, L., Tyler, R., Markovic, V., et al. (2018). ., Pitx2 deficiency and associated human disease: insights from the zebrafish model. *Hum. Mol. Genet.* 27, 1675–1695. doi: 10.1093/hmg/ddy074

Holly, V. L., WIden, S. A., Famulski, J. K., and Waskiewicz, A. J. (2014). Sfrp1a and Sfrp5 function as positive regulators of Wnt and BMP signaling during early retinal development. *Dev. Biol.* 388, 192–204. doi: 10.1016/j.ydbio.2014.01.012

Ivanova, A. S., Korotkova, D. D., Ermakova, G. V., Martynova, N. Y., Zaraisky, A. G., and Tereshina, M. B. (2018). Ras-dva small GTPases lost during evolution of amniotes regulate regeneration in anamniotes. *Sci. Rep.* 8:13035. doi: 10.1038/s41598-018-30811-0

Ivanova, A. S., Shandarin, I. N., Ermakova, G. V., Minin, A. A., Tereshina, M. B., and Zaraisky, A. G. (2015). , The secreted factor Ag1 missing in higher vertebrates regulates fins regeneration in Danio rerio. *Sci. Rep.* 5,:8123. doi: 10.1038/srep08123

Ji, Y., Buel, S., and Amack, J. (2016). Mutations in zebrafish pitx2 model congenital malformations in axenfeld-rieger syndrome but do not disrupt left-right placement of visceral organs. *Dev. Biol.* 416, 69–81. doi: 10.1016/j.ydbio.2016.06.010

Kannabiran, C., and Klintworth, G. K. (2006). TGFBI gene mutations in corneal dystrophies. *Hum. Mutat.* 27, 615–625.

Kulesa, P., Bailey, C., Kasemeier-Kulesa, J., and McLennan, R. (2010). Cranial neural crest migration: new rules for an old road. *Dev. Biol.* 344, 543–554. doi: 10.1016/j.ydbio.2010.04.010

Langenberg, T., Kahana, A., Wszalek, J., and Halloran, M. (2008). ., The eye organizes neural crest cell migration. *Dev. Dyn.* 237, 1645–1652. doi: 10.1002/dvdy.21577

Lauter, G., Söll, I., and Hauptmann, G. (2011). Two-color fluorescent *in situ* hybridization in the embryonic zebrafish brain using differential detection systems. *BMC Dev. Biol.* 11:43. doi: 10.1186/1471-213X-11-43

Lister, J., Cooper, C., Ngyen, K., Modrell, M., Grant, K., and Raible, D. (2006). Zebrafish foxd3 is required for development of a subset of neural crest derivatives. *Dev. Biol.* 290, 92–104. doi: 10.1016/j.ydbio.2005.11.014

Liu, P., and Johnson, R. (2010). Lmx1b is required for murine trabecular meshwork formation and for the maintenance of corneal transparency. *Dev. Dyn.* 239, 2161–2171. doi: 10.1002/dvdy.22347

Liu, Y., and Semina, E. (2012). Pitx2 deficiency results in abnormal ocular and craniofacial development in zebrafish. *PLoS One* 7:e30896. doi: 10.1371/journal.pone.0030896

Lucey, M. M., Wang, Y., Bustin, M., and Duncan, M. K. (2008). Differential expression of the HMGN family of chromatin proteins during ocular development. *Gene Expr. Patterns* 8, 433–437. doi: 10.1016/j.gep.2008.04.002

Lupo, G., Gestri, G., O'Brien, M., Denton, R. M., Chandraratna, R. A., Ley, S. V., et al. (2011). Retinoic acid receptor signaling regulates choroid fissure closure through independent mechanisms in the ventral optic cup and periocular mesenchyme. *Proc. Natl. Acad. Sci. U.S.A.* 108, 8698–8703. doi: 10.1073/pnas.1103802108

Matt, N., Dupe, V., Garnier, J., Dennefeld, C., Chambon, P., Mark, M., et al. (2005). Retinoic acid-dependent eye morphogenesis is orchestrated by neural crest cells. *Development* 132, 4789–4800. doi: 10.1242/dev.02031

Matt, N., Ghyselinck, N. B., Pellerin, I., and Dupe, V. (2008). Impairing retinoic acid signalling in the neural crest cells is sufficient to alter entire eye morphogenesis. *Dev. Biol.* 320, 140–148. doi: 10.1016/j.ydbio.2008.04.039

McMahon, C., Gestri, G., Wilson, S., and Link, B. (2009). Lmx1b is essential for survival of periocular mesenchymal cells and influences fgf-mediated retinal pattering in zebrafish. *Dev. Biol.* 332, 287–298. doi: 10.1016/j.ydbio.2009.05.577

Nielsen, N. S., Poulsen, E. T., Lukassen, M. V., Chao Shern, C., Mogensen, E. H., Weberskov, C. E., et al. (2020). Biochemical mechanisms of aggregation in TGFBI-linked corneal dystrophies. *Prog. Retin. Eye Res.* 100843. (in press). doi: 10.1016/j.preteyeres.2020.100843

Poulaki, V., and Colby, K. (2008). Genetics of anterior and stromal corneal dystrophies. *Semin. Ophthalmol.* 23, 9–17. doi: 10.1080/08820530701745173

Reis, L., Tyler, R., Kloss, V. B., Schilter, K., Levin, A., Lowry, R. B., et al. (2012). Pitx2 and Foxc1 spectrum of mutations in ocular syndromes. *Eur. J. Hum. Genet.* 20, 1224–1233. doi: 10.1038/ejhg.2012.80

Richardson, J., Gauert, A., Montecinos, L., Fanlo, L., Alhashem, Z., Assar, R., et al. (2016). Leader cells define directionality of trunk, but not cranial, neural crest cell migration. *Cell Rep.* 15, 2076–2088. doi: 10.1016/j.celrep.2016.04.067

Seo, S., Chen, L., Liu, W., Zhao, D., Schultz, K., Sasman, A., et al. (2017). ., FoxC1 and FoxC2 in the neural crest are required for the ocular anterior segment development. *Invest. Ophthalmol. Vis. Sci.* 58, 1368–1377. doi: 10.1167/iovs.16-21217

Shioda, S., Takenoya, F., Wada, N., Hirabayashi, T., Seki, T., and Nakamachi, T. (2016). Pleiotropic and retinoprotective functions of PACAP. *Anat. Sci. Int.* 91, 313–324. doi: 10.1007/s12565-016-0351-0

Stewart, R., Arduini, B., Berghmans, S., George, R., Kanki, J., Henion, P., et al. (2006). Zebrafish foxd3 is selectively required for neural crest specification, migration, and survival. *Dev. Biol.* 292, 174–188. doi: 10.1016/j.ydbio.2005.12.035

Trainor, P., and Tam, P. (1995). Cranial paraxial mesoderm and the neural crest cells of the mouse embryo: co-distribution in the craniofacial mesenchyme but distinct segregation in the branchial arches. *Development* 121, 2569–2582.

Van Der Meulen, K. L., Vocking, O., Meshram, N. N., and Famulski, J. K. (2019). Spatiotemporal characterization of anterior segment mesenchyme heterogeneity during anterior segment development. *BioRxiv* [preprint]. doi: 10.1101/726257,

Volkmann, B. A., Zinkevich, N. S., Mustonen, A., Schilter, K. F., Bosenko, D. V., Reis, L. M., et al. (2011). Potential novel mechanism for Axenfeld-Rieger syndrome: deletion of a distant region containing regulatory elements of PITX2. *Invest. Ophthalmol. Vis. Sci.* 52, 1450–1459. doi: 10.1167/iovs.10-6060

Volkmann Kloss, B., Reis, L., Bremond-Gignac, D., Glaser, T., and Semina, E. (2012). Analysis of FoxD3 sequence variation in human ocular disease. *Mol. Vis.* 18, 1740–1749.

Wang, W., Melville, D., Montero-Balaguer, M., Hatzopoulos, A., and Knapik, E. (2011). Tfap2a and Foxd3 regulate early steps in the development of the neural crest progenitor population. *Dev. Biol.* 360, 173–185. doi: 10.1016/j.ydbio.2011.09.019

Williams, A., and Bohnsack, B. (2015). Neural crest derivatives in oular development: discerning the eye of the storm. *Birth Defects Res. Part C* 105, 87–95. doi: 10.1002/bdrc.21095

Wu, S., Adams, B. A., Fradinger, E. A., and Sherwood, N. M. (2006). Role of two genes encoding PACAP in early brain development in zebrafish. *Ann. N. Y. Acad .Sci.* 1070, 602–621. doi: 10.1196/annals.1317.091

Zhao, Y., Sorenson, C. M., and Sheibani, N. (2015). Cytochrome P450 1B1 and primary congenital glaucoma. *J. Ophthalmic. Vis. Res.* 10, 60–67. doi: 10.4103/2008-322X.156116

Conflict of Interest: The authors declare that the research was conducted in the absence of any commercial or financial relationships that could be construed as a potential conflict of interest.

frontiers in Cell and Developmental Biology

REVIEW
published: 16 June 2020
doi: 10.3389/fcell.2020.00438

Migrasome and Tetraspanins in Vascular Homeostasis: Concept, Present, and Future

Yaxing Zhang[1], Jing Wang[2], Yungang Ding[3], Jiongshan Zhang[1], Yan Xu[4], Jingting Xu[5], Shuhui Zheng[6] and Hongzhi Yang[1]**

[1] Department of Traditional Chinese Medicine, The Third Affiliated Hospital, Sun Yat-sen University, Guangzhou, China, [2] Department of Ophthalmology, Qingdao Fubai Eye Hospital, Qingdao, China, [3] Department of Ophthalmology, Qingdao Ludong Eye Hospital, Qingdao, China, [4] Department of Gastrointestinal Endoscopy, Guangzhou Cadre Health Management Center/Guangzhou Eleventh People's Hospital, Guangzhou, China, [5] Biofeedback Laboratory, Xinhua College of Sun Yat-sen University, Guangzhou, China, [6] Research Center for Translational Medicine, The First Affiliated Hospital, Sun Yat-sen University, Guangzhou, China

Cell migration plays a critical role in vascular homeostasis. Under noxious stimuli, endothelial cells (ECs) migration always contributes to vascular repair, while enhanced migration of vascular smooth muscle cells (VSMCs) will lead to pathological vascular remodeling. Moreover, vascular activities are involved in communication between ECs and VSMCs, between ECs and immune cells, et al. Recently, Ma et al. (2015) discovered a novel migration-dependent organelle "migrasome," which mediated release of cytoplasmic contents, and this process was defined as "migracytosis." The formation of migrasome is precisely regulated by tetraspanins (TSPANs), cholesterol and integrins. Migrasomes can be taken up by neighboring cells, and migrasomes are distributed in many kinds of cells and tissues, such as in blood vessel, human serum, and in ischemic brain of human and mouse. In addition, the migrasome elements TSPANs are wildly expressed in cardiovascular system. Therefore, TSPANs, migrasomes and migracytosis might play essential roles in regulating vascular homeostasis. In this review, we will discuss the discoveries of migration-dependent migrasome and migracytosis, migrasome formation, the basic differences between migrasomes and exosomes, the distributions and functions of migrasome, the functions of migrasome elements TSPANs in vascular biology, and discuss the possible roles of migrasomes and migracytosis in vascular homeostasis.

Keywords: cell migration, migrasome, migracytosis, tetraspanins, vascular homeostasis

OPEN ACCESS

Edited by:
Mitsugu Fujita,
Kindai University, Japan

Reviewed by:
Peter Monk,
University of Sheffield,
United Kingdom
María Yáñez-Mó,
Autonomous University of Madrid,
Spain

****Correspondence:***
Yaxing Zhang
zhangyaxingstar@126.com
Hongzhi Yang
hzyang1960@163.com

Specialty section:
This article was submitted to Cell Adhesion and Migration, a section of the journal Frontiers in Cell and Developmental Biology

Received: *16 March 2020*
Accepted: *11 May 2020*
Published: *16 June 2020*

Citation:
Zhang Y, Wang J, Ding Y, Zhang J, Xu Y, Xu J, Zheng S and Yang H (2020) Migrasome and Tetraspanins in Vascular Homeostasis: Concept, Present, and Future. Front. Cell Dev. Biol. 8:438. doi: 10.3389/fcell.2020.00438

BLOOD VESSELS AND VASCULAR HOMEOSTASIS

The vasculature is one of the first functional organs to form during embryogenesis and matures into a closed cardiovascular system, adding up to about 90,000 km in total length in adults (Eelen et al., 2018). Structurally, blood vessels are primarily made up of three layers: *tunica interna* (*intima*), *tunica media* (*media*), and *tunica externa* (*adventitia*), which is a network of connective tissue, including collagen fibers, fibroblasts, *vasa vasorum*, nerve endings, progenitor/stem cells, myofibroblasts, pericytes, lymphocytes, macrophages, and dendritic cells et al. (Moos et al., 2005; Hu and Xu, 2011; Campbell et al., 2012; Wilting and Chao, 2015; Halper, 2018; Zhang Y. et al., 2018); while lymphatic capillaries are thin-walled vessels of approximately 30–80 μm in diameter, composed of a single layer of oak-leaf-shaped lymphatic ECs that differ in many ways from blood vascular ECs (Alitalo, 2011). Almost all tissues, except for cartilage, cornea and lens et al., in the

body rely on blood vessels for a continuous supply of nutrients and oxygen, and on lymphatic vessels to collect excess protein-rich fluid that has extravasated from blood vessels and transport it back into blood circulation, and these vessels provide gateways for immune surveillance (Alitalo, 2011; Potente et al., 2011; Eelen et al., 2018). Additionally, blood vessels take part in controlling systemic pH and temperature homeostasis (Eelen et al., 2018).

During adult life, the maintenance of vascular homeostasis is the result of balancing vascular damage and injury with repair and regeneration, while also integrating environmental cues to optimize vascular function and blood vessel growth, thus ensuring adequate supply of oxygen and nutrients to tissues, and maintaining other functions mentioned above (Marsboom and Rehman, 2018). Vascular remodeling denotes morphological changes and reorganization of vessel wall structure, morphologically, all three layers of the arterial wall are concurrently affected by neointimal hyperplasia, medial thickening, and adventitial fibrosis attributable to the interaction of leukocyte recruitment, VSMCs accumulation, and endothelial recovery, in response to various noxious stimuli, such as hemodynamic stress, mechanical injury, inflammation, or hypoxia et al. (Schober, 2008; Zhang et al., 2016, 2017). All these lead to decrease in cross-sectional vessel diameters and increase in the thickness of the arterial wall. Therefore, vascular homeostasis maintenance is an active process, involved in the growth, migration and death of vascular cells, activation of immune cells in vasculature, as well as the generation and degradation of ECM, all these coordinate with environmental cues to maintain the function of blood vessels (Moos et al., 2005; Liu et al., 2014; Zhang and Dong, 2014; Zhang and Li, 2017).

CELL MIGRATION IN DEVELOPMENT, IMMUNE DEFENSE AND VASCULAR HOMEOSTASIS

Cell migration plays an essential role in a variety of physiological and pathological processes (Le Clainche and Carlier, 2008). During developmental processes, cell migration is fundamental to the establishment of the embryonic architecture like gastrulation (Keller, 2005), and migration is also required for neural crest cells colonization (Szabo and Mayor, 2018). Recently, *Yu Li* group indicated that migration-dependent migrasomes release developmental cues, including Cxcl12, into defined locations in embryos to modulate organ morphogenesis during zebrafish gastrulation (Jiang et al., 2019). The immune defensive function of most immune cells depends on their ability to migrate through complex microenvironments, either randomly to patrol for the presence of antigens or directionally to reach their next site of action (Moreau et al., 2018). In cardiovascular system, ECs migration occurs during vasculogenesis and angiogenesis, and also in damaged vessels to restore vessel integrity, VSMCs migrate to the intima and proliferate to contribute to neointimal lesions under pathophysiological conditions (Michaelis, 2014; Wang et al., 2015; Zhang et al., 2016). Therefore, cell migration is the key event during the regulation of vascular homeostasis.

THE DISCOVERIES OF MIGRATION-DEPENDENT MIGRASOME AND MIGRACYTOSIS

Porter et al. (1945) and Taylor and Robbins (1963) have observed the long projections from the surface of cells, and long tubular structures as migrating cells retracted from the substratum, respectively. Oppenheimer and Humphreys (1971), Culp and Black (1972), and Terry and Culp (1974) isolated the specific macromolecules, which remain on substrates after treating with chelating agents. Morphological and biochemical analyses showed that these SAMs are finger-like extensions and contain relatively large amounts of cell surface components that participate in cell adhesion, such as fibronectin, proteoglycans, and gangliosides (Rosen and Culp, 1977; Culp et al., 1979; Rollins and Culp, 1979; Murray and Culp, 1981; Mugnai et al., 1984; Barletta et al., 1989). SAMs are analogous to the retraction fibers of migrating cells that are also enriched with TSPANs (Penas et al., 2000; Zhang and Huang, 2012; Yamada et al., 2013). Besides TSPANs, SAMs also contain large amounts of TSPANs associated proteins, but not focal adhesion proteins, and thus resemble the footprints (Yamada et al., 2013). Although these structures wildly present in different cell types, however, they have received little attention, their structure, characterization and function are less well-known.

Ma et al. (2015) observed and characterized an extracellular membrane-bound vesicular structure, which are PLSs relate to

Abbreviations: BRB, blood–retina barrier; CAMs, cell adhesion molecules; circRNA, circular RNA; CPQ, carboxypeptidase Q; dsDNA, double-stranded DNA; ECs, endothelial cells; ECL1, extracellular loop 1; ECM, extracellular matrix; EOGT, EGF domain-specific O-linked *N*-acetylglucosaminetransferase; FZD4, Frizzled-4; GPCR, G-protein-coupled receptor; HCASMCs, human coronary artery smooth muscle cells; HDLECs, human dermal lymphatic endothelial cells; HDMECs, human dermal microvascular endothelial cells; HGF, hepatocyte growth factor; HLVECs, human liver endothelial cells; HMAECs, human mammary artery endothelial cells; HMEC-1, human microvascular endothelial cell line-1; HRCECs, human retinal capillary endothelial cells; HSP, heat shock protein; HSVECs, human saphenous vein endothelial cells; HUVECs, human umbilical vein endothelial cells; iBRECs, microvascular endothelial cells of the bovine retina; ICAM-1, intercellular adhesion molecule-1; KO, knockout; LAMP1, lysosomal associated membrane protein 1; MASMCs, mouse aortic smooth muscle cells; MCASMCs, mouse carotid artery smooth muscle cells; MEF, mouse embryonic fibroblast; miRNA, microRNA; MLUECs, mouse lung endothelial cells; MLVECs, mouse liver endothelial cells; MMP, matrix metalloproteinase; MRVECs, mouse retinal vascular endothelial cells; mtDNA, mitochondrial DNA; mtRNA, mitochondrial RNA; MT1-MMP, membrane-type 1 matrix metalloproteinase; MVB, multivesicular bodies; NDP, norrie disease protein, also referred to as norrin; NDST1, bifunctionalheparan sulfate *N*-deacetylase/*N*-sulfotransferase 1; NeuN, Neuronal Nuclei; NRK, normal rat kidney cell; PDGF-BB, platelet derived growth factor-BB; PIGK, phosphatidylinositol glycan anchor biosynthesis, class K; piRNA, PIWI-interacting RNA; PLSs, pomegranate-like structures; RAECs, rat aortic endothelial cells; RTK, Receptor tyrosine kinase; SAGE, serial analysis of gene expression; SAMs, substrate-attached materials; siRNA-TSPAN29, TSPAN29-specific small interfering RNA; snoRNA, small nucleolar RNA; snRNA, small nuclear RNA; ssDNA, single-stranded DNA; SUMF2, sulfatase modifying factor 2; TEMs, TSPAN-enriched microdomains; TEMAs, tetraspanin- and cholesterol-enriched macrodomains; TM1, transmembrane region 1; tRNA, transfer RNA; TSG101, tumor susceptibility gene 101; TSPANs, tetraspanins; tsRNAs, tRNA-derived small RNAs; VCAM-1, vascular cell adhesion molecule-1; VEGF, vascular endothelial growth factor; VEGFR-3, VEGF receptor 3; VSMCs, vascular smooth muscle cells; WGA, wheat-germ agglutinin.

cells. They found that a cell will leave retraction fibers behind it, and vesicles grow on the tips or at the intersections of retraction fibers during the process of migration; eventually, the retraction fibers break up, and PLSs, as a package of vesicles and cytosolic contents enclosed within a single limiting membrane, are released into the medium or directly taken up by surrounding cells (da Rocha-Azevedo and Schmid, 2015; Ma et al., 2015). The formation of these PLSs is dependent on both migration and actin polymerization, thus, they named these PLSs "migrasomes," which average lifespan is about 400 min, this migration-dependent release mechanism is named "migracytosis" (Ma et al., 2015).

THE MOLECULAR MECHANISM OF MIGRASOMES FORMATION

As migrasomes are membrane structures, therefore, membrane-localized proteins and the organization of membrane are essential for migrasomes formation. TSPANs family, which includes 33 members in human beings (Hemler, 2008; Rubinstein, 2011), are abundant in membranes of various types of endocytic organelles and in exosomes (Zoller, 2009; van Niel et al., 2018), and are also essential components of migrasomes (**Table 1**). TSPANs contain a number of shared structural features, including TM1, TM2, TM3 and TM4, a very short intracellular loop (typically four amino acids) between TM2 and TM3, a short ECL1 between TM1 and TM2, a large ECL2 between TM3 and TM4, short amino- and carboxy-terminal tails, and a large central pocket inside the intramembranous region bounded by the four transmembrane helices (Hemler, 2005; Zoller, 2009; Zimmerman et al., 2016; Umeda et al., 2020). The Glu219 in TSPAN28 is the critical residue for cholesterol molecule binding at the central cavity, TSPAN10 also possesses a polar residue in this position, while most other TSPANs have a polar residue one helical turn earlier, with other cholesterol-binding residues highly conserved throughout evolution, offering a potential mechanism for how TSPANs might detect cholesterol or other membrane lipids (Zimmerman et al., 2016). The TEMs, including TSPANs, a set of TSPANs-associated proteins and a high concentration of cholesterol, is a functional unit in cell plasma membranes (Yanez-Mo et al., 2009; Huang et al., 2019). The physiological and pathological functions of TSPANs family genes have been investigated and confirmed by the established TSPANs KO mice (**Supplementary Table 1**).

During the discovery of migrasomes, *Yu Li* group identified that TSPAN4 is abundant in migrasomes membrane, and acts as the clearest migrasomes marker (Ma et al., 2015). Overexpression of TSPAN1, 2, 3, 4, 5, 6, 7, 9, 13, 18, 25, 26, 27, and 28 enhance the formation of migrasomes, and TSPAN1, 2, 4, 6, 7, 9, 18, 27, and 28 have strong effects (Huang et al., 2019). KO of TSPAN4 impairs migrasomes formation in MGC-803 cells and NRK, while deficiency of TSPAN4 in L929 cells did not impair migrasomes formation, presumably due to the presence of other migrasomes-forming TSPANs (Huang et al., 2019). TSPAN4, TSPAN7, cholesterol and integrins are necessary for migrasomes formation (Wu et al., 2017; Huang et al., 2019; Jiang et al., 2019). TSPAN4 in migrasomes is about four times higher than in retraction fibers, cholesterol is enriched about 40-fold in migrasomes relative to retraction fibers, and integrins are highly enriched on migrasomes and are only present at very low levels on retraction fibers (Wu et al., 2017; Huang et al., 2019). The activated integrin α5 is mainly enriched on the bottom side of migrasomes while TSPAN4 is on the upper side (Wu et al., 2017). Mechanistically, when a cell migrates, integrins enable cell migration and the correct pairing of integrin with its specific ECM partner protein provides the adhesion for retraction fiber tethering, and retraction fibers are formed at the back of the migrating cells (Wu et al., 2017). The mechanical stress exerted along the retraction fibers triggers clustering of TSPANs, such as TSPAN4, TSPAN7, and cholesterol molecules, leading to the formation of "TEMAs," which enriched causes stiffening of the plasma membrane, thus, facilitating a new migrasome formation (Huang et al., 2019; Jiang et al., 2019; Tavano and Heisenberg, 2019).

THE BASIC DIFFERENCES BETWEEN MIGRASOMES AND EXOSOMES

Both migrasomes and exosomes are the extracellular membrane-bound vesicular structures, however, the comparison of migrasomes and exosomes proteomics indicates that the two structures share only 27% (158) proteins, and there is still much difference among size, contents, TSPANs expression profiles, classical membrane markers, specific protein markers, and the process of release (da Rocha-Azevedo and Schmid, 2015; Ma et al., 2015; Ibrahim and Marban, 2016; Wu et al., 2017; Chen et al., 2018; Schmidt-Pogoda et al., 2018; van Niel et al., 2018; Huang et al., 2019; Jeppesen et al., 2019; Jiang et al., 2019; Pegtel and Gould, 2019; Zhao et al., 2019; Kalluri and LeBleu, 2020; **Table 1**).

Based on these above, TSPAN4/7 and integrin α1, α3, α5, β1 et al., which are expressed in the membrane of migrasomes, can act as essential structure markers for migrasomes (Ma et al., 2015; Wu et al., 2017; Schmidt-Pogoda et al., 2018; Huang et al., 2019; Jiang et al., 2019). NDST1, PIGK, CPQ and EOGT, which are enriched in migrasomes, but are absent or barely detectable in exosomes, are specific protein markers for migrasomes (Zhao et al., 2019). The transmission electron microscopy is used to detected ultrastructure of migrasomes *in situ* within cultured cells (Chen et al., 2018). A recent study by *Yu Li* group indicated that WGA is a probe for convenient, rapid detection of migrasomes in both fixed and living cells (Chen et al., 2019). The detail methods for visualizing migrasomes have also been described in two articles of "Detection of Migrasomes" and "WGA is a probe for migrasomes" by *Yu Li* group (Chen et al., 2018, 2019).

THE DISTRIBUTIONS AND FUNCTIONS OF MIGRASOMES

Studies in the past 5 years indicated that migrasomes are distributed in many cell types *in vitro*, including NRK, mouse

TABLE 1 | The basic characteristics of migrasomes and exosomes.

Indexes	Exosomes	Migrasomes	References
Diameters	30–200 nm	0.5–3 μm	Ma et al., 2015; Pegtel and Gould, 2019
Contents	Membrane organizers, enzymes, lipids, chaperon proteins, intracellular trafficking proteins, cell adhesion proteins, signal transduction proteins, cell-type-specific proteins, biogenesis factors, histones, nucleic acids (DNA: mtDNA, dsDNA, ssDNA, viral DNA; RNA: mRNA, miRNA, Pre-miRNA, Y-RNA, circRNA, mtRNA, tRNA, tsRNA, snRNA, snoRNA, piRNA), amino acids, glycoconjugates, and metabolites et al.	Vesicles, membrane proteins, contractile proteins, cytoskeleton proteins, enzymes, chaperon proteins, vesicle traffic proteins, receptors, cell adhesion proteins, extracellular proteins, DNA or RNA binding proteins, complement system proteins, signal transduction proteins, lipids, et al.	Ma et al., 2015; Schmidt-Pogoda et al., 2018; van Niel et al., 2018; Pegtel and Gould, 2019; Kalluri and LeBleu, 2020
TSPANs profiles	TSPAN6, 8, 24, 25, 26, 27, 28, 29, 30, et al.	TSPAN4, TSPAN7, et al.	Ma et al., 2015; van Niel et al., 2018; Jiang et al., 2019; Pegtel and Gould, 2019
Classical membrane markers	TSPAN28, TSPAN29, TSPAN30, TSG101, et al.	TSPAN4, TSPAN7, Integrin α5 and β1, et al.	Ibrahim and Marban, 2016; Wu et al., 2017; Jiang et al., 2019
Specific protein markers	SUMF2, LAMP1	NDST1, PIGK, CPQ, EOGT	Ma et al., 2015; Ibrahim and Marban, 2016; Zhao et al., 2019
Release	By fusion of MVBs with plasma membrane	By breaking the retraction fibers	Ma et al., 2015

mtDNA, mitochondrial DNA; dsDNA, double-stranded DNA; ssDNA, single-stranded DNA; miRNA, microRNA; circRNA, circular RNA; mtRNA, mitochondrial RNA; tRNA, transfer RNA; tsRNAs, tRNA-derived small RNAs; snRNA, small nuclear RNA; snoRNA, small nucleolar RNA; piRNA, PIWI-interacting RNA; TSG101, tumor susceptibility gene 101; SUMF2, sulfatase modifying factor 2; LAMP1, lysosomal associated membrane protein 1; NDST1, bifunctionalheparan sulfate N-deacetylase/N-sulfotransferase 1, PIGK, phosphatidylinositol glycan anchor biosynthesis, class K, CPQ, carboxypeptidase Q; EOGT, EGF domain-specific O-linked N-acetylglucosaminetransferase; MVB, multivesicular bodies.

embryonic fibroblasts (MEF and NIH3T3), mouse melanoma cell (B16), mouse embryonic stem cells, mouse hippocampal neurons and mouse bone marrow-derived macrophages, and murine microglia, human keratinocyte (HaCaT), human breast cancer cell (MDA-MB-231), human colon cancer cell (HCT116), human adenocarcinoma cell (SW480), human gastric carcinoma cell (MGC803), human ovarian adenocarcinoma cell (SKOV-3) (Ma et al., 2015; Schmidt-Pogoda et al., 2018). Moreover, migrasomes are also distributed in various organs, such as human stroke specimens, mouse eye, rat lung, rat/mouse intestine (Ma et al., 2015; Schmidt-Pogoda et al., 2018; **Figure 1**). They tend to be present inside cavity such as pulmonary alveoli or blood vessel, for example, in intestine, migrasomes are inside blood capillaries or lymph capillaries, in the lamina propria of ileum crypts, or in connective tissue (Ma et al., 2015). The mice model study indicate that migrasomes can be detected in the brain of the ischemic hemispheres of mice feeding standard diet, and high-salt diet induces massive migrasomes formation in microglia/macrophages and leads to reduce numbers of anti-inflammatory F4/80$^+$-microglia/macrophages and astrocytes after cerebral ischemia (Schmidt-Pogoda et al., 2018). F4/80$^+$-migrasomes are co-localized with NeuN, which is expressed in nuclei and cytoplasm of neurons, and there is a significant correlation between the extent of migrasome formation and the number of shrunk neurons (Schmidt-Pogoda et al., 2018). These findings suggest that migrasome, which incorporates and dispatches the cytosol of surrounding neurons, might act as a novel, sodium chloride-driven mechanism in acute ischemic stroke pathophysiology (Schmidt-Pogoda et al., 2018). However, the precise regulatory mechanisms between migrasome formation and neuronal loss still need further investigation. Recently, the physiological roles of migrasomes in living animals has been investigated by using the zebrafish embryo as a model system, the results indicated that migrasomes were enriched on a cavity underneath the embryonic shield where they served as chemoattractants to ensure the correct positioning of dorsal forerunner cells vegetally next to the embryonic shield, thus coordinating organ morphogenesis during zebrafish gastrulation (Jiang et al., 2019). Surprisingly, *Yu Li* group found that migrasomes are present in human serum, but their origin and function are not clear (Zhao et al., 2019). Therefore, to discuss and investigate its roles in vascular biology is an interesting topic.

THE CURRENT UNDERSTANDING OF TETRASPANINS FAMILY IN VASCULAR HOMEOSTASIS

Migracytosis, a cell migration-dependent mechanism for releasing intracellular contents into external environment, and migrasomes, the vesicular structures that mediate migracytosis, are involved in cell–cell communications, as that the releasing contents can be taken up by surrounding cells (Ma et al., 2015; Chen et al., 2018). Based on their distribution *in vivo* and *in vitro*, it seems that they may play essential roles in maintaining vascular homeostasis. However, there are few literatures discussed the functions of migrasomes and migracytosis in blood vessel. Therefore, to understand the vascular function of TSPANs,

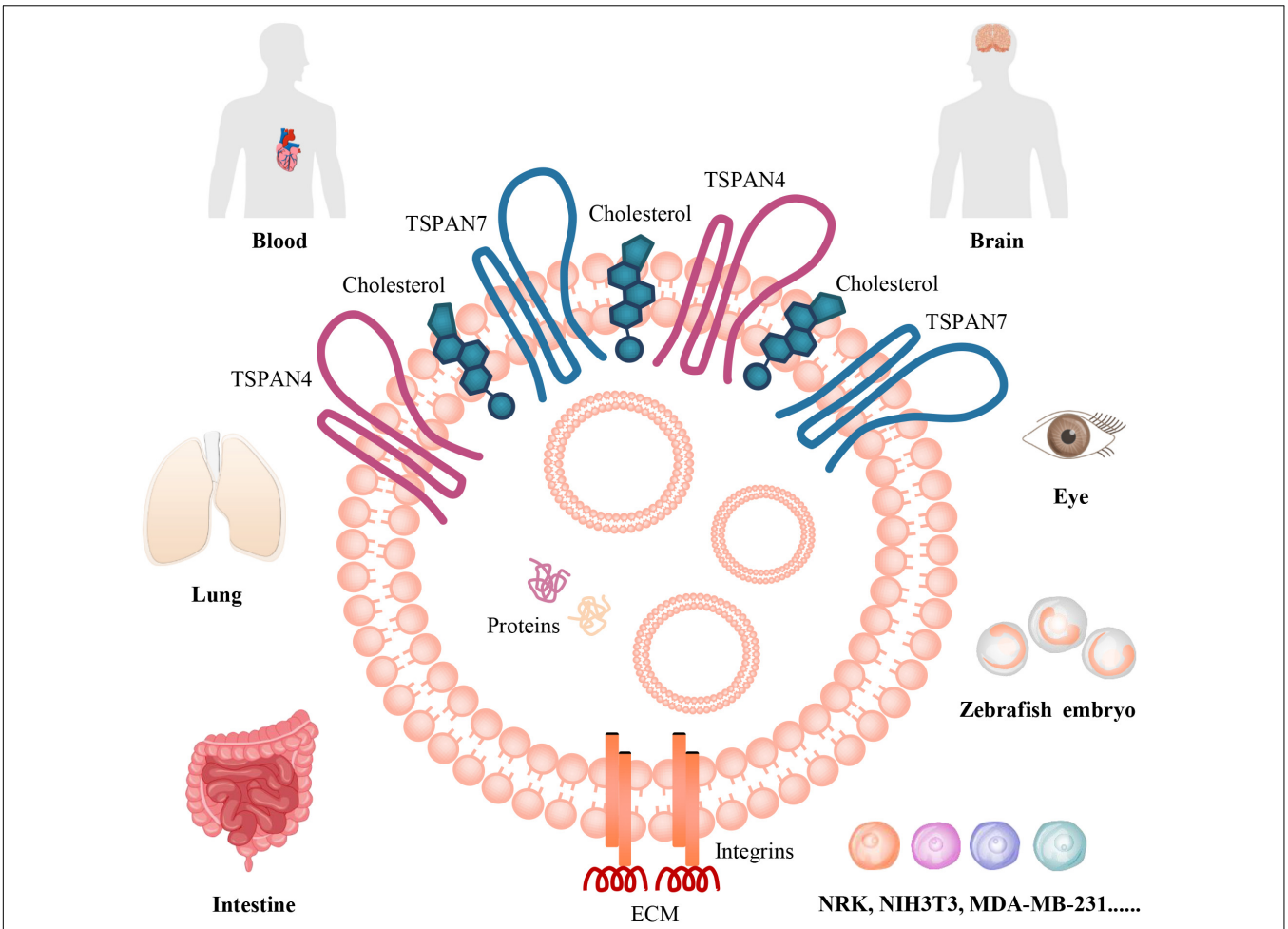

FIGURE 1 | The organization and distributions of migrasomes. Migrasome, which is an extracellular membrane-bound vesicular structure and includes cytosolic proteins and small vesicles in the cavity, is organized by TSPANs, cholesterol, and integrins. The matching of specific integrin-ECM pairs determine when and where migrasome can be generated *in vivo*. They are distributed in human blood and stroke specimens; in mouse brain and eye, rat lung, rat/mouse intestine; in zebrafish embryo. They are also found in numerous cancer cells, such as MDA-MB-231, SKOV-3, HCT116, SW480, MGC803, B16; in normal rat or mouse cells, including NRK, NIH3T3, mouse embryonic stem cells, hippocampal neurons and bone marrow-derived macrophages, and microglia; and in HaCaT *in vitro*.

which are the key elements of migrasomes, may help us to investigate and understand the possible roles of migrasomes and migracytosis in vascular homeostasis in the near future.

Bailey et al. (2011) have investigated TSPANs expression at the mRNA level in human ECs by analyzing largescale transcriptomic data from publicly available SAGE experiments. They found that HUVECs expressed 23 TSPANs and human liver endothelium expressed 17 TSPANs. The RNA-seq analyses and RNA-arrays for TSPANs family genes expressed in HCASMCs, MASMCs and mouse carotid arteries indicate that all TSPANs except for TSPAN16 and TSPAN19 are detectable in these cells and tissue (Zhao et al., 2017). More than one half of TSPANs family genes are significantly reduced by TGF-β1, while only *TSPAN2*, *12*, *13*, and *22* are up-regulated, and *TSPAN2* shows the most dramatic change by TGF-β1 (Zhao et al., 2017). Myocardin, which is another master regulator of VSMCs differentiation, increases 8 *TSPANs* genes expression, including *TSPAN2, 7, 10, 11, 12, 15, 21, 33*, and *TSPAN2* showed the greatest up-regulation (Zhao et al., 2017). The expression profiles of TSPANs family genes in ECs and VSMCs indicate that they may play critical roles in vascular biology, such as migration (**Table 2**).

TSPAN2 is extensively expressed in medial layer VSMCs of aortas, bladder, brain, lung, skeletal muscle, stomach, heart, spleen, kidney and liver, however, the levels of TSPAN2 is decreased in mouse carotid arteries after ligation injury and in failed human arteriovenous fistula samples after occlusion by dedifferentiated neointimal VSMCs (Zhao et al., 2017). TSPAN2 acts as a suppressor of VSMCs proliferation and migration, and plays important role in the pathogenesis of occlusive vascular diseases (Zhao et al., 2017). Mechanistically, transcription of TSPAN2 in VSMCs is regulated by 2 parallel pathways, TGF-β1/SMAD and myocardin/serum response factor, *via* distinct binding sites in the vicinity of the TSPAN2 promoter (Zhao et al., 2017). Additionally, the single-nucleotide polymorphism located in the regulatory region (G allele at rs12122341) of TSPAN2 is strongly associated with atherosclerosis in large arteries

TABLE 2 | The effects of TSPANs in vascular cells migration.

TSPANs	Expression	Migration	References
TSPAN2	HUVECs, HCASMCs, MASMCs	HCASMCs↓	Bailey et al., 2011; Zhao et al., 2017
TSPAN27	HUVECs, HDMECs, HRCECs, MLUECs, MLVECs, HCASMCs, MASMCs	HUVECs↓, MLU/VECs↓	Nagao and Oka, 2011; Wei et al., 2014; Zhao et al., 2017
TSPAN8	HUVECs, RAECs, HCASMCs, MASMCs	RAECs↑	Nazarenko et al., 2010; Bailey et al., 2011; Zhao et al., 2017
TSPAN12	HUVECs, HLVECs, MRVECs, HCASMCs, MASMCs	HUVECs↑	Bailey et al., 2011; Bucher et al., 2017; Zhao et al., 2017; Zhang C. et al., 2018
TSPAN24	HUVECs, HLVECs, MLUECs, iBRECs, HDLECs, HMEC-1, HCASMCs, MASMCs	HUVECs↑, MLUECs↑	Yanez-Mo et al., 1998; Deissler et al., 2007; Takeda et al., 2007; Bailey et al., 2011; Iwasaki et al., 2013; Zhao et al., 2017
TSPAN28/30	HUVECs, HLVECs, HSVECs, HMAECs, iBRECs, HDLECs, HCASMCs, MASMCs	HUVECs↑	Yanez-Mo et al., 1998; Klein-Soyer et al., 2000; Deissler et al., 2007; Bailey et al., 2011; Iwasaki et al., 2013; Tugues et al., 2013; Zhao et al., 2017
TSPAN29	HUVECs, HLVECs, HSVECs, HMAECs, iBRECs, HDLECs, HCASMCs, MCASMCs, MASMCs	HUVECs↑, HSVECs↑, HMAECs↑, HCASMCs↑, HDLECs↑, iBRECs↑	Yanez-Mo et al., 1998; Klein-Soyer et al., 2000; Deissler et al., 2007; Kotha et al., 2009; Bailey et al., 2011; Iwasaki et al., 2013; Zhao et al., 2017
TSPAN3/4/5/6/7/9/13/14/18/25/31	HUVECs, HLVECs, HCASMCs, MASMCs	?	Bailey et al., 2011; Zhao et al., 2017
TSPAN11/15/23	HUVECs, HCASMCs, MASMCs	?	Bailey et al., 2011; Zhao et al., 2017
TSPAN17	HLVECs, HCASMCs, MASMCs	?	Bailey et al., 2011; Zhao et al., 2017
TSPAN1/10/20/21/22/26/32/33	HCASMCs, MASMCs	?	Zhao et al., 2017
TSPAN19	HUVECs	?	Bailey et al., 2011

HUVECs, human umbilical vein endothelial cells; HCASMCs, human coronary artery smooth muscle cells; MASMCs, mouse aortic smooth muscle cells; HDMECs, human dermal microvascular endothelial cells; HRCECs, human retinal capillary endothelial cells; MLUECs, mouse lung endothelial cells; MLVECs, mouse liver endothelial cells; RAECs, rat aortic endothelial cells; HLVECs, human liver endothelial cells; MRVECs, mouse retinal vascular endothelial cells; iBRECs, microvascular endothelial cells of the bovine retina; HDLECs, human dermal lymphatic endothelial cells; HMEC-1, human microvascular endothelial cell line-1; HSVECs, human saphenous vein endothelial cells; HMAECs, human mammary artery endothelial cells; MCASMCs, mouse carotid artery smooth muscle cells.

(Ninds Stroke Genetics Network [SIGN] and International Stroke Genetics Consortium [ISGC], 2016). However, the function of TSPAN2 in ECs is not clear.

TSPANC8 subgroup, which have the eight cysteine residues in their large extracellular loops, includes TSPAN5, 10, 14, 15, 17, and 33 (Matthews et al., 2018). TSPAN5 is highly expressed in neocortex, hippocampus, amygdala and in Purkinje cells in the cerebellum of mouse (Garcia-Frigola et al., 2000), and its expression is prominent in both atrial and trabeculated ventricular chambers of the heart on embryonic day 10, indicated that it might be involved in heart development (Garcia-Frigola et al., 2001). TSPAN14 is the major TSPANs of TSPANC8 subgroup in HUVECs and is essential for normal ADAM10 surface expression and activity, while TSPAN33 is the major TSPANs of TSPANC8 subgroup in the erythrocyte lineage and is essential for normal ADAM10 expression (Haining et al., 2012). The vascular functions of TSPANC8 subgroup members still need further investigation.

TSPAN18 is highly expressed in ECs, TSPAN18-knockdown ECs have impaired Ca^{2+} mobilization, and impaired histamine- and thrombin-induced von Willebrand Factor release (Noy et al., 2019). Mechanistically, TSPAN18 interacts with Orai1, which is a major entry route for extracellular Ca^{2+} in non-excitable cells (Noy et al., 2019). Thus, TSPAN18 is essential for Ca^{2+} homeostasis and inflammatory responses in ECs.

Among TSPANs, TSPAN8, TSPAN24, TSPAN12, and TSPAN29 are the main TSPANs family members that facilitate angiogenesis (Hemler, 2014; Bucher et al., 2017; Heo and Lee, 2020). Gesierich et al. (2006) firstly reported that TSPAN8 is the strongest angiogenesis inducer, as that overexpression of TSPAN8 in tumor cells markedly increases angiogenesis *in vivo* and *in vitro*, and co-culture of TSPAN8 knockdown tumor cells or the exosomes-depleted supernatant with HUVECs markedly inhibit HUVECs tube formation *in vitro* (Gesierich et al., 2006; Akiel et al., 2016). Mechanistically, the tumor cells released exosomes containing TSPAN8 are taken up by target cells via ligands for TSPAN8-associated molecules, and induce angiogenic gene transcription and modulate the RNA profile in ECs or adjacent fibroblasts, and exosomes expressing TSPAN8-CD49d complex preferentially bind ECs, thus initiating an angiogenic loop by inducing TSPAN8 itself expression on sprouting ECs (Gesierich et al., 2006; Nazarenko et al., 2010; Mu et al., 2020). The contribution of TSPAN8 and TSPAN24 on angiogenesis has also been confirmed by TSPAN8-KO mice, TSPAN24-KO mice and TSPAN8/24 double-KO mice (Takeda et al., 2007; Zhao et al., 2018a,b) (**Supplementary Table 1**). Mechanistically, promotion of angiogenesis by tumor-derived exosomes and rescue of impaired angiogenesis in KO mice by wild type-serum exosomes depend on the association of TSPAN8 and TSPAN24 with GPCR and RTK in ECs and tumor cells (Zhao

et al., 2018b; Mu et al., 2020). Most importantly, the TSPAN24-integrin complex as a functional unit, and the YRSL motif of TSPAN24 plays key role in TSPAN24-mediated angiogenesis (Sincock et al., 1999; Zhang et al., 2002; Zuo et al., 2010; Liu et al., 2011; Peng et al., 2013; Huang et al., 2016). Based on its effects on angiogenesis, TSPAN24 gene delivery promotes angiogenesis and improves skin temperature in rat hindlimb ischemia model (Liu et al., 2011), enhances myocardial angiogenesis and improves left ventricular function in rat acute myocardial infarction model (Wang et al., 2006; Fu et al., 2015), and the beneficial effect of TSPAN24 on myocardial angiogenesis has also been confirmed in a pig myocardial infarction model (Zuo et al., 2009). In contrast, the oxygen-induced retinal neovascularization and angiogenesis in three tumors models are not decreased in TSPAN24-null mice (Takeda et al., 2007; Deng et al., 2012; Copeland et al., 2013a; Li et al., 2013), indicated that the contributions of TSPAN24 in angiogenesis might be models/diseases dependent. TSPAN24 maintains vascular stability by balancing the forces of cell adhesion and cytoskeletal tension as that TSPAN24 deficiency increases actin cytoskeletal traction by elevating RhoA signaling and diminishes actin cortical meshwork by decreasing Rac1 activity (Zhang et al., 2011). Similar to its influence in angiogenesis, the effect of TSPAN24 on vascular permeability might also be model-dependent as that TSPAN24 deletion did not affect VEGF-induced vascular permeability (Takeda et al., 2011). Moreover, TSPAN24 acts as a molecular linker between MT1-MMP and α3β1 integrin in ECs: MT1-MMP, through its hemopexin domain, associates tightly with TSPAN24, thus forming α3β1 integrin/TSPAN24/MT1-MMP ternary complexes, which is essential for a normal pattern of MT1-MMP-dependent collagenolysis (Yanez-Mo et al., 2008). Thus, TSPAN24 is a key regulator of MT1-MMP in mediating endothelial homeostasis.

TSPAN12, which is expressed in retinal vasculature, has been extensively investigated in ophthalmology (Junge et al., 2009; Nikopoulos et al., 2010; Yang et al., 2011; Seo et al., 2016; Bucher et al., 2017; Lai et al., 2017; Zhang C. et al., 2018). Physiologically, TSPAN12 acts as a key regulator for retinal vascular development by activating NDP- but not Wnt-induced FZD4/β-catenin signaling, early loss of TSPAN12 in ECs causes lack of intraretinal capillaries and increased the expression of ECs-specific adhesion molecule cadherin5, consistent with premature vascular quiescence, late loss of TSPAN12 strongly impairs BRB maintenance without affecting vascular morphogenesis, pericyte coverage, or perfusion, thus, the endothelial TSPAN12 contributes to vascular morphogenesis and BRB formation in developing mice and BRB maintenance in adult mice (Junge et al., 2009; Zhang C. et al., 2018). Mechanistically, TSPAN12 is an essential component of the NDP receptor complex and interacts with FZD4 and NDP *via* its extracellular loops, consistent with an action as co-receptor that enhances FZD4 ligand selectivity for NDP, which signaling is required for normal retinal angiogenesis and BRB function (Lai et al., 2017). Based on its role in retinal angiogenesis during development, mutations in TSPAN12 or large deletions of TSPAN12 cause familial exudative vitreoretinopathy in human (Nikopoulos et al., 2010; Yang et al., 2011; Seo et al., 2016), in contrast, the anti-TSPAN12 antibody, which inhibits ECs migration and tube formation, ameliorates vasoproliferative retinopathy *via* suppressing β-Catenin signaling in rodent models of retinal neovascular disease (Bucher et al., 2017). The function of TSPAN12 in retinal vasculature, especially in retinal ECs, is relatively clear; however, its functions in large arteries are not fully understood.

TSPAN29 promotes angiogenesis and lymphangiogenesis *via* forming functional complexes between VEGFR-3 and integrin α5 and α9, therefore, tumor-induced and inflammation-induced lymphangiogenesis, and tumor-induced angiogenesis are decreased in TSPAN29-KO mice (Iwasaki et al., 2013) (**Supplementary Table 1**). Intravitreous injections of siRNA-TSPAN29 or anti-TSPAN29 antibodies are therapeutically effective for laser-induced retinal and choroidal neovascularization in mice, and injecting siRNA-TSPAN29 markedly suppresses HGF- or VEGF-induced subconjunctival angiogenesis *in vivo* (Kamisasanuki et al., 2011). Using anti-TSPAN29 monoclonal antibody, three independent experiments revealed that TSPAN29 participates in ECs migration during wound repair *in vitro*, and TSPAN29 is required for platelet-induced HUVECs proliferation (Klein-Soyer et al., 2000; Ko et al., 2006; Deissler et al., 2007). Mechanistically, TSPAN29, TSPAN28, and TSPAN24 localize at cell–cell junctions of ECs and are associated with each other and those of TSPAN29 and TSPAN24 with α3β1 integrin, which are essential for ECs motility, as that monoclonal antibodies directed to both TSPAN24 and TSPAN28 as well as monoclonal antibody specific for α3 integrin, are able to inhibit ECs migration in the process of wound healing (Yanez-Mo et al., 1998). However, another study indicated that ablation of TSPAN29 does not affect proliferation, apoptosis or angiogenesis in primary prostate tumors (Copeland et al., 2013b). Similar to TSPAN24, TSPAN29-dependent angiogenesis might also be model-dependent and perhaps other TSPANs compensates for the absence of TSPAN29 (Hemler, 2014). TSPAN29 also associates with integrins in VSMCs (Scherberich et al., 1998), the neutralization antibody for TSPAN29 reduces the proliferation and migration of VSMCs, and results in a 31% reduction in neointima formation in a mouse carotid ligation injury model, in contrast, overexpression of TSPAN29 leads to 43% increase in neointima (Kotha et al., 2009). To further understand how TSPAN29 regulate adverse VSMCs phenotypes, Herr et al. (2014) used TSPAN29 lentiviral shRNA to knockdown TSPAN29 expression in VSMCs, and found that TSPAN29 deficiency is sufficient to profoundly disrupt cellular actin arrangement and endogenous cell contraction by interfering with RhoA signaling.

In contrast to TSPAN8/12/24/29, ECs TSPAN27 restrains pathologic angiogenesis (Wei et al., 2014). Deficiency of TSPAN27 significantly enhances the migration and invasion of ECs, and markedly increases vascular morphogenesis to various stimuli, however, slightly promotes ECs proliferation and survival (Wei et al., 2014). Mechanistically, TSPAN27 modulates CAMs trafficking by preventing lipid raft aggregation and dissociating CAMs from lipid rafts, and TSPAN27-ganglioside-CD44 signaling restrains angiogenesis by inhibiting ECs adhesiveness and motility (Wei et al., 2014). Therefore, the balance of these TSPANs in regulating angiogenesis is critical for vascular homeostasis.

TSPAN30, which is localized in late endosomes/lysosomes and on the plasma membrane in ECs, contributes to several cell functions relevant to initiation and progression of angiogenesis, such as adhesion and migration of vascular ECs, mechanistically, TSPAN30 associates with both integrin β1 and VEGFR-2 to form functional complexes to modulate VEGFR2 signaling and internalization (Tugues et al., 2013). TSPAN30 also colocalizes with von Willebrand factor and P-selectin to reside in the membrane of Weibel-Palade bodies of ECs (Vischer and Wagner, 1993). Similarly, TSPAN30 coclusters with P-selectin on the plasma membrane of activated ECs, it is thus an essential cofactor to leukocyte recruitment by endothelial P-selectin (Doyle et al., 2011). Other TSPANs are also known to organize leukocyte adhesion molecules into microdomains (Ley, 2011). For example, TSPAN24 and TSPAN29 are components of the endothelial docking structure for adherent leukocytes by their association with ICAM-1 and VCAM-1 in ECs (Barreiro et al., 2005). However, their requirement for leukocyte adhesion is not as stringent as that of TSPAN30 (Ley, 2011). TSPAN28, a putative receptor for hepatitis C virus, is up-regulated in ECs of early atherosclerotic lesions, and it has the potential to substantially enhance monocyte adhesion *via* relocalizing and increasing membrane clustering of ICAM-1 and VCAM-1 (Pileri et al., 1998; Rohlena et al., 2009). Moreover, TSPAN28 interaction with Rac1 through its cytoplasmic C-terminal region limits the GTPase activation within the plasma membrane during cell adhesion and migration (Tejera et al., 2013). As described above, overexpression of TSPAN28 can enhance migrasomes formation in NRK (Huang et al., 2019), however, whether TSPAN28 can influence migrasomes formation in vascular cells has not been investigated.

PERSPECTIVE

TSPANs family, which is known to be important in vesicle formation and targeting of vesicles to recipient cell, is involved in a multitude of biological processes, such as development, fertilization, platelet aggregation, parasite and viral infection, immune response induction, metastasis suppression and tumor progression, ophthalmology, synaptic contacts at neuromuscular junctions, maintenance of skin integrity (Hemler, 2003; Levy and Shoham, 2005; Zoller, 2009; Bailey et al., 2011; Rana and Zoller, 2011; Charrin et al., 2014; Colombo et al., 2014; van Niel et al., 2018; Jiang et al., 2019). Moreover, TSPANs are widely expressed in hematopoietic and vascular cells, such as ECs and VSMCs, and are also participated in both physiological and pathological processes related to thrombosis, hemostasis, angiogenesis and vascular injuries (including vascular cells migration), thus emerging novel roles in regulating vascular biology (Zhang et al., 2009; **Table 2**).

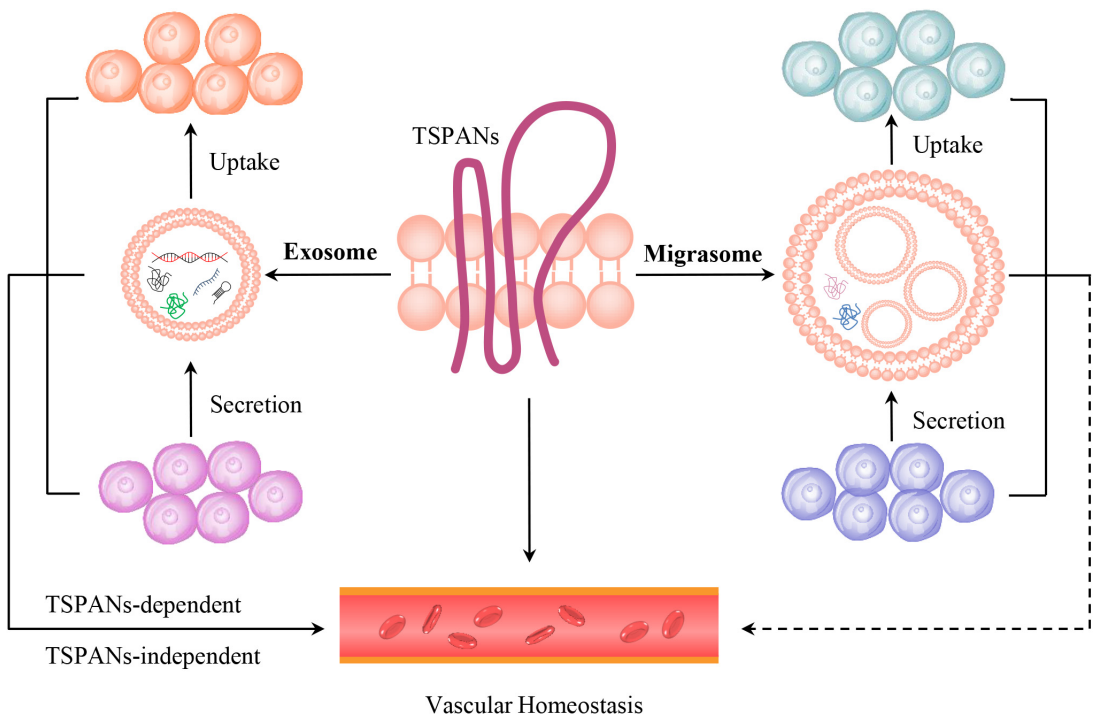

FIGURE 2 | The models of TSPANs, exosomes and migrasomes in vascular homeostasis. TSPANs are the key organizators of both exosome and migrasome. TSPANs can regulate vascular homeostasis directly. Exosomes, which contain selected proteins, lipids, nucleic acids, amino acids, glycoconjugates and metabolites et al., are secreted by one cell and taken up by another cell, thus transferring signals through cell–cell communication and influencing vascular homeostasis in TSPANs-dependent or independent manners. Migrasomes, which are distributed in blood circulation and blood vessel, contain bioactive cargos, and are also secreted by one cell and taken up by the surrounding cells. Therefore, migrasomes might influence vascular homeostasis *via* cell–cell communication.

As we have discussed above, migrasomes are organized by TSPANs, cholesterol, integrins and other unidentified molecules, and migracytosis releases cellular contents at a specific location, these cellular contents can be taken up by other cells which travel to that site, indicates that biochemical and spatial information from outgoing cells can be acquired by incoming cells (Ma et al., 2015; Schmidt-Pogoda et al., 2018; Zhao et al., 2019). Considered that migrasomes are distributed in blood vessel, human serum, and in infarcted brain parenchyma of human stroke patients, the contraction and relaxation, vascular repair, and immune responses occurred in blood vessels require vascular cells or immune cells migration, and the localized communication between ECs and VSMCs, and between ECs and immune cells, et al. (Ma et al., 2015; Eelen et al., 2018; Schmidt-Pogoda et al., 2018; Zhao et al., 2019), thus, there is not surprising that migration-dependent migrasomes and migracytosis might play important roles in these processes and act as novel players in mediating vascular homeostasis.

It should be noticed that TSPANs are expressed in the membranes of both exosomes and migrasomes (da Rocha-Azevedo and Schmid, 2015; Ma et al., 2015; Ibrahim and Marban, 2016; Wu et al., 2017; Chen et al., 2018, 2019; Schmidt-Pogoda et al., 2018; Huang et al., 2019; Jiang et al., 2019; Pegtel and Gould, 2019; Tavano and Heisenberg, 2019; Zhao et al., 2019). The exosomes play essential roles in ECs dysfunction and regeneration, VSMCs migration, ischemic heart disease, cardiac hypertrophy and fibrosis by transferring their bioactive cargos, such as microRNAs and proteins (Ibrahim and Marban, 2016; Barile et al., 2017; Chang et al., 2018; Tong et al., 2018; Baruah and Wary, 2019; Ranjan et al., 2019). Moreover, cancer cells released exosomes containing TSPAN8 are critical for angiogenesis, as that they can be taken up and initiate angiogenic genes transcription and modulate the RNA profile in ECs or adjacent fibroblasts (Gesierich et al., 2006; Nazarenko et al., 2010; Mu et al., 2020). However, it is not known whether the tumor cells-expressed migraomses can be taken up by ECs *in vivo*, and influence tumor-induced angiogenesis and subsequently tumor growth, and what will happen if these tumor-derived migrasomes reaches organs distant from the tumor? These should be carefully investigated in the near future. Therefore, exosomes- or migrasomes-dependent or independent effects of TSPANs, the TSPANs-dependent or independent effects of exosomes or migrasomes in modulating vascular biology, and the relationships between exosomes and migrasomes in regulating vascular homeostasis should be distinguished and investigated (**Figure 2**).

The formation of migrasome depends on the matching of specific integrin-ECM pairs, there are 18 α and 8 β integrins in mammals, and each ECM protein has a specific spatial and temporal distribution pattern in a given organism, which will determine when and where migrasome can be generated *in vivo* (Wu et al., 2017). As we have mentioned above, migrasomes display temporal and spatial distributions during the development of zebrafish embryos (Jiang et al., 2019). The percentage of containing in migrasomes is organ-, tissue- or cell type-dependent. Migrasomes in ischemic brain are mainly composed of contractile proteins actin and myosin, cytoskeleton and annexin proteins, while enzymes are the most (31%) contents and much of them are involved in metabolic processes in migrasomes from NRK (Ma et al., 2015; Schmidt-Pogoda et al., 2018; Zhao et al., 2019). The zebrafish embryonic migrasomes are enriched for a host of chemokines, morphogens, cytokines and growth factors, including Tgfβ2, Il1β, PdgfD, Cxcl12b, Wnt11, Mydgf, DllD, Cxcl12a, Bmp1, Wnt8a, Chd, Bmp7a, Cxcl18a.1, Wnt5b, Lefty1 and Bmp2, and migrasomes regulate organ morphogenesis by delivering Cxcl12a/b for Cxcl12a (ligand)-Cxcr4b (receptor) signaling (Jiang et al., 2019). However, the compositions of vascular migrasomes, the origins and targets of migrasomes in human serum, and the pathways of migrasomes entering the circulatory system are not clear (Zhao et al., 2019). Are migrasomes in human serum related to certain cardiovascular diseases, and can they be used as a diagnostic marker (Zhao et al., 2019)? Therefore, these seem that the possible roles of migrasomes and migracytosis in cardiovascular system might be mainly dependent on their origins, compositions, levels, temporal distribution patterns, and locations.

AUTHOR CONTRIBUTIONS

YZ and HY contributed to concept and idea. YZ, JZ, and YX prepared the figures and tables. YZ, JW, YD, SZ, and JX wrote the manuscript. All authors have read and agreed to the published version of the manuscript.

FUNDING

This work was supported by Project funded by China Postdoctoral Science Foundation, grant number 2019M653238, the Natural Science Foundation of Guangdong Province, grant numbers 2018A030313657 and 2018A030313733, the National Natural Science Foundation of China, grant numbers 81900376 and 81901447, and Guangdong famous Traditional Chinese Medicine inheritance studio construction project, grant number 20180137.

ACKNOWLEDGMENTS

We apologize to all of the authors whose invaluable work we could not discuss or cite in this review due to space constraints. We should thank Bi Mingmin and Fang Chun for the technical preparation of figures.

SUPPLEMENTARY MATERIAL

The Supplementary Material for this article can be found online at: https://www.frontiersin.org/articles/10.3389/fcell.2020.00438/full#supplementary-material

REFERENCES

Akiel, M. A., Santhekadur, P. K., Mendoza, R. G., Siddiq, A., Fisher, P. B., and Sarkar, D. (2016). Tetraspanin 8 mediates AEG-1-induced invasion and metastasis in hepatocellular carcinoma cells. *FEBS Lett.* 590, 2700–2708. doi: 10.1002/1873-3468.12268

Alitalo, K. (2011). The lymphatic vasculature in disease. *Nat. Med.* 17, 1371–1380. doi: 10.1038/nm.2545

Bailey, R. L., Herbert, J. M., Khan, K., Heath, V. L., Bicknell, R., and Tomlinson, M. G. (2011). The emerging role of tetraspanin microdomains on endothelial cells. *Biochem. Soc. Trans.* 39, 1667–1673. doi: 10.1042/BST20110745

Barile, L., Moccetti, T., Marban, E., and Vassalli, G. (2017). Roles of exosomes in cardioprotection. *Eur. Heart. J.* 38, 1372–1379. doi: 10.1093/eurheartj/ehw304

Barletta, E., Mugnai, G., and Ruggieri, S. (1989). Morphological characteristics and ganglioside composition of substratum adhesion sites in a hepatoma cell line (CMH5123 cells) during different phases of growth. *Exp. Cell Res.* 182, 394–402. doi: 10.1016/0014-4827(89)90244-9

Barreiro, O., Yanez-Mo, M., Sala-Valdes, M., Gutierrez-Lopez, M. D., Ovalle, S., Higginbottom, A., et al. (2005). Endothelial tetraspanin microdomains regulate leukocyte firm adhesion during extravasation. *Blood* 105, 2852–2861. doi: 10.1182/blood-2004-09-3606

Baruah, J., and Wary, K. K. (2019). Exosomes in the regulation of vascular endothelial cell regeneration. *Front. Cell. Dev. Biol.* 7:353. doi: 10.3389/fcell.2019.00353

Bucher, F., Zhang, D., Aguilar, E., Sakimoto, S., Diaz-Aguilar, S., Rosenfeld, M., et al. (2017). Antibody-mediated inhibition of Tspan12 ameliorates vasoproliferative retinopathy through suppression of beta-catenin signaling. *Circulation* 136, 180–195. doi: 10.1161/CIRCULATIONAHA.116.025604

Campbell, K. A., Lipinski, M. J., Doran, A. C., Skaflen, M. D., Fuster, V., and McNamara, C. A. (2012). Lymphocytes and the adventitial immune response in atherosclerosis. *Circ. Res.* 110, 889–900. doi: 10.1161/CIRCRESAHA.111.263186

Chang, X., Yao, J., He, Q., Liu, M., Duan, T., and Wang, K. (2018). Exosomes from women with preeclampsia induced vascular dysfunction by delivering sFlt (soluble Fms-like tyrosine kinase)-1 and sEng (soluble endoglin) to endothelial cells. *Hypertension* 72, 1381–1390. doi: 10.1161/HYPERTENSIONAHA.118.11706

Charrin, S., Jouannet, S., Boucheix, C., and Rubinstein, E. (2014). Tetraspanins at a glance. *J. Cell Sci.* 127(Pt 17), 3641–3648. doi: 10.1242/jcs.154906

Chen, L., Ma, L., and Yu, L. (2019). WGA is a probe for migrasomes. *Cell Discov.* 5:13.

Chen, Y., Li, Y., Ma, L., and Yu, L. (2018). Detection of migrasomes. *Methods Mol. Biol.* 1749, 43–49. doi: 10.1007/978-1-4939-7701-7_5

Colombo, M., Raposo, G., and Thery, C. (2014). Biogenesis, secretion, and intercellular interactions of exosomes and other extracellular vesicles. *Annu. Rev. Cell Dev. Biol.* 30, 255–289. doi: 10.1146/annurev-cellbio-101512-122326

Copeland, B. T., Bowman, M. J., and Ashman, L. K. (2013a). Genetic ablation of the tetraspanin CD151 reduces spontaneous metastatic spread of prostate cancer in the TRAMP model. *Mol. Cancer Res.* 11, 95–105. doi: 10.1158/1541-7786.MCR-12-0468

Copeland, B. T., Bowman, M. J., Boucheix, C., and Ashman, L. K. (2013b). Knockout of the tetraspanin Cd9 in the TRAMP model of de novo prostate cancer increases spontaneous metastases in an organ-specific manner. *Int. J. Cancer* 133, 1803–1812. doi: 10.1002/ijc.28204

Culp, L. A., and Black, P. H. (1972). Release of macromolecules from BALB-c mouse cell lines treated with chelating agents. *Biochemistry* 11, 2161–2172. doi: 10.1021/bi00761a024

Culp, L. A., Murray, B. A., and Rollins, B. J. (1979). Fibronectin and proteoglycans as determinants of cell-substratum adhesion. *J. Supramol. Struct.* 11, 401–427. doi: 10.1002/jss.400110314

da Rocha-Azevedo, B., and Schmid, S. L. (2015). Migrasomes: a new organelle of migrating cells. *Cell Res.* 25, 1–2. doi: 10.1038/cr.2014.146

Deissler, H., Kuhn, E. M., Lang, G. E., and Deissler, H. (2007). Tetraspanin CD9 is involved in the migration of retinal microvascular endothelial cells. *Int. J. Mol. Med.* 20, 643–652.

Deng, X., Li, Q., Hoff, J., Novak, M., Yang, H., Jin, H., et al. (2012). Integrin-associated CD151 drives ErbB2-evoked mammary tumor onset and metastasis. *Neoplasia* 14, 678–689. doi: 10.1593/neo.12922

Doyle, E. L., Ridger, V., Ferraro, F., Turmaine, M., Saftig, P., and Cutler, D. F. (2011). CD63 is an essential cofactor to leukocyte recruitment by endothelial P-selectin. *Blood* 118, 4265–4273. doi: 10.1182/blood-2010-11-321489

Eelen, G., de Zeeuw, P., Treps, L., Harjes, U., Wong, B. W., and Carmeliet, P. (2018). Endothelial cell metabolism. *Physiol. Rev.* 98, 3–58. doi: 10.1152/physrev.00001.2017

Fu, H., Tan, J., and Yin, Q. (2015). Effects of recombinant adeno-associated virus-mediated CD151 gene transfer on the expression of rat vascular endothelial growth factor in ischemic myocardium. *Exp. Ther. Med.* 9, 187–190. doi: 10.3892/etm.2014.2079

Garcia-Frigola, C., Burgaya, F., Calbet, M., de Lecea, L., and Soriano, E. (2000). Mouse Tspan-5, a member of the tetraspanin superfamily, is highly expressed in brain cortical structures. *Neuroreport* 11, 3181–3185. doi: 10.1097/00001756-200009280-00027

Garcia-Frigola, C., Burgaya, F., de Lecea, L., and Soriano, E. (2001). Pattern of expression of the tetraspanin Tspan-5 during brain development in the mouse. *Mech. Dev.* 106, 207–212. doi: 10.1016/s0925-4773(01)00436-1

Gesierich, S., Berezovskiy, I., Ryschich, E., and Zoller, M. (2006). Systemic induction of the angiogenesis switch by the tetraspanin D6.1A/CO-029. *Cancer Res.* 66, 7083–7094. doi: 10.1158/0008-5472.can-06-0391

Haining, E. J., Yang, J., Bailey, R. L., Khan, K., Collier, R., Tsai, S., et al. (2012). The TspanC8 subgroup of tetraspanins interacts with A disintegrin and metalloprotease 10 (ADAM10) and regulates its maturation and cell surface expression. *J. Biol. Chem.* 287, 39753–39765. doi: 10.1074/jbc.M112.416503

Halper, J. (2018). Basic components of vascular connective tissue and extracellular matrix. *Adv. Pharmacol.* 81, 95–127. doi: 10.1016/bs.apha.2017.08.012

Hemler, M. E. (2003). Tetraspanin proteins mediate cellular penetration, invasion, and fusion events and define a novel type of membrane microdomain. *Annu. Rev. Cell Dev. Biol.* 19, 397–422. doi: 10.1146/annurev.cellbio.19.111301.153609

Hemler, M. E. (2005). Tetraspanin functions and associated microdomains. *Nat. Rev. Mol. Cell Biol.* 6, 801–811. doi: 10.1038/nrm1736

Hemler, M. E. (2008). Targeting of tetraspanin proteins–potential benefits and strategies. *Nat. Rev. Drug Discov.* 7, 747–758. doi: 10.1038/nrd2659

Hemler, M. E. (2014). Tetraspanin proteins promote multiple cancer stages. *Nat. Rev. Cancer* 14, 49–60. doi: 10.1038/nrc3640

Heo, K., and Lee, S. (2020). TSPAN8 as a novel emerging therapeutic target in cancer for monoclonal antibody therapy. *Biomolecules* 10:388. doi: 10.3390/biom10030388

Herr, M. J., Mabry, S. E., and Jennings, L. K. (2014). Tetraspanin CD9 regulates cell contraction and actin arrangement via RhoA in human vascular smooth muscle cells. *PLoS One* 9:e106999. doi: 10.1371/journal.pone.0106999

Hu, Y., and Xu, Q. (2011). Adventitial biology: differentiation and function. *Arterioscler. Thromb. Vasc. Biol.* 31, 1523–1529. doi: 10.1161/ATVBAHA.110.221176

Huang, Y., Zucker, B., Zhang, S., Elias, S., Zhu, Y., Chen, H., et al. (2019). Migrasome formation is mediated by assembly of micron-scale tetraspanin macrodomains. *Nat. Cell Biol.* 21, 991–1002. doi: 10.1038/s41556-019-0367-5

Huang, Z., Miao, X., Patarroyo, M., Nilsson, G. P., Pernow, J., and Li, N. (2016). Tetraspanin CD151 and integrin alpha6beta1 mediate platelet-enhanced endothelial colony forming cell angiogenesis. *J. Thromb. Haemost.* 14, 606–618. doi: 10.1111/jth.13248

Ibrahim, A., and Marban, E. (2016). Exosomes: fundamental biology and roles in cardiovascular physiology. *Annu. Rev. Physiol.* 78, 67–83. doi: 10.1146/annurev-physiol-021115-104929

Iwasaki, T., Takeda, Y., Maruyama, K., Yokosaki, Y., Tsujino, K., Tetsumoto, S., et al. (2013). Deletion of tetraspanin CD9 diminishes lymphangiogenesis in vivo and in vitro. *J. Biol. Chem.* 288, 2118–2131. doi: 10.1074/jbc.M112.424291

Jeppesen, D. K., Fenix, A. M., Franklin, J. L., Higginbotham, J. N., Zhang, Q., Zimmerman, L. J., et al. (2019). Reassessment of exosome composition. *Cell* 177, 428–445.e18. doi: 10.1016/j.cell.2019.02.029

Jiang, D., Jiang, Z., Lu, D., Wang, X., Liang, H., Zhang, J., et al. (2019). Migrasomes provide regional cues for organ morphogenesis during zebrafish gastrulation. *Nat. Cell Biol.* 21, 966–977. doi: 10.1038/s41556-019-0358-6

Junge, H. J., Yang, S., Burton, J. B., Paes, K., Shu, X., French, D. M., et al. (2009). TSPAN12 regulates retinal vascular development by promoting Norrin- but not Wnt-induced FZD4/beta-catenin signaling. *Cell* 139, 299–311. doi: 10.1016/j.cell.2009.07.048

Kalluri, R., and LeBleu, V. S. (2020). The biology, function, and biomedical applications of exosomes. *Science* 367:eaau6977. doi: 10.1126/science.aau6977

Kamisasanuki, T., Tokushige, S., Terasaki, H., Khai, N. C., Wang, Y., Sakamoto, T., et al. (2011). Targeting CD9 produces stimulus-independent antiangiogenic effects predominantly in activated endothelial cells during angiogenesis: a novel antiangiogenic therapy. *Biochem. Biophys. Res. Commun.* 413, 128–135. doi: 10.1016/j.bbrc.2011.08.068

Keller, R. (2005). Cell migration during gastrulation. *Curr. Opin. Cell Biol.* 17, 533–541. doi: 10.1016/j.ceb.2005.08.006

Klein-Soyer, C., Azorsa, D. O., Cazenave, J. P., and Lanza, F. (2000). CD9 participates in endothelial cell migration during in vitro wound repair. *Arterioscler. Thromb. Vasc. Biol.* 20, 360–369. doi: 10.1161/01.atv.20.2.360

Ko, E. M., Lee, I. Y., Cheon, I. S., Kim, J., Choi, J. S., Hwang, J. Y., et al. (2006). Monoclonal antibody to CD9 inhibits platelet-induced human endothelial cell proliferation. *Mol. Cells* 22, 70–77.

Kotha, J., Zhang, C., Longhurst, C. M., Lu, Y., Jacobs, J., Cheng, Y., et al. (2009). Functional relevance of tetraspanin CD9 in vascular smooth muscle cell injury phenotypes: a novel target for the prevention of neointimal hyperplasia. *Atherosclerosis* 203, 377–386. doi: 10.1016/j.atherosclerosis.2008.07.036

Lai, M. B., Zhang, C., Shi, J., Johnson, V., Khandan, L., McVey, J., et al. (2017). TSPAN12 is a norrin co-receptor that amplifies Frizzled4 ligand selectivity and signaling. *Cell Rep.* 19, 2809–2822. doi: 10.1016/j.celrep.2017.06.004

Le Clainche, C., and Carlier, M. F. (2008). Regulation of actin assembly associated with protrusion and adhesion in cell migration. *Physiol. Rev.* 88, 489–513. doi: 10.1152/physrev.00021.2007

Levy, S., and Shoham, T. (2005). The tetraspanin web modulates immune-signalling complexes. *Nat. Rev. Immunol.* 5, 136–148. doi: 10.1038/nri1548

Ley, K. (2011). CD63 positions CD62P for rolling. *Blood* 118, 4012–4013. doi: 10.1182/blood-2011-08-372318

Li, Q., Yang, X. H., Xu, F., Sharma, C., Wang, H. X., Knoblich, K., et al. (2013). Tetraspanin CD151 plays a key role in skin squamous cell carcinoma. *Oncogene* 32, 1772–1783. doi: 10.1038/onc.2012.205

Liu, W. F., Zuo, H. J., Chai, B. L., Peng, D., Fei, Y. J., Lin, J. Y., et al. (2011). Role of tetraspanin CD151-alpha3/alpha6 integrin complex: implication in angiogenesis CD151-integrin complex in angiogenesis. *Int. J. Biochem. Cell Biol.* 43, 642–650. doi: 10.1016/j.biocel.2011.01.004

Liu, Y., Chen, H., and Liu, D. (2014). Mechanistic perspectives of calorie restriction on vascular homeostasis. *Sci. China Life Sci.* 57, 742–754. doi: 10.1007/s11427-014-4709-z

Ma, L., Li, Y., Peng, J., Wu, D., Zhao, X., Cui, Y., et al. (2015). Discovery of the migrasome, an organelle mediating release of cytoplasmic contents during cell migration. *Cell Res.* 25, 24–38. doi: 10.1038/cr.2014.135

Marsboom, G., and Rehman, J. (2018). Hypoxia signaling in vascular homeostasis. *Physiology* 33, 328–337. doi: 10.1152/physiol.00018.2018

Matthews, A. L., Koo, C. Z., Szyroka, J., Harrison, N., Kanhere, A., and Tomlinson, M. G. (2018). Regulation of leukocytes by TspanC8 tetraspanins and the "molecular scissor" ADAM10. *Front. Immunol.* 9:1451. doi: 10.3389/fimmu.2018.01451

Michaelis, U. R. (2014). Mechanisms of endothelial cell migration. *Cell. Mol. Life Sci.* 71, 4131–4148. doi: 10.1007/s00018-014-1678-0

Moos, M. P., John, N., Grabner, R., Nossmann, S., Gunther, B., Vollandt, R., et al. (2005). The lamina adventitia is the major site of immune cell accumulation in standard chow-fed apolipoprotein E-deficient mice. *Arterioscler. Thromb. Vasc. Biol.* 25, 2386–2391. doi: 10.1161/01.ATV.0000187470.31662.fe

Moreau, H. D., Piel, M., Voituriez, R., and Lennon-Dumenil, A. M. (2018). Integrating physical and molecular insights on immune cell migration. *Trends Immunol.* 39, 632–643. doi: 10.1016/j.it.2018.04.007

Mu, W., Provaznik, J., Hackert, T., and Zoller, M. (2020). Tspan8-tumor extracellular vesicle-induced endothelial cell and fibroblast remodeling relies on the target cell-selective response. *Cells* 9:E319. doi: 10.3390/cells9020319

Mugnai, G., Tombaccini, D., and Ruggieri, S. (1984). Ganglioside composition of substrate-adhesion sites of normal and virally-transformed Balb/c 3T3 cells. *Biochem. Biophys. Res. Commun.* 125, 142–148. doi: 10.1016/s0006-291x(84)80346-0

Murray, B. A., and Culp, L. A. (1981). Multiple and masked pools of fibronectin in murine fibroblast cell–substratum adhesion sites. *Exp. Cell Res.* 131, 237–249. doi: 10.1016/0014-4827(81)90229-9

Nagao, K., and Oka, K. (2011). HIF-2 directly activates CD82 gene expression in endothelial cells. *Biochem. Biophys. Res. Commun.* 407, 260–265. doi: 10.1016/j.bbrc.2011.03.017

Nazarenko, I., Rana, S., Baumann, A., McAlear, J., Hellwig, A., Trendelenburg, M., et al. (2010). Cell surface tetraspanin Tspan8 contributes to molecular pathways of exosome-induced endothelial cell activation. *Cancer Res.* 70, 1668–1678. doi: 10.1158/0008-5472.CAN-09-2470

Nikopoulos, K., Gilissen, C., Hoischen, A., van Nouhuys, C. E., Boonstra, F. N., Blokland, E. A., et al. (2010). Next-generation sequencing of a 40 Mb linkage interval reveals TSPAN12 mutations in patients with familial exudative vitreoretinopathy. *Am. J. Hum. Genet.* 86, 240–247. doi: 10.1016/j.ajhg.2009.12.016

Ninds Stroke Genetics Network [SIGN], and International Stroke Genetics Consortium [ISGC] (2016). Loci associated with ischaemic stroke and its subtypes (SiGN): a genome-wide association study. *Lancet Neurol.* 15, 174–184. doi: 10.1016/S1474-4422(15)00338-5

Noy, P. J., Gavin, R. L., Colombo, D., Haining, E. J., Reyat, J. S., Payne, H., et al. (2019). Tspan18 is a novel regulator of the Ca(2+) channel orai1 and von willebrand factor release in endothelial cells. *Haematologica* 104, 1892–1905. doi: 10.3324/haematol.2018.194241

Oppenheimer, S. B., and Humphreys, T. (1971). Isolation of specific macromolecules required for adhesion of mouse tumour cells. *Nature* 232, 125–127. doi: 10.1038/232125a0

Pegtel, D. M., and Gould, S. J. (2019). Exosomes. *Annu. Rev. Biochem.* 88, 487–514. doi: 10.1146/annurev-biochem-013118-111902

Penas, P. F., Garcia-Diez, A., Sanchez-Madrid, F., and Yanez-Mo, M. (2000). Tetraspanins are localized at motility-related structures and involved in normal human keratinocyte wound healing migration. *J. Invest. Dermatol.* 114, 1126–1135. doi: 10.1046/j.1523-1747.2000.00998.x

Peng, D., Zuo, H., Liu, Z., Qin, J., Zhou, Y., Li, P., et al. (2013). The tetraspanin CD151-ARSA mutant inhibits angiogenesis via the YRSL sequence. *Mol. Med. Rep.* 7, 836–842. doi: 10.3892/mmr.2012.1250

Pileri, P., Uematsu, Y., Campagnoli, S., Galli, G., Falugi, F., Petracca, R., et al. (1998). Binding of hepatitis C virus to CD81. *Science* 282, 938–941. doi: 10.1126/science.282.5390.938

Porter, K. R., Claude, A., and Fullam, E. F. (1945). A study of tissue culture cells by electron microscopy: methods and preliminary observations. *J. Exp. Med.* 81, 233–246. doi: 10.1084/jem.81.3.233

Potente, M., Gerhardt, H., and Carmeliet, P. (2011). Basic and therapeutic aspects of angiogenesis. *Cell* 146, 873–887. doi: 10.1016/j.cell.2011.08.039

Rana, S., and Zoller, M. (2011). Exosome target cell selection and the importance of exosomal tetraspanins: a hypothesis. *Biochem. Soc. Trans.* 39, 559–562. doi: 10.1042/bst0390559

Ranjan, P., Kumari, R., and Verma, S. K. (2019). Cardiac fibroblasts and cardiac fibrosis: precise role of exosomes. *Front. Cell. Dev. Biol.* 7:318. doi: 10.3389/fcell.2019.00318

Rohlena, J., Volger, O. L., van Buul, J. D., Hekking, L. H., van Gils, J. M., Bonta, P. I., et al. (2009). Endothelial CD81 is a marker of early human atherosclerotic plaques and facilitates monocyte adhesion. *Cardiovasc. Res.* 81, 187–196. doi: 10.1093/cvr/cvn256

Rollins, B. J., and Culp, L. A. (1979). Glycosaminoglycans in the substrate adhesion sites of normal and virus-transformed murine cells. *Biochemistry* 18, 141–148. doi: 10.1021/bi00568a022

Rosen, J. J., and Culp, L. A. (1977). Morphology and cellular origins of substrate-attached material from mouse fibroblasts. *Exp. Cell Res.* 107, 139–149. doi: 10.1016/0014-4827(77)90395-0

Rubinstein, E. (2011). The complexity of tetraspanins. *Biochem. Soc. Trans.* 39, 501–505. doi: 10.1042/BST0390501

Scherberich, A., Moog, S., Haan-Archipoff, G., Azorsa, D. O., Lanza, F., and Beretz, A. (1998). Tetraspanin CD9 is associated with very late-acting integrins in human vascular smooth muscle cells and modulates collagen matrix reorganization. *Arterioscler. Thromb. Vasc. Biol.* 18, 1691–1697. doi: 10.1161/01.atv.18.11.1691

Schmidt-Pogoda, A., Strecker, J. K., Liebmann, M., Massoth, C., Beuker, C., Hansen, U., et al. (2018). Dietary salt promotes ischemic brain injury and is

associated with parenchymal migrasome formation. *PLoS One* 13:e0209871. doi: 10.1371/journal.pone.0209871

Schober, A. (2008). Chemokines in vascular dysfunction and remodeling. *Arterioscler. Thromb. Vasc. Biol.* 28, 1950–1959. doi: 10.1161/ATVBAHA.107.161224

Seo, S. H., Kim, M. J., Park, S. W., Kim, J. H., Yu, Y. S., Song, J. Y., et al. (2016). Large deletions of TSPAN12 cause familial exudative vitreoretinopathy (FEVR). *Invest. Ophthalmol. Vis. Sci.* 57, 6902–6908.

Sincock, P. M., Fitter, S., Parton, R. G., Berndt, M. C., Gamble, J. R., and Ashman, L. K. (1999). PETA-3/CD151, a member of the transmembrane 4 superfamily, is localised to the plasma membrane and endocytic system of endothelial cells, associates with multiple integrins and modulates cell function. *J. Cell Sci.* 112(Pt 6), 833–844.

Szabo, A., and Mayor, R. (2018). Mechanisms of neural crest migration. *Annu. Rev. Genet.* 52, 43–63. doi: 10.1146/annurev-genet-120417-031559

Takeda, Y., Kazarov, A. R., Butterfield, C. E., Hopkins, B. D., Benjamin, L. E., Kaipainen, A., et al. (2007). Deletion of tetraspanin Cd151 results in decreased pathologic angiogenesis in vivo and in vitro. *Blood* 109, 1524–1532. doi: 10.1182/blood-2006-08-041970

Takeda, Y., Li, Q., Kazarov, A. R., Epardaud, M., Elpek, K., Turley, S. J., et al. (2011). Diminished metastasis in tetraspanin CD151-knockout mice. *Blood* 118, 464–472. doi: 10.1182/blood-2010-08-302240

Tavano, S., and Heisenberg, C. P. (2019). Migrasomes take center stage. *Nat. Cell Biol.* 21, 918–920. doi: 10.1038/s41556-019-0369-3

Taylor, A. C., and Robbins, E. (1963). Observations on microextensions from the surface of isolated vertebrate cells. *Dev. Biol.* 6, 660–673. doi: 10.1016/0012-1606(63)90150-7

Tejera, E., Rocha-Perugini, V., Lopez-Martin, S., Perez-Hernandez, D., Bachir, A. I., Horwitz, A. R., et al. (2013). CD81 regulates cell migration through its association with Rac GTPase. *Mol. Biol. Cell* 24, 261–273. doi: 10.1091/mbc.E12-09-0642

Terry, A. H., and Culp, L. A. (1974). Substrate-attached glycoproteins from normal and virus-transformed cells. *Biochemistry* 13, 414–425. doi: 10.1021/bi00700a004

Tong, Y., Ye, C., Ren, X. S., Qiu, Y., Zang, Y. H., Xiong, X. Q., et al. (2018). Exosome-mediated transfer of ACE (angiotensin-converting enzyme) from adventitial fibroblasts of spontaneously hypertensive rats promotes vascular smooth muscle cell migration. *Hypertension* 72, 881–888. doi: 10.1161/HYPERTENSIONAHA.118.11375

Tugues, S., Honjo, S., Konig, C., Padhan, N., Kroon, J., Gualandi, L., et al. (2013). Tetraspanin CD63 promotes vascular endothelial growth factor receptor 2-beta1 integrin complex formation, thereby regulating activation and downstream signaling in endothelial cells in vitro and in vivo. *J. Biol. Chem.* 288, 19060–19071. doi: 10.1074/jbc.M113.468199

Umeda, R., Satouh, Y., Takemoto, M., Nakada-Nakura, Y., Liu, K., Yokoyama, T., et al. (2020). Structural insights into tetraspanin CD9 function. *Nat. Commun.* 11:1606. doi: 10.1038/s41467-020-15459-7

van Niel, G., D'Angelo, G., and Raposo, G. (2018). Shedding light on the cell biology of extracellular vesicles. *Nat. Rev. Mol. Cell Biol.* 19, 213–228. doi: 10.1038/nrm.2017.125

Vischer, U. M., and Wagner, D. D. (1993). CD63 is a component of Weibel-Palade bodies of human endothelial cells. *Blood* 82, 1184–1191. doi: 10.1182/blood.v82.4.1184.1184

Wang, G., Jacquet, L., Karamariti, E., and Xu, Q. (2015). Origin and differentiation of vascular smooth muscle cells. *J. Physiol.* 593, 3013–3030. doi: 10.1113/JP270033

Wang, L., Yang, J., Liu, Z. X., Chen, B., Liu, J., Lan, R. F., et al. (2006). [Gene transfer of CD151 enhanced myocardial angiogenesis and improved cardiac function in rats with experimental myocardial infarction]. *Zhonghua Xin Xue Guan Bing Za Zhi* 34, 159–163.

Wei, Q., Zhang, F., Richardson, M. M., Roy, N. H., Rodgers, W., Liu, Y., et al. (2014). CD82 restrains pathological angiogenesis by altering lipid raft clustering and CD44 trafficking in endothelial cells. *Circulation* 130, 1493–1504. doi: 10.1161/circulationaha.114.011096

Wilting, J., and Chao, T. I. (2015). "Integrated vascular anatomy," in *Pan Vascular Medicine*, ed. P. Lanzer (Berlin: Springer), 193–241. doi: 10.1007/978-3-642-37078-6_252

Wu, D., Xu, Y., Ding, T., Zu, Y., Yang, C., and Yu, L. (2017). Pairing of integrins with ECM proteins determines migrasome formation. *Cell Res.* 27, 1397–1400. doi: 10.1038/cr.2017.108

Yamada, M., Mugnai, G., Serada, S., Yagi, Y., Naka, T., and Sekiguchi, K. (2013). Substrate-attached materials are enriched with tetraspanins and are analogous to the structures associated with rear-end retraction in migrating cells. *Cell Adh. Migr.* 7, 304–314. doi: 10.4161/cam.25041

Yanez-Mo, M., Alfranca, A., Cabanas, C., Marazuela, M., Tejedor, R., Ursa, M. A., et al. (1998). Regulation of endothelial cell motility by complexes of tetraspan molecules CD81/TAPA-1 and CD151/PETA-3 with alpha3 beta1 integrin localized at endothelial lateral junctions. *J. Cell Biol.* 141, 791–804. doi: 10.1083/jcb.141.3.791

Yanez-Mo, M., Barreiro, O., Gonzalo, P., Batista, A., Megias, D., Genis, L., et al. (2008). MT1-MMP collagenolytic activity is regulated through association with tetraspanin CD151 in primary endothelial cells. *Blood* 112, 3217–3226. doi: 10.1182/blood-2008-02-139394

Yanez-Mo, M., Barreiro, O., Gordon-Alonso, M., Sala-Valdes, M., and Sanchez-Madrid, F. (2009). Tetraspanin-enriched microdomains: a functional unit in cell plasma membranes. *Trends Cell Biol.* 19, 434–446. doi: 10.1016/j.tcb.2009.06.004

Yang, H., Xiao, X., Li, S., Mai, G., and Zhang, Q. (2011). Novel TSPAN12 mutations in patients with familial exudative vitreoretinopathy and their associated phenotypes. *Mol. Vis.* 17, 1128–1135.

Zhang, C., Lai, M. B., Pedler, M. G., Johnson, V., Adams, R. H., Petrash, J. M., et al. (2018). Endothelial cell-specific inactivation of TSPAN12 (tetraspanin 12) reveals pathological consequences of barrier defects in an otherwise intact vasculature. *Arterioscler. Thromb. Vasc. Biol.* 38, 2691–2705. doi: 10.1161/atvbaha.118.311689

Zhang, F., Kotha, J., Jennings, L. K., and Zhang, X. A. (2009). Tetraspanins and vascular functions. *Cardiovasc. Res.* 83, 7–15. doi: 10.1093/cvr/cvp080

Zhang, F., Michaelson, J. E., Moshiach, S., Sachs, N., Zhao, W., Sun, Y., et al. (2011). Tetraspanin CD151 maintains vascular stability by balancing the forces of cell adhesion and cytoskeletal tension. *Blood* 118, 4274–4284. doi: 10.1182/blood-2011-03-339531

Zhang, X. A., and Huang, C. (2012). Tetraspanins and cell membrane tubular structures. *Cell. Mol. Life Sci.* 69, 2843–2852. doi: 10.1007/s00018-012-0954-0

Zhang, X. A., Kazarov, A. R., Yang, X., Bontrager, A. L., Stipp, C. S., and Hemler, M. E. (2002). Function of the tetraspanin CD151-alpha6beta1 integrin complex during cellular morphogenesis. *Mol. Biol. Cell* 13, 1–11. doi: 10.1091/mbc.01-10-0481

Zhang, Y. X., Xu, J. T., You, X. C., Wang, C., Zhou, K. W., Li, P., et al. (2016). Inhibitory effects of hydrogen on proliferation and migration of vascular smooth muscle cells via down-regulation of mitogen/activated protein kinase and ezrin-radixin-moesin signaling pathways. *Chin. J. Physiol.* 59, 46–55. doi: 10.4077/CJP.2016.BAE365

Zhang, Y., and Dong, E. (2014). New insight into vascular homeostasis and injury-reconstruction. *Sci. China Life Sci.* 57, 739–741. doi: 10.1007/s11427-014-4719-x

Zhang, Y., and Li, H. (2017). Reprogramming interferon regulatory factor signaling in cardiometabolic diseases. *Physiology* 32, 210–223. doi: 10.1152/physiol.00038.2016

Zhang, Y., Tan, S., Xu, J., and Wang, T. (2018). Hydrogen therapy in cardiovascular and metabolic diseases: from bench to bedside. *Cell. Physiol. Biochem.* 47, 1–10. doi: 10.1159/000489737

Zhang, Y., Zhang, X. J., and Li, H. (2017). Targeting interferon regulatory factor for cardiometabolic diseases: opportunities and challenges. *Curr. Drug Targets* 18, 1754–1778. doi: 10.2174/1389450116666150804110412

Zhao, J., Wu, W., Zhang, W., Lu, Y. W., Tou, E., Ye, J., et al. (2017). Selective expression of TSPAN2 in vascular smooth muscle is independently regulated by TGF-beta1/SMAD and myocardin/serum response factor. *FASEB J.* 31, 2576–2591. doi: 10.1096/fj.201601021R

Zhao, K., Erb, U., Hackert, T., Zoller, M., and Yue, S. (2018a). Distorted leukocyte migration, angiogenesis, wound repair and metastasis in Tspan8 and Tspan8/CD151 double knockout mice indicate complementary activities of Tspan8 and CD51. *Biochim. Biophys. Acta Mol. Cell Res.* 1865, 379–391. doi: 10.1016/j.bbamcr.2017.11.007

Zhao, K., Wang, Z., Hackert, T., Pitzer, C., and Zoller, M. (2018b). Tspan8 and Tspan8/CD151 knockout mice unravel the contribution of tumor and host

exosomes to tumor progression. *J. Exp. Clin. Cancer Res.* 37:312. doi: 10.1186/s13046-018-0961-6

Zhao, X., Lei, Y., Zheng, J., Peng, J., Li, Y., Yu, L., et al. (2019). Identification of markers for migrasome detection. *Cell Discov.* 5:27. doi: 10.1038/s41421-019-0093-y

Zimmerman, B., Kelly, B., McMillan, B. J., Seegar, T. C. M., Dror, R. O., Kruse, A. C., et al. (2016). Crystal structure of a full-length human tetraspanin reveals a cholesterol-binding pocket. *Cell* 167, 1041–1051.e11. doi: 10.1016/j.cell.2016.09.056

Zoller, M. (2009). Tetraspanins: push and pull in suppressing and promoting metastasis. *Nat. Rev. Cancer* 9, 40–55. doi: 10.1038/nrc2543

Zuo, H. J., Lin, J. Y., Liu, Z. Y., Liu, W. F., Liu, T., Yang, J., et al. (2010). Activation of the ERK signaling pathway is involved in CD151-induced angiogenic effects on the formation of CD151-integrin complexes. *Acta Pharmacol. Sin.* 31, 805–812. doi: 10.1038/aps.2010.65

Zuo, H. J., Liu, Z. X., Liu, X. C., Yang, J., Liu, T., Wen, S., et al. (2009). Assessment of myocardial blood perfusion improved by CD151 in a pig myocardial infarction model. *Acta Pharmacol. Sin.* 30, 70–77. doi: 10.1038/aps.2008.10

Conflict of Interest: The authors declare that the research was conducted in the absence of any commercial or financial relationships that could be construed as a potential conflict of interest.

frontiers in Cell and Developmental Biology

REVIEW
published: 17 September 2020
doi: 10.3389/fcell.2020.583226

Mechanical Cues Affect Migration and Invasion of Cells From Three Different Directions

*Claudia Tanja Mierke**

Faculty of Physics and Earth Science, Peter Debye Institute of Soft Matter Physics, Biological Physics Division, University of Leipzig, Leipzig, Germany

Cell migration and invasion is a key driving factor for providing essential cellular functions under physiological conditions or the malignant progression of tumors following downward the metastatic cascade. Although there has been plentiful of molecules identified to support the migration and invasion of cells, the mechanical aspects have not yet been explored in a combined and systematic manner. In addition, the cellular environment has been classically and frequently assumed to be homogeneous for reasons of simplicity. However, motility assays have led to various models for migration covering only some aspects and supporting factors that in some cases also include mechanical factors. Instead of specific models, in this review, a more or less holistic model for cell motility in 3D is envisioned covering all these different aspects with a special emphasis on the mechanical cues from a biophysical perspective. After introducing the mechanical aspects of cell migration and invasion and presenting the heterogeneity of extracellular matrices, the three distinct directions of cell motility focusing on the mechanical aspects are presented. These three different directions are as follows: firstly, the commonly used invasion tests using structural and structure-based mechanical environmental signals; secondly, the mechano-invasion assay, in which cells are studied by mechanical forces to migrate and invade; and thirdly, cell mechanics, including cytoskeletal and nuclear mechanics, to influence cell migration and invasion. Since the interaction between the cell and the microenvironment is bi-directional in these assays, these should be accounted in migration and invasion approaches focusing on the mechanical aspects. Beyond this, there is also the interaction between the cytoskeleton of the cell and its other compartments, such as the cell nucleus. In specific, a three-element approach is presented for addressing the effect of mechanics on cell migration and invasion by including the effect of the mechano-phenotype of the cytoskeleton, nucleus and the cell's microenvironment into the analysis. In precise terms, the combination of these three research approaches including experimental techniques seems to be promising for revealing bi-directional impacts of mechanical alterations of the cellular microenvironment on cells and internal mechanical fluctuations or changes of cells on the surroundings. Finally, different approaches are discussed and thereby a model for the broad impact of mechanics on cell migration and invasion is evolved.

Keywords: cell mechanics, confinement, extracellular matrix, inhomogeneities, elasticity, viscosity, cancer cells, stiffness

OPEN ACCESS

Edited by:
Wassim Abou-Kheir, American University of Beirut, Lebanon

Reviewed by:
Andrea Dimitracopoulos, University of Cambridge, United Kingdom
Nagaraj Balasubramanian, Indian Institute of Science Education and Research, Pune, India

***Correspondence:**
Claudia Tanja Mierke
claudia.mierke@uni-leipzig.de

Specialty section:
This article was submitted to Cell Adhesion and Migration, a section of the journal Frontiers in Cell and Developmental Biology

Received: *14 July 2020*
Accepted: *24 August 2020*
Published: *17 September 2020*

Citation:
Mierke CT (2020) Mechanical Cues Affect Migration and Invasion of Cells From Three Different Directions. Front. Cell Dev. Biol. 8:583226. doi: 10.3389/fcell.2020.583226

INTRODUCTION TO CELL MIGRATION AND INVASION

Cellular motility is a crucial task in many physiological functions, such as wound healing processes after tissue injury, and pathological functions. The pathological functions encompass, for instance, the migration and invasion of a malignant subset of cancer cells out of the primary tumor during cancer metastasis or the entire invasive growth mode of the primary tumor mass switching toward an aggressive and invasive state. Cancer metastasis represents a multistep consecutive process that is precisely regulated by specific biochemical and mechanical cues of the nearby microenvironment of the cancer cell. Tugging forces evoked by the migration and invasion of cells through the extracellular matrix network can be produced *in vitro* and combined with a classical 3D cell invasion assay, where the cells are plated on top of these matrices, which is termed mechano-invasion assay. It has been shown that these tugging forces induced and further promoted the invasion of cells into these matrices (Menon and Beningo, 2011). By using this assay, it was possible to reveal mechanisms regulating the invasion of cells due to randomly applied tugging on the fibers of the extracellular matrix network.

Among these genes fostering the invasiveness of cancer cells are those needed for governing of the activity of protrusive structures, such as invadopodia, in cancer cells. As these genes are elevated, it is proposed that invadopodia are assembled, whose activity is increased due to mechanical probing (Alexander et al., 2008; Albiges-Rizo et al., 2009).

In line with the hypothesis that decreased adhesion causes an enhancement in the invasive capacity of a cell, it has been detected that a wide variety of cell adhesion genes were diminished in their expression rather than increasingly expressed. In specific, the expression of ITGB3, the integrin β3 receptor subunit, has been seen to be decreased due to mechanical stimulation. In agreement with the expression results, the overexpression of the integrin β3 impaired the increase in invasion that commonly takes place after the stimulation, and thereby provides another proof that integrin β3 needs to be decreased in its expression due to mechanical cues to facilitate the cellular reaction toward the mechanical probing.

As fibronectin is necessary for accessing the mechanical stimulus through a process referred to as mechanosensing (Menon and Beningo, 2011), it seems to be likely that downregulation of integrin β3 is evoked by a regulatory feedback mechanism, which is triggered through the process of mechanosensing via the integrin β3. Apart from it, it is possible that another integrin, such as integrin β1 can take over this function and facilitate the downregulation through crosstalk associated mechanism. Nevertheless, it was intriguing that a well-known mechanoreceptor is downregulated due to mechanical probing.

As living cells and tissue are no static arrangement of building blocks withstanding all external mechanical cues, it is necessary to address alterations of cells and tissues during the process of cell migration and invasion through extracellular matrix environments. Consequently, the migration and invasion of cells is generally subject to ongoing fluctuations due to alterations of the mechanical cytoskeleton-based phenotype of cells, the matrix mechanical phenotype, encompassing composition, concentration, cross-linking, and degree of homogeneity, and the nuclear and other organelle mechanical phenotype, which plays a crucial role in narrow confinements restricting the movements at cellular length scale. However, an issue that has been excluded for a long time, was the inhomogeneity of extracellular matrix scaffolds affecting the migratory capacity of cells. Commonly, the mechanics-based approaches include mostly only a one-way based task focusing on the alteration of one specific phenotype in revealing some insights into the mechanisms of cell migration and invasion (Wolf et al., 2007; Fisher et al., 2009; **Figure 1**). Thereby, only one of the three major mechanical phenotypes, such as the matrix phenotype, the cytoskeletal phenotype, and the nuclear and other organelle phenotype are changed and its impact on at least one other phenotype is determined. More holistic two-way or three-way approaches may be promising that elucidate the interaction between cells and their microenvironment from different ways based on different directions, since there are still discrepancies between different approaches, such as the impact of cell stiffness/deformability (**Figure 2**; Guck et al., 2005; Mierke et al., 2011a,b; Mierke, 2019a), forces (Mierke et al., 2008; Koch et al., 2012; Kai et al., 2016), or mechanical linkages within cellular compartments and the surrounding extracellular matrix (Destaing et al., 2014; Kim and Wirtz, 2015; Martino et al., 2018; Fischer et al., 2020). Thereby, at least two phenotypes are altered to investigate the impact on the others in both directions and reveal a more complex regulatory phenomenon. The migration modes employed by cells grow steadily (Mierke, 2020), which therefore can be attributed to the growing number of biophysical techniques. However, these biophysical techniques enable the novel two-ways and three-way approaches. In line with this, a contradictory hypothesis is

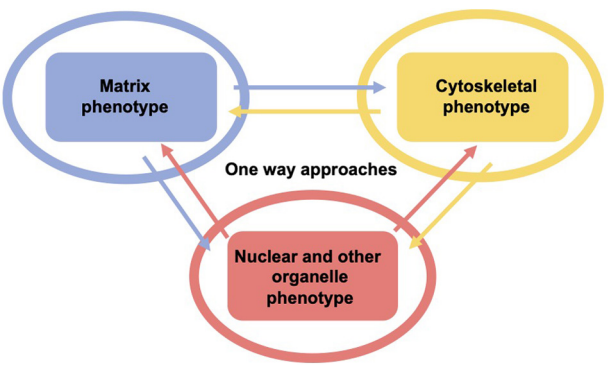

FIGURE 1 | One-way approaches are utilized to analyze the three major mechanical properties including surrounding matrix, the cell's cytoskeleton and its major the organelle the nucleus and other organelles. Hence, there are the cytoskeletal mechano-phenotype and the nuclear and other organelle mechano-phenotype. There is only one mechanical phenotype at a time that alters the matrix (blue), the cytoskeleton (yellow), and the cell nucleus and other organelles (red) in this type of approach, which is referred to as one-way approach, such as in the majority of classical migration and invasion assay.

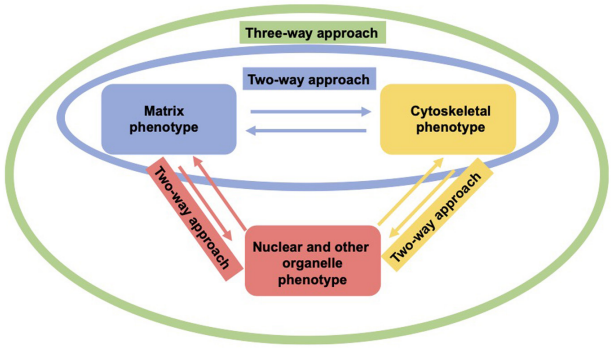

FIGURE 2 | Two-way or three-approaches are an improved method for investigating the three major mechanical properties. In a two-way approach two mechanical phenotypes are altered to reveal the impact in both directions (red, yellow, and green). In a three-way approach, all three mechanical phenotypes are altered to uncover their interdependence (green).

put forward which challenges the well-known general hypothesis that cell stiffness/deformability generally has the same effect on cell migration and invasion (Mierke, 2019a). Since cancer cell types differ largely in their biochemical and genetic phenotypes, it cannot be generally assumed, for example, that increased deformability of cells leads to increased migration and invasion by confined 3D scaffolding structures of the extracellular matrix (Jonietz, 2012; Alibert et al., 2017). Instead, one can rather hypothesize that the differences between the different cell types have different effects on the mechanical phenotype that promotes or hinders migration in interaction with other cell type-specific characteristics. Consequently, it cannot be assumed that a general and cell type-independent increased cell deformability generally causes increased migration and invasion of 3D matrix inclusions.

DIMENSIONALITY AND HETEROGENEITY OF MICROENVIRONMENTS EMPLOYED FOR CELL MOTILITY ANALYSIS

On 2D substrates, cells sense, adhere to, and generate force toward a single surface mostly homogenous substrate. In 3D microenvironments the surroundings differ vastly in topology, rigidity, and uniformity form the 2D situation (Caswell and Zech, 2018). The heterogeneity of extracellular matrix mechanical cues seems to be based on dynamic cellular interactions and matrix remodeling processes evoked by cells (Malandrino et al., 2018). Primarily cancer cells and stroma cells contribute to the matrix remodeling events. This causes the extracellular matrix to become a complex mechanical issue (Malandrino et al., 2018). Tissues are commonly comprised of extracellular matrix proteins, various types of cells, blood-fueled vascular regions, in addition to a collection of signal transduction proteins for intercellular communications. When determining the structural architectures and functions of extracellular matrices, it seems promising to have a complete list of these constituents, including a list of all proteins in each intended matrix and an even more comprehensive list of all proteins that influence or process matrices in certain situations, which is referred to as a matrisome (Hynes and Naba, 2012).

Apart from these common features, the proportions within the different anatomical spaces vary considerably. On the one hand there are typically unique mechanical properties of specific tissue types (Akhtar et al., 2011). Inside tissues the architecture of them is dictated by the function (Hynes and Naba, 2012). On the other hand, tissues can look quite inhomogeneous on smaller length scales, where cells experience and perceive mechanical property changes within tissue regions (Khadpekar et al., 2019). There is also a special type of movement in cell collections referred to as asmataxis. In asmataxis, cooperative migration is transferred due to inhomogeneity, resulting in a long-ranged self-patterning of the cells, such as skeletal myoblast C2C12 cells (Khadpekar et al., 2019). Asmataxis fulfills a functional role in the spatial multicellular patterning of tissues during the physiological development of tissues or in artificial tissue engineering. Similarly, asmataxis can play a crucial task in disease states such as the progression of malignant cancer. In specific to promote the patterning of whole tissues, a reaction-diffusion model has been proposed (Turing, 1952). In line with this many diffusion-based patterning mechanisms have been envisioned and shown to be relevant in this process (Heller and Fuchs, 2015). Apart from diffusion, mechanical cues also perform a critical role in the formation of patterned tissues (Krieg et al., 2008; Shen et al., 2008; Mammoto and Ingber, 2010; Poh et al., 2014). Cells have been demonstrated to align due to topographical cues (Charest et al., 2007; Soleas et al., 2015), shear stress (Choi et al., 2014; Ostrowski et al., 2014), and cyclic strain (Liu et al., 2008; Greiner et al., 2013). The alignment of cells can be thoroughly controlled by the varying stiffness of the underlying substrate (Suk et al., 2012).

In engineered materials, the mechanical properties of the matrix are regulated by its microstructure. At exactly the same structural length scale in biomaterials, the composition and architecture differ widely among various tissue types, inside individual tissues and crucially also with the chronological age of the tissue and the development of diseases, such as cancer, acute or chronic inflammations (Akhtar et al., 2011).

Apart from structural mechanical cues, the fluid flow through the environment of the extracellular matrix can also alter the behavior of the embedded cells to align with the fluid flow (Malek and Izumo, 1996; Ng and Swartz, 2003; Miteva et al., 2010; Poduri et al., 2017). Moreover, it has been demonstrated that cells can sense the variations of tissue rigidities through the focal adhesion (FA) protein talin, which is engaged to cell-matrix receptors, such as integrins and subsequently, it is recruited to nascent FAs (Austen et al., 2015).

All in all, the heterogeneity of tissues on a cellular length scale, such as inhomogeneities of the extracellular matrix scaffold has been ignored in many bioengineered migration and invasion assays, when analyzing the cells in a 3D microenvironment. In addition, the dynamical remodeling of the microenvironment of cells has often been excluded from motility examinations of invading cells. The mechanical probing of extracellular matrices

has just become a novel research focus, since the tensile stress acting on extracellular matrices supports the induction and enhancement of cell invasion. Finally, it has also been observed to have an effect on the function of the cells and the entire tissue, and even to contribute to a profound reshaping of tissues after injury during the healing process or to the differentiation of cells into tissues.

CELL PROTRUSIONS IN MIGRATION AND INVASION

Cell migration through 3D microenvironments depends on cellular contractile forces and is regulated by the substrate rigidity (Lo et al., 2000; Liu et al., 2008; Mierke et al., 2008, 2011b). There are at least two completely different structures with which cells are confronted on their route of cell migration and invasion through tissues. Firstly, the basement membranes, which assemble thin sheet like structures to anchor cells, including epithelial and endothelial cells, and subsequently to enclose entire tissues or organs. The basement membrane protects these tissues or organs from the underlying interstitial extracellular matrix, by forming a complex 3D structural architecture that is characterized by fibrillar collagens and has pores of varying sizes that allow the cells to enter/penetrate tissue or organs. Against this background, it is obviously not surprising that cells have the capacity to accommodate a wide variety of distinct migration modes in a 3D matrix (Mierke, 2019b, 2020), which either include the morphological appearance of protrusions/proturberances or even provide a mechanism to perform the specific migration mode (Friedl and Alexander, 2011). Within extracellular 3D matrices, cells exhibit a considerable amount of plasticity and are capable of alternating the migration mode in dependence of intrinsic and extrinsic parameters (Friedl and Alexander, 2011). The capability of cells to migrate and penetrate within collective sheets or strands further increases the intricacy of migration characteristics (Mayor and Etienne-Manneville, 2016). However, the focus of this review is on the individual migration and invasion of cells including the specific mechanisms of actin-driven protrusion formation. However, it seems probable that the mechanisms of protrusion at the leading edge are apparently the same as those found in leading cells in collectively migrating groups of cells. Invasive cells can interact with the underlying tissue, whereby they insert protrusive structures, such as invadopodia. Cells can move through and penetrate 3D microenvironments using at least two different major modes, the protrusion-based mode or the blebbing-based mode involving membrane detached rounded membrane bubbles (Mierke et al., 2018).

Caveolae Serve as Mechanosensitive Membrane Invaginations

The transitions between different shapes of cells and their various functions requires plasticity and a specific part of this specialization takes place at the cell's plasma membrane. An intrinsic characteristic of the plasma membrane of mammalian cells is their plasticity, a property essential for the perception and transduction of signals and for the capacity to cope with tension alterations caused by their environment or their own biomechanical characteristics. The caveolae are membrane invaginations that are mechanosensitive and are coupled to actin filaments (Röhlich and Allison, 1976; Singer, 1979; Valentich et al., 1997). Caveolae constitute unique invaginated membrane nanodomains that are key players in the organization of signal transduction, the homeostasis of lipids and the accommodation to membranous tension. Caveolin 1 has been identified as a major compound of caveolae (Rothberg et al., 1992), which is co-localized with the CD24 that supports actin-based cell migration in 3D collagen matrices through elevated contractile forces (Mierke et al., 2011a). Since caveolae are commonly linked to actin stress fibers, they contribute to membrane tension and the shape of cells.

The plasticity of the organization of caveolae is based on three different forms: flattened caveolae, single caveolae and clustered caveolae (Parton et al., 1994; Kiss and Botos, 2009). Caveolae are not evenly distributed in the several types of mammalian cells. They are very common in mechanically challenged cells including adipocytes, endothelial cells, fibroblasts, and muscle cells, but are practically non-existent in neurons and lymphocytes (Nassoy and Lamaze, 2012; Parton and del Pozo, 2013). It has been shown that caveolae are crucial for the regulation of multiple cascades of signaling, including several mechanisms of mechanotransduction (Parton and del Pozo, 2013). Caveolae perform a pivotal role in lipid homeostasis, and the deficiency of caveolar components leads to lipodystrophy in both mouse models and humans (Pilch and Liu, 2011). In addition, caveolae are involved in the buffering of mechanical stress at the plasma membrane (Sinha et al., 2011), what might possibly understand the occurrence of muscular dystrophies, myopathies and cardiopathies in mice and humans with mutations in caveolar components, since muscle cells are permanently subjected to mechanical stress across their plasma membrane (Galbiati et al., 2001; Garg and Agarwal, 2008; Rajab et al., 2010).

The unique feature of caveolae, its physical connection and functional interaction with the actin cytoskeleton, and particularly with the stress fibers. Since mechanically stressed cells are capable of accommodating the mechanical alterations of their microenvironment, cells should restructure their plasma membrane and actin cytoskeleton. The connection of caveolae with tension fibers can guarantee the coupling and communication between these two mechanosensors, the actin cytoskeleton and the plasma membrane, which is necessary to sustain plasma membrane integrity and to guarantee proper signaling in reply to physical signals (Echarri and Del Pozo, 2015). For example, in matrix-directed cell migration, the membrane tension is used to pull back the rear end of the migrating cell (Hetmanski et al., 2019). Invasive cancer cells traveling along the 3D cell-derived matrix of fibrillar collagen and fibronectin (Cukierman et al., 2001) can track the topology of the fibrils with defined lamellipodial and filopodial projections at the cell's leading edge (Paul et al., 2015a; Caswell and Zech, 2018), similar to cells moving on 2D substrates. The rear retraction zone of the cell is rounded and swiftly displaced with a limited number of small retraction fibers, and adhesion complexes

(Hetmanski et al., 2019). Without a chemotactic gradient, the direction of migration along matrix fibrils is assumed to be provided by the physical characteristics of the matrix, such as the strain stiffening of the matrix (Van Helvert and Friedl, 2016). Thereby, the polarization of the cells is maintained that is needed for the guided directional movement.

Invadosomes Encompass Invadopodia and Podosomes

Generally, to migrate and invade tissues efficiently, cells need to explore and sense their microenvironmental properties, such as matrix properties or fluid flow. Thereby, they need to adapt their own cytoskeletal, nuclear, organelle, or plasma membrane mechanics and alter their surrounding matrix confinement by degradation, secretion of matrix cross-linking molecules, or exert forces to apply tensile stress on their environment. In the following, the matrix environment in *in vitro* cell culture assays can be modified to promote the migration and invasion of cells, such as cancer cells or fibroblasts. Since transient mechanical stress can provoke the maturation of invadopodia and consequently promote their migration and invasion through 3D confinements, it is necessary to understand how the mechanotransduction can signal from the outside in the cells to finally facilitate the motility of cells in 3D (first direction: structure-based apporach). These invadopodia can be analyzed in greater depths by either altering the cytoskeletal mechanical characteristics, the mechanical linkage between cellular organelles, such as the nucleus or mitochondria or by probing the surrounding extracellular matrix scaffold directly with mechanical load (second direction, extrinsic mechanics-based approach) or indirectly via the alteration of the structural cues within the matrix scaffold (third direction, cell mechanics-based approach).

Invadosomes can be seen as mechano-adhesive structures involved in the regulation of the invasive capacity of cells through their ability to breakdown the extracellular matrix (Albiges-Rizo et al., 2009; Linder, 2009; Destaing et al., 2011; Murphy and Courtneidge, 2011; Saltel et al., 2011; Boateng et al., 2012). The new term invadosome has been defined to cover the term invadopodia in cancer cells and podosomes in untransformed cells, comprising dendritic cells, endothelial cells, macrophages, osteoclasts and vascular smooth muscle cells (Marchisio et al., 1987; Gaidano et al., 1990; Kanehisa et al., 1990; Miyauchi et al., 1990; Hai et al., 2002; Moreau et al., 2003; Burns and Thrasher, 2004; Destaing et al., 2014). From a historical perspective, the terms podosome and invadopodia characterize exactly the same structure, which in epithelial cells and fibroblasts is determined by the expression of a constitutively active variant of the tyrosine kinase Src (Tarone et al., 1985; Chen, 1989). However, invadopodia and podosomes still exhibit fine variations in molecular content, dynamics and structure (Destaing et al., 2014).

Invadosomes represent hot-spots of intensified actin polymerization. The invadosome structure is comprised of two continuously polymerizing actin arrangements represented by long pillars of tightly bundled F-actin filaments aligned perpendicular to the substrate. This structure is referred to as the heart of the invadosome structure, in which an actin cluster is formed, consisting of radial F-actin filaments parallel to the substrate (Luxenburg et al., 2007; Winograd-Katz et al., 2011). Consequently, a single invadosome is identified by a dense F-actin core covered by a closed ring of adhesion molecules that colocalize on the actin cluster cloud. Multiple extracellular matrix receptors, including CD44, β1, β3, and β5 integrins, have been detected in invadosomes (Zambonin-Zallone et al., 1989; Jurdic et al., 2006; Destaing et al., 2010; Schmidt et al., 2011). Within these invadosomes, the associated receptors can sustain the localization of multiple adaptor proteins including those identified in FAs encompassing tyrosine kinases, such as focal adhesion kinase (FAK), Pyk2, and Src, small GTPases. Among these small GTPases are Cdc42, Rac and Rho, and adaptor molecules, such as p130Cas, paxillin, and vinculin. In the end, these invadosomes essentially perform two main tasks, such as exerting actin-rich and adhesive cellular protrusions or components and governing polarized secretory signaling pathways that manage the precisely regulated supply of metalloproteases required for the degradation of the extracellular matrix.

Coupling Functions of Src and Its Substrates Between Actin-Based Adhesion and Matrix Breakdown

c-Src belongs to the family of tyrosine kinases that possess generally a distinct domain structure, encompassing a myristoylated N-terminal domain that directs Src toward membranes, two Src-homology-protein-binding domains (SH2 and SH3), and a catalytic domain shared by tyrosine-kinases. The activation of Src is facilitated through the impairment of the intramolecular interactions of SH2 with the phosphorylated Tyr527, when specific phosphatases targeting this Tyr residue and thereby causing an "opening" of the entire protein (Roskoski, 2004). Apart from its kinase activity, Src performs an adaptor function that controls the liberation of its SH2 and SH3 domains, which can interact with a variety of molecules. Similar to integrins, the alteration of c-Src activity is facilitated through conformational states, which are referred to as on "open" and "closed" conformational state due to the intracellular governance. Within the invadosome, the oscillation of conformational changes of Src controls the cellular functions. In specific detail, a constitutive active Src mutant, termed SrcY527F, has been expressed in Src-, Yes-, and Fyn-deficient (SYF) fibroblasts (Kelley et al., 2010), where it can induce the protrusion of invadosomes in a wide variety of different cell types. However, this type of invadosome is not capable of breaking down the surrounding extracellular matrix. This result indicates that the cycling of the Src activation cycle seems to be a fundamental and necessary mechanism for linking the acto-adhesive system and the breakdown activity of the extracellular matrix.

The targeted molecules of Src contribute also to this linking mechanism. Cortactin represents a Src substrate that may perform a function in the maturation of invadosomes, whereby

it controls the secretory release of matrix-metalloproteinases (MMPs) within invadopodia (Clark et al., 2007; Clark and Weaver, 2008; Buschman et al., 2009). The localization of cortactin to predicted future spots of the breakdown of the extracellular matrix occurs prior to the trafficking of proteases (Artym et al., 2006). There are two novel substrates of the Src kinase, termed Tks4 and Tks5, which were characterized to function in an essential manner in the organization of invadosomes (Courtneidge, 2012). Beyond their function in the dynamics of PIP2 and the five SH3 domains that facilitate scaffolding activity, Tks4 and Tsk5 are components of the Nox3 protein complex involved in ROS synthesis, which is required for the breakdown activity of invadosomes. The functional connection between Tks4 and Tsk5 is not yet clearly elucidated, however, it may be rather obvious that they fulfill crucial tasks in governing of the linkage of the acto-adhesive system and the breakdown activity toward the extracellular matrix environment. The expression of Tks5 in Tks4$^{-/-}$ mouse embryonic fibroblasts (MEFs), which express an active Src mutant, referred to as SrcY527F, can sufficiently rescue the normal assembly of invadosomes without the capacity to breakdown the extracellular matrix. Apart from the ratio between Tks5/Tks4, the phosphorylation of Tks4 is supposed to be crucial for the governance of this linkage. In fact, the expression of the Tks4Y25/373/508F triple mutant rescues the sustained generation of the invadosome in Tks4$^{-/-}$ MEFs, whereas their breakdown activity is not restored (Buschman et al., 2009; Branch et al., 2012). These data suggest a regime in which the linkage between the acto-adhesive mechanism and the breakdown rate of the extracellular matrix relies on the molecular dynamics of invadosome governors. Up to now, it is assumed that the linkage of these two functionalities is exclusively controlled by mutants that alter the adaptive cycle of conformational modification or the phosphorylation dynamics. Therefore, the coupling of these two processes strongly relies on accurate cycling of the activation/inhibition of the principal invadosome governors. However, there may be differences between invadopodia and podosomes (Yamaguchi et al., 2005; Oikawa et al., 2008, Artym et al., 2011). Thus, it has been speculated that there exists a maturation process enabling a transition between the two protrusive states (Destaing et al., 2014).

Filopodia

There is much evidence that elevated activity of lamellipodia favored increased 3D migration, invasion and metastasis. In addition, there is ample evidence that lamellipodial regulators, which comprise the compounds of the race activator Tiam-1 and the WAVE complex, are attenuated in metastatic cancer (Malliri et al., 2002; Silva et al., 2009; Sowalsky et al., 2015; Vaughan et al., 2015). It is probable, therefore, that other types of F-actin-based protrusions can supplement or counterbalance the migration into 3D. Filopodia fulfill various tasks in migrating cells, such as detecting and adapting to the chemical and physical environment, establishment of cell–cell adhesions when closing epithelial membranes with zippers and developing protrusions (Mattila and Lappalainen, 2008). Similarly, the exertion of filopodia has also been associated with the cancer invasion and the malignant progression of cancer encompassing metastasis. Fascin, which belongs to the actin bundling proteins that encourage filopodial exertion, is increasingly expressed in a variety of metastatic tumors in mice and humans (Vignjevic et al., 2007; Tan et al., 2013; Li et al., 2014; Schoumacher et al., 2014; Huang et al., 2015). In addition, the expression of myosin X is initiated by the expression of the gain-of-function mutant p53 to facilitate metastasis in mouse models of pancreatic cancer and to be implicated in the poor performance in breast cancer (Arjonen et al., 2014).

Bone morphogenetic protein (BMP) signaling has been found to stimulate the expression of ARHGEF9b in tip endothelial cells to activate Cdc42 and produce filopodia through formin like 3 (FMNL3; Wakayama et al., 2015). Filopodia through formin like 3 was also involved in angiogenesis in mammalian tissues, pointing to a conserved mechanistic pathway. Fascin fulfills a crucial task in the bundling of F-actin within filopodia in cancer and additionally induces the exertion of filopodia in tip cells of the endothelium. However, fascin also impacts the process of angiogenesis in a moderate manner (Ma et al., 2013), which highlights its functional role as a filopodial regulator that performs more redundant tasks in this specific cell type.

There are different types of filopodia, such as long filopodia-like protrusions. It has been seen that a small amount of long filopodia-like protrusions occurs near the periphery of breast cancer cells as they begin to move into the lung parenchyma and interstitium-like environments (Shibue et al., 2012). Long filopodia-like protrusions initiate the connection to the extracellular matrix in metastatic breast cancer cells through the coupled interaction of the RhoGTPase-formin axis, such as Rif-mDia2, and the integrin signaling axis, such as ILK-Parvin-Pix-Cdc42-PAK-cofilin, to prolong the lifetime of the long filopodia-like protrusions, which drives the formation of adhesions and the generation of proliferative signals through FAK–ERK signaling, subsequently supporting tumorigenesis (Shibue et al., 2012, 2013).

Filopodia can also foster the migration and invasion of cancer cells in the extracellular matrix environment. In specific, the local co-trafficking of α5β1 integrins and receptor tyrosine kinases (RTKs), encompassing the epidermal growth factor receptor 1, provide the interaction between cell–matrix adhesion receptors and RTKs (Paul et al., 2015a) and thereby repress the activity of Rac. However, they induce the activation of RhoA at the frontline of the cell's leading edge to protrude actin-spike protrusions at the front edge of the invading cancer cells (Jacquemet et al., 2013). Due to the activation of RhoA actin-spike protrusions are created in breast and lung carcinoma cell lines that express the gain-of-function mutant p53. These specific protuberances are clearly distinguishable from lamellipodia as they do not have dendritic actin sheaths and consist of numerous small filopodia that emerge in the direction of migration in cells moving in extracellular 3D matrices and in *in vivo* tissues (Paul et al., 2015a,b). Filopodial actin spikes necessitate the formin FHOD3 that is activated through the phosphorylation downstream of the RhoA–ROCK elements. The density and structural organization of filopodia inside these protrusions lead to the hypothesis that they fulfill a crucial function in the generation of protrusive forces.

FIRST DIRECTION (STRUCTURE-BASED APPROACH): COMMONLY EMPLOYED INVASION ASSAYS WHERE STRUCTURAL AND STRUCTURAL-BASED MECHANICAL ENVIRONMENTAL CUES ARE ALTERED

There exists a number of studies that deal with varying concentrations of extracellular matrix proteins polymerizing into a fibrillar scaffold suitable for the migration and invasion of multiple cell types (**Figure 3**; Mierke et al., 2011b; Wolf et al., 2013; van Helvert et al., 2018; Anguiano et al., 2020; Le et al., 2020). When one parameter is altered usually the others may be changed accordingly, which has to be taken into account or it needs to be omitted by adapting the experimental approach. There are some examples of such interdependencies provided in **Figure 3**. The most commonly employed matrices are hydrogels, which constitute polymeric fibrous networks capable of retaining a large amount of water or any liquid withholding up to 95–99% of its weight. They are biomimetic in nature, as their high-water contents and diffusive transport characteristics are closely related to that of natural extracellular matrix (Spiller et al., 2011). Most hydrogels are even biocompatible, like those made with natural polymers such as agarose, alginate, chitosan, collagen, dextran, fibrin, gelatin, hyaluronic acid (HA), Matrigel, and silk (Vega et al., 2017) and those obtained from synthetic gels on the basis of polyacrylic acid (PAA), poly(ethylene glycol) (PEG), poly(hydroxyethyl methacrylate) (PHEMA), poly(vinyl alcohol) (PVA), and poly(propylene fumarate) (Hunt et al., 2014). Another feature of hydrogels that is extremely beneficial in the field of tumor environments and regenerative medicine is their strong functionalization capacity, which enables them to be easily adapted for enhanced cell adhesion and mechanical characteristics or continuous release of growth factors, cytokines including chemokines and pharmaceuticals (Buwalda et al., 2017).

Hydrogel Concentration

The invasion of cancer cells turned out to follow a biphasic response toward the stiffness of the extracellular matrix microenvironment (Ahmadzadeh et al., 2017). The risk of breast cancer is 4–6 times higher when mammographic density is elevated (Boyd et al., 1998, 2001; McCormack and dos Santos Silva, 2006), whereby mammographic density becomes a major independent risk parameter for breast cancer (Boyd et al., 1998, 2002; McCormack and dos Santos Silva, 2006). This rise in mass density is associated with a considerably elevated accumulation

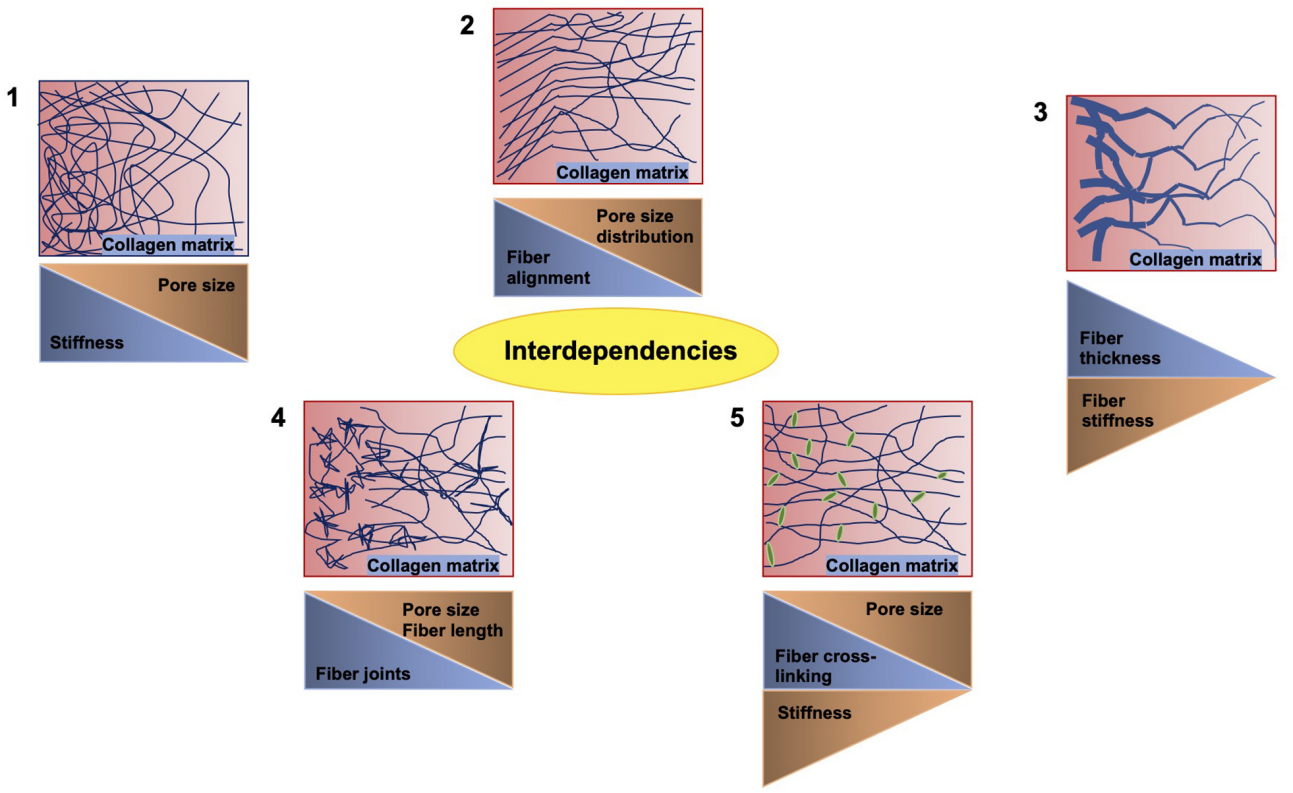

FIGURE 3 | Crucial interdependencies between structural and mechanical cues of 3D collagen fiber matrices. When the stiffness of the matrix is altered, the pore size is inversely altered **(1)**. When the fiber alignment is modulated, the pore size distribution is affected **(2)**. When the fiber thickness is varied, the stiffness of the fiber is altered accordingly **(3)**. When inhomogeneities, such as joints, are increased, the fiber length and pore size are decreased **(4)**. Similarly, the cross-linking of the fibers reduces the pore size, but decreases the stiffness **(5)**.

of extracellular matrix proteins, especially collagen I (Guo et al., 2001; Boyd et al., 2002; Li et al., 2005), which is partially accountable for the general rise in stiffness in mammary tumors (Paszek et al., 2005; Lopez et al., 2011). Rigidity of matrix has been proven to encourage a malignant phenotype in cancer cells (Paszek et al., 2005; Alexander et al., 2008; Provenzano et al., 2009; Tilghman et al., 2010), increases the migration and invasion (Pelham and Wang, 1997; Lo et al., 2000; Kostic et al., 2009; Menon and Beningo, 2011), and impacts the intracellular signaling, pathways, causing consequently elevated proliferation (Wozniak et al., 2004; Klein et al., 2009; Provenzano et al., 2009). Even though it is obvious that matrix stiffness is a major determinant of tumor progression, the mechanisms whereby cells react to alterations in matrix stiffness are not yet fully comprehended. In parallel to the abundance of collagen, the alignment of the collagen fibers seems to have a decisive function in the progression of tumors. Changes in the arrangement and orientation of collagen fibers have been characterized and tumor-associated collagen signatures (TACS) have been recognized (Riching et al., 2014), which become apparent in a predictable manner throughout the progression of the tumor. In specific, the accumulation of aligned collagen fibers oriented perpendicular to the tumor margin, which are referred to as TACS-3, establishes motorways on which cancer cells are monitored to travel *in vivo* (Provenzano et al., 2006), and is associated with enhanced invasion and metastasis in murine models (Provenzano et al., 2008).

Hydrogel Composition

The nanostructure of the extracellular matrix and specific collection of the extracellular matrix molecules is precisely guided in a tissue-specific manner during tissue development to provide proper functions of cells and entire organs (Smith et al., 2017). Alterations of the composition in extracellular matrix scaffold and the mechanical phenotype are observed in the course of the progression of most degenerative diseases and show the outcome of aging or, as a compensatory effort of the tissue, maintain its proper function (Kim et al., 2000; Parker et al., 2014; Klaas et al., 2016). At present, these alterations in compliance of the extracellular matrix are regarded as prognostically valuable for solid tumors (Calvo et al., 2013; Hayashi and Iwata, 2015; Reid et al., 2017).

Knowledge of the function of mechanical and structural elements within the extracellular matrix may constitute an indispensable foundation for cancer therapy (Karuppuswamy et al., 2014). However, due to the interlinked alterations of these factors in traditional extracellular matrix model schemes, it is commonly challenging to separately distinguish these distinct parameters (Jiang et al., 2015; Hwang et al., 2016; Jun et al., 2018; Huang et al., 2020). To overcome this difficulty, an electrospun fibrous gel matrix, adjustable for elasticity/porosity, was designed, consisting of photocrosslinked gelatinous microfibers (chemical gels crosslinked in the nanometer range) with highly controlled binding, such as fiber-bound gels in the tenth of a micrometer range (Gurave et al., 2020; Huang et al., 2020) (**Figure 4**). This arrangement permits an independent manipulation of the microscopic fiber elasticity and porosity of the matrix, in other words the mechanical and structural requirements of the extracellular matrix can be adjusted independently. The elasticity of the fibers was coordinated with photocrosslinking parameters (Huang et al., 2020). The porosity of the material was modified by adjusting the level of inter-fiber cohesion (**Figure 4**). The interference of these elements of the fibrous gel matrix on the migratory capacity of tumorigenic MDA-MB-231 cells and non-tumorigenic MCF-10A cells have been quantitatively examined. MDA-MB-231 cells exhibited the strongest level of MMP-independent invasion into the matrix, which consisted of fibers with a Young's modulus of 20 kPa and a small level of interfiber cohesion, whereas MCF-10A cells under the identical matrix circumstances demonstrated non-invasive performance

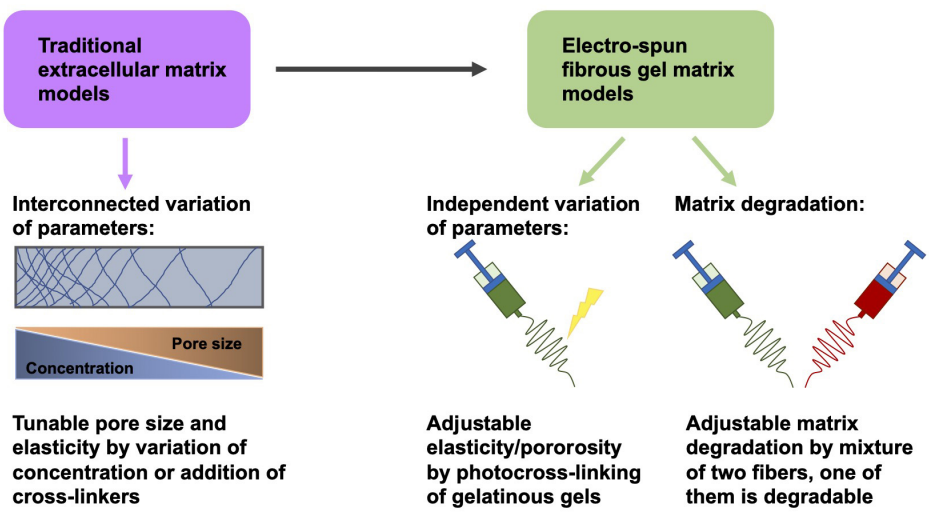

FIGURE 4 | Variation of matrix parameters independently of one another. Instead of traditional fibrous matrix gels, electrospun fibrous gels are employed to obtain gels whose elasticity/porosity can be adapted independently of other parameters, such as pore size and concentration.

(Huang et al., 2020). In addition, there are also biodegradable polymers that can be generated through electrospinning (Kai et al., 2014; Jiang et al., 2015).

There exists vastly divers types of hydrogels: firstly, physical or reversible gels in which the framework of the polymer network is achieved by physical cross-linkages such as micellar crystallites, helix formation, hydrogen bonds or hydrophobic forces, that can be "broken" (reversed) by altering the conditions of the solution, such as pH, temperature, salt concentration, and ionic strength (Caló and Khutoryanskiy, 2015), and secondly, chemical or permanent-type gels in which the cross-linked polymers are attached covalently. An essential feature for cartilage tissue engineering is the fact that hydrogels possess adaptable mechanical characteristics that are connected to the level of cross-linking and are determined by the existence and amount of the charge. Charged hydrogels modify their hydration in dependence of the pH level and their geometry when they are subjected to the electromagnetic field (Takahashi et al., 2014).

Special Relevance of Collagen Type I for Cancer Cell Migration and Invasion

Several global transcriptomic or proteomic studies revealed special candidates that foster the onset of colon carcinogenesis due to elevated or reduced expression levels, however, among them are those additionally altered in locally improved or metastatic colorectal cancer (Langlois et al., 2014; Naba et al., 2014; Yuzhalin et al., 2018a). In specific, the proteomics analysis of the detergent-insoluble portions of paired primary tumors of the colon and liver metastases in comparison to neighboring non-tumorous tissues demonstrated the specific accumulation of the pathological material in the core matrisome and several collagen-modifying enzymes including MMPs, A Disintegrin And Metalloproteinase (ADAM)s and Lysyl oxidase homolog 1 (LOXL1; Naba et al., 2014). Desmoplasia and disturbances of collagen are a characteristic of colorectal cancer, and several collagens, the most frequent of which are type I, VI, VII, VIII, X, XI, and XVIII, have been identified in colorectal cancer specimens collected (Skovbjerg et al., 2009; Kantola et al., 2014; Sole et al., 2014; Burke et al., 2015; Qiao et al., 2015; Shang et al., 2018; Yuzhalin et al., 2018b). The type I collagen has been seen to be elevated in cancerous tissues compared to normal tissues (Zou et al., 2013). In accordance with this finding, type I collagen mRNAs in the blood of colorectal cancer patients were also elevated over healthy individuals (Zou et al., 2013; Rodia et al., 2016). Consequently, second harmonic generation of fibrillar collagen content imaging has proven clinical usefulness in the stratification of high-grade cancers and its value in forecasting disease outcome in colorectal cancer patients (Birk et al., 2014; Burke et al., 2015).

The most thoroughly investigated type I collagen receptors are integrins α1β1, α2β1, α10β1, and α11β1 (**Figure 5**; Barczyk et al., 2009). After identification of their GFOGER sequence, the activation of these receptors can be switched on by various ligands such as collagen type I (Knight et al., 2000). Among these collagen receptors, the α1β1 integrin represents the most expressed one in colon carcinoma (Boudjadi et al., 2013). Moreover, the expression of the β1 integrin subunit in tumors correlates with diminished overall survival and decreased disease-free survival in a broad-ranged cohort of colorectal cancer patients (Liu et al., 2015). In specific, the β1 integrin is found in the serum of colorectal cancer patients, and the degree of its expression seems to strongly correspond with the levels of aggressiveness and the occurrence of micrometastases (Assent et al., 2015). The overexpression of the β1 integrin is tightly coupled with the malignant progression of colorectal cancer and consequently ends up in the colorectal metastasis of the targeted organs, such as the liver (Sun et al., 2014; Assent et al., 2015). In

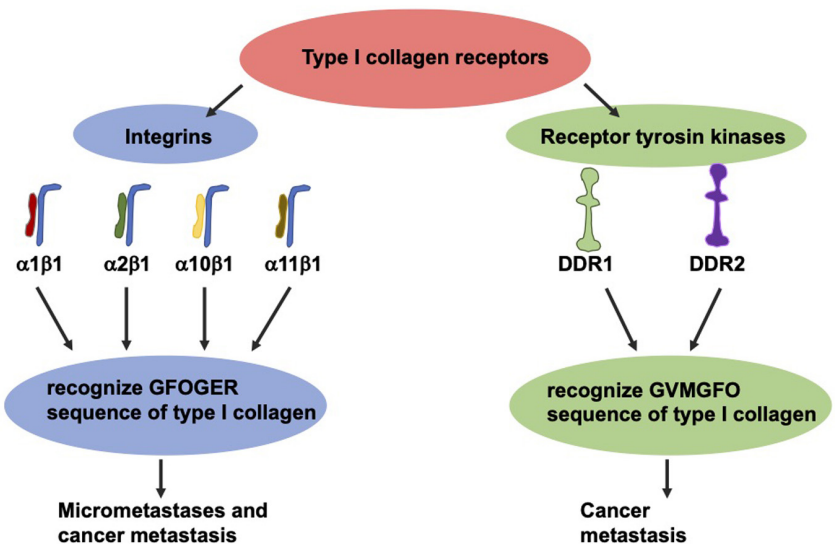

FIGURE 5 | The two groups of type I collagen receptors, the integrins and the discoidin domain receptors. These two types recognize different sequence motifs in type I collagen.

line with this, the β1 integrin expression is decreased *in vitro* due to sensing of 3D type I collagen (Assent et al., 2015; Saby et al., 2016).

Collagen can also transduce signals to cells via two RTKs discoidin domain receptors (DDRs), referred to as DDR1 and DDR2 (**Figure 5**). Each of which are able to interfere with type I collagen (Rammal et al., 2016) and fulfill an essential part in the progression of the cancer disease (Saby et al., 2016). These receptors, featuring tyrosine kinase activity, identify the GVMGFO sequence of type I collagen (Konitsiotis et al., 2008) and undergo fairly tardy and persistent activation (Vogel et al., 1997). DDR1 is highly expressed in colon carcinoma and encourages the development of metastases in invasive colon carcinoma (Chen et al., 2011; Jeitany et al., 2018, Sirvent and Lafitte, 2018). With respect to DDR2, high levels of expression were linked to higher abundances of T4, lymph node metastases, peritoneal dissemination and a poor prognosis, indicating that DDR2 expression appears to be an efficacious therapeutic objective (Sasaki et al., 2017).

Hydrogel Gradients

A technique for the fabrication of type I collagen hydrogels with precisely controlled and reproducible physical density and mechanical stiffness gradients by avoiding damage to the collagen fibril structure and omitting additional chemical alterations is highly needed (Kayal et al., 2020). In order to encourage the development of appropriate substrates, key knowledge must be gained about the influence of local stiffness gradients both in respect of the value of the principal stiffness and the slope of the gradient. A set of model substrates with collagen hydrogels was generated and characterized, in which predefined stiffness gradients were established and analyzed. Therefore, tissue engineering technology was adapted to generate gradients in RAFT-stabilized collagen hydrogels (Cheema and Brown, 2013; Levis et al., 2015) by constructing molds and 3D printing molds to obtain model collagen hydrogels with well specified stiffness gradients. These collagen constructs were employed to examine the impact of stiffness gradient and stiffness magnitude on the elongation and orientation of cells *in vitro* (Kayal et al., 2020).

A gradient hydrogel constitutes a hydrogel which exhibits a gradual and continuously spatio-temporal variation in at least one of its properties (Genzer and Bhat, 2008). Gradient hydrogels provide outstanding engineering instruments for the native-like, biomimetic cellular microenvironment. They also enable the determination of a broad range of property levels in a single specimen, which is ideal for high-throughput screenings (Sant et al., 2010). Gradients may be physical or biochemical or a mixture of the two and may also contain a time dimension. Gradient hydrogels can be produced by several techniques that typically entail the initiation of precursor solution crosslinking, such as photopolymerization, the enzyme-catalyzed technique and thermally initiated gradient (Vega et al., 2017). When crosslinking enhances stiffness, the first covered hydrogel area behaves predominantly elastic, whereas the last covered area, that has been subjected to UV light the longest, exhibits a higher rate of crosslinking and is the stiffest. Hence, a gradient of stiffness is generated (Hudalla and Murphy, 2015). Apart from UV-light cross-linking, specific enzymes including tyrosinases, transferases, and peroxidases can be utilized to catalyze covalent cross-linking of hydrogel precursors and subsequently to modify hydrogels (Teixeira et al., 2012).

Biochemical gradients are gradients in concentration of the bioactive molecules, such as morphogens, which encompass a broad variety of substances including growth and transcription factors, chemokines, and cytokines. Biocompatible hydrogels can be based on natural and some synthetic polymers, that exhibit inherent bioactive characteristics. The bioactivity of hydrogels can be increased through distinct functionalization, which covers covalent binding of peptides and proteins (Hesse et al., 2017) or exopolysaccharides (Rederstorff et al., 2017) to the polymers of the hydrogel. Moreover, the elevation of bioactivity can be gained through additional specific affinity binding, which is facilitated by incorporating specific collagen binding sequences to the envisioned peptide/protein to be easily attached and connected into the collagen-based hydrogel (Hesse et al., 2018). In general, synthetic hydrogels are functionalized in a way that they become better suited for cell adhesion through the incorporation of cell-adhesive ligands, such as RGD(S) peptides, which presents the key element of the adhesion of cells to fibronectin (Moreira Teixeira et al., 2014).

Porous Hydrogels

Porous hydrogels can be manufactured in multiple ways: firstly by producing the gel matrix scaffold with completely encapsulated biodegradable units (Zhao et al., 2013), secondly, by the production of hydrogel fibers through electrospinning or 3D bioprinting (Murphy and Atala, 2014; Bracaglia et al., 2017), thirdly, by the implementation of porogens, such as polymer microspheres (Fan and Wang, 2017; Gupta et al., 2017), or fourthly by usage of 3D laser perforation (Ahrem et al., 2014). Under mechanical stress, hydrogel frameworks also have an elongation gradient; the surface hydrogel layer dampens more elongation than the middle and deep layers (Brady et al., 2017).

The multi-branched PEG-based gradient hydrogel stage acts as biomimetic cell niche with autonomously adjustable matrix stiffness and biochemical ligand density, such as the CRGDS peptide (Tong et al., 2016). Both gradients were implemented in a timed manner, such as firstly the mechanical gradient and secondly the chemical gradient. Thereby, a gradient of UV exposure can be applied over the precursor solvent or over hydrogels with well-defined mechanical gradients (Tong et al., 2016).

Cell-Derived Matrix Cross-Linking Molecules

Apart from the photo-crosslinked fibers, fibers can be crosslinked through biomolecules that are either cell-secreted or externally added to the migration and invasion assays. Among them are fibronectin, HA, and lysyl oxidase (**Figure 6**). In living tissues, the core of the matrisome comprises five different classes of macromolecules, namely collagens, fibronectin, hyaluronans, laminins, and proteoglycans. In the majority of tissues, fibrillar collagen is the primary source of extracellular matrix. Cells

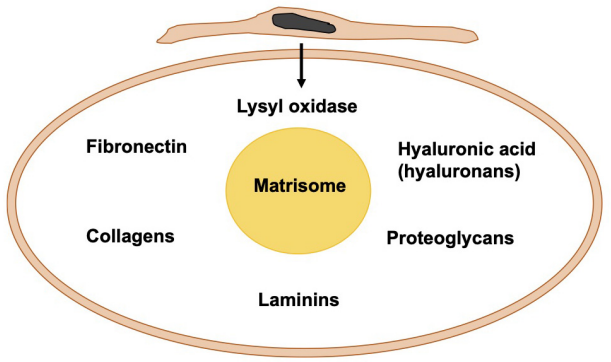

FIGURE 6 | Cell-derived matrix cross-linking molecules create the matrisome.

integrated into fibrillar collagen interfere with it via their surface receptors, such as integrins and DDRs. On one side, cells receive signals from the extracellular matrix that alter their functionalities and response. On the other side, all cells inside the tumor surroundings, for example, cancer cells, cancer-associated fibroblasts, endothelial cells, and immune cells produce and release matrix macromolecules under the regulation of several extracellular cues.

Fibronectin

An old classical focus of cancer research has been on the obvious changes in stiffness, as the near stroma of most tumors usually stiffens and thickens due to an accumulation of type I collagen and fibronectin (Miles and Sikes, 2014; Pickup et al., 2014). The factors that govern the balance between the deposition of the matrix and its degradation in the course of the disturbances of the tissue remodeling processes are required for enlightening the mechanisms that control a large set of normal and pathological processes. In fibronectin null cells, the polymerization of fibronectin into the extracellular matrix microenvironment is necessary for the accumulation of type I collagen and thrombospondin-1 and that the retention of fibronectin fibrils of the extracellular matrix demands the constant polymerization of a fibronectin matrix. Beyond that, the integrin ligation by itself is inadequate to sustain the extracellular matrix fibronectin in the complete lack of fibronectin accumulation. It has been shown that maintenance of thrombospondin-1 and collagen I in fibrillar constructions located inside the extracellular matrix relies on an effective fibronectin matrix. An undamaged fibronectin matrix is crucial for preserving the configuration of the cell–matrix adhesion sites. However, in total lack of fibronectin and fibronectin polymerization, neither α5β1 integrins nor tensin can attach to fibrillar cell–matrix adhesions (Sottile and Hocking, 2002).

The deposition of fibronectin into the extracellular matrix enhances the adhesion-dependent cell contractility (Hocking et al., 2000). Entire populations of cells are able to switch toward a dormant and stalled stage, which is induced by the assembly of an organized, fibrillar fibronectin matrix through cell–matrix adhesion via αvβ3 and α5β1 integrins, ROCK-generated tension, and the stimulation of TGFβ2 (Barney et al., 2020). The outgrowth of cancer cells after a dormancy period necessitates the MMP-2-driven breakdown of fibronectin (Barney et al., 2020). The impairment of the fibronectin polymerization facilitates a loss of collagen I matrix fibrils and an associated elevation in the amounts of endocytosed type I collagen (Shi et al., 2010). In addition, the membrane type matrix metalloproteinase 1 (MT1-MMP, synonymously referred to as MMP14) is critical for the regulation of the turnover of fibronectin (Shi and Sottile, 2011). The assembly of the matrix is generally triggered through extracellular matrix glycoproteins that connect to distinct cell surface receptors, such as dimerized fibronectin, which binds to α5β1 integrins. The binding of fibronectin to a receptor fosters the fibronectin self-association facilitated through the N-terminal assembly domain and primes in a structural manner the actin cytoskeleton to generate cellular contractility. Alterations in the conformational state of fibronectin lead to the liberation of additional binding sites, that contribute to the assembly of fibrils and consequently to their transformation into a stabilized and insoluble state. After their assembly, the fibronectin matrix governs the organization of tissues insofar that it manages the assembly of additional extracellular matrix proteins (Singh et al., 2010).

In breast cancer, the stiffening of the tissue through the accumulation of fibronectin and collagen is linked to an advanced progression of the disease at both locations, the site of the primary tumor and metastatic sites (Libring et al., 2020). Intracellular and soluble fibronectin is at first lost during the transformation of the tumor, whereas it is restored in all lines exhibiting epithelial-mesenchymal plasticity. Non-transformed mammary epithelial cells cannot cause accumulation of fibronectin matrices except when transglutaminase 2, which functions as a fibronectin cross-linking enzyme, is overexpressed. On the contrary, breast cancer cells alter the fibronectin matrix output of fibroblasts in a phenotype-specific fashion. In addition, different levels of accumulation were found according to whether the fibroblasts are conditioned to replicate paracrine signaling or endocrine signaling events of the metastatic niche. In the paracrine signaling, fibroblasts stimulated with breast cancer cell cultures of high epithelial-mesenchymal plasticity have been shown to lead to the largest accumulation of the fibronectin matrix. In endocrine signaling, mesenchymal breast cancer cells generate extracellular vesicles, which cause the highest levels of matrix formation through conditioned fibroblasts. Consequently, it has been revealed that there exists a dynamic interplay between cancer cells and surrounding stromal cells inside the tumor microenvironment. During that interplay, the amount of fibronectin and its degree of fibrillarization within the extracellular matrix are adapted to the specific stage of progress of the disease (**Figure 7**). In contrast, in invasive cancers, these fibrils reorient themselves vertically to the boundary of the tumor and serve as so-called tracks for the migration of cancer cells across the basement membrane (Yang et al., 2011; Clark and Vignjevic, 2015; Bayer et al., 2019).

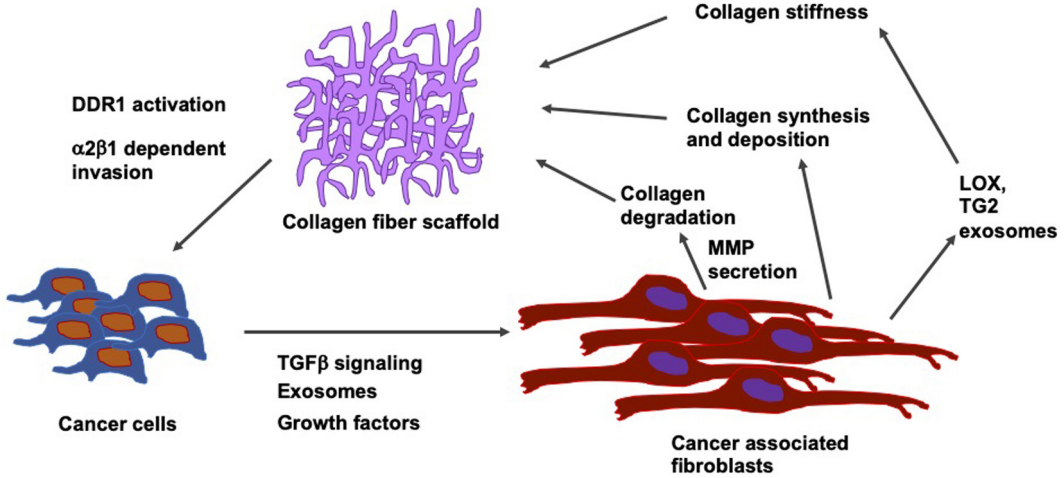

FIGURE 7 | Relation between type I collagen fiber scaffolds and cells including their tumor microenvironment, such as cancer associated fibroblasts (CAFs). Cancer cells secrete TGF- β, growth factors and exosomes. CAFs influences collagen synthesis and deposit collagen and release LOX and transglutaminase 2 (TG2) exosome that subsequently increases the collagen stiffness.

Hyaluronic Acid

Apart from fibronectin, the matrices can also be altered mechanically through HA. The adhesion/homing molecule CD44, participating in cell-cell and cell–matrix adhesion, constitutes the major cell surface receptor for HA (Lesley et al., 1992). The transcription machinery of YAP1/TAZ and TEA domain transcription factor (TEAD) activates the transcription of CD44 by coupling to the CD44 promoter at TEAD binding sites, thereby encouraging the propagation of malignant pleural mesothelioma (MPM) cell lines (Tanaka et al., 2017). Apart from CD44, the receptor for hyaluronic acid-mediated motility (RHAMM) synonymously referred to as HMMR, IHABP, or CD168, acts as a receptor for HA (Turley et al., 2002).

The aberrant expression of RHAMM that is generally not present in normal tissues, fosters the proliferation, migration and invasion of cells and consequently causes the resistance to pharmacological drugs in distinct types of tumors encompassing breast (Wang et al., 2014), lung (Wang et al., 2016) and liver cancers (He et al., 2015). Moreover, HA enhances the migration and invasion of cells in MPM cells via RHAMM (Shigeeda et al., 2017). Receptor for hyaluronic acid-mediated motility is transcriptionally regulated through Yes-associated protein 1 (YAP1) and transcriptional co-activator with PDZ-binding motif (TAZ), whose own expressions are found to be elevated in cancer cells during their malignant progression (McCarthy et al., 2018; Ye et al., 2020). It is obvious that YAP1/TAZ and TEAD complexes couple to a specific location within the RHAMM promoter and thus are capable of governing cell migration and invasion in breast cancer cell lines (Wang et al., 2014). In line with this, it has been shown that inhibitors, such as Verteprofin and CA3, both suppress the mesothelioma phenotype that encompasses cell migration and invasion, spheroid assembly and subsequently the formation of the primary tumor (Kandasamy et al., 2020). In specific, these two reagents cause apoptosis in mesothelioma cells. It is known that the persistently active YAP1 expression abolishes the action of the inhibitors, which leads to the hypothesis that impairment of the YAP1/TAZ/TEAD signaling is a prerequisite for the effectiveness of Verteporfin and CA3 in mesothelioma cells.

Under normal physiological circumstances, the stabilization and activation of YAP1/TAZ are closely guided through the phosphorylation within the Hippo pathway (Lei et al., 2008; Liu et al., 2010; Zhao et al., 2010). However, under pathological conditions, when this pathway is dysregulated, it has been revealed that this can lead to aberrant stabilization and activation of YAP1/TAZ protein, resulting in tumor development, progression, metastasis, and even recurrence (Ma et al., 2015; Zanconato et al., 2016). Moreover, by acquiring cancer stem cell-like characteristics, it can elicit a resistance to drugs (Lian et al., 2010; Cordenonsi et al., 2011; Touil et al., 2014; Zhao et al., 2014; Tanaka et al., 2017).

Lysyl Oxidase

The extracellular matrix can be seen as a vastly fluctuating system, which permanently undergoes a process of continuous conversion driven by the cells that populate it. As a consequence, neighboring cells are forced to adapt their behavior (Butcher et al., 2009). In the microenvironment of the tumor, abnormal extracellular matrix dynamical processes are prevalent and account for the course of progression, transformation and dispersal of cancer cells. One hallmark of cancer, for example, is the excessive production and secretion of extracellular matrix proteins encompassing collagen I, II, III, V, and IX, that all cause fibrosis of tissues (Zhu et al., 1995; Kauppila et al., 1998; Kalluri and Zeisberg, 2006; Huijbers et al., 2010; Pickup et al., 2014). The tissue fibrosis, in turn, raises the stiffness of the surrounding microenvironment of the tumor compared to the surrounding tissue, thereby accelerating the progression of the cancer by lowering the concentrations of the tumor suppressors PTEN and HOXA9 within the cancer

cells (Mouw et al., 2014; Pickup et al., 2014). It has been revealed how breast adenocarcinoma cells release lysyl oxidase, a substance that crosslinks extracellular matrix proteins, resulting in secondary stiffening of the extracellular matrix scaffold to ease invasion (Levental et al., 2009). This rise in stiffness also affects the surrounding cells, including the development of cancer-associated fibroblasts (Calvo et al., 2013) and tumor-activated macrophages (Acerbi et al., 2015).

In identifying key features of the extracellular matrix to alleviate these transformations, the matrix mechanics of the tumor environment has an outstanding character (Kalluri and Weinberg, 2009). For instance, in the course of the epithelial to mesenchymal transition (EMT), where polarized epithelial cells are transferred toward more motile mesenchymal cells during biological processes including embryogenesis and the malignant progression of cancer (Chen et al., 2017), laminin-rich extracellular matrix is able to abolish EMT, whereas fibronectin-rich extracellular matrix fosters the transformation of it (Chen et al., 2013). Stiffening behavior of the surrounding microenvironment has also been reported to support the EMT of breast cancer cells that consequently enhances its invasive capacity and malignant progression encompassing cancer metastasis (Wie et al., 2015), whereby the polarity of tissues provides elevated resistance to death in mammary cancer cells (Weaver et al., 2002).

Cell-Derived Matrix-Degrading Molecules

Another major focus of cancer research is the investigation of the matrix-degradation through cell secreted molecules such as MMPs, including MT-MMP1 (synonymously referred to as MMP-14) (Wolf et al., 2003, 2007; Sabeh et al., 2009) and MMP-2 (Clark and Weaver, 2008), whose substrates are collagen and fibronectin, as well as MMP-9 (Jacob and Prekeris, 2015), which all have demonstrated to fulfill a major role in the malignant progression of the tumor. In colorectal cancer, the co-culture of tumor associated macrophages and colorectal cancer cells elevates the generation of cancer-derived MMP-2 and MMP-9 (Kang et al., 2010).

The basement membrane surrounding tissues or vessels and the fibrillar collagen-based interstitial matrix represent physical barriers for cell migration and invasion (Willis et al., 2013). A dense, cross-linked extracellular matrix is mainly assembled by type I collagen (Hanahan and Weinberg, 2000; Chambers et al., 2002). Extracellular matrix molecules can also be broken down extracellularly through the employment of proteases such as MMPs, plasminogen activators, and plasmin (Hynes, 1990; Marchina and Barlati, 1996; Shapiro, 1998). In line with this, the dense extracellular matrix scaffold serves also as barrier and can be overcome in two different ways, one mechanical mode without the degradation of the extracellular matrix (Friedl et al., 2001; Wolf et al., 2003, 2007) and one enzymatic mode involving collagenolytic activity through MMPs, such as mainly MT1-MMP in the course of cancer invasion (Stetler-Stevenson and Yu, 2001; Itoh and Nagase, 2002; Hojilla et al., 2003; Cruz-Munoz et al., 2006).

Even though leukocytes (and amoeboid cancer cells, which travel through the extracellular matrix using hydrostatic pressure and membrane swellings referred to as blebs) apparently migrate protease-independently, mesenchymal cancer cells have to free their route through focusing breakdown activity. MT1-MMP can be considered a membrane-bound matrix metalloprotease that performs a distinct, non-redundant function in the invasion of a number of cancer cell types (Sabeh et al., 2009). In contrast, the principal protrusion of invasive cancer cells has the potential to attract and regulate the extracellular matrix fiber alignment (without large-scale degradation). An integrin-rich and actin-rich area of collagen decomposition has been identified, which lies behind it but still in front of the nucleus (Wolf et al., 2007).

The Arp2/3 activator N-WASP has been revealed to fulfill a crucial task in focal proteolytic decomposition of the extracellular matrix. The actin polymerization facilitated by N-WASP encourages the infiltration of MT1-MMP at actin hot spots, which are accumulations of F-actin at places of interaction and contact with the extracellular matrix. MT1-MMP is bound to these actin hotspot herds by means of an actin-binding domain located inside the cytoplasmic tail. Thus, N-WASP-facilitated actin polymerization guides protease activity by producing actin hotspots in immediate vicinity of matrix fibrils intended for breakdown in invasive cells (Yu et al., 2012). The WASP family member WASH fosters the Arp2/3-driven polymerization of actin on late endosomes, and provides tubules that are able to fuse with the plasma membrane at locations of FAs that provide cell matrix adhesion (Monteiro et al., 2013). Therefore, various Arp2/3 nucleation promoting factors, which operate at multiple subcellular sites, could combine to control a matrix degradation regime at areas of extracellular matrix contact to eliminate the extracellular matrix barrier and thereby ease the cell protrusion. In view of the fact that the size of the matrix pores is a major limitation for the transmigration of moving cells (Wolf et al., 2013), it is intriguing to assume that sites of cell-matrix contact in front of the nucleus could serve as a narrowing belt that is liberated by these focal proteolytic processes in invasive cancer cells.

In the maturation phase of invadopodia, they accomplish to be proteolytically active, consisting of a process marked by the identification and/or secretion of specific functional MMP enzymes (**Figure 8**). The three members of the MMP family compromise MMP-2, MMP-9 and MT1-MMP that are linked within invadopodia (Jacob and Prekeris, 2015). Of special interest for this pivotal finding is MMP-2, which has fibronectin type II repeats that attach to its collagen substrate (Polette et al., 2004). MMP-2 is targeted on invadopodia, where it is released into the extracellular surroundings to breakdown the extracellular matrix (Clark and Weaver, 2008). Most interestingly, the overexpression of cofilin in multiple invasive cancer cell lines enhances the cellular invasiveness and increases the enzymatic activity of MMP-2 (Yap et al., 2005; Dang et al., 2006). In contrast, the reduction of cofilin expression lowers the maturation of invadopodia and subsequently, the enzymatic activity of MMP-2 (Wang et al., 2007; Tahtamouni et al., 2013).

A hypothesis takes on a necessary function for the membrane-tethered collagenase MT1-MMP through its capacity to

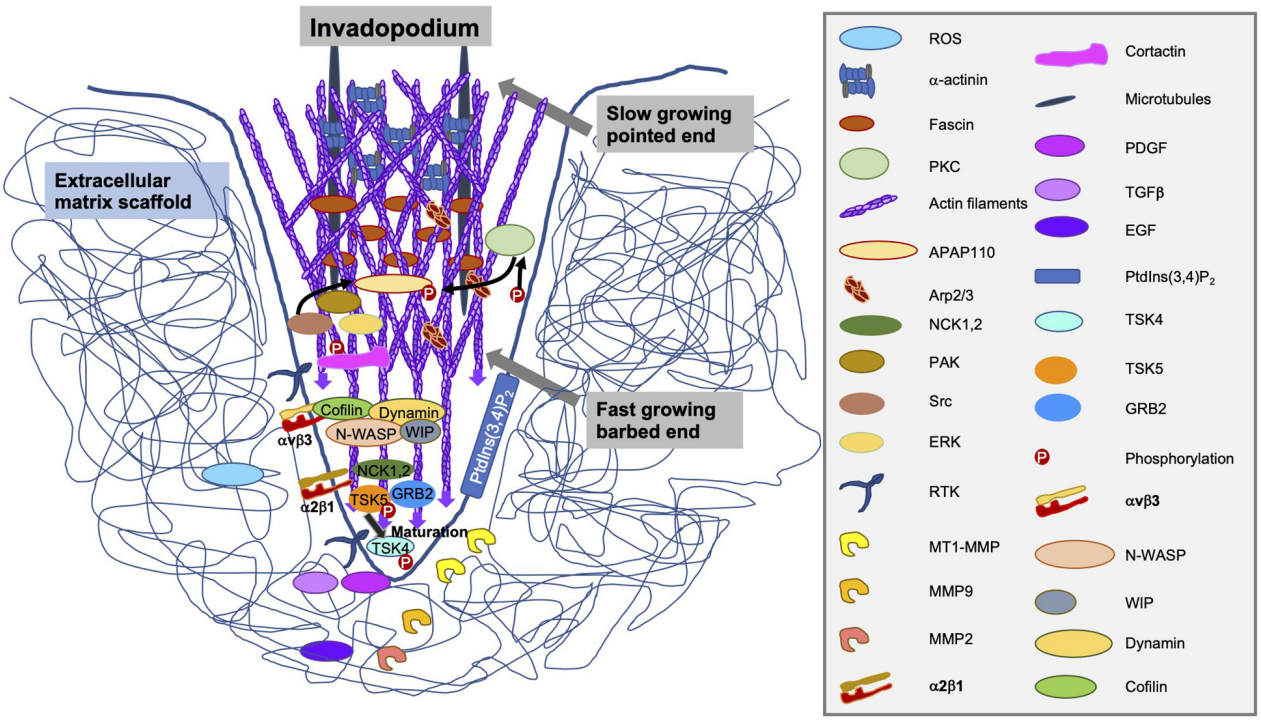

FIGURE 8 | Structure, components and secreted enzymes of an invadopodium.

proteolytically breakdown matrix components including type I collagen (Seiki, 2003; Sabeh et al., 2004; Fisher et al., 2006; Li et al., 2008). These results strongly indicate that MT1-MMP-expressing cancer cells have the intrinsic ability to move through the extracellular matrix scaffold according to the collagenolytic activity of this enzyme. However, clinical trials aiming these enzymes have revealed no promising outcomes (Coussens et al., 2002).

When cancer cells expressing MT1-MMP, such as HT1080s cells, are trapped in the dense physiologically networked type I collagen scaffolds, such as 2.0–5.0 g/l type I collagen, and broad-spectrum inhibitors of MMPs are supplemented, no MMP-independent invasion is reported (Sabeh et al., 2004; Fisher et al., 2006). Cells secrete metalloproteinases, including these MMPs, to breakdown the tight collagen matrix scaffold and enhance the pore size to encourage the invasion of cells. This phenomenon is more evident when the density of the fibers is high and the spaces between the fibers are considerably reduced compared to the size of the cell body (Fraley et al., 2015). Incorporating the activity of MMPs in the model leads to an enhancement of cell invasion at higher collagen concentrations, consistent with melanoma invasion data. The MMP-dependent reshaping of the fibers also offers the necessary room for cell proliferation in the close proximity of the cells. Consequently, the elimination of MMPs is proven to decrease cell proliferation (Bott et al., 2010). However, there is no one-way alteration, since a single alteration has usually side effects, which impacts migration and invasion, that has to be taken into account. The rigidity of the matrix also influences the proliferation of the cells in a Rho-based mode. Enhancement of matrix stiffness and Rho activity initiates phosphorylation of FAK at Y397 sites, which has been associated with an acceleration of cell migration and invasion (Mierke et al., 2017).

Differences in Matrix Remodeling Mechanisms Between Normal and Malignant Cells

Metastasizing breast carcinoma cells can utilize normal mammary branching mechanisms during organ morphogenesis to elevate their tissue-invasive activity. The mechanisms of breast cancer invasion revealed that MT1-MMP fulfils a functional role, while the closely related proteinase MT2-MMP (synonymously referred to as MMP-15) does not appear to be associated, although it acts as a predominant proteolytic participant in bifurcation morphogenesis and the invasion of carcinoma cells *in vivo*. In contrast, the epithelial cell-specific aiming of MT1-MMP in normal mammary glands leaves the branching unaffected, while the loss of the proteinase in the carcinoma cells reverses the invasion, maintains the matrix structure, and totally prevents metastasis. In contrast, in the normal mammary gland, extracellular matrix reshaping and morphogenesis is only removed when MT1-MMP expression is specifically eliminated from the periductal stroma. These results reveal the complementary but diverse mechanisms that govern the developmental schemes compared to those for redesigning the neoplastic matrix (Feinberg et al., 2018).

Complicated signal transduction cues govern the cancer invasion in 3D extracellular matrices confinements, such as MMP-dependent and MMP-independent mechanisms. Lysophosphatidic-acid-triggered HT1080 cell invasion necessitates MT1-MMP-dependent collagenolysis to obtain matrix voids of nuclear width. These spaces are referred to as single-cell invasion tunnels (SCITs). When SCITs are generated, cells manage to migrate MMP-independent inside them. Apart from cancer cells, endothelial cells, smooth muscle cells and fibroblasts can produce SCITs during their invasion, which leads to the hypothesis that the generation of SCIT is a basic element of cellular motility inside 3D matrices. Precisely regulated signaling actions are necessary for the generation of SCITs. MT1-MMP, Cdc42 and its downstream effectors, including myotonic dystrophy kinase-related Cdc42-binding kinase (MRCK) and p21 protein-activated kinase 4 (PAK4), protein kinase Cα and Rho-associated coiled-coil-containing protein kinases (ROCK-1 and ROCK-2) guide the synchronization required for SCIT construction. Finally, MT1-MMP and Cdc42 are fundamental compounds of a cointegrated invasion signaling system that is capable of directing single cell invasion in 3D collagen matrices (Fisher et al., 2009).

SECOND DIRECTION (EXTRINSIC MECHANICS-BASED APPROACH): MECHANO-INVASION ASSAYS

Apart from the biochemically based metastatic cascade, with increasing understanding of the metastatic progression, there are also a number of mechanical parameters that favor the initiation of the multi-stage metastatic cascade (Kumar and Weaver, 2009). A broad range of mechanical forces are observed within the surrounding tissue environment of cancers. In contrast, an enormous amount of research has concentrated exclusively on the elevated rigidity of the tumor stroma (Paszek et al., 2005; Kostic et al., 2009; Levental et al., 2009). However, when employing an *in vitro* mechano-invasion assay (Menon and Beningo, 2011) the impact of various kinds of mechanical cues can be examined on the capacity of a cell to migrate and invade through matrix scaffolds. Mechanical stimulation takes the form of temporary tugging forces generated through magnetic beads coincidentally connected to anisotropic collagen and fibronectin fibers (**Figure 9**). These forces are not sufficiently strong to cause stretching of the entire material, nor is the transient strain oriented in a specific axis of the substrate.

In biomechanical research, a major focus is on alterations of the structure and mechanics of the entire tissue, and another major focus is on local biophysical alterations affecting the geometry and topology of the surrounding extracellular matrix. Primarily, an early focus has been on pronounced alterations in stiffness, as in most cases the tumor nearby stroma commonly becomes more rigid and dense that has been caused by an elevated generation of collagen type I and fibronectin (Miles and Sikes, 2014; Pickup et al., 2014). This enhancement in matrix rigidity may foster an elevation in cancer cell proliferation, migration and invasion (Alexander et al., 2008; Kostic et al., 2009; Parekh and Weaver, 2009; Ulrich et al., 2009; Tilghman et al., 2010; Charras and Sahai, 2014; Jerrell and Parekh, 2014; Umesh et al., 2014). Beyond the matrix rigidity, stroma-associated cells, such as the highly contractile myofibroblasts, generate forces within the extracellular matrix environment, when they remodel and invade through the extracellular matrix (Goffin et al., 2006; Shieh, 2011; Tripathi et al., 2012). In the course of the remodeling action of the matrix, a tugging force is produced and transferred toward the surrounding collagen fibers that are further bundled and rearranged (Goffin et al., 2006; Castella et al., 2010; Murrell et al., 2015; Oudin et al., 2016a). The occurrence of myofibroblasts and the forces they exert have been implicated in enhanced invasion and motility of cancer cells (De Wever et al., 2008; Elkabets et al., 2011; Fuyuhiro et al., 2012).

The transient mechanical strain can be evoked by embedding magnetic particles inside hydrogels, such as 3D collagen fiber matrices and exerting displacements on those beads with an external permanent magnet. This approach seems to be appropriate to mirror the magnitude and organization of the forces, which are caused by residual normal fibroblasts or fibrosarcoma cells, through transient tugging on fibers inside collagen–fibronectin matrices. Consequently, this approach increases the level of invasive cells, when they are *per se* highly metastatic cells, such as human fibrosarcoma cells (Menon and Beningo, 2011). This indicates that random transient tugging forces seem to deliver mechanical cues, which can be employed to foster the invasion of metastatic cancer cells.

These distinct mechanical cues and even more can be detected within the extracellular matrix through mechanoreceptors of the plasma membrane (Gasparski and Beningo, 2015). The integrin receptor family is involved in mechanoreception and its relevance in mechanotransduction has been extensively examined (Roca-Cusachs et al., 2012; Ross et al., 2013). It is generally known that cellular structures including filopodia, lamellipodia and invadosomes, encompassing invadopodia, and podosomes, react to mechanical stimuli (Schwarz and Gardel, 2012; Mrkonjic et al., 2016).

Transient Mechanical Strain Affects Highly Invasive Cells

Transient mechanical strain facilitates maturation of invadopodia, elongation of invadopodia and subsequently a pronounced migration and invasion of cells into hydrogels due to this mechanical load (Menon and Beningo, 2011; Gasparski et al., 2017). Hence, enhanced invasion due to this mechanical stimulus necessitates the cells to be invasive by themselves, since non-invasive cells cannot be induced to be invasive. This mechanical signal is utilized especially by metastasizing cancer cells. Cofilin and fibronectin are required to react to mechanical stimuli. The expression of cofilin in cancer cells is required to maintain their invasive potential (Walter et al., 2009; Menon and Beningo, 2011; Nagai et al., 2011). Cofilin activity is governed through LIM kinase 1 (LIMK1) phosphorylation at its Ser3 position. Unphosphorylated cofilin interacts with F-actin filaments to trigger actin polymerization, whereas phosphorylated cofilin cannot fulfill this task. Consequently,

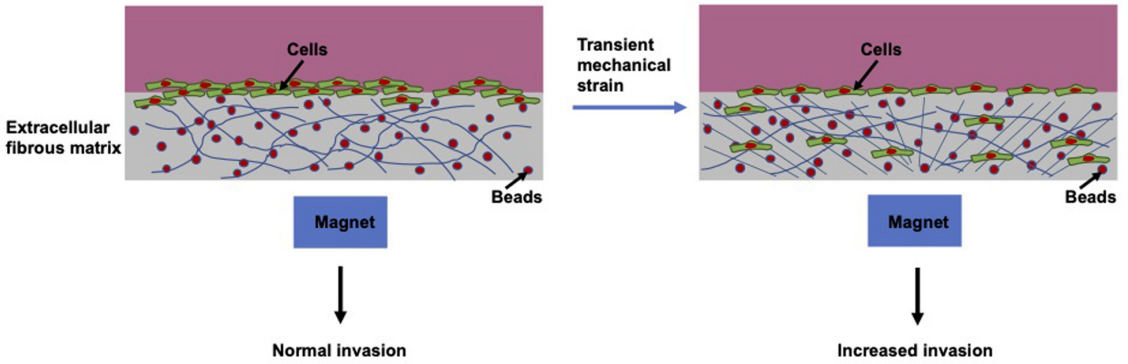

FIGURE 9 | Schematic drawing of mechano-invasion assay.

exclusively active, unphosphorylated cofilin interferes with actin polymerization through the production of free barbed-ends (Blanchoin et al., 2000).

The integrin β3-encoding gene is specifically expressed, which confirmed its functional role in sensing this type of mechanical probing. The downregulation of integrin β3 expression raises the maturation of invadopodia due to stimulation, whereas a knocked down expression of cofilin creates invadopodia that are insensitive to stimulation. As a consequence of encouraging maturation of invadopodia, there is a concomitant enhancement of MMP activity levels linked to invadopodia. Tugging forces have been established as intrinsically supportive of metastatic cell invasion, and they continue to deliver a mechanical stimulus for the foundation of mechanically initiated maturation of invadopodia (Gasparski et al., 2017).

The integrin β3 forms pairs with integrin αv or integrin αIIb to create the heterodimeric integrin molecules. These integrin β3-containing heterodimers interact with arginine–glycine–aspartic acid (RGD) domains of fibronectin (Xiong et al., 2002). Since fibronectin is necessary for the enhanced reaction of cells in this kind of mechano-invasion experiments (Menon and Beningo, 2011), the decreased expression of integrin β3 by mechanical stimulation is fascinating. In addition, it is understood that the levels of expression of integrin β3 may differ in several cancer types and that this variation in expression can influence cell invasion (Jin and Varner, 2004; Sheldrake and Patterson, 2009; Seguin et al., 2015). When the downward regulation of the integrin β3 would be mandatory for the cells to perceive the mechanical stimulus and generate an increased invasion, overexpression of integrin β3 would impede the amplification of the invasion. In fact, it has been shown that cells overexpressing integrin β3 cannot react to mechanical stimulation, as they did not exhibit increased invasion compared to controls, indicating that downregulation of integrin β3 is necessary for increased invasion as a consequence of stimulation.

Interaction Between Transient Strain and Expression of Proteins

Multiple cases of integrin crosstalk have been documented in which the attachment of one integrin to its ligand results in a disturbance in the expression or activity of other integrins. This type of crosstalk exists between integrin β3 and another fibronectin-binding family member, integrin β1 (Gonzalez et al., 2010). However, there is no crosstalk between integrin β1 and β3 subunits in the invasive reaction due to mechanical stimulation (Gasparski et al., 2017). Is there a relationship between integrin β3 subunits and cofilin? Cofilin severs actin filaments and matures invadopodia (Yamaguchi et al., 2005). In the mechano-invasion assay, cells treated with cofilin siRNA cannot sense the mechanical stimulation and exhibit no increased invasion, instead they displayed a basal invasiveness (Menon and Beningo, 2011). Since cofilin activity is governed by its phosphorylation at Ser3, which is referred to as Ser3 phospho-cofilin (Pollard and Borisy, 2003), it is supposed that mechanically triggered cells exhibit decreased amounts of Ser3 phospho-cofilin (inactive form) compared to non-stimulated controls. Moreover, when cofilin activity relies on integrin β3 expression, overexpression of integrin β3 is expected to elevate the amount of inactive phospho-cofilin due to mechanical strain. It has been observed that levels of Ser3 phospho-cofilin are reduced due to mechanical stimulation, which leads to the hypothesis that more cofilin needs to be in its active state after mechanical stimulation. This elevation in the amount of active cofilin is driven through decreased expression of the integrin β3 mechanoreceptor (Gasparski et al., 2017).

Cofilin activity facilitated actin polymerization is necessary for invadopodia maturation. Thus, knockdown of cofilin is expected to impair the elongation of invadopodia triggered by mechanical stimulation of cells. In line with this, MMP-2 represents a hallmark of invadopodia-based invasion. But it has been found that HT1080 cells have an MMP-independent nuclear piston invasion mechanism that demands integrin β3 activity (Petrie et al., 2017). It is a fascinating concept that a cell employs the expression of integrin β3 to choose between various invasion modes (Mierke, 2019b, 2020), so that down-regulation favors MMP-dependent invasion, whereas the normal integrin levels of β3 expression foster an MMP-independent nuclear piston invasion mode. The actin filament-severing activity of cofilin is controlled through LIMK1-dependent phosphorylation (Arber et al., 1998; Pollard and Borisy, 2003; Yamaguchi et al., 2005). Apparently, there exists a model signal transduction pathway

that combines integrin β3 and cofilin activity and subsequently the ripening of invadopodia. It has been proposed that the engagement and activation of integrins causes the activation of Rac1, a Rho-GTPase regulated through integrin β3 within focal complexes (Morgan et al., 2009). Therefore, the hypothesis is that mechanical stimulation decreases the expression of integrin β3, which in turn decreases the activation of Rac1. In opposition to other investigations, in which Rac1 expression strengthened the migration and invasion of cells (Kunschmann et al., 2019). It is hypothesized that various types of force use distinct signal transduction pathways, in which the force is primarily modulated by the interaction of cells with various ligands.

It has been determined that an increased stiffness of the invasion assay matrix (4.5 g/l) had no effect on the increase of invasion through tugging forces compared to a less stiff matrix (2.5 g/l). Besides, an increase in stiffness only, without the tugging force, has not raised the invasion level (Menon and Beningo, 2011). However, this is in contrast to other studies where stiffness *per se* may increase the invasiveness of another metastatic cancer cell line, the MDA-MB-231 breast cancer cells, or even normal MCF10A epithelial cells (Fischer et al., 2017, 2020). However, it may be that different cell types respond differently to stiffness changes. Following the first finding, it can be assumed that highly invasive cells are able to distinguish a tugging force from an alteration in matrix stiffness and interpret the signal in a different way, which supports the hypothesis of differential sensing of forces within extracellular matrices or tissues. This type of mechanical signaling may exist in every extracellular microenvironment and is obviously utilized by the heavily metastatic cancer cells to encourage invasiveness, whereas non-invasive cells do not evidently have the ability to exploit this special type of mechanical signature.

Role of PAK in Mechano-Invasion

The p21-activated kinase 1 (PAK1) belongs to the six-member PAK serine-threonine-protein kinase family. It encompasses three major domains: firstly, a kinase domain in the C-terminus, secondly, an autoinhibitory domain and thirdly, a p21-binding domain (Kumar et al., 2017; Rane and Minden, 2018). The auto-inhibitory domain of PAK abolishes the catalytic activity of its own kinase domain. A single PAK1 molecule is normally inactive, but is activated when its auto-inhibitory domain connects to the kinase domain of another molecule (Kumar et al., 2017). PAK1 governs cytoskeletal remodeling, cell migration and invasion, metastasis and angiogenesis (Hammer et al., 2013; Hammer and Diakonova, 2015; Kumar and Li, 2016). The PAK family crucially connects Rho family of GTPases with several cytoskeletal processes. For instance, Rac1 interacts with PAK1 signal transduction in cell migration and invasion (Meyer Zum Büschenfelde et al., 2018; Mierke et al., 2020). Significant findings also suggest that PAK1 is implicated in numerous types of cancer, in particular in the control of the capability of invasive cells to metastasize (Hammer et al., 2013; Hammer and Diakonova, 2015; Yang et al., 2015; Kumar and Li, 2016).

In fact, a decrease in integrin β3 signaling due to mechanical stimuli, such as transient tugging force, is connected to the activity of PAK1 (Gasparski et al., 2019). It is well established that PAK1 exhibits a reduced activity under mechanical challenge, as evidenced by a reduction in Ser144 phosphorylation. However, this phosphorylation deficit can be restored when integrin β3 is overexpressed. PAK1 mutants display a coordinated reaction in the expression and activity of the MMP-2 enzyme, in addition to prolongation of invadopodia, as a reaction to stimulation. These findings have led to the recognition of a novel mechanosensitive reaction in human fibrosarcoma involving PAK1 as a signal generator which is downstream of integrin β3. There is an established cascading pathway linking integrin β3 to the control of cofilin activity, although its part in this mechanosensitive process is largely unclear. Integrin β3 transmits signals to Rac1 that result in the activation of PAK1 at the membrane through PAK1 autophosphorylation (Morgan et al., 2009). PAK1 can phosphorylate LIMK1 at the Tyr507 position, which decreases cofilin activity through phosphorylation of cofilin at its Ser3 position (del Pozo et al., 2000; Pollard and Borisy, 2003). Nevertheless, it is not established whether this route is of any relevance for the statement that transient mechanical stimulation leads to an elevation of cofilin activity and consequently to an intensified invasion through the maturation of the invadopodia. Most probably, this route could be scaled down, as this would generate more active, unphosphorylated cofilin, resulting in the maturation of invadopodia.

In human fibrosarcoma cells, the expression of PAK1 is reduced and also its phosphorylation (decreased phospho-Ser144 levels) due to transient stimulation. When integrin β3 is overexpressed, phospho-PAK1 levels are elevated in stimulated cells, indicating that PAK1 is in fact more active. When mutants of PAK1 were expressed in these cells, the so-called kinase-dead mutants displayed enhanced cell invasion, invadopodia maturation and related MMP-2 release. On the contrary, constitutively active PAK1 mutants exhibit a lower invasion, smaller invadopodia and reduced MMP-2 activity. These findings indicate that a reduction in PAK1 activity is required for fibrosarcoma cells to increase their invasiveness as a response to mechanical excitation.

Mechanical Cues Induce Directed Motility

Directed cell movement, such as cancer stem cells, provided by contact guidance within aligned collagenous extracellular matrices represents a crucial point for the dissemination of breast cancers throughout tissues (Ray et al., 2017). The physical microenvironment impacts multiple fundamental cellular functions encompassing the migration of cells (van Helvert et al., 2018). Cell migration can be directed through the rigidity of the microenvironment by employing a process referred to as durotaxis (Lo et al., 2000). Durotaxis, migration to increasing stiffness, is involved in physiological and pathological mechanisms ranging from developmental processes (Flanagan et al., 2002; Sundararaghavan et al., 2009) to malignant progression of cancer (Butcher et al., 2009; Levental et al., 2009; Ulrich et al., 2009; Lachowski et al., 2017). Durotaxis necessitates cells to be able of firstly sensing a mechanical cue (mechanosensing), secondly directing their motility toward

the mechanical stimulus (referred to as mechanically directed motility due to anisotropic mechanics), and thirdly migrating in a directed manner to the stimulus. These processes are critical for durotaxis, however, the molecular mechanisms governing them are mainly elusive.

Cells can react to mechanical requirements of the local microenvironment by changing their actin cytoskeleton in a dynamic fashion at FAs (Choquet et al., 1997; Butcher et al., 2009). In accordance with such findings, mathematical and experimental simulations pointed to the fact that the acto-myosin cytoskeleton in FAs provides an alternating traction force necessary for mechanically guided motility, and the directional motility toward a mechanical impulse (Plotnikov et al., 2012; Wu et al., 2017). Nevertheless, the mechanisms that govern these FA cytoskeletal dynamics, and the special part that these mechanisms perform as mechanosensors, in mechanically directed motility, and in durotaxis, still need to be unraveled.

The Ena/VASP family member Ena/VASPlike (EVL) is a new type of regulator of actin polymerization in FAs, and EVL-facilitated actin polymerization has been identified to control cell matrix adhesion and mechanosensors. In addition, EVL plays a decisive part in managing the mechanically directed motility of normal and cancer cells, encourages durotactic invasion and, intriguingly, the inhibition of myosin contractility does not hamper this mechanism. Importantly, suppression of EVL expression interferes with the durotactic 3D invasion of cancer cells. In extension, the reaction to chemotactic (biochemical) stimulation is amplified in cells with decreased EVL expression, indicating that EVL uniquely facilitates the reaction to mechanical stimuli. A scheme is put forward in which EVL-driven FA actin polymerization strengthens FAs while mechanically paced, which thereby improves mechanosensors, mechanically oriented motility and durotaxis (Puleo et al., 2019).

The expression of MENA or VASP failed to re-establish the diminished adhesion phenotypes in EVL KD cells, and by using chimeric mutants it was determined that the EVH1 domain of EVL is singular amongst the Ena/VASP proteins and is particularly relevant for the proper operation of EVL in FAs. These observational findings reinforce the growing evidence that Ena/VASP proteins, formerly assumed to be exchangeable in functional terms (Laurent et al., 1999), fulfill a singular and distinctive function in the regularity of FAs. For this purpose, MENA, for instance, singularly attaches to the integrin α5 and acts as a modulator of adhesion signal transduction through an actin-independent machinery (Gupton et al., 2012), and VASP works with the rap-1 interacting molecule (RIAM) and zyxin to govern the fluctuations of the integrin β1 (Worth et al., 2010) and the intactness of actin stress fibers (Smith et al., 2010). Thus, whereas data establish EVL as the principal Ena/VASP protein in charge of actin polymerization-based cell–matrix adhesion, MENA and VASP contribute substantially, but inevitably, to FAs. Most significantly, prior investigations have demonstrated that MENA has a critical importance in fostering chemotaxis and haptotaxis (Goswami et al., 2009; Oudin et al., 2016a,b), which are both regimes of directed cell migration that rely on soluble or fixed ligand gradients. Consequently, these findings support the hypothesis that Ena/VASP proteins are involved in a variety of tasks in directed cell migration and invasion. The important thing is that these proteins could probably be instrumental in incorporating biochemical and mechanical cues from the cell microenvironment to manage migration in physiological and pathological frameworks.

THIRD DIRECTION (CELL MECHANICS-BASED APPROACH): CELL MECHANICS ARE ALTERED TO REGULATE CELL MIGRATION AND INVASION

Dissimilar to intracellular proteins, which are persistently replaced (Jennissen, 1995), extracellular matrix proteins are extraordinary long-lived proteins (Shapiro et al., 1991; Sivan et al., 2006). Therefore, it is very likely that the cell mechanical properties will be altered to enable the migration and invasion of the cells. In concrete terms, the mechanical performance of animal cells is governed by a matrix of stiff protein filaments referred to as the cytoskeleton. The cytoskeleton is a noteworthy piece of material that is kept out of balance by a multitude of molecular mechanisms involving chemical energy (Mackintosh and Schmidt, 2010). The molecular motors that harness the energy generated during ATP hydrolysis to travel alongside actin filaments and microtubules constitute an integral part of this process (Howard, 2001). A strong evidence exists that the myosin II motors interacting with the actin filaments can actively enhance cell stiffness by producing a contractile prestress (Wang et al., 2001; Fernandez et al., 2006; Gallet et al., 2009; Kollmannsberger et al., 2011; Crow et al., 2012). Measurements with pure actin networks have demonstrated that these meshes become severely stiffened when either an external or an internal stress is imposed (Mizuno et al., 2007; Koenderink et al., 2009). Cells can leverage this non-linear stress answer to rapidly adjust their stiffness in the wake of extracellular environment stiffness alterations (Solon et al., 2007; Mitrossilis et al., 2010).

As fibrin gels stiffen strongly when probed by an external load, it can be proposed that active cell contraction enhances the elastic modulus of fibrin gels (Storm et al., 2005; Brown et al., 2009; Piechocka et al., 2010). Therefore, the linear elastic modulus, G_0, of fibrinogen solutions including or excluding cells during its polymerization has been determined through macroscopic shear rheology. When cells are absent, G_0 immediately raises and becomes a plateau after roughly 3 h. This increase reflects the rapid fibrin polymerization to a space-filling elastic scaffolding to be followed by a more retarded process of covalent crosslinking by FXIIIa (Standeven et al., 2007; Münster et al., 2013). In the presence of cells, an immediate elevation of G_0 occurs, however, 4 h are required to obtain a constant G_0 value. In specific, the rise of G_0 has been revealed to be biphasic, with a bending around 2 h. The first phase of scaffolding stiffening probably resembles the same scaffolding formation process that arises without cells. The second phase of scaffolding stiffening roughly concurs with the beginning of cell spreading (Jansen et al., 2013). Finally, the entire network is shifted toward a stress-stiffened regime.

In the majority of studies, the term cell mechanics has been employed to explore the effect of mechanical alterations inside cells on their microenvironment and even on the cellular functions, such as cell migration and invasion (**Figure 10**). In the following, the parts of the distinct cellular compartments, such as nucleus and other major organelles, or major cellular structures, such as actin filaments and myosin filaments, are briefly highlighted.

Cytoskeletal Mechanics

A major contributor of cytoskeletal mechanics are actin filaments. The actin cytoskeleton is composed of semi-flexible actin filaments, myosin motors, and cross-linking proteins. *De novo* actin polymerization seems to be crucial for the generation of actin fibers in migrating cells (Hotulainen and Lappalainen, 2006), whereas accumulation of existing actin filament fragments is most probable in stationary cells in a steady-state surrounding (Tojkander et al., 2012).

During the adaptation procedure, the actin cytoskeleton reshapes itself to better withstand the external stress (Salbreux et al., 2012; Blanchoin et al., 2014; Mueller et al., 2017). In this way, actomyosin networks cross-linked by α-actinin and other cross-linking proteins are capable of adjusting to external forces through rapid mechanical reactions, in which stress relaxation appears on the time axis of seconds (Mizuno et al., 2007; Kasza et al., 2010; Schmoller et al., 2010; Dasanayake et al., 2011). However, cytoskeletal responses such as the (de)polymerization of actin or the activation of myosin II, where chemical energy is progressively transferred into mechanical force, results in delayed transformation of the actomyosin scaffolds on a time axis of minutes (Besser and Schwarz, 2007,; Ni and Papoian, 2019). As a consequence of the myosin-dominant mechanochemical dynamism, actomyosin networks are prone to contraction (Levayer and Lecuit, 2012; Floyd et al., 2019).

Apart from actin filament polymerization based protrusive forces, it has been hypothesized that the suppression of myosin contractility has an impact on the directionality of cell movement (Puleo et al., 2019). There is an upregulation of genes/proteins such as Ubiquitin domain−containing protein 1 (UBTD 1) that interact with E2 enzymes of the ubiquitin–proteasome system due to environmental cues, such as stiff matrices (Torrino et al., 2019). Rather unexpected is the fact that suppression of myosin activity had no impact on mechanically guided directed motility. Myosin contractility is involved in single-cell (Raab et al., 2012) and collective cell durotaxis (Sunyer et al., 2016) and commonly in cell migration (Vallenius, 2013). Nevertheless, no clear role of myosin in the process of perceiving directed mechanical stimuli has been documented. Even though it influences long-distance migration, the perception of directional impulses can be managed by various molecular processes (Mouneimne et al., 2004, 2006).

Significantly, the repression of myosin contractility disturbed the contraction of the back of the cell when motility was mechanically aligned, which is in agreement with previous findings (Sunyer et al., 2016). Consequently, myosin may be superfluous for targeting the cells to a mechanical stimulus (mechanically directed motility), but it is nevertheless essential for long-distance migration toward enhanced stiffness (durotaxis). Due to this complexity, future work is required to completely characterize the specific function of myosin in each of these distinct mechanically governed processes. Moreover, it has turned out that microtubules and intermediate filaments account

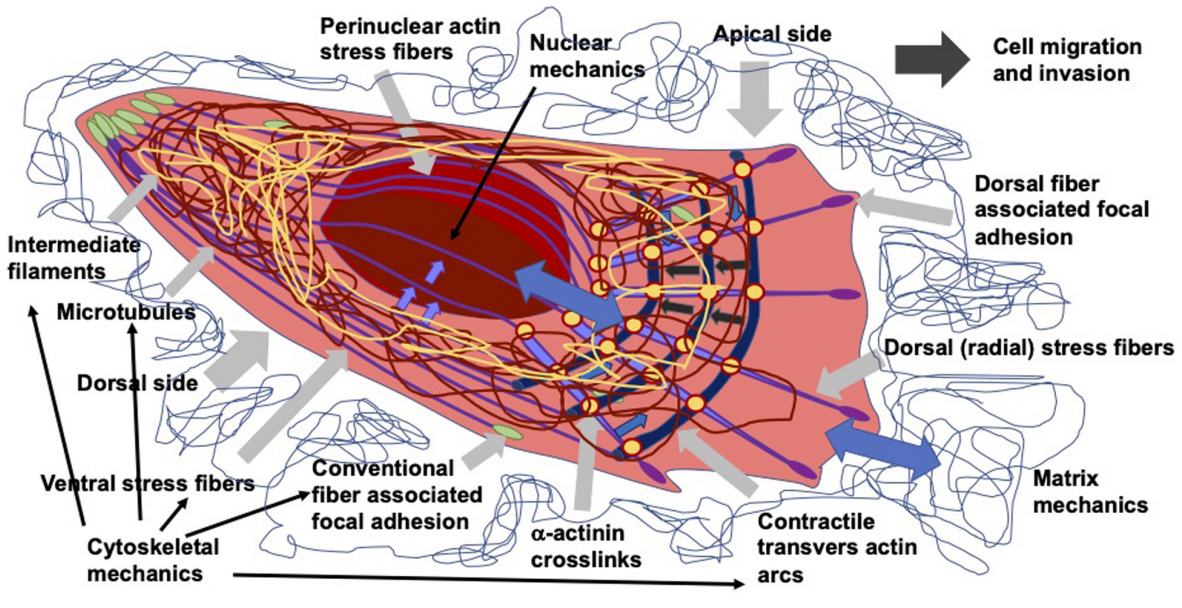

FIGURE 10 | Interaction between the cell's cytoskeletal mechanics, nuclear mechanics and the matrix mechanics impacts cell migration and invasion through environmental confinements.

for cell mechanics in a similar manner as actin filaments, which needs also to be taken into account.

Nuclear and Other Organelle Mechanics

Since the nucleus is the largest and stiffest organelle within a cell (2- to 10-fold stiffer as the neighboring cytoplasm), it represents a major obstacle for the migration and invasion of cells through narrow subcellular-sized constrictions (Lammerding, 2011; Liu et al., 2014; Mierke, 2017; Krause et al., 2019). The positioning and transport of the nucleus is performed by the coordinated actions of protrusion of the leading edge, integrin adhesion to the ambient environment, contractile actin cytoskeleton fibers, microtubules and the linker of the cytoskeleton and nucleoskeleton (LINC) complex that physically couples the chromatin to the cytoskeleton. This leads to a fluctuating force accumulation at the front and a contraction of the back while removing the rear integrin from the extracellular matrix, thereby displacing the nucleus to the front. Accordingly, during cell migration, alternating pulling and pushing cycles operate on the cell nucleus, resulting in what is known as the multi-stage translocation cycle of the cell nucleus (Friedl et al., 2011; Wolf et al., 2013; Wu et al., 2014; Thomas et al., 2015; Jayo et al., 2016; McGregor et al., 2016).

The steps comprise firstly the exertion of pressure on the nuclear membrane in the direction of migration due to the external constriction, secondly the incipient deformation of the nucleus due to the formation of a local incident retarding the migration, thirdly the sliding of the compressed and deformed nucleus through the pore and fourthly the backward release, combined with a fast forward pushing and rounding (recoil) of the nucleus (Friedl et al., 2011). Hence, the migration and invasion are retarded in the second step, which is consistent with the physical barrier role of the nucleus and seems to be a storage phase of deformation energy that is released as propulsive energy during the fourth phase enabling elevated movement.

Subsequently, the nucleus is rate-limiting for the migration of cells through subcellular pores or 3D extracellular matrix scaffolds (Jia et al., 2005; Wolf et al., 2007; Beadle et al., 2008; Friedl et al., 2011). The shape and the size of the nuclei can be quite diverse due to the specific cell type and distinct stimulation or treatment of cells. The entire stiffness of the nucleus of intact cells relies on several structural determinants, encompassing A-type lamins being a component of the nuclear lamin network underneath nuclear membrane and the organization of chromatin (Pajerowski et al., 2007; Swift et al., 2013; Stephens et al., 2017).

The chromatin packing state changes continuously depending on transcriptional requirements, the level of DNA repair and the specific cell cycle phase. Any of these events bring about modifications in the DNA organization, with temporary and reversible transformations from dense heterochromatin to more open euchromatin due to histone acetylation or demethylation (Sarma and Reinberg, 2005; Hizume et al., 2010; Unnikrishnan et al., 2010) that consequently cause chromatin decondensation, nuclear softening and ultimately its enlargement (Toth et al., 2004; Chalut et al., 2012).

Despite of this, the majority of cells exhibit in 3D substrates rather egg-shaped or spherical shaped nuclei with a diameter between 5 and 15 μm (Jaalouk and Lammerding, 2009). Under extracellular matrix confinement close to the nuclear diameter, or in the presence of cell-derived proteolytic tissue degradation activity generating a low resistance migratory path that resembles close to the largest cell diameter, the migration and invasion is not hindered (Wolf et al., 2013). In contrary, in an ambient constriction by an extracellular matrix, the cell nucleus has to deform and adjust to the matrix confinements, while simultaneously constituting a mechanical impediment that gradually retards the migration and invasion (Fu et al., 2012; Wolf et al., 2013; McGregor et al., 2016; Thiam et al., 2016).

The nuclear mechanics have been shown to be regulated by cytoskeletal components, such as actin filaments (Fischer et al., 2020). Beyond the nucleus, the mechanical properties of other organelles, such as mitochondria, Golgi apparatus or endoplasmic reticulum can impact the overall mechano-phenotype and thereby impact the behavior of cells, such as cell migration and invasion.

FUTURE DIRECTION OF CELL MECHANICS RESEARCH FACILITATING MOTILITY

Combined approaches of the three different directions seem to be promising to gain new insights into the mechanical processes and how matrix mechanics, cell mechanics and nuclear and other organelle mechanics are interrelated. There is generally a bidirectional interaction between cells and the surrounding extracellular matrix with a special focus on the mechanical phenotypes of cells and matrices. The ultimate goal seems to be still on tunable mechanical cues applied to 3D engineered matrices with varied biochemical and embedded cell compositions. Another focus of future research will lie on the co-culture approaches, where the surrounding cells, such as cancer associated fibroblasts or macrophages and cancer associated endothelial cells can foster or impair the migration and invasion of cancer cells by possibly affecting mechanical phenotype of cancer cells, including the cytoskeletal as well as the nuclear and other organelle phenotype, or the mechano-phenotype of extracellular matrices.

AUTHOR CONTRIBUTIONS

CTM wrote the manuscript and prepared all the figures.

FUNDING

This work was supported by the DFG (MI1211/18-1 and INST268/357-1 FUGG), EFRE-SAB infrastructure (No. 100299919). and SMWK TG70 No. 22110853. The author acknowledges support from the German Research Foundation (DFG) and Universität Leipzig within the program of Open Access Publishing.

REFERENCES

Acerbi, I., Cassereau, L., Dean, I., Shi, Q., Au, A., Park, C., et al. (2015). Human breast cancer invasion and aggression correlates with ECM stiffening and immune cell infiltration. *Integr. Biol.* 7, 1120–1134. doi: 10.1039/c5ib00040h

Ahmadzadeh, H., Webster, M. R., Beher, R., Valencia, A. M. J., Wirtz, D., Weeraratna, A. T., et al. (2017). Modeling the two-way feedback between contractility and matrix realignment reveals a nonlinear mode of cancer cell invasion. *PNAS* 114, E1617–E1626.

Ahrem, H., Pretzel, D., Endres, M., Conrad, D., Courseau, J., Müller, H., et al. (2014). Laser-structured bacterial nanocellulose hydrogels support ingrowth and differentiation of chondrocytes and show potential as cartilage implants. *Acta Biomater.* 10, 1341–1353. doi: 10.1016/j.actbio.2013.12.004

Akhtar, R., Sherratt, M. J., Cruickshank, K., and Derby, B. (2011). Characterizing the elastic properties of tissues. *Mater. Today* 14, 96–105. doi: 10.1016/s1369-7021(11)70059-1

Albiges-Rizo, C., Destaing, O., Fourcade, B., Planus, E., and Block, M. R. (2009). Actin machinery and mechanosensitivity in invadopodia, podosomes and focal adhesions. *J. Cell Sci.* 122, 3037–3049. doi: 10.1242/jcs.052704

Alexander, N. R., Branch, K. M., Parekh, A., Clark, E. S., Iwueke, I. C., Guelcher, S. A., et al. (2008). Extracellular matrix rigidity promotes invadopodia activity. *Curr. Biol.* 18, 1295–1299. doi: 10.1016/j.cub.2008.07.090

Alibert, C., Goud, B., and Manneville, J. B. (2017). Are cancer cells really softer than normal cells? *Bio Cell* 109, 167–189. doi: 10.1111/boc.201600078

Anguiano, M., Morales, X., Castilla, C., Pena, A. R., Ederra, C., Martínez, M., et al. (2020). The use of mixed collagen-matrigel matrices of increasing complexity recapitulates the biphasic role of cell adhesion in cancer cell migration: ECM sensing, remodeling and forces at the leading edge of cancer invasion. *PLoS One* 15:e0220019. doi: 10.1371/journal.pone.0220019

Arber, S., Barbayannis, F. A., Hanser, H., Schneider, C., Stanyon, C. A., Bernard, O., et al. (1998). Regulation of actin dynamics through phosphorylation of cofilin by LIM-kinase. *Nature* 393, 805–809. doi: 10.1038/31729

Arjonen, A., Kaukonen, R., Mattila, E., Rouhi, P., Hognas, G., Sihtoet, H., et al. (2014). Mutant p53-associated myosin-X upregulation promotes breast cancer invasion and metastasis. *J. Clin. Invest.* 124, 1069–1082. doi: 10.1172/jci67280

Artym, V. V., Matsumoto, K., Mueller, S. C., and Yamada, K. M. (2011). Dynamic membrane remodeling at invadopodia differentiates invadopodia from podosomes. *Eur. J. Cell Biol.* 90, 172–180. doi: 10.1016/j.ejcb.2010.06.006

Artym, V. V., Zhang, Y., Seillier-Moiseiwitsch, F., Yamada, K. M., and Mueller, S. C. (2006). Dynamic interactions of cortactin and membrane type 1 matrix metalloproteinase at invadopodia: defining the stages of invadopodia formation and function. *Cancer Res.* 66, 3034–3043. doi: 10.1158/0008-5472.can-05-2177

Assent, D., Bourgot, I., Hennuy, B., Geurts, P., Noel, A., Foidart, J. M., et al. (2015). A membrane-type-1 matrix metalloproteinase (MT1-MMP)-discoidin domain receptor 1 axis regulates collagen-induced apoptosis in breast cancer cells. *PLoS One* 10:e0116006. doi: 10.1371/journal.pone.0116006

Austen, K., Ringer, P., Mehlich, A., Chrostek-Grashoff, A., Kluger, C., Klingner, C., et al. (2015). Extracellular rigidity sensing by talin isoform-specific mechanical linkages. *Nat. Cell Biol.* 17, 1597–1606. doi: 10.1038/ncb3268

Barczyk, M., Carracedo, S., and Gullberg, D. (2009). Integrins. *Cell Tissue Res.* 339, 269–280.

Barney, L. E., Hall, C. L., Schwartz, A. D., Parks, A. N., Sparages, C., Platt, M. O., et al. (2020). Tumor cell-organized fibronectin maintenance of a dormant breast cancer population. *Sci. Adv.* 6:eaaz4157. doi: 10.1126/sciadv.aaz4157

Bayer, S. V., Grither, W. R., Brenot, A., Hwang, P. Y., Barcus, C. E., Ernst, M., et al. (2019). DDR2 controls breast tumor stiffness and metastasis by regulating integrin mediated mechanotransduction in CAFs. *eLife* 8:e45508.

Beadle, C., Assanah, M. C., Monzo, P., Vallee, R., Rosenfeld, S. S., and Canoll, P. (2008). The role of myosin II in glioma invasion of the brain. *Mol. Biol. Cell* 19, 3357–3368. doi: 10.1091/mbc.e08-03-0319

Besser, A., and Schwarz, U. S. (2007). Coupling biochemistry and mechanics in cell adhesion: a model for inhomogeneous stress fiber contraction. *New J. Phys.* 9:425. doi: 10.1088/1367-2630/9/11/425

Birk, J. W., Tadros, M., Moezardalan, K., Nadyarnykh, O., Forouhar, F., Anderson, J., et al. (2014). Second harmonic generation imaging distinguishes both high-grade dysplasia and cancer from normal colonic mucosa. *Dig. Dis. Sci.* 59, 1529–1534. doi: 10.1007/s10620-014-3121-7

Blanchoin, L., Boujemaa-Paterski, R., Sykes, C., and Plastino, J. (2014). Actin dynamics, architecture, and mechanics in cell motility. *Physiol. Rev.* 94, 235–263. doi: 10.1152/physrev.00018.2013

Blanchoin, L., Pollard, T. D., and Mullins, R. D. (2000). Interactions of ADF/cofilin, Arp2/3 complex, capping protein and profilin in remodeling of branched actin filament networks. *Curr. Biol.* 10, 1273–1282. doi: 10.1016/s0960-9822(00)00749-1

Boateng, L. R., Cortesio, C. L., and Huttenlocher, A. (2012). Src-mediated phosphorylation of mammalian Abp1 (DBNL) regulates podosome rosette formation in transformed fibroblasts. *J. Cell Sci.* 125, 1329–1341. doi: 10.1242/jcs.096529

Bott, K., Upton, Z., Schrobback, K., Ehrbar, M., Hubbell, J. A., Lutolf, M. P., et al. (2010). The effect of matrix characteristics on fibroblast proliferation in 3D gels. *Biomaterials* 31, 8454–8464. doi: 10.1016/j.biomaterials.2010.07.046

Boudjadi, S., Carrier, J. C., and Beaulieu, J.-F. (2013). Integrin a1 subunit is up-regulated in colorectal cancer. *Biomark. Res.* 9:96.

Boyd, N. F., Dite, G. S., Stone, J., Gunasekara, A., English, D. R., McCredie, M. R. E., et al. (2002). Heritability of mammographic density, a risk factor for breast cancer. *N. Engl. J. Med.* 347, 886–894.

Boyd, N. F., Lockwood, G. A., Byng, J. W., Tritchler, D. L., and Yaffe, M. L. (1998). Mammographic densities and breast cancer risk. *Cancer Epidemiol. Biomarkers Prev.* 7, 1133–1144.

Boyd, N. F., Martin, L. J., Stone, J., Greenberg, C., Minkin, S., and Yaffe, M. J. (2001). Mammographic densities as a marker of human breast cancer risk and their use in chemo-prevention. *Curr. Oncol. Rep.* 3, 314–321. doi: 10.1007/s11912-001-0083-7

Bracaglia, L. G., Smith, B. T., Watson, E., Arumugasaamy, N., Mikos, A. G., and Fisher, J. P. (2017). 3D printing for the design and fabrication of polymer-based gradient scaffolds. *Acta Biomater.* 56, 3–13. doi: 10.1016/j.actbio.2017.03.030

Brady, M. A., Talvard, L., Vella, A., and Ethier, C. R. (2017). Bio-inspired design of a magnetically active trilayered scaffold for cartilage tissue engineering. *J. Tissue Eng. Regen. Med.* 11, 1298–1302. doi: 10.1002/term.2106

Branch, K. M., Hoshino, D., and Weaver, A. M. (2012). Adhesion rings surround invadopodia and promote maturation. *Biol. Open* 1, 711–722. doi: 10.1242/bio.20121867

Brown, A. E., Litvinov, R. I., Discher, D. E., Purohit, P. K., and Weisel, J. W. (2009). Multiscale mechanics of fibrin polymer: gel stretching with protein unfolding and loss of water. *Science* 325, 741–744. doi: 10.1126/science.1172484

Burke, K., Smid, M., Dawes, R. P., Timmermans, M. A., Salzman, P., van Deurzen, C. H. M., et al. (2015). Using second harmonic generation to predict patient outcome in solid tumors. *BMC Cancer* 15:929. doi: 10.1186/s12885-015-1911-8

Burns, S., and Thrasher, A. J. (2004). Dendritic cells: the bare bones of immunity. *Curr. Biol.* 14, R965–R967.

Buschman, M. D., Bromann, P. A., Cejudo-Martin, P., Wen, F., Pass, I., and Courtneidge, S. A. (2009). The novel adaptor protein Tks4 (SH3PXD2B) is required for functional podosome formation. *Mol. Biol. Cell* 20, 1302–1311. doi: 10.1091/mbc.e08-09-0949

Butcher, D. T., Alliston, T., and Weaver, V. M. (2009). A tense situation: forcing tumour progression. *Nat. Rev. Cancer* 9, 108–122. doi: 10.1038/nrc2544

Buwalda, S. J., Vermonden, T., and Hennink, W. E. (2017). Hydrogels for therapeutic delivery: current developments and future directions. *Biomacromolecules* 18, 316–330. doi: 10.1021/acs.biomac.6b01604

Caló, E., and Khutoryanskiy, V. V. (2015). Biomedical applications of hydrogels: a review of patents and commercial products. *Eur. Polym. J.* 65, 252–267. doi: 10.1016/j.eurpolymj.2014.11.024

Calvo, F., Ege, N., Grande-Garcia, A., Hooper, S., Jenkins, R. P., Chaudhry, S. I., et al. (2013). Mechanotransduction and YAP-dependent matrix remodelling is required for the generation and maintenance of cancer-associated fibroblasts. *Nat. Cell Biol.* 15, 637–646. doi: 10.1038/ncb2756

Castella, L. F., Buscemi, L., Godbout, C., Meister, J.-J., and Hinz, B. (2010). A new lock-step mechanism of matrix remodelling based on subcellular contractile events. *J. Cell Sci.* 123, 1751–1760. doi: 10.1242/jcs.066795

Caswell, P. T., and Zech, T. (2018). Actin-based cell protrusion in a 3D matrix. *Trends Cell Biol.* 28, 823–834. doi: 10.1016/j.tcb.2018.06.003

Chalut, K. J., Höpfler, M., Lautenschläger, F., Boyde, L., Chan, C. J., Ekpenyong, A., et al. (2012). Chromatin decondensation and nuclear softening accompany Nanog downregulation in embryonic stem cells. *Biophys. J.* 103, 2060–2070. doi: 10.1016/j.bpj.2012.10.015

Chambers, A. F., Groom, A. C., and MacDonald, I. C. (2002). Dissemination and growth of cancer cells in metastatic sites. *Nat. Rev. Cancer* 2, 563–572. doi: 10.1038/nrc865

Charest, J. L., Garcia, A. J., and King, W. P. (2007). Myoblast alignment and differentiation on cell culture substrates with microscale topography and model chemistries. *Biomaterials* 28, 2202–2210. doi: 10.1016/j.biomaterials.2007.01.020

Charras, G., and Sahai, E. (2014). Physical influences of the extracellular environment on cell migration. *Nat. Rev. Mol. Cell Biol.* 15, 813–824. doi: 10.1038/nrm3897

Cheema, U., and Brown, R. A. (2013). Rapid fabrication of living tissue models by collagen plastic compression: understanding three-dimensional cell matrix repair in vitro. *Adv. Wound Care* 2, 176–184. doi: 10.1089/wound.2012.0392

Chen, C. T., Yamaguchi, H., Lee, H. J. Y., Lee, H.-H., Xia, W., Yu, W.-H., et al. (2011). Dual targeting of tumor angiogenesis and chemotherapy by endostatincytosine deaminase-uracil phosphoribosyl transferase. *Mol. Cancer Ther.* 10, 1327–1336. doi: 10.1158/1535-7163.mct-10-1117

Chen, Q. K., Lee, K., Radisky, D. C., and Nelson, C. M. (2013). Extracellular matrix proteins regulate epithelial-mesenchymal transition in mammary epithelial cells. *Differentiation* 86, 126–132. doi: 10.1016/j.diff.2013.03.003

Chen, T., You, Y., Jiang, H., and Wang, Z. Z. (2017). Epithelial-mesenchymal transition (EMT): a biological process in the development, stem cell differentiation, and tumorigenesis. *J. Cell Physiol.* 232, 3261–3272. doi: 10.1002/jcp.25797

Chen, W. T. (1989). Proteolytic activity of specialized surface protrusions formed at rosette contact sites of transformed cells. *J. Exp. Zool.* 251, 167–185. doi: 10.1002/jez.1402510206

Choi, J. S., Piao, Y., and Seo, T. S. (2014). Circumferential alignment of vascular smooth muscle cells in a circular microfluidic channel. *Biomaterials* 35, 63–70. doi: 10.1016/j.biomaterials.2013.09.106

Choquet, D., Felsenfeld, D. P., and Sheetz, M. P. (1997). Extracellular matrix rigidity causes strengthening of integrin-cytoskeleton linkages. *Cell* 88, 39–48. doi: 10.1016/s0092-8674(00)81856-5

Clark, A. G., and Vignjevic, D. M. (2015). Modes of cancer cell invasion and the role of the microenvironment. *Curr. Opin. Cell Biol.* 36, 13–22. doi: 10.1016/j.ceb.2015.06.004

Clark, E. S., and Weaver, A. M. (2008). A new role for cortactin in invadopodia: regulation of protease secretion. *Eur. J. Cell Biol.* 87, 581–590. doi: 10.1016/j.ejcb.2008.01.008

Clark, E. S., Whigham, A. S., Yarbrough, W. G., and Weaver, A. M. (2007). Cortactin is an essential regulator of matrix metalloproteinase secretion and extracellular matrix degradation in invadopodia. *Cancer Res.* 67, 4227–4235. doi: 10.1158/0008-5472.can-06-3928

Cordenonsi, M., Zanconato, F., Azzolin, L., Forcato, M., Rosato, A., Frasson, C., et al. (2011). The Hippo transducer TAZ confers cancer stem cell-related traits on breast cancer cells. *Cell* 147, 759–772. doi: 10.1016/j.cell.2011.09.048

Courtneidge, S. A. (2012). Cell migration and invasion in human disease: the Tks adaptor proteins. *Biochem. Soc. Trans.* 40, 129–132. doi: 10.1042/bst20110685

Coussens, L. M., Fingleton, B., and Matrisian, L. M. (2002). Matrix metalloproteinase inhibitors and cancer: trials and tribulations. *Science* 295, 2387–2392. doi: 10.1126/science.1067100

Crow, A., Webster, K. D., Hohlfeld, E., Ng, W. P., Geissler, P., and Fletcher, D. A. (2012). Contractile equilibration of single cells to step changes in extracellular stiffness. *Biophys. J.* 102, 443–451. doi: 10.1016/j.bpj.2011.11.4020

Cruz-Munoz, W., Sanchez, O. H., Di Grappa, M., English, J. L., Hill, R. P., and Khokha, R. (2006). Enhanced metastatic dissemination to multiple organs by melanoma and lymphoma cells in timp-3–/– mice. *Oncogene* 25, 6489–6496. doi: 10.1038/sj.onc.1209663

Cukierman, E., Pankov, R., Stevens, D. R., and Yamada, K. M. (2001). Taking cell-matrix adhesions to the third dimension. *Science* 294, 1708–1712. doi: 10.1126/science.1064829

Dang, D., Bamburg, J. R., and Ramos, D. M. (2006). Alphavbeta3 integrin and cofilin modulate K1735 melanoma cell invasion. *Exp. Cell Res.* 312, 468–477. doi: 10.1016/j.yexcr.2005.11.011

Dasanayake, N. L., Michalski, P. J., and Carlsson, A. E. (2011). General mechanism of actomyosin contractility. *Phys. Rev. Lett.* 107:118101.

De Wever, O., Demetter, P., Mareel, M., and Bracke, M. (2008). Stromal myofibroblasts are drivers of invasive cancer growth. *Int. J. Cancer* 123, 2229–2238. doi: 10.1002/ijc.23925

del Pozo, M. A., Price, L. S., Alderson, N. B., Ren, X. D., and Schwartz, M. A. (2000). Adhesion to the extracellular matrix regulates the coupling of the small GTPase Rac to its effector PAK. *EMBO J.* 19, 2008–2014. doi: 10.1093/emboj/19.9.2008

Destaing, O., Block, M. R., Planus, E., and Albiges-Rizo, C. (2011). Invadosome regulation by adhesion signaling. *Curr. Opin. Cell Biol.* 23, 597–606. doi: 10.1016/j.ceb.2011.04.002

Destaing, O., Petropoulos, C., and Albiges-Rizo, C. (2014). Coupling between acto-adhesive machinery and ECM degradation in invadosomes. *Cell Adh. Migr.* 8, 256–262. doi: 10.4161/cam.28558

Destaing, O., Planus, E., Bouvard, D., Oddou, C., Badowski, C., Bossy, V., et al. (2010). β1A integrin is a master regulator of invadosome organization and function. *Mol. Biol. Cell* 21, 4108–4119. doi: 10.1091/mbc.e10-07-0580

Echarri, A., and Del Pozo, M. A. (2015). Caveolae – mechanosensitive membrane invaginations linked to actin filaments. *J. Cell Sci.* 128, 2747–2758. doi: 10.1242/jcs.153940

Elkabets, M., Gifford, A. M., Scheel, C., Nilsson, B., Reinhardt, F., Bray, M.-A., et al. (2011). Human tumors instigate granulin-expressing hematopoietic cells that promote malignancy by activating stromal fibroblasts in mice. *J. Clin. Invest.* 121, 784–799. doi: 10.1172/jci43757

Fan, C., and Wang, D. A. (2017). Macroporous hydrogel scaffolds for three-dimensional cell culture and tissue engineering. *Tissue Eng. Part B Rev.* 23, 451–461. doi: 10.1089/ten.teb.2016.0465

Feinberg, T. Y., Zheng, H., Liu, R., Wicha, M. S., Yu, S. M., and Weiss, S. J. (2018). Divergent matrix-remodeling strategies distinguish developmental from neoplastic mammary epithelial cell invasion programs. *Dev. Cell* 47, 145–160. doi: 10.1016/j.devcel.2018.08.025

Fernandez, P., Pullarkat, P. A., and Ott, A. (2006). A master relation defines the nonlinear viscoelasticity of single fibroblasts. *Biophys. J.* 90, 3796–3805. doi: 10.1529/biophysj.105.072215

Fischer, T., Hayn, A., and Mierke, C. T. (2020). Effect of nuclear stiffness on cell mechanics and migration of human breast cancer cells. *Front. Cell Dev. Biol.* 8:393. doi: 10.3389/fcell.2020.00393

Fischer, T., Wilharm, N., Hayn, A., and Mierke, C. T. (2017). Matrix and cellular mechanical properties are the driving factors for facilitating human cancer cell motility into 3D engineered matrices. *Conver. Sci. Phys. Oncol.* 3:044003. doi: 10.1088/2057-1739/aa8bbb

Fisher, K. E., Pop, A., Koh, W., Anthis, N. J., Saunders, W. B., and Davis, G. E. (2006). Tumor cell invasion of collagen matrices requires coordinate lipid agonist-induced G protein and membrane-type matrix metalloproteinase-1-dependent signaling. *Mol. Cancer* 5:69.

Fisher, K. E., Sacharidou, A., Stratman, A. N., Mayo, A. M., Fisher, S. B., Mahan, R. D., et al. (2009). MT1-MMP- and Cdc42-dependent signaling co-regulate cell invasion and tunnel formation in 3D collagen matrices. *J. Cell Sci.* 122(Pt 24), 4558–4569. doi: 10.1242/jcs.050724

Flanagan, L. A., Ju, Y.-E., Marg, B., Osterfield, M., and Janmey, P. A. (2002). Neurite branching on deformable substrates. *Neuroreport* 13, 2411–2415. doi: 10.1097/00001756-200212200-00007

Floyd, C., Papoian, G. A., and Jarzynski, C. (2019). Quantifying dissipation in actomyosin networks. *Interface Focus* 9:20180078. doi: 10.1098/rsfs.2018.0078

Fraley, S. I., Wu, P.-H., He, L., Feng, Y., Krisnamurthy, R., Longmore, G. D., et al. (2015). Three-dimensional matrix fiber alignment modulates cell migration and MT1-MMP utility by spatially and temporally directing protrusions. *Sci. Rep.* 5:14580.

Friedl, P., and Alexander, S. (2011). Cancer invasion and the micro- environment: plasticity and reciprocity. *Cell* 147, 992–1009. doi: 10.1016/j.cell.2011.11.016

Friedl, P., Borgmann, S., and Brocker, E. B. (2001). Amoeboid leukocyte crawling through extracellular matrix: lessons from the dictyostelium paradigm of cell movement. *J. Leukoc Biol.* 70, 491–509.

Friedl, P., Wolf, K., and Lammerding, J. (2011). Nuclear mechanics during cell migration. *Curr. Opin. Cell Biol.* 23, 55–64. doi: 10.1016/j.ceb.2010.10.015

Fu, Y., Chin, L. K., Bourouina, T., Liu, A. Q., and VanDongen, A. M. (2012). Nuclear deformation during breast cancer cell transmigration. *Lab Chip* 12, 3774–3778. doi: 10.1039/c2lc40477j

Fuyuhiro, Y., Yashiro, M., Noda, S., Matsuoka, J., Hasegawa, T., Kato, Y., et al. (2012). Cancer-associated orthotopic myofibroblasts stimulates the motility of

gastric carcinoma cells. *Cancer Sci.* 103, 797–805. doi: 10.1111/j.1349-7006.2012.02209.x

Gaidano, G., Bergui, L., Schena, M., Gaboli, M., Cremona, O., Marchisio, P. C., et al. (1990). Integrin distribution and cytoskeleton organization in normal and malignant monocytes. *Leukemia* 4, 682–687.

Galbiati, F., Razani, B., and Lisanti, M. P. (2001). Caveolae and caveolin-3 in muscular dystrophy. *Trends Mol. Med.* 7, 435–441. doi: 10.1016/s1471-4914(01)02105-0

Gallet, F., Arcizet, D., Bohec, P., and Richert, A. (2009). Power spectrum of out-ofequilibrium forces in living cells: amplitude and frequency dependence. *Soft. Matter.* 5, 2947–2953. doi: 10.1039/b901311c

Garg, A., and Agarwal, A. K. (2008). Caveolin-1: a new locus for human lipodystrophy. *J. Clin. Endocrinol. Metab.* 93, 1183–1185. doi: 10.1210/jc.2008-0426

Gasparski, A. N., and Beningo, K. A. (2015). Mechanoreception at the cell membrane: More than the integrins. *Arch. Biochem. Biophys.* 586, 20–26. doi: 10.1016/j.abb.2015.07.017

Gasparski, A. N., Ozarkar, S., and Beningo, K. A. (2017). Transient mechanical strain promotes the maturation of invadopodia and enhances cancer cell invasion in vitro. *J. Cell Sci.* 130, 1965–1978. doi: 10.1242/jcs.199760

Gasparski, A. N., Wilson, J. T., Banerjee, A., and Beningo, K. A. (2019). The role of PAK1 in the maturation of invadopodia during transient mechanical stimulation. *Front. Cell Dev. Biol.* 7:269. doi: 10.3389/fcell.2019.00269

Genzer, J., and Bhat, R. R. (2008). Surface-bound soft matter gradients. *Langmuir* 24, 2294–2317. doi: 10.1021/la7033164

Goffin, J. M., Pittet, P., Csucs, G., Lussi, J. W., Meister, J.-J., and Hinz, B. (2006). Focal adhesion size controls tension-dependent recruitment of alpha-smooth muscle actin to stress fibers. *J. Cell Biol.* 172, 259–268. doi: 10.1083/jcb.200506179

Gonzalez, A. M., Bhattacharya, R., DeHart, G. W., and Jones, J. C. R. (2010). Transdominant regulation of integrin function: mechanisms of crosstalk. *Cell Signal.* 22, 578–583. doi: 10.1016/j.cellsig.2009.10.009

Goswami, S., Philippar, U., Sun, D., Patsialou, A., Avraham, J., Wang, W., et al. (2009). Identification of invasion specific splice variants of the cytoskeletal protein mena present in mammary tumor cells during invasion in vivo. *Clin. Exp. Metastasis* 26, 153–159. doi: 10.1007/s10585-008-9225-8

Greiner, A. M., Chen, H., Spatz, J. P., and Kemkemer, R. (2013). Cyclic tensile strain controls cell shape and directs actin stress fiber formation and focal adhesion alignment in spreading cells. *PLoS One* 8:e77328. doi: 10.1371/journal.pone.0077328

Guck, J., Schinkinger, S., Lincoln, B., Wottawah, F., Ebert, S., Romeyke, M., et al. (2005). Optical deformability as an inherent cell marker for testing malignant transformation and metastatic competence. *Biophys. J.* 88, 3689–3698. doi: 10.1529/biophysj.104.045476

Guo, Y. P., Martin, L. J., Hanna, W., Banerjee, D., Miller, N., Fishell, E., et al. (2001). Growth factors and stromal matrix proteins associated with mammographic densities. *Cancer Epidemiol. Biomarkers Prev.* 10, 243–248.

Gupta, V., Khan, Y., Berkland, C. J., Laurencin, C. T., and Detamore, M. S. (2017). Microsphere-based scaffolds in regenerative engineering. *Annu. Rev. Biomed. Eng.* 19, 135–161. doi: 10.1146/annurev-bioeng-071516-044712

Gupton, S. L., Riquelme, D., Hughes-Alford, S. K., Tadros, J., Rudina, S. S., Hynes, R. O., et al. (2012). Mena binds α5 integrin directly and modulates α5β1 function. *J. Cell Biol.* 198, 657–676. doi: 10.1083/jcb.201202079

Gurave, P. M., Singh, S., Yadav, A., Nandan, B., and Srivastava, R. K. (2020). Electrospinning of a near gel resin to produce cross-linked fibrous matrices. *Langmuir* 36, 2419–2426. doi: 10.1021/acs.langmuir.9b03870

Hai, C. M., Hahne, P., Harrington, E. O., and Gimona, M. (2002). Conventional protein kinase C mediates phorbol-dibutyrate-induced cytoskeletal remodeling in a7r5 smooth muscle cells. *Exp. Cell Res.* 280, 64–74. doi: 10.1006/excr.2002.5592

Hammer, A., and Diakonova, M. (2015). Tyrosyl phosphorylated serine-threonine kinase PAK1 is a novel regulator of prolactin-dependent breast cancer cell motility and invasion. *Adv. Exp. Med. Biol.* 846, 97–137. doi: 10.1007/978-3-319-12114-7_5

Hammer, A., Rider, L., Oladimeji, P., Cook, L., Li, Q., Mattingly, R. R., et al. (2013). Tyrosyl phosphorylated PAK1 regulates breast cancer cell motility in response to prolactin through filamin. *A. Mol. Endocrinol.* 27, 455–465. doi: 10.1210/me.2012-1291

Hanahan, D., and Weinberg, R. A. (2000). The hallmarks of cancer. *Cell* 100, 57–70.

Hayashi, K., and Iwata, M. (2015). Stiffness of cancer cells measured with an AFM indentation method. *J. Mech. Behav. Biomed. Mater.* 49, 105–111. doi: 10.1016/j.jmbbm.2015.04.030

He, X., Liao, W., Li, Y., Wang, Y., Chen, Q., Jin, J., et al. (2015). Upregulation of hyaluronan-mediated motility receptor in hepatocellular carcinoma predicts poor survival. *Oncol. Lett.* 10, 3639–3646. doi: 10.3892/ol.2015.3773

Heller, E., and Fuchs, E. (2015). Tissue patterning and cellular mechanics. *J. Cell Biol.* 211, 219–231. doi: 10.1083/jcb.201506106

Hesse, E., Freudenberg, U., Niemietz, T., Greth, C., Weisser, M., Hagmann, S., et al. (2018). Peptide-functionalized starPEG/heparin hydrogels direct mitogenicity, cell morphology and cartilage matrix distribution in vitro and in vivo. *J. Tissue Eng. Regen. Med.* 12, 229–239. doi: 10.1002/term.2404

Hesse, E., Freudenberg, U., Niemietz, T., Greth, C., Weisser, M., Renz, Y., et al. (2017). Peptide-functionalised cell instructive hydrogel system for cartilage tissue engineering. *Bone Joint J.* 99(Suppl. 1):82.

Hetmanski, J. H. R., Belly, H., Busnelli, I., Waring, T., Nair, R. V., Sokleva, V., et al. (2019). Membrane tension orchestrates rear retraction in matrix-directed cell migration. *Dev. Cell* 51, 460.e10–475.e10.

Hizume, K., Araki, S., Hata, K., Prieto, E., Kundu, T. K., Yoshikawa, K., et al. (2010). Nano-scale analyses of the chromatin decompaction induced by histone acetylation. *Arch. Histol. Cytol.* 73, 149–163. doi: 10.1679/aohc.73.149

Hocking, D. C., Sottile, J., and Langenbach, K. J. (2000). Stimulation of integrin-mediated cell contractility by fibronectin polymerization. *J. Biol. Chem.* 275, 10673–10682. doi: 10.1074/jbc.275.14.10673

Hojilla, C. V., Mohammed, F. F., and Khokha, R. (2003). Matrix metalloproteinases and their tissue inhibitors direct cell fate during cancer development. *Br. J. Cancer* 89, 1817–1821. doi: 10.1038/sj.bjc.6601327

Hotulainen, P., and Lappalainen, P. (2006). Stress fibers are generated by two distinct actin assembly mechanisms in motile cells. *J. Cell Biol.* 173, 383–394. doi: 10.1083/jcb.200511093

Howard, J. (2001). *Mechanics of Motor Proteins and the Cytoskeleton*. Sunderland MA: Sinauer.

Huang, D., Nakamura, Y., Ogata, A., and Kidoaki, S. (2020). Characterization of 3D matrix conditions for cancer cell migration with elasticity/porosity-independent tunable microfiber gels. *Polym. J.* 52, 333–344. doi: 10.1038/s41428-019-0283-3

Huang, F.-K., Han, S., Xing, B., Huang, J., Liu, B., Bordeleau, F., et al. (2015). Targeted inhibition of fascin function blocks tumour invasion and metastatic colonization. *Nat. Commun.* 6, 1–14.

Hudalla, G. H., and Murphy, W. L. (2015). *Mimicking the Extracellular Matrix: The Intersection of Matrix Biology and Biomaterials*. London: Royal Society of Chemistry.

Huijbers, I. J., Iravani, M., Popov, S., Robertson, D., Al-Sarraj, S., Jones, C., et al. (2010). A role for fibrillar collagen deposition and the collagen internalization receptor endo180 in glioma invasion. *PLoS One* 5:e9808. doi: 10.1371/journal.pone.0009808

Hunt, J. A., Chen, R., van Veen, T., and Bryan, N. (2014). Hydrogels for tissue engineering and regenerative medicine. *J. Mater. Chem. B* 2, 5319–5338.

Hwang, P. T. J., Murdock, K., Alexander, G. C., Salaam, A. D., Ng, J. I., Lim, D. J., et al. (2016). Poly(-caprolactone)/gelatin composite electrospun scaffolds with porous crater-like structures for tissue engineering. *J. Biomed. Mater. Res. A* 104, 1017–1029. doi: 10.1002/jbm.a.35614

Hynes, R. O. (1990). *Fibronectins*. New York, NY: Springer-Verlag.

Hynes, R. O., and Naba, A. (2012). Overview of the matrisome—An inventory of extracellular matrix constituents and functions. *Cold Spring Harb. Perspect. Biol.* 4:a004903. doi: 10.1101/cshperspect.a004903

Itoh, Y., and Nagase, H. (2002). Matrix metalloproteinases in cancer. *Essays Biochem.* 38, 21–36.

Jaalouk, D. E., and Lammerding, J. (2009). Mechanotransduction gone awry. *Nat. Rev. Mol. Cell Biol.* 10, 63–73. doi: 10.1038/nrm2597

Jacob, A., and Prekeris, R. (2015). The regulation of MMP targeting to invadopodia during cancer metastasis. *Front. Cell Dev. Biol.* 3:4. doi: 10.3389/fcell.2015.00004

Jacquemet, G., Green, D. M., Bridgewater, R. E., von Kriegsheim, A., Humphries, M. J., Norman, J. C., et al. (2013). RCP-driven alpha5beta1 recycling suppresses

Rac and promotes RhoA activity via the RacGAP1- IQGAP1 complex. *J. Cell Biol.* 202, 917–935. doi: 10.1083/jcb.201302041

Jansen, K. A., Bacabac, R. G., Piechocka, I. K., and Koenderink, G. H. (2013). cells actively stiffen fibrin networks by generating contractile stress. *Biophys. J.* 105, 2240–2251. doi: 10.1016/j.bpj.2013.10.008

Jayo, A., Malboubi, M., Antoku, S., Chang, W., Ortiz-Zapater, E., Groen, C., et al. (2016). Fascin regulates nuclear movement and deformation in migrating cells. *Dev. Cell* 38, 371–383. doi: 10.1016/j.devcel.2016.07.021

Jeitany, M., Leroy, C., Tosti, P., Lafitte, M., Le Guet, J., Simon, V., et al. (2018). Inhibition of DDR1-BCR signalling by nilotinib as a new therapeutic strategy for metastatic colorectal cancer. *EMBO Mol. Med.* 10:e7918.

Jennissen, H. P. (1995). Ubiquitin and the enigma of intracellular protein degradation. *Biochemistry* 231, 1–30. doi: 10.1111/j.1432-1033.1995.tb20665.x

Jerrell, R. J., and Parekh, A. (2014). Cellular traction stresses mediate extracellular matrix degradation by invadopodia. *Acta Biomater.* 10, 1886–1896. doi: 10.1016/j.actbio.2013.12.058

Jia, Z., Barbier, L., Stuart, H., Amraei, M., Pelech, S., Dennis, J. W., et al. (2005). Tumor cell pseudopodial protrusions. Localized signaling domains coordinating cytoskeleton remodeling, cell adhesion, glycolysis, RNA translocation, and protein translation. *J. Biol. Chem.* 280, 30564–30573. doi: 10.1074/jbc.m501754200

Jiang, T., Carbone, E. J., Lo, K. W. H., and Laurencin, C. T. (2015). Electrospinning of polymer nanofibers for tissue regeneration. *Prog. Polym. Sci.* 46, 1–24. doi: 10.1016/j.progpolymsci.2014.12.001

Jin, H., and Varner, J. (2004). Integrins: roles in cancer development and as treatment targets. *Br. J. Cancer* 90, 561–565. doi: 10.1038/sj.bjc.6601576

Jonietz, E. (2012). Mechanics: the forces of cancer. *Nature* 491, S56–S57.

Jun, I., Han, H.-S., Edwards, J. R., and Jeon, H. (2018). Electrospun fibrous scaffolds for tissue engineering: viewpoints on architecture and fabrication. *Int. J. Mol. Sci.* 19:745. doi: 10.3390/ijms19030745

Jurdic, P., Saltel, F., Chabadel, A., and Destaing, O. (2006). Podosome and sealing zone: specificity of the osteoclast model. *Eur. J. Cell Biol.* 85, 195–202. doi: 10.1016/j.ejcb.2005.09.008

Kai, D., Liow, S. S., and Loh, X. J. (2014). Biodegradable polymers for electrospinning: Towards biomedical applications. *Mater. Sci. Eng. C Mater* 45, 659–670. doi: 10.1016/j.msec.2014.04.051

Kai, F. B., Laklai, H., and Weaver, V. M. (2016). Force matters: biomechanical regulation of cell invasion and migration in disease. *Trends Cell Biol.* 26, 486–497. doi: 10.1016/j.tcb.2016.03.007

Kalluri, R., and Weinberg, R. A. (2009). The basics of epithelial-mesenchymal transition. *J. Clin. Invest.* 119, 1420–1428. doi: 10.1172/jci39104

Kalluri, R., and Zeisberg, M. (2006). Fibroblasts in cancer. *Nat. Rev. Cancer* 6, 392–401.

Kandasamy, S., Adhikary, G., Rorke, E. A., Friedberg, J. S., Mickle, M. B., Alexander, H. A., et al. (2020). The YAP1 signaling inhibitors, verteporfin and CA3, suppress the mesothelioma cancer stem cell phenotype. *Mol. Cancer Res.* 18, 343–351. doi: 10.1158/1541-7786.mcr-19-0914

Kanehisa, J., Yamanaka, T., Doi, S., Turksen, K., Heersche, J. N., Aubin, J. E., et al. (1990). A band of F-actin containing podosomes is involved in bone resorption by osteoclasts. *Bone* 11, 287–293. doi: 10.1016/8756-3282(90)90082-a

Kang, J. C., Chen, J. S., Lee, C. H., Chang, J. J., and Shieh, Y. S. (2010). Intratumoral macrophage counts correlate with tumor progression in colorectal cancer. *J. Surg. Oncol.* 102, 242–248. doi: 10.1002/jso.21617

Kantola, T., Vayrynen, J. P., Klintrup, K., Makela, J., Karppinen, S. M., Pihlajaniemi, T., et al. (2014). Serum endostatin levels are elevated in colorectal cancer and correlate with invasion and systemic inflammatory markers. *Br. J. Cancer* 111, 1605–1613. doi: 10.1038/bjc.2014.456

Karuppuswamy, P., Venugopal, J. R., Navaneethan, B., Laiva, A. L., Sridhar, S., and Ramakrishna, S. (2014). Functionalized hybrid nanofibers to mimic native ECM for tissue engineering applications. *Appl. Surf. Sci.* 322, 162–168. doi: 10.1016/j.apsusc.2014.10.074

Kasza, K. E., Broedersz, C. P., Koenderink, G. H., Lin, Y. C., Messner, W., Millman, E. A., et al. (2010). Actin filament length tunes elasticity of flexibly cross-linked actin networks. *Biophys. J.* 99, 1091–1100. doi: 10.1016/j.bpj.2010.06.025

Kauppila, S., Stenbäck, F., Risteli, J., Jukkola, A., and Risteli, L. (1998). Aberrant type I and type III collagen gene expression in human breast cancer in vivo. *J. Pathol.* 186, 262–268. doi: 10.1002/(sici)1096-9896(1998110)186:3<262::aid-path191>3.0.co;2-3

Kayal, C., Moeendarbary, E., Shipley, R. J., and Phillips, J. B. (2020). Mechanical response of neural cells to physiologically relevant stiffness gradients. *Adv. Healthcare Mater.* 9:1901036. doi: 10.1002/adhm.201901036

Kelley, L. C., Ammer, A. G., Hayes, K. E., Martin, K. H., Machida, K., Jia, L., et al. (2010). Oncogenic Src requires a wild-type counterpart to regulate invadopodia maturation. *J. Cell Sci.* 123, 3923–3932. doi: 10.1242/jcs.075200

Khadpekar, A., Mistry, K., Dwivedi, N., Paspunurwar, A., Tandaiya, P., and Majumder, A. (2019). Asamataxis: a cooperative relayed migration in response to subsurface inhomogeneity leads to long-range self-patterning of cells. *bioRxiv* [Preprint]. doi: 10.1101/799437

Kim, D. H., and Wirtz, D. (2015). Cytoskeletal tension induces the polarized architecture of the nucleus. *Biomaterials* 48, 161–172. doi: 10.1016/j.biomaterials.2015.01.023

Kim, H. E., Dalal, S. S., Young, E., Legato, M. J., Weisfeldt, M. L., and D'Armiento, J. (2000). Disruption of the myocardial extracellular matrix leads to cardiac dysfunction. *J. Clin. Invest.* 106, 857–866. doi: 10.1172/jci8040

Kiss, A. L., and Botos, E. (2009). Ocadaic acid retains caveolae in multicaveolar clusters. *Pathol. Oncol. Res.* 15, 479–486. doi: 10.1007/s12253-008-9139-4

Klaas, M., Kangur, T., Viil, J., Mäemets-Allas, K., Minajeva, A., Vadi, K., et al. (2016). The alterations in the extracellular matrix composition guide the repair of damaged liver tissue. *Sci. Rep.* 6:27398.

Klein, E. A., Yin, L., Kothapalli, D., Castagnino, P., Byfield, F. J., Xu, T., et al. (2009). Cell-cycle control by physiological matrix elasticity and in vivo tissue stiffening. *Curr. Biol.* 19, 1511–1518. doi: 10.1016/j.cub.2009.07.069

Knight, G., Morton, L. F., Peachey, A. R., Tuckwell, D. S., Farndale, R. W., and Barnes, M. J. (2000). The collagen-binding A-domains of integrins alpha(1)beta(1) and alpha(2)beta(1) recognize the same specific amino acid sequence, GFOGER, in native (triple-helical) collagens. *J. Biol. Chem.* 275, 35–40. doi: 10.1074/jbc.275.1.35

Koch, T. M., Münster, S., Bonakdar, N., Butler, J. P., and Fabry, B. (2012). 3D traction forces in cancer cell invasion. *PLoS One* 7:e33476. doi: 10.1371/journal.pone.0033476

Koenderink, G. H., Dogic, Z., Nakamura, F., Bendix, P. M., MacKintosh, F. C., Hartwig, J. H., et al. (2009). An active biopolymer network controlled by molecular motors. *Proc. Natl. Acad. Sci. U.S.A.* 106, 15192–15197. doi: 10.1073/pnas.0903974106

Kollmannsberger, P., Mierke, C. T., and Fabry, B. (2011). Nonlinear viscoelasticity of adherent cells is controlled by cytoskeletal tension. *Soft. Matter.* 7, 3127–3132. doi: 10.1039/c0sm00833h

Konitsiotis, A. D., Raynal, N., Bihan, D., Hohenester, E., Farndale, R. W., and Leitinger, B. (2008). Characterization of high affinity binding motifs for the discoidin domain receptor DDR2 in collagen. *J. Biol. Chem.* 283, 6861–6868. doi: 10.1074/jbc.m709290200

Kostic, A., Lynch, C. D., and Sheetz, M. P. (2009). Differential matrix rigidity response in breast cancer cell lines correlates with the tissue tropism. *PLoS One* 4:e6361. doi: 10.1371/journal.pone.0006361

Krause, M., Yang, F. W., te Lindert, M., Isermann, P., Schepens, J., Maas, R. J. A., et al. (2019). Cell migration through three-dimensional confining pores: speed accelerations by deformation and recoil of the nucleus. *Phil. Trans. R. Soc. B* 374:20180225. doi: 10.1098/rstb.2018.0225

Krieg, M., Arboleda-Estudillo, Y., Puech, P.-H., Käfer, J., Graner, F., Müller, D. J., et al. (2008). Tensile forces govern germ-layer organization in zebrafish. *Nat. Cell Biol.* 10, 429–436. doi: 10.1038/ncb1705

Kumar, R., and Li, D. Q. (2016). PAKs in human cancer progression: from inception to cancer therapeutic to future oncobiology. *Adv. Cancer Res.* 130, 137–209. doi: 10.1016/bs.acr.2016.01.002

Kumar, R., Sanawar, R., Li, X., and Li, F. (2017). Structure, biochemistry, and biology of PAK kinases. *Gene* 605, 20–31. doi: 10.1016/j.gene.2016.12.014

Kumar, S., and Weaver, V. M. (2009). Mechanics, malignancy, and metastasis: the force journey of a tumor cell. *Cancer Metastasis Rev.* 28, 113–127. doi: 10.1007/s10555-008-9173-4

Kunschmann, T., Puder, S., Fischer, T., Steffen, A., Rottner, K., and Mierke, C. T. (2019). The small GTPase Rac1 increases cell surface stiffness and enhances 3D migration into extracellular matrices. *Sci. Rep.* 9, 1–18.

Lachowski, D., Cortes, E., Pink, D., Chronopoulos, A., Karim, S. A., Morton, J. P., et al. (2017). Substrate rigidity controls activation and durotaxis in pancreatic stellate cells. *Sci. Rep.* 7:2506.

Lammerding, J. (2011). Mechanics of the nucleus. *Compr. Physiol.* 1, 783–807.

Langlois, B., Saupe, F., Rupp, T., Arnold, C., van der Heyden, M., Orend, G., et al. (2014). AngioMatrix, a signature of the tumor angiogenic switch-specific matrisome, correlates with poor prognosis for glioma and colorectal cancer patients. *Oncotarget* 5, 10529–10545. doi: 10.18632/oncotarget.2470

Laurent, V., Loisel, T. P., Harbeck, B., Wehman, A., Gröbe, L., Jockusch, B. M., et al. (1999). Role of proteins of the Ena/VASP family in actin-based motility of Listeria monocytogenes. *J. Cell Biol.* 144, 1245–1258. doi: 10.1083/jcb.144.6.1245

Le, C. C., Bennasroune, A., Langlois, B., Salesse, S., Boulagnon-Rombi, C., Morjani, H., et al. (2020). Functional interplay between collagen network and cell behavior within tumor microenvironment in colorectal cancer. *Front. Oncol.* 10:527. doi: 10.3389/fonc.2020.00527

Lei, Q. Y., Zhang, H., Zhao, B., Zha, Z. Y., Bai, F., Pei, X. H., et al. (2008). TAZ promotes cell proliferation and epithelial-mesenchymal transition and is inhibited by the hippo pathway. *Mol. Cell Biol.* 28, 2426–2436. doi: 10.1128/mcb.01874-07

Lesley, J., He, Q., Miyake, K., Hamann, A., Hyman, R., and Kincade, P. W. (1992). Requirements for hyaluronic acid binding by CD44: a role for the cytoplasmic domain and activation by antibody. *J. Exp. Med.* 175, 257–266. doi: 10.1084/jem.175.1.257

Levayer, R., and Lecuit, T. (2012). Biomechanical regulation of contractility: spatial control and dynamics. *Trends Cell Biol.* 22, 61–81. doi: 10.1016/j.tcb.2011.10.001

Levental, K. R., Yu, H., Kass, L., Lakins, J. N., Egeblad, M., Erler, J. T., et al. (2009). Matrix crosslinking forces tumor progression by enhancing integrin signaling. *Cell* 139, 891–906. doi: 10.1016/j.cell.2009.10.027

Levis, H. J., Kureshi, A. K., Massie, I., Morgan, L., Vernon, A. J., and Daniels, J. T. (2015). Tissue engineering the cornea: the evolution of RAFT. *Funct. Biomater.* 6, 50–65. doi: 10.3390/jfb6010050

Li, A., Morton, J. P., Ma, Y. F., Karim, S. A., Zhou, Y., and Faller, W. J. (2014). Fascin is regulated by slug, promotes progression of pancreatic cancer in mice, and is associated with patient outcomes. *Gastroenterology* 146, 1386–1396. doi: 10.1053/j.gastro.2014.01.046

Li, T., Sun, L., Miller, N., Nicklee, T., Woo, J., Hulse-Smith, L., et al. (2005). The association of measured breast tissue characteristics with mammographic density and other risk factors for breast cancer. *Cancer Epidemiol. Biomarkers Prev.* 14, 343–349. doi: 10.1158/1055-9965.epi-04-0490

Li, X. Y., Ota, I., Yana, I., Sabeh, F., and Weiss, S. J. (2008). Molecular dissection of the structural machinery underlying the tissue-invasive activity of membrane type-1 matrix metalloproteinase. *Mol. Biol. Cell* 19, 3221–3233. doi: 10.1091/mbc.e08-01-0016

Lian, I., Kim, J., Okazawa, H., Zhao, J., Zhao, B., Yu, J., et al. (2010).). The role of YAP transcription coactivator in regulating stem cell self-renewal and differentiation. *Genes Dev.* 24, 1106–1118. doi: 10.1101/gad.1903310

Libring, S., Shinde, A., Chanda, M. K., Nuru, M., George, H., Saleh, A. M., et al. (2020). The dynamic relationship of breast cancer cells and fibroblasts in fibronectin accumulation at primary and metastatic tumor. *Sites Cancers* 12:1270. doi: 10.3390/cancers12051270

Linder, S. (2009). Invadosomes at a glance. *J. Cell Sci.* 122, 3009–3013. doi: 10.1242/jcs.032631

Liu, B., Qu, M.-J., Qin, K.-R., Li, H., Li, Z.-K., Shen, B.-R., et al. (2008). Role of cyclic strain frequency in regulating the alignment of vascular smooth muscle cells in vitro. *Biophys. J.* 94, 1497–1507. doi: 10.1529/biophysj.106.098574

Liu, C. Y., Zha, Z. Y., Zhou, X., Zhang, H., Huang, W., Zhao, D., et al. (2010). The hippo tumor pathway promotes TAZ degradation by phosphorylating a phosphodegron and recruiting the SCF{beta}-TrCP E3 ligase. *J. Biol. Chem.* 285, 37159–37169. doi: 10.1074/jbc.m110.152942

Liu, H., Wen, J., Xiao, Y., Liu, J., Hopyan, S., Radisic, M., et al. (2014). In situ mechanical characterization of the cell nucleus by atomic force microscopy. *ACS Nano* 8, 3821–3828. doi: 10.1021/nn500553z

Liu, Q. Z., Gao, X. H., Chang, W. J., Gong, H. F., Fu, C. G., Zhang, W., et al. (2015). Expression of ITGB1 predicts prognosis in colorectal cancer: a large prospective study based on tissue microarray. *Int. J. Clin. Exp. Pathol.* 8, 12802–12810.

Lo, C. M., Wang, H. B., Dembo, M., and Wang, Y. L. (2000). Cell movement is guided by the rigidity of the substrate. *Biophys. J.* 79, 144–152. doi: 10.1016/s0006-3495(00)76279-5

Lopez, J. I., Kang, I., You, W.-K., McDonald, D. M., and Weaver, V. M. (2011). In situ force mapping of mammary gland transformation. *Integr. Biol.* 3, 910–921. doi: 10.1039/c1ib00043h

Luxenburg, C., Geblinger, D., Klein, E., Anderson, K., Hanein, D., Geiger, B., et al. (2007). The architecture of the adhesive apparatus of cultured osteoclasts: from podosome formation to sealing zone assembly. *PLoS One* 2:e179. doi: 10.1371/journal.pone.0000179

Ma, Y., Reynolds, L. E., Li, A., Stevenson, R. P., Hodivala-Dilke, K. M., Yamashiro, S., et al. (2013). Fascin 1 is dispensable for developmental and tumour angiogenesis. *Biol. Open* 2, 1187–1191. doi: 10.1242/bio.20136031

Ma, Y., Yang, Y., Wang, F., Wie, Q., and Qin, H. (2015). Hippo-YAP signaling pathway: a new paradigm for cancer therapy. *Int. J. Cancer* 137, 2275–2286. doi: 10.1002/ijc.29073

Mackintosh, F. C., and Schmidt, C. F. (2010). Active cellular materials. *Curr. Opin. Cell Biol.* 22, 29–35. doi: 10.1016/j.ceb.2010.01.002

Malandrino, A., Mak, M., Kamm, R. D., and Moeendarbary, E. (2018). Complex mechanics of the heterogeneous extracellular matrix in cancer. *Extreme Mech. Lett.* 21, 25–34. doi: 10.1016/j.eml.2018.02.003

Malek, A. M., and Izumo, S. (1996). Mechanism of endothelial cell shape change and cytoskeletal remodeling in response to fluid shear stress. *J. Cell Sci.* 109, 713–726.

Malliri, A., van der Kammen, R. A., Clark, K., van der Valk, M., Michiels, F., and Collard, J. G. (2002). Mice deficient in the Rac activator Tiam1 are resistant to Ras-induced skin tumours. *Nature* 417, 867–871. doi: 10.1038/nature00848

Mammoto, T., and Ingber, D. E. (2010). Mechanical control of tissue and organ development. *Development* 137, 1407–1420. doi: 10.1242/dev.024166

Marchina, E., and Barlati, S. (1996). Degradation of human plasma and extracellular matrix fibronectin by tissue type plasminogen activator and urokinase. *Int. J. Biochem. Cell Biol.* 28, 1141–1150. doi: 10.1016/1357-2725(96)00055-6

Marchisio, P. C., Cirillo, D., Teti, A., Zambonin-Zallone, A., and Tarone, G. (1987). Rous sarcoma virus-transformed fibroblasts and cells of monocytic origin display a peculiar dot-like organization of cytoskeletal proteins involved in microfilament-membrane interactions. *Exp. Cell Res.* 169, 202–214. doi: 10.1016/0014-4827(87)90238-2

Martino, F., Perestrelo, A. R., Vinarský, V., Pagliari, S., and Forte, G. (2018). Cellular mechanotransduction: from tension to function. *Front. Physiol.* 9:824. doi: 10.3389/fphys.2018.00824

Mattila, P. K., and Lappalainen, P. (2008). Filopodia: molecular architecture and cellular functions. *Nat. Rev. Mol. Cell Biol.* 9, 446–454. doi: 10.1038/nrm2406

Mayor, R., and Etienne-Manneville, S. (2016). The front and rear of collective cell migration. *Nat. Rev. Mol. Cell Biol.* 17, 97–109. doi: 10.1038/nrm.2015.14

McCarthy, J. B., El-Ashry, D., and Turley, E. A. (2018). Hyaluronan, cancer-associated fibroblasts and the tumor microenvironment in malignant progression. *Front. Cell Dev. Biol.* 6:48. doi: 10.3389/fcell.2018.00048

McCormack, V. A., and dos Santos Silva, I. (2006). Breast density and parenchymal patterns as markers of breast cancer risk: a meta-analysis. *Cancer Epidemiol. Biomarkers Prev.* 15, 1159–1169. doi: 10.1158/1055-9965.epi-06-0034

McGregor, A. L., Hsia, C. R., and Lammerding, J. (2016). Squish and squeeze—the nucleus as a physical barrier during migration in confined environments. *Curr. Opin. Cell Biol.* 40, 32–40. doi: 10.1016/j.ceb.2016.01.011

Menon, S., and Beningo, K. A. (2011). Cancer cell invasion is enhanced by applied mechanical stimulation. *PLoS One* 6:e17277. doi: 10.1371/journal.pone.0017277

Meyer Zum Büschenfelde, U., Brandenstein, L. I., von Elsner, L., Flato, K., Holling, T., Zenker, M., et al. (2018). RIT1 controls actin dynamics via complex formation with RAC1/CDC42 and PAK1. *PLoS Genet.* 14:e1007370. doi: 10.1371/journal.pgen.1007370

Mierke, C. T. (2017). Physical role of nuclear and cytoskeletal confinements in cell migration mode selection and switching. *AIMS Biophys.* 4, 615–658. doi: 10.3934/biophy.2017.4.615

Mierke, C. T. (2019a). The role of the optical stretcher is crucial in the investigation of cell mechanics regulating cell adhesion and motility. *Front. Cell Dev. Biol.* 7:184. doi: 10.3389/fcell.2019.00184

Mierke, C. T. (2019b). The matrix environmental and cell mechanical properties regulate cell migration and contribute to the invasive phenotype of cancer cells. *Rep. Prog. Phys.* 82:064602. doi: 10.1088/1361-6633/ab1628

Mierke, C. T. (2020). Cell mechanics drives migration modes. *Biophys. Rev. Lett.* 15, 1–34. doi: 10.1142/s1793048020300017

Mierke, C. T., Bretz, N., and Altevogt, P. (2011a). Contractile forces contribute to increased glycosylphosphatidylinositol-anchored receptor CD24-facilitated cancer cell invasion. *J. Biol. Chem.* 286, 34858–34871. doi: 10.1074/jbc.m111.245183

Mierke, C. T., Frey, B., Fellner, M., Herrmann, M., and Fabry, B. (2011b). Integrin α5β1 facilitates cancer cell invasion through enhanced contractile forces. *J. Cell Sci.* 124, 369–383. doi: 10.1242/jcs.071985

Mierke, C. T., Fischer, T., Puder, S., Kunschmann, T., Soetje, B., and Ziegler, W. H. (2017). Focal adhesion kinase activity is required for actomyosin contractility based invasion of cells into dense 3D matrices. *Sci. Rep.* 7:42780.

Mierke, C. T., Puder, S., Aermes, C., Fischer, T., and Kunschmann, T. (2020). Effect of PAK inhibition on cell mechanics depends on Rac1. *Front. Cell Dev. Biol.* 8:13. doi: 10.3389/fcell.2020.00013

Mierke, C. T., Sauer, F., Grosser, S., Puder, S., Fischer, T., and Käs, J. A. (2018). The two faces of enhanced stroma: Stroma acts as a tumor promoter and a steric obstacle. *NMR Biomed.* 31:e3831. doi: 10.1002/nbm.3831

Mierke, C. T., Zitterbart, D. P., Kollmannsberger, P., Raupach, C., Schlötzer-Schrehardt, U., Goecke, T. W., et al. (2008). Breakdown of the endothelial barrier function in tumor cell transmigration. *Biophys. J.* 94, 2832–2846. doi: 10.1529/biophysj.107.113613

Miles, F. L., and Sikes, R. A. (2014). Insidious changes in stromal matrix fuel cancer progression. *Mol. Cancer Res.* 12, 297–312. doi: 10.1158/1541-7786.mcr-13-0535

Miteva, D. O., Rutkowski, J. M., Dixon, J. B., Kilarski, W., Shields, J. D., and Swartz, M. A. (2010). Transmural flow modulates cell and fluid transport functions of lymphatic endothelium. *Circ. Res.* 106, 920–931. doi: 10.1161/circresaha.109.207274

Mitrossilis, D., Fouchard, J., Pereira, D., Postic, F., Richert, A., Saint-Jean, M., et al. (2010). Real-time single cell response to stiffness. *Proc. Natl. Acad. Sci. U.S.A.* 107, 16518–16523. doi: 10.1073/pnas.1007940107

Miyauchi, A., Hruska, K. A., Greenfield, E. M., Duncan, R., Alvarez, J., Barattolo, R., et al. (1990). Osteoclast cytosolic calcium, regulated by voltage-gated calcium channels and extracellular calcium, controls podosome assembly and bone resorption. *J. Cell Biol.* 111, 2543–2552. doi: 10.1083/jcb.111.6.2543

Mizuno, D., Tardin, C., Schmidt, C. F., and Mackintosh, F. C. (2007). Nonequilibrium mechanics of active cytoskeletal networks. *Science* 315, 370–373. doi: 10.1126/science.1134404

Monteiro, P., Rossé, C., Castro-Castro, A., Irondelle, M., Lagoutte, E., Paul-Gilloteaux, P., et al. (2013). Endosomal WASH and exocyst complexes control exocytosis of MT1-MMP at invadopodia. *J. Cell Biol.* 203, 1063–1079. doi: 10.1083/jcb.201306162

Moreau, V., Tatin, F., Varon, C., and Geìnot, E. (2003). Actin can reorganize into podosomes in aortic endothelial cells, a process controlled by Cdc42 and RhoA. *Mol. Cell Biol.* 23, 6809–6822. doi: 10.1128/mcb.23.19.6809-6822.2003

Moreira Teixeira, L. S., Patterson, J., and Luyten, F. P. (2014). Skeletal tissue regeneration: where can hydrogels play a role? *Int Orthop* 38, 1861–1876. doi: 10.1007/s00264-014-2402-2

Morgan, M. R., Byron, A., Humphries, M. J., and Bass, M. D. (2009). Giving off mixed signals–distinct functions of alpha5beta1 and alphavbeta3 integrins in regulating cell behavior. *IUBMB Life* 61, 731–738. doi: 10.1002/iub.200

Mouneimne, G., DesMarais, V., Sidani, M., Scemes, E., Wang, W., Song, X., et al. (2006). Spatial and temporal control of cofilin activity is required for directional sensing during chemotaxis. *Curr. Biol.* 16, 2193–2205. doi: 10.1016/j.cub.2006.09.016

Mouneimne, G., Soon, L., DesMarais, V., Sidani, M., Song, X., Yip, S.-C., et al. (2004). Phospholipase C and cofilin are required for carcinoma cell directionality in response to EGF stimulation. *J. Cell Biol.* 166, 697–708. doi: 10.1083/jcb.200405156

Mouw, J. K., Yui, Y., Damiano, L., Bainer, R. O., Lakins, J. N., Acerbi, I., et al. (2014). Tissue mechanics modulate microRNA-dependent PTEN expression to regulate malignant progression. *Nat. Med.* 20, 360–367. doi: 10.1038/nm.3497

Mrkonjic, S., Destaing, O., and Albiges-Rizo, C. (2016). Mechanotransduction pulls the strings of matrix degradation at invadosome. *Matrix Biol.* 5, 190–203. doi: 10.1016/j.matbio.2016.06.007

Mueller, J., Szep, G., Nemethova, M., de Vries, I., Lieber, A. D., Winkler, C., et al. (2017). Load adaptation of lamellipodial actin networks. *Cell* 171, 188–200. doi: 10.1016/j.cell.2017.07.051

Münster, S., Jawerth, L. M., Leslie, B. A., Weitz, J. I., Fabry, B., and Weitz, D. A. (2013). Strain history dependence of the nonlinear stress response of fibrin and collagen networks. *Proc. Natl. Acad. Sci. U.S.A.* 110, 12197–12202. doi: 10.1073/pnas.1222787110

Murphy, D. A., and Courtneidge, S. A. (2011). The 'ins' and 'outs' of podosomes and invadopodia: characteristics, formation and function. *Nat. Rev. Mol. Cell Biol.* 12, 413–426. doi: 10.1038/nrm3141

Murphy, S. V., and Atala, A. (2014). 3D bioprinting of tissues and organs. *Nat. Biotechnol.* 32, 773–785. doi: 10.1038/nbt.2958

Murrell, M., Oakes, P. W., Lenz, M., and Gardel, M. L. (2015). Forcing cells into shape: the mechanics of actomyosin contractility. *Nat. Rev. Mol. Cell Biol.* 16, 486–498. doi: 10.1038/nrm4012

Naba, A., Clauser, K. R., Whittaker, C. A., Carr, S. A., Tanabe, K. K., and Hynes, R. O. (2014). Extracellular matrix signatures of human primary metastatic colon cancers and their metastases to liver. *BMC Cancer* 14:518. doi: 10.1186/1471-2407-14-518

Nagai, S., Moreno, O., Smith, C. A., Ivanchuk, S., Romagnuolo, R., Golbourn, B., et al. (2011). Role of the cofilin activity cycle in astrocytoma migration and invasion. *Genes Cancer* 2, 859–869. doi: 10.1177/1947601911431839

Nassoy, P., and Lamaze, C. (2012). Stressing caveolae new role in cell mechanics. *Trends Cell Biol.* 22, 381–389. doi: 10.1016/j.tcb.2012.04.007

Ng, C. P., and Swartz, M. A. (2003). Fibroblast alignment under interstitial fluid flow using a novel 3-D tissue culture model. *Am. J. Physiol. Heart Circ. Physiol.* 284, H1771–H1777.

Ni, Q., and Papoian, G. A. (2019). Turnover versus treadmilling in actin network assembly and remodeling. *Cytoskeleton* 76, 562–570. doi: 10.1002/cm.21564

Oikawa, T., Itoh, T., and Takenawa, T. (2008). Sequential signals toward podosome formation in NIH-src cells. *J. Cell Biol.* 182, 157–169. doi: 10.1083/jcb.200801042

Ostrowski, M., Huang, N. F., Walker, T. W., Verwijlen, T., Poplawski, C., Khoo, A. S., et al. (2014). Microvascular endothelial cells migrate upstream and align against the shear stress field created by impinging flow. *Biophys. J.* 106, 366–374. doi: 10.1016/j.bpj.2013.11.4502

Oudin, M. J., Jonas, O., Kosciuk, T., Broye, L. C., Guido, B. C., Wyckoff, J., et al. (2016a). Tumor cell-driven extracellular matrix remodeling drives haptotaxis during metastatic progression. *Cancer Discov.* 6, 516–531. doi: 10.1158/2159-8290.cd-15-1183

Oudin, M. J., Miller, M. A., Klazen, J. A. Z., Kosciuk, T., Lussiez, A., Hughes, S. K., et al. (2016b). MenaINV mediates synergistic cross-talk between signaling pathways driving chemotaxis and haptotaxis. *Mol. Biol. Cell* 27, 3085–3094. doi: 10.1091/mbc.e16-04-0212

Pajerowski, J. D., Dahl, K. N., Zhong, F. L., Sammak, P. J., and Discher, D. E. (2007). Physical plasticity of the nucleus in stem cell differentiation. *Proc. Natl Acad. Sci. U.S.A.* 104, 15619–15624. doi: 10.1073/pnas.0702576104

Parekh, A., and Weaver, A. M. (2009). Regulation of cancer invasiveness by the physical extracellular matrix environment. *Cell Adh. Migr.* 3, 288–292. doi: 10.4161/cam.3.3.8888

Parker, M. W., Rossi, D., Peterson, M., Smith, K., Sikström, K., White, E. S., et al. (2014). Fibrotic extracellular matrix activates a profibrotic positive feedback loop. *J. Clni. Invest.* 124, 1622–1635. doi: 10.1172/jci71386

Parton, R. G., and del Pozo, M. A. (2013). Caveolae as plasma membrane sensors, protectors and organizers. *Nat. Rev. Mol. Cell Biol.* 14, 98–112. doi: 10.1038/nrm3512

Parton, R. G., Joggerst, B., and Simons, K. (1994). Regulated internalization of caveolae. *J. Cell Biol.* 127, 1199–1215. doi: 10.1083/jcb.127.5.1199

Paszek, M. J., Zahir, N., Johnson, K. R., Lakins, J. N., Rozenberg, G. I., Gefen, A., et al. (2005). Tensional homeostasis and the malignant phenotype. *Cancer Cell* 8, 241–254. doi: 10.1016/j.ccr.2005.08.010

Provenzano, P. P., Inman, D. R., Eliceiri, K. W., Trier, S. M., and Keely, P. J. (2008). Contact guidance mediated three-dimensional cell migration is regulated by Rho/ROCK-dependent matrix reorganization. *Biophys. J.* 95, 5374–5384. doi: 10.1529/biophysj.108.133116

Paul, N. R., Allen, J. L., Chapman, A., Morlan-Mairal, M., Zindy, E., Jacquemet, G., et al. (2015a). α5β1 integrin recycling promotes Arp2/ 3-independent cancer

cell invasion via the formin. FHOD3. *J. Cell Biol.* 210, 1013–1031. doi: 10.1083/jcb.201502040

Paul, N. R., Jacquemet, G., and Caswell, P. T. (2015b). Endocytic trafficking of integrins in cell migration. *Curr. Biol.* 25, R1092–R1105.

Pelham, R. J. Jr., and Wang, Y. I. (1997). Cell locomotion and focal adhesions are regulated by substrate flexibility. *Proc. Natl. Acad. Sci. U.S.A.* 94, 13661–13665. doi: 10.1073/pnas.94.25.13661

Petrie, R. J., Harlin, H. M., Korsak, L. I. T., and Yamada, K. M. (2017). Activating the nuclear piston mechanism of 3D migration in tumor cells. *J. Cell Biol.* 216, 93–100. doi: 10.1083/jcb.201605097

Pickup, M. W., Mouw, J. K., and Weaver, V. M. (2014). The extracellular matrix modulates the hallmarks of cancer. *EMBO Rep.* 15, 1243–1253. doi: 10.15252/embr.201439246

Piechocka, I. K., Bacabac, R. G., Potters, M., MacKintosh, F. C., and Koenderink, G. H. (2010). Structural hierarchy governs fibrin gel mechanics. *Biophys. J.* 98, 2281–2289. doi: 10.1016/j.bpj.2010.01.040

Pilch, P. F., and Liu, L. (2011). Fat caves: caveolae, lipid trafficking and lipid metabolism in adipocytes. *Trends Endocrinol. Metab.* 22, 318–324. doi: 10.1016/j.tem.2011.04.001

Plotnikov, S. V., Pasapera, A. M., Sabass, B., and Waterman, C. M. (2012). Force fluctuations within focal adhesions mediate ECM-rigidity sensing to guide directed cell migration. *Cell* 151, 1513–1527. doi: 10.1016/j.cell.2012.11.034

Poduri, A., Chang, A. H., Raftrey, B., Rhee, S., Van, M., and Red-Horse, K. (2017). Endothelial cells respond to the direction of mechanical stimuli through SMAD signaling to regulate coronary artery size. *Development* 144, 3241–3252. doi: 10.1242/dev.150904

Poh, Y.-C., Chen, J., Hong, Y., Zhang, S., Chen, J., Wu, D. C., et al. (2014). Generation of organized germ layers from a single mouse embryonic stem cell. *Nat. Commun.* 5:4000.

Polette, M., Nawrocki-Raby, B., Gilles, C., Clavel, C., and Birembaut, P. (2004). Tumour invasion and matrix metalloproteinases. *Crit. Rev. Oncol. Hematol.* 49, 179–186. doi: 10.1016/j.critrevonc.2003.10.008

Pollard, T. D., and Borisy, G. G. (2003). Cellular motility driven by assembly and disassembly of actin filaments. *Cell* 112, 453–465. doi: 10.1016/s0092-8674(03)00120-x

Provenzano, P. P., Eliceiri, K. W., Campbell, J. M., Inman, D. R., White, J. G., Keely, P. J., et al. (2006). Collagen reorganization at the tumor-stromal interface facilitates local invasion. *BMC Med.* 4:38. doi: 10.1186/1741-7015-4-38

Provenzano, P. P., Inman, D. R., Eliceiri, K. W., and Keely, P. J. (2009). Matrix density- induced mechanoregulation of breast cell phenotype, signaling and gene expression through a FAK-ERK linkage. *Oncogene* 28, 4326–4343. doi: 10.1038/onc.2009.299

Puleo, J. I., Parker, S. S., Roman, M. R., Watson, A. W., Eliato, K. R., Peng, L., et al. (2019). Mechanosensing during directed cell migration requires dynamic actin polymerization at focal adhesions. *J. Cell Biol.* 218, 4215–4235. doi: 10.1083/jcb.201902101

Qiao, J., Fang, C. Y., Chen, S. X., Wang, X.-Q., Cui, S.-J., Liu, X.-H., et al. (2015). Stroma derived COL6A3 is a potential prognosis marker of colorectal carcinoma revealed by quantitative proteomics. *Oncotarget* 6, 29929–29946. doi: 10.18632/oncotarget.4966

Raab, M., Swift, J., Dingal, P. C. D. P., Shah, P., Shin, J.-W., and Discher, D. E. (2012). Crawling from soft to stiff matrix polarizes the cytoskeleton and phosphoregulates myosin-II heavy chain. *J. Cell Biol.* 199, 669–683. doi: 10.1083/jcb.201205056

Rajab, A., Straub, V., McCann, L. J., Seelow, D., Varon, R., Barresi, R., et al. (2010). Fatal cardiac arrhythmia and long-QT syndrome in a new form of congenital generalized lipodystrophy with muscle rippling (CGL4) due to PTRF-CAVIN mutations. *PLoS Genet.* 6:e1000874. doi: 10.1371/journal.pgen.1000874

Rammal, H., Saby, C., Magnien, K., Van-Gulick, L., Garnotel, R., Buache, E., et al. (2016). Discoidin domain receptors: potential actors and targets in cancer. *Front. Pharmacol.* 7:55. doi: 10.3389/fphar.2016.00055

Rane, C. K., and Minden, A. (2018). P21 activated kinase signaling in cancer. *Semin. Cancer Biol.* 54, 40–49. doi: 10.1016/j.semcancer.2018.01.006

Ray, A., Slama, Z. M., Morford, R. K., Madden, S. A., and Provenzano, P. P. (2017). Enhanced directional migration of cancer stem cells in 3D aligned collagen matrices. *Biophys. J.* 112, 1023–1036. doi: 10.1016/j.bpj.2017.01.007

Rederstorff, E., Rethore, G., Weiss, P., Sourice, S., Beck-Cormier, S., Mathieu, E., et al. (2017). Enriching a cellulose hydrogel with a biologically active marine exopolysaccharide for cell-based cartilage engineering. *J. Tissue Eng. Regen. Med.* 11, 1152–1164. doi: 10.1002/term.2018

Reid, S. E., Kay, E. J., Neilson, L. J., Henze, A.-T., Serneels, J., McGhee, E. J., et al. (2017). Tumor matrix stiffness promotes metastatic cancer cell interaction with endothelium. *EMBO J.* 36, 2373–2389. doi: 10.15252/embj.201694912

Riching, K. M., Cox, B. L., Salick, M. R., Pehlke, C., Riching, A. S., Ponik, S. M., et al. (2014). 3D collagen alignment limits protrusions to enhance breast cancer cell persistence. *Biophys. J.* 107, 2546–2558. doi: 10.1016/j.bpj.2014.10.035

Roca-Cusachs, P., Iskratsch, T., and Sheetz, M. P. (2012). Finding the weakest link: exploring integrin-mediated mechanical molecular pathways. *J. Cell Sci.* 125, 3025–3038. doi: 10.1242/jcs.095794

Rodia, M. T., Ugolini, G., Mattei, G., Montroni, I., Zattoni, D., Ghignone, F., et al. (2016). Systematic large-scale meta-analysis identifies a panel of two mRNAs as blood biomarkers for colorectal cancer detection. *Oncotarget* 7, 30295–30306. doi: 10.18632/oncotarget.8108

Röhlich, P., and Allison, A. C. (1976). Oriented pattern of membrane-associated vesicles in fibroblasts. *J. Ultrastruct. Res.* 57, 94–103. doi: 10.1016/s0022-5320(76)80059-7

Roskoski, R. Jr. (2004). Src protein-tyrosine kinase structure and regulation. *Biochem. Biophys. Res. Commun.* 324, 1155–1164. doi: 10.1016/j.bbrc.2004.09.171

Ross, T. D., Coon, B. G., Yun, S., Baeyens, N., Tanaka, K., Ouyang, M., et al. (2013). Integrins in mechanotransduction. *Curr. Opin. Cell Biol.* 25, 613–618.

Rothberg, K. G., Heuser, J. E., Donzell, W. C., Ying, Y.-S., Glenney, J. R., and Anderson, R. G. W. (1992). Caveolin, a protein component of caveolae membrane coats. *Cell* 68, 673–682. doi: 10.1016/0092-8674(92)90143-z

Sabeh, F., Ota, I., Holmbeck, K., Birkedal-Hansen, H., Soloway, P., Balbin, M., et al. (2004). Tumor cell traffic through the extracellular matrix is controlled by the membrane-anchored collagenase MT1-MMP. *J. Cell Biol.* 167, 769–781. doi: 10.1083/jcb.200408028

Sabeh, F., Shimizu-Hirotam, R., and Weiss, S. J. (2009). Protease-dependent versus-independent cancer cell invasion programs: three-dimensional amoeboid movement revisited. *J. Cell Biol.* 185, 11–19. doi: 10.1083/jcb.200807195

Saby, C., Buache, E., Brassart-Pasco, S., El Btaouri, H., Courageot, M. P., Van Gulick, L., et al. (2016). Type I collagen aging impairs discoidin domain receptor 2-mediated tumor cell growth suppression. *Oncotarget* 7, 24908–24927. doi: 10.18632/oncotarget.8795

Salbreux, G., Charras, G., and Paluch, E. (2012). Actin cortex mechanics and cellular morphogenesis. *Trends Cell Biol.* 22, 536–545. doi: 10.1016/j.tcb.2012.07.001

Saltel, F., Daubon, T., Juin, A., Ganuza, I. E., Veillat, V., and Geinot, E. (2011). Invadosomes: intriguing structures with promise. *Eur. J. Cell Biol.* 90, 100–107. doi: 10.1016/j.ejcb.2010.05.011

Sant, S., Hancock, M. J., Donnelly, J. P., Iyer, D., and Khademhosseini, A. (2010). Biomimetic gradient hydrogels for tissue engineering. *Can. J. Chem. Eng.* 88, 899–911. doi: 10.1002/cjce.20411

Sarma, K., and Reinberg, D. (2005). Histone variants meet their match. *Nat. Rev. Mol. Cell Biol.* 6, 139–149. doi: 10.1038/nrm1567

Sasaki, S., Ueda, M., Iguchi, T., Kaneko, M., Nakayama, H., Watanabe, T., et al. (2017). DDR2 expression is associated with a high frequency of peritoneal dissemination and poor prognosis in colorectal cancer. *Anticancer Res.* 37, 2587–2591. doi: 10.21873/anticanres.11603

Schmidt, S., Nakchbandi, I., Ruppert, R., Kawelke, N., Hess, M. W., Pfaller, K., et al. (2011). Kindlin-3-mediated signaling from multiple integrin classes is required for osteoclast-mediated bone resorption. *J. Cell Biol.* 192, 883–897. doi: 10.1083/jcb.201007141

Schmoller, K., Fernandez, P., Arevalo, R., Blair, D., and Bausch, A. (2010). Cyclic hardening in bundled actin networks. *Nat. Commun.* 1:134.

Schoumacher, M., El-Marjou, F., Laé, M., Kambou, N., Louvard, D., Robine, S., et al. (2014). Conditional expression of fascin increases tumor progression in a mouse model of intestinal cancer. *Eur. J. Cell Biol.* 93, 388–395. doi: 10.1016/j.ejcb.2014.08.002

Schwarz, U. S., and Gardel, M. L. (2012). United we stand: integrating the actin cytoskeleton and cell-matrix adhesions in cellular mechanotransduction. *J. Cell Sci.* 125, 3051–3060. doi: 10.1242/jcs.093716

Seguin, L., Desgrosellier, J. S., Weis, S. M., and Cheresh, D. A. (2015). Integrins and cancer: regulators of cancer stemness, metastasis, and drug resistance Trends. *Cell Biol.* 25, 234–240. doi: 10.1016/j.tcb.2014.12.006

Seiki, M. (2003). Membrane-type 1 matrix metalloproteinase: a key enzyme for tumor invasion. *Cancer Lett.* 194, 1–11. doi: 10.1016/s0304-3835(02)00699-7

Shang, J., Wang, F., Chen, P., Wang, X., Ding, F., Liu, S., et al. (2018). Co-expression network analysis identified COL8A1 is associated with the progression and prognosis in human colon adenocarcinoma. *Dig. Dis. Sci.* 63, 1219–1228. doi: 10.1007/s10620-018-4996-5

Shapiro, S. D. (1998). Matrix metalloproteinase degradation of extracellular matrix: biological consequences. *Curr. Opin. Cell Biol.* 10, 602–608. doi: 10.1016/s0955-0674(98)80035-5

Shapiro, S. D., Endicott, S. K., Province, M. A., Pierce, J. A., and Campbell, E. J. (1991). Marked longevity of human lung parenchymal elastic fibers deduced from prevalence of d-aspartate and nuclear weapons-related radiocarbon. *J. Clin. Invest.* 87, 1828–1834. doi: 10.1172/jci115204

Sheldrake, H. M., and Patterson, L. H. (2009). Function and antagonism of beta3 integrins in the development of cancer therapy. *Curr. Cancer Drug. Targets* 9, 519–540. doi: 10.2174/156800909788486713

Shen, C. J., Fu, J., and Chen, C. S. (2008). Patterning cell and tissue function. *Cell. Mol. Bioeng.* 1, 15–23. doi: 10.1007/s12195-008-0005-y

Shi, F., Harman, J., Fujiwara, K., and Sottile, J. (2010). Collagen I matrix turnover is regulated by fibronectin polymerization. *Am. J. Physiol. Cell Physiol.* 298, C1265–C1275.

Shi, F., and Sottile, J. (2011). MT1-MMP regulates the turnover and endocytosis of extracellular matrix fibronectin. *J. Cell Sci.* 124(Pt 23), 4039–4050. doi: 10.1242/jcs.087858

Shibue, T., Brooks, M. W., Inan, M. F., Reinhardt, F., and Weinberg, R. A. (2012). The outgrowth of micrometastases is enabled by the formation of filopodium-like protrusions. *Cancer Discov.* 2, 706–721. doi: 10.1158/2159-8290.cd-11-0239

Shibue, T., Brooks, M. W., and Weinberg, R. A. (2013). An integrin-linked machinery of cyto- skeletal regulation that enables experimental tumor initiation and metastatic colonization. *Cancer Cell* 24, 481–498. doi: 10.1016/j.ccr.2013.08.012

Shieh, A. C. (2011). Biomechanical forces shape the tumor microenvironment. *Ann. Biomed. Eng.* 39, 1379–1389. doi: 10.1007/s10439-011-0252-2

Shigeeda, W., Shibazaki, M., Yasuhira, S., Masuda, T., Tanita, T., Kaneko, Y., et al. (2017). Hyaluronic acid enhances cell migration and invasion via the YAP1/TAZ-RHAMM axis in malignant pleural mesothelioma. *Oncotarget* 8, 93729–93740. doi: 10.18632/oncotarget.20750

Silva, J. J. M., Ezhkova, E., Silva, J., Heart, S., Castillo, M., Campos, Y., et al. (2009). Cyfip1 is a putative invasion suppressor in epithelial cancers. *Cell* 137, 1047–1061. doi: 10.1016/j.cell.2009.04.013

Singer, I. I. (1979). Microfilament bundles and the control of pinocytotic vesicle distribution at the surfaces of normal and transformed fibroblasts. *Exp. Cell Res.* 122, 251–264. doi: 10.1016/0014-4827(79)90302-1

Singh, P., Carraher, C., and Schwarzbauer, J. E. (2010). Assembly of fibronectin extracellular matrix. *Annu. Rev. Cell Dev. Biol.* 26, 397–419.

Sinha, B., Köster, D., Ruez, R., Gonnord, P., Bastiani, M., Abankwa, D., et al. (2011). Cells respond to mechanical stress by rapid disassembly of caveolae. *Cell* 144, 402–413. doi: 10.1016/j.cell.2010.12.031

Sirvent, A., and Lafitte, M. (2018). DDR1 inhibition as a new therapeutic strategy for colorectal cancer. *Mol. Cell Oncol.* 5:e1465882. doi: 10.1080/23723556.2018.1465882

Sivan, S. S., Tsitron, E., Wachtel, E., Roughley, P., Sakkee, N., van der Ham, F., et al. (2006). Age-related accumulation of pentosidine in aggrecan and collagen from normal and degenerate human intervertebral discs. *Biochem. J.* 399, 29–35. doi: 10.1042/bj20060579

Skovbjerg, H., Anthonsen, D., Lothe, I. M., Tveit, K. M., Kure, E. H., and Vogel, L. K. (2009). Collagen mRNA levels changes during colorectal cancer carcinogenesis. *BMC Cancer* 9:136. doi: 10.1186/1471-2407-9-136

Smith, L., Cho, S., and Discher, D. E. (2017). Mechanosensing of matrix by stem cells: from contractility and matrix heterogeneity to cardiogenesis and muscle stem cells. *Semin. Cell Dev. Biol.* 71, 84–98. doi: 10.1016/j.semcdb.2017.05.025

Smith, M. A., Blankman, E., Gardel, M. L., Luettjohann, L., Waterman, C. M., and Beckerle, M. C. (2010). A zyxin-mediated mechanism for actin stress fiber maintenance and repair. *Dev. Cell* 19, 365–376. doi: 10.1016/j.devcel.2010.08.008

Sole, X., Crous-Bou, M., Cordero, D., Olivares, D., Guinó, E., Sanz-Pamplona, R., et al. (2014). Discovery and validation of new potential biomarkers for early detection of colon cancer. *PLoS One* 9:e106748. doi: 10.1371/journal.pone.0106748

Soleas, J. P., Waddell, T. K., and McGuigan, A. P. (2015). Topographically grooved gel inserts for aligning epithelial cells during air–liquid-interface culture. *Biomater. Sci.* 3, 121–133. doi: 10.1039/c4bm00237g

Solon, J., Levental, I., Sengupta, K., Georges, P. C., and Janmey, P. A. (2007). Fibroblast adaptation and stiffness matching to soft elastic substrates. *Biophys. J.* 93, 4453–4461. doi: 10.1529/biophysj.106.101386

Sottile, J., and Hocking, D. C. (2002). Fibronectin polymerization regulates the composition and stability of extracellular matrix fibrils and cell-matrix adhesions. *Mol. Biol. Cell* 13, 3546–3559. doi: 10.1091/mbc.e02-01-0048

Sowalsky, A. G., Sager, R., Schaefer, R. J., Bratslavsky, G., Pandolfi, P. P., Balk, S. P., et al. (2015). Loss of Wave1 gene defines a subtype of lethal prostate cancer. *Oncotarget* 6, 12383–12391. doi: 10.18632/oncotarget.3564

Spiller, K. L., Maher, S. A., and Lowman, A. M. (2011). Hydrogels for the repair of articular cartilage defects. *Tissue Eng. Part B Rev.* 17, 281–299. doi: 10.1089/ten.teb.2011.0077

Standeven, K. F., Carter, A. M., Grant, P. J., Weisel, J. W., Chernysh, I., Masova, L., et al. (2007). Functional analysis of fibrin gamma-chain cross-linking by activated factor XIII: determination of a cross-linking pattern that maximizes clot stiffness. *Blood* 110, 902–907. doi: 10.1182/blood-2007-01-066837

Stephens, A. D., Banigan, E. J., Adam, S. A., Goldman, R. D., and Marko, J. F. (2017). Chromatin and lamin A determine two different mechanical response regimes of the cell nucleus. *Mol. Biol. Cell* 28, 1984–1996. doi: 10.1091/mbc.e16-09-0653

Stetler-Stevenson, W. G., and Yu, A. E. (2001). Proteases in invasion: matrix metalloproteinases. *Semin. Cancer Biol.* 11, 143–152. doi: 10.1006/scbi.2000.0365

Storm, C., Pastore, J. J., MacKintosh, F. C., Lubensky, T. C., and Janmey, P. A. (2005). Nonlinear elasticity in biological gels. *Nature* 435, 191–194. doi: 10.1038/nature03521

Suk, Y., Vincent, L. G., Lee, A. R., Kretchmer, K. C., Chirasatitsin, S., Dobke, M. K., et al. (2012). The alignment and fusion assembly of adipose-derived stem cells on mechanically patterned matrices. *Biomaterials* 33, 6943–6951. doi: 10.1016/j.biomaterials.2012.06.057

Sun, C., Zargham, R., Shao, Q., Gui, X., Marcus, V., Lazaris, A., et al. (2014). Association of CD98, integrin beta1, integrin beta3 and Fak with the progression and liver metastases of colorectal cancer. *Pathol. Res. Pract.* 210, 668–674. doi: 10.1016/j.prp.2014.06.016

Sundararaghavan, H. G., Monteiro, G. A., Firestein, B. L., and Shreiber, D. I. (2009). Neurite growth in 3D collagen gels with gradients of mechanical properties. *Biotechnol. Bioeng.* 102, 632–643. doi: 10.1002/bit.22074

Sunyer, R., Conte, V., Escribano, J., Elosegui-Artola, A., Labernadie, A., Valon, L., et al. (2016). Collective cell durotaxis emerges from long-range intercellular force transmission. *Science* 353, 1157–1161. doi: 10.1126/science.aaf7119

Swift, J., Ivanovska, I. L., Buxboim, A., Harada, T., Dingal, P. C., Pinter, J., et al. (2013). Nuclear lamin-A scales with tissue stiffness and enhances matrix-directed differentiation. *Science* 341:1240104. doi: 10.1126/science.1240104

Tahtamouni, L. H., Shaw, A. E., Hasan, M. H., Yasin, S. R., and Bamburg, J. R. (2013). Non-overlapping activities of ADF and cofilin-1 during the migration of metastatic breast tumor cells. *BMC Cell Biol.* 14:45. doi: 10.1186/1471-2121-14-45

Takahashi, R., Wu, Z. L., Arifuzzaman, M., Nonoyama, T., Nakajima, T., Kurokawa, T., et al. (2014). Control superstructure of rigid polyelectrolytes in oppositely charged hydrogels via programmed internal stress. *Nat. Commun.* 5:4490.

Tan, V. Y., Lewis, S. J., Adams, J. C., and Martin, R. M. (2013). Association of fascin-1 with mortality, disease progression and metastasis in carcinomas: a systematic review and meta-analysis. *BMC Med.* 11:52. doi: 10.1186/1741-7015-11-52

Tanaka, K., Osada, H., Murakami-Tonami, Y., Horio, Y., Hida, T., and Sekido, Y. (2017). Statin suppresses Hippo pathway-inactivated malignant mesothelioma cells and blocks the YAP/CD44 growth stimulatory axis. *Cancer Lett.* 385, 215–224. doi: 10.1016/j.canlet.2016.10.020

Tarone, G., Cirillo, D., Giancotti, F. G., Comoglio, P. M., and Marchisio, P. C. (1985). Rous sarcoma virus-transformed fibroblasts adhere primarily at discrete

protrusions of the ventral membrane called podosomes. *Exp. Cell Res.* 159, 141–157. doi: 10.1016/s0014-4827(85)80044-6

Teixeira, L. S., Feijen, J., van Blitterswijk, C. A., Dijkstra, P. J., and Karperien, M. (2012). Enzyme-catalyzed crosslinkable hydrogels: emerging strategies for tissue engineering. *Biomaterials* 33, 1281–1290. doi: 10.1016/j.biomaterials.2011.10.067

Thiam, H.-R., Vargas, P., Carpi, N., Crespo, C. L., Raab, M., Terriac, E., et al. (2016). Perinuclear Arp2/3-driven actin polymerization enables nuclear deformation to facilitate cell migration through complex environments. *Nat. Commun.* 7:10997.

Thomas, D. G., Yenepalli, A., Denais, C. M., Rape, A., Beach, J. R., Wang, Y. L., et al. (2015). Non-muscle myosin IIB is critical for nuclear translocation during 3D invasion. *J. Cell Biol.* 210, 583–594. doi: 10.1083/jcb.201502039

Tilghman, R. W., Cowan, C. R., Mih, J. D., Koryakina, Y., Gioeli, D., Slack-Davis, J. K., et al. (2010). Matrix rigidity regulates cancer cell growth and cellular phenotype. *PLoS One* 5:e12905. doi: 10.1371/journal.pone.0012905

Tojkander, S., Gateva, G., and Lappalainen, P. (2012). Actin stress fibers—assembly, dynamics and biological roles. *J. Cell Sci.* 125(Pt 8), 1855–1864. doi: 10.1242/jcs.098087

Tong, X., Jiang, J., Zhu, D., and Yan, F. (2016). Hydrogels with dual gradients of mechanical and biochemical cues for deciphering cell-niche interactions. *ACS Biomater. Sci. Eng.'* 2, 845–852. doi: 10.1021/acsbiomaterials.6b00074

Torrino, S., Roustan, F.-R., Kaminski, L., Bertero, T., Pisano, S., Ambrosetti, D., et al. (2019). UBTD1 is a mechano-regulator controlling cancer aggressiveness. *EMBO Rep.* 20:e46570.

Toth, K. F., Knoch, T. A., Wachsmuth, M., Frank-Stöhr, M., Stöhr, M., Bacher, C. P., et al. (2004). Trichostatin A-induced histone acetylation causes decondensation of interphase chromatin. *J. Cell Sci.* 117, 4277–4287. doi: 10.1242/jcs.01293

Touil, Y., Igoudjil, W., Corvaisier, M., Dessein, A.-F., Vandomme, J., Monté, D., et al. (2014). Colon cancer cells escape 5FU chemotherapy-induced cell death by entering stemness and quiescence associated with the c-Yes/YAP axis. *Clin. Cancer Res.* 20, 837–846. doi: 10.1158/1078-0432.ccr-13-1854

Tripathi, M., Billet, S., and Bhowmick, N. A. (2012). Understanding the role of stromal fibroblasts in cancer progression. *Cell Adh. Migr.* 6, 231–235. doi: 10.4161/cam.20419

Turing, A. (1952). The chemical basis of morphogenesis. *Bull. Math. Biol.* 237, 37–72.

Turley, E. A., Noble, P. W., and Bourguignon, L. Y. (2002). Signaling properties of hyaluronan receptors. *J. Biol. Chem.* 277, 4589–4592. doi: 10.1074/jbc.r100038200

Ulrich, T. A., de Juan Pardo, E. M., and Kumar, S. (2009). The mechanical rigidity of the extracellular matrix regulates the structure, motility, and proliferation of glioma cells. *Cancer Res.* 69, 4167–4174. doi: 10.1158/0008-5472.can-08-4859

Umesh, V., Rape, A. D., Ulrich, T. A., and Kumar, S. (2014). Microenvironmental stiffness enhances glioma cell proliferation by stimulating epidermal growth factor receptor signaling. *PLoS One* 9:e101771. doi: 10.1371/journal.pone.0101771

Unnikrishnan, A., Gafken, P. R., and Tsukiyama, T. (2010). Dynamic changes in histone acetylation regulate origins of DNA replication. *Nat. Struct. Mol. Biol.* 17, 430–437. doi: 10.1038/nsmb.1780

Valentich, J. D., Popov, V., Saada, J. I., and Powell, D. W. (1997). Phenotypic characterization of an intestinal subepithelial myofibroblast cell line. *Am. J. Physiol.* 272, C1513–C1524.

Vallenius, T. (2013). Actin stress fibre subtypes in mesenchymal-migrating cells. *Open Biol.* 3:130001. doi: 10.1098/rsob.130001

Van Helvert, S., and Friedl, P. (2016). Strain stiffening of fibrillar collagen during individual and collective cell migration identified by AFM nanoindentation. *ACS Appl. Mater. Interfaces* 8, 21946–21955. doi: 10.1021/acsami.6b01755

van Helvert, S., Storm, C., and Friedl, P. (2018). Mechanoreciprocity in cell migration. *Nat. Cell Biol.* 20, 8–20. doi: 10.1038/s41556-017-0012-0

Vaughan, L., Tan, C.-T., Chapman, A., Nonaka, D., Mack, N. A., Smith, D., et al. (2015). HUWE1 ubiquitylates and degrades the RAC activator TIAM1 promoting cell-cell adhesion disassembly, migration, and invasion. *Cell Rep.* 10, 88–102. doi: 10.1016/j.celrep.2014.12.012

Vega, S. L., Kwon, M. Y., and Burdick, J. A. (2017). Recent advances in hydrogels for cartilage tissue engineering. *Eur. Cell Mater.* 33, 59–75. doi: 10.22203/ecm.v033a05

Vignjevic, D., Schoumacher, M., Gavert, N., Janssen, K.-P., Jih, G., Laé, M., et al. (2007). Fascin, a novel target of beta-catenin-TCF signaling, is expressed at the invasive front of human colon cancer. *Cancer Res.* 67, 6844–6853. doi: 10.1158/0008-5472.can-07-0929

Vogel, W., Gish, G. D., Alves, F., and Pawson, T. (1997). The discoidin domain receptor tyrosine kinases are activated by collagen. *Mol. Cell* 1, 13–23. doi: 10.1016/s1097-2765(00)80003-9

Wakayama, Y., Fukuhara, S., Ando, K., Matsuda, M., and Mochizuki, N. (2015). Cdc42 mediates Bmp-induced sprouting angiogenesis through Fmnl3-driven assembly of endothelial filopodia in zebrafish. *Dev. Cell* 32, 109–122. doi: 10.1016/j.devcel.2014.11.024

Walter, M., Liang, S., Ghosh, S., Hornsby, P. J., and Li, R. (2009). Interleukin 6 secreted from adipose stromal cells promotes migration and invasion of breast cancer cells. *Oncogene* 28, 2745–2755. doi: 10.1038/onc.2009.130

Wang, D., Narula, N., Azzopardi, S., Smith, R. S., Nasar, A., Altorki, N. K., et al. (2016). Expression of the receptor for hyaluronic acid mediated motility (RHAMM) is associated with poor prognosis and metastasis in non-small cell lung carcinoma. *Oncotarget* 7, 39957–39969. doi: 10.18632/oncotarget.9554

Wang, N., Naruse, N., Stamenović, D., Fredberg, J. J., Mijailovich, S. M., Tolić-Nørrelykke, I. M., et al. (2001). Mechanical behavior in living cells consistent with the tensegrity model. *Proc. Natl. Acad. Sci. U.S.A.* 98, 7765–7770. doi: 10.1073/pnas.141199598

Wang, W., Eddy, R., and Condeelis, J. (2007). The cofilin pathway in breast cancer invasion and metastasis. *Nat. Rev. Cancer* 7, 429–440. doi: 10.1038/nrc2148

Wang, Z., Wu, Y., Wang, H., Zhang, Y., Mei, L., Fang, X., et al. (2014). Interplay of mevalonate and Hippo pathways regulates RHAMM transcription via YAP to modulate breast cancer cell motility. *Proc Natl Acad Sci U.S.A* 111, E89–E98.

Weaver, V. M., Lelièvre, S., Lakins, J. N., Chrenek, M. A., Jones, J. C. R., Giancotti, F., et al. (2002). Beta4 integrin-dependent formation of polarized three- dimensional architecture confers resistance to apoptosis in normal and malignant mammary epithelium. *Cancer Cell* 2, 205–216. doi: 10.1016/s1535-6108(02)00125-3

Wie, S. C., Fattet, L., Tsai, J. H., Guo, Y., Pai, V. H., Majeski, H. E., et al. (2015). Matrix stiffness drives epithelial-mesenchymal transition and tumour metastasis through a TWIST1-G3BP2 mechanotransduction pathway. *Nat. Cell Biol.* 17, 678–688. doi: 10.1038/ncb3157

Willis, A. L., Sabeh, F., Li, X.-Y., and Weiss, S. J. (2013). Extracellular matrix determinants and the regulation of cancer cell invasion stratagems. *J. Microsc.* 251, 250–260. doi: 10.1111/jmi.12064

Winograd-Katz, S. E., Brunner, M. C., Mirlas, N., and Geiger, B. (2011). Analysis of the signaling pathways regulating Src-dependent remodeling of the actin cytoskeleton. *Eur. J. Cell Biol.* 90, 143–156. doi: 10.1016/j.ejcb.2010.07.006

Wolf, K., Mazo, I., Leung, H., Engelke, K., von Andrian, U. H., Deryugina, E. I., et al. (2003). Compensation mechanism in tumor cell migration: mesenchymal-amoeboid transition after blocking of pericellular proteolysis. *J. Cell Biol.* 160, 267–277.

Wolf, K., Te Lindert, M., Krause, M., Alexander, S., Te Riet, J., Willis, A. L., et al. (2013). Physical limits of cell migration: control by ECM space and nuclear deformation and tuning by proteolysis and traction force. *J. Cell Biol.* 201, 1069–1084. doi: 10.1083/jcb.201210152

Wolf, K., Wu, Y. I., Liu, Y., Geiger, J., Tam, E., Overall, C., et al. (2007). Multi-step pericellular proteolysis controls the transition from individual to collective cancer cell invasion. *Nat. Cell Biol.* 9, 893–904. doi: 10.1038/ncb1616

Worth, D. C., Hodivala-Dilke, K., Robinson, S. D., King, S. J., Morton, P. E., Gertler, F. B., et al. (2010). Alpha v beta3 integrin spatially regulates VASP and RIAM to control adhesion dynamics and migration. *J. Cell Biol.* 189, 369–383. doi: 10.1083/jcb.200912014

Wozniak, M. A., Modzelewska, K., Kwong, L., and Keely, P. J. (2004). Focal adhesion regulation of cell behavior. *Biochim. Biophys. Acta* 1692, 103–119.

Wu, J., Kent, I., Shekhar, N., Chancellor, T. J., Mendonca, A., Dickinson, R., et al. (2014). Actomyosin pulls to advance the nucleus in a migrating tissue cell. *Biophys. J.* 106, 7–15. doi: 10.1016/j.bpj.2013.11.4489

Wu, Z., Plotnikov, S. V., Moalim, A. Y., Waterman, C. M., and Liu, J. (2017). two distinct actin networks mediate traction oscillations to confer focal adhesion. *Mechanosensing Biophys. J.* 112, 780–794. doi: 10.1016/j.bpj.2016.12.035

Xiong, J.-P., Stehle, T., Zhang, R., Joachimiak, A., Frech, M., Goodman, S. L., et al. (2002). Crystal structure of the extracellular segment of integrin alpha

Vbeta3 in complex with an Arg-Gly-Asp ligand. *Science* 296, 151–155. doi: 10.1126/science.1069040

Yamaguchi, H., Lorenz, M., Kempiak, S., Sarmiento, C., Coniglio, S., Symons, M., et al. (2005). Molecular mechanisms of invadopodium formation: the role of the N-WASP-Arp2/3 complex pathway and cofilin. *J. Cell Biol.* 168, 441–452.

Yang, G., Zhang, X., and Shi, J. (2015). MiR-98 inhibits cell proliferation and invasion of non-small cell carcinoma lung cancer by targeting PAK1. *Int. J. Clin. Exp. Med.* 8, 20135–20145.

Yang, N., Mosher, R., Seo, S., Beebe, D., and Friedl, A. (2011). Syndecan-1 in breast cancer stroma fibroblasts regulates extracellular matrix fiber organization and carcinoma cell motility. *Am. J. Pathol.* 178, 325–335. doi: 10.1016/j.ajpath.2010.11.039

Yap, C. T., Simpson, T. I., Pratt, T., Price, D. J., and Maciver, S. K. (2005). The motility of glioblastoma tumour cells is modulated by intracellular cofilin expression in a concentration-dependent manner. *Cell Motil. Cytoskeleton* 60, 153–165. doi: 10.1002/cm.20053

Ye, S., Liu, Y., Fuller, A. M., Katti, R., Ciotti, G. E., Chor, S., et al. (2020). TGFβ and hippo pathways cooperate to enhance sarcomagenesis and metastasis through the hyaluronan-mediated motility receptor (HMMR). *Mol. Cancer Res.* 18, 560–573. doi: 10.1158/1541-7786.mcr-19-0877

Yu, X., Zech, T., McDonald, L., Gonzalez, E. G., Li, A., Macpherson, I., et al. (2012). N-WASP coordinates the delivery and F- actin-mediated capture of MT1-MMP at invasive pseudopods. *J. Cell Biol.* 199, 527–544. doi: 10.1083/jcb.201203025

Yuzhalin, A. E., Gordon-Weeks, A. N., Tognoli, M. L., Jones, K., Markelc, B., Konietzny, R., et al. (2018a). Colorectal cancer liver metastatic growth depends on PAD4-driven citrullination of the extracellular matrix. *Nat. Commun.* 9:4783.

Yuzhalin, A. E., Urbonas, T., Silva, M. A., Muschel, R. J., and Gordon-Weeks, A. N. (2018b). A core matrisome gene signature predicts cancer outcome. *Br. J. Cancer* 118, 435–440. doi: 10.1038/bjc.2017.458

Zambonin-Zallone, A., Teti, A., Grano, M., Rubinacci, A., Abbadini, M., Gaboli, M., et al. (1989). Immunocytochemical distribution of extracellular matrix receptors in human osteoclasts: a beta 3 integrin is colocalized with vinculin and talin in the podosomes of osteoclastoma giant cells. *Exp. Cell Res.* 182, 645–652. doi: 10.1016/0014-4827(89)90266-8

Zanconato, F., Cordenonsi, M., and Piccolo, S. (2016). YAP/TAZ at the roots of cancer. *Cancer Cell* 29, 783–803. doi: 10.1016/j.ccell.2016.05.005

Zhao, B., Li, L., Tumaneng, K., Wang, C. Y., and Guan, K. L. (2010). A coordinated phosphorylation by Lats and CK1 regulates YAP stability through SCF(beta-TRCP). *Genes Dev.* 24, 72–85. doi: 10.1101/gad.1843810

Zhao, W., Jin, X., Cong, Y., Lui, Y., and Fu, J. (2013). Degradable natural polymer hydrogels for articular cartilage tissue engineering. *J. Chem. Technol. Biotechnol.* 88, 327–339. doi: 10.1002/jctb.3970

Zhao, Y., Khanal, P., Savage, P., She, Y. M., Cyr, T. D., and Yang, X. (2014). YAP-induced resistance of cancer cells to antitubulin drugs is modulated by a Hippo-independent pathway. *Cancer Res.* 74, 4493–4503. doi: 10.1158/0008-5472.can-13-2712

Zhu, G. G., Risteli, L., Mäkinen, M., Risteli, J., Kauppila, A., and Stenbäck, F. (1995). Immunohistochemical study of type I collagen and type I pN-collagen in benign and malignant ovarian neoplasms. *Cancer* 75, 1010–1017. doi: 10.1002/1097-0142(19950215)75:4<1010::aid-cncr2820750417>3.0.co;2-o

Zou, X., Feng, B., Dong, T., Yan, G., Tan, B., Shen, H., et al. (2013). Upregulation of type I collagen during tumorigenesis of colorectal cancer revealed by quantitative proteomic analysis. *J. Proteomics* 94, 473–485. doi: 10.1016/j.jprot.2013.10.020

Conflict of Interest: The author declares that the research was conducted in the absence of any commercial or financial relationships that could be construed as a potential conflict of interest.

frontiers in Cell and Developmental Biology

ORIGINAL RESEARCH
published: 15 October 2020
doi: 10.3389/fcell.2020.575227

Syndecan-4 Modulates Cell Polarity and Migration by Influencing Centrosome Positioning and Intracellular Calcium Distribution

*Daniel Becsky[1†], Kitti Szabo[1†], Szuzina Gyulai-Nagy[1], Tamas Gajdos[2], Zsuzsa Bartos[3], Arpad Balind[4], Laszlo Dux[1], Peter Horvath[4], Miklos Erdelyi[2], Laszlo Homolya[3] and Aniko Keller-Pinter[1]**

[1] Department of Biochemistry, Faculty of Medicine, University of Szeged, Szeged, Hungary, [2] Department of Optics and Quantum Electronics, Faculty of Science and Informatics, University of Szeged, Szeged, Hungary, [3] Institute of Enzymology, Research Centre for Natural Sciences, Hungarian Academy of Sciences Center of Excellence, Budapest, Hungary, [4] Institute of Biochemistry, Biological Research Centre, Hungarian Academy of Sciences, Szeged, Hungary

Efficient cell migration requires cellular polarization, which is characterized by the formation of leading and trailing edges, appropriate positioning of the nucleus and reorientation of the Golgi apparatus and centrosomes toward the leading edge. Migration also requires the development of an asymmetrical front-to-rear calcium (Ca^{2+}) gradient to regulate focal adhesion assembly and actomyosin contractility. Here we demonstrate that silencing of syndecan-4, a transmembrane heparan sulfate proteoglycan, interferes with the correct polarization of migrating mammalian myoblasts (i.e., activated satellite stem cells). In particular, syndecan-4 knockdown completely abolished the intracellular Ca^{2+} gradient, abrogated centrosome reorientation and thus decreased cell motility, demonstrating the role of syndecan-4 in cell polarity. Additionally, syndecan-4 exhibited a polarized distribution during migration. Syndecan-4 knockdown cells exhibited decreases in the total movement distance during directional migration, maximum and vectorial distances from the starting point, as well as average and maximum cell speeds. Super-resolution direct stochastic optical reconstruction microscopy images of syndecan-4 knockdown cells revealed nanoscale changes in the actin cytoskeletal architecture, such as decreases in the numbers of branches and individual branch lengths in the lamellipodia of the migrating cells. Given the crucial importance of myoblast migration during embryonic development and postnatal muscle regeneration, we conclude that our results could facilitate an understanding of these processes and the general role of syndecan-4 during cell migration.

Keywords: syndecan-4, proteoglycan, cell polarity, super-resolution microscopy, actin, calcium, centrosome, cell migration

OPEN ACCESS

Edited by:
Claudia Tanja Mierke, Leipzig University, Germany

Reviewed by:
Shihuan Kuang, Purdue University, United States
Rosario Donato, University of Perugia, Italy

****Correspondence:***
Aniko Keller-Pinter
keller.aniko@med.u-szeged.hu

† These authors have contributed equally to this work

Specialty section:
This article was submitted to Cell Adhesion and Migration, a section of the journal Frontiers in Cell and Developmental Biology

Received: *22 June 2020*
Accepted: *17 August 2020*
Published: *15 October 2020*

Citation:
Becsky D, Szabo K, Gyulai-Nagy S, Gajdos T, Bartos Z, Balind A, Dux L, Horvath P, Erdelyi M, Homolya L and Keller-Pinter A (2020) Syndecan-4 Modulates Cell Polarity and Migration by Influencing Centrosome Positioning and Intracellular Calcium Distribution. Front. Cell Dev. Biol. 8:575227. doi: 10.3389/fcell.2020.575227

INTRODUCTION

Cell migration is a fundamentally important factor in various physiological and pathological processes, including morphogenesis, immune surveillance, tissue regeneration, and cancer cell metastasis (Ridley et al., 2003). Cell motility and directed migration require the establishment of cell polarization, defined as the formation of distinct front and rear cellular areas. This process is characterized by the emergence of an actin-mediated lamellipodial membrane protrusion, which

forms the leading edge, as well as the development of a retracting tail. The leading edge protrusions depend on polarized intracellular signaling processes. Polarization is also defined by the positioning of the cell nucleus and reorientation of the Golgi network and microtubule organizing center toward the leading edge (Vicente-Manzanares et al., 2005; Zhang and Wang, 2017). Cell motility is orchestrated by the formation of integrin-dependent adhesions to the surrounding matrix and the detachment of these adhesions from distinct regions at the rear of the cell (Lauffenburger and Horwitz, 1996; Ridley et al., 2003). These mechanisms direct the cell motility cycle and are required for cell migration in response to various factors. However, the mechanism by which this motility system integrates extracellular signals with cell polarity and cytoskeletal remodeling to promote directionally persistent migration remains unclear.

Calcium (Ca^{2+}) has been identified as an essential factor in cell migration. Ca^{2+} forms an increasing front–rear gradient that is involved in the disassembly of focal adhesions and, consequently, the rear-end retraction and the movement of the cell. This essential front–rear polarity is maintained by restricting the spontaneous formation of lamellipodia at the trailing edges of migrating cells (Tsai et al., 2015; Kim et al., 2016). The steering of membrane protrusions is directed by a localized Ca^{2+} influx created by stretch-activated Ca^{2+} channels in the front of a migrating cell, whereas other types of Ca^{2+} influx have been reported to mediate the detachment of rear protrusions (Kim et al., 2016). However, previous reports describing the coordination of cell migration by the Ca^{2+} gradient have provided limited insights into cell motility and the formation of these gradients.

Syndecans are a family of four transmembrane proteoglycans, each of which comprises a variable N-terminal ectodomain, a highly conserved short transmembrane and a C-terminal cytoplasmic domains (Zimmermann and David, 1999). Three syndecans are distributed in a tissue-specific manner (Xian et al., 2010; Elfenbein and Simons, 2013): syndecan-1 is mainly present in epithelial cells, syndecan-2 is expressed in mesenchymal cell types and developing neural tissues, whereas syndecan-3 is present in neural tissues and the developing musculoskeletal system. In contrast, syndecan-4 is expressed ubiquitously (Xian et al., 2010). Usually, the ectodomains of syndecans contain three heparan sulfate chains attached to a serine residue via tetrasaccharide linkers (Carey, 1997), although syndecan-1 and syndecan-3 possess additional chondroitin sulfate chains. The interactions of the ectodomain with extracellular matrix molecules, fibronectin, matrix metalloproteinases, growth factors and other cell surface receptors (e.g., integrins) activate downstream signaling pathways. The cytoplasmic domain comprises a variable region unique to each member of the syndecan family, as well as two conserved regions that interact with four-point-one, ezrin, radixin, and moesin (FERM) proteins; Src kinase; and cortactin (Granes et al., 2003). In syndecan-4, the variable region binds and activates the catalytic domain of protein kinase C α (PKCα) (Koo et al., 2006), as well as directly binds α-actinin in a beta-integrin-independent manner (Greene et al., 2003). The ability of syndecan-4 to link the extracellular matrix and cytoskeleton enables this proteoglycan to contribute to several outside-in and inside-out signaling events, such as the sequestration and concentration of matrix components, as well as effects on cell–matrix adhesion, endocytosis, exosome biogenesis or cytokinesis (Keller-Pinter et al., 2010; Elfenbein and Simons, 2013; Afratis et al., 2017). Syndecan-4 also regulates the activity of the small GTPase Rac1 (Bass et al., 2007; Keller-Pinter et al., 2017) and the level of intracellular Ca^{2+} (Liu et al., 2012; Gopal et al., 2015), and contributes to the phosphorylation of focal adhesion kinase (FAK) (Wilcox-Adelman et al., 2002).

Syndecans play an important role in tissue regeneration (Chung et al., 2016). For example, the skeletal muscle is renewed constantly in response to injury, exercise or muscle diseases. During the repair process, activated stem (i.e., satellite) cells form myoblasts that proliferate, migrate to the injured site, differentiate and fuse into polynuclear myotubes (Schultz and McCormick, 1994; Hawke and Garry, 2001). Syndecan-4 is a cell surface marker of both quiescent and proliferating satellite cells (Cornelison et al., 2001). Although syndecan-4 knockout mice cannot regenerate damaged muscle tissue (Cornelison et al., 2004), the details of the underlying mechanism remain unknown. Previously, we reported that syndecan-4 affects myoblast proliferation by modulating myostatin signaling and the G1/S transition in cell cycle (Keller-Pinter et al., 2018), and directional persistence of random cell migration is affected by syndecan-4-mediated Tiam-1 expression and distribution (Becsky et al., 2020). In this study, we demonstrated that syndecan-4 knockdown induced nanoscale alterations in the lamellipodial actin fiber structure of migrating myoblasts. Moreover, we found that syndecan-4 distributes asymmetrically during cell migration and determines cellular polarity by influencing the positioning of centrosomes and the development of the front–rear Ca^{2+} gradient. Although several previous reports have described a role for syndecan-4 in cell migration, here we present a super-resolution structure of the actin cytoskeleton. Moreover, this is the first report to describe the role of syndecan-4 in the development of the Ca^{2+} gradient and centrosome positioning in a migrating cell.

MATERIALS AND METHODS

Cell Culture and Plasmids

C2C12 mouse myoblast cells (ATCC; Manassas, VA, United States) were cultured in high-glucose Dulbecco's modified Eagle's medium containing 4.5 g/L glucose, 584 mg/L glutamine and 110 mg/L pyruvate (Corning, NY, United States) supplemented with 65 μg/mL gentamicin (Lonza, Basel, Switzerland), and 20% fetal bovine serum (Gibco/Thermo Fisher Scientific, Waltham, MA, United States). To achieve syndecan-4 knockdown, C2C12 cells were transfected stably with plasmids expressing short hairpin RNAs (shRNAs) specific for mouse syndecan-4 (shSDC4#1 and shSDC4#2) or a scrambled target sequence. The plasmids were obtained from OriGene (TR513122; Rockville, MD, United States) and targeted the following sequences: 5'-GAA CTG GAA GAG AAT GAG GTC ATT CCT AA-3' (shSDC4#1), 5'-GCG GCG TGG TAG GCA TCC TCT TTG CCG TT-3' (shSDC4#2) and 5'-GCA CTA

CCA GAG CTA ACT CAG ATA GTA CT-3' (scrambled). X-tremeGENE transfection reagent (Roche, Basel, Switzerland) was used for the transfection procedures. Transfected cells were then selected in medium containing 4 μg/mL puromycin (Sigma-Aldrich, St. Louis, MO, United States).

Time-Lapse Imaging of Live Cells

Cells were seeded into the reservoirs of 2-well cell culture silicon inserts at a density of 3×10^4 cells/well (Ibidi, Martinsried, Germany). The inserts were designed to ensure directional cell migration, with a defined cell-free gap of 500 μm. Upon cellular attachment, the medium was replaced with serum-reduced medium for 24 h to suppress cell division. After nuclear staining with Hoechst 33342 (0.5 μg/mL) for 1 h and washing with PBS, the insert was removed and the migration of cells into the cell-free zone was screened. Time-lapse images were captured in 20 min intervals for 8 h at 37°C and 5% CO_2 using the PerkinElmer Operetta (PerkinElmer, Inc., Waltham, MA, United States) high-content imaging system with a 20 × objective (20 × long WD; NA = 0.45, working distance: 7.8 mm; field of view: 675 × 509; depth of focus: 4.6 μm; optical xy resolution: 0.7 μm).

Single-Cell Tracking of Cultured Myoblasts

Time-lapse microscopy was used to quantify the migratory parameters. Single cells were tracked manually from frame to frame using the ImageJ (National Institutes of Health, Bethesda, MD, United States)[1] and CellTracker[2] (Piccinini et al., 2016) software programs. Nuclear tracking was used to follow the migration of individual cells. Dying or damaged cells were excluded from the analysis. The length of total path, maximum distance from the origin, as well as the average and maximum cell speeds were calculated. The vectorial distance of migration (i.e., real shift of the cell) from the origin was also quantified. Individual migratory tracks into the cell-free zone were visualized.

Wound Scratch Assay

For the wound scratch assay, cells were grown in 6-well plates until they reached confluence. After 24 h incubation in serum-reduced medium, cell-free zones were created by scratching the cell layer with a P200 pipette tip. Images of the cell-free zone were captured immediately (0 h), 4 and 8 h after wounding, using a Leica DMi1 phase-contrast microscope (Leica Microsystems, Wetzlar, Germany). Between imaging periods, the cells were incubated at 37°C and 5% CO_2. The area of the cell-free zone was measured using Digimizer image analysis software (MedCalc Software bvba, Ostend, Belgium). The closure of the cell-free area was calculated as follows: (area of cell-free zone at t_{0h} - area of cell-free zone at t_{xh})/area of cell-free zone at t_{0h}.

Fluorescence Staining

For fluorescence cytochemistry, the cells subjected to wounding were fixed at indicated time points, stained with fluorescence markers, and studied to evaluate the migratory cells in the scratched area. For centrosome staining, cells were fixed with methanol 2, 4, and 6 h after scratching. After permeabilization with 0.5% Tween-20 (Sigma-Aldrich), the samples were blocked in 4% bovine serum albumin (BSA; Sigma-Aldrich), and stained with a mouse monoclonal anti-γ-tubulin antibody (1:200; Sigma-Aldrich) at 4°C overnight, followed by incubation with an Alexa Fluor 488-conjugated anti-mouse secondary antibody (Jackson ImmunoResearch, Cambridgeshire, United Kingdom) a day later.

To visualize the actin filaments, cells subjected to the above-described scratch assay were fixed with a methanol-free 4% formaldehyde solution (Thermo Fischer Scientific) 2 h after wounding. After permeabilization with 0.3% Triton X-100 (Sigma-Aldrich) and blocking in 4% BSA (Sigma-Aldrich), the actin filaments were stained with Alexa Fluor 647-conjugated phalloidin (A22287, Thermo Fisher Scientific).

For syndecan-4 immunostaining, myoblasts were fixed with 4% formaldehyde solution 2 h after wounding, permeabilized with 0.3% Triton X-100, and blocked with 1% BSA. Rabbit polyclonal anti-syndecan-4 primary antibody (immunogen: synthetic peptide surrounding amino acid 184 of human syndecan 4; PA1-32485; Invitrogen, Carlsbad, CA, United States) was visualized with the appropriate Alexa Fluor 568-conjugated (Invitrogen), or Alexa Fluor 488-conjugated secondary antibody (Jackson ImmunoResearch, Cambridgeshire, United Kingdom) secondary antibody. For double immunostaining experiments, cells were fixed with 4% formaldehyde solution, permeabilized with 0.1% Triton X-100 and blocked with 3% BSA. Focal adhesions were marked with mouse monoclonal anti-FAK primary antibody (sc-271126; Santa Cruz Biotechnology, Dallas, TX, United States) and with Alexa Fluor 488-conjugated secondary antibody (Jackson ImmunoResearch, Cambridgeshire, United Kingdom). The *cis*-Golgi network was stained by mouse monoclonal anti-GM130 antibody (610822; BD Biosciences, San Jose, CA, United States), and followed by incubation with CF568-conjugated secondary antibody (Biotinum, Fremont, CA, United States). Nuclei were counterstained with Hoechst 33258 (0.01 mg/mL, Sigma-Aldrich).

Quantification of Centrosome Positioning

The positions of centrosomes were analyzed to quantify cell polarity, based on a previous characterization of centrosome reorientation in response to a scratch (Etienne-Manneville and Hall, 2001). Anti-γ-tubulin-stained samples were inspected and imaged using a Nikon Eclipse Ti-E microscope frame (Nikon Instruments Inc., Melville, NY, United States) with epifluorescent illumination using 20 × objective (Nikon Plan fluor 20 × DIC N2, NA = 0.50). The images were analyzed using ImageJ software.

Two hours after wounding, only the migrating cells next to the scratched area were analyzed. For selected cells adjacent to the cell-free zone, the direction of migration was designated as perpendicular to the wound edge, the nucleus was set as the origin, and a 30°circular sector facing the direction of wound closure was assigned. Centrosomes situated within this assigned area were scored as correctly oriented. To monitor the time

[1] https://imagej.nih.gov/ij/

[2] http://celltracker.website/

dependency of centrosome reorientation in different cell lines, the position of centrosomes was analyzed 2, 4, and 6 h after wounding in the 1st and 2nd row of myoblasts in the different cell lines along the wound edge based on the method described by Gotlieb et al. (1983). The position of centrosomes was considered "toward" the wound edge (between the nucleus and the wound edge), "middle" (along the side the nucleus), or "away" (between the nucleus the monolayer behind the cells).

Super-Resolution dSTORM Imaging

Super-resolution direct stochastic optical reconstruction microscopy (dSTORM) measurements were performed using a custom-made inverted microscope based on a Nikon Eclipse Ti-E frame. After conditioning (through spatial filtering via fiber coupling and beam expansion), the applied laser beams were focused into the back focal plane of the microscope objective (Nikon CFI Apo 100 ×, NA = 1.49) to produce a collimated beam on the sample. The angle of illumination was then set through a tilting mirror mounted into a motorized gimbal holder and placed into the conjugate plane of the sample. All dSTORM images were captured under epi-illumination at an excitation wavelength of 634 nm (Thorlabs HL63133DG: 637 nm, P_{max} = 170 mW in a Thorlabs TCLDM9 TE-Cooled mount set to 19°C). The laser intensity was controlled via a Thorlabs LDC500 laser driver and set to an output of 2–4 kW/cm^2 on the sample plane. An additional laser (Nichia: 405 nm, P_{max} = 60 mW) was used for reactivation. Images were captured using an Andor iXon3 897 BV EMCCD digital camera (512 pixels × 512 pixels; pixel size: 16 μm). The size of the illuminated sample region was matched to the size of the detector, which determined the field of view (80 × 80 μm^2). Typically, the frame stacks for dSTORM super-resolution images were captured at a reduced image size (i.e., crop mode). A fluorescence filter set (Semrock, LF405/488/561/635-A-000 dichroic mirror with a BLP01-647R-25 emission filter) was used to select and separate the excitation and emission lights in the microscope. During measurements, the perfect focus system of the microscope was used to maintain focus on the sample at a precision level of < 30 nm. Immediately before measurement, the sample storage buffer was replaced with a GLOX switching buffer (van de Linde et al., 2011), and the sample was mounted on a microscope slide. During a typical imaging session, 20,000 frames were captured at an exposure time of 20 or 30 ms. The image stacks were analyzed using rainSTORM localization software (Rees et al., 2013) and reconstructed using the built-in Simple Histogram method with a super-pixel size of 13.33 nm. The Thompson-precision (Thompson et al., 2002) and PSF size acceptance ranges were set to 0–35 nm and 0.7–1.5 pixels, respectively.

Nanoscale Analysis of the Actin Cytoskeletal Structure

After dSTORM imaging, phalloidin-stained samples were subjected to a nanoscale analysis of the actin cytoskeleton. The dSTORM images of lamellipodial actin structures were processed using ImageJ software. The super-resolution images were converted to grayscale, adjusted to a fixed threshold, and noise filtered. The ImageJ Skeletonize function was used to create binary skeletonized images. Then the Skeleton Analysis plugin was used to calculate the number of branches belonging to each skeleton in every image and to measure the length of each individual branch. To describe the difference between the cortical actin-rich region and the inner actin-depleted area of the lamellipodial actin network, three areas (each 126 × 124 px) were randomly selected in the external region (with a width of 350 px beneath the plasma membrane) and three in the inner, internal region of the lamellipodia. Then the average number of branches and average length of the individual branches were measured in each of these selected rectangles and compared.

Evaluation of Syndecan-4 Immunostaining

Wide-field fluorescence images of syndecan-4 immunostained samples were acquired by a Nikon Eclipse Ti-E microscope (Nikon Instruments Inc.) with 40 × (Nikon CFI Plan Fluor 40 ×, NA = 0.75) and 100 × (Nikon CFI Plan Apo DM Lambda 100 × Oil, NA = 1.45) objectives, and pseudo-colored using ImageJ. The contours of the individual cells were drawn, and the average pixel intensity within the border of the cells were quantified following background correction. The intensity value of each pixel was measured within the selected area and the sum of the intensities was divided by the area of the cell to obtain the average syndecan-4 intensity value of the individual cells. Furthermore, cells were partitioned into 4 quadrants considering the nucleus as the origin, a 90°circular sector facing the direction of the wound closure was assigned, and the syndecan-4 signal intensity within this area was quantified.

Assessment of Intracellular Ca^{2+} Distribution

As control, scrambled and two syndecan-4-targeted myoblast cell lines were seeded onto glass 8-well chambered coverslips (ibidi GmbH, Gräfelfing, Germany) at 1 × 10^4 cells/well density and grown for 24 h in serum-reduced medium. The confluent cultures were scratched as described above and further incubated for 2 h. Subsequently, the cells were subjected to 2 μM Fluo-4 AM and 3 μM Fura Red AM (Thermo Fisher Scientific) in serum-free D-MEM containing 50 μM Verapamil (Sigma) for 30 min at 37°C and 5% CO_2. Verapamil was included to block the activity of multidrug transporters hindering effective dye loading. After several thorough washing steps, the green (493–572 nm) and far red (609–797 nm) fluorescence images were simultaneously acquired at 488 and 458 nm excitations, respectively, using a Zeiss 710 LSM laser scanning fluorescence confocal microscope with a Plan-Apochromat 40 × (N.A. = 1.4) oil immersion objective. The images were analyzed by ImageJ 1.49g software (National Institutes of Health, Bethesda, MD, United States). Ratio images were generated using the Ratio Plus Plug-in. For quantitative analysis, the Fluo-4 and Fura Red fluorescence intensities were determined along the axis of migrating cells starting from the leading edge. After background

correction, ratios of green and red fluorescence were calculated. The slope of the intracellular Ca^{2+} distribution was determined by least squares method.

Statistical Analysis

Differences between groups were analyzed using a one-way ANOVA, followed by the Scheffe *post hoc* test or Student's *t*-test. GraphPad Prism 7.0 (GraphPad Software Inc., San Diego, CA, United States) was used for graphing and statistical analyses. The data are expressed as means + standard errors of the means. A $p < 0.05$ was considered significantly different.

RESULTS

Syndecan-4 Knockdown Decreases Directional Cell Migration

Initially, we evaluated the expression of syndecan-4 in C2C12 myoblasts transfected stably with plasmids expressing shRNA specific for syndecan-4 (shSDC4#1 and SDC4#2 cell lines) using Western blotting technique. A more significant reduction in syndecan-4 expression was observed in shSDC4#1 cells vs. shSDC4#2 cells, whereas the scrambled sequence had no effect on syndecan-4 level (**Supplementary Figure 1**).

We then measured the effect of syndecan-4 knockdown on directional migration *in vitro* into cell-free zones created using cell culture inserts for an 8 h period (**Supplementary Movies 1–4**). During this analysis, we observed significant decreases in the length of total movement, the vectorial distance, the maximum distance from the origin, as well as the average and maximum cell speeds in both the shSDC4#1 and shSDC4#2 cell lines (**Figure 1A**), whereas no significant difference was observed between the non-transfected and scrambled cell lines (**Figure 1A**). Moreover, we observed a greater reduction in migratory parameters in shSDC4#1 cells (**Figure 1**), consistent with the previous observation of greater syndecan-4 suppression in this line. An evaluation of the migratory tracks of individual cells depicts the positions of the x and y coordinates corresponding to the paths taken by each cell during the indicated time (as z; **Figure 1B**). The migratory tracks of highly motile control cells crossed each other in the middle of the cell-free zone (black area in the center of each image), whereas those of syndecan-4 knockdown cells hardly moved from the original x-y positions during the 8 h experimental period. We then prepared histograms to depict the percentages of cells within each velocity range (**Figure 1C**). Notably, the histograms of the non-transfected and scrambled cells formed bell-shaped curves, whereas those of both silenced cell lines exhibited a left-skewed distribution suggesting the higher ratio of less motile cells.

Representative images in **Figure 2A** depict a scratch wound in a confluent culture at 0, 4, and 8 h. Quantification of the wound closures revealed a reduced closure of the cell-free zone in both syndecan-4 knockdown lines (**Figure 2B**). No significant difference was observed between non-transfected and scrambled cells (**Figure 2B**).

Syndecan-4 Affects the Nanoscale Architecture of the Actin Cytoskeleton, as Determined by Super-Resolution dSTORM

Cell motility is regulated by both extracellular factors and internal signaling mechanisms, including actin cytoskeletal remodeling. As syndecan-4 plays a crucial role in the organization of the actin cytoskeleton (Baciu et al., 2000; Elfenbein and Simons, 2013; Cavalheiro et al., 2017), we evaluated actin filaments using wide-field fluorescence microscopy (**Figures 3A,B,D,E,G,H,J,K**) and single-molecule localization super-resolution dSTORM imaging (lower magnification: **Figures 3A,D,G,J**; higher magnification: **Figures 3C,F,I,L**). Notably, our super-resolution dSTORM images reveal the sub-diffraction structure of the actin cytoskeleton and enable a more sophisticated experimental comparison of control and syndecan-4 knockdown samples. The reduced fluorescence background and enhanced resolution enabled visualization of the orientations and densities of individual actin bundles.

Next, wound scratch assays were performed to study the lamellipodial actin networks in migrating cells. To prove the migratory phenotype of the cells next to the cell-free zone, we stained the focal adhesions by anti-FAK antibody in the different cell lines, and FAK-stained focal adhesions were observed at the end of the stress fibers (**Supplementary Figure 2**). Interestingly, both the size and the number of focal adhesions decreased in syndecan-4 knockdown cells (**Supplementary Figure 2**). The cells next to the scratched areas were analyzed after actin filament labeling of the samples. For every sample, a panoramic map of individual wide-field fluorescence images was generated to cover the whole area of cell culture around the scratch wound (**Supplementary Figures 3–6**), and the lamellipodia of the migrating cells next to the wound were analyzed by dSTORM. Representative areas of the panoramic maps are shown in **Figures 3A,D,G,J**. Notably, syndecan-4 silencing altered the organization of the actin cytoskeleton (**Figure 3**) by hindering the development of actin structures (**Figures 3G–L**). The non-transfected and scrambled cells exhibited well-developed actin filaments (**Figures 3A–F**), whereas this filamentous actin cytoskeletal structure was less pronounced, and the lamellipodial actin network was less organized in syndecan-4 knockdown cells (**Figures 3G–L**). Next, dSTORM images of the actin cytoskeleton were converted to binary images (**Figure 4A**) and analyzed further to quantify nanoscale changes in the actin network (**Figure 4B**). An analysis of binary images of the lamellipodial actin filaments (**Figure 4A**) revealed decreases in both the number of branches and the lengths of individual branches in the lamellipodial actin networks of syndecan-4 knockdown cells (**Figure 4C**).

As the binary images suggested the presence of an actin-depleted inner region some micrometers away from the leading edge in syndecan-4 knockdown cell lines, next we quantified the nanoscale changes of the cortical (external) and the inner area of the lamellipodial actin network in the cell lines (**Figure 4D**). Both the average number of

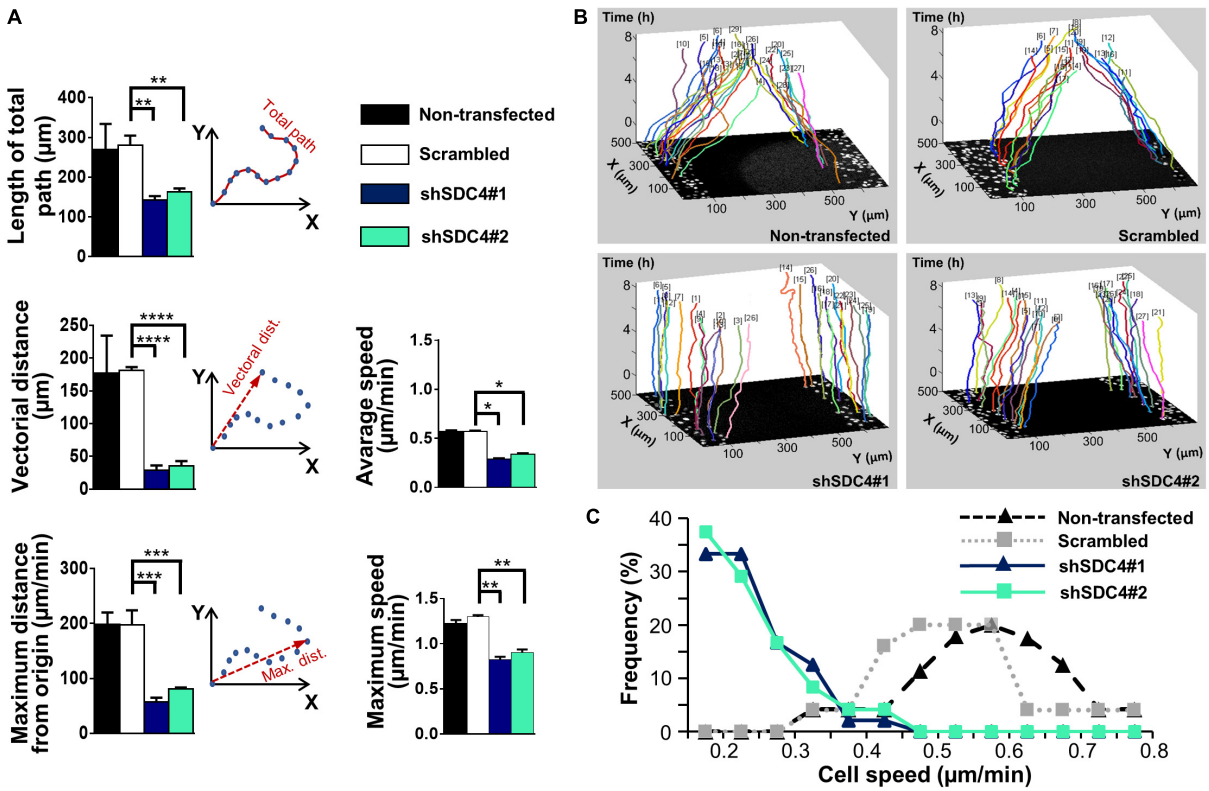

FIGURE 1 | The role of syndecan-4 in the directional migration of myoblasts. **(A)** Migration of non-transfected, scrambled, and syndecan-4-silenced (shSDC4#1 and shSDC4#2) C2C12 myoblasts to a cell-free zone was assessed after the removal of a cell culture insert. The total length of movement, maximum distance from the starting point, vectorial distance (i.e., real displacement of the cells), and the average and maximum cell speeds during directional migration are presented. The total duration of live cell microscopy was 8 h, at a frame rate of 3/1 h. Four independent experiments were conducted, with 60–87 cells/cell line and 5–6 fields of view/experiment. Data are presented as means + standard errors of the means; *$p < 0.05$, **$p < 0.01$, ***$p < 0.001$, and ****$p < 0.0001$. **(B)** Representative three-dimensional migration tracks. Different colors represent the total migrations of individual myoblasts; x and y axes: position of the cell (µm), *z*-axis: time (h). **(C)** Histograms depict the distributions of cells from different lines according to cell speed (intervals of 0.05 µm/min). The frequencies of cells from each line with average speeds within each interval were evaluated and are presented on the *y*-axis.

branches (in each skeleton) and the lengths of individual branches decreased in the inner region as compared to the external region of the lamellipodia in syndecan-4 knockdown cells, indicating the inhomogeneous lamellipodial actin structure in these cells (i.e., actin-rich external region and actin-depleted inner area).

Syndecan-4 Affects Centrosome Positioning and Cell Polarity

Appropriate polarization of the cell (Lauffenburger and Horwitz, 1996), adequate positioning of the cellular compartments (Petrie et al., 2009), and dynamic reconstruction of the actin cytoskeleton (Gardel et al., 2010; Parsons et al., 2010) are required for efficient cell migration. As syndecan-4 silencing was shown to reduce myoblast migration, we next studied the polarization of syndecan-4 knockdown cells using centrosome localization, an indicator of cell polarity in migrating cells (Etienne-Manneville and Hall, 2001; Zhang and Wang, 2017). Specifically, the exact positions of the centrosomes were observed on immunostained samples obtained 2, 4, and 6 h after a wound scratch assay (**Figure 5A**, **Table 1**, and **Supplementary Figures 7–9**). Fluorescence images were captured after centrosome (anti-γ-tubulin) staining and used to generate panoramic maps of the entire scratched area (**Supplementary Figures 7–9**).

Two h after wounding, cells adjacent to the cell-free area were investigated using the nuclei as the points of reference (i.e., origins). The areas around the nuclei were divided into 30° sectors, and centrosomes located in the 30°circular sector facing toward the cell-free area were considered properly oriented (**Figure 5B**). **Figure 5C** depicts the numbers of centrosomes in the various sectors from experiments involving the different cell lines. Notably, syndecan-4 knockdown was associated with significantly fewer centrosomes in the 30°circular sector facing toward the cell-free zone, indicating an improper reorientation of the centrosomes in these cells (**Figures 5C,D**). In contrast, nearly all centrosomes of the scrambled and non-transfected cells were localized to this 30°circular sector facing toward the cell-free area, indicating precise and proper regulation of centrosome positioning in these controls (**Figures 5C,D**). There was no significant difference between the non-transfected and scrambled cells (**Figure 5D**). To analyze the time dependency

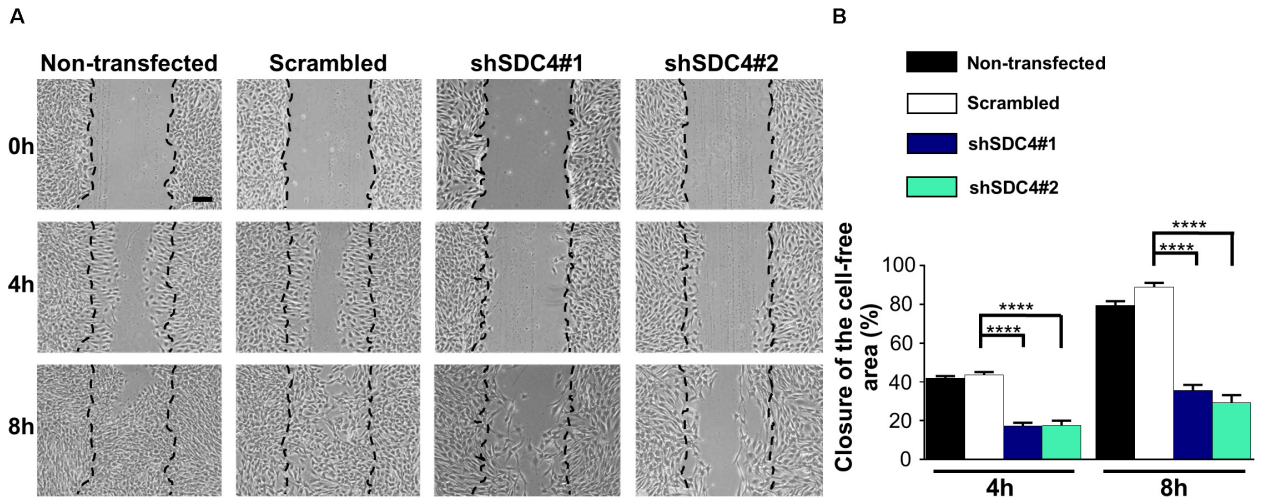

FIGURE 2 | Syndecan-4 influences the closure of the cell-free zone. **(A)** Representative microscopy images taken 0, 4, and 8 h after the initiation of a wound scratch assay. Dashed lines indicate the position of the cell-free zone at 0 h. Scale bar: 200 μm. **(B)** Quantification of the closure of the cell-free area in cultures of non-transfected, scrambled, and syndecan-4-silenced (shSDC4#1 and shSDC4#2) cells; $n = 4$ independent experiments. Data are shown as means + standard errors of the means; $^{****}p < 0.0001$.

of centrosome reorientation, the position of centrosomes was studied 2, 4, and 6 h after wounding (**Table 1**). The number of centrosomes facing the wound edge increased in all cell lines during the 6 h period in both 1st and 2nd row. Analysis of centrosome position along the wound edge revealed that in 83% of the scrambled cells in the first row the centrosomes were located toward the wound edge (between the nucleus and the wound edge) 2 h after wounding and 94% of the cells 6 h following wounding (**Table 1**). In contrast, only 25–27% of the syndecan-4 silenced cells presented centrosomes with "toward" position 6 h after wounding. In scrambled cells, only a few number of cells exhibited "middle" (along the side the nucleus), or "away" (between the nucleus the monolayer behind the cells) localized centrosomes 6 h after scratching. Based on these results, the reorientation of centrosomes during migration is delayed in syndecan-4 knockdown cells.

Polarized Distribution of Syndecan-4 During Migration

The former experiments demonstrated that syndecan-4 influences cellular polarity indicated by the impaired centrosome positioning and migration properties of myoblasts. Next we examined the intracellular distribution of syndecan-4 in control (scrambled) and syndecan-4 silenced cell lines in wide-field fluorescence images. According to immunostaining experiments, the amount of syndecan-4, considering all fluorescence signal intensities, was significantly higher in control cells than in syndecan-4 silenced cell lines (**Figures 6A,B**). Syndecan-4 accumulates in the quadrant of the migrating cells facing the wounded area (**Figure 6A**) which points the direction of migration (**Figure 6C**). Comparing the amount of syndecan-4 accumulated in the quadrant facing the wounded area (**Figure 6C**) to the total of syndecan-4 level of the cells did not depict significant difference between the cell lines (**Figure 6D**). Based on these results, the distribution of syndecan-4 does not change as a result of silencing; only the total amount of syndecan-4 is lower in knockdown cells.

Since the wide-field images showed cytoplasmic syndecan-4 staining, next we performed confocal imaging. The representative confocal image (**Figure 6E**) depicts the weak cell membrane localization of syndecan-4 in a migrating cell. Since earlier we showed the co-localization of syndecan-4 with the anti-GM130 Golgi marker and syndecan-4 is a member of focal adhesions, next we tested the co-distribution of syndecan-4 with FAK and GM130 (**Figures 6F,G**). The observed localization of syndecan-4 in the focal adhesions and *cis*-Golgi (**Figures 6F,G**) can explain the vacuolar and punctate signals of syndecan-4 staining. Moreover, earlier we have shown that the phospho-(Ser179 in human, Ser183 in mouse) syndecan-4 accumulates in the cytoplasm during cytokinesis (Keller-Pinter et al., 2010). Therefore, we cannot exclude, that the syndecan-4 signal in our migrating cells partially originates from the cytoplasmic phosphorylated form.

Syndecan-4 Knockdown Abrogates the Intracellular Ca^{2+} Gradient in Migrating Cells

Normally, migrating cells exhibit a gradual increase in Ca^{2+} levels along the axis of migration. Accordingly, we next assessed the distribution of intracellular Ca^{2+} in syndecan-4-silenced C2C12 cells and compered to that seen in cells transfected with a scrambled target sequence. The front–rear Ca^{2+} distribution was studied in cells adjacent to the cell-free area in a scratch-wounded confluent culture (**Figure 7A**). As expected, the intracellular Ca^{2+} concentration increased from the leading edge to the rear in control scrambled cells in (**Figures 7B,C**). In contrast, this Ca^{2+} gradient was completely abolished in syndecan-4-knockdown cells (**Figures 7B,C**). Since it has been reported that Fura Red

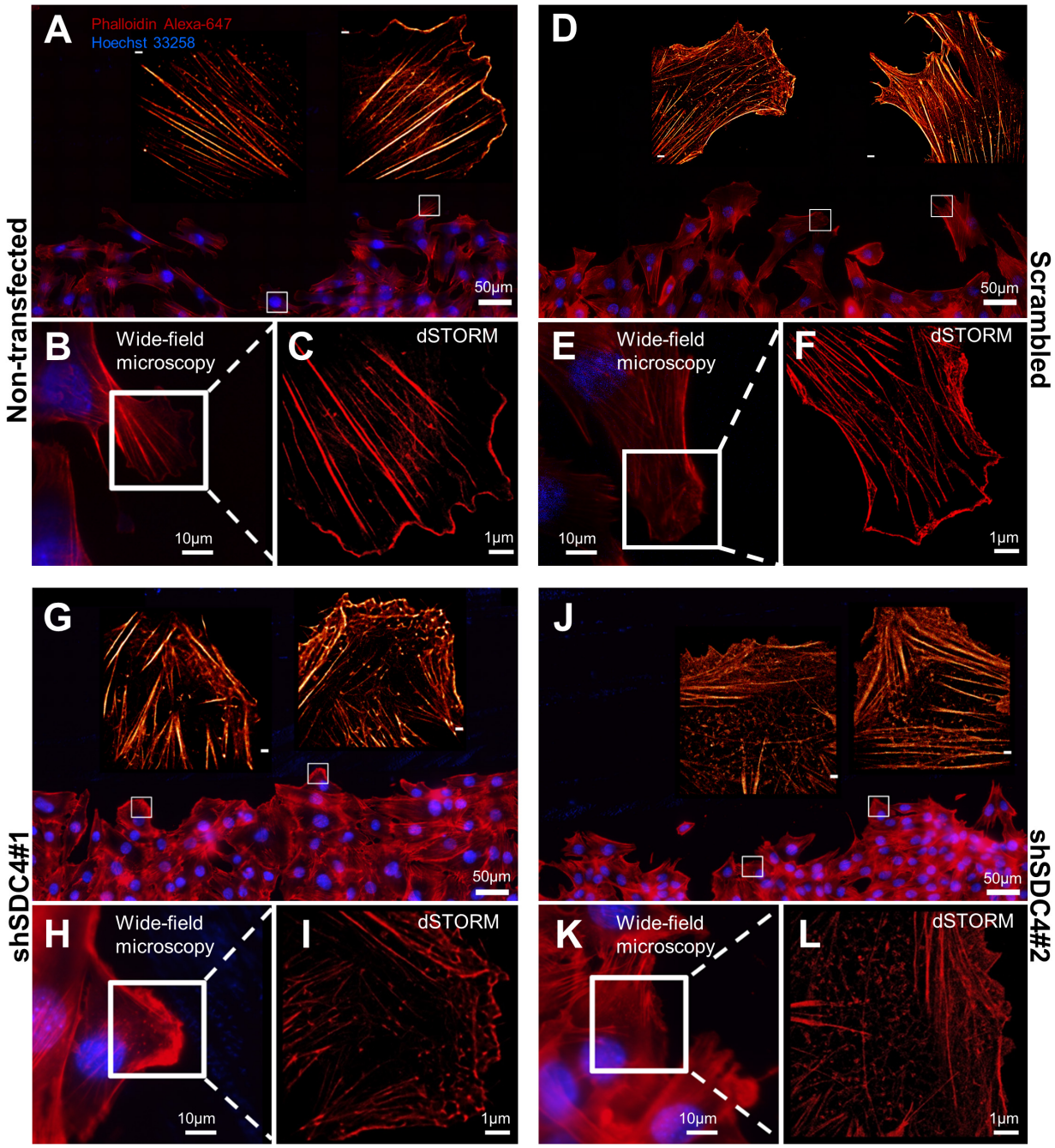

FIGURE 3 | Direct stochastic optical reconstruction microscopy (dSTORM) analysis of the actin cytoskeleton after syndecan-4 silencing. Representative wide-field fluorescence and super-resolution dSTORM images depict the actin skeletons of the cells adjacent to the cell-free zone in cultures of non-transfected **(A–C)**, scrambled **(D–F)**, shSDC4#1 **(G–I),** and shSDC4#2 **(J–L)** cell lines. Confluent monolayers were subjected to wound scratching. The cells were fixed 2 h later, and the actin filaments were stained with Alexa Fluor 647-conjugated phalloidin (red). Wide-field fluorescence images were obtained around the cell-free zone (**A,D,G,J,** higher magnification: **B,E,H,K**). Full panoramic maps of the scratched areas are shown in **Supplementary Figures 3–6**. The insets of the wide-field fluorescence images depict dSTORM images of the lamellipodial regions of migrating cells adjacent to the cell-free zone **(A,B,D,E,G,H,J,K).** Representative dSTORM images of lamellipodial actin structures are embedded in the original low-magnification images (**A,D,G,J**; bar: 1 µm) or are shown in separate higher magnification panels **(C,F,I,L)**. Nuclei are stained by Hoechst 33258 (blue).

tend to accumulate in the mitochondria (Thomas et al., 2000), we explored whether the punctate structures can be observed in the Ca^{2+} indicator-loaded cell are mitochondria. Either control or syndecan-4-silenced cells exhibited distinct distribution for the Ca^{2+} indicators and the mitochondrial dye MitoTracker Deep Red (**Supplementary Figure 10**), demonstrating that neither

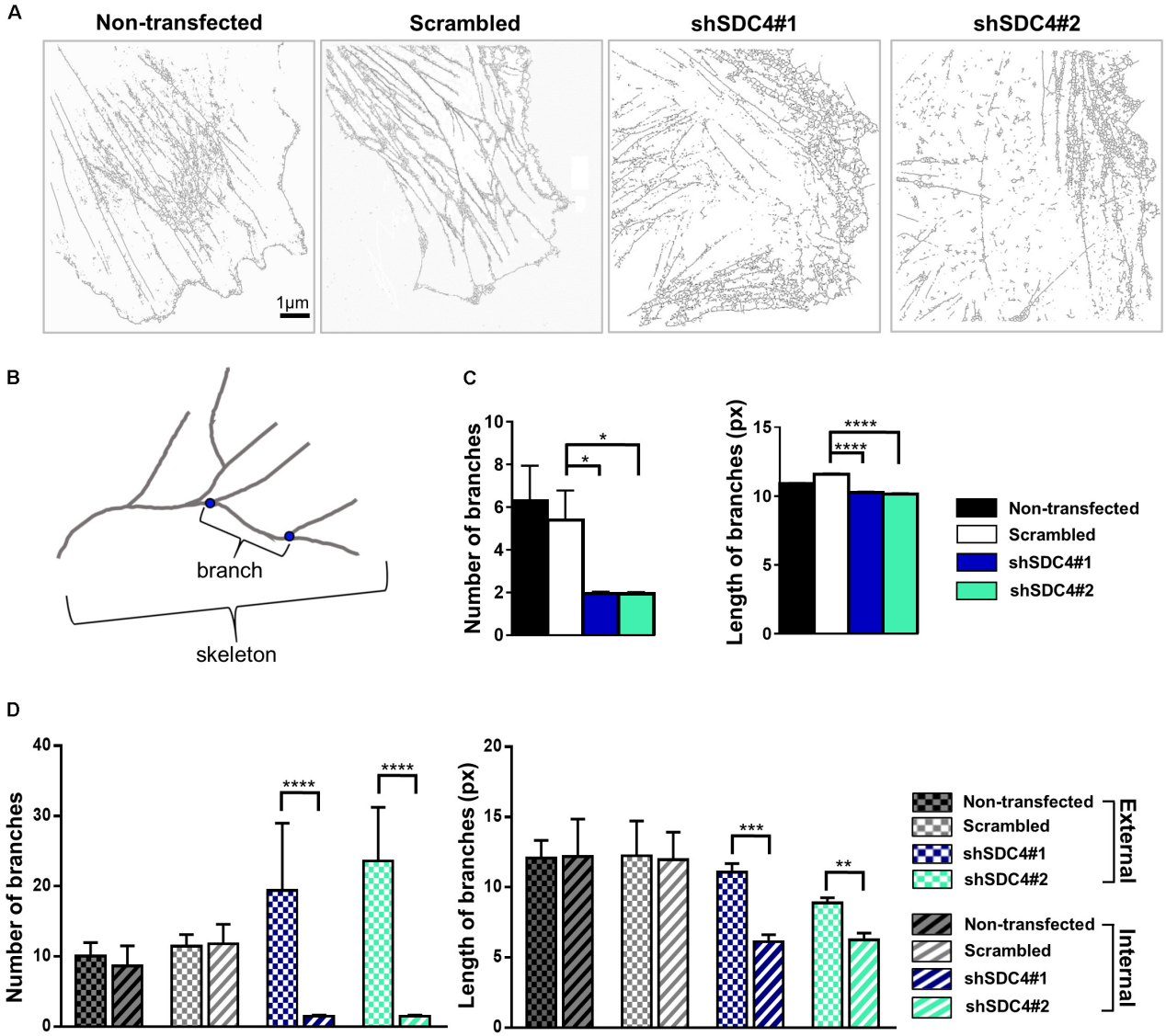

FIGURE 4 | Skeletal analysis of dSTORM images of the lamellipodial actin network. The phalloidin-stained lamellipodial actin cytoskeletons of non-transfected, scrambled, and syndecan-4-silenced (shSDC4#1 and shSDC4#2) cells were analyzed. Representative binary images converted from dSTORM images of the actin cytoskeleton are shown **(A)**. Within the actin network, branching points divide the skeletons into smaller branches **(B)**. The number of branches in the skeletons and the lengths of individual branches in the lamellipodial actin network in the whole binary images were quantified **(C)**. To measure the differences between the external and the internal region of the lamellipodial actin network, the average number and length of branches were compared in randomly selected areas (three areas in both external and internal regions, each 126 × 124 pixels in size) of the binary images **(D)**. Binary images of 5 cells/cell line were studied. Numbers of analyzed skeletons: 5,560–8,450/cell line; numbers of analyzed branches: 26,723–32,813/cell line. Number of analyzed skeletons in a single 126 × 124 pixels area: 2–69, number of analyzed branches in a single 126 × 124 pixels area: 32–336. Data are shown as means + standard errors of the means; $^{*}p < 0.05$, $^{**}p < 0.01$, $^{***}p < 0.001$, and $^{****}p < 0.0001$.

Fluo-4 nor Fura Red accumulated in the mitochondria in our experiments. To exclude the possibility that alteration in the green and red fluorescence ratios is due to redistribution of organelles, in which one Ca^{2+} indicator accumulated more than the other, we performed an analysis, in which high intensity pixels (2.5-fold over mean cellular fluorescence) were omitted. Similar results were obtained this way to that shown in **Figure 7** and **Supplementary Figure 10**, demonstrating that indeed the intracellular front-rear Ca^{2+} gradient was diminished by syndecan-4-silencing. In summary, our findings demonstrate the essential role of syndecan-4 in cell polarity.

DISCUSSION

Cell migration is an essential component of several physiological and pathological processes, including tissue regeneration. During regeneration of the skeletal muscle tissue, myoblasts (i.e.,

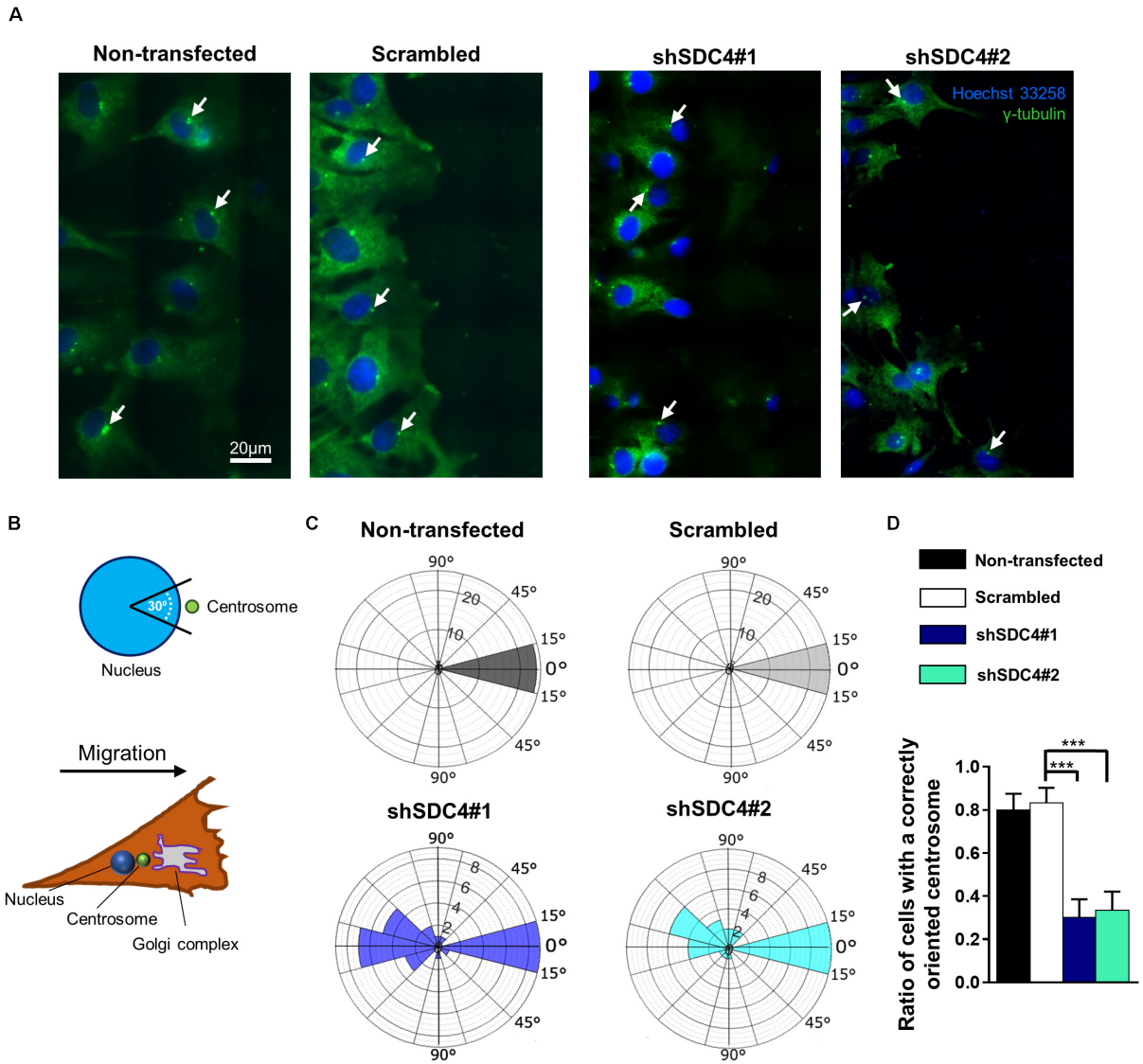

FIGURE 5 | Syndecan-4 affects centrosome positioning during migration. **(A)** Representative wide-field fluorescence images of the studied cell lines depict the positions of centrosomes 2 h after scratching. Anti-γ-tubulin-labeled centrosomes and Hoechst 33258-stained nuclei are shown in green and blue, respectively. Arrows indicate the centrosomes. **(B)** Schematic representation of a polarized migratory cell. To quantify the positions of centrosomes, the nucleus was set as the origin, and centrosomes located in the 30°circular sector facing toward the direction of wound closure were considered properly located. **(C)** Pie charts (i.e., polar histograms) show the localization of centrosomes in different cell lines. The plane was partitioned into 30°circular sectors with the nucleus as the origin. The radius of each circular sector represents the number of cells with centrosomes located in that 30° sector. $N = 3$ independent experiments. Thirty cells were analyzed per cell line. **(D)** Quantification of the results shown in **(C)**. The graph presents the ratios of centrosomes in the 30° sector facing the cell-free area. Data are shown as means + standard errors of the means; ***$p < 0.001$.

activated satellite cells, skeletal muscle stem cells) proliferate, differentiate, migrate and fuse to form tubular, multi-nuclear myotubes. Accordingly, during muscle development and regeneration, myoblasts must be capable of migration to promote the cell–cell interactions and myoblast fusion required for muscle fiber formation. Syndecans, a family of transmembrane proteoglycans, have been reported to play crucial roles in tissue regeneration (Chung et al., 2016). We demonstrated previously that syndecan-4 could influence myoblast proliferation, as syndecan-4 silencing reduced cell cycle progression from the G1 to the S phase and reduced the formation of mature myostatin, a negative regulator of muscle growth (Keller-Pinter et al., 2018). Syndecan-4 knockout mice also exhibited a decreased capacity for skin wound repair and angiogenesis (Echtermeyer et al., 2001), as well as inability to regenerate skeletal muscle following cardiotoxin-induced muscle necrosis (Cornelison et al., 2004). In summary, syndecan-4 appears to play an essential role in skeletal muscle development and regeneration, although the exact mechanism underlying this phenomenon remains unclear

TABLE 1 | Comparison of the effect of syndecan-4 silencing on centrosome reorientation in the 1st and 2nd row of myoblasts along the wound edge.

	Time after scratch											
	2 h				4 h				6 h			
	Non-transfected	Scrambled	shSDC4#1	shSDC4#2	Non-transfected	Scrambled	shSDC4#1	shSDC4#2	Non-transfected	Scrambled	shSDC4#1	shSDC4#2
Toward												
1st	80 ± 4.0	83 ± 1.0	8 ± 1.0	7 ± 1.5	86 ± 2.5	88 ± 1.0	15 ± 1.0	14 ± 2.0	94 ± 4.0	92 ± 3.0	27 ± 3.5	25 ± 3.5
2nd	84 ± 1.5	87 ± 2.5	6 ± 1.5	4 ± 0.5	84 ± 0.5	89 ± 5.0	12 ± 1.0	16 ± 2.0	97 ± 2.0	98 ± 1.5	35 ± 2.5	27 ± 2.5
Middle												
1st	8 ± 1.0	8 ± 1.5	22 ± 2.0	20 ± 3.0	2 ± 4.5	4 ± 2.0	17 ± 2.5	19 ± 3.0	2 ± 2.0	5 ± 1.5	16 ± 1.5	23 ± 1.0
2nd	6 ± 0.5	7 ± 1.0	18 ± 3.0	15 ± 5.5	7 ± 6.5	5 ± 8.0	21 ± 1.0	14 ± 3.0	2 ± 2.5	1 ± 0.5	17 ± 2.5	12 ± 1.5
Away												
1st	12 ± 3.0	9 ± 2.5	70 ± 3.0	73 ± 4.5	12 ± 2.0	8 ± 1.0	71 ± 1.5	67 ± 1.0	4 ± 2.0	3 ± 1.5	57 ± 2.0	52 ± 2.5
2nd	10 ± 1.0	6 ± 1.5	76 ± 1.5	81 ± 5.0	9 ± 6.0	11 ± 3.0	67 ± 2.0	70 ± 1.0	1 ± 0.5	1 ± 1.0	52 ± 5.0	61 ± 1.0

Four independent experiments, n = 100–100 cells/cell lines in each row.

(Cornelison et al., 2004). Moreover, little is known about the specific role of syndecan-4 in mammalian myoblast migration.

Syndecan-4 was shown previously to affect migration in various cell types, including fibroblasts (Bass et al., 2007), endothelial cells (Chaudhuri et al., 2005), and hepatic stellate cells (Yin et al., 2017). This proteoglycan may also contribute to disease development by influencing the migration of tumor cells, such as lung adenocarcinoma (Toba-Ichihashi et al., 2016) and hepatoma (Charni et al., 2009); dendritic cells in the context of allergic rhinitis (Polte et al., 2015) and B-cells in the context of arthritis (Endo et al., 2015). A role for syndecan-4 has also been implicated in trophoblast migration and, consequently, the pathogenesis of preeclampsia (Jeyarajah et al., 2019). Importantly, Shin et al. (2013) reported that syndecan-4 overexpression increased the migration of turkey satellite cells and increased the activation of RhoA GTPase, and these motile phenomena required the cytoplasmic domain of syndecan-4. Other studies observed reduced motility following syndecan-4 knockdown in different cell types, consistent with our current observations, whereas high syndecan-4 level promoted migration (Toba-Ichihashi et al., 2016; Yin et al., 2017; Jeyarajah et al., 2019). Previous analyses of C2C12 mouse myoblast cells revealed that syndecan-4 was the most prominent heparan sulfate proteoglycan in these cells when compared with syndecan-1, syndecan-2, syndecan-3, glypican, or perlecan (Keller-Pinter et al., 2018), thus suggesting an important role for syndecan-4 in this cell type. However, the observed upregulation of syndecan-1, syndecan-2, and syndecan-3 mRNAs after syndecan-4 silencing (Keller-Pinter et al., 2018) suggests that other members of the syndecan family may compensate at least partially for the loss of syndecan-4. Given the importance of syndecan-4 in cell migration and cytoskeletal organization, we hypothesized that this proteoglycan would affect cellular polarity, centrosome positioning, and intracellular Ca^{2+} distribution during cell migration. We recently reported that syndecan-4 affects random migration and the directional persistence of migration in C2C12 cells during 18 h movement (Becsky et al., 2020). Here we show the effect of syndecan-4 silencing on Ca^{2+} distribution, centrosome positioning, and actin nanostructure after 8 h directional migration following wound scratching. Interestingly, the average speed values of the migrating C2C12 cells were similar in the case of both random (Becsky et al., 2020) and directional migration.

Cell polarization and the associated rearrangement of the actin cytoskeleton and cell–matrix relationships are key factors in cell migration. In addition to the integrins, syndecan-4 plays a pivotal role in the formation of focal adhesions. Specifically, syndecan-4 directly binds fibronectin to promote cell adhesions, thereby affecting cell migration, whereas the syndecan-4/PKCα/RhoA signaling axis promotes focal adhesion formation (Matthews et al., 2008; Yin et al., 2017). Furthermore, the downregulation of syndecan-4 was shown to suppress integrin-mediated cell adhesion by inhibiting FAK phosphorylation (Qin et al., 2017). Moreover, the cytoplasmic domain of syndecan-4 interacts directly with α-actinin (Greene et al., 2003), leading to associations with other adhesion molecules, such as vinculin and zyxin (Cavalheiro et al., 2017), as well as the actin cytoskeleton (Choi et al., 2008). In a recent study on endothelial cells, syndecan-4 knockdown was shown to induce the decoupling of vinculin from F-actin filaments (Cavalheiro et al., 2017). Interestingly, the interaction of PKCα and α-actinin with syndecan-4 was shown to be reciprocal (Chaudhuri et al., 2005). Moreover, syndecan-4 has been identified as a binding partner of dynamin II GTPase via its PH domain, and the resultant complex is a key regulator of focal adhesion and stress fiber formation in migrating cells (Yoo et al., 2005). Therefore, syndecan-4 serves as a central mediator in focal adhesion formation by bridging the interactions between integrins, fibronectin and intracellular molecules. Here we showed, that both the number and size of FAK stained focal adhesions were decreased in syndecan-4 knockdown cells during migration. Consequently, the loss of syndecan-4 would affect cell motility via multiple mechanisms, including the observed changes in the lamellipodial actin cytoskeletal structure.

As noted above, intracellular Ca^{2+} plays a crucial role in cell migration. Both Ca^{2+} influx from the extracellular

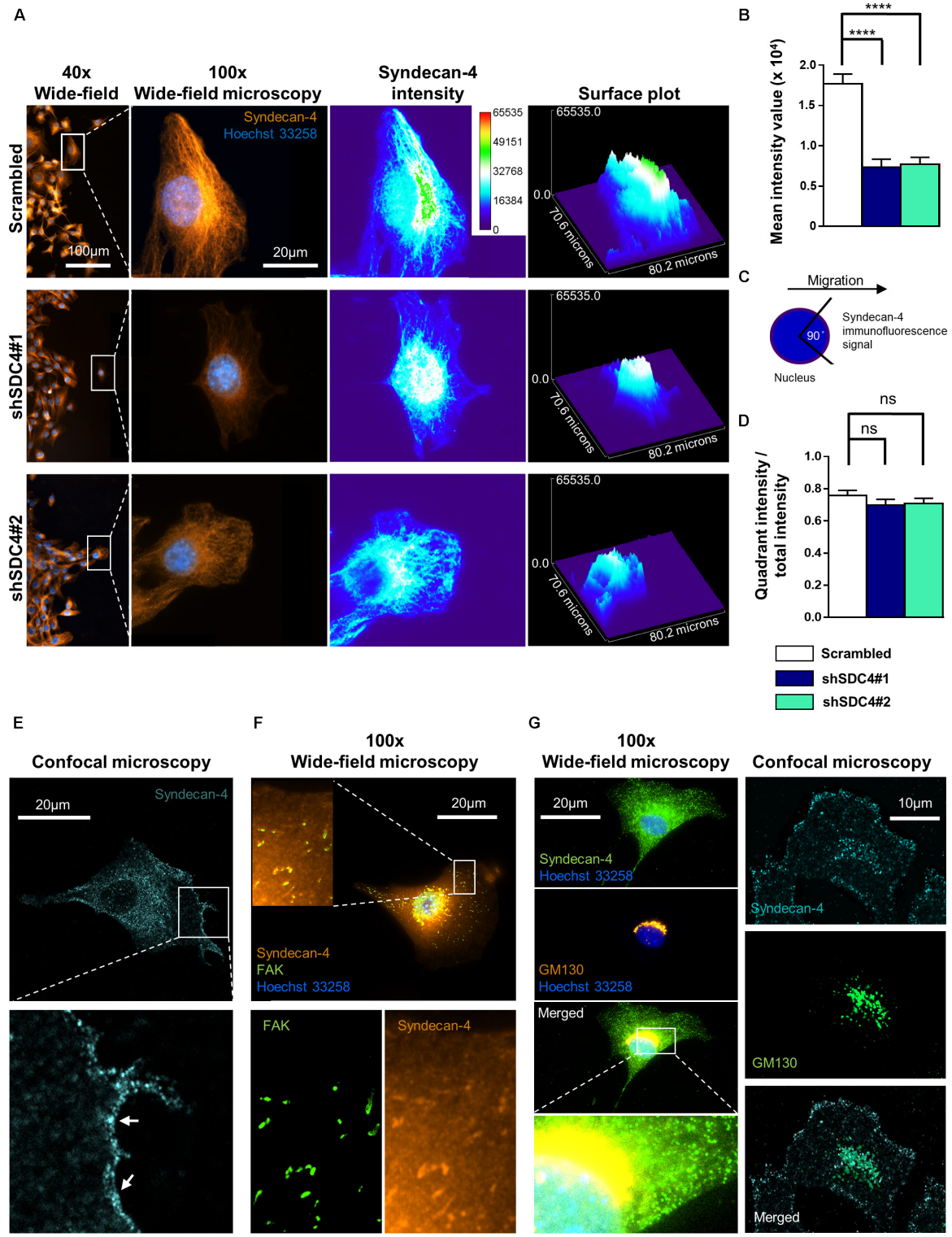

FIGURE 6 | Asymmetric distribution of syndecan-4 in migrating myoblasts. **(A)** Representative images show syndecan-4 distribution following staining with Alexa Fluor 568 fluorophore (orange). Nuclei are stained by Hoechst 33258 (blue). Representative pseudo-color images (2D and 3D) depict syndecan-4 signal intensity as indicated by the calibration bar. **(B)** The mean intensity values of the cells were quantified. **(C)** Cells were partitioned into 4 quadrants considering the nucleus as the origin; and a 90°circular sector facing the direction of the wound closure was assigned and the syndecan-4 signal intensity within this area was quantified. **(D)** The ratio of signal intensity of the quadrant pointing into the direction of migration (see schematic figure, **C**), and the total syndecan-4 intensity of the cell was calculated

(Continued)

FIGURE 6 | Continued
and compared in the different cell lines. Data are reported as means + standard errors of the means, $n = 30$ cells/cell line were analyzed; ns: not significant; ****$p < 0.0001$. **(E)** Representative confocal image depicts the cell membrane localization (arrows) of syndecan-4 in a migrating scrambled cell. **(F)** Representative wide-field fluorescence image of syndecan-4 and FAK staining in a migrating scrambled cell. **(G)** Representative wide-field fluorescence and confocal image of GM130 (*cis*-Golgi marker) and syndecan-4 double staining in migrating scrambled cells.

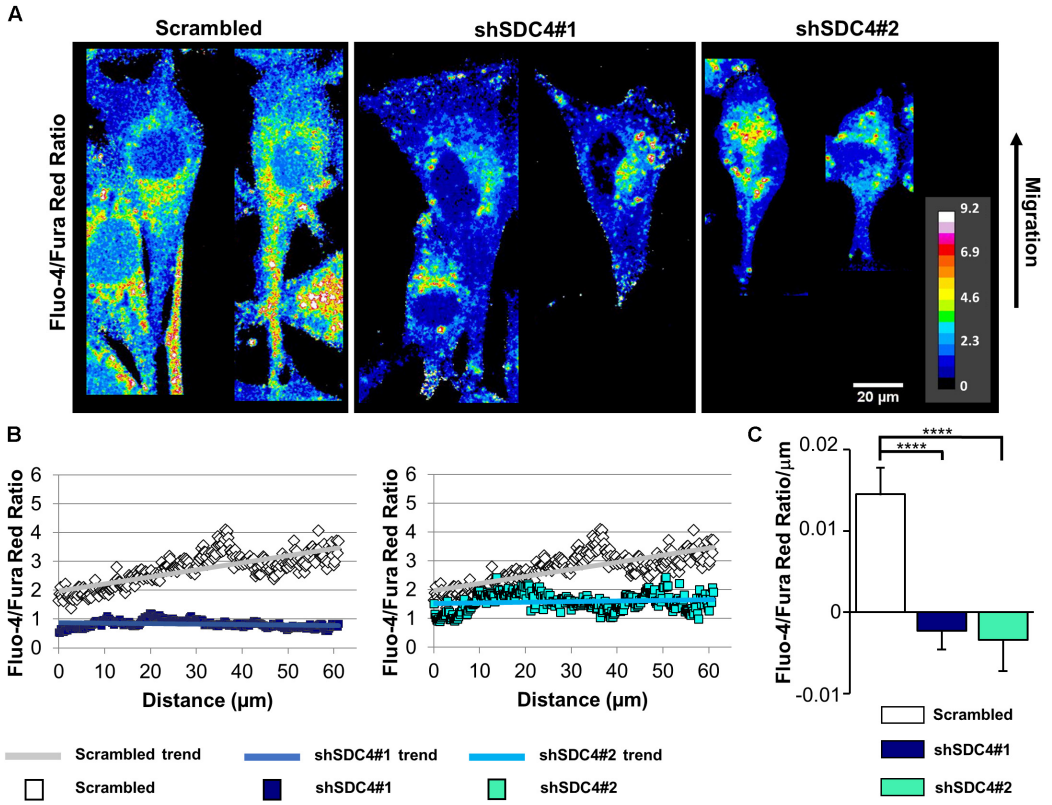

FIGURE 7 | Effect of syndecan-4 silencing on the distribution of intracellular Ca^{2+} in migrating myoblasts. **(A)** The ratio of Fluo-4 and Fura Red fluorescence, an indicator of the intracellular Ca^{2+} level, is shown in the representative pseudo-color images of scrambled, shSDC4#1, and shSDC4#2 cells. **(B)** The ratio of Fluo-4 and Fura Red fluorescence was determined along the migration axis from the leading edge to the rear of cells following scratch wounding. The mean fluorescence ratios are presented as a function of the distance from the leading edge. **(C)** The slopes of Fluo-4/Fura Red ratios along the migration axis in scrambled and syndecan-4 knockdown cells. Migrating cells next to the cell-free zones ($n = 8$–12) revealed that syndecan-4 knockdown completely abolished Ca^{2+} gradient development in migrating cells. Data are shown as the means + standard errors of the means; ****$p < 0.0001$.

space via different plasma membrane Ca^{2+} channels and Ca^{2+} release from intracellular stores (primarily the endoplasmic reticulum) contribute to the cytosolic Ca^{2+} concentration. In addition to contractility, changes in the intracellular Ca^{2+} affect the activities of calmodulin-dependent enzymes and actin-crosslinking proteins, thus playing a key role in the assembly of adhesions and junctions. Migrating cells establish a front-to-rear Ca^{2+} gradient, which increases toward the rear of the cell. Importantly, our findings suggest that syndecan-4 influences the development of this Ca^{2+} gradient, as demonstrated by its absence in syndecan-4 knockdown cells in association with decreased migration.

Syndecan-4 was shown earlier to influence Ca^{2+} concentrations in different cell types. In podocytes, syndecan-4 knockdown reduced the cell surface expression of the transient receptor potential cation channel subfamily C member (TRPC) 6 channel and consequently reduced the Ca^{2+} concentration (Liu et al., 2012). In contrast, another study of fibroblasts reported that the TRPC7 Ca^{2+} channel was more likely to be open in the absence of syndecan-4, resulting in an increased Ca^{2+} concentration (Gopal et al., 2015). However, a direct interaction has not been reported between syndecan-4 and TRPC7 (Afratis et al., 2017). Furthermore, the single knockdown of syndecan-4 in HaCaT keratinocytes did not affect the Ca^{2+} concentration, whereas the simultaneous silencing of both syndecan-1 and syndecan-4 decreased the cytosolic Ca^{2+} concentration in a TRPC4 channel-dependent manner (Gopal et al., 2015).

The development of Ca^{2+} gradient and the phosphorylation of FAK (Tyr397) are important for focal adhesion assembly and disassembly. Signaling via syndecan-4 is required for focal adhesion formation (Woods and Couchman, 2001), and syndecan-4 favors FAK phosphorylation (Wilcox-Adelman et al.,

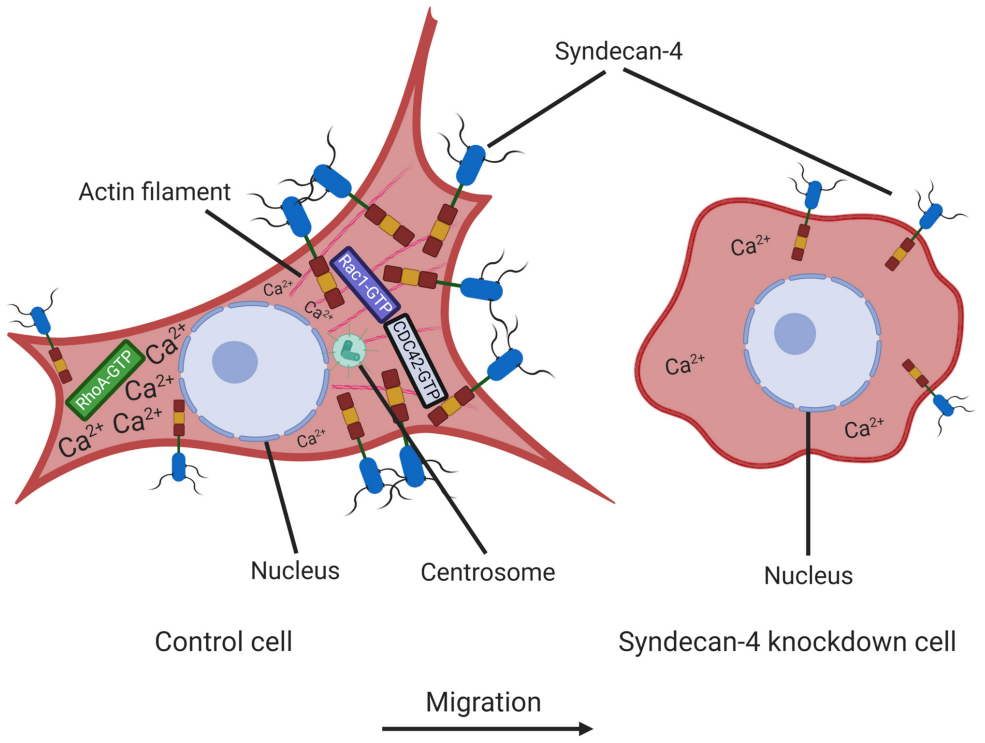

FIGURE 8 | Schematic representation of the effect of syndecan-4 knockdown on cell polarity and migration. The intracellular distribution of Ca^{2+} and syndecan-4 in non-transfected control **(A)** and syndecan-4 knockdown **(B)** myoblasts. In migrating cells, the formation of protruding leading edges are driven by Rac1/CDC42-GTPases favoring the generation of focal contacts, while the retraction and detachment occur at rear edges driven by RhoA-GTP. Syndecan-4 distributes asymmetrically in migrating cells; and syndecan-4 knockdown resulted in the improper positioning of centrosomes, the absence of a front–rear Ca^{2+} gradient and disturbances in the nanoscale structures of the actin fibers. These abnormalities led to decreases in cell polarity and migration. The figure was created with BioRender.com.

2002). The accumulation of phospho-FAK on the frontal side has been investigated and demonstrated in previous studies (Swaney et al., 2006; Carey et al., 2016; Gonzalez Malagon et al., 2018). The polarized distribution of syndecan-4 can affect both Ca^{2+} gradient and local phospho-FAK level. Furthermore, low amount of syndecan-4 in the rear of the migrating cells can contribute to focal adhesion disassembly.

As noted above, the localization of the centrosome is an indicator of polarization in a migrating cell (Etienne-Manneville and Hall, 2001; Zhang and Wang, 2017). To our knowledge, our study is the first to evaluate the effects of syndecan-4 on centrosome positioning, the Ca^{2+} gradient, and the consequent effects on cell polarity. In our previous report of the role of syndecan-4 in cytokinesis, we demonstrated the polarized distribution of the phospho-Ser179 syndecan-4, which accumulated in the intercellular bridges during cytokinesis (Keller-Pinter et al., 2010). The role for syndecan-4 in regulating the activity of RhoA and Rac1 had previously described (Bass et al., 2007; Keller-Pinter et al., 2017), which are crucial regulators of cell polarity. Here we demonstrated that syndecan-4 knockdown led to centrosome disorientation, which indicated improper cell polarization. Further studies are needed to determine the signaling processes leading to syndecan-4-dependent centrosome orientation. As the orientation of the centrosome-nucleus axis depends on a balance of actin- and microtubule-mediated forces (Elric and Etienne-Manneville, 2014), structural changes in the actin cytoskeleton may contribute to the observed mislocalization of centrosomes. Furthermore, changes in the quantity and, presumably, the localization of Rac1 GTPase in syndecan-4-knockdown cells may also affect centrosome positioning and polarity. The latter postulation is supported by an earlier observation that Rac1 activity and membrane protrusions are localized to the leading edges of migrating syndecan-4-sufficient cells, resulting in persistent migration, whereas syndecan-4-null cells migrate randomly (Bass et al., 2007).

The front-to-rear cell polarity required for migration depends on the activities of various members of the small GTPase Rho family. The rear of a migrating cell is defined by high levels of RhoA activity and subsequent actomyosin contractility, in addition to an increased Ca^{2+} concentration and the activation of Ca^{2+}-dependent proteases required to cleave focal adhesion proteins. Interestingly, Tsai and colleagues suggested the presence of crosstalk between Ca^{2+} signaling and Rho GTPases that would

coordinate the oscillations of these factors in the leading edges of migrating cells (Tsai et al., 2015). As noted, phospho-Ser179 syndecan-4 regulates both Rac1 GTPase activity (Keller-Pinter et al., 2017) and intracellular Ca^{2+} level (Gopal et al., 2015). It would be interesting to determine whether these processes are coordinated simultaneously by syndecan-4 during cell migration.

CONCLUSION

In conclusion, we have identified new effects of syndecan-4 in the regulation of cell migration. Specifically, syndecan-4 silencing greatly reduces the migratory abilities of myoblasts. Presumably, this effect is due to a disturbance in cell polarization, which can be inferred from the shift in centrosome positioning relative to the nucleus and the absence of the intracellular Ca^{2+} gradient (**Figure 8**). The reduced migration capability might also be attributed to changes in the nanoscale structure of the lamellipodial actin cytoskeleton and reductions in cell–matrix adhesions. Our findings therefore elucidate the multiple roles of syndecan-4 in myoblast cell migration, although these findings are likely applicable to other cell types, given the ubiquitous expression of syndecan-4. This increase in general knowledge about cell migration will likely facilitate the development of strategies for the further exploration of a wide range of physiological and pathological migratory processes.

DATA AVAILABILITY STATEMENT

All datasets presented in this study are included in the article/**Supplementary Material**.

AUTHOR CONTRIBUTIONS

AK-P and LH conceived and designed the experiments. DB, KS, TG, SG-N, AB, ZB, LH, and AK-P performed the experiments. DB, KS, SG-N, LH, and AK-P analyzed the results. AK-P wrote the manuscript with inputs from DB, KS, SG-N, LH, TG, and ME. AK-P, ME, PH, LH, and LD edited the manuscript. DB and KS contributed equally to this work. AK-P was the principal investigator of the study. All authors contributed to the article and approved the submitted version.

FUNDING

This research was supported by the National Research, Development and Innovation Office of Hungary [grant nos: GINOP-2.3.2-15-2016-00040 (MYOTeam), EFOP-3.6.2-16-2017-00006, NKFI FK 134684, and NKFI K 132446]. The work was further supported by the János Bolyai Research Scholarship of the Hungarian Academy of Sciences (to AK-P), UNKP-19-4-SZTE-23 New National Excellence Program of the Ministry for Innovation and Technology Sciences (to AK-P), the National Research, Development and Innovation Fund (grant no. OTKA_K 128123 to LH), and was conducted with support from the Szeged Scientists Academy under the sponsorship of the Hungarian Ministry of Human Capacities (grant no. EMMI:13725-2/2018/INTFIN, to SG-N). The dSTORM measurements were funded by the Hungarian Brain Research Programme (grant no. 2017-1.2.1-NKP-2017-00002); the National Research, Development and Innovation Office of Hungary (grant nos. GINOP-2.3.2-15-2016-00036) and an EU-funded Hungarian Grant (grant no. EFOP-3.6.1-16-2016-00008). For live-cell microscopy imaging AB and PH acknowledge support from the LENDULET-BIOMAG Grant (grant no. 2018-342) and the European Regional Development Funds (grant nos. GINOP-2.3.2-15-2016-00006, GINOP-2.3.2-15-2016-00026, and GINOP-2.3.2-15-2016-00037).

ACKNOWLEDGMENTS

We thank Zita Makráné Felhõ, Lászlóné Csontos (University of Szeged) and Gyöngyi Bézsenyi (RCNS, Budapest) for their excellent technical assistance. We are also grateful to Fanni Gergely (Cancer Research UK, Cambridge) for her suggestions with centrosome staining.

SUPPLEMENTARY MATERIAL

The Supplementary Material for this article can be found online at: https://www.frontiersin.org/articles/10.3389/fcell.2020.575227/full#supplementary-material

REFERENCES

Afratis, N. A., Nikitovic, D., Multhaupt, H. A., Theocharis, A. D., Couchman, J. R., and Karamanos, N. K. (2017). Syndecans - key regulators of cell signaling and biological functions. *FEBS J.* 284, 27–41. doi: 10.1111/febs.13940

Baciu, P. C., Saoncella, S., Lee, S. H., Denhez, F., Leuthardt, D., and Goetinck, P. F. (2000). Syndesmos, a protein that interacts with the cytoplasmic domain of syndecan-4, mediates cell spreading and actin cytoskeletal organization. *J. Cell Sci.* 113(Pt 2), 315–324.

Bass, M. D., Roach, K. A., Morgan, M. R., Mostafavi-Pour, Z., Schoen, T., Muramatsu, T., et al. (2007). Syndecan-4-dependent Rac1 regulation determines directional migration in response to the extracellular matrix. *J. Cell Biol.* 177, 527–538. doi: 10.1083/jcb.200610076

Becsky, D., Gyulai-Nagy, S., Balind, A., Horvath, P., Dux, L., and Keller-Pinter, A. (2020). Myoblast migration and directional persistence affected by syndecan-4-mediated tiam-1 expression and distribution. *Int. J. Mol. Sci.* 21:823. doi: 10.3390/ijms21030823

Carey, D. J. (1997). Syndecans: multifunctional cell-surface co-receptors. *Biochem J.* 327(Pt 1), 1–16. doi: 10.1042/bj3270001

Carey, S. P., Goldblatt, Z. E., Martin, K. E., Romero, B., Williams, R. M., and Reinhart-King, C. A. (2016). Local extracellular matrix alignment directs cellular protrusion dynamics and migration through Rac1 and FAK. *Integr. Biol.* 8, 821–835. doi: 10.1039/c6ib00030d

Cavalheiro, R. P., Lima, M. A., Jarrouge-Boucas, T. R., Viana, G. M., Lopes, C. C., Coulson-Thomas, V. J., et al. (2017). Coupling of vinculin to F-actin demands

Syndecan-4 proteoglycan. *Matrix Biol.* 63, 23–37. doi: 10.1016/j.matbio.2016.12.006

Charni, F., Friand, V., Haddad, O., Hlawaty, H., Martin, L., Vassy, R., et al. (2009). Syndecan-1 and syndecan-4 are involved in RANTES/CCL5-induced migration and invasion of human hepatoma cells. *Biochim. Biophys. Acta* 1790, 1314–1326. doi: 10.1016/j.bbagen.2009.07.015

Chaudhuri, P., Colles, S. M., Fox, P. L., and Graham, L. M. (2005). Protein kinase Cdelta-dependent phosphorylation of syndecan-4 regulates cell migration. *Circ. Res.* 97, 674–681. doi: 10.1161/01.RES.0000184667.82354.b1

Choi, Y., Kim, S., Lee, J., Ko, S. G., Lee, W., Han, I. O., et al. (2008). The oligomeric status of syndecan-4 regulates syndecan-4 interaction with alpha-actinin. *Eur. J. Cell Biol.* 87, 807–815. doi: 10.1016/j.ejcb.2008.04.005

Chung, H., Multhaupt, H. A., Oh, E. S., and Couchman, J. R. (2016). Minireview: syndecans and their crucial roles during tissue regeneration. *FEBS Lett.* 590, 2408–2417. doi: 10.1002/1873-3468.12280

Cornelison, D. D., Filla, M. S., Stanley, H. M., Rapraeger, A. C., and Olwin, B. B. (2001). Syndecan-3 and syndecan-4 specifically mark skeletal muscle satellite cells and are implicated in satellite cell maintenance and muscle regeneration. *Dev. Biol.* 239, 79–94. doi: 10.1006/dbio.2001.0416

Cornelison, D. D., Wilcox-Adelman, S. A., Goetinck, P. F., Rauvala, H., Rapraeger, A. C., and Olwin, B. B. (2004). Essential and separable roles for Syndecan-3 and Syndecan-4 in skeletal muscle development and regeneration. *Genes Dev.* 18, 2231–2236. doi: 10.1101/gad.1214204

Echtermeyer, F., Streit, M., Wilcox-Adelman, S., Saoncella, S., Denhez, F., Detmar, M., et al. (2001). Delayed wound repair and impaired angiogenesis in mice lacking syndecan-4. *J. Clin. Invest.* 107, R9–R14. doi: 10.1172/jci10559

Elfenbein, A., and Simons, M. (2013). Syndecan-4 signaling at a glance. *J. Cell Sci.* 126(Pt 17), 3799–3804. doi: 10.1242/jcs.124636

Elric, J., and Etienne-Manneville, S. (2014). Centrosome positioning in polarized cells: common themes and variations. *Exp. Cell Res.* 328, 240–248. doi: 10.1016/j.yexcr.2014.09.004

Endo, T., Ito, K., Morimoto, J., Kanayama, M., Ota, D., Ikesue, M., et al. (2015). Syndecan 4 Regulation of the development of autoimmune arthritis in mice by modulating B cell migration and germinal center formation. *Arthritis Rheumatol.* 67, 2512–2522. doi: 10.1002/art.39193

Etienne-Manneville, S., and Hall, A. (2001). Integrin-mediated activation of Cdc42 controls cell polarity in migrating astrocytes through PKCzeta. *Cell* 106, 489–498. doi: 10.1016/s0092-8674(01)00471-8

Gardel, M. L., Schneider, I. C., Aratyn-Schaus, Y., and Waterman, C. M. (2010). Mechanical integration of actin and adhesion dynamics in cell migration. *Annu. Rev. Cell Dev. Biol.* 26, 315–333. doi: 10.1146/annurev.cellbio.011209.122036

Gonzalez Malagon, S. G., Lopez Munoz, A. M., Doro, D., Bolger, T. G., Poon, E., Tucker, E. R., et al. (2018). Glycogen synthase kinase 3 controls migration of the neural crest lineage in mouse and Xenopus. *Nat. Commun.* 9:1126. doi: 10.1038/s41467-018-03512-5

Gopal, S., Sogaard, P., Multhaupt, H. A., Pataki, C., Okina, E., Xian, X., et al. (2015). Transmembrane proteoglycans control stretch-activated channels to set cytosolic calcium levels. *J. Cell Biol.* 210, 1199–1211. doi: 10.1083/jcb.201501060

Gotlieb, A. I., Subrahmanyan, L., and Kalnins, V. I. (1983). Microtubule-organizing centers and cell migration: effect of inhibition of migration and microtubule disruption in endothelial cells. *J. Cell Biol.* 96, 1266–1272. doi: 10.1083/jcb.96.5.1266

Granes, F., Berndt, C., Roy, C., Mangeat, P., Reina, M., and Vilaro, S. (2003). Identification of a novel Ezrin-binding site in syndecan-2 cytoplasmic domain. *FEBS Lett.* 547, 212–216. doi: 10.1016/s0014-5793(03)00712-9

Greene, D. K., Tumova, S., Couchman, J. R., and Woods, A. (2003). Syndecan-4 associates with alpha-actinin. *J. Biol. Chem.* 278, 7617–7623. doi: 10.1074/jbc.M207123200

Hawke, T. J., and Garry, D. J. (2001). Myogenic satellite cells: physiology to molecular biology. *J. Appl. Physiol.* 91, 534–551. doi: 10.1152/jappl.2001.91.2.534

Jeyarajah, M. J., Jaju Bhattad, G., Kops, B. F., and Renaud, S. J. (2019). Syndecan-4 regulates extravillous trophoblast migration by coordinating protein kinase C activation. *Sci. Rep.* 9:10175. doi: 10.1038/s41598-019-46599-6

Keller-Pinter, A., Bottka, S., Timar, J., Kulka, J., Katona, R., Dux, L., et al. (2010). Syndecan-4 promotes cytokinesis in a phosphorylation-dependent manner. *Cell Mol. Life Sci.* 67, 1881–1894. doi: 10.1007/s00018-010-0298-6

Keller-Pinter, A., Szabo, K., Kocsis, T., Deak, F., Ocsovszki, I., Zvara, A., et al. (2018). Syndecan-4 influences mammalian myoblast proliferation by modulating myostatin signalling and G1/S transition. *FEBS Lett.* 592, 3139–3151. doi: 10.1002/1873-3468.13227

Keller-Pinter, A., Ughy, B., Domoki, M., Pettko-Szandtner, A., Letoha, T., Tovari, J., et al. (2017). The phosphomimetic mutation of syndecan-4 binds and inhibits Tiam1 modulating Rac1 activity in PDZ interaction-dependent manner. *PLoS One* 12:e0187094. doi: 10.1371/journal.pone.0187094

Kim, J. M., Lee, M., Kim, N., and Heo, W. D. (2016). Optogenetic toolkit reveals the role of Ca2+ sparklets in coordinated cell migration. *Proc. Natl. Acad. Sci. U.S.A.* 113, 5952–5957. doi: 10.1073/pnas.1518412113

Koo, B. K., Jung, Y. S., Shin, J., Han, I., Mortier, E., Zimmermann, P., et al. (2006). Structural basis of syndecan-4 phosphorylation as a molecular switch to regulate signaling. *J. Mol. Biol.* 355, 651–663. doi: 10.1016/j.jmb.2005.09.087

Lauffenburger, D. A., and Horwitz, A. F. (1996). Cell migration: a physically integrated molecular process. *Cell* 84, 359–369. doi: 10.1016/s0092-8674(00)81280-5

Liu, Y., Echtermeyer, F., Thilo, F., Theilmeier, G., Schmidt, A., Schulein, R., et al. (2012). The proteoglycan syndecan 4 regulates transient receptor potential canonical 6 channels via RhoA/Rho-associated protein kinase signaling. *Arterioscler. Thromb. Vasc. Biol.* 32, 378–385. doi: 10.1161/atvbaha.111.241018

Matthews, H. K., Marchant, L., Carmona-Fontaine, C., Kuriyama, S., Larrain, J., Holt, M. R., et al. (2008). Directional migration of neural crest cells in vivo is regulated by Syndecan-4/Rac1 and non-canonical Wnt signaling/RhoA. *Development* 135, 1771–1780. doi: 10.1242/dev.017350

Parsons, J. T., Horwitz, A. R., and Schwartz, M. A. (2010). Cell adhesion: integrating cytoskeletal dynamics and cellular tension. *Nat. Rev. Mol. Cell Biol.* 11, 633–643. doi: 10.1038/nrm2957

Petrie, R. J., Zhao, B., Bedford, F., and Lamarche-Vane, N. (2009). Compartmentalized DCC signalling is distinct from DCC localized to lipid rafts. *Biol. Cell* 101, 77–90. doi: 10.1042/bc20070108

Piccinini, F., Kiss, A., and Horvath, P. (2016). CellTracker (not only) for dummies. *Bioinformatics* 32, 955–957. doi: 10.1093/bioinformatics/btv686

Polte, T., Petzold, S., Bertrand, J., Schutze, N., Hinz, D., Simon, J. C., et al. (2015). Critical role for syndecan-4 in dendritic cell migration during development of allergic airway inflammation. *Nat. Commun.* 6:7554. doi: 10.1038/ncomms8554

Qin, Y., Zhu, Y., Luo, F., Chen, C., Chen, X., and Wu, M. (2017). Killing two birds with one stone: dual blockade of integrin and FGF signaling through targeting syndecan-4 in postoperative capsular opacification. *Cell Death Dis.* 8, e2920. doi: 10.1038/cddis.2017.315

Rees, E. J., Erdelyi, M., Kaminski-Schierle, G. S., Knight, A. E., and Kaminski, C. F. (2013). Elements of image processing in localisation microscopy. *J. Opt.* 15:094012.

Ridley, A. J., Schwartz, M. A., Burridge, K., Firtel, R. A., Ginsberg, M. H., Borisy, G., et al. (2003). Cell migration: integrating signals from front to back. *Science* 302, 1704–1709. doi: 10.1126/science.1092053

Schultz, E., and McCormick, K. M. (1994). Skeletal muscle satellite cells. *Rev. Physiol. Biochem. Pharmacol.* 123, 213–257.

Shin, J., McFarland, D. C., and Velleman, S. G. (2013). Migration of turkey muscle satellite cells is enhanced by the syndecan-4 cytoplasmic domain through the activation of RhoA. *Mol. Cell Biochem.* 375, 115–130. doi: 10.1007/s11010-012-1534-1

Swaney, J. S., Patel, H. H., Yokoyama, U., Head, B. P., Roth, D. M., and Insel, P. A. (2006). Focal adhesions in (myo)fibroblasts scaffold adenylyl cyclase with phosphorylated caveolin. *J. Biol. Chem.* 281, 17173–17179. doi: 10.1074/jbc.M513097200

Thomas, D., Tovey, S. C., Collins, T. J., Bootman, M. D., Berridge, M. J., and Lipp, P. (2000). A comparison of fluorescent Ca2+ indicator properties and their use in measuring elementary and global Ca2+ signals. *Cell Calcium* 28, 213–223. doi: 10.1054/ceca.2000.0152

Thompson, R. E., Larson, D. R., and Webb, W. W. (2002). Precise nanometer localization analysis for individual fluorescent probes. *Biophys. J.* 82, 2775–2783. doi: 10.1016/s0006-3495(02)75618-x

Toba-Ichihashi, Y., Yamaoka, T., Ohmori, T., and Ohba, M. (2016). Up-regulation of Syndecan-4 contributes to TGF-beta1-induced epithelial to mesenchymal transition in lung adenocarcinoma A549 cells. *Biochem. Biophys. Rep.* 5, 1–7. doi: 10.1016/j.bbrep.2015.11.021

Tsai, F. C., Kuo, G. H., Chang, S. W., and Tsai, P. J. (2015). Ca2+ signaling in cytoskeletal reorganization, cell migration, and cancer metastasis. *Biomed. Res. Int.* 2015:409245. doi: 10.1155/2015/409245

van de Linde, S., Loschberger, A., Klein, T., Heidbreder, M., Wolter, S., Heilemann, M., et al. (2011). Direct stochastic optical reconstruction microscopy with standard fluorescent probes. *Nat. Protoc.* 6, 991–1009. doi: 10.1038/nprot.2011.336

Vicente-Manzanares, M., Webb, D. J., and Horwitz, A. R. (2005). Cell migration at a glance. *J. Cell Sci.* 118(Pt 21), 4917–4919. doi: 10.1242/jcs.02662

Wilcox-Adelman, S. A., Denhez, F., and Goetinck, P. F. (2002). Syndecan-4 modulates focal adhesion kinase phosphorylation. *J. Biol. Chem.* 277, 32970–32977. doi: 10.1074/jbc.M201283200

Woods, A., and Couchman, J. R. (2001). Syndecan-4 and focal adhesion function. *Curr. Opin. Cell Biol.* 13, 578–583. doi: 10.1016/s0955-0674(00)00254-4

Xian, X., Gopal, S., and Couchman, J. R. (2010). Syndecans as receptors and organizers of the extracellular matrix. *Cell Tissue Res.* 339, 31–46. doi: 10.1007/s00441-009-0829-3

Yin, L., Qi, Y., Xu, Y., Xu, L., Han, X., Tao, X., et al. (2017). Dioscin inhibits HSC-T6 cell migration via adjusting SDC-4 expression: insights from iTRAQ-based quantitative proteomics. *Front. Pharmacol.* 8:665. doi: 10.3389/fphar.2017.00665

Yoo, J., Jeong, M. J., Cho, H. J., Oh, E. S., and Han, M. Y. (2005). Dynamin II interacts with syndecan-4, a regulator of focal adhesion and stress-fiber formation. *Biochem. Biophys. Res. Commun.* 328, 424–431. doi: 10.1016/j.bbrc.2004.12.179

Zhang, J., and Wang, Y. L. (2017). Centrosome defines the rear of cells during mesenchymal migration. *Mol. Biol. Cell* 28, 3240–3251. doi: 10.1091/mbc.E17-06-0366

Zimmermann, P., and David, G. (1999). The syndecans, tuners of transmembrane signaling. *FASEB J.* 13(Suppl.), S91–S100. doi: 10.1096/fasebj.13.9001.s91

Conflict of Interest: The authors declare that the research was conducted in the absence of any commercial or financial relationships that could be construed as a potential conflict of interest.

frontiers in Cell and Developmental Biology

BRIEF RESEARCH REPORT
published: 20 October 2020
doi: 10.3389/fcell.2020.588851

Netrin-1/DCC Signaling Differentially Regulates the Migration of Pax7, Nkx6.1, Irx2, Otp, and Otx2 Cell Populations in the Developing Interpeduncular Nucleus

*Isabel M. García-Guillén[1,2], Antonia Alonso[1,2], Nicanor Morales-Delgado[1,2,3], Belén Andrés[4], Luis Puelles[1,2], Guillermina López-Bendito[4], Faustino Marín[1,2] and Pilar Aroca[1,2]**

[1] Department of Human Anatomy and Psychobiology, School of Medicine, University of Murcia, Murcia, Spain, [2] Biomedical Research Institute of Murcia (IMIB-Arrixaca), Murcia, Spain, [3] Department of Histology and Anatomy, School of Medicine, Miguel Hernández University, Alicante, Spain, [4] Instituto de Neurociencias de Alicante, CSIC, Universidad Miguel Hernández, Alicante, Spain

OPEN ACCESS

Edited by:
Vladimir Sytnyk,
University of New South Wales,
Australia

Reviewed by:
Andrea Wizenmann,
University of Tübingen, Germany
Hisham F. Bahmad,
American University of Beirut,
Lebanon

***Correspondence:**
Pilar Aroca
pilaroca@um.es

Specialty section:
This article was submitted to Cell Adhesion and Migration, a section of the journal Frontiers in Cell and Developmental Biology

Received: 29 July 2020
Accepted: 30 September 2020
Published: 20 October 2020

Citation:
García-Guillén IM, Alonso A, Morales-Delgado N, Andrés B, Puelles L, López-Bendito G, Marín F and Aroca P (2020) Netrin-1/DCC Signaling Differentially Regulates the Migration of Pax7, Nkx6.1, Irx2, Otp, and Otx2 Cell Populations in the Developing Interpeduncular Nucleus. Front. Cell Dev. Biol. 8:588851. doi: 10.3389/fcell.2020.588851

The interpeduncular nucleus (IPN) is a hindbrain structure formed by three main subdivisions, the prodromal (Pro) domain located at the isthmus (Ist), and the rostral and caudal interpeduncular domains (IPR, IPC) within rhombomere 1 (r1). Various cell populations can be detected in the IPN through the expression of the *Nkx6.1*, *Otp*, *Otx2*, *Pax7,* and/or *Irx2* transcription factors. These cell populations follow independent dorsoventral tangential and radial migratory routes targeting the ventral paramedian region of Ist and r1. Here we set out to examine the influence of the Netrin-1/DCC pathway on these migrations, since it is known to regulate other processes of neuronal migration in the brain. To this end, we analyzed IPN development in late gestational wild-type and DCC$^{-/-}$ mice, using mainly *in situ* hybridization (ISH) to identify the cells expressing each of the aforementioned genes. We found that the migration of *Nkx6.1*$^{+}$ and *Irx2*$^{+}$ cells into the Pro domain was strongly disrupted by the loss of DCC, as occurred with the migration of *Pax7*$^{+}$, *Irx2*$^{+}$, and *Otp*$^{+}$ cells that would normally form the IPR. In addition, there was mild impairment of the migration of the *Pax7*$^{+}$ and *Otx2*$^{+}$ cells that form the IPC. These results demonstrate that the Netrin-1/DCC signaling pathway is involved in the migration of most of the IPN populations, mainly affecting those of the Pro and IPR domains of this nucleus. There are psychiatric disorders that involve the medial habenula (mHb)-IPN system, so that this experimental model could provide a basis to study their neurodevelopmental etiology.

Keywords: neuronal tangential migration, axon guidance, Netrin1, DCC, transcription factors, rhombomeres, chemoattractant molecules, interpeduncular nucleus (IPN)

Abbreviations: IPN, interpeduncular nucleus; Pro, prodromal; IPR, interpeduncular rostral; IPC, interpeduncular caudal; Ist, isthmus; r1, rhombomere 1; r1-r, rhombomere 1 rostral; r1-c, rhombomere 1 caudal; r2, rhombomere 2; mHb, medial habenula; VZ, ventricular zone.

INTRODUCTION

Neuronal migration is an important feature of brain development, in some cases involving the displacement of considerable cell populations toward different coordinates. In addition to the classic examples of migration, such as that in the precerebellar nuclei (Bloch-Gallego et al., 2005), recent data has shown that complex migratory events contribute to the formation of the interpeduncular nucleus (IPN) (Lorente-Cánovas et al., 2012; Moreno-Bravo et al., 2014; Ruiz-Reig et al., 2019). In vertebrates, the IPN is a complex hindbrain structure and it is the principal target of the retroflex tract that comes from the medial habenula (mHb) (Herkenham and Nauta, 1979; Contestabile and Flumerfelt, 1981). In behavioral and functional studies, the mHb-IPN pathway has been implicated in learning and memory, affective states and mood-related psychiatric conditions (Klemm, 2004; Hikosaka, 2010). However, the development of the IPN has only recently been studied, in particular in the chick (Lorente-Cánovas et al., 2012) and mouse (Moreno-Bravo et al., 2014; Ruiz-Reig et al., 2019).

Our previous experimental study in the chick demonstrated that the IPN is formed in the rostral (prepontine) hindbrain, containing cells from both alar and basal populations (Lorente-Cánovas et al., 2012). Each of the IPN populations follows a specific dorsoventral migratory trajectory from its original periventricular position, ultimately converging at a more medial site and settling down in a sub-pial location across the median floor plate of the isthmus (Ist) and hindbrain rhombomere 1 (r1) (Lorente-Cánovas et al., 2012; Moreno-Bravo et al., 2014). At the end of this process, the so-called rostral (IPR) and caudal (IPC) domains of the IPN lie in the rostral and caudal parts of r1 (r1-r, r1-c), respectively, while the smaller rostral prodromal (Pro) domain is located in the isthmic region. In terms of the molecular regionalization of this nucleus, we identified at least four distinct neuronal populations that expressed the *Pax7* (alar plate origin), and *Nkx6.1*, *Otp* or *Otx2* (distinct basal plate origins) transcription factors.

Based on their morphology, migratory routes, location and gene expression, the same neuronal populations that form the chick IPN also appear to generate the mouse IPN (García-Guillén et al., unpublished; Moreno-Bravo et al., 2014; Ruiz-Reig et al., 2019). Moreover, Otx2 activity is required for the tangential migration of the IPC cells that normally express this gene (Ruiz-Reig et al., 2019), and a conditional mutant of *Shh*, the gene responsible for the formation of the floorplate, alters the migration of the $Pax7^+$, $Nkx6.1^+$, Otp^+, and $Otx2^+$ cells that would normally form the distinct parts of the IPN (Moreno-Bravo et al., 2014). These earlier studies showed that the IPN emerges as a plurisegmental and heterogeneous alar/basal formation whose correct development depends on the proper migration and positioning of several neuronal populations. However, the molecular mechanisms underlying these independent migratory events are still largely unknown, other than the need for SHH at the floor plate (Moreno-Bravo et al., 2014).

One of the molecular mechanisms that regulates neuronal migration in the brain is the Netrin-1/DCC (Deleted in Colorectal Cancer) pathway (Bashaw and Klein, 2010; Marín et al., 2010; Evsyukova et al., 2013). Netrin-1 is expressed in the floorplate of the central nervous system and it acts as an attractive molecule in conjunction with its receptor, DCC (Fearon et al., 1990; Hedrick et al., 1994; Keino-Masu et al., 1996). Floorplate-derived Netrin-1/DCC signaling is known to steer the migration of several neuronal populations in the hindbrain. Indeed, it is required for the dorsoventral tangential migration of noradrenergic neurons of the locus coeruleus (Shi et al., 2008) and for the migration of precerebellar rhombic lip neurons (Alcántara et al., 2000; de Diego et al., 2002; Bloch-Gallego et al., 2005), including inferior olivary neurons (Bloch-Gallego et al., 2005; Marcos et al., 2009) and neurons of the basilar pontine nuclei (Kratochwil et al., 2017). In terms of the IPN, *Netrin-1* is expressed in the floor plate of the rostral hindbrain where this nucleus develops, while *Dcc* is expressed by the migrating $Otx2^+$ cells that enter the IPC (Ruiz-Reig et al., 2019).

Taking all this into account, we have studied the possible functional role of the Netrin-1/DCC pathway in regulating the dorsoventral tangential and/or radial migrations of the diverse IPN populations. To this end, we analyzed IPN development in an experimental mouse model devoid of DCC activity, demonstrating that practically all the selective cell migration to the IPN is altered in these mice.

MATERIALS AND METHODS

Animals and Embryo Processing

All mice were maintained according to the European Union guidelines (2010/63/EU) and Spanish law (Royal Decree 53/2013 and Royal Decree 1386/2018) regarding the care and handling of research animals. All procedures were performed according to protocols approved by the University of Murcia Ethical Committee for Animal Experimentation. Swiss albino mice bred at the University of Murcia were used to analyze gene expression during development (**Figure 1**). The *Dcc* knock-out mice (Fazeli et al., 1997) were generated and kindly provided by Marc Tessier-Lavigne (The Rockefeller University; New York, United States).

In all cases, the day of vaginal post-coital plug detection was regarded as embryonic day 0.5 (E0.5). E15.5 and E18.5 embryos of undetermined sex were extracted from the pregnant dams after sacrifice, genotyped and fixed overnight in 4% paraformaldehyde (PFA) prepared in phosphate-buffered saline (PBS, pH 7.4). For the studies of the transgenic mice, embryos from the same litter were matched in pairs of +/+ and −/− mice for each experiment. The embryo's brain was dissected out, post-fixed at 4°C in the PFA for 24 h (E15.5 embryos) or 48 h (E18.5 embryos), and then washed in PBS. The brains were then embedded in 4% agarose in PBS, and sagittal vibratome sections (80 μm thick) were subsequently processed for *in situ* hybridization (ISH) and in some cases, followed by immunohistochemistry (IHC).

RNA Probes

Digoxigenin-labeled riboprobes were synthesized from cDNA constructs kindly provided by M. Tessier-Lavigne (*Netrin-1* and

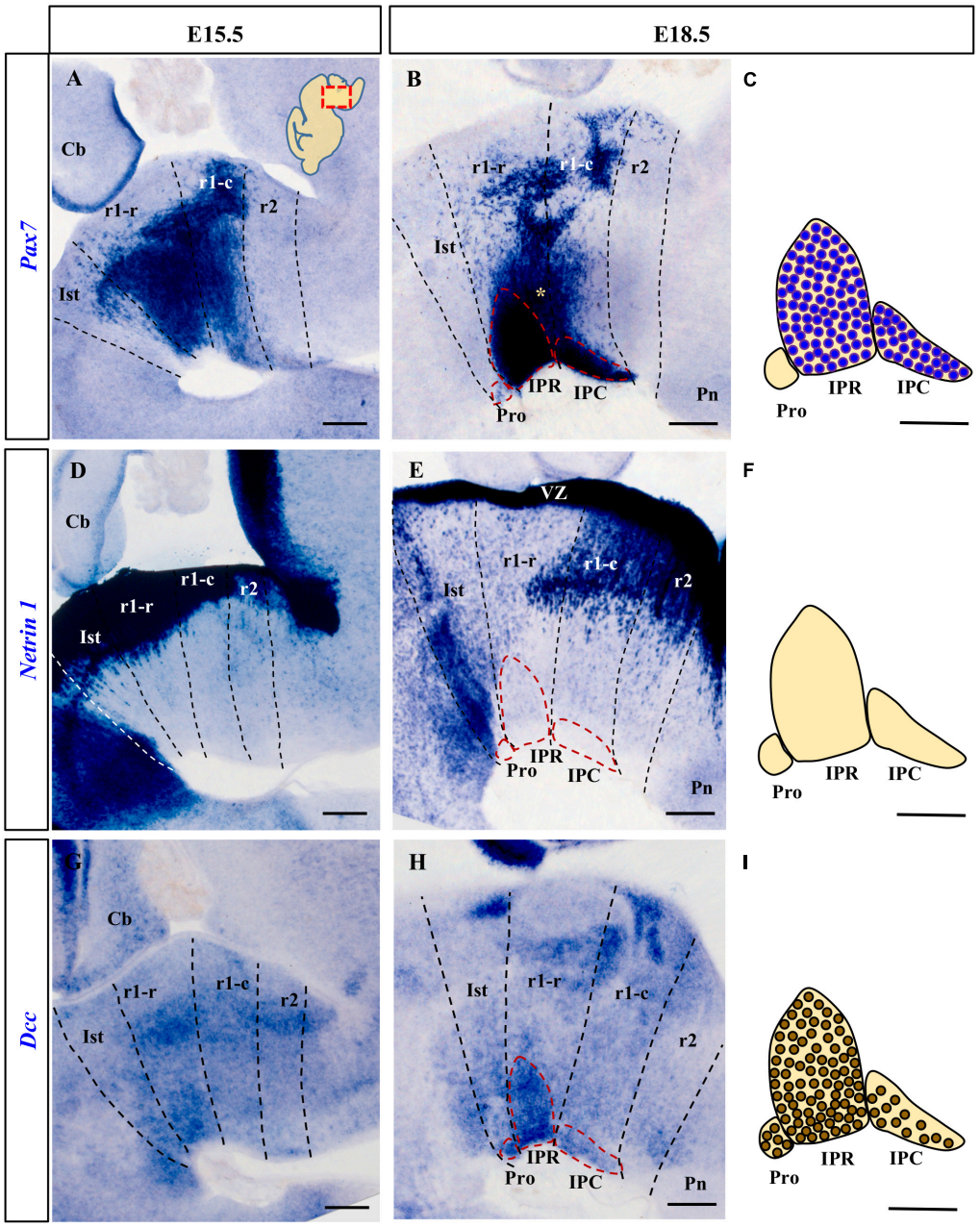

FIGURE 1 | Comparison of *Pax7*, *Netrin-1* and *Dcc* rostral hindbrain expression in sections from E15.5 and E18.5 mouse embryos processed for ISH (see section Materials and Methods). In this and the other figures, the images are from parasagittal sections centered on the IPN in the rostral hindbrain. In each image the rostral end is to the left. The dashed lines represent the intersegmental boundaries delimiting the Ist, r1-r, r1-c and r2. **(A,B)** *Pax7* is a marker for the majority of cells of the developing IPN. At E15.5 the *Pax7*$^{+}$ cells are migrating in the mantle layer, while at E18.5 they are forming the IPR and the IPC. **(D,E)** *Netrin-1* is expressed strongly by the floor plate in the Ist and r1 where the IPN develops from the early (data not shown) to later stages, at E15.5 and E18.5. **(G,H)** At E15.5, *Dcc* is expressed by IPN neurons migrating to the IPN to become part of the three portions of the nucleus (Pro, IPR, and IPC) at E18.5. **(C,F,I)** Scheme of sagittal sections of the IPN at E18.5, from top to bottom representing: the expression of *Pax7* by cells in the IPR and IPC, the absence of *Netrin-1* expression in the nucleus, and the expression of the netrin receptor *Dcc* by IPR, IPC and (unlike *Pax7*) Pro cells. Pro, prodromal; IPR, interpeduncular rostral; IPC, interpeduncular caudal; Ist, isthmus; r1-r, rhombomere 1 rostral; r1-c, rhombomere 1 caudal; r2, rhombomere 2; Pn, pontine nuclei; VZ, ventricular zone; Cb, cerebellum. **(A,B,D,E,G,H)** scale bars = 200 μm, **(C,F,I)** scale bars = 50 μm.

Dcc: Rockefeller University, NY, United States), A. Simeone (*Otp* and *Otx2*: Inst. Genetics and Biophysics, Naples, Italy) and O. Marín (*Nkx6.1*: King's College London, United Kingdom). A *Pax7* cDNA clone (Riken 5330440B08, NCBI accession number AK133693) was obtained from Source BioScience (Nottingham, United Kingdom) and an *Irx2* cDNA clone (MGC 27958, IMAGE

3592499, NCBI accession number BC029750) from ImaGenes GmbH (Berlin, Germany).

In situ Hybridization and Immunohistochemistry

Floating sagittal sections were processed for ISH with digoxigenin-labeled antisense RNA probes using the protocol of Nieto et al. (1996) adapted for floating vibratome sections. To detect the hybridized probes, the sections were incubated overnight with alkaline phosphatase (AP)-conjugated anti-digoxigenin antibody, and the NBT/BCIP substrates were used to detect AP activity, producing a blue chromogenic precipitate. The sections were then washed in saline solution and post-fixed.

To combined IHC with ISH, the sections were incubated with a monoclonal mouse anti-Pax7 antibody (Developmental Studies Hybridoma Bank) after ISH, diluted 1:80 in Tris-buffered saline with 0.1% Tween 20 and 20% of sheep serum. The binding of this antibody was detected with a biotinylated goat anti-mouse IgG secondary antibody (Sigma) diluted 1:200 in Tris-buffered saline with 0.1% Tween 20 and 5% sheep serum and after several washes in Tris-buffered saline with 0.05% Tween 20, it was visualized with avidin-biotin-peroxidase (VECTASTAIN Elite ABC kit from Vector), following the manufacturer's indications. Peroxidase was detected by standard protocols, using diaminobenzidine-tetrahydrochloride (DAB) and hydrogen peroxide as substrates to produce a brown chromogenic precipitate. Finally, the sections were mounted, dehydrated and then coverslipped with Eukitt. Digital photographs were taken on a Leica microscope (DMR HC) equipped with a Zeiss Axiovision digital camera.

RESULTS

We analyzed the expression of *Netrin-1*, *Dcc* and the genes indicated, characterizing the distinct IPN neuronal populations in the brain sections from both wild-type and DCC$^{-/-}$ mice, situating them relative to the Ist, r1-r, r1-c and rhombomere 2 (r2) boundaries. We identified these boundaries based on the mapping of these regions and the expression data available in chick and mouse brains (Aroca and Puelles, 2005; Aroca et al., 2006; Lorente-Cánovas et al., 2012; Alonso et al., 2013; Watson et al., 2017).

The Netrin-1 Receptor DCC Is Expressed in the Developing Interpeduncular Nucleus

We first analyzed *Netrin-1* and *Dcc* mRNA expression in the IPN territory at several stages of development, identified by the position of the migrated *Pax7*$^+$ cells. According to previous studies in the chick (Lorente-Cánovas et al., 2012), the *Pax7*$^+$ IPN population originates in the alar plate of the ventricular zone (VZ) throughout r1 (r1-r and r1-c), from where the cells first translocate tangentially into the mantle of the medial basal plate, and then, they migrate radially toward the pial surface. In the mouse, we found that the *Pax7*$^+$ cells began to reach the median IPN locus at E15.5 (**Figure 1A**) and by E18.5, *Pax7* is expressed strongly by neurons in the IPR and IPC, but not by those in isthmic Pro (**Figures 1B,C**). In addition to the cells in the IPN, at this stage there was still a large population of cells that express *Pax7* migrating en route to that nucleus (yellow asterisk in **Figure 1B**). Other labeled populations remain stable in the periventricular stratum, probably corresponding to the prospective populations of the ventral tegmental and sphenoid nuclei (Moreno-Bravo et al., 2014). From early stages of development (E11.5 and E13.5), *Netrin-1* is intensely expressed in the VZ of the hindbrain floor plate, including that of Ist and r1 (data not shown). This VZ contains the cell bodies of the radial glia that constitute the main cell population in the floor plate. At stages E15.5 and E18.5 (**Figures 1D,E**), *Netrin-1* was also expressed by some neuron populations within the basal mantle of Ist and r1 but not in the IPN complex itself (**Figures 1E,F**).

In terms of the Netrin-1 receptor, *Dcc* was expressed in the VZ throughout the Ist and r1 at E11.5 and E13.5 (data not shown). At E15.5, there were numerous *Dcc*$^+$ cells in the mantle layer of these segments and a population of *Dcc*$^+$ neurons begin to arrive at the IPN locus (**Figure 1G**). By E18.5, the *Dcc*$^+$ population in the IPN had increased markedly, distributed across its three rostro-caudal domains: Pro, IPR and IPC (**Figures 1H,I**). A stream of *Dcc*$^+$ cells was also evident along the radial migratory pathway to the IPN.

Comparing the expression of *Dcc* and *Pax7*, there was a clear overlap in the expression of both markers in the IPR and IPC domains of the IPN, while the Pro domain was *Pax7*$^-$ and *Dcc*$^+$ (compare **Figures 1B,C,H,I**). These expression patterns complemented the distribution of *Otx2* cells within the IPC (Ruiz-Reig et al., 2019) and they were consistent with the possible regulation of the migration of the different components of the IPN by Netrin-1/DCC signaling, particularly given the uniform *Dcc* expression in the migrating IPN cells and the presence of *Netrin-1* in their target region, the rostral hindbrain floorplate.

The Migration of Five Independent IPN Neuronal Populations Is Differentially Disrupted in DCC$^{-/-}$ Embryos

Considering the aforementioned hypothesis, we evaluated the migration of the *Nkx6.1*$^+$, *Irx2*$^+$, *Pax7*$^+$, *Otp*$^+$, and *Otx2*$^+$ IPN cell populations in E18.5 DCC$^{-/-}$ and wild-type mice. *Irx2* was recently identified as a conspicuous marker for the IPN in a screening of genes expressed in this structure (García-Guillén et al., unpublished), while the other markers indicated have been characterized previously (Lorente-Cánovas et al., 2012; Moreno-Bravo et al., 2014; Ruiz-Reig et al., 2019).

In wild-type embryos, *Nkx6.1* expressing cells were only observed in the Pro domain in the isthmic region of the IPN (**Figure 2A**). This *Nkx6.1*$^+$ population was significantly smaller in DCC$^{-/-}$ embryos, such that only a few cells reached their final location in the Pro domain (**Figure 2B**). In addition, anomalous ectopic patches of *Nxk6.1*$^+$ cells were evident in the isthmic tegmentum (yellow arrows in **Figure 2B**), probably corresponding to disorientated cells from this population.

The *Irx2*$^+$ population was distributed in the Pro and IPR in wild-type embryos (**Figure 2C** and data not shown), yet there were no *Irx2*$^+$ cells in these two compartments of the DCC$^{-/-}$

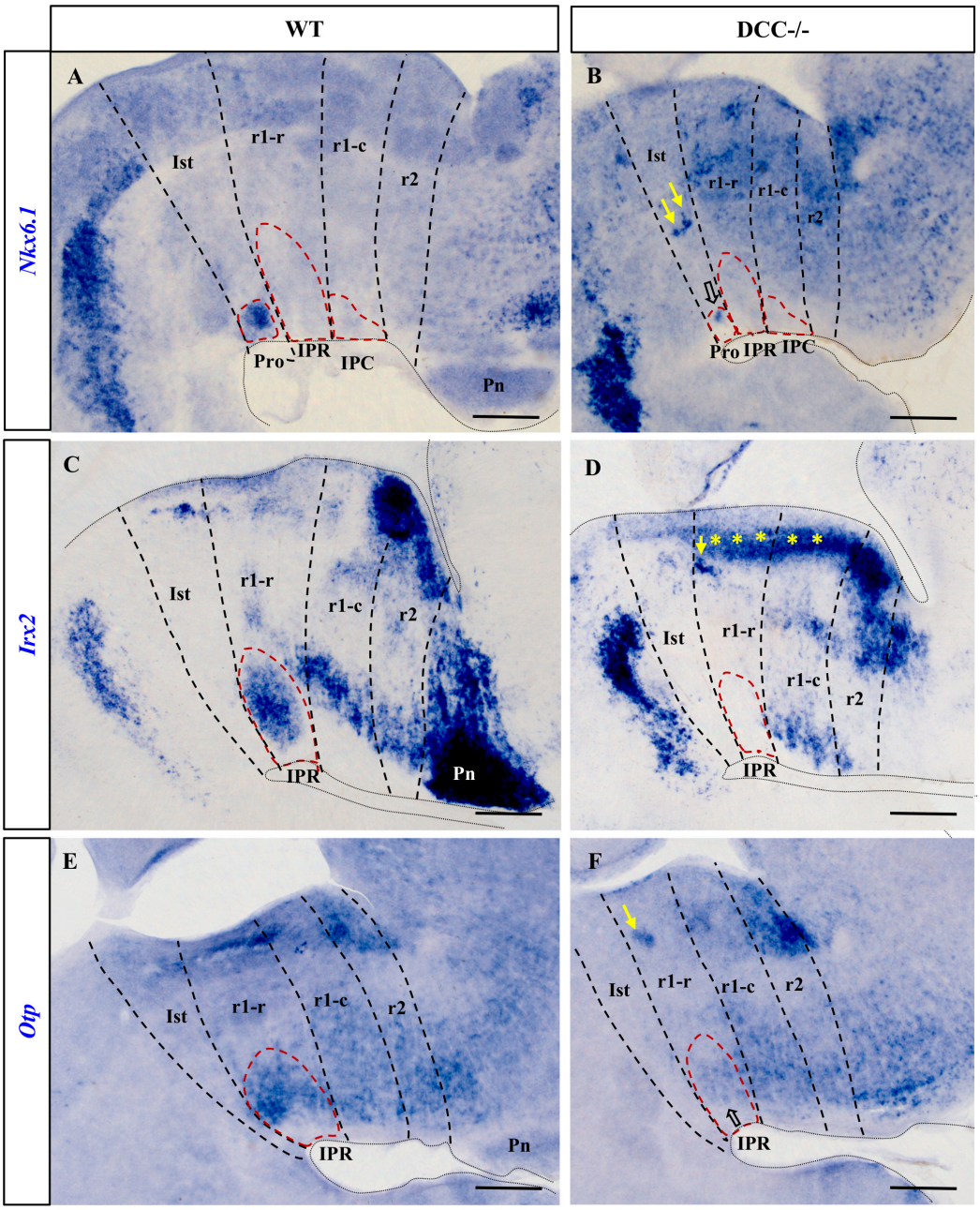

FIGURE 2 | Comparison of *Nkx6.1*, *Irx2* and *Otp* expression in sections processed for ISH from wild-type and DCC$^{-/-}$ brains at E18.5. **(A,C,E)** Sections of wild-type brains showing the expression of these genes. *Nkx6.1* **(A)** is expressed by the cells in the Pro, *Otp* **(E)** by cells in the IPR and *Irx2* **(C)** is expressed both in the Pro and the IPR, although *Irx2* expression in the Pro is not visualized here because this image corresponds to a medial sagittal section and the Pro lies more laterally. Along with **(C)**, the images **(D,E,F)** correspond to medial sagittal sections where the Pro and the IPC are absent. **(B,D,F)** Sections of DCC$^{-/-}$ brains showing the respective expression of these genes. There are no *Irx2* cells in the IPR **(D)** or in the Pro (data not shown), whereas *Nkx6.1* **(B)** and *Otp* **(F)** are almost absent in the Pro and IPR respectively, with some cells that have reached their correct location in the IPN in the latter two cases (open arrows). In these three images, yellow arrows indicate patches of cells that have ceased to migrate toward the IPN, probably as a consequence of the absence of DCC. Yellow asterisks in **(D)** indicate an aberrant band of *Irx2*$^{+}$ cells that appear not to have completed the migratory process through the mantle in DCC$^{-/-}$ mice. Pro, prodromal; IPR, interpeduncular rostral; IPC, interpeduncular caudal; Ist, isthmus; r1-r, rhombomere 1 rostral; r1-c, rhombomere 1 caudal; r2, rhombomere 2; Pn, pontine nuclei. Scale bars = 200 μm.

IPN (**Figure 2D**). Rather, such cells appeared to accumulate densely in the corresponding periventricular stratum, as well as in ectopic patches within the r1 tegmentum (yellow asterisks and yellow arrow in **Figure 2D**), reflecting their disturbed migration. *Irx2* is also a marker of the pontine nuclei, such that the disruption to the expression of this gene also reflects the failure of

these nuclei to develop in DCC$^{-/-}$ embryos. The effects on these structures may have been expected since Netrin-1/DCC signaling was demonstrated to regulate migration to the pontine nuclei (Alcántara et al., 2000).

Like the *Irx2*$^{+}$expressing cells, *Otp*$^{+}$ cells in wild-type embryos were mainly observed in the IPR (**Figure 2E**), whereas these cells were almost completely absent from this structure in DCC$^{-/-}$ embryos (**Figure 2F**). We also observed a dense group of ectopic *Otp*$^{+}$ cells in the r1 tegmental mantle of DCC$^{-/-}$ embryos that may have had their migration arrested (yellow arrow in Figurr 2F).

To analyze the effect of Netrin-1/DCC signaling on the development of the *Otx2*$^{+}$and *Pax7*$^{+}$ IPN populations, it must be borne in mind that *Pax7* is expressed extensively in the IPR, including the medial and lateral aspects of this structure (**Figures 3A,B**). By contrast, the most medial population in the IPC is *Otx2*$^{+}$ (**Figure 3A**), with *Pax7*$^{+}$ cells situated laterally (**Figure 3B** and diagram in **Figure 4B**). These patterns in mice are similar to those observed for the same genes in the chick IPN (Lorente-Cánovas et al., 2012).

The migration of *Pax7*$^{+}$ cells into the medial aspect of the IPR domain almost completely disappeared in DCC$^{-/-}$ embryos (compare **Figure 3E** with 3F). Caudally, the *Pax7*$^{+}$ population of the IPC was much reduced relative to that in the wild-type brains (compare **Figure 3B** with 3G). However, there were a few *Pax7*$^{+}$ neurons that succeeded in reaching their final destination in the IPC (**Figure 3G**). Hence, the migration of *Pax7*$^{+}$ cells into the IPR is more strongly affected than that into the IPC. On the other hand, there appear to be dense ectopic clusters of *Pax7*$^{+}$ cells within both the r1-r and r1-c (yellow arrows in **Figures 3F,G**) that might correspond to cells arrested in their migration, as indicated above.

In the DCC$^{-/-}$ embryos there appeared to be a reduced group of *Otx2*$^{+}$ cells that reach their destination in the IPC. However, a large part of the *Otx2*$^{+}$ did not reach the IPC at all, which was an incomplete structure in these embryos when compared to the wild-type brains (**Figure 3C**). Consistent with this disrupted migration, we observed a dense mass of ectopic *Otx2* cells arrested in the r1-c mantle layer (yellow arrows in **Figure 3D**).

By analyzing the migration of these cell populations to the IPN, we conclude that there is a general but differential impairment of their migration, such that migration of the Pro and IPR populations (*Nkx6.1*, *Irx2*, *Otp*, *Pax7*) was more compromised than that of the IPC cells (*Pax7*, *Otx2*).

DISCUSSION

In this study, we first reveal that the Netrin-1 receptor DCC is expressed extensively in the neurons forming the three rostrocaudal portions of the developing IPN (Pro, IPR and IPC) (**Figure 4A**). When we analyzed the migration of five molecularly identified neuronal populations of the IPN in DCC$^{-/-}$ mice (*Nkx6.1*$^{+}$, *Pax7*$^{+}$, *Irx2*$^{+}$, *Otp*$^{+}$, and *Otx2*$^{+}$ cells) we found that, as expected, the absence of this Netrin-1 receptor severely disrupts the migration of these diverse elements into the three portions of the IPN (**Figures 4C–H**). In these conditions, the IPN populations are born and specified but their migration is impaired, which hinders the formation of a normally constituted IPN complex.

Our earlier studies demonstrated that the migration of various neuronal populations into the IPN is crucial for the development of this nucleus (Lorente-Cánovas et al., 2012). These neuronal populations have different dorsoventral origins (*Pax7* and *Irx2* in the alar plate, *Otp* across the alar and basal plates, *Nkx6.1* and *Otx2* in the basal plate) and different rostrocaudal fates within the IPN (*Nkx6.1* and *Irx2* in the Pro; *Pax7*, *Otp* and *Irx2* in the IPR; and *Pax7* and *Otx2* in the IPC). These features of the different regions reflect the variant molecular profiles of the three neuromeric units that form the IPN complex, the Ist, r1-r and r1-c units, the latter two behaving histogenetically as independent neuromeres (Aroca and Puelles, 2005; Alonso et al., 2013).

Remarkably, the anteroposterior extent of the IPN is restricted to the rostral hindbrain area under the influence of the isthmic organizer (Crossley et al., 1996), that is thought to stop at the r1/r2 boundary (Aroca and Puelles, 2005). The rostrocaudal gradient of efficient FGF8 signaling delivered through the Ist and r1 (Aroca and Puelles, 2005) possibly accounts for part of the segmental differences in migration behavior and targeting, either directly or indirectly. Irrespective of such anteroposterior segmental differences, the Netrin-1/DCC pathway clearly emerges as a general shared mechanism that is crucial for the normal targeting of diverse cell populations to the plurineuromeric ventral subpial IPN complex.

Notably, several of the IPN cell populations studied have their origins in the lateral part of the basal plate, or even in the neighboring alar plate, such that they first have to migrate tangentially within the periventricular stratum to approach the paramedian region, where their final radial migration into the IPN occurs, adjacent to the local floor plate (Lorente-Cánovas et al., 2012). Our study shows that the absence of DCC affects both the tangential and radial migrations of the IPN cells. Nevertheless, some of them manage to migrate tangentially down to the paramedian region, failing thereafter in their final radial migration, while only a few are able to reach the IPN locus. This ability of some DCC-deficient cells to migrate suggests that additional mechanisms other than the Netrin-1/DCC pathway also influence these tangential and radial migrations.

In terms of the involvement of the Netrin-1/DCC pathway in IPN development, it would appear to first participate in the tangential dorsoventral migration of DCC^{+} cells, such that they would be attracted by the floorplate source of Netrin-1, in accordance with their known attractive interaction (Finci et al., 2015). The subsequent radial migration of these cells could be mediated by the attractive role of a second accumulation of Netrin-1 protein in the pial surface of the hindbrain paramedian region (Yung et al., 2018). Alternatively, the floor plate Netrin-1 (Yung et al., 2018; present data) could become a repulsive cue in collaboration with the Unc5 receptors (Hong et al., 1999) that are expressed by the developing IPN (van den Heuvel et al., 2013). Either of these two mechanisms (attractive sub-pial Netrin-1 or repulsive floorplate Netrin-1) could cause the radial migration of DCC^{+} cells toward their final sub-pial location after they have completed their tangential migration.

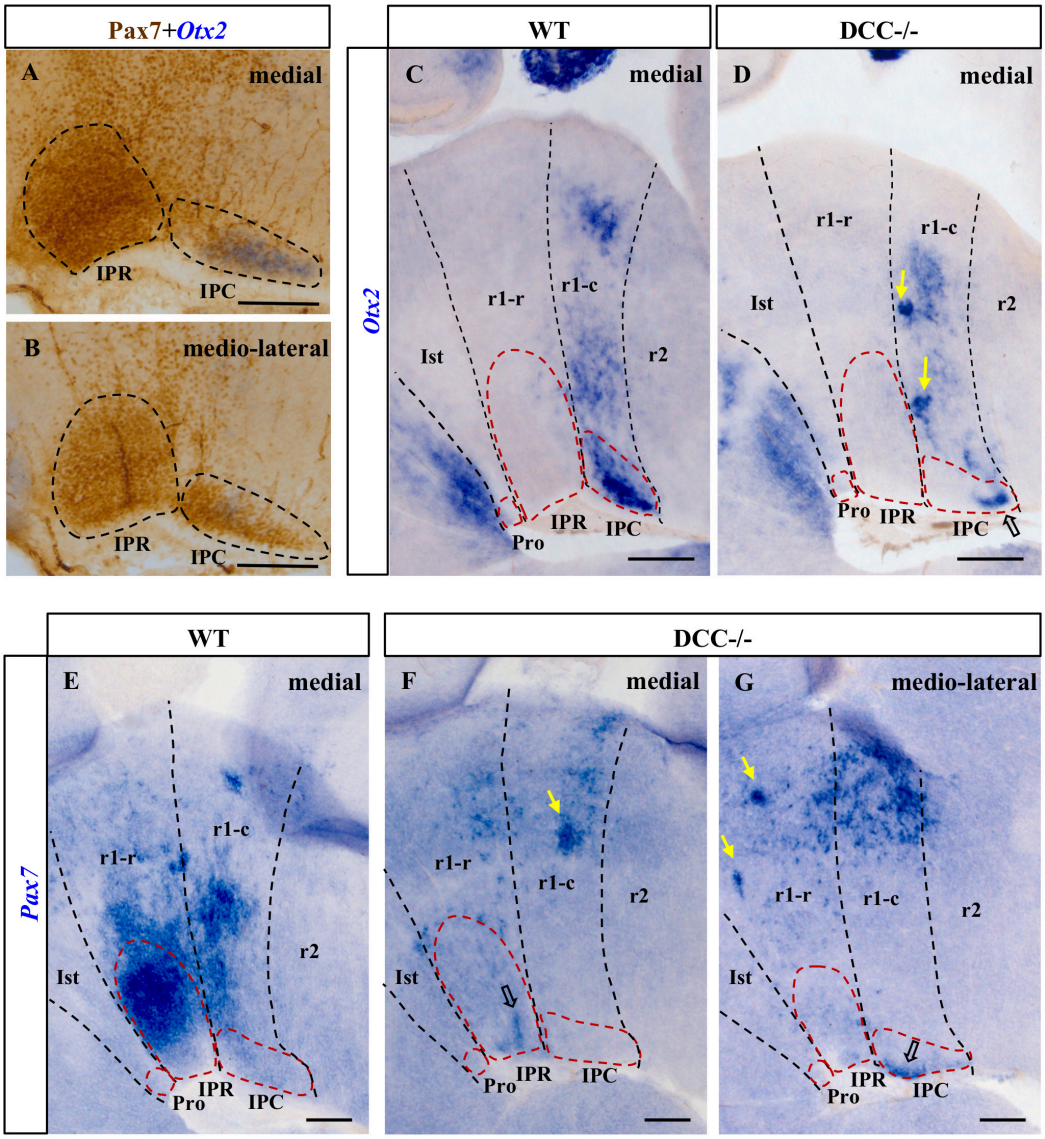

FIGURE 3 | Comparison of the *Otx2* and *Pax7* expression in sections from E18.5 wild-type and DCC$^{-/-}$ brains processed for ISH plus IHC **(A,B)** or ISH alone **(C–G)**. **(A,B)** Parasagittal sections of the IPN in an E18.5 wild-type brain after dual ISH-IHC showing the expression of Pax7 (IHC: brown precipitate) and *Otx2* (ISH: blue precipitate) in the IPN. While Pax7 is expressed in the entire IPR, there are two independent populations in the IPC: the *Otx2*$^{+}$ population located in the most medial part of the IPC **(A)**, while the Pax7^{+} population is placed laterally to the *Otx2* population **(B)**. Therefore, the medio-lateral Pax7^{+} population embraces the medial *Otx2* population in the IPC. **(C,E)** Sections of wild-type brains showing the expression of these genes. *Otx2* is expressed by cells in the IPC (medially: **C**) while *Pax7* is expressed in the IPR **(**medially: **E)** and the IPC **(**medio-laterally: data not shown**)**. We cannot see *Pax7* expression in the IPC in **(E)** as this image is a medial sagittal section, and the caudal expression of *Pax7* is observable more laterally. **(D,F,G)** Sections of DCC$^{-/-}$ brains showing the expression of these genes. A large part of the *Otx2*$^{+}$ population in the IPC is absent, although some cells have reached their correct location in the caudal IPC (open arrow in **D**). The rostral *Pax7* population has almost completely disappeared from the IPR, with only a few cells arriving at their destination **(**open arrow in **F)**, whereas the caudal population seems to be less severely affected since more *Pax7*$^{+}$ cells reach their correct location in the IPC (open arrow in **G**). In the latter three images, the yellow arrows point to patches of cells that appear to have halted their migration to the IPN as a consequence of the absence of DCC. Pro, prodromal; IPR, interpeduncular rostral; IPC, interpeduncular caudal; Ist, isthmus; r1-r, rhombomere 1 rostral; r1-c, rhombomere 1 caudal; r2, rhombomere 2. **(A,B)** scale bars = 50 μm, **(C,D,E,F,G)** scale bars = 200 μm.

There are many homeodomain transcription factors that regulate tangential migration (Chédotal and Rijli, 2009). For example, concerning the transcription factors expressed in the IPN, *Nkx6.1* is involved in the tangential migration of branchiomotor neurons (Müller et al., 2003), while *Otp* is involved in the migration of diencephalic dopaminergic neurons (Ryu et al., 2007; Löhr et al., 2009) and some hypothalamic neurons (Acampora et al., 1999; Blechman et al., 2007). In terms of the IPN complex, we know that the transcription factor Otx2 is needed for the tangential migration of the *Otx2*$^{+}$ cells of

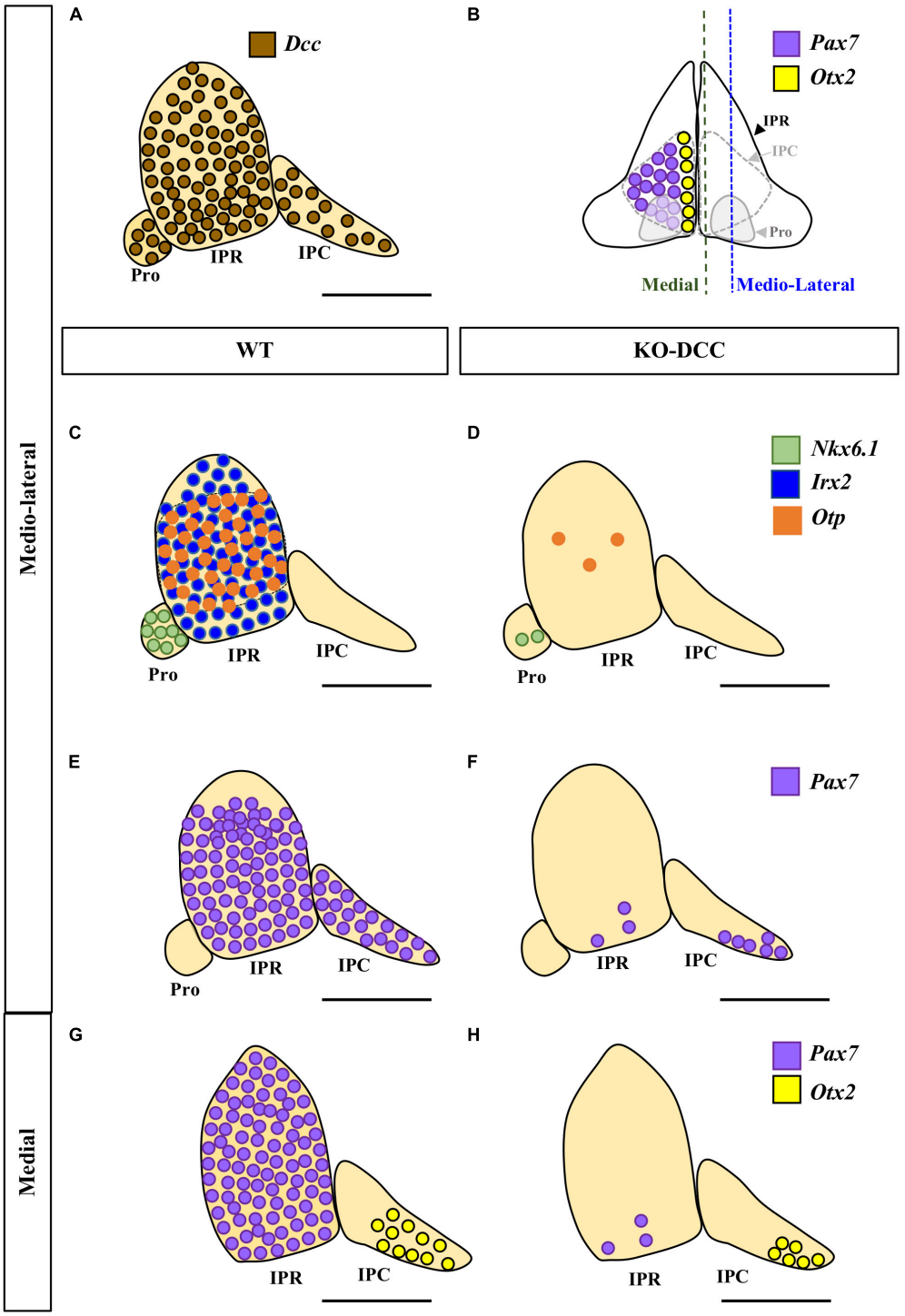

FIGURE 4 | Comparison of the wild-type and DCC$^{-/-}$ phenotypes of the IPN. **(A,C,E,G)** Sagittal diagrams showing the distribution of *Dcc* (brown circles), *Nkx6.1* (green circles), *Irx2* (blue circles), *Otp* (orange circles), *Pax7* (purple circles) and *Otx2* (yellow circles) expressing cells in the IPN. **(B)** Scheme of a frontal view of the IPN at E18.5 in which its sub-regions and the distribution of the caudal populations of the IPN are shown, with the *Pax7*$^{+}$ population embracing the *Otx2*$^{+}$ population. **(D,F,H)** Sagittal diagrams of the IPN in DCC$^{-/-}$ brains following the aforementioned color codes. By comparing **(C)** and **(D)** we can see that the *Nkx6.1*$^{+}$ population disappears almost entirely in the Pro of the DCC$^{-/-}$ brains. Similarly, a large part of the *Otp*$^{+}$ population disappears from the IPR while the *Irx2*$^{+}$ population is completely absent in these mutants. The *Pax7*$^{+}$ population of the IPR disappears almost completely (compare **E** to **F**, and **G** to **H**). However, the *Pax7*$^{+}$ population in the IPC (located medio-laterally) is less affected (compare **E** to **F**) than the aforementioned rostral populations. Similarly, the *Otx2*$^{+}$ population of the IPC (located medially) is less affected than the other populations of the IPN, although a large part of this population has also disappeared (compare **G** to **H**). Pro, prodromal; IPR, interpeduncular rostral; IPC, interpeduncular caudal. Scale bars = 50 μm.

the IPC within the r1-c medial basal plate, as shown in knockout mice (Ruiz-Reig et al., 2019). In this model, *Otx2*$^{-/-}$ cells down-regulate their DCC expression, leading to the proposal that the Netrin-1/DCC pathway might participate in the tangential migration of this neuronal population.

On the other hand, the role of the floor plate derived morphogen SHH in the migration of the IPN populations was also investigated (Moreno-Bravo et al., 2014). SHH is a well-known organizer that participates in the formation of various ventral neuronal cell types (Placzek and Briscoe, 2005). In a *Shh*-conditional mutant (Moreno-Bravo et al., 2014), the basal plate is smaller and the basal *Nkx6.1* population disappears at the interpeduncular Pro portion. However, the alar *Pax7* population migrates ventrally possibly due to remnant Netrin-1 protein expressed in the floorplate of this mutant.

Although Netrin-1 has already been proposed as a potential regulator of migratory targeting to the IPN (Aroca et al., 2006; Moreno-Bravo et al., 2014; Ruiz-Reig et al., 2019), this issue had not been directly addressed to date. Our results indicate that along with the previously demonstrated involvement of *Otx2* (Ruiz-Reig et al., 2019) and SHH (Moreno-Bravo et al., 2014), the Netrin-1/DCC signaling system fulfils an important role in the independent IPN migrations examined. Regarding the molecular identity of the 5 groups of migrating IPN cells identified, it would be necessary to identify additional transcription factors, as well as other extra- and intracellular signaling molecules involved in cell migration.

In the absence of DCC, ectopic cells that express each of the markers analyzed accumulate in the basal mantle zone. These apparently correspond to cells whose migration is arrested or misdirected due to their inability to respond to the source of Netrin-1, provided either by the floor plate or by the paramedian sub-pial surface (see above). The different morphology and distribution of the ectopic cell clusters observed for each studied gene might be related to the respective molecular identities and places of origin. The presence of these dense ectopic groups of cells suggests that cell survival has not been affected in the absence of DCC and indeed, the loss of DCC does not normally produce cell death in other experimental models, consistent with the proapoptotic role of this molecule (Mehlen et al., 1998). Moreover, Netrin-1 has been shown to act as a survival factor (Llambi et al., 2001), which could explain the survival of IPN neurons despite residing in abnormal ectopic environments.

Overall, the data presented here, in conjunction with the known roles of the mHb-IPN system, indicate that the loss of Netrin-1/DCC signaling probably leads to multiple malformations in the IPN, which would be expected to cause severe brain dysfunction. In fact, lesion or genetic/pharmacological manipulation of the mHb-IPN system in experimental models leads to dysfunctional brain syndromes like depression (Xu et al., 2018), schizophrenia (Lecourtier et al., 2004), and substance use (reviewed by McLaughlin et al., 2017).

We assume that more subtle (or selective) deficits or variations of this multiple migrational mechanism might be caused by given DCC genetic variants. This may help explain the association of different genetic variants of Netrin-1 and DCC with depression, schizophrenia or substance use (Vosberg et al., 2020). This association of Netrin-1/DCC with certain psychiatric disorders can be related to the expression of these factors in the ventral tegmental area, nucleus accumbens and orbitofrontal cortex, all part of the limbic system (Flores et al., 2005; Grant et al., 2007, 2014; Flores, 2011; Vosberg et al., 2020). Interestingly, and as inferred from our results, the emergence of such psychiatric disorders could also be associated with the effects of pathogenic variants of DCC leading to IPN maldevelopment, especially considering that this nucleus is also a limbic structure connected to the ventral tegmental area (Groenewegen et al., 1986; Klemm, 2004; McLaughlin et al., 2017).

CONCLUSION

We demonstrate that the Netrin-1/DCC pathway is involved in the migration of the IPN. We have not quantified the differences between the studied conditions from a statistical point of view. However, the qualitative results we show regarding deficits in cell migration are sufficient for our purpose, since we are not proposing any quantitative conclusions, nor a hypothesis that implies quantitative postulates. As such, we have not considered it necessary to perform a quantitative and/or statistical analysis to support the conclusions of this work. Our finding is important not only to understand the development of this structure, but also as a basis to study the possible neuroembryological etiology of brain disorders related to the habenulo-interpeduncular system. Further studies will be needed to ascertain experimentally if the known genetic *Dcc* variants also affect the migration of the different IPN populations, and eventually to analyze the resulting cellular and molecular features as well as the connectivity of this nucleus in these experimental conditions. It would be also interesting to discern additional cellular or molecular mechanisms regulating IPN migration together with Netrin-1/DCC.

DATA AVAILABILITY STATEMENT

The original contributions presented in the study are included in the article, further inquiries can be directed to the corresponding author.

ETHICS STATEMENT

The animal study was reviewed and approved by Ethics Committee of the University of Murcia.

AUTHOR CONTRIBUTIONS

PA conceived and designed the research. IG-G and PA performed the experiments. IG-G, FM, and PA analyzed the data. AA and NM-D collaborated in the probe synthesis, image analysis, and figure preparation. BA took care of the transgenic mice colony, obtaining and genotyping the embryos. GL-B established and

maintained the transgenic mouse colony at her institution. GL-B and LP provided funding for this study. IG-G, FM, and PA wrote the manuscript. IG-G, AA, NM-D, GL-B, LP, FM, and PA edited the manuscript. All the authors contributed to the article and approved the final version submitted.

FUNDING

This work was funded by the Seneca Foundation to LP (Autonomous Community of Murcia, Excellency Research contract, reference: 19904/GERM/15; 5672 Fundación Séneca; project name: Genoarchitectonic Brain Development and Applications to Neurodegenerative Diseases and Cancer) and by the Knowledge Generation Program of the Spanish Government to GL-B (PGC2018-096631-B-I00). IG-G was recipient of a predoctoral fellowship of the FPU program from the University of Murcia.

ACKNOWLEDGMENTS

Infrastructure support was provided by the University of Murcia and IMIB-Arrixaca Institute of Murcia. We thank Mark Sefton at BiomedRed for editorial support. The Pax7 antibody was developed by A. Kawakami, M. Kimura-Kawakami, T. Nomura, and H. Fujisawa and it was obtained from the Developmental Studies Hybridoma Bank (created by the NICHD of the NIH and maintained at The University of Iowa, Department of Biology, Iowa City, IA, United States).

REFERENCES

Acampora, D., Postiglione, M. P., Avantaggiato, V., Di Bonito, M., Vaccarino, F. M., Michaud, J., et al. (1999). Progressive impairment of developing neuroendocrine cell lineages in the hypothalamus of mice lacking the Orthopedia gene. *Genes Dev.* 13, 2787–2800. doi: 10.1101/gad.13.21.2787

Alcántara, S., Ruiz, M., De Castro, F., Soriano, E., and Sotelo, C. (2000). Netrin 1 acts as an attractive or as a repulsive cue for distinct migrating neurons during the development of the cerebellar system. *Development* 127, 1359–1372.

Alonso, A., Merchán, P., Sandoval, J. E., Sánchez-Arrones, L., Garcia-Cazorla, A., Artuch, R., et al. (2013). Development of the serotonergic cells in murine raphe nuclei and their relations with rhombomeric domains. *Brain Struct. Funct.* 218, 1229–1277. doi: 10.1007/s00429-012-0456-8

Aroca, P., Lorente-Cánovas, B., Mateos, F. R., and Puelles, L. (2006). Locus coeruleus neurons originate in alar rhombomere 1 and migrate into the basal plate: studies in chick and mouse embryos. *J. Comp. Neurol.* 496, 802–818. doi: 10.1002/cne.20957

Aroca, P., and Puelles, L. (2005). Postulated boundaries and differential fate in the developing rostral hindbrain. *Brain Res. Rev.* 49, 179–190. doi: 10.1016/j.brainresrev.2004.12.031

Bashaw, G. J., and Klein, R. (2010). Signaling from axon guidance receptors. *Cold Spring Harb. Perspect. Biol.* 2:a001941. doi: 10.1101/cshperspect.a001941

Blechman, J., Borodovsky, N., Eisenberg, M., Nabel-Rosen, H., Grimm, J., and Levkowitz, G. (2007). Specification of hypothalamic neurons by dual regulation of the homeodomain protein Orthopedia. *Development* 134, 4417–4426. doi: 10.1242/dev.011262

Bloch-Gallego, E., Causeret, F., Ezan, F., Backer, S., and Hidalgo-Sánchez, M. (2005). Development of precerebellar nuclei: instructive factors and intracellular mediators in neuronal migration, survival and axon pathfinding. *Brain Res. Rev.* 49, 253–266. doi: 10.1016/j.brainresrev.2005.01.003

Chédotal, A., and Rijli, F. M. (2009). Transcriptional regulation of tangential neuronal migration in the developing forebrain. *Curr. Opin. Neurobiol.* 19, 139–145. doi: 10.1016/j.conb.2009.04.005

Contestabile, R. A., and Flumerfelt, B. A. (1981). Afferent connections of the interpeduncular nucleus and the topographic organization of the habenulo-interpeduncular pathway: an HRP study in the rat. *J. Comp. Neurol.* 196, 253–270. doi: 10.1002/cne.901960206

Crossley, P. H., Martinez, S., and Martin, G. R. (1996). Midbrain development induced by FGF8 in the chick embryo. *Nature* 380, 66–68. doi: 10.1038/380066a0

de Diego, I., Kyriakopoulou, K., Karagogeos, D., and Wassef, M. (2002). Multiple influences on the migration of precerebellar neurons in the caudal medulla. *Development* 129, 297–306.

Evsyukova, I., Plestant, C., and Anton, E. S. (2013). Integrative Mechanisms of Oriented Neuronal Migration in the Developing Brain. *Annu. Rev. Cell Dev. Biol.* 29, 299–353. doi: 10.1146/annurev-cellbio-101512-122400

Fazeli, A., Dickinson, S. L., Hermiston, M. L., Tighe, R. V., Steen, R. G., Small, C. G., et al. (1997). Phenotype of mice lacking functional Deleted in colorectal cancer (Dcc) gene. *Nature* 386, 796–804. doi: 10.1038/386796a0

Fearon, E. R., Cho, K. R., Nigro, J. M., Kern, S. E., Simons, J. W., Ruppert, J. M., et al. (1990). Identification of a chromosome 18q gene that is altered in colorectal cancers. *Science* 247, 49–56. doi: 10.1126/science.2294591

Finci, L., Zhang, Y., Meijers, R., and Wang, J. H. (2015). Signaling mechanism of the netrin-1 receptor DCC in axon guidance. *Prog. Biophys. Mol. Biol.* 118, 153–160. doi: 10.1016/j.pbiomolbio.2015.04.001

Flores, C. (2011). Role of netrin-1 in the organization and function of the mesocorticolimbic dopamine system. *J. Psychiatry Neurosci.* 36, 296–310. doi: 10.1503/jpn.100171

Flores, C., Manitt, C., Rodaros, D., Thompson, K. M., Rajabi, H., Luk, K. C., et al. (2005). Netrin receptor deficient mice exhibit functional reorganization of dopaminergic systems and do not sensitize to amphetamine. *Mol. Psychiatry* 10, 606–612. doi: 10.1038/sj.mp.4001607

Grant, A., Hoops, D., Labelle-Dumais, C., Prévost, M., Rajabi, H., Kolb, B., et al. (2007). Netrin-1 receptor-deficient mice show enhanced mesocortical dopamine transmission and blunted behavioural responses to amphetamine. *Eur. J. Neurosci.* 26, 3215–3228. doi: 10.1111/j.1460-9568.2007.05888.x

Grant, A., Manitt, C., and Flores, C. (2014). Haloperidol treatment downregulates DCC expression in the ventral tegmental area. *Neurosci. Lett.* 575, 58–62. doi: 10.1016/j.neulet.2014.05.030

Groenewegen, H. J., Ahlenius, S., Haber, S. N., Kowall, N. W., and Nauta, W. J. H. (1986). Cytoarchitecture, fiber connections, and some histochemical aspects of the interpeduncular nucleus in the rat. *J. Comp. Neurol.* 249, 65–102. doi: 10.1002/cne.902490107

Hedrick, L., Cho, K. R., Fearon, E. R., Wu, T. C., Kinzler, K. W., and Vogelstein, B. (1994). The DCC gene product in cellular differentiation and colorectal tumorigenesis. *Genes Dev.* 8, 1174–1183. doi: 10.1101/gad.8.10.1174

Herkenham, M., and Nauta, W. J. H. (1979). Efferent connections of the habenular nuclei in the rat. *J. Comp. Neurol.* 187, 19–47. doi: 10.1002/cne.901870103

Hikosaka, O. (2010). The habenula: from stress evasion to value-based decision-making. *Nat. Rev. Neurosci.* 11, 503–513. doi: 10.1038/nrn2866

Hong, K., Hinck, L., Nishiyama, M., Poo, M. M., Tessier-Lavigne, M., and Stein, E. (1999). A ligand-gated association between cytoplasmic domains of UNC5 and DCC family receptors converts netrin-induced growth cone attraction to repulsion. *Cell* 97, 927–941. doi: 10.1016/S0092-8674(00)80804-1

Keino-Masu, K., Masu, M., Hinck, L., Leonardo, E. D., Chan, S. S. Y., Culotti, J. G., et al. (1996). Deleted in Colorectal Cancer (DCC) encodes a netrin receptor. *Cell* 87, 175–185. doi: 10.1016/S0092-8674(00)81336-7

Klemm, W. R. (2004). Habenular and interpeduncularis nuclei: shared components in multiple-function networks. *Med. Sci. Monit.* 10, RA261–RA273.

Kratochwil, C. F., Maheshwari, U., and Rijli, F. M. (2017). The long journey of pontine nuclei neurons: from rhombic lip to cortico-ponto-cerebellar circuitry. *Front. Neural Circuits* 11:33. doi: 10.3389/fncir.2017.00033

Lecourtier, L., Neijt, H. C., and Kelly, P. H. (2004). Habenula lesions cause impaired cognitive performance in rats: implications for schizophrenia. *Eur. J. Neurosci.* 19, 2551–2560. doi: 10.1111/j.0953-816X.2004.03356.x

Llambi, F., Causeret, F., Bloch-Gallego, E., and Mehlen, P. (2001). Netrin-1 acts as a survival factor via its receptors UNC5H and DCC. *EMBO J.* 20, 2715–2722. doi: 10.1093/emboj/20.11.2715

Löhr, H., Ryu, S., and Driever, W. (2009). Zebrafish diencephalic A11-related dopaminergic neurons share a conserved transcriptional network with neuroendocrine cell lineages. *Development* 136, 1007–1017. doi: 10.1242/dev.033878

Lorente-Cánovas, B., Marín, F., Corral-San-Miguel, R., Hidalgo-Sánchez, M., Ferrán, J. L., Puelles, L., et al. (2012). Multiple origins, migratory paths and molecular profiles of cells populating the avian interpeduncular nucleus. *Dev. Biol.* 361, 12–26. doi: 10.1016/j.ydbio.2011.09.032

Marcos, S., Backer, S., Causeret, F., Tessier-Lavigne, M., and Bloch-Gallego, E. (2009). Differential roles of Netrin-1 and its receptor DCC in inferior olivary neuron migration. *Mol. Cell. Neurosci.* 41, 429–439. doi: 10.1016/j.mcn.2009.04.008

Marín, O., Valiente, M., Ge, X., and Tsai, L.-H. (2010). Guiding neuronal cell migrations. *Cold Spring Harb. Perspect. Biol.* 2:a001834. doi: 10.1101/cshperspect.a001834

McLaughlin, I., Dani, J. A., and De Biasi, M. (2017). The medial habenula and interpeduncular nucleus circuitry is critical in addiction, anxiety, and mood regulation. *J. Neurochem.* 142, 130–143. doi: 10.1111/jnc.14008

Mehlen, P., Rabizadeh, S., Snipas, S. J., Assa-Munt, N., Salvesen, G. S., and Bredesen, D. E. (1998). The DCC gene product induces apoptosis by a mechanism requiring receptor proteolysis. *Nature* 395, 801–804. doi: 10.1038/27441

Moreno-Bravo, J. A., Perez-Balaguer, A., Martinez-Lopez, J. E., Aroca, P., Puelles, L., Martinez, S., et al. (2014). Role of Shh in the development of molecularly characterized tegmental nuclei in mouse rhombomere 1. *Brain Struct. Funct.* 219, 777–792. doi: 10.1007/s00429-013-0534-6

Müller, M., Jabs, N., Lorke, D. E., Fritzsch, B., and Sander, M. (2003). Nkx6.1 controls migration and axon pathfinding of cranial branchio-motoneurons. *Development* 130, 5815–5826. doi: 10.1242/dev.00815

Nieto, M. A., Patel, K., and Wilkinson, D. G. (1996). In Situ hybridization analysis of chick embryos in whole mount and tissue sections. *Methods Cell Biol.* 51, 219–235. doi: 10.1016/s0091-679x(08)60630-5

Placzek, M., and Briscoe, J. (2005). The floor plate: multiple cells, multiple signals. *Nat. Rev. Neurosci.* 6, 230–240. doi: 10.1038/nrn1628

Ruiz-Reig, N., Rakotobe, M., Bethus, I., Le Menn, G., Huditz, H. I., Marie, H., et al. (2019). Developmental requirement of homeoprotein Otx2 for specific habenulo-interpeduncular subcircuits. *J. Neurosci.* 39, 1005–1019. doi: 10.1523/JNEUROSCI.1818-18.2018

Ryu, S., Mahler, J., Acampora, D., Holzschuh, J., Erhardt, S., Omodei, D., et al. (2007). Orthopedia homeodomain protein is essential for diencephalic dopaminergic neuron development. *Curr. Biol.* 17, 873–880. doi: 10.1016/j.cub.2007.04.003

Shi, M., Guo, C., Dai, J. X., and Ding, Y. Q. (2008). DCC is required for the tangential migration of noradrenergic neurons in locus coeruleus of mouse brain. *Mol. Cell. Neurosci.* 39, 529–538. doi: 10.1016/j.mcn.2008.07.023

van den Heuvel, D. M. A., Hellemons, A. J. C. G. M., and Pasterkamp, R. J. (2013). Spatiotemporal expression of repulsive guidance molecules (RGMs) and their receptor neogenin in the mouse brain. *PLoS One* 8:e55828. doi: 10.1371/journal.pone.0055828

Vosberg, D. E., Leyton, M., and Flores, C. (2020). The Netrin-1/DCC guidance system: dopamine pathway maturation and psychiatric disorders emerging in adolescence. *Mol. Psychiatry* 25, 297–307. doi: 10.1038/s41380-019-0561-567

Watson, C., Shimogori, T., and Puelles, L. (2017). Mouse Fgf8-Cre-LacZ lineage analysis defines the territory of the postnatal mammalian isthmus. *J. Comp. Neurol.* 525, 2782–2799. doi: 10.1002/cne.24242

Xu, C., Sun, Y., Cai, X., You, T., Zhao, H., Li, Y., et al. (2018). Medial Habenula-interpeduncular nucleus circuit contributes to Anhedonia-like behavior in a rat model of depression. *Front. Behav. Neurosci.* 12:238. doi: 10.3389/fnbeh.2018.00238

Yung, A. R., Druckenbrod, N. R., Cloutier, J. F., Wu, Z., Tessier-Lavigne, M., and Goodrich, L. V. (2018). Netrin-1 Confines Rhombic Lip-Derived Neurons to the CNS. *Cell Rep.* 22, 1666–1680. doi: 10.1016/j.celrep.2018.01.068

Conflict of Interest: The authors declare that the research was conducted in the absence of any commercial or financial relationships that could be construed as a potential conflict of interest.

frontiers in Cell and Developmental Biology

ORIGINAL RESEARCH
published: 29 October 2020
doi: 10.3389/fcell.2020.577201

The Planar Polarity Component VANGL2 Is a Key Regulator of Mechanosignaling

*Sek-Shir Cheong[1], Khondoker M. Akram[1], Carlos Matellan[2], Sally Yunsun Kim[1], David C. A. Gaboriau[3], Matthew Hind[1,4], Armando E. del Río Hernández[2], Mark Griffiths[1,5] and Charlotte H. Dean[1,6]**

[1] National Heart and Lung Institute, Imperial College London, London, United Kingdom, [2] Cellular and Molecular Biomechanics Laboratory, Department of Bioengineering, Imperial College London, London, United Kingdom, [3] Facility for Imaging by Light Microscopy, National Heart and Lung Institute, Faculty of Medicine, Imperial College London, London, United Kingdom, [4] National Institute for Health Research, Respiratory Biomedical Research Unit, Royal Brompton & Harefield NHS Foundation Trust, London, United Kingdom, [5] Peri-Operative Medicine Department, St Bartholomew's Hospital, London, United Kingdom, [6] MRC Harwell Institute, Harwell Campus, Oxfordshire, United Kingdom

VANGL2 is a component of the planar cell polarity (PCP) pathway, which regulates tissue polarity and patterning. The *Vangl2*^{Lp} mutation causes lung branching defects due to dysfunctional actomyosin-driven morphogenesis. Since the actomyosin network regulates cell mechanics, we speculated that mechanosignaling could be impaired when VANGL2 is disrupted. Here, we used live-imaging of precision-cut lung slices (PCLS) from *Vangl2*$^{Lp/+}$ mice to determine that alveologenesis is attenuated as a result of impaired epithelial cell migration. *Vangl2*$^{Lp/+}$ tracheal epithelial cells (TECs) and alveolar epithelial cells (AECs) exhibited highly disrupted actomyosin networks and focal adhesions (FAs). Functional assessment of cellular forces confirmed impaired traction force generation in *Vangl2*$^{Lp/+}$ TECs. YAP signaling in *Vangl2*^{Lp} airway epithelium was reduced, consistent with a role for VANGL2 in mechanotransduction. Furthermore, activation of RhoA signaling restored actomyosin organization in *Vangl2*$^{Lp/+}$, confirming RhoA as an effector of VANGL2. This study identifies a pivotal role for VANGL2 in mechanosignaling, which underlies the key role of the PCP pathway in tissue morphogenesis.

Keywords: VANGL2, planar cell polarity, mechanosignaling, cell migration, focal adhesion, traction force, RhoA, YAP signaling

OPEN ACCESS

Edited by:
Claudia Tanja Mierke, Leipzig University, Germany

Reviewed by:
Andre Goffinet, Catholic University of Louvain, Belgium
Xiaowei Lu, University of Virginia, United States

***Correspondence:**
Charlotte H. Dean
c.dean@imperial.ac.uk

Specialty section:
This article was submitted to Cell Adhesion and Migration, a section of the journal Frontiers in Cell and Developmental Biology

Received: *28 June 2020*
Accepted: *08 October 2020*
Published: *29 October 2020*

Citation:
Cheong S-S, Akram KM, Matellan C, Kim SY, Gaboriau DCA, Hind M, del Río Hernández AE, Griffiths M and Dean CH (2020) The Planar Polarity Component VANGL2 Is a Key Regulator of Mechanosignaling. Front. Cell Dev. Biol. 8:577201. doi: 10.3389/fcell.2020.577201

INTRODUCTION

The planar cell polarity (PCP) pathway is a non-canonical Wnt pathway, best known for controlling the collective polarization of cells across the plane of a cell sheet, a phenomenon referred to as PCP. In *Drosophila*, the mutually exclusive location of Vangl/Pk and Fz/Dsh/Diego complexes at the proximal and distal side within a cell gives rise to PCP (Goodrich and Strutt, 2011). More broadly, across different organisms, this core set of protein components govern diverse developmental processes through regulation of directed cell migration (DCM) (Henderson et al., 2018). In DCM, groups of cells within the tissue plane adopt multicellular polarization and move in a cohesive manner with the coordination of RhoA-mediated actomyosin contractile activity at the rear and Rac1/Cdc42-induced pushing force at the front, while maintaining cell–cell contacts (Friedl and Gilmour, 2009; Mayor and Carmona-Fontaine, 2010). Our previous studies have shown that the

PCP pathway is required for embryonic lung and kidney development (Yates et al., 2010a,b, 2013). More recently, it has been shown that the PCP pathway plays a central role in alveologenesis and adult lung homeostasis (Poobalasingam et al., 2017; Zhang et al., 2020) and is important for normal repair of the lung epithelium following injury (Poobalasingam et al., 2017). Both embryonic and adult PCP mouse mutants display abnormal actomyosin distribution (Yates et al., 2010b; Poobalasingam et al., 2017). Although PCP is known to regulate actin cytoskeleton remodeling through its downstream effector RhoA (Munoz-Soriano et al., 2012; Davey and Moens, 2017; Henderson et al., 2018), the function of the PCP pathway in mechanosignaling, the process by which mechanical cues can rapidly trigger signaling mechanisms that lead to cytoskeletal re-organization and modulation of cell shape or movement, has not been determined.

The actin cytoskeleton consists of polymerized actin filaments (F-actin), which serve as a scaffold for non-muscle myosin II to form the actomyosin contractile system. Mechanical stresses can activate RhoA, which promotes the formation of stress fibers and stimulates the phosphorylation of myosin light chain 2 (MLC2) through Rho-associated kinase (ROCK) (Sun et al., 2016). The intracellular actin cytoskeleton is linked to focal adhesions (FAs) via proteins such as paxillin, talin, and vinculin. These FA complexes mediate bidirectional signaling between cell and extracellular matrix (ECM) via the mechanosensitive transmembrane integrin proteins and the intracellular actin filaments (Mitra et al., 2005; Hopkins et al., 2019). During migration, increased mechanosignaling leads to integrin clustering at FAs, which triggers the autophosphorylation of FA kinase (FAK). This in turn stimulates the recruitment of FA proteins such as paxillin and vinculin to further reinforce the FA maturation (Hamadi et al., 2005; Mitra et al., 2005).

Given the role of the PCP pathway in DCM and our previous observations of disrupted actomyosin network in the lungs (Yates et al., 2010b; Poobalasingam et al., 2017), we hypothesized that VANGL2 could play a key role in mechanosignaling. Interestingly, a previous study described a link between the PCP/WNT5A-Frizzled-DVL pathway with YAP (Park et al., 2015), a mechanotransducer that converts mechanical stimuli into biochemical signals by regulating gene expression in response to mechanical cues (Jaalouk and Lammerding, 2009). Moreover, YAP deficiency caused lung branching defects (Lin et al., 2017), similar to that of *Vangl2*^{Lp}.

The *Looptail* mutant mouse (*Vangl2*^{Lp}) carries a missense mutation, S464N, in the *Vangl2* gene. *Vangl2*^{Lp} is a dominant negative mutation that not only impairs the transport of mutant VANGL2 from endoplasmic reticulum to the Golgi but also blocks wildtype (WT) VANGL2 protein being trafficked to membrane, thereby resulting in loss of function. The dominant nature of the *Vangl2*^{Lp} mutation has been well established in mouse genetic studies and *in vitro* cell systems (Kibar et al., 2001; Murdoch, 2001; Gao et al., 2011; Belotti et al., 2012; Yin et al., 2012; Seo et al., 2017). Although homozygotes die around birth, heterozygotes are viable as adults but display a number of phenotypes including looped tails which led to their name and lung defects (Yates et al., 2010b; Poobalasingam et al., 2017). In addition to disruption of VANGL2, the Looptail mutation also affects additional PCP components such as Prickle2 (Pryor et al., 2014), Frizzled3 (Montcouquiol et al., 2006), and its homolog Vangl1 (Yin et al., 2012) making this a powerful tool for studies of the Wnt/PCP pathway. Thus, using *Vangl2*^{Lp}, we assessed whether VANGL2 dysfunction affects normal cellular mechanics and mechanosignaling. Real-time imaging of *Vangl2*$^{Lp/+}$ precision-cut lung slices (PCLSi) and wound-healing assays with primary lung epithelial cells reveal that VANGL2 is required for normal alveologenesis and wound repair via its role in DCM. We provide mechanistic evidence that VANGL2 disruption affects FA complexes, stress fiber formation, and MLC2 activation, leading to defective intracellular contractility via RhoA signaling. These abnormalities result in impaired traction force generation and deficiency of the mechanotransducer YAP. This study demonstrates that VANGL2 has an important role in mechanosignaling, which underlies the key functions of PCP pathway in regulating tissue morphogenesis and repair.

RESULTS

Live Imaging of Alveologenesis in *Vangl2*$^{Lp/+}$ PCLS Reveals Impaired Cell Migration

Using the PCLSi technique recently established by our team (Akram et al., 2019a), we investigated whether the alveologenesis defects we previously reported in *Vangl2*$^{Lp/+}$ mice were due to impaired cell migration (Poobalasingam et al., 2017).

Precision-cut lung slices (300 μm thick) from WT and *Vangl2*$^{Lp/+}$ P3 littermate lungs were labeled with FITC-conjugated epithelial cell-specific marker EpCAM and time-lapse live imaging of *ex vivo* alveologenesis was conducted for 13 h (**Supplementary Figure S1A**). EpCAM specifically labeled epithelial cells but not macrophages within PCLS, as confirmed by dual staining of EpCAM and CD11c (macrophage marker) (**Supplementary Figure S1B**). Time-lapse image sequences were subsequently analyzed to track and quantify epithelial cell motility.

Disruption of *Vangl2* significantly inhibited mean net epithelial cell migration (a total linear migration of a cell from "start point" to the "end point" in 13 h) compared to WT control PCLS (1.88 vs 2.50 μm respectively; $p = 0.0001$) (**Figures 1A–C** and **Supplementary Videos 1, 2**). A large proportion of epithelial cells were relatively sessile and migrated less than 2 μm both in WT and *Vangl2*$^{Lp/+}$ lung slices. However, the number of highly motile epithelial cells which migrated between 5 and 11 μm was more than double in WT PCLS compared to that of *Vangl2*$^{Lp/+}$ littermates (12 vs 5%, respectively; $p = 0.0007$) (**Figure 1D**). MTT metabolic assays confirmed that viability was equally maintained in WT and *Vangl2*$^{Lp/+}$ slices at the end of time-lapse imaging (**Figure 1E**).

In addition to live imaging, we compared alveologenesis in PCLS from WT and *Vangl2*$^{Lp/+}$ P3 mice cultured in serum-free DMEM for 72 h. Lung slices were then embedded in paraffin,

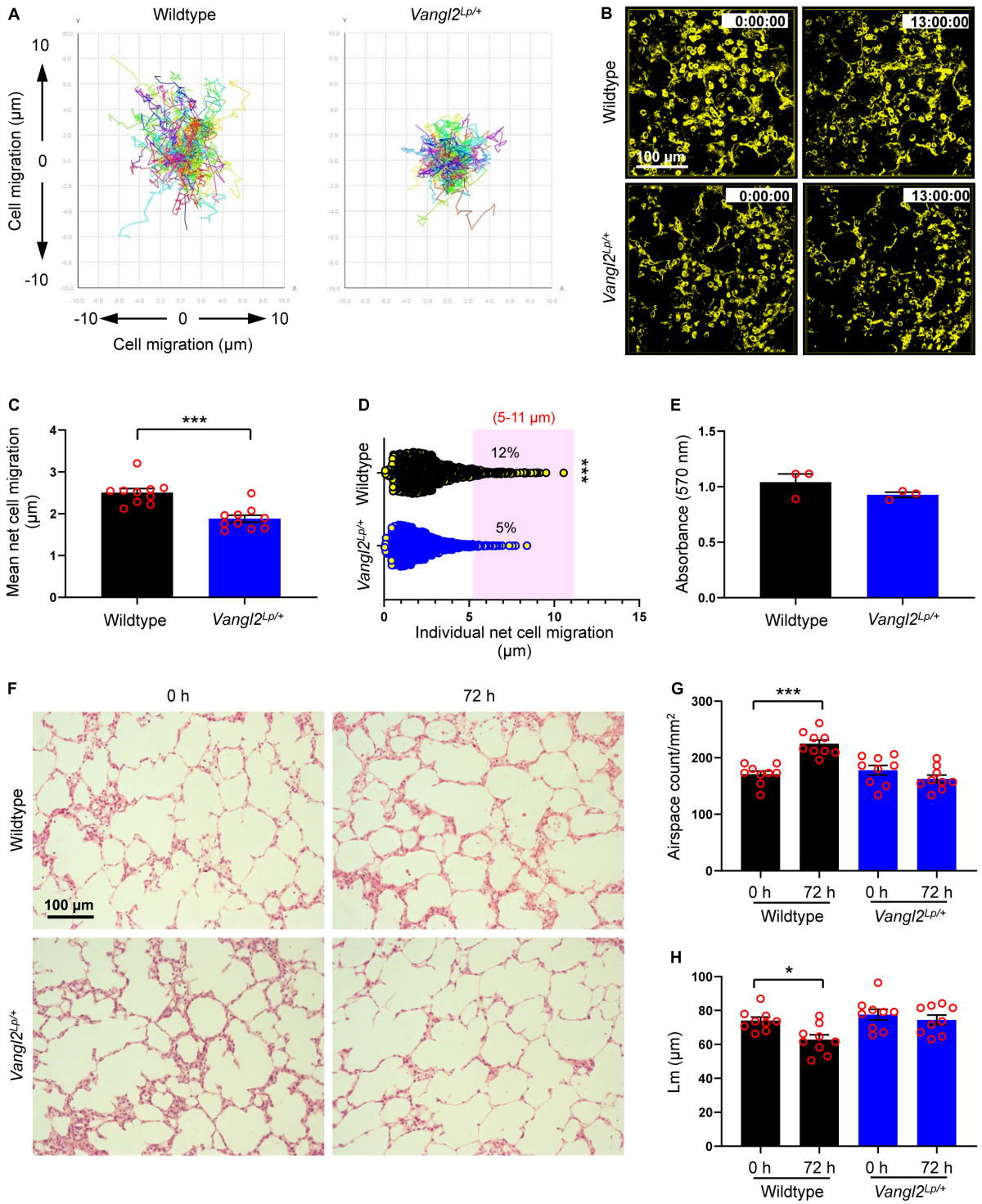

FIGURE 1 | Alveolar epithelial cell migration is disrupted in *Vangl2*$^{Lp/+}$ mice during *ex vivo* alveologenesis. **(A)** Traces of individual cell tracking over 13 h in a single field from wildtype and *Vangl2*$^{Lp/+}$ P3 mouse PCLS. **(B)** Deconvolved widefield 3D z-stack images extracted from 13 h time-lapse videos (**Supplementary Videos 1, 2**) of wildtype (top panels) and *Vangl2*$^{Lp/+}$ (bottom panels) P3 PCLS labeled with EpCAM-FITC. **(C)** Mean net epithelial cell migration over 13 h of time-lapse imaging of P3 PCLS. *n* = 3 independent experiments using three separate mice for each group; at least three fields were quantified from each lung slice from each mouse per group per experiment. Each dot represents mean net epithelial cell migration per field. Mann–Whitney *U*-test, ***$p = 0.0001$. **(D)** Individual net cell migration in wildtype and *Vangl2*$^{Lp/+}$ P3 PCLS after 13 h of time-lapse imaging (each dot represents a single cell). A total of 1248 cells in wildtype and 1635 cells in *Vangl2*$^{Lp/+}$ P3 PCLS were tracked. Cells fall within the area highlighted in pink were highly motile and migrated between 5 and 11 μm. *n* = 3 independent

(Continued)

FIGURE 1 | Continued
experiments using three separate mice for each group. Mann–Whitney *U*-test, ***$p = 0.0007$. **(E)** MTT cell viability assay comparing wildtype and *Vangl2*$^{Lp/+}$ P3 PCLS at the end of 13 h time-lapse; $n = 3$ independent experiments using three separate mice, with duplicate slices per condition per experiment; Mann–Whitney *U*-test. **(F)** H&E-stained sections from P3 PCLS at 0 and 72 h *ex vivo* culture of wildtype (top panels) and *Vangl2*$^{Lp/+}$ (bottom panels) mice. Airspace count **(G)** and mean linear intercept (Lm) **(H)** obtained from H&E sections of P3 PCLS of wildtype and *Vangl2*$^{Lp/+}$ mice at 0 and 72 h; $n = 3$ independent experiments using three separate mice, three H&E sections from each PCLS from each mouse were quantified per group per experiment. Each dot represents counts per field; one-way ANOVA with Tukey's *post hoc* test, ***$p < 0.001$, *$p < 0.05$. All data are presented as mean ± SEM.

cut into 3 μm sections, and stained with hematoxylin and eosin (H&E) for imaging and subsequent morphometric analyses. Alveologenesis was compared by quantifying the number of airspaces and mean linear intercept (Lm). A smaller Lm value indicates more alveoli. In WT PCLS, the number of airspaces per square millimeter (mm^2) area increased by 31% (171 vs 225 airspaces/mm^2 at 0 and 72 h, respectively; $p < 0.001$), and the Lm values decreased (74.07 vs 62.84 μm at 0 and 72 h, respectively; $p < 0.05$) after 72 h of culture (**Figures 1F–H**), indicating that alveologenesis continued *ex vivo* (Pieretti et al., 2014; Akram et al., 2019a). By contrast, the number of airspaces and Lm values remained unaltered in *Vangl2*$^{Lp/+}$ lung slices after *in vitro* culture for the same duration (178 vs 163 airspaces/mm^2; Lm: 77.58 vs 74.49 μm at 0 and 72 h, respectively) (**Figures 1F–H**). MTT assays confirmed that cell viability was unaffected in WT and *Vangl2*$^{Lp/+}$ PCLS after 72 h of culture (**Supplementary Figure S1C**). Taken together, our data show that functional deficiency of *Vangl2* perturbs alveolar epithelial cell (AEC) migration, thereby hindering postnatal alveologenesis.

Vangl2 Is Required for Wound Repair and Directed Cell Migration

Next we investigated cell migration and repair capacity in *Vangl2*$^{Lp/+}$ primary lung epithelial cells. We isolated tracheal epithelial cells (TECs) from WT and *Vangl2*$^{Lp/+}$ mice and cultured them to confluence before inflicting a scratch wound in the cell monolayers and comparing the wound-healing capacity in WT and *Vangl2*$^{Lp/+}$ TECs. The percentage of wound area healed was reduced by 20% in *Vangl2*$^{Lp/+}$ TECs (63.24% in *Vangl2*$^{Lp/+}$ vs 85.36% in WT; $p = 0.029$) (**Figures 2A,B**) or (0.75 vs 1.00 *Vangl2*$^{Lp/+}$ relative to WT TECs; $p = 0.029$) (**Figures 2A,C**).

Given the role of the PCP pathway in establishing cell polarity during DCM (Amano et al., 1996), we then assessed whether impaired cell migration in *Vangl2*$^{Lp/+}$ TECs may be attributed to aberrant cell polarity at the leading edge of a scratch wound. Cells were fixed at 20 h post-scratch and immunostained with Golgi marker GM130 to distinguish polarized and non-polarized cells as previously described (Etienne-Manneville and Hall, 2001; Cory, 2011; Poobalasingam et al., 2017). Interestingly, Golgi apparatus appeared randomly localized in *Vangl2*$^{Lp/+}$ TECs at the leading edge compared with leading WT TECs, which showed a higher proportion of cells with the Golgi facing the direction of migration (**Figure 2E**). Quantitative analysis of GM130 position demonstrated that around 62% of the WT TECs at the leading edge were polarized compared with only 44% in *Vangl2*$^{Lp/+}$ TECs ($p = 0.029$) (**Figure 2F**). These data confirmed that in primary lung epithelial cells, VANGL2 plays a role in wound repair following injury by regulating cell polarity during DCM.

VANGL2 Dysfunction Leads to Highly Disrupted Actin Cytoskeleton and Focal Adhesions

To investigate whether impaired cell mechanics were associated with the cell migration defects in *Vangl2*$^{Lp/+}$ lungs, we first investigated actin cytoskeleton organization and FA integrity in adult WT and *Vangl2*$^{Lp/+}$ epithelial cells. Phalloidin stained stress fibers throughout WT TECs (**Figure 3A**). In contrast, *Vangl2*$^{Lp/+}$ TECs exhibited diffuse and highly disrupted actin filaments that were sparsely distributed and barely visible (**Figure 3B**). Cortical actin was visible in both WT and *Vangl2*$^{Lp/+}$ TECs. These microscopic changes in actin distribution within adult *Vangl2*$^{Lp/+}$ epithelial cells are consistent with our previous findings of aberrant actin distribution and regulation in whole embryonic homozygous and heterozygous *Vangl2*^{Lp} lung tissues (Poobalasingam et al., 2017).

Immunostaining for the FA protein, paxillin, in WT TECs demonstrated a high number of elongated FAs at the tips of stress fibers and small dot-like FAs at the cell periphery (**Figure 3A**). This was strikingly different from *Vangl2*$^{Lp/+}$ TECs, in which FAs were markedly reduced and large FAs capping stress fibers were rarely present (**Figure 3B**). Quantification of both mean FA size and FA density (total FA area normalized to total cell area) revealed a substantial reduction in *Vangl2*$^{Lp/+}$ TECs ($p < 0.01$) (**Figures 3C,D**). Similarly, compared to WT cells (**Figure 3E**), AECs isolated from *Vangl2*$^{Lp/+}$ mutant mice also exhibited highly disordered actin cytoskeleton (**Figure 3F**) and a dramatic reduction in both mean FA size and density ($p < 0.01$) (**Figures 3G,H**). Immunostaining with pan-cytokeratin, an epithelial cell marker, was performed for TECs and AECs in each experiment to confirm the purity of epithelial cell populations (**Supplementary Figure S2**).

To further validate our findings, we conducted *VANGL2* knockdown by siRNA transfection in human AECs (A549). The siRNA knockdown efficiency was assessed by qRT-PCR, as shown in **Supplementary Figure S3A**. In agreement with the findings described above, *VANGL2*-depleted A549 cells recapitulated overt anomalies in both actin cytoskeleton and FAs (**Figures 4A–D**). These morphological aberrations resembled A549 cells treated with different actomyosin inhibitors: para-nitroblebbistatin (blebbistatin; an inhibitor of non-muscle myosin II ATPase activity) (Képiró et al., 2014), ROCK inhibitor, Y-27632 (Uehata et al., 1997), and actin polymerization inhibitor, cytochalasin D (Schliwa, 1982) (**Figures 4E–N**). Scratch assays conducted in A549 cells treated with blebbistatin or

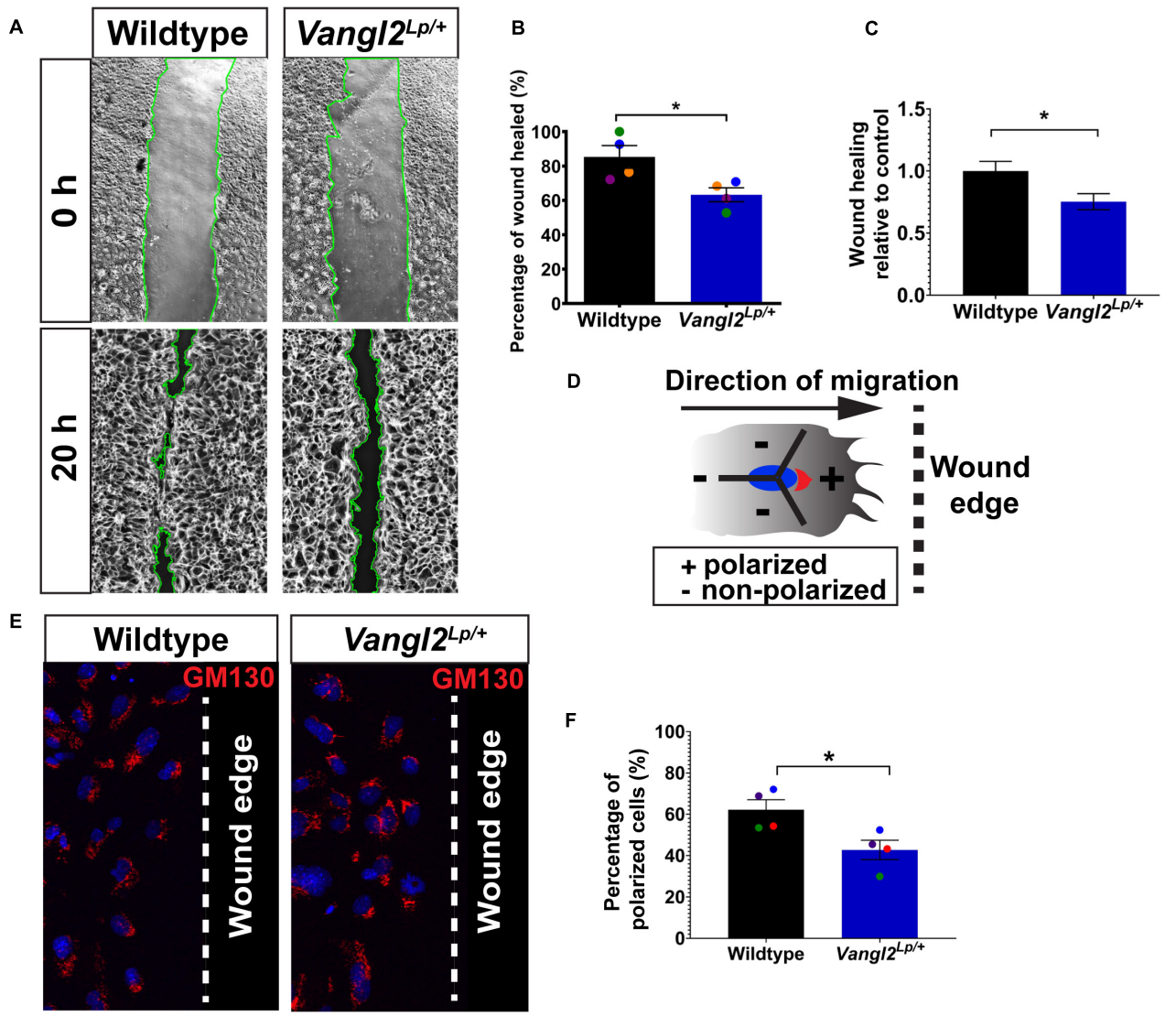

FIGURE 2 | Cell polarity and wound-healing are impaired in *Vangl2*$^{Lp/+}$ TECs. **(A)** Representative images showing wildtype (left panels) and *Vangl2*$^{Lp/+}$ TECs (right panels) at 0 and 20 h post-scratch. Wound edges are indicated by green lines. **(B)** Percentage of wound healed measured at 20 h post-scratch in wildtype and *Vangl2*$^{Lp/+}$ TECs. $n = 4$ independent experiments; TECs from three mice were pooled for each group per experiment; three technical replicates for each group per experiment; each dot represents mean percentage of wound healed per experiment. Mann–Whitney *U*-test, $^*p = 0.029$. **(C)** Wound-healing rate in *Vangl2*$^{Lp/+}$ relative to wildtype control. $n = 4$ independent experiments. Mann–Whitney *U*-test, $^*p = 0.029$. **(D)** Schematic to illustrate polarized or non-polarized cells at leading edge as determined by the 120° arc drawn from the center of a nucleus (blue) facing the direction of migration (arrow). Golgi (red) that are located within the 120° arc (+) were considered as polarized, whereas cells with the entire or majority of the Golgi localized outside the 120° arc were classed as non-polarized. Arrow shows the direction of migration and dotted line indicates the wound edge. **(E)** Immunostaining for Golgi marker GM130 (red) in fixed wildtype and *Vangl2*$^{Lp/+}$ TECs at 20 h post-scratch. Nuclei were labeled with DAPI (blue). Dotted line indicates the wound edge. **(F)** Percentage of polarized cells at 20 h post-scratch in wildtype and *Vangl2*$^{Lp/+}$ TECs. $n = 4$ independent experiments; TECs from three mice were pooled for each group per experiment; three technical replicates for each group per experiment; each dot represents mean percentage of wound healed per experiment. Mann–Whitney *U*-test, $^*p < 0.05$. All data are presented as mean ± SEM.

cytochalasin D also showed significantly impaired cell migration (**Supplementary Figures S3B–E**) as shown in primary *Vangl2*^{Lp} TECs (**Figure 2**). Altogether, these results suggest that disrupted FAs and actin cytoskeleton in *VANGL2*-deficient cells contribute to impaired cell migration.

Since FAK is known to be one of the major kinases that regulate the formation and maturation of FAs (Hamadi et al., 2005), we next investigated whether phosphorylated FAK (pFAK; active form) is affected in *Vangl2*$^{Lp/+}$ TECs. Immunostaining for pFAK-Y397 revealed an altered pFAK pattern in *Vangl2*$^{Lp/+}$ TECs (**Figure 4O**). However, it was technically challenging to obtain sufficient materials from primary cells to quantify pFAK levels by western blotting, therefore, given the similar phenotype observed in both *Vangl2*$^{Lp/+}$ primary cells and *VANGL2*-depleted A549s, lysates from control- or *VANGL2*-siRNA-treated A549 cells were used to quantify pFAK and total

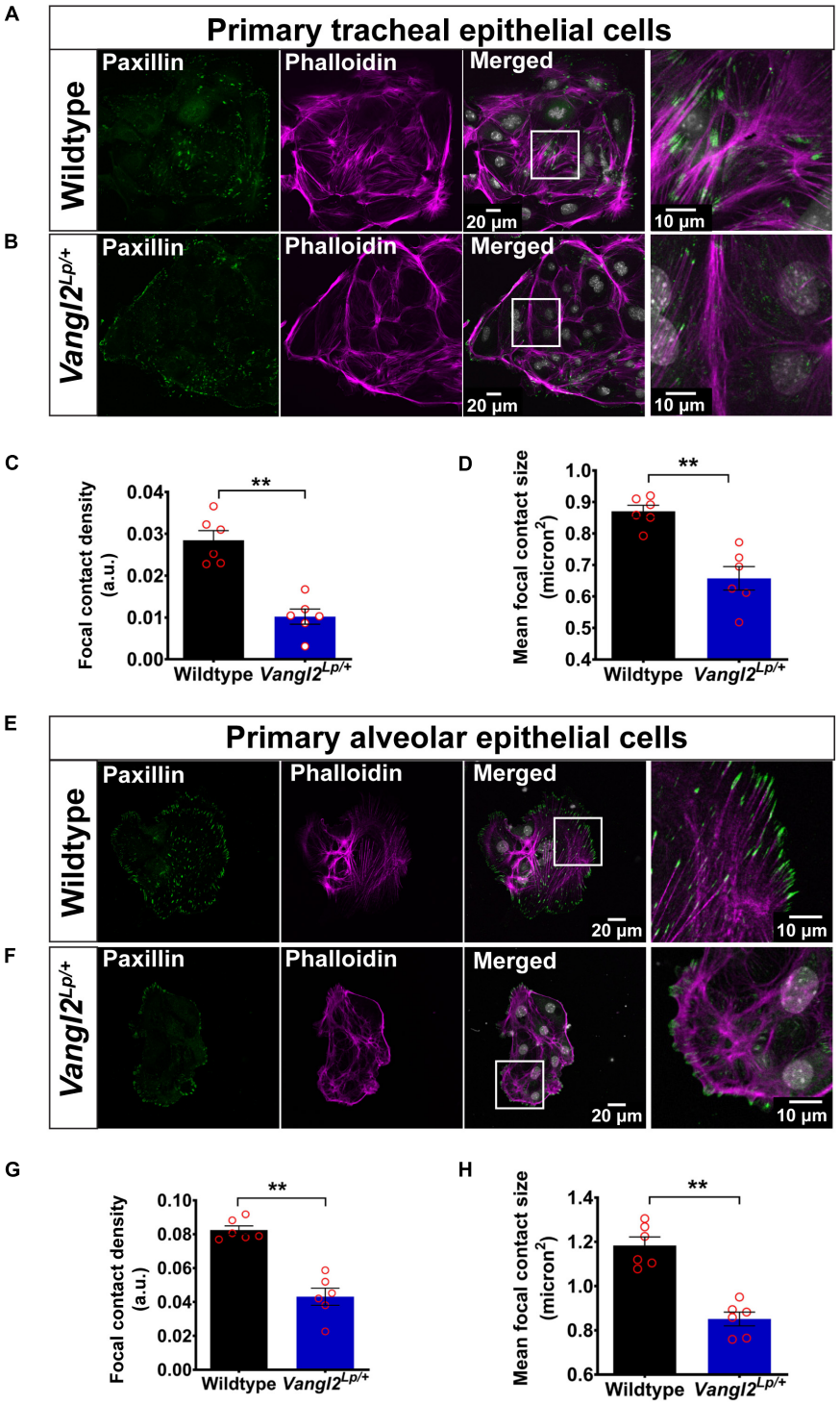

FIGURE 3 | VANGL2 dysfunction leads to highly disrupted actin cytoskeleton and focal adhesions. Representative images showing wildtype **(A)** and *Vangl2*$^{Lp/+}$ **(B)** TECs labeled with phalloidin (magenta) to visualize F-actin and paxillin (green) to stain focal contacts. Nuclei were stained with DAPI (gray). Quantification of focal contact density **(C)** and mean focal contact size (micron^2) **(D)** in wildtype and *Vangl2*$^{Lp/+}$ TECs. $n = 3$ independent experiments; TECs from three mice were pooled for each group per experiment; two technical replicates for each group per experiment; images from at least three fields were taken per technical replicate; each dot represents mean value per technical replicate. Mann–Whitney *U*-test, $^{**}p < 0.01$. Representative images showing wildtype **(E)** and *Vangl2*$^{Lp/+}$ **(F)** AECs labeled with phalloidin (magenta) and paxillin (green). Nuclei were labeled with DAPI (gray). Quantification of focal contact density **(G)** and mean focal contact size (micron^2) **(H)** in wildtype and *Vangl2*$^{Lp/+}$ AECs. $n = 3$ independent experiments; AECs from one mouse per group for each experiment; two technical replicates for each group per experiment; at least three fields were taken per technical replicate; each dot represents mean value per technical replicate. Mann–Whitney *U*-test, $^{**}p < 0.01$. All data are presented as mean ± SEM.

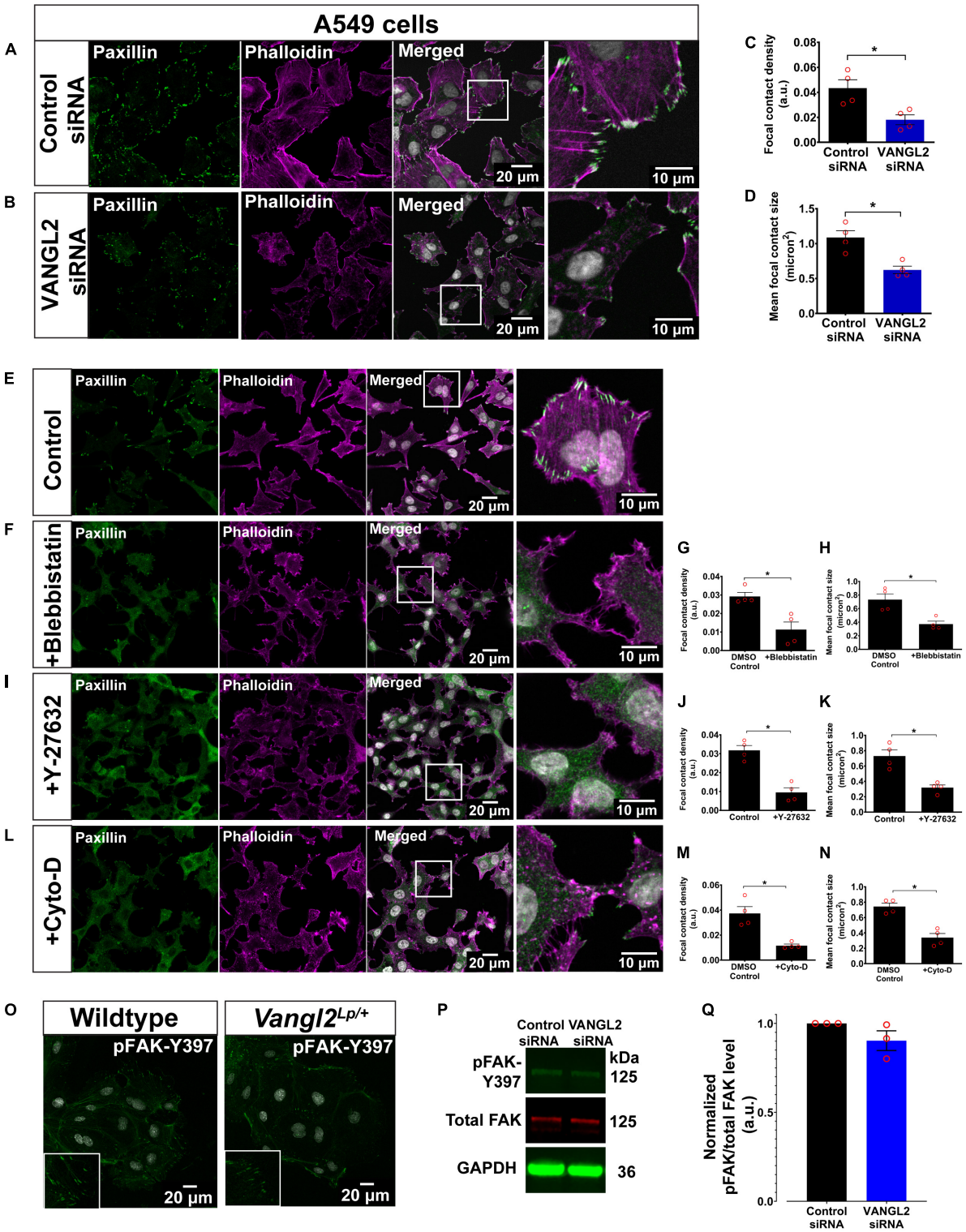

FIGURE 4 | A549 treated with actomyosin inhibitors phenocopy actin cytoskeleton and focal adhesion aberrations following siRNA knockdown of *VANGL2*. Representative images showing A549 transfected with **(A)** control siRNA or **(B)** *VANGL2* siRNA. A549 labeled with phalloidin (magenta) to visualize F-actin and paxillin (green) for focal contacts. Nuclei were stained with DAPI (gray). Quantification of focal contact density **(C)** and mean focal contact size (micron^2) **(D)** in control siRNA- or *VANGL2* siRNA-treated A549 cells. $n = 4$ independent experiments; two technical replicates for each group per experiment; each dot represents mean value per experiment. Mann–Whitney *U*-test, $^*p < 0.05$. Representative images showing control A549 without treatment **(E)**, A549 treated with 25 μM blebbistatin

(Continued)

FIGURE 4 | Continued
for 30 min **(F)**, 10 μM Y-27632 for 1 h **(I)**, or 0.5 μM cytochalasin D for 30 min **(L)**, and their corresponding focal contact density and mean focal contact size quantification **(G,H,J,K,M,N)**. No morphological difference was observed in the DMEM-DMSO control or DMEM only control cells so only representative control cell images are shown. Cells were stained with phalloidin (magenta) and paxillin (green). Nuclei were stained with DAPI (gray). **(O)** Representative images showing wildtype and *Vangl2*$^{Lp/+}$ TECs stained with pFAK-Y397 (green). Nuclei were stained with DAPI (gray). Representative western blots show the levels of pFAK-Y397 (green), total FAK (red), reference protein GAPDH (green) **(P)**, and quantification of pFAK levels normalized to total FAK levels **(Q)**. See **Supplementary Figure S4** for whole western blot. $n = 3$ independent experiments. All data are presented as mean ± SEM.

FAK levels. Our results showed a slight reduction in normalized pFAK levels following *VANGL2*-siRNA knockdown. However, the difference was not significant ($p = 0.16$) (**Figures 4P,Q** and **Supplementary Figure S4**).

VANGL2 Disruption Inhibits Phospho-MLC2-Mediated Traction Force Generation

Phosphorylated MLC2 (pMLC2) induces actomyosin contractility and enables cells to generate forces required for cell adhesion and cell motility (Amano et al., 1996; Pandya et al., 2017). Thus, we next interrogated whether MLC2 activation is affected in *Vangl2*$^{Lp/+}$ TECs. Dual staining of pMLC2 and phalloidin demonstrated high levels of pMLC2 intermittently distributed along the F-actin bundles in WT TECs (**Figure 5A**). In contrast, a marked reduction in pMLC2 was observed in *Vangl2*$^{Lp/+}$ TECs, with an overall decreased formation of actomyosin bundles (**Figure 5B**). Relative fluorescence intensity (RFI) analysis revealed a significant decrease in pMLC2 in *Vangl2*$^{Lp/+}$ TECs compared with their WT counterparts ($p = 0.029$) (**Figure 5C**).

To determine whether the abnormal actomyosin organization may affect the ability of *Vangl2*$^{Lp/+}$ TECs to exert forces on substrates, we measured traction forces applied by TECs, using elastic micropillars. TECs were seeded on an array of elastic polydimethylsiloxane (PDMS) micropillars coated with rat-tail collagen I and the deflection of each pillar, which was proportional to cellular traction force was assessed (**Figure 5D**). Our results showed that traction forces were predominantly distributed around the cell periphery, in both WT and *Vangl2*$^{Lp/+}$ TECs (**Figures 5E,F**). Quantitative analysis of the mean maximum forces exerted on the pillars indicated that *Vangl2*$^{Lp/+}$ TECs generated significantly less traction forces (mean: 322 pN, median: 276 pN) compared with WT TECs (mean: 582 pN, median: 487 pN) ($p < 0.001$) (**Figure 5G**). These data demonstrate that functional VANGL2 is required for the formation of optimal actomyosin networks that drive traction force generation.

Rho Activator Restores Actomyosin Organization in *Vangl2*^{Lp}/+

Planar cell polarity is known to regulate actin cytoskeleton remodeling through its downstream effector RhoA signaling (Munoz-Soriano et al., 2012; Davey and Moens, 2017; Henderson et al., 2018). Thus, we next investigated whether exogenous activation of RhoA signaling could rescue the actomyosin defects in adult *Vangl2*$^{Lp/+}$. *Vangl2*$^{Lp/+}$ TECs were treated with Rho activator II, CN03, for 3 h. Immediately after treatment, cells were fixed and labeled with phalloidin and anti-pMLC2 antibody. Untreated *Vangl2*$^{Lp/+}$ TECs were used as a control (**Figure 5H**). Confocal images showed that CN03 treatment led to striking changes in actomyosin organization in *Vangl2*$^{Lp/+}$ TECs. CN03 treatment markedly increased the formation of stress fibers and pMLC2 expression was considerably enhanced (**Figure 5I**), demonstrating that actomyosin defects caused by VANGL2 disruption can be ameliorated by exogenously activating RhoA signaling.

Reduced YAP Signaling in *Vangl2*^{Lp} Mutant Lungs

Nuclear YAP is used as a read-out of active mechanosignaling and recent data have shown that YAP deficiency has profound effects on lung development (Lin et al., 2017). In order for cells to process the mechanical signals, intracellular mechanotransducers, such as YAP, that can detect and respond to mechanical cues play an essential role. To determine whether YAP signaling is affected in *Vangl2*^{Lp} lungs, we next performed immunohistochemistry of YAP on embryonic E18.5 WT, heterozygous, and homozygous *Vangl2*^{Lp} lung sections and compared the percentage of airway epithelial cells that were positive for nuclear (active) YAP. Interestingly, as shown in **Figures 6A–C**, the percentage of cells with nuclear YAP was significantly decreased in the airways of *Vangl2*$^{Lp/+}$ (18.38%; $p < 0.001$) and *Vangl2*$^{Lp/Lp}$ (11.97%; $p < 0.001$) lungs compared with WT control (30.71%). To determine whether reduced active nuclear YAP is also associated with increased cytoplasmic sequestration of non-active, phospho-YAP in *Vangl2*^{Lp} lung sections, immunofluorescence of pYAP (Ser127) was performed on embryonic E18.5 WT, heterozygous, and homozygous *Vangl2*^{Lp} lung cryosections. RFI analysis revealed a significant increase in cytoplasmic pYAP in the airways of *Vangl2*$^{Lp/Lp}$ lungs compared with WT control ($p < 0.05$) (**Supplementary Figure S5**). RFI of pYAP was also higher in *Vangl2*^{Lp} heterozygous lungs, though this did not reach statistical significance (**Supplementary Figure S5**). Consistent with our previous findings (Yates et al., 2010b; Poobalasingam et al., 2017), lung architectural defects were also observed in *Vang2*$^{Lp/+}$ and *Vang2*$^{Lp/Lp}$ lungs. Nuclear YAP was also present in a proportion of mesenchymal cells. However, due to the altered architecture in *Vangl2*^{Lp} lungs, this was difficult to quantify and therefore restricted our quantification to the airways only.

As well as examining YAP at the protein level, we assessed the transcript levels of known YAP target genes: *Ctgf* (connective tissue growth factor) (Zhao et al., 2008), *Cyr61* (cysteine rich angiogenic inducer 61) (Choi et al., 2015), and *Ankrd1* (ankyrin

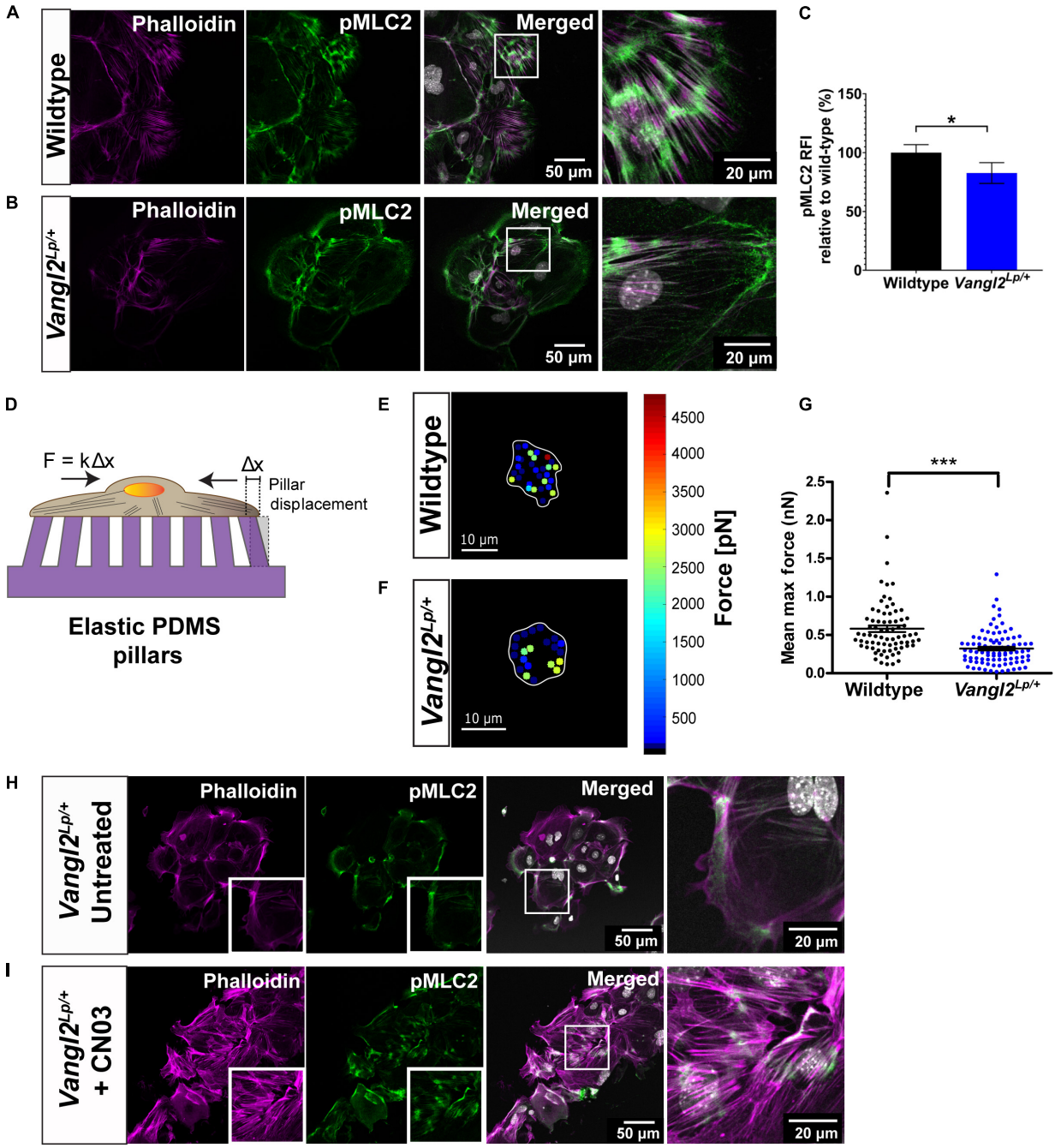

FIGURE 5 | VANGL2 regulates MLC2 activation and force generation via RhoA signaling. Representative images showing wildtype **(A)** and *Vangl2*$^{Lp/+}$ **(B)** TECs stained with pMLC2 (green) and phalloidin (magenta). Nuclei are shown in gray (DAPI). **(C)** Quantification of pMLC2 relative fluorescence intensity (RFI) in *Vangl2*$^{Lp/+}$ relative to wildtype (presented as mean ± SEM). $n = 3$ independent experiments; TECs from three mice were pooled for each group per experiment; two technical replicates for each group per experiment; at least three fields were taken per technical replicate. Mann–Whitney *U*-test, $^{*}p < 0.05$. **(D)** Schematic representation of the elastic micropillars used to measure cellular traction forces. Cells were seeded on a rat-tail collagen I coated array of micropillars and incubated at 37°C with 5% CO_2 for 24 h. Individual pillar deflection from its original position in the array (Δx) is tracked via time-lapse microscopy and converted to traction force based on the pillar spring constant ($k = 1.36$ nN/µm). Heat maps of the traction forces distribution in a representative wildtype **(E)** and *Vangl2*$^{Lp/+}$ **(F)** TEC. Cell boundary is outlined in white. **(G)** Quantification of the mean maximum traction forces exerted by wildtype ($n = 75$ cells) and *Vangl2*$^{Lp/+}$ TECs ($n = 92$ cells) on the micropillars (presented as mean ± SEM). $n = 2$ independent experiments; in each experiment, tracheas from three separate mice were pooled for each group; two technical replicates for each group per experiment; each dot represents mean maximum traction force per cell. Two-tailed unpaired Student's *t*-test, $^{***}p < 0.001$. Representative images showing *Vangl2*$^{Lp/+}$ TECs without treatment **(H)** and *Vangl2*$^{Lp/+}$ TECs treated with Rho activator, CN03 **(I)**. TECs were stained with pMLC2 (green) and phalloidin (magenta). Nuclei were stained with DAPI (gray). $n = 3$ independent experiments; TECs from three mice were pooled for each group per experiment; two technical replicates for each group per experiment.

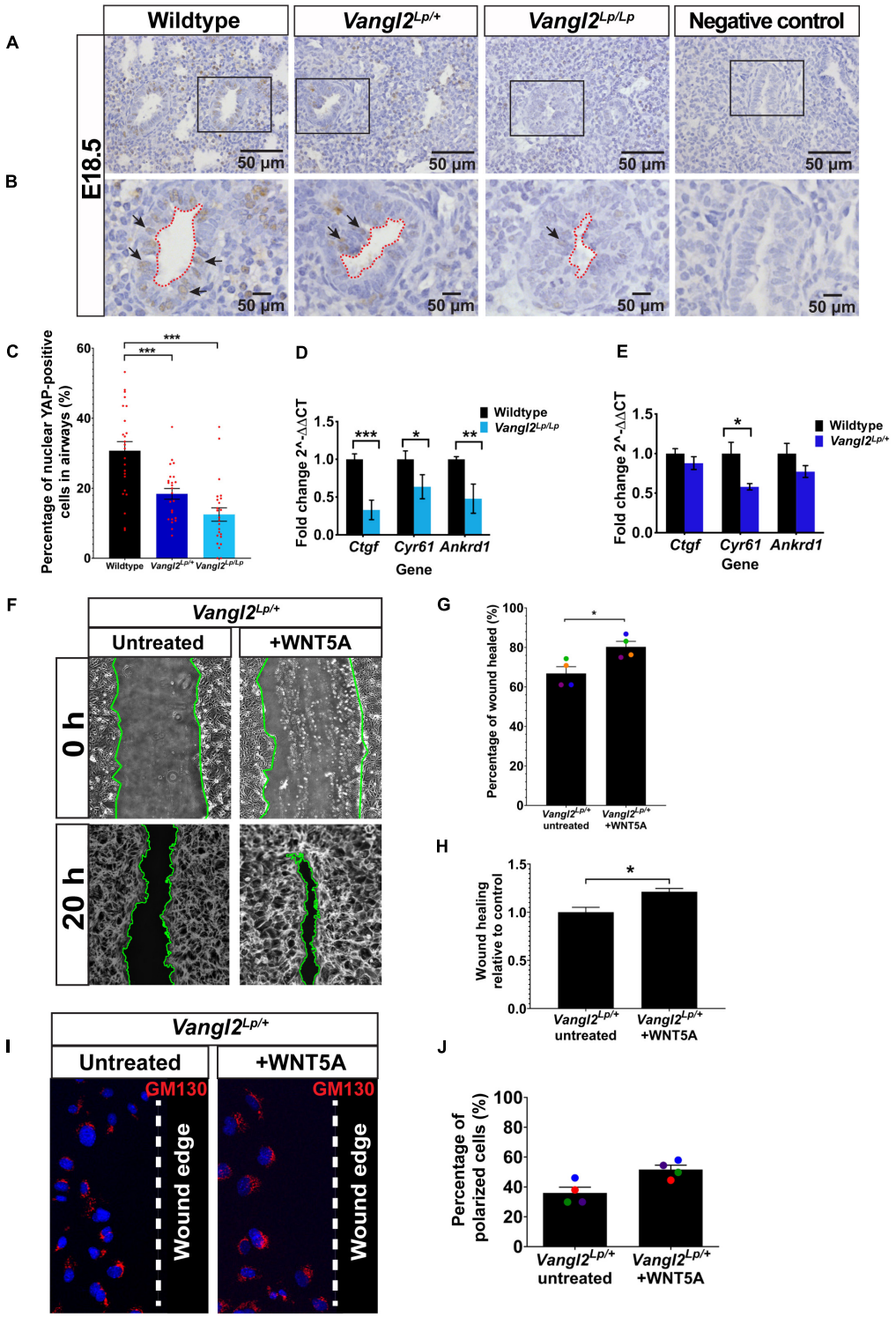

FIGURE 6 | Reduced YAP signaling in embryonic *Vangl2*^{Lp} airways and WNT5A rescues cell migration defects in *Vangl2*$^{Lp/+}$. **(A,B)** Representative images show immunostaining for YAP in E18.5 wildtype, heterozygous *Vangl2*$^{Lp/+}$, and homozygous *Vangl2*$^{Lp/Lp}$ mouse lungs. Sections were counterstained with hematoxylin. Negative controls with primary antibody omitted are shown. Insets **(B)** show the morphology of airway lumen. Arrows indicate nuclear YAP staining. **(C)** Percentage of nuclear YAP-positive cells in the airways. $n = 3$ mice per group; eight airways were quantified per mouse; a total of 1389 cells (wildtype), 1381 cells (*Vangl2*$^{Lp/+}$), and 995 cells (*Vangl2*$^{Lp/Lp}$) were analyzed (presented as mean ± SEM); one-way ANOVA with Tukey's *post hoc* test, ***$p < 0.001$. Histograms show transcript levels for YAP target genes: *Ctgf*, *Cyr61*, and *Ankrd1* in E18.5 wildtype vs *Vangl2*$^{Lp/Lp}$ **(D)** and adult wildtype vs *Vangl2*$^{Lp/+}$ lungs **(E)**. $n = 3$ independent experiments;

(Continued)

FIGURE 6 | Continued
three mice per genotype; each experiment was run in triplicate. Data are presented as mean ± SEM; Mann–Whitney *U*-test, $*p < 0.05$, $**p < 0.01$, $***p < 0.001$. **(F)** Representative images showing untreated and WNT5A-treated *Vangl2*$^{Lp/+}$ TECs at 0 and 20 h post-scratch. Wound edges are indicated by green lines. Percentage of wound healed 20 h after wound scratch in untreated *Vangl2*$^{Lp/+}$ TECs and *Vangl2*$^{Lp/+}$ TECs treated with WNT5A **(G)** and wound-healing rate in WNT5A-treated *Vangl2*$^{Lp/+}$ TECs in relative to untreated *Vangl2*$^{Lp/+}$ TEC controls **(H)**. Data are presented as mean ± SEM. $n = 4$ independent experiments; TECs from three mice were pooled for each group per experiment; three technical replicates for each group per experiment; each dot represents mean percentage of wound healed per experiment. Mann–Whitney *U*-test, $*p < 0.05$. **(I)** Immunostaining for Golgi marker (GM130; red) in fixed untreated and WNT5A-treated *Vangl2*$^{Lp/+}$ TECs 20 h post-scratch to determine cell polarity at leading edge. Nuclei were labeled with DAPI (blue) and dotted line indicates the wound edge. **(J)** Percentage of polarized cells 20 h post-scratch in untreated and WNT5A-treated *Vangl2*$^{Lp/+}$ TECs (presented as mean ± SEM). $n = 4$ independent experiments; TECs from three mice were pooled for each group per experiment; three technical replicates for each group per experiment. Mann–Whitney *U*-test.

repeat domain-containing protein 1) (Choi et al., 2015) by qRT-PCR, using total RNA extracted from E18.5 and adult WT and *Vangl2*^{Lp} mutant lungs. In agreement with our immunostaining data, qRT-PCR results showed a significant reduction in transcript levels of *Ctgf* ($p < 0.001$), *Cyr61* ($p < 0.05$), and *Ankrd1* ($p < 0.01$) in embryonic (E18.5) *Vangl2*$^{Lp/Lp}$ lungs (**Figure 6D**). However, in adult *Vangl2*$^{Lp/+}$ lungs, where only heterozygous tissue was available due to neonatal lethality of homozygotes, only *Cyr61* transcript levels were significantly decreased compared to WT littermate lungs ($p < 0.05$) (**Figure 6E**). There was a slight reduction in *Ctgf* and *Ankrd1* levels but the difference in these genes was not statistically significant in the adult (**Figure 6E**). These results suggest that YAP signaling is dysfunctional in *Vangl2*^{Lp} mutant lungs.

WNT5A Rescues Cell Migration Defects in *Vangl2*$^{Lp/+}$ TECs

WNT5A is a known ligand for the PCP pathway (Qian et al., 2007; Komiya and Habas, 2008; Witze et al., 2008) and plays a key role in both alveologenesis and the response to lung injury (Poobalasingam et al., 2017; Nabhan et al., 2018; Li et al., 2020). However, it is still unclear which downstream Wnt pathway(s) respond to WNT5A following injury to facilitate repair.

Thus, we tested whether addition of exogenous WNT5A would improve cell migration in *Vangl2*$^{Lp/+}$ TECs. Interestingly, scratch assay results demonstrated that treatment with WNT5A consistently increased the percentage of wound area healed (80.3%) compared with untreated *Vangl2*$^{Lp/+}$ TECs (66.8%) (**Figures 6F,G**). Relative wound-healing rate showed a 1.21-fold increase in WNT5A-treated *Vangl2*$^{Lp/+}$ TECs ($p = 0.0434$) (**Figure 6H**). Next, we tested whether the effect of WNT5A on cell migration was due to restoration of cell polarity. Analysis of the GM130 staining revealed that WNT5A treatment increased the percentage of polarized cells at the leading edge (54.38% cells were polarized) compared with 35.94% in untreated *Vangl2*$^{Lp/+}$ TECs. However, the difference was not statistically significant ($p = 0.0571$) (**Figures 6I,J**).

DISCUSSION

Our previous work has shown that the PCP pathway is important for development, homeostasis, and repair of the lungs, highlighting the fundamental role of this pathway in lung biology (Yates et al., 2010b, 2013; Poobalasingam et al., 2017). In various tissues, planar polarity is regulated by molecular gradients of key molecules, for example, Frizzled, or by physical forces, for example, the anisotropic forces that regulate PCP and wing blade shaping in *Drosophila* (Gao et al., 2011; Aw et al., 2016; Henderson et al., 2018). Mechanical forces play an essential role in branching morphogenesis during lung development, helping to shape the airway epithelium (Kim and Nelson, 2012; Varner et al., 2015). Similarly, cyclic mechanical strain associated with mechanical or spontaneous ventilation is a key determinant of survival in patients with injured lungs. Moreover, dysregulation of mechanical forces can have detrimental effects on lung function leading to tissue injury and disease (Kim and Nelson, 2012; Waters et al., 2012; Varner et al., 2015).

Mechanobiology is concerned with how cells sense and translate forces to regulate cell behaviors like morphogenesis and migration by converting mechanical stimuli into biochemical signals through mechanoregulators. Both mechanosignaling and PCP signaling result in modulation of the actin cytoskeleton but how these two pathways are connected at the molecular level is not understood. A growing number of studies have begun to discern the importance of mechanoregulators like YAP in lung development and repair. In particular, YAP is critical for lung branching morphogenesis *in utero* while TAZ deletion affects post-natal alveologenesis leading to an emphysema-like phenotype in adult mice (van Soldt et al., 2019; Isago et al., 2020). YAP and TAZ also regulate regeneration of the adult mouse lungs in response to *Streptococcus pneumoniae*-mediated injury (Lacanna et al., 2019). Here we have shown that mechanoregulation of the planar polarity pathway via *Vangl2* is integral to PCP driven cell behaviors such as DCM and morphogenesis.

Our previous data showed that perturbed VANGL2 function in *Vangl2*$^{Lp/+}$ mice leads to disorganization of the actin cytoskeleton, resulting in alveologenesis defects (Poobalasingam et al., 2017). Zhang et al. (2020) recently reported similar alveologenesis defects in different *Vangl2*$^{f/f}$ conditional mouse mutants, further supporting the role for PCP pathway in lung development. In this study, we used live imaging to show conclusively that VANGL2 has an important role in cell migration. Reduced movement of AECs and impaired alveologenesis was evident in *Vangl2*$^{Lp/+}$ PCLS compared to WT. To dissect the cellular mechanisms underlying this reduced cell migration, we used primary TECs and AECs isolated from adult WT and *Vangl2*$^{Lp/+}$ mice, as well as siRNA intervention in A549 cells. We demonstrated using *in vitro* wound-healing assays that *Vangl2*$^{Lp/+}$ TECs exhibited reduced DCM. In *Vangl2*$^{Lp/+}$ TEC monolayers, cells at the leading edge of the wound did

not display coordinated polarity. In migrating cells, crosstalk between PCP proteins and cytoskeletal components is required for polarized organization of the cytoskeleton that underlies front-rear polarity (Raman et al., 2018). The *Vangl2*^{Lp} mutation is known to affect trafficking of VANGL2 protein to the membrane (Gao et al., 2011; Seo et al., 2017) and we have previously shown a reduction in β-catenin at the cell membranes in *Vangl2*$^{Lp/+}$ lungs (Poobalasingam et al., 2017). Membrane associated β-catenin is important to maintain proper actin cytoskeleton structure and cell tension (Abreu-Blanco et al., 2012), together with the data shown in this manuscript our findings indicate that VANGL2 dysfunction disrupts the actin cytoskeleton and thereby affects the polarization of the cytoskeleton required for DCM.

Mechanosensing, the process by which cells assess their environment to respond to mechanical cues, relies on the formation of FAs, through which cells can apply force generated by actomyosin-mediated contractility (Evans and Calderwood, 2007; Geiger et al., 2009). Our results demonstrated that VANGL2 regulates FA size and density, a phenotype that is likely to affect mechanosignaling. To measure the traction forces generated by *Vangl2*$^{Lp/+}$ cells as a functional readout of the underlying cytoskeletal defects leading to the FA changes in *Vangl2*$^{Lp/+}$ cells, we employed micropillar arrays. These arrays are composed of uniformly spaced needle-like microposts of user-defined rigidity that allow discrete attachment of a cell. This enables sensitive quantification of traction force by measuring the deflection of pillars, using a simple mathematical model as shown in **Figure 5D** (Yang et al., 2011; Chronopoulos et al., 2016). We demonstrated significantly reduced cellular traction force when VANGL2 function is disrupted.

We also showed that addition of a Rho activator restored MLC2 activation and actomyosin organization in *Vangl2*$^{Lp/+}$ cells, confirming that VANGL2 regulates actomyosin contractility via its effector RhoA. This is in line with previous work showing inhibition of ROCK (a downstream effector of RhoA) by selective inhibitor Y-27632 leads to reduced MLC2 phosphorylation (Unbekandt et al., 2014). Altogether, our findings demonstrate a direct role for VANGL2, a core PCP component, in the regulation of traction force generation for the first time. The correlation between FA size and magnitude of force exerted at the FA has been a longstanding debate, previous studies having shown either a positive linear (Balaban et al., 2001; Schwarz et al., 2002; Goffin et al., 2006) or inverse relationship (Beningo et al., 2001), as well as more complicated findings that suggest positive correlation is limited to early FA growth and is diminished in mature FAs (Stricker et al., 2011). Our findings in this study have shown a concomitant decrease in FA size and traction force in *Vangl2*$^{Lp/+}$ TEC, which support a positive correlation between FA size and force applied at FA.

Park et al. (2015) previously found that YAP/TAZ can act as downstream effectors of the non-canonical/PCP pathway in mediating cell migration and osteogenic differentiation via Frizzled and ROR. Our study has discovered that *Vangl2*^{Lp} is associated with reduced nuclear (active) YAP and increased cytoplasmic phospho-YAP (non-active) in the lung epithelium. Since YAP provides a read-out of mechanosignaling activity (Dupont et al., 2011; Wada et al., 2011; Dobrokhotov et al., 2018), our data provide evidence that VANGL2 has an active role in mechanosignaling.

Narrow or collapsed airway lumens are a feature of genetically modified mouse mutants of the PCP pathway (Yates et al., 2010b; Poobalasingam et al., 2017) and mechanical forces are important for airway branching morphogenesis (Varner et al., 2015). Moreover, YAP deficiency, which results in defective mechanical force generation, disrupts lung branching morphogenesis in mice (Lin et al., 2017). The reduction in YAP activity detected in the airways of *Vangl2*^{Lp} mice suggests that the collapsed airway lumen that are a prominent feature of embryonic *Vangl2*^{Lp} mouse lungs could result from the perturbation of tensile forces within *Vangl2*^{Lp} airway epithelial cells, as a result of defective mechanosignaling.

Our findings also raise important questions for future investigation. pFAK is known to regulate the formation of stress fibers and FAs (Schiller and Fässler, 2013; Oakes and Gardel, 2014; Sun et al., 2016). Immunostaining for pFAK did not reveal overt changes in pFAK distribution or pattern in heterozygous *Vangl2*$^{Lp/+}$ TECs, suggesting that the loss of pFAK may not provide a significant contribution to the highly disrupted cytoskeletal organization and FA structures in *Vangl2*$^{Lp/+}$ cells. It is also possible that homozygous *Vangl2*$^{Lp/Lp}$ cells would exhibit more discernible differences in the pFAK distribution and protein level compared to their heterozygous counterparts. However, since *Vangl2*$^{Lp/Lp}$ mice are not viable after birth, we could not assess TECs from homozygous mice.

WNT5A is most frequently regarded as a non-canonical Wnt ligand that regulates the PCP pathway (Qian et al., 2007; Komiya and Habas, 2008; Witze et al., 2008). In the lungs, WNT5A has emerged as an important mediator of alveologenesis and repair following injury (Poobalasingam et al., 2017; Nabhan et al., 2018; Li et al., 2020). While evidence shows that VANGL2 has a central role in WNT5A-mediated PCP signaling (Babayeva et al., 2011; Poobalasingam et al., 2017; Yang et al., 2017; Rao-Bhatia et al., 2020), surprisingly, we demonstrated that WNT5A improved cell migration in *Vangl2*$^{Lp/+}$ cells. These findings indicate that WNT5A can still induce cell migration when VANGL2 function is perturbed. There are a number of possibilities as to how this could transpire. For example, it is possible that in the absence of an intact PCP pathway, WNT5A signals via the alternative canonical Wnt/β-catenin pathway in *Vangl2*^{Lp}. In some contexts, canonical Wnt signaling is increased in response to disrupted PCP signaling (Weidinger and Moon, 2003; Westfall et al., 2003). However, we did not find any change in canonical Wnt signaling in adult *Vangl2*$^{Lp/+}$ lungs (Poobalasingam et al., 2017). It is also possible that in *Vangl2*$^{Lp/+}$ lungs, some functional VANGL2 protein remains and this is sufficient to transduce WNT5A to promote wound-healing. Studies have shown that WNT5A can bind to a number of different receptors to mediate PCP signaling in diverse cell contexts. One prominent receptor that WNT5A binds to mediate actin cytoskeleton remodeling via the PCP pathway is ROR2 (Nishita et al., 2010; Gao et al., 2011). In particular, ROR2 has an important role in the phosphorylation of VANGL2 in response to WNT5A (Gao et al., 2011). Recently, two separate studies reported that an axis of WNT5A-ROR (Li et al., 2020) or WNT5A-ROR2-VANGL2 (Zhang et al., 2020)

is required for alveologenesis, based on the similar phenotypes observed in a number of different conditional mouse mutants of these genes. Intriguingly, WNT5A has been shown to bind to ROR2 to mediate cell invasion independently of the PCP pathway (Enomoto et al., 2009) and ROR1/ROR2 can act as direct receptors for WNT5A to recruit guanine exchange factors (GEFs) and activate Rac1 and RhoA (Yu et al., 2016), supporting the idea that WNT5A can signal through more than one route. In addition to ROR2, RYK is another receptor that binds to WNT5A and VANGL2 to regulate PCP signaling (Andre et al., 2012; Duan et al., 2017). It remains unclear which is the predominant WNT5A receptor that mediates PCP signaling in *Vangl2*^{Lp} lungs and further studies will be required to comprehensively address this.

WNT5A is a current target of interest for treatment of several lung diseases in which there is aberrant expression of this ligand including: chronic obstructive pulmonary disease (COPD)/emphysema, idiopathic pulmonary arterial hypertension (IPAH), bronchopulmonary dysplasia (BPD), and interstitial pneumonia (UIP) (Vuga et al., 2009; Baarsma et al., 2017; Yuan et al., 2019; Li et al., 2020; Sucre et al., 2020; Vladar and Königshoff, 2020). In addition, WNT5A has an important role in progenitor cell induction following lung injury (Nabhan et al., 2018). It is also notable that several independent datasets from emphysema patients, in which repair capacity is diminished, show significant downregulation of *VANGL2* and *WNT5A* (Ezzie et al., 2012; Poobalasingam et al., 2017; Zhang et al., 2020). However, contradictory findings with regard to pro-repair/migratory (Witze et al., 2008; Vuga et al., 2009; Gao et al., 2011; Poobalasingam et al., 2017; Yuan et al., 2019; Li et al., 2020; Zhang et al., 2020) or anti-repair effects (Baarsma et al., 2017; Wu et al., 2019; Sucre et al., 2020) of WNT5A suggest that the complex mechanism of action of WNT5A may be cell type or tissue context-dependent or may differ depending on the balance between PCP and other signaling pathways, such as canonical Wnt signaling. Thus, it will be important to carry out further detailed investigation of how WNT5A stimulates repair in *Vangl2*$^{Lp/+}$ mice.

Our study shows that beyond establishing tissue patterning, VANGL2, a core PCP component, plays a pivotal role in the regulation of cell mechanobiology. We provide mechanistic evidence that VANGL2 modulates cellular mechanics, including FA complexes, actomyosin organization, actomyosin-mediated contractility and traction force generation via RhoA signaling (**Figure 7**). We identify a positive correlation between VANGL2 and YAP signaling and show that VANGL2 controls cell migration through its direct role in mechanosignaling. This work represents an important advance in our understanding of VANGL2 function by demonstrating an indispensable role for this core PCP component in mechanosignaling for the first time.

MATERIALS AND METHODS

Animals

All animal maintenance and procedures were conducted in compliance with the requirements of the Animal (Scientific Procedures) Act 1986. Animal work was approved by the South Kensington and St Mary's AWERB committee, Imperial College London. Mice were genotyped by MRC Harwell (Oxford, United Kingdom). *Vangl2*$^{Lp/+}$ mice carry a heterozygous substitution mutation S464N that results in loss of function of VANGL2 (Kibar et al., 2001; Murdoch, 2001); WT littermates were used as controls. Mice were maintained on a C3H/HeH background (MRC Harwell, Oxford) and were housed in specific pathogen-free conditions and given food and water *ad libitum*. Male or female adult mice aged 8–12 weeks were used for alveolar and TEC isolation in this study; whereas PCLS were obtained from postnatal day 3 (P3) mouse lungs. Mice were humanely killed by intraperitoneal pentobarbital injection.

Precision-Cut Lung Slicing and *in vitro* Culture

Precision-cut lung slices were obtained from WT and *Vangl2*$^{Lp/+}$ littermate P3 mouse lungs as previously described (Akram et al., 2019a,b). Briefly, P3 mice were culled and the anterior chest and neck wall was excised. A small opening was made in the anterior wall of the trachea just below the cricoid cartilage. A 25G rigid metallic cannula was inserted through the trachea. The lungs were inflated by injecting 0.2 ml of 37°C warm, 1.5% low-gelling temperature agarose (Sigma–Aldrich) prepared with 1 × HBSS/HEPES buffer (Life Technologies). Agarose was injected to inflate both lungs keeping them *in situ* within the chest cavity at a volume that enabled lungs to be fully inflated without hyper- or sub-optimal inflation. After inflation, agarose was solidified by applying ice to the chest cavity for 1 min. The lungs were excised from the body along with heart and trachea and immersed in ice-cold serum-free (SF)-DMEM (Gibco), and kept on ice until slicing. Left lung lobes were isolated and cut transversely at 300 μm using an automated vibratome (Compresstome® VF-300-0Z; Precisionary Instruments LLC) in ice-cold HBSS/HEPES buffer. Slices were obtained from the middle 2/3rd of the lobe, to ensure similar sized slices, and placed in a 24-well plate in ice-cold SF-DMEM for all experiments. PCLS were then incubated at 37°C for 2 h and washed twice with warm SF-DMEM to remove excess agarose from the tissue. Slices were incubated for a further 1 h in SF-DMEM at 37°C. These PCLS were then used for time-lapse imaging and *ex vivo* alveologenesis (**Supplementary Figure S1A**).

Isolation of Mouse Alveolar Epithelial Cells

Mice were culled and metallic cannula was inserted through the trachea as described above. The lungs were gently flushed with PBS and 1 ml of Dispase (50 U/ml; Corning; Cat# 354235) was injected into the lungs, followed by 200 μl of 1% low-gelling temperature agarose (Sigma–Aldrich) dissolved in SF-DMEM (Gibco). After injection, ice was applied to the chest cavity for 1 min to solidify agarose and prevent Dispase leakage. Lungs were excised from the body. Tracheas were collected for isolation of trachea epithelial cells as described below. Heart and connective tissues were removed before immersing the lungs in 1.5 ml of ice-cold Dispase solution (50 U/ml; Corning), and incubated

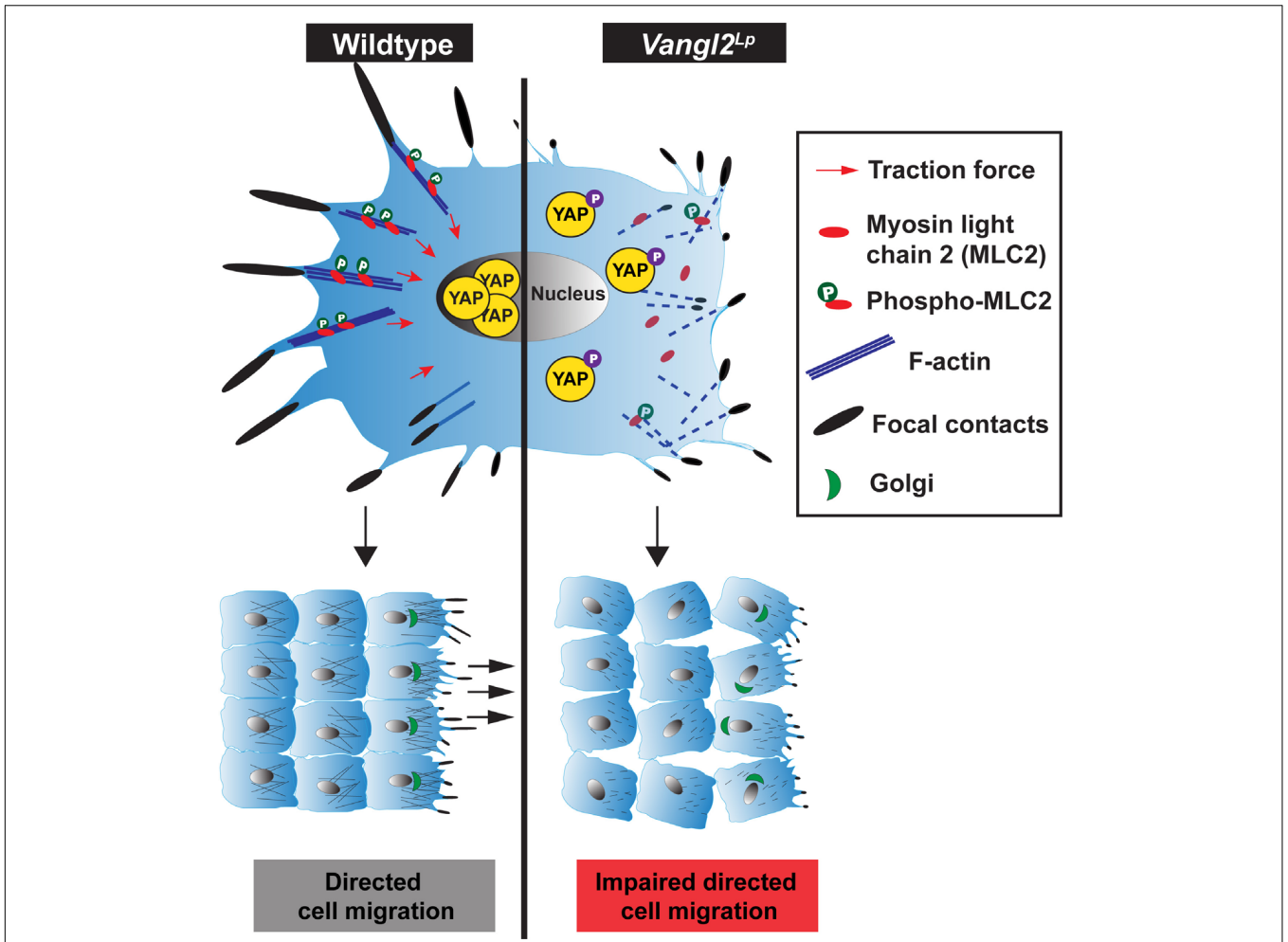

FIGURE 7 | Comparison of cellular mechanics in wildtype and *Vangl2*^{Lp} cells. (Left) In a normal cell, VANGL2 regulates the activation of myosin light chain 2 (MLC2) and F-actin and induces intracellular contractility. This gives rise to the generation of cellular traction force (red arrows) and promotes the formation of focal adhesion complexes. High mechanical cues within a cell then activate YAP signaling, rendering the translocation of YAP to the nucleus, leading to the transcriptional induction of YAP target genes. The optimal coordination of focal complexes, actomyosin contractile activity at the rear and pushing force at the front, as well as VANGL2-regulated cell polarity enables directed cell migration. (Right) In a *Vangl2*^{Lp} cell, VANGL2 dysfunction leads to highly disrupted actin cytoskeleton, aberrant focal complex formation, and inhibition of MLC2 activation. This causes defective actomyosin-mediated contractility, which hampers traction force generation. Attenuated mechanosignaling within the cell inhibits activation of mechanosensitive protein YAP. YAP is phosphorylated, rendering its sequestration in the cytoplasm, thereby causing the transcriptional suppression of YAP target genes. Perturbation of traction force generation, aberrant focal contact formation, the lack of pushing force caused by highly disrupted actin cytoskeleton, and defective VANGL2-regulated cell polarity impede directed cell migration.

at room temperature for 45 min. Lung lobes were separated and connective tissues were discarded. Lung lobes were then homogenized using forceps in 3 ml of DMEM/HEPES/DNase medium [DMEM medium (Gibco) containing 25 mM HEPES (Gibco), 1% penicillin and streptomycin (Sigma–Aldrich), and 50 U/ml DNase I (Thermo Fisher Scientific)]. The homogenized mixture was sequentially passed through 100, 70, and 30 μm cell strainers into a 15 ml centrifuge tube. The cell suspension was centrifuged at 550 × *g* for 5 min at 4°C to pellet the cells. Supernatant and a translucent layer of residual agarose above the cell pellet were carefully removed. Cells were then resuspended in 1 ml of DMEM/HEPES/DNase medium to perform cell counting. Cells were centrifuged at 300 × *g* for 5 min at 4°C and resuspended in MACS buffer (Miltenyi Biotec) with appropriate amount of CD31 (Miltenyi Biotec; Cat# 130-097-418) and CD45 microbeads (Miltenyi Biotec; Cat# 130-052-301) and incubated at 4°C for 20 min. The cell suspension was then passed through the MACS magnetic column and unwanted endothelial (CD31) and hematopoietic cells (CD45) were magnetically labeled and removed from the cell suspension. An appropriate amount of CD326 (EpCAM) microbeads (Miltenyi Biotec; Cat# 130-105-958) was then added to the cell suspension and incubated at 4°C for 20 min. After incubation, EpCAM-positive AECs were eluted from the magnetic column. AEC suspension was centrifuged at 300 × *g* for 5 min at 4°C and was resuspended in an appropriate amount of AEC growth medium [DMEM/F-12 medium (Gibco) containing 15 mM HEPES (Gibco), 4 mM glutamine (Life Technologies), 0.03% $NaHCO_3$ (Sigma–Aldrich),

0.25 μg/ml Fungizone (Gibco), 10 U penicillin-streptomycin (Sigma–Aldrich), 1 × Insulin-Transferrin-Selenium (ITS; Life Technologies), 0.1 μg/ml Cholera toxin (Sigma–Aldrich), 25 ng/ml epidermal growth factor (EGF; Sigma–Aldrich), 30 μg/ml bovine pituitary extract (BPE; Gibco), and 5% fetal bovine serum (FBS; Gibco)]. AECs were seeded into Lab-Tek Permanox chamber slides (VWR) pre-coated with 50 μg/ml rat-tail collagen I (Gibco; diluted with 0.02 M acetic acid) and grown at 37°C with 5% CO_2. AECs were fixed for immunostaining after 72 h culture.

Isolation of Mouse Tracheal Epithelial Cells

Mouse TECs were isolated as previously described (Lam et al., 2010). Tracheas were separated from the lung lobes into ice-cold SF-Ham's F-12 medium (Gibco) and the esophagus and connective tissues were carefully removed using forceps. Tracheas were then cut lengthwise to expose the lumen. Three tracheas from mice of the same genotype were pooled for each sample. Tracheas were then incubated with SF-Ham's F-12 medium (Gibco) containing 0.15% Pronase (Roche; Cat# 10165921001) in a 15 ml tube overnight at 4°C. Cells were gently dissociated from tracheas by inverting the tubes. Equal volume of Ham's F-12 supplemented with 20% FBS was added and tubes were inverted several times. Tracheas were transferred to a new tube containing fresh Ham's F-12 supplemented with 10% FBS and the tube was inverted several times. This step was repeated twice and then all supernatant was collected and centrifuged at 390 × *g* for 10 min at 4°C to pellet the cells before discarding the supernatant. Cells were gently resuspended in DNase I solution (0.5 mg/ml; Sigma–Aldrich; dissolved in SF-Ham's F-12 medium) and incubated on ice for 5 min. Cells were then centrifuged at 390 × *g* for 5 min at 4°C with the slowest break speed and supernatant was discarded. Cells were then resuspended in TEC medium [DMEM/F-12 medium (Gibco) containing 15 mM HEPES, 4 mM glutamine, 0.03% $NaHCO_3$, 0.25 μg/ml Fungizone, and 10 U penicillin-streptomycin] supplemented with 10% FBS, seeded onto a six-well plate and incubated at 37°C for 4 h. This allowed fibroblasts to attach to the dish while TECs remained floating in the supernatant. The supernatant was then collected, centrifuged at 390 × *g* for 5 min at 4°C, and cell pellets were resuspended in an appropriate amount of pre-warmed TEC Plus medium [TEC medium enriched with 1 × ITS, 0.1 μg/ml Cholera toxin, 25 ng/ml EGF, 30 μg/ml BPE, 5% FBS, and 0.1 μM retinoic acid (Sigma–Aldrich)] to perform cell counting. After cell counting, TECs were diluted with appropriate amount of TEC Plus medium and grown at 37°C with 5% CO_2. All dishes and coverslips used to culture TECs were pre-coated with 50 μg/ml rat-tail collagen I (Gibco; diluted with 0.02 M acetic acid). TECs were fixed for immunostaining after 72 h culture.

Culture of Human Alveolar Epithelial Cell Line A549

Human alveolar adenocarcinoma A594 cells were purchased from American Type Culture Collection (ATCC). Cells were grown at 37°C with 5% CO_2 in DMEM (Gibco) containing 10% FBS.

Live Staining of PCLS and Time-Lapse Imaging

P3 PCLS from WT and *Vangl2*$^{Lp/+}$ mice were stained with FITC-conjugated EpCAM (EpCAM-FITC) antibody following the protocol described in Akram et al. (2019a). Briefly, PCLS were incubated for 1 h at 37°C in the dark with EpCAM-FITC antibody at 1:200 (Thermo Fisher Scientific; Cat# 11-5791-80) (500 μl antibody solution per well) prepared in phenol red-free SF-DMEM (Life Technologies). Slices were then washed three times with phenol red-free SF-DMEM. For time-lapse imaging, the EpCAM-FITC labeled PCLS were placed at the center of the well of an uncoated Ibidi 24-well μ-plate (Ibidi). Then, a 0.4 μm pore, 12 mm transwell (Corning) was placed onto the PCLS, with the rim of the transwell removed to allow the transwell filter to contact the slice at the bottom of the well. Image media, containing EpCAM-FITC at 1:500 in phenol red-free SF-DMEM, was then added to the upper chamber (500 μl) and bottom chamber (300 μl). A 1.66 g metal flat washer (M8-5/16th inches diameter) was placed on top of the transwell housing to keep the PCLS in place throughout the duration of imaging. The PCLS were then left in the incubator for 2 h, ensuring the cells were all labeled and allowing the PCLS to settle down prior to image acquisition. The 24-well plate was then transferred to a pre-equilibrated and humidified incubator chamber (37°C, 5% CO_2 and air oxygen levels, ∼21%) of an inverted Zeiss Axio Observer widefield epifluorescence microscope. Imaging was conducted using a long working distance 40×/0.7NA air objective lens. In each experiment, a duplicate slice was imaged for each experimental group (WT and *Vangl2*$^{Lp/+}$). A maximum of four slices were imaged in a single time-lapse experiment. Images were captured using GFP filter, excitation 450–490 nm, emission 500–550 nm (for EpCAM-FITC) from four fields per slice for 13 h at 15 min intervals. Ten images were captured along the *z*-axis with 1 μm step-gap to make a z-stack from each slice. Channel color was changed during video post-processing to aid visualization.

Cell Tracking Using Icy Software

Icy (version 1.9.8.0), an open source bioimaging analysis software, was used for cell tracking and migration quantification during time-lapse imaging following previously described protocol (Fabrice de Chaumont et al., 2012; Akram et al., 2019a). Briefly, raw time-lapse sequences from each field of a lung slice were acquired into Icy and EpCAM-positive cells were tracked. Results were manually verified to ensure tracking was correct. EpCAM-FITC-positive cells were tracked for quantification of epithelial cell migration. FITC-channel was selected from best-focused slice from a z-stack for tracking. Cell migration in the *X*–*Y* plane only (not the *Z*-plane) was recorded. Two aspects of tracking data were considered: (1) Net cell migration during time-lapse period (13 h), in which the mean value was calculated to present how much linear distance in the *X*–*Y* axis ("Start" point to "End" point) a cell had migrated (Akram et al., 2019b). A mean value of migrated distances of total number of cells from

each field is presented as "mean net cell migration." (2) The net distance migrated by individual cells in a field within the specified time period in each experimental group was also investigated. To determine the proportion of highly motile cells, the percentage of cells that migrated between 5 and 11 μm per field within a defined time period (13 h) was quantified. Two to four fields from each slice were analyzed. Three independent experiments were conducted using three mice per group.

PCLS *in vitro* Culture

P3 PCLS from WT and *Vangl2*$^{Lp/+}$ mice were cultured in SF-DMEM for 72 h (**Supplementary Figure S1A**) following a previously described protocol (Akram et al., 2019a). Briefly, unlabeled 300 μm thick PCLS from P3 WT and *Vangl2*$^{Lp/+}$ mice were cultured in SF-DMEM in a 24-well plate (1 PCLS per well in 1 ml medium) for 72 h under normal culture conditions (37°C, 5% CO_2). Medium was changed every alternate day. Slices were fixed with 10% formalin for 30 min at room temperature for histology sectioning and morphometric analysis.

Morphometric Analysis of PCLS

To evaluate alveologenesis, mean linear intercept (Lm) and the number of airspaces were quantified in H&E-stained P3 PCLS cultured in SF-DMEM for 72 h (Poobalasingam et al., 2017). P3 WT and *Vangl2*$^{Lp/+}$ PCLS from 0 and 72 h culture were fixed as above, embedded in paraffin, keeping the slice surfaces horizontal to the block and sectioned at 4 μm thickness. Sections were deparaffinized and stained with H&E. Images were captured using a Leica DM2500 widefield microscope and a ×20, 0.7 NA objective lens. For quantification of Lm, a grid of eight horizontal lines was superimposed on images from H&E sections, using FIJI (Schindelin et al., 2012; Poobalasingam et al., 2017). The number of times alveolar cells/walls intercepted the line was counted and Lm was calculated using the following equation: Lm = NL/X, where N = number of lines counted, L = length of line, and X = total number of intercepts counted. Three fields per lung section, and three sections per PCLS from three mice for each group were imaged. The number of alveolar spaces/airspace per field was counted and presented as number of airspaces per millimeter square area. Alveolar spaces were quantified from the same visual fields used for Lm quantification. Fields of view containing blood vessels or airways were omitted from analysis.

MTT Assay

To assess viability of the cells within PCLS, for each experiment, similar size PCLS were placed into wells of a 24-well plate in duplicate (1 slice per well). MTT assay (Sigma–Aldrich) was performed according to manufacturer's instructions and protocol described in Akram et al. (2019a). Briefly, 500 μl of 10% MTT solution prepared in SF-DMEM was added per well, per slice and incubated at 37°C for 1 h. Formazan crystals that formed within the viable cells were solubilized by adding an equal volume of DMSO for 10 min at 37°C. 200 μl of eluted formazan solution from each slice was placed into individual wells of a 96-well plate. Absorbance (OD) was measured at 570 nm and corrected at 690 nm using a plate reader. MTT was performed on post time-lapse PCLS and on 72 h *ex vivo* cultured PCLS.

siRNA Transfection

siRNA transfection was performed on A549 cells using DharmaFECT 1 Transfection Reagent (Dharmacon) according to the manufacturer's instructions. A549 cells were cultured in DMEM (Gibco) containing 10% FBS for 18 h before siRNA transfection. Cells were transfected with a final concentration of 20 nM siRNA and cultured for further 48 h before immunostaining or RNA extraction for qRT-PCR analysis. Four independent experiments were conducted. Non-targeting (control) and *VANGL2* siRNA oligos used in this study are as follows: ON-TARGETplus VANGL2 siRNA (Dharmacon; Cat# L-010581-00-0020) and siGENOME non-targeting siRNA pool #2 (Dharmacon; Cat# D-001206-14-20).

Scratch Wound Assay

A total of 50,000 WT and *Vangl2*$^{Lp/+}$ TECs in TEC Plus medium (described above) were seeded on rat-tail collagen I (Gibco)-coated coverslips (diameter: 13 mm; Sarstedt) and medium was changed after 48 h. After culturing for 72 h, a single scratch wound was made across the center of confluent TEC monolayers using a 200 μl pipette tip. Wells were gently washed with PBS to remove floating cells and replaced with fresh TEC Plus medium. Wells were imaged at t = 0 using an inverted Zeiss Axio Observer widefield epifluorescence microscope in a pre-equilibrated and humidified incubator chamber (37°C, 5% CO_2 and air oxygen levels, ∼21%). Images were taken using an EC Plan-Neofluar 10x/0.30 objective lens and tiling method was used to image the entire coverslip. Cells were then cultured for a further 20 h and images were taken using the same protocol at t = 20 h. For WNT5A treatment, *Vangl2*$^{Lp/+}$ TECs were cultured with TEC Plus medium supplemented with 1 μg/ml recombinant WNT5A (R&D Systems; Cat# 645-WN). The percentage of wound healed was calculated by drawing around the outline of the scratch using the freehand tool in FIJI and subtracting the area at t = 20 h from the area at t = 0 h. Four independent experiments were conducted, and each individual experiment contained pooled TECs from three mice per sample.

For actomyosin inhibitor studies, A549 cells were seeded at 40,000 cells/well in eight-well chamber slides (VWR) pre-coated with 50 μg/ml rat-tail collagen I (Gibco) and cultured for 48 h in DMEM supplemented with 10% FBS until cells reached confluence. Cells were then serum starved for 24 h before treatment with 25 μM blebbistastin (Cambridge Bioscience; Cat# CAY13891) or 0.5 μM cytochalasin D (Sigma–Aldrich; Cat# C8273) diluted in DMEM supplemented with 0.5% FBS. Since blebbistatin and cytochalasin D were reconstituted using DMSO and the final concentrations of DMSO in the working media were 0.08 and 0.025%, respectively. Control media for blebbistatin and cytochalasin D in scratch assays was 0.5% FBS-DMEM containing 0.08 and 0.025% DMSO, respectively. Scratch assays, wound imaging, and measurement of wound healed were performed as detailed above.

Quantification of Polarized Cells

Tracheal epithelial cells were fixed 20 h post-scratch and dual stained with a Golgi marker, GM130 (1:200; Becton Dickinson

Biosciences; Cat# 610822) and DAPI (1:500; Sigma; Cat# D9542) that labeled the nuclei. Detailed immunocytochemistry protocol is described below. After staining, images were captured on a Leica SP8 inverted confocal microscope using a HC PL APO 10x/0.40 objective lens. Cell directionality during migration was quantified as previously described (Etienne-Manneville and Hall, 2001; Cory, 2011; Poobalasingam et al., 2017). Using the line tool in FIJI, a cross with a 120° arc facing the direction of migration was drawn from the center of the nucleus in cells at the leading edge. Golgi were considered polarized if they were located within the 120° arc facing the direction of migration; whereas cells with the entire or majority of the Golgi localized outside the 120° arc were classed as non-polarized. Golgi orientation was quantified from four independent experiments, with each individual experiment containing pooled TECs from three mice per sample.

Immunohistochemistry

Lung tissues were fixed in 4% paraformaldehyde (PFA), dehydrated in ethanol and embedded in paraffin, and sectioned at 4 μm thickness. Sections were deparaffinized and rehydrated using standard protocols: Gentaclear and descending ethanol concentrations. Sections were then incubated in 3% H_2O_2 for 5 min at room temperature, followed by 1 h blocking with PBS containing horse serum provided by the Vectastain Elite ABC kit (Vector Labs) at room temperature, and incubation with rabbit anti-YAP antibody (1:400; Cell Signaling Technology; Cat# 14074) overnight at 4°C. Next, sections were incubated with biotinylated antibody from the Vectastain Elite ABC HRP kit for 30 min at RT, followed by Vectastain Elite ABC reagent mixture for 30 min at RT. Then, sections were incubated with peroxidase substrate, diaminobenzidine (DAB) (BD Bioscience) following the manufacturers' instructions. Stain development was quenched by rinsing slides in tap water. Slides were counterstained with hematoxylin and mounted with DPX mountant (Solmedia). Images were taken on a Leica DM2500 widefield microscope with a 40× objective lens. The total number of cells and the number of nuclear YAP-positive cells in the airways were quantified using FIJI software. Three mice were analyzed per genotype and eight airways were quantified per mouse. Negative controls, where the primary antibody was omitted, were included in each experiment.

Immunofluorescence

Cells were seeded on rat-tail collagen I-coated Lab-Tek Permanox chamber slide (VWR) or coverslips (diameter: 13 mm; Sarstedt). For Rho activation experiment, TECs were treated with 1 μg/ml of Rho activator II, CN03 (Cytoskeleton Inc; Cat# CN03–A) for 3 h. For treatment with actomyosin inhibitors, A549 cells were treated with blebbistastin (Cambridge Bioscience; Cat# CAY13891) at 25 μM for 30 min, ROCK inhibitor Y-27632 (Sigma–Aldrich; Cat# Y0503) at 10 μM for 1 h, or cytochalasin D (Sigma–Aldrich; Cat# C8273) at 0.5 μM for 30 min. Since blebbistatin and cytochalasin D were reconstituted using DMSO, media containing DMSO were used as control. Cells were fixed in 4% PFA for 10 min at RT, washed in PBS, permeabilized with 0.2% Triton X-100 in PBS at RT for 5 min, followed by 1 h blocking with PBSBT (3% BSA, 0.1% Triton X-100 in PBS) at RT for 1 h. After blocking, cells were incubated with primary antibodies diluted in PBSBT blocking buffer at 4°C overnight. Primary antibodies used in this study are as follows: rabbit anti-paxillin Y113 (1:100; Abcam; Cat# ab32084), rabbit anti-pFAK Tyr397 (1:100; CST; Cat# 3283), rabbit anti-pMLC2 Ser19 (1:50; CST; Cat# 3671), rabbit anti-GM130 (1:200; BD Biosciences; Cat# 610822), mouse anti-pan-cytokeratin (1:200; Sigma–Aldrich; C2931). After five washes in PBS, cells were then incubated with rhodamine phalloidin (1:100; Biotium; Cat# 00027) and species-specific Alexa Fluor 488 and 647 secondary antibodies (1:500; Thermo Fisher Scientific) at RT for 1 h. After washing in PBS, cell nuclei were labeled with DAPI (Sigma–Aldrich). Coverslips were then mounted with ProLong Gold Antifade Mountant (Invitrogen; Cat# P36930). Cells were imaged on a Leica SP8 inverted confocal microscope using a HC PL APO 40x/1.30 oil objective lens. For quantification of polarized cells experiment, images were captured with a HC PL APO 10x/0.40 air objective lens.

Lung cryosections from E18.5 WT, *Vangl2*$^{Lp/+}$, and *Vangl2*$^{Lp/Lp}$ mice were immunostained with mouse anti-pan-cytokeratin (1:200; Sigma–Aldrich; C2931) and rabbit anti-pYAP Ser127 (1:100; CST; Cat# 4911). Sections were then incubated with species-specific Alexa Fluor 488 and 647 secondary antibodies (1:500; Thermo Fisher Scientific). Cell nuclei were labeled with DAPI (Sigma–Aldrich) and sections were then mounted with ProLong Gold Antifade Mountant (Invitrogen; Cat# P36930). Lung airways were imaged on a Leica SP8 inverted confocal microscope using a HC PL APO 40x/1.30 oil objective lens. For quantification of cytoplasmic pYAP levels, images of the nuclei stained with DAPI were thresholded, resulting in a binary mask of the nuclei. This mask was overlaid on the pYAP immunofluorescence image and subtracted from the pYAP mask. The mean fluorescent intensity was measured giving the average YAP expression in the cytoplasm.

For immunofluorescent staining of fixed PCLS, first P3 PCLS were dual stained as above with EpCAM-FITC (1:200; Thermo Fisher Scientific; Cat# 11-5791-80) and silicon rhodamine far-red fluorophore-conjugated DNA minor groove binder bisbenzimide (SiR-DNA) at (1:300; Tebu-Bio Ltd.; Cat# SC007). PCLS were fixed with 10% buffered formalin then blocked and permeabilized with PBSBT blocking buffer (1% BSA, 0.5% Triton X-100 in PBS) in the dark for 1 h at RT. Samples were then incubated with anti-mouse CD11c-PE conjugated primary antibody (1:200; Biolegend; Cat# 117307) overnight at 4°C to label macrophages. After incubation, EpCAM-FITC, CD11c-PE, and SiR-DNA triple-labeled PCLS were washed and mounted onto glass slides with ProLong Gold Antifade Mountant (Invitrogen; Cat# P36930). Images were taken using a Zeiss Axio Observer inverted microscope, with Lumencor Spectra X LED light source and Hamamatsu Flash 4.0 camera, using 40×/0.7 NA, air objective lens. The z-stacks of images were deconvolved as above and best-focused single slice images were analyzed. For some experiments, channel colors were changed during image post-processing to aid visualization.

Quantification of Focal Adhesions

Cell FAs were imaged on a Leica SP8 inverted confocal microscope using a HC PL APO 40x/1.30 oil objective lens. Quantification of FAs was performed using FIJI software. First, a raw image was split into three channels: DAPI, Alexa Fluor 488-conjugated paxillin, and rhodamine-conjugated phalloidin. The single channel paxillin image was thresholded to highlight the paxillin staining and "analyze particles" tool was used to measure the size of paxillin (FAs) in the unit of micron^2. A size filter of " $>$ 0.1 micron^2 to infinity" was used to exclude non-specific noise. A list of measurements was produced and each of them represented a single FA size. The result was exported to Excel and the mean FA size was calculated using the Excel "average" function. The total FA area was also calculated by summing all the FA areas. For the quantification of FA density, phalloidin channel was also analyzed to measure the total cell area (micron^2). "Threshold" tool was used to exclude the cell-free area. Any noise outside the cells was manually removed using the drawing tool. Cell areas were then selected and "measure" tool in FIJI was used, which produced the total cell area in micron^2. The result was exported to the Excel. The FA density = total FA area normalized to total cell area.

RNA Extraction and Quantitative RT-PCR

Total RNA was extracted from WT, *Vangl2*$^{Lp/+}$, and *Vangl2*$^{Lp/Lp}$ mouse lung tissues and A549 cells using the RNeasy mini kit (Qiagen) according to the manufacturer's protocols. For mouse lung tissues, a two-step homogenization was carried out using a FastPrep-24^{TM} Tissue Homogenizer (MP Biomedicals) followed by a QIAshredder kit (Qiagen) following the manufacturer's instructions. RNA concentration and quality was assessed using the TapeStation 2200 (Agilent). 1 μg of total RNA was reverse-transcribed to cDNA using the High-Capacity cDNA Reverse Transcription kit (Applied Biosystems). Quantitative RT-PCR (qRT-PCR) was performed using TaqMan Fast Advanced Master Mix (Life Technologies) and run on a Viia7 Real-Time PCR System (Applied Biosystems). For mouse cDNA, *B2m* and *Hprt* were used as reference genes; whereas *B2M* and *GUSB* were used as reference genes for human cDNA. Relative transcript levels were analyzed using the $2^{-\Delta\Delta CT}$ method. Three mice were used per group and all samples were tested in triplicate. All primers used in this study were purchased from Life Technologies as follows: *Ctgf (*Mm01192933_g1), *Cyr61 (*Mm00487498_m1), *Ankrd1 (*Mm00496512_m1), *B2m (*Mm00437762_m1), *Hprt (*Mm03024075_m1), *B2M* (Hs00187842_m1), *GUSB* (Hs00939627_m1), and *VANGL2* (Hs00393412_m1).

Protein Extraction and Western Blotting

A549 cells were lyzed in lysis buffer containing 0.1% Triton X-100 (Sigma–Aldrich), 1 × protease inhibitor cocktail (PIC; Roche), 1 × PhosSTOP^{TM} (Roche), 1 mM phenylmethylsulfonyl fluoride (PMSF; Sigma–Aldrich), and 5 μg/ml sodium deoxycholate (Sigma–Aldrich) in PBS for 15 min. Lysates were collected with a cell scraper and sonicated for 5 s. Lysates were then centrifuged at 4°C, 14,000 × *g* for 30 min and supernatant was collected and stored at −80°C until use. The concentrations of protein samples were quantified using the Pierce BCA Protein Assay Kit (Thermo Fisher Scientific) according to the manufacturer's instructions. Protein samples were subjected to SDS-PAGE and transferred onto polyvinylidene difluoride (PVDF) membranes (Thermo Fisher Scientific). After blocking with TBSBT blocking buffer (0.1% Tween-20, 5% BSA in TBS) for 1 h at RT, membranes were incubated with rabbit anti-phospho-FAK Y397 (1:1000; CST; Cat# 3283) and mouse anti-FAK (1:3000; CST; Cat# 05-537) primary antibodies overnight at 4°C. After washing in TBS containing 0.1% Tween-20, membranes were incubated with IRDye 800CW goat anti-rabbit IgG secondary antibody (1:15,000; LI-COR Biosciences; Cat# 925-32211) and IRDye 680RD goat anti-mouse IgG secondary antibody (1:10,000; LI-COR Biosciences; Cat# 925-68070) at RT for 1 h. Immunodetection was performed using an Odyssey infrared imaging system (LI-COR) and western blots were analyzed using the LI-COR Image Studio Lite Software.

Elastic Pillar Arrays

Elastic micropillar arrays were fabricated in PDMS as previously described (Chronopoulos et al., 2016). Briefly, PDMS (Sylgard 184, Dow Corning) was mixed with its curing agent in a 10:1 ratio according to the manufacturer's specification, poured on the silicon mold, and cured at 60°C for 1 h. After curing, pillars were peeled from the mold in PBS and store at 4°C. Prior to cell seeding, pillars were coated with 50 μg/ml rat-tail collagen I diluted in 0.02 M acetic acid and incubated at 37°C for 1 h. After incubation, collagen solution covering the pillars was carefully replaced with PBS followed by TEC Plus medium. TECs were then counted and seeded on the pillar microarrays submerged in TEC Plus medium and incubated at 37°C at 5% CO_2 for 24 h before analysis. Time-lapse imaging (1 frame per second for 1 min) of individual cells was acquired on an inverted microscope (Eclipse Ti; Nikon) with a sCMOS camera (Neo sCMOS Andor) in a pre-equilibrated and humidified incubator chamber. Each sample was analyzed for a maximum of 30 min to ensure cell viability. Data were analyzed with a custom MATLAB script to track individual pillar deflection, and a cell-free area was used to subtract stage drift. Traction forces were calculated from pillar deflections using the spring constant (k = 1.36 nN/μm) of the pillars.

Quantification and Statistical Analysis

All graphs and statistical tests were produced in GraphPad Prism 8. All data are presented as mean ± standard error of mean (SEM). D'Agostino–Pearson test was performed to determine the normality of data. Non-parametric datasets were analyzed using Mann–Whitney *U*-test (comparison of two groups), or Kruskal–Wallis with Dunn's multiple comparisons test (comparison of more than two groups). Normally distributed datasets were analyzed using two-tailed unpaired Student's *t*-test (comparison of two groups), or one-way ANOVA with Tukey's *post hoc* test (comparison of more than two groups). Details of the statistical tests used, the value of *n*, and number of experiments performed are all detailed in the figure legends. $P < 0.05$ was considered statistically significant.

DATA AVAILABILITY STATEMENT

The raw data supporting the conclusions of this article will be made available by the authors, without undue reservation.

ETHICS STATEMENT

The animal study was reviewed and approved by the South Kensington and St Mary's AWERB Committee, Imperial College London.

AUTHOR CONTRIBUTIONS

S-SC, CD, and MG designed the study and supervised the project. S-SC, KA, CM, and SK performed experiments. S-SC, KA, and CM analyzed the data. S-SC, KA, CM, MG, and CD wrote the manuscript. DG processed the movies and provided imaging expertise. CD, MG, AR, and MH provided conceptual advice. MH and CD acquired funding. All authors discussed the results and contributed to editing the manuscript.

FUNDING

This project was funded by the Royal Brompton Hospital and Harefield hospitals charity (Grant No. B1064) and an award from Mr. and Mrs. Youssef Mansour. The Facility for Imaging by Light Microscopy (FILM) at Imperial College London was part supported by funding from the Wellcome Trust (Grant 104931/Z/14/Z) and BBSRC (Grant BB/L015129/1).

ACKNOWLEDGMENTS

We thank MRC Harwell Institute for animal husbandry. We thank Andreas Bruckbauer and Stephen Rothery for microscope training and advice. We thank Lorraine Lawrence for help with lung tissue sectioning.

SUPPLEMENTARY MATERIAL

The Supplementary Material for this article can be found online at: https://www.frontiersin.org/articles/10.3389/fcell.2020.577201/full#supplementary-material

REFERENCES

Abreu-Blanco, M. T., Watts, J. J., Verboon, J. M., and Parkhurst, S. M. (2012). Cytoskeleton responses in wound repair. *Cell. Mol. Life Sci.* 69, 2469–2483. doi: 10.1007/s00018-012-0928-2

Akram, K. M., Yates, L. L., Mongey, R., Rothery, S., Gaboriau, D. C. A., Sanderson, J., et al. (2019a). Live imaging of alveologenesis in precision-cut lung slices reveals dynamic epithelial cell behaviour. *Nat. Commun.* 10:1178.

Akram, K. M., Yates, L. L., Mongey, R., Rothery, S., Gaboriau, D. C., Sanderson, J., et al. (2019b). Time-lapse imaging of alveologenesis in mouse precision-cut lung slices. *Bio Protoc.* 9:e3403.

Amano, M., Ito, M., Kimura, K., Fukata, Y., Chihara, K., Nakano, T., et al. (1996). Phosphorylation and activation of myosin by Rho-associated kinase (Rho-kinase). *J. Biol. Chem.* 271, 20246–20249. doi: 10.1074/jbc.271.34.20246

Andre, P., Wang, Q., Wang, N., Gao, B., Schilit, A., Halford, M. M., et al. (2012). The Wnt coreceptor Ryk regulates Wnt/planar cell polarity by modulating the degradation of the core planar cell polarity component Vangl2. *J. Biol. Chem.* 287, 44518–44525. doi: 10.1074/jbc.M112.414441

Aw, W., Heck, B., Joyce, B., and Devenport, D. (2016). Transient tissue-scale deformation coordinates alignment of planar cell polarity junctions in the mammalian skin. *Curr. Biol.* 26, 2090–2100. doi: 10.1016/j.cub.2016.06.030

Baarsma, H. A., Skronska-Wasek, W., Mutze, K., Ciolek, F., Wagner, D. E., John-Schuster, G., et al. (2017). Noncanonical WNT-5A signaling impairs endogenous lung repair in COPD. *J. Exp. Med.* 214, 143–163. doi: 10.1084/jem.20160675

Babayeva, S., Zilber, Y., and Torban, E. (2011). Planar cell polarity pathway regulates actin rearrangement, cell shape, motility, and nephrin distribution in podocytes. *Am. J. Physiol. Renal Physiol.* 300, F549–F560. doi: 10.1152/ajprenal.00566.2009

Balaban, N. Q., Schwarz, U. S., Riveline, D., Goichberg, P., Tzur, G., Sabanay, I., et al. (2001). Force and focal adhesion assembly: a close relationship studied using elastic micropatterned substrates. *Nat. Cell Biol.* 3, 466–472. doi: 10.1038/35074532

Belotti, E., Puvirajesinghe, T. M., Audebert, S., Baudelet, E., Camoin, L., Pierres, M., et al. (2012). Molecular characterisation of endogenous Vangl2/Vangl1 heteromeric protein complexes. *PLoS One* 7:e46213. doi: 10.1371/journal.pone.0046213

Beningo, K. A., Dembo, M., Kaverina, I., Small, J. V., and Wang, Y. L. (2001). Nascent focal adhesions are responsible for the generation of strong propulsive forces in migrating fibroblasts. *J. Cell Biol.* 153, 881–887. doi: 10.1083/jcb.153.4.881

Choi, H. J., Zhang, H., Park, H., Choi, K. S., Lee, H. W., Agrawal, V., et al. (2015). Yes-associated protein regulates endothelial cell contact-mediated expression of angiopoietin-2. *Nat. Commun.* 6:6943. doi: 10.1038/ncomms7943

Chronopoulos, A., Robinson, B., Sarper, M., Cortes, E., Auernheimer, V., Lachowski, D., et al. (2016). ATRA mechanically reprograms pancreatic stellate cells to suppress matrix remodelling and inhibit cancer cell invasion. *Nat. Commun.* 7:12630. doi: 10.1038/ncomms12630

Cory, G. (2011). Scratch-wound assay. *Methods Mol. Biol.* 769, 25–30. doi: 10.1007/978-1-61779-207-6_2

Davey, C. F., and Moens, C. B. (2017). Planar cell polarity in moving cells: think globally, act locally. *Development* 144, 187–200. doi: 10.1242/dev.122804

de Chaumont, F., Dallongeville, S., Chenouard, N., Hervé, N., Pop, S., Provoost, T., et al. (2012). Icy: an open bioimage informatics platform for extended reproducible research. *Nat. Methods* 9, 690–696. doi: 10.1038/nmeth.2075

Dobrokhotov, O., Samsonov, M., Sokabe, M., and Hirata, H. (2018). Mechanoregulation and pathology of YAP/TAZ via Hippo and non-Hippo mechanisms. *Clin. Transl. Med.* 7:23.

Duan, X., Gao, Y., and Liu, Y. (2017). Ryk regulates Wnt5a repulsion of mouse corticospinal tract through modulating planar cell polarity signaling. *Cell Discov.* 3:17015. doi: 10.1038/celldisc.2017.15

Dupont, S., Morsut, L., Aragona, M., Enzo, E., Giulitti, S., Cordenonsi, M., et al. (2011). Role of YAP/TAZ in mechanotransduction. *Nature* 474, 179–184. doi: 10.1038/nature10137

Enomoto, M., Hayakawa, S., Itsukushima, S., Ren, D. Y., Matsuo, M., Tamada, K., et al. (2009). Autonomous regulation of osteosarcoma cell invasiveness by Wnt5a/Ror2 signaling. *Oncogene* 28, 3197–3208. doi: 10.1038/onc.2009.175

Etienne-Manneville, S., and Hall, A. (2001). Integrin-mediated activation of Cdc42 controls cell polarity in migrating astrocytes through PKCζ. *Cell* 106, 489–498. doi: 10.1016/s0092-8674(01)00471-8

Evans, E. A., and Calderwood, D. A. (2007). Forces and bond dynamics in cell adhesion. *Science* 316, 1148–1154. doi: 10.1126/science.1137592

Ezzie, M. E., Crawford, M., Cho, J.-H., Orellana, R., Zhang, S., Gelinas, R., et al. (2012). Gene expression networks in COPD: microRNA and mRNA regulation. *Thorax* 67, 122–131. doi: 10.1136/thoraxjnl-2011-200089

Friedl, P., and Gilmour, D. (2009). Collective cell migration in morphogenesis, regeneration and cancer. *Nat. Rev. Mol. Cell Biol.* 10, 445–457. doi: 10.1038/nrm2720

Gao, B., Song, H., Bishop, K., Elliot, G., Garrett, L., English, M. A., et al. (2011). Wnt signaling gradients establish planar cell polarity by inducing Vangl2 phosphorylation through Ror2. *Dev. Cell* 20, 163–176. doi: 10.1016/j.devcel.2011.01.001

Geiger, B., Spatz, J. P., and Bershadsky, A. D. (2009). Environmental sensing through focal adhesions. *Nat. Rev. Mol. Cell Biol.* 10, 21–33. doi: 10.1038/nrm2593

Goffin, J. M., Pittet, P., Csucs, G., Lussi, J. W., Meister, J. J., and Hinz, B. (2006). Focal adhesion size controls tension-dependent recruitment of α-smooth muscle actin to stress fibers. *J. Cell Biol.* 172, 259–268. doi: 10.1083/jcb.200506179

Goodrich, L. V., and Strutt, D. (2011). Principles of planar polarity in animal development. *Development* 138, 1877–1892. doi: 10.1242/dev.054080

Hamadi, A., Bouali, M., Dontenwill, M., Stoeckel, H., Takeda, K., and Rondé, P. (2005). Regulation of focal adhesion dynamics and disassembly by phosphorylation of FAK at tyrosine 397. *J. Cell Sci.* 118, 4415–4425. doi: 10.1242/jcs.02565

Henderson, D. J., Long, D. A., and Dean, C. H. (2018). Planar cell polarity in organ formation. *Curr. Opin. Cell Biol.* 55, 96–103. doi: 10.1016/j.ceb.2018.06.011

Hopkins, A. M., Pineda, A. D. A., Winfree, L. M., Brown, G. T., Laukoetter, M. G., and Nusrat, A. (2019). Organized migration of epithelial cells requires control of adhesion and protrusion through Rho kinase effectors. *Am. J. Physiol. Gastrointest. Liver Physiol.* 292, G806–G817. doi: 10.1152/ajpgi.00333.2006

Isago, H., Mitani, A., Mikami, Y., Horie, M., Urushiyama, H., Hamamoto, R., et al. (2020). Epithelial expression of YAP and TAZ is sequentially required in lung development. *Am. J. Respir. Cell Mol. Biol.* 62, 256–266. doi: 10.1165/rcmb.2019-0218oc

Jaalouk, D. E., and Lammerding, J. (2009). Mechanotransduction gone awry. *Nat. Rev. Mol. Cell Biol.* 10, 63–73. doi: 10.1038/nrm2597

Képiró, M., Várkuti, B. H., Végner, L., Vörös, G., Hegyi, G., Varga, M., et al. (2014). Para-nitroblebbistatin, the non-cytotoxic and photostable myosin II inhibitor. *Angew. Chem. Int. Ed.* 53, 8211–8215. doi: 10.1002/anie.201403540

Kibar, Z., Vogan, K. J., Groulx, N., Justice, M. J., Underhill, D. A., and Gros, P. (2001). *Ltap*, a mammalian homolog of *Drosophila Strabismus/Van Gogh*, is altered in the mouse neural tube mutant Loop-tail. *Nat. Genet.* 28, 251–255. doi: 10.1038/90081

Kim, H. Y., and Nelson, C. M. (2012). Extracellular matrix and cytoskeletal dynamics during branching morphogenesis. *Organogenesis* 8, 56–64. doi: 10.4161/org.19813

Komiya, Y., and Habas, R. (2008). Wnt signal transduction pathways. *Organogenesis* 4, 68–75. doi: 10.4161/org.4.2.5851

Lacanna, R., Wolfson, M. R., Tian, Y., Lacanna, R., Liccardo, D., Zhang, P., et al. (2019). Yap/Taz regulate alveolar regeneration and resolution of lung inflammation. *J. Clin. Invest.* 129, 2107–2122. doi: 10.1172/jci125014

Lam, H. C., Choi, A. M. K., and Ryter, S. W. (2010). Isolation of mouse respiratory epithelial cells and exposure to experimental cigarette smoke at air liquid interface. *J. Vis. Exp.* 48:2513. doi: 10.3791/2513

Li, C., Smith, S. M., Peinado, N., Gao, F., Li, W., Lee, M. K., et al. (2020). WNT5a-ROR signaling is essential for alveologenesis. *Cells* 9:384. doi: 10.3390/cells9020384

Lin, C., Yao, E., Zhang, K., Jiang, X., Croll, S., Thompson-Peer, K., et al. (2017). YAP is essential for mechanical force production and epithelial cell proliferation during lung branching morphogenesis. *eLife* 6:e21130. doi: 10.7554/eLife.21130

Mayor, R., and Carmona-Fontaine, C. (2010). Keeping in touch with contact inhibition of locomotion. *Trends Cell Biol.* 20, 319–328. doi: 10.1016/j.tcb.2010.03.005

Mitra, S. K., Hanson, D. A., and Schlaepfer, D. D. (2005). Focal adhesion kinase: in command and control of cell motility. *Nat. Rev. Mol. Cell Biol.* 6, 56–68. doi: 10.1038/nrm1549

Montcouquiol, M., Sans, N., Huss, D., Kach, J., Dickman, J. D., Forge, A., et al. (2006). Asymmetric localization of Vangl2 and Fz3 indicate novel mechanisms for planar cell polarity in mammals. *J. Neurosci.* 26, 5265–5275. doi: 10.1523/JNEUROSCI.4680-05.2006

Munoz-Soriano, V., Belacortu, Y., and Paricio, N. (2012). Planar cell polarity signaling in collective cell movements during morphogenesis and disease. *Curr. Genomics* 13, 609–622. doi: 10.2174/138920212803759721

Murdoch, J. N. (2001). Severe neural tube defects in the loop-tail mouse result from mutation of Lpp1, a novel gene involved in floor plate specification. *Hum. Mol. Genet.* 10, 2593–2601. doi: 10.1093/hmg/10.22.2593

Nabhan, A. N., Brownfield, D. G., Harbury, P. B., Krasnow, M. A., and Desai, T. J. (2018). Single-cell Wnt signaling niches maintain stemness of alveolar type 2 cells. *Science* 359, 1118–1123. doi: 10.1126/science.aam6603

Nishita, M., Enomoto, M., Yamagata, K., and Minami, Y. (2010). Cell/tissue-tropic functions of Wnt5a signaling in normal and cancer cells. *Trends Cell Biol.* 20, 346–354. doi: 10.1016/j.tcb.2010.03.001

Oakes, P. W., and Gardel, M. L. (2014). Stressing the limits of focal adhesion mechanosensitivity. *Curr. Opin. Cell Biol.* 30, 68–73. doi: 10.1016/j.ceb.2014.06.003

Pandya, P., Orgaz, J. L., and Sanz-Moreno, V. (2017). Actomyosin contractility and collective migration: may the force be with you. *Curr. Opin. Cell Biol.* 48, 87–96. doi: 10.1016/j.ceb.2017.06.006

Park, H. W., Kim, Y. C., Yu, B., Moroishi, T., Mo, J. S., Plouffe, S. W., et al. (2015). Alternative Wnt signaling activates YAP/TAZ. *Cell* 162, 780–794. doi: 10.1016/j.cell.2015.07.013

Pieretti, A. C., Ahmed, A. M., Roberts, J. D., and Kelleher, C. M. (2014). A novel in vitro model to study alveologenesis. *Am. J. Respir. Cell Mol. Biol.* 50, 459–469. doi: 10.1165/rcmb.2013-0056OC

Poobalasingam, T., Yates, L. L., Walker, S. A., Pereira, M., Gross, N. Y., Ali, A., et al. (2017). Heterozygous Vangl2 Looptail mice reveal novel roles for the planar cell polarity pathway in adult lung homeostasis and repair. *Dis. Models Mech.* 10, 409–423. doi: 10.1242/dmm.028175

Pryor, S. E., Massa, V., Savery, D., Andre, P., Yang, Y., Greene, N. D., et al. (2014). Vangl-dependent planar cell polarity signalling is not required for neural crest migration in mammals. *Development* 141, 3153–3158. doi: 10.1242/dev.111427

Qian, D., Jones, C., Rzadzinska, A., Mark, S., Zhang, X., Steel, K. P., et al. (2007). Wnt5a functions in planar cell polarity regulation in mice. *Dev. Biol.* 306, 121–133. doi: 10.1016/j.ydbio.2007.03.011

Raman, R., Pinto, C. S., and Sonawane, M. (2018). Polarized organization of the cytoskeleton: regulation by cell polarity proteins. *J. Mol. Biol.* 430, 3565–3584. doi: 10.1016/j.jmb.2018.06.028

Rao-Bhatia, A., Zhu, M., Yin, W.-C., Coquenlorge, S., Zhang, X., Woo, J., et al. (2020). Hedgehog-activated Fat4 and PCP pathways mediate mesenchymal cell clustering and villus formation in gut development. *Dev. Cell* 52, 647–658. doi: 10.1016/j.devcel.2020.02.003

Schiller, H. B., and Fässler, R. (2013). Mechanosensitivity and compositional dynamics of cell-matrix adhesions. *EMBO Rep.* 14, 509–519. doi: 10.1038/embor.2013.49

Schindelin, J., Arganda-Carreras, I., Frise, E., Kaynig, V., Longair, M., Pietzsch, T., et al. (2012). Fiji: an open-source platform for biological-image analysis. *Nat. Methods* 9, 676–682. doi: 10.1038/nmeth.2019

Schliwa, M. (1982). Action of cytochalasin D on cytoskeletal networks. *J. Cell Biol.* 92, 79–91. doi: 10.1083/jcb.92.1.79

Schwarz, U. S., Balaban, N. Q., Riveline, D., Bershadsky, A., Geiger, B., and Safran, S. A. (2002). Calculation of forces at focal adhesions from elastic substrate data: the effect of localized force and the need for regularization. *Biophys. J.* 83, 1380–1394. doi: 10.1016/S0006-3495(02)73909-X

Seo, H. S., Habas, R., Chang, C., and Wang, J. (2017). Bimodal regulation of Dishevelled function by Vangl2 during morphogenesis. *Hum. Mol. Genet.* 26, 2053–2061. doi: 10.1093/hmg/ddx095

Stricker, J., Aratyn-Schaus, Y., Oakes, P. W., and Gardel, M. L. (2011). Spatiotemporal constraints on the force-dependent growth of focal adhesions. *Biophys. J.* 100, 2883–2893. doi: 10.1016/j.bpj.2011.05.023

Sucre, J. M. S., Vickers, K. C., Benjamin, J. T., Plosa, E. J., Jetter, C. S., Cutrone, A., et al. (2020). Hyperoxia injury in the developing lung is mediated by mesenchymal expression of Wnt5A. *Am. J. Respir. Crit. Care Med.* 201, 1249–1262. doi: 10.1164/rccm.201908-1513oc

Sun, Z., Guo, S. S., and Fässler, R. (2016). Integrin-mediated mechanotransduction. *J. Cell Biol.* 215, 445–456. doi: 10.1083/jcb.201609037

Uehata, M., Ishizaki, T., and Satoh, H. (1997). Calcium sensitization of smooth muscle mediated by a Rho-associated protein kinase in hypertension. *Nature* 389, 990–994. doi: 10.1038/40187

Unbekandt, M., Croft, D. R., Crighton, D., Mezna, M., McArthur, D., McConnell, P., et al. (2014). A novel small-molecule MRCK inhibitor blocks cancer cell invasion. *Cell Commun. Signal.* 12:54. doi: 10.1186/s12964-014-0054-x

van Soldt, B. J., Qian, J., Li, J., Tang, N., Lu, J., and Cardoso, W. V. (2019). Yap and its subcellular localization have distinct compartment-specific roles in the developing lung. *Development* 146:dev175810. doi: 10.1242/dev.175810

Varner, V. D., Gleghorn, J. P., Miller, E., Radisky, D. C., and Nelson, C. M. (2015). Mechanically patterning the embryonic airway epithelium. *Proc. Natl. Acad. Sci. U.S.A.* 112, 9230–9235. doi: 10.1073/pnas.1504102112

Vladar, E. K., and Königshoff, M. (2020). Noncanonical Wnt planar cell polarity signaling in lung development and disease. *Biochem. Soc. Trans.* 48, 231–243. doi: 10.1042/BST20190597

Vuga, L. J., Ben-Yehudah, A., Kovkarova-Naumovski, E., Oriss, T., Gibson, K. F., Feghali-Bostwick, C., et al. (2009). WNT5A is a regulator of fibroblast proliferation and resistance to apoptosis. *Am. J. Respir. Cell Mol. Biol.* 41, 583–589. doi: 10.1165/rcmb.2008-0201OC

Wada, K. I., Itoga, K., Okano, T., Yonemura, S., and Sasaki, H. (2011). Hippo pathway regulation by cell morphology and stress fibers. *Development* 138, 3907–3914. doi: 10.1242/dev.070987

Waters, C. M., Roan, E., and Navajas, D. (2012). Mechanobiology in lung epithelial cells: measurements, perturbations, and responses. *Compr. Physiol.* 2, 1–29. doi: 10.1002/cphy.c100090

Weidinger, G., and Moon, R. T. (2003). When Wnts antagonize Wnts. *J. Cell Biol.* 162, 753–755. doi: 10.1083/jcb.200307181

Westfall, T. A., Brimeyer, R., Twedt, J., Gladon, J., Olberding, A., Furutani-Seiki, M., et al. (2003). Wnt-5/pipetail functions in vertebrate axis formation as a negative regulator of Wnt/β-catenin activity. *J. Cell Biol.* 162, 889–898. doi: 10.1083/jcb.200303107

Witze, E. S., Litman, E. S., Argast, G. M., Moon, R. T., and Ahn, N. G. (2008). Wnt5a control of cell polarity and directional movement by polarized redistribution of adhesion receptors. *Science* 320, 365–370. doi: 10.1126/science.1151250

Wu, X., van Dijk, E. M., Ng-Blichfeldt, J.-P., Bos, I. S., Ciminieri, C., Königsho, M., et al. (2019). Mesenchymal WNT-5A/5B signaling represses lung alveolar epithelial progenitors. *Cells* 25:1147. doi: 10.3390/cells8101147

Yang, M. T., Fu, J., Wang, Y. K., Desai, R. A., and Chen, C. S. (2011). Assaying stem cell mechanobiology on microfabricated elastomeric substrates with geometrically modulated rigidity. *Nat. Protoc.* 6, 187–213. doi: 10.1038/nprot.2010.189

Yang, W., Garrett, L., Feng, D., Elliott, G., Liu, X., Wang, N., et al. (2017). Wnt-induced Vangl2 phosphorylation is dose-dependently required for planar cell polarity in mammalian development. *Cell Res.* 27, 1466–1484. doi: 10.1038/cr.2017.127

Yates, L. L., Papakrivopoulou, J., Long, D. A., Goggolidou, P., Connolly, J. O., Woolf, A. S., et al. (2010a). The planar cell polarity gene Vangl2 is required for mammalian kidney-branching morphogenesis and glomerular maturation. *Hum. Mol. Genet.* 19, 4663–4676. doi: 10.1093/hmg/ddq397

Yates, L. L., Schnatwinkel, C., Murdoch, J. N., Bogani, D., Formstone, C. J., Townsend, S., et al. (2010b). The PCP genes Celsr1 and Vangl2 are required for normal lung branching morphogenesis. *Hum. Mol. Genet.* 19, 2251–2267. doi: 10.1093/hmg/ddq104

Yates, L. L., Schnatwinkel, C., Hazelwood, L., Chessum, L., Paudyal, A., Hilton, H., et al. (2013). Scribble is required for normal epithelial cell-cell contacts and lumen morphogenesis in the mammalian lung. *Dev. Biol.* 373, 267–280. doi: 10.1016/j.ydbio.2012.11.012

Yin, H., Copley, C. O., Goodrich, L. V., and Deans, M. R. (2012). Comparison of phenotypes between different Vangl2 mutants demonstrates dominant effects of the Looptail mutation during hair cell development. *PLoS One* 7:e31988. doi: 10.1371/journal.pone.0031988

Yu, J., Chen, L., Cui, B., Widhopf, G. F., Shen, Z., Wu, R., et al. (2016). Wnt5a induces ROR1/ROR2 heterooligomerization to enhance leukemia chemotaxis and proliferation. *J. Clin. Investig.* 126, 585–598. doi: 10.1172/JCI83535

Yuan, K., Shamskhou, E., Orcholski, M., Nathan, A., Reddy, S., Honda, H., et al. (2019). Loss of endothelium-derived Wnt5a is associated with reduced pericyte recruitment and small vessel loss in pulmonary arterial hypertension. *Circulation* 139, 1710–1724. doi: 10.1161/CIRCULATIONAHA.118.037642

Zhang, K., Yao, E., Lin, C., Chou, Y., Wong, J., Li, J., et al. (2020). A mammalian Wnt5a – Ror2 – Vangl2 axis controls the cytoskeleton and confers cellular properties required for alveologenesis. *eLife* 9:e53688.

Zhao, B., Ye, X., Yu, J., Li, L., Li, W., Li, S., et al. (2008). TEAD mediates YAP-dependent gene induction and growth control. *Genes Dev.* 22, 1962–1971. doi: 10.1101/gad.1664408

Conflict of Interest: The authors declare that the research was conducted in the absence of any commercial or financial relationships that could be construed as a potential conflict of interest.

frontiers in Cell and Developmental Biology

ORIGINAL RESEARCH
published: 05 November 2020
doi: 10.3389/fcell.2020.593879

Inhomogeneities in 3D Collagen Matrices Impact Matrix Mechanics and Cancer Cell Migration

*Alexander Hayn, Tony Fischer and Claudia Tanja Mierke**

Biological Physics Division, Faculty of Physics and Earth Sciences, Peter Debye Institute for Soft Matter Physics, University of Leipzig, Leipzig, Germany

Cell motility under physiological and pathological conditions including malignant progression of cancer and subsequent metastasis are founded on environmental confinements. During the last two decades, three-dimensional cell migration has been studied mostly by utilizing biomimetic extracellular matrix models. In the majority of these studies, the *in vitro* collagen scaffolds are usually assumed to be homogenous, as they consist commonly of one specific type of collagen, such as collagen type I, isolated from one species. These collagen matrices should resemble *in vivo* extracellular matrix scaffolds physiologically, however, mechanical phenotype and functional reliability have been addressed poorly due to certain limitations based on the assumption of homogeneity. How local variations of extracellular matrix structure impact matrix mechanics and cell migration is largely unknown. Here, we hypothesize that local inhomogeneities alter cell movement due to alterations in matrix mechanics, as they frequently occur in *in vivo* tissue scaffolds and were even changed in diseased tissues. To analyze the effect of structural inhomogeneities on cell migration, we used a mixture of rat tail and bovine dermal collagen type I as well as pure rat and pure bovine collagens at four different concentrations to assess three-dimensional scaffold inhomogeneities. Collagen type I from rat self-assembled to elongated fibrils, whereas bovine collagen tended to build node-shaped inhomogeneous scaffolds. We have shown that the elastic modulus determined with atomic force microscopy in combination with pore size analysis using confocal laser scanning microscopy revealed distinct inhomogeneities within collagen matrices. We hypothesized that elastic modulus and pore size govern cancer cell invasion in three-dimensional collagen matrices. In fact, invasiveness of three breast cancer cell types is altered due to matrix-type and concentration indicating that these two factors are crucial for cellular invasiveness. Our findings revealed that local matrix scaffold inhomogeneity is another crucial parameter to explain differences in cell migration, which not solely depended on pore size and stiffness of the collagen matrices. With these three distinct biophysical parameters, characterizing structure and mechanics of the studied collagen matrices, we were able to explain differences in the invasion behavior of the studied cancer cell lines in dependence of the used collagen model.

Keywords: structural homogeneity, cancer, invasion, extracellular matrix, motility, atomic force microscope, elasticity, stiffness

OPEN ACCESS

Edited by:
Maurizio Onisto, University of Padua, Italy

Reviewed by:
Marco Franchi, University of Bologna, Italy
Anke Bruning-Richardson, University of Huddersfield, United Kingdom

***Correspondence:**
Claudia Tanja Mierke
claudia.mierke@uni-leipzig.de

Specialty section:
This article was submitted to Cell Adhesion and Migration, a section of the journal Frontiers in Cell and Developmental Biology

Received: *11 August 2020*
Accepted: *08 October 2020*
Published: *05 November 2020*

Citation:
Hayn A, Fischer T and Mierke CT (2020) Inhomogeneities in 3D Collagen Matrices Impact Matrix Mechanics and Cancer Cell Migration. Front. Cell Dev. Biol. 8:593879. doi: 10.3389/fcell.2020.593879

INTRODUCTION

Metastasis caused by spreading of malignant cells represents the most harmful and dangerous aspect of cancer. Moreover, metastasis represents a prominent hallmark of the metastatic cascade (Pantel and Brakenhoff, 2004), that leads to secondary tumors at distant sites, which includes the capacity of cancer cells to efficiently invade different surrounding tissues (Gupta and Massagué, 2006), formed mainly by the specific extracellular matrices (ECMs). Changing the physical properties of the ECM protein meshwork (Krause et al., 2019) structures requires a highly adaptive behavior of invading cancer cells (Mierke, 2019a). Three-dimensional (3D) confined networks are relevant *in vitro* model systems to study cancer cell migration (Holle et al., 2019). Thereby adjustability and reproducibility represent a tunable and controlled microenvironment that is highly constructive to mimic ECM characteristics (Bersini et al., 2014) that cancer cells face *in vivo*.

In many studies, collagens of different origins or various collagen matrix compositions are utilized for 3D invasion assays. Implications for the migration behavior of cancer cells are the consequence. Howbeit, migration studies concerning cancer cell invasion into crafted 3D microenvironments are done in enormity, using several techniques and different materials (Hakkinen et al., 2011; Paul et al., 2016, 2017). In a growing number of studies, the spreading of cancer cells in defined environments is more focused on structural parameters and physical characteristics and their direct influence on the migratory behavior (Paszek et al., 2005; Wolf et al., 2009; Pathak and Kumar, 2012; Stroka and Konstantopoulos, 2014; Clark and Vignjevic, 2015; Carey et al., 2016; Um et al., 2017). Amongst others, inhomogeneity (Friedl and Alexander, 2011), matrix mechanics (Fischer et al., 2017) and confinements (Wolf et al., 2013) can drastically affect the migration potential.

Obviously, distinct parameters of the microenvironmental scaffold can stimulate and support the migration of specific cancer cells, whereas other parameters seem to rather constrain and impair the invasiveness of specific cancer cells (Wolf et al., 2013; Charras and Sahai, 2014). However, if these parameters impact the migration of all cancer cell types, or even all types of cells, in a universal manner is still on debate (Mierke, 2019b).

Apart from a broad field of techniques encompassing transwell migration assays or 3D invasion assays and many more, the material of the engineered ECM plays an even more crucial role concerning the cancer cell migration on top and into these distinct microenvironments (Wolf et al., 2009). Engineered matrices polymerized of collagen type I, which is the most abundant ECM protein in mammals, serve as a physiological *in vitro* model system (Paul et al., 2016).

Since hydrogels are used to investigate cancer cell behavior, collagen type I from bovine dermis and rat tail tendon are prominently employed for matrix engineering (Brown, 1982; Behrens et al., 1989; Liebersbach and Sanderson, 1994; Friedl et al., 1997; Wolf et al., 2009, 2013; Willis et al., 2013; Mohammadi et al., 2015; Sapudom et al., 2015, 2019; Krause et al., 2019). In many cases, even mixtures of rat and bovine collagen are used (Koch et al., 2012; Lang et al., 2015; Lautscham et al., 2015; Fischer et al., 2017, 2020; Kunschmann et al., 2019; Riedel et al., 2019; Sauer et al., 2019; Mierke et al., 2020). Although those collagen matrices are made of the same type of collagen (namely type I), they can assemble to a totally different network exhibiting different physical properties (Wolf et al., 2009; Paul et al., 2016).

To what extend collagens of different origin and composition directly influence the cancer cell invasive phenotype, due to the altered biomechanical and topological properties of the various ECM systems, is mostly unknown. Thus, in this study, we analyzed three different collagen compositions for 3D cancer cell invasion, each of them at four different collagen concentrations. We compared the invasion behavior into these matrices for three different human breast cancer cell lines, such as MDA-MB-231, ZR-75, and MCF-7. Furthermore, we analyzed the matrix mechanics concerning elasticity and pore size of crafted 3D microenvironments varying in structural inhomogeneity. In fact, we found that the cancer cell invasion varies due to structural differences of these matrices. In specific detail, it has turned out that inhomogeneities of the 3D microenvironment, most importantly on the cell level, crucially influence the invasive phenotype of cancer cells.

RESULTS

Characterization of Cell Line Specific Invasion in Different 3D Models

In order to obtain precise and distinct data for the invasion of human breast cancer cell lines, we generated different types of collagen networks from distinct collagen compositions. Therefore, we used commonly employed collagen compositions from collagen type I, such as pure collagens from rat tail (R) and bovine skin (B) and a 1:2 mixture of both (RB) collagen sources.

For a detailed insight in matrix dependent invasion, we altered the collagen concentrations from 1.5 g/l to 3.0 g/l, in steps of 0.5 g/l, respectively. By changing collagen concentration, we engineered loose (1.5 g/l), slightly loose (2.0 g/l), slightly dense (2.5 g/l) and dense (3.0 g/l) fibrillary networks. For all concentrations of all compositions, we seeded highly invasive MDA-MB-231, moderate invasive MCF-7 and minor invasive ZR75-1 cells separately on top of the collagen networks and let them invade for 3 days (**Figure 1A**). We analyzed the percentage of invasive cells (**Figure 1B**) and determined the invasion depths (**Figure 1C**) in dependence of the collagen composition and concentration. Further, we measured the invasion profiles (**Supplementary Figures S1A–C**), which show the probability for cells to be encountered in a certain depth also called their cumulative probability.

In summary, the cell line dependent invasion into R collagens exhibited a significantly higher invasive capacity (**Supplementary Figure S1A**) for MDA-MB-231 cells compared to a hindered invasion of MCF-7 cells and arrested ZR75-1 cells. The invasion of all three cell lines was somehow promoted at dense collagen matrices.

For R collagens, we found that MDA-MB-231 cells displayed a significantly ($p = 0.001$, or less) increased percentage of invasive cells (**Figure 1B**, left) with elevating collagen concentrations,

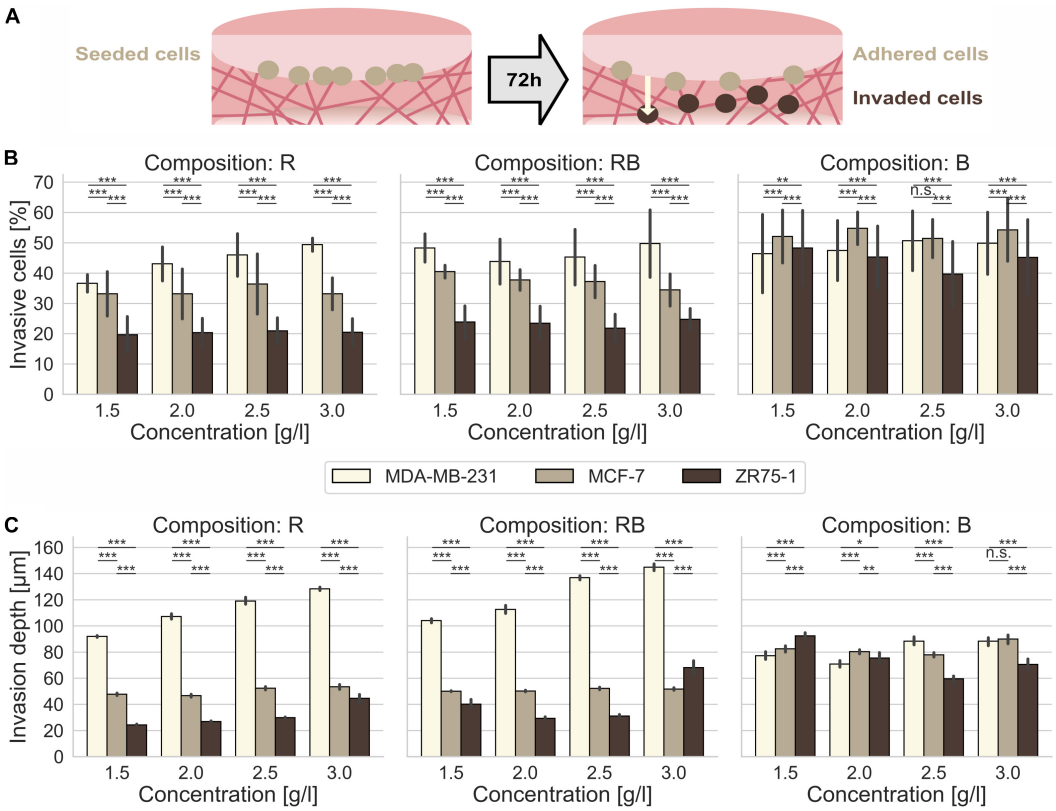

FIGURE 1 | Cancer cell invasion. Effect of collagen monomer concentration on the invasiveness and invasion depth for human MDA-MB-231, MCF-7 and ZR75-1 breast cancer cells into crafted scaffolds of rat collagen (R), bovine skin collagen (B) and a 1:2 mixture or rat and bovine collagen (RB). **(A)** Sketch of the invasion assay. Cells are seeded on top of the collagen gels and invaded the matrices for 72 h. **(B)** The invasiveness and **(C)** the invasion depth for three observed human breast cancer cell lines in dependence of the collagen monomer concentration for three different collagen compositions (R, left; RB, middle; B, right). Data are presented as the means and SD for at least 5–12 repetitions in 4–6 independent experiments. Significance notions were derived from Welch's unequal variance *t*-test, ***$p \leq 0.001$, **$p \leq 0.01$, *$p \leq 0.05$, n.s., not significant. One-way ANOVA test revealed *** significance for all conditions **(A,B)**.

from 36.6% ± 2.9% for loose collagen up to 49.4% ± 2.2% for dense collagens (**Supplementary Table S1**). In addition, the invasion depths (**Figure 1C**, left) increased significantly (p = 0.001, or less) with increasing concentration from 92.0 µm ± 7.1 µm for loose collagens up to 128.4 µm ± 11.9 µm for dense collagens. These results confirm the highly aggressive character of this cancer cell line. MCF-7 cells invaded R collagens with similar percentages of invasive cells at all concentrations, in the range of 33.1% ± 8.2% to 36.4% ± 9.9% (**Supplementary Table S1**). Invasion depths did not alter drastically in the range of 46.7 µm ± 8.8 µm up to 53.5 µm ± 14.5 µm (**Supplementary Table S1**). ZR75-1 cells invaded R collagens with stagnating percentages of invasive cells in the range of 19.7% ± 6.0% up to 21.0% ± 4.3% (**Supplementary Table S1**). Invasion depths were slightly but significantly (p = 0.001, or less) increased from 24.3 µm ± 6.1 µm in loose collagens up to 29.9 µm ± 5.3 µm in slightly dense collagens and considerably promoted in dense collagens (44.6 µm ± 29.7 µm). In summary, MDA-MB-231 cells invaded R collagens with significantly higher (p = 0.001, or less) percentages of invasive cells and penetrated these networks significantly deeper (p = 0.001, or less) at all concentrations compared to MCF-7 (1.5-fold invasion rate and 2.4-fold deeper invasion for dense collagens) and to ZR75-1 cells (2.4-fold invasion rate and 2.9-fold deeper invasion for dense collagen matrices).

MDA-MB-231 cells invaded with high percentages of invasive cells (**Figure 1B**, middle) into RB collagen matrices over all concentrations, in the range of 43.8% ± 7.4% up to 50.0% ± 11.1% invasive cells (**Supplementary Table S1**). Increasing collagen concentration significantly (p = 0.001, or less) promoted the invasion depths (**Figure 1C**, middle) from 104.1 µm ± 14.4 µm for loose collagens up to 145.0 µm ± 25.6 µm for dense collagens. However, for MCF-7 cells, we found a decreasing invasion ratio (**Figure 1B**, middle) with increasing collagen concentration, from 40.5% ± 2.1% for loose collagen matrices to 34.4% ± 5.3% for dense collagen matrices. Invasion depths (**Figure 1C**, middle) over all concentrations barely changed from 50.1 µm ± 2.8 µm up to 52.3 µm ± 8.7 µm (**Supplementary Table S1**). ZR75-1 cells invaded RB collagens less intense over all concentrations with invasion ratios (**Figure 1B**, middle) in the range of 23.5% ± 5.6% to 24.8% ± 3.6% (**Supplementary Table S1**). Invasion depths

(**Figure 1C**, middle) were low for intermediate concentrations (2.0 g/l and 2.5 g/l), upshifted for loose and drastically increased for dense collagens (**Supplementary Table S1**). In summary, MDA-MB-231 cells aggressively invaded RB collagens deeply at high invasion rates. Compared to MCF-7 cells and ZR75-1 cells the percentage of invasive MDA-MB-231 cells and their invasion depths are significantly higher (p = 0.001, or less) at all concentrations. MDA-MB-231 cells invaded with a 1.2-fold (loose collagens) up to 1.5-fold (dense collagens) higher invasion rates compared to MCF-7 cells and a 2-fold (loose and dense collagens) higher invasion rate compared to ZR75-1 cells. The invasion depths of MDA-MB-231 cells were 2.1-fold (loose collagens) to 2.8-fold (dense collagens) higher compared to MCF-7 cells and 2.1-fold (dense collagens) up to 2.6-fold (loose collagens) higher than ZR75-1 cells.

The invasive potential (**Supplementary Figure S1B**) increased for MDA-MB-231 cells with increasing RB collagen concentration. For MCF-7 cells and ZR75-1 cells, no clear trend in the invasive potential could be seen. However, the invasion into RB collagen matrices was promoted at loose and dense collagen matrices by increased invasion rates and/or invasion depths compared to the intermediate concentrations for all three investigated cancer cell lines.

MDA-MB-231 cells invaded B collagens at a higher percentage of invasive cells (**Figure 1B**, right) over all concentrations, in the range from 46.4% ± 12.9% up to 50.7% ± 9.8%. In fact, their invasiveness slightly increased for denser collagen matrices (2.5 g/l and 3.0 g/l) compared to looser collagen matrices (1.5 g/l and 2.0 g/l). The invasion depths (**Figure 1C**, right) varied between 70.8 μm ± 25.1 μm and 88.4 μm ± 31.5 μm and were increased at denser collagen matrices (**Supplementary Table S1**). MCF-7 cells invaded these collagens (**Figure 1B**, right) with higher invasion rates (51.4% ± 6.3% up to 54.8% ± 5.4%) and deeper (**Figure 1C**, right) compared to MDA-MB-231 cells, with one exception at 2.5 g/l collagens. MCF-7 invasion depths are in the range from 77.9 μm ± 15.4 μm up to 90.0 μm ± 28.4 μm (**Supplementary Table S1**). ZR75-1 cells invaded B collagen matrices with high percentage of invasive cells (**Figure 1B**, right) and invasion depth (**Figure 1C**, right). Values decreased from 48.3% ± 12.4% and 92.4 μm ± 34.7 μm for loose collagen matrices to 39.7% ± 10.8% and 59.6 μm ± 25.8 μm for slightly dense collagens and again increased to 45.2% ± 12.5% and 70.6 μm ± 36.6 μm for dense collagen matrices. The invasiveness into B collagen matrices was promoted for each of the three cancer cell lines, which was underlined by their invasion profiles (**Supplementary Figure S1**C). However, MCF-7 cells invaded these collagen matrices with a higher invasion rate and predominantly deeper (except for 2.5 g/l collagens) compared to MDA-MB-231 cells. ZR75-1 cells displayed a promoted invasiveness at looser collagen matrices by means of invasion depth relating to the percent of invasive cells.

In fact, MDA-MB-231 cells invaded denser collagens more numerous and deeper for all observed collagen compositions (**Supplementary Figures S2A,B**). The ability of this cell line to penetrate 3D networks deeply was inhibited for networks solely made of bovine skin collagens, although their high invasiveness was not influenced by the collagen composition. MCF-7 cells invaded R and RB collagen matrices moderately in their invasiveness and invasion depth. Contrarily, they very aggressive hiked through B collagen matrices with high ratio of invasive cells and invasion depths (**Supplementary Figures S2A,B**). ZR75-1 cells were predominantly inhibited in the invasion of R and RB networks and considerable promoted in B collagen matrices due to their percentage of invaded cells and their invasion depths (**Supplementary Figures S2A,B**). Among all collagen compositions, dense collagen matrices promote these cells to invade surpassing deep.

Effect of Collagen Composition on the Human Breast Cancer Collective Invasiveness

For the invasion into R collagen matrices (**Figure 2**, left) and RB collagen matrices (**Figure 2**, middle), we found no raised proclivity to migrate in collectives for MDA-MB-231 cells and for MCF-7 cells (**Supplementary Table S1**). On the opposite, ZR75-1 cells showed a significantly higher (p = 0.001, or less; p = 0.002 and p = 0.63 as exception for 3.0 g/l RB collagens) affinity to invade these collagen matrices at all concentrations collectively. For B collagen matrices (**Figure 2**, right) the affinity for MDA-MB-231 cells and MCF-7 cells to invade through collective migration forms was not altered contrary to the migration of ZR75-1. Obviously, for invading these networks the ratio of clustered cells among the invaded cells decreased with increasing concentration to the level of MDA-MB-231 cells and MCF-7 cells (**Supplementary Table S1**). Thus, the predominant number of invasive cells invaded B collagens as single cells for all observed cell lines.

Considering the cancer cell invasion as depicted above and concerning the differences and changes in migration mode for invading different 3D collagen microenvironments we focused on the characteristics of these networks assuming that there are underlying structural details that bias the differences in the observed migratory behavior.

Collagen Composition Influences Structural Characteristics of Collagen Matrices

Analyses of representative confocal laser scanning microscopy (CLSM) image stacks provided adequate insight into different structures (**Figure 3**) with increasing collagen monomer concentrations for R, RB, and B collagens. Obviously, R collagens formed distinct fibril bundles arranging progressively in dominantly developed node structures with increasing concentration. RB collagen fibrils arranged in apparent finer bundles that distributed more laminar compared to R collagens and at least formed large node-like structures. In contrast to R and RB networks, B collagen fibrils arranged in consecutive compact and dense node structures that dominated wide areas at an increasing rate with increasing concentration.

For reliable insight into network characteristics, we analyzed the structure of R, RB and B collagens considering network pore size as a crucial parameter. Therefore, we recorded 3D cubic image stacks (**Figure 4A**) with a CLSM and analyzed them with

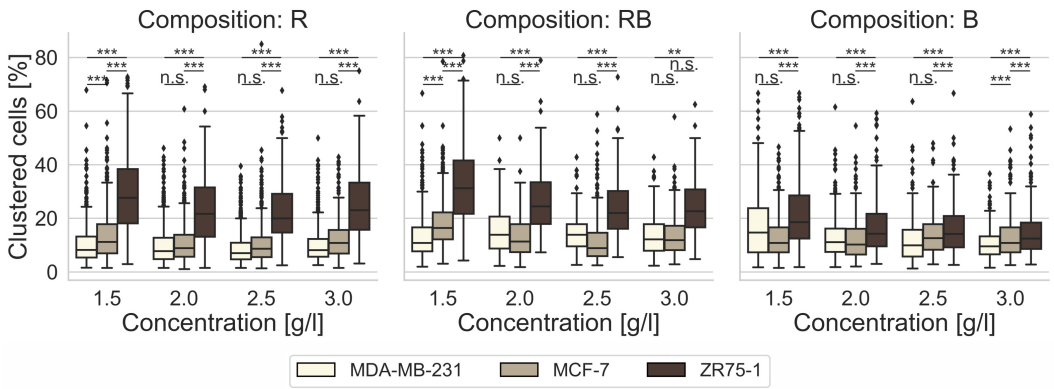

FIGURE 2 | Cell clustering. Impact of cell line specific migration, as percentage of clustered cells among invaded cells, after 3 days of invasion into 3D collagen matrices of different monomer concentration and different collagen composition (R, left; RB, middle; B, right). Significance notions were derived from Welch's unequal variance *t*-test, $^{***}p \leq 0.001$, $^{**}p \leq 0.01$, n.s. not significant. Boxes are confined by 25th and 75th percentile, horizontal lines are the medians, whiskers describe 5th and 95th percentile. One-way ANOVA test revealed *** significance.

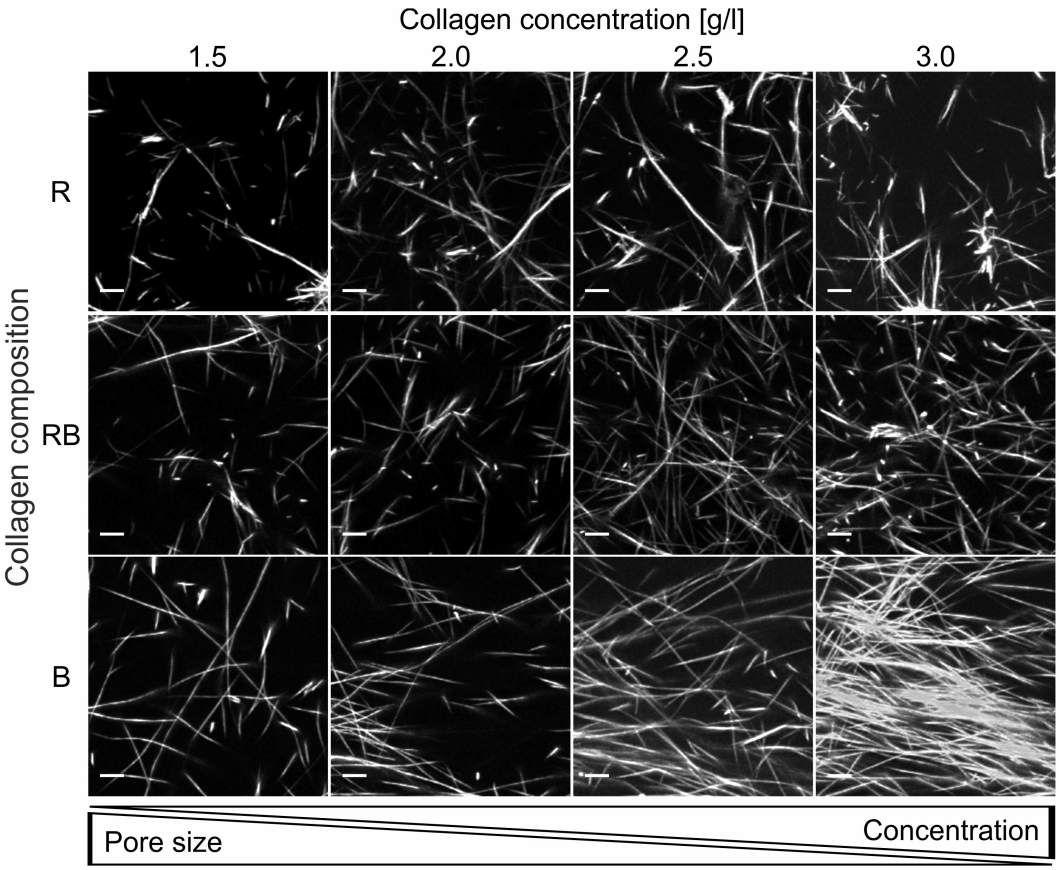

FIGURE 3 | Collagen insight. Projection of representative collagen stacks for each concentration and composition. Dimensions are 50 μm × 50 μm and 10 slices (2.5 μm) are summed up. Scale bars are 5 μm. The collagen stacks were stained with TAMRA-SE for fluorescence and imaged with a CLSM using a 40x NA/1.10 water immersion objective.

an advanced pore size analysis (**Figure 4B**), published previously (Fischer et al., 2019). We found that all observed collagen compositions featured networks with significantly decreasing pore sizes by increasing collagen concentrations (**Supplementary Table S2**) ($p = 0.01$, or less for R collagens, $p = 0.05$ or less for RB and B collagens). The R collagen matrix pore size (**Figure 4C**)

decreased from 7.7 μm ± 1.4 μm for loose collagen matrices to 5.8 μm ± 0.4 μm for dense collagen matrices. The pore size of RB collagen matrices (**Figure 4C**) decreased from 7.3 μm ± 0.7 μm for loose collagen matrices to 5.9 μm ± 1.3 μm for dense collagen matrices. B collagen pore size (**Figure 4C**) decreased from 6.9 μm ± 1.5 μm for loose collagen matrices to 5.2 μm ± 1.6 μm for dense collagen matrices.

Another essential parameter for characterizing collagen networks is their elasticity in terms of stiffness (namely Young's Modulus). Therefore, we used an atomic force microscopy (AFM) device and a well-accepted technique (Sapudom et al., 2015, 2019; Fischer et al., 2017). Thereby, we indented the collagen networks with a modified cantilever and measured their elastic response (**Figure 5A**). We found that R collagens significantly ($p = 0.001$, or less) increased their stiffness with increased collagen concentration from 63.0 Pa ± 48.5 Pa for loose collagen matrices up to 292.9 Pa ± 321.9 Pa for dense collagen matrices. Likewise, RB collagen matrices were significantly stiffer ($p = 0.001$, or less) due to increased concentration, namely 101.2 Pa ± 68.5 Pa for loose collagen matrices up to 326.2 Pa ± 260.1 Pa for dense collagen matrices. The stiffness of B collagens significantly ($p = 0.001$, or less) changed from looser to denser collagen matrices but showed no significant change between 1.5 g/l and 2.0 g/l ($p = 0.09$) as well as between 2.5 g/l and 3.0 g/l ($p = 1.12$) collagen matrices. The Young's modulus amounted to 76.1 Pa ± 135.7 Pa (1.5 g/l), 84.6 Pa ± 256.3 Pa (2.0 g/l), 159.0 Pa ± 333.9 Pa (2.5 g/l) and 141.5 Pa ± 501.7 Pa (3.0 g/l). In summary, this contemplation characterized RB collagen matrices as being stiffer compared to R collagen matrices and B collagen matrices over the observed concentration spectra.

In fact, R and RB collagen matrices were predominantly stiffer than B collagen matrices (**Supplementary Table S2**) which is at the first glance conflictive to their visual appearance (**Figure 5B**) and the results of the pore size determination linking smaller pores to higher collagen concentrations (**Supplementary Figure S3**). Due to elasticity measurements, it is undisputed that higher concentrated collagen matrices are stiffer than lower concentrated collagen matrices and thus smaller pores can be linked to stiffer gels. Thus, one would expect the highest stiffness for B collagen matrices with the smallest pores (**Supplementary Figure S3**) among the observed collagen compositions. Analyzing elasticity measurements unpretentiously (assuming collagens being homogeneous) leads to such contrariety. The importance for analyzing structural characteristics reasonably was to estimate the necessary grade of accuracy or an adequate structure-centered view. In this case, we decided to analyze near the cell level by considering the inhomogeneities within the collagen matrices.

Applying an advanced approach, considering gel and node-like areas (**Figure 5B**), we observed significantly ($p = 0.001$, or less) different elasticities among all collagen concentrations and compositions (**Figures 5C–E**). Node-like areas in R collagen matrices (**Figure 5C**) were 1.8-fold to 2.7-fold stiffer than their corresponding softer matrix counterparts. The stiffness of R collagen matrices increased from 55.4 Pa ± 32.3 Pa for loose collagen matrices up to 222.7 Pa ± 118.5 Pa for dense collagen matrices. Node stiffness increased from 100.0 Pa ± 58.5 Pa for loose collagen matrices up to 608.9 Pa ± 390.4 Pa for dense collagen matrices (**Supplementary Table S2**). Gel stiffness increased for RB collagen matrices (**Figure 5D**) from 85.7 Pa ± 34.1 Pa for loose collagens up to 264.3 Pa ± 151.0 Pa for dense collagens, whereas the stiffness of node-like areas were 1.9-fold to 2.1-fold stiffer and increased from 174.5 Pa ± 72.1 Pa for loose collagen matrices to 546.5 Pa ± 285.1 Pa for dense collagen matrices. B collagen matrices (**Figure 5E**) possessed 3.0-fold to 6.0-fold stiffer node-like areas exhibiting a matrix stiffness increasing from 56.1 Pa ± 17.5 Pa for loose collagen matrices up to 116.9 Pa ± 77.7 Pa for dense collagen matrices. Node stiffness increased from 168.8 Pa ± 170.4 Pa for loose collagen matrices up to 706.4 Pa ± 667.4 Pa for dense collagen matrices.

In summary, RB collagen matrices were stiffer than R collagen matrices in mostly all cases and B collagen matrices possessed the highest ratio between stiffer and softer areas and at denser collagens the stiffest nodes and softest gels. Finally, the increasing fraction of B collagen concentration stiffened the networks at apparent spots (node-like areas). For B collagens, the collagen monomers relocated at compact and dense structures and soft gel counterparts. R collagens formed networks with largest pores and a less stiff structure. RB collagen matrices are found somehow in between R and B collagen matrices, when considering pore size and elasticity. These findings justify and necessitate the introduction of another biophysical parameter to distinguish the network homogeneity.

Salient differences in the distribution of collagen structures arise in dependence of the collagen composition. To analyze these differences, we investigated the collagens regarding their matrix scaffold inhomogeneity and introduced a novel parameter representing the structural inhomogeneities of the different networks (**Figure 6**). Obviously, the networks solely made of rat collagen and the collagens mixed from rat and bovine collagen differ significantly ($p = 0.05$ or less at 2.0 g/l, else $p = 0.01$ or less) in their matrix scaffold inhomogeneity compared to collagens solely made of bovine collagens at all concentrations. Between rat and mixed collagens no significant ($p = 0.72$ and higher) difference could be measured. Likewise, there is no significance within the single collagen compositions over the concentration spectra ($p = 1.55$ and higher). Although a slightly trend to decreased matrix scaffold inhomogeneity with increased collagen concentration can be observed.

DISCUSSION

The invasion of cancer cells is a complex process. The change of the cell shape (Lyons et al., 2016; Baskaran et al., 2020), the softening the cell body and/or the nucleus (Fischer et al., 2020), the enzymatic-degradation of the matrix (Gialeli et al., 2011; Wolf and Friedl, 2011), the switch between migration modes (Friedl and Wolf, 2010) are some of well-founded methods that cancer cells use to overcome steric barriers and thus efficiently invade confined networks.

In the past, the majority of cancer cell migration and invasion assays have utilized homogeneous, such as flat two-dimensional substrates (Ridley et al., 2003; Geiger et al., 2009), rather than

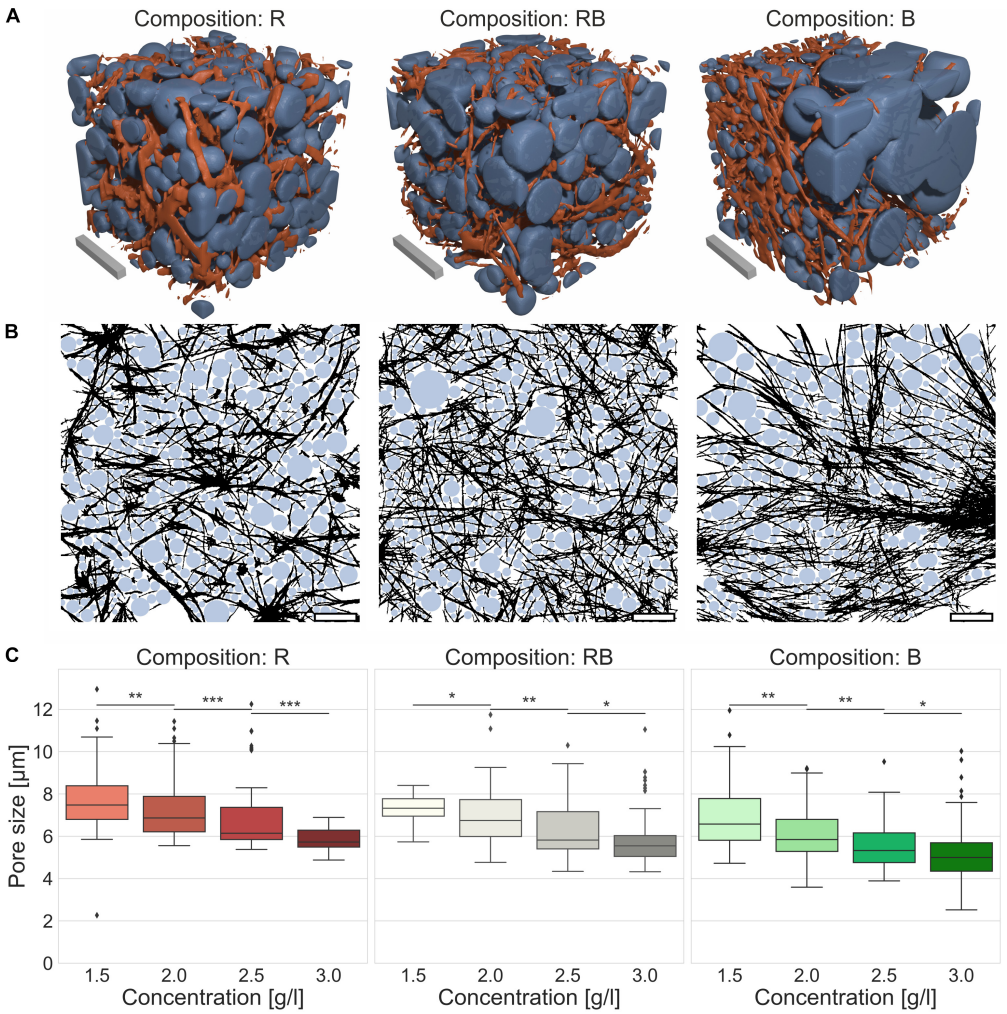

FIGURE 4 | Pore size. Pore size as a crucial parameter to determine matrix properties. **(A)** Visualizations of detected pores of the collagen fiber matrices were assumed as spherical bubbles (blue) betted amongst collagen fibers (orange) for different collagen compositions (Rat (R), left; Rat/Bovine (RB), middle; Bovine (B), right). Scale bars are 20 µm. **(B)** Graphical realization (2D) of detected pores in exemplary image stacks for the three different collagen compositions (R, left; RB, middle; B, right). Scale bars are 20 µm. **(C)** Measurements of the pore size for the three collagen compositions conditional on the collagen monomer concentration. Significance notions were derived from Mann-Whitney *U* test, $^{***}p \leq 0.001$, $^{**}p \leq 0.01$, $^{*}p \leq 0.05$, n.s., not significant. Boxes are confined by 25th and 75th percentile, horizontal lines are the medians, whiskers describe 5th and 95th percentile. Kruskal–Wallis test revealed *** significance.

inhomogeneous 3D extracellular matrix scaffolds. In almost all 3D motility assays based on extracellular matrix, it was assumed that the microenvironment is homogeneous on the cellular scale. In our study, dealing with the mechanical characteristics of 3D collagen matrices, we observed a discrepancy within the literature that no single homogeneous mechanical parameter reflects the mechanical phenotype of the matrices.

Every reaction that cancer cells show is forced by the interaction with their environment. It is accepted that a certain stiffness is needed to exert adherence-based forces to the matrix components (Paszek et al., 2005; Wisdom et al., 2018). Furthermore, a tradeoff between pore size and stiffness is crucial for invasion (Lang et al., 2015). Therefore, it is useful to observe the invasion of cancer cells and gain insights into structural and mechanical properties of the microenvironment, as these support the invasion of the cancer cells. Cancer cell invasion into collagen model systems is an important method to characterize the spread of cancer. It is known that cancer cells successfully invade different tissues *in vivo* (Wolf and Friedl, 2011; Clark and Vignjevic, 2015). Collagen matrix models aim to mimic such different tissues *in vitro* (Wolf et al., 2009; Herrmann et al., 2014; Shamir and Ewald, 2014; Paul et al., 2016). It is accepted that alterations in matrix mechanics frequently occur in tissue scaffolds *in vivo* (Khadpekar et al., 2019) and inherently were altered in diseased tissues (Akhtar et al., 2011; Lu et al., 2012). To understand *in vivo* incidents with the help of *in vitro* models the inhomogeneity of the microenvironment is an important aspect.

For exhaustive investigations, we decided to examine the invasion of three human breast cancer cell lines, with different migratory potential, into three standard collagen models. Further,

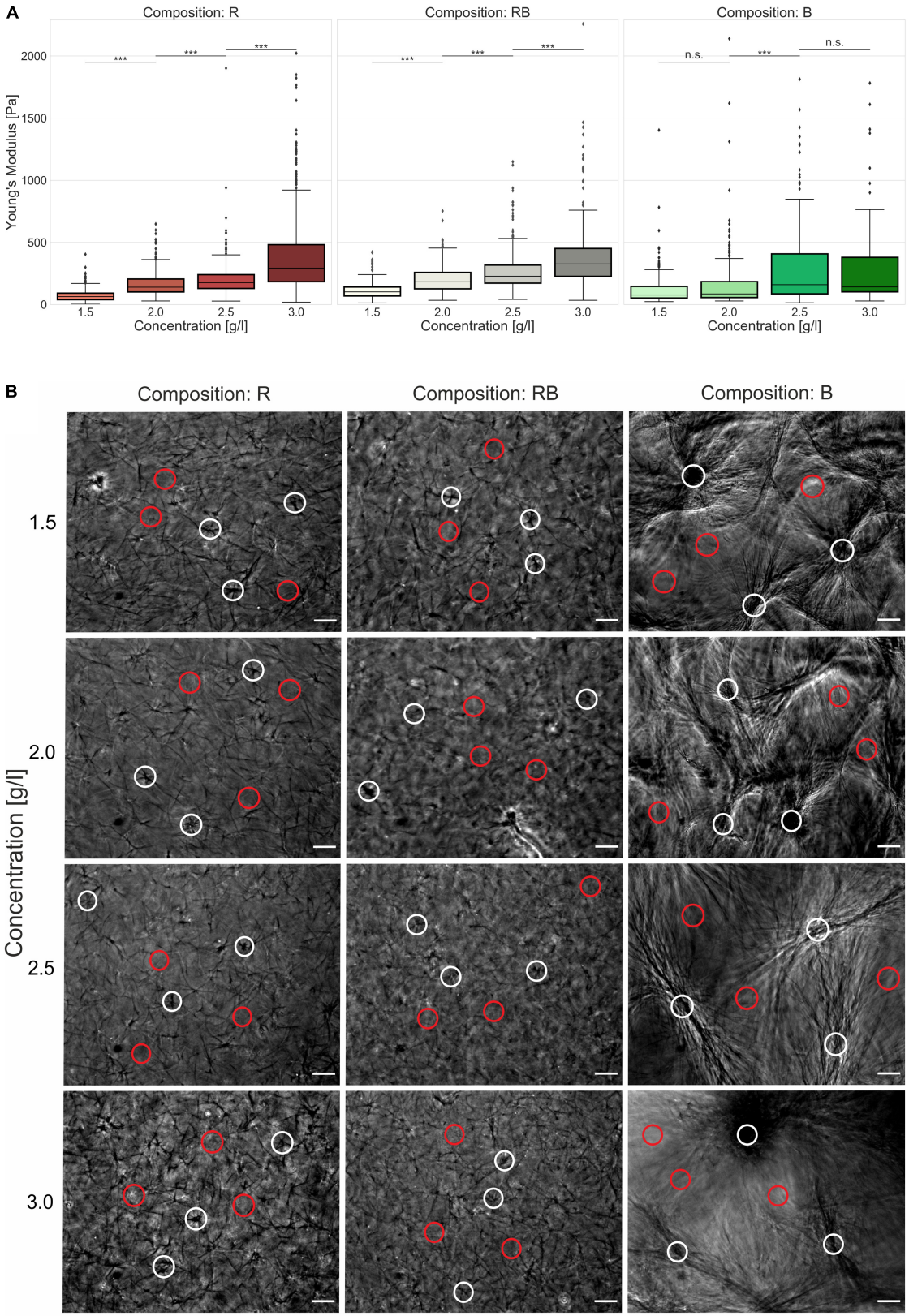

FIGURE 5 | Continued

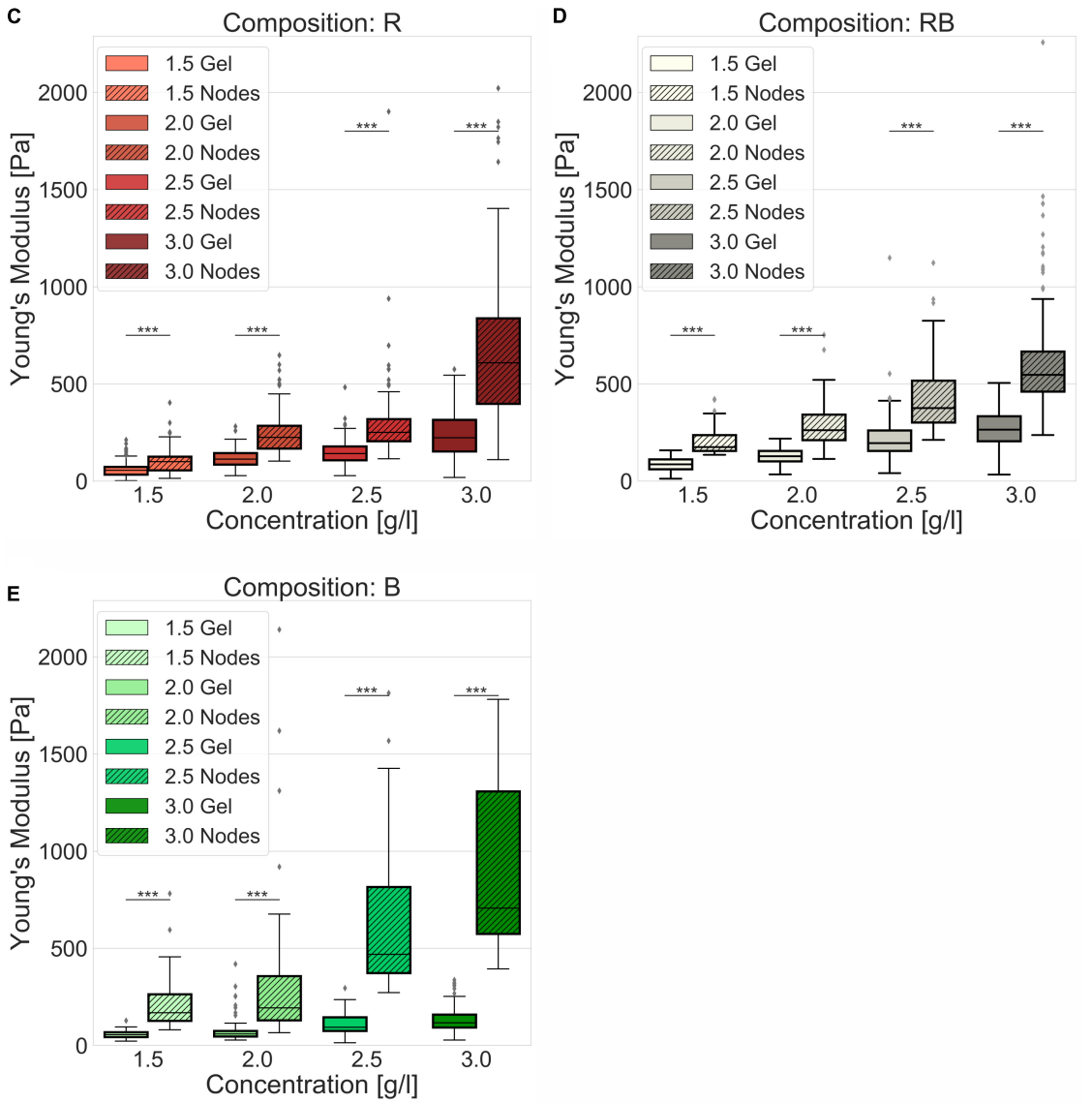

FIGURE 5 | Elasticity. Elasticity of engineered collagen matrices. **(A)** Young's modulus (stiffness) was ascertained by scanning force measurements (realized by a tipless cantilever attached with a 45 μm bead) for different collagen compositions (R, left; RB, middle; B, right) dependent on the collagen monomer concentration. **(B)** Exemplary phase contrast images of collagens that were used for AFM measurements. Representative indentations at node-containing regions of the collagen matrices were marked as white circles and indentations at gel regions of the collagen matrices were marked as red circles for different collagen compositions and collagen monomer concentrations. Scale bars are 50 μm. **(C–E)** Advanced stiffness consideration with focus on soft gel ranges and stiff node-like areas for **(C)** R collagen networks **(D)** RB collagen networks and **(E)** B collagen networks dependent on the collagen monomer concentration. Significance notions were derived from Mann–Whitney *U* test, ***$p \leq 0.001$, n.s., not significant. Boxes are confined by 25th and 75th percentile, horizontal lines are the medians, whiskers describe 5th and 95th percentile. Kruskal–Wallis test revealed *** significance for all conditions **(A,C–E)**.

we observed the structure of the collagens to classify their mechanics and intrinsic topology to obtain an explanation for the determined invasion behavior.

The invasion of highly invasive MDA-MB-231 cancer cells into collagens from rat tail and collagens mixed from rat tail and bovine skin was as high as expected. Those networks could also mirror the moderate and inhibited invasion of intermediary invasive ZR75-1 and of weakly invasive MCF-7 cancer cells.

It was rather unexpected that the cell migration into bovine collagens of all three cancer cell lines was impaired. Highly invasive MDA-MB-231 (**Supplementary Figure S6**) cancer cells were hindered to penetrate the matrices deeply whilst weakly invasive MCF-7 (**Supplementary Figure S7**) cancer cells tend to invade bovine matrices excessively. Intermediary invasive ZR75-1 (**Supplementary Figure S8**) cells changed their migration from predominantly collective invasion to single cell migration

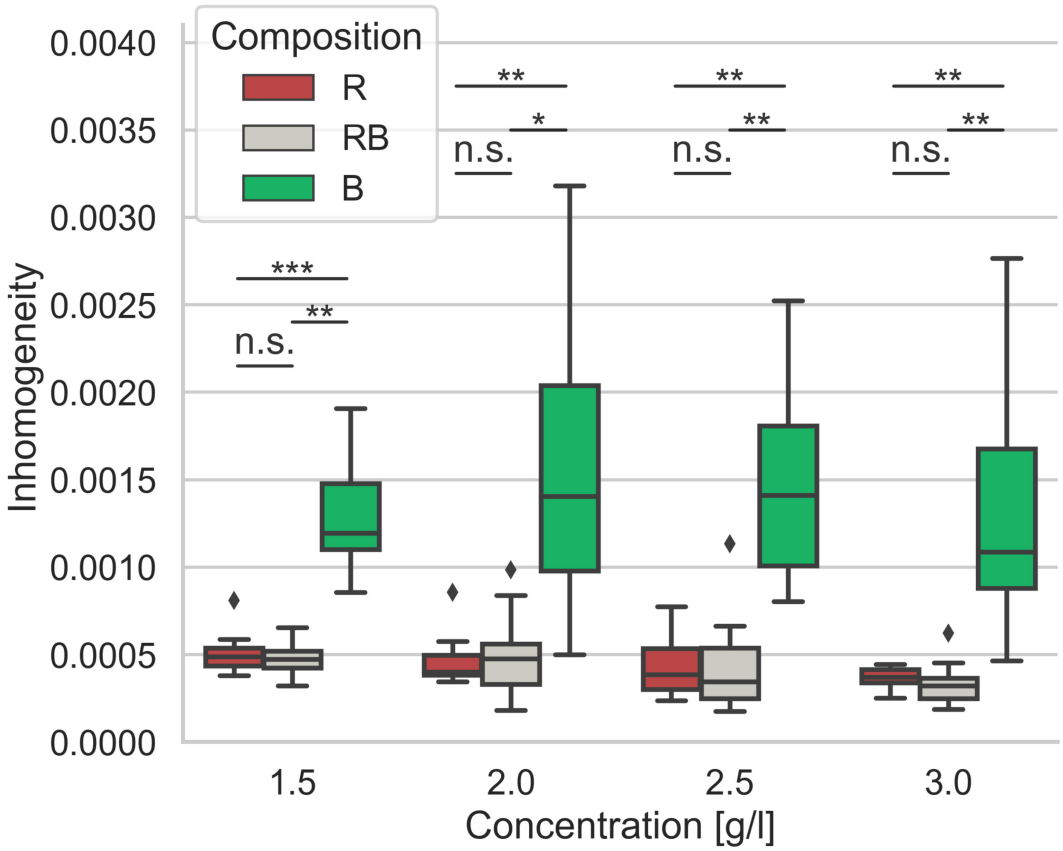

FIGURE 6 | Inhomogeneity. Matrix scaffold inhomogeneity of networks of different collagen compositions for concentrations ranging from 1.5 g/l to 3.0 g/l. Each boxplot contains data of at least 8 – 13 image stacks obtained from different independent measurements. Significance notions were derived from Mann-Whitney *U* test, ***$p \leq 0.001$, **$p \leq 0.01$, *$p \leq 0.05$, n.s., not significant. Boxes are confined by 25th and 75th percentile, horizontal lines are the medians, whiskers describe 5th and 95th percentile. Kruskal–Wallis test revealed *** significance.

accompanied by an aptness to invade bovine networks deeply with a high ratio of invasive cells.

In accordance with existing studies, we have shown that both stiffness and pore size govern the invasion of cancer cells into 3D-enclosed matrices (Wolf and Friedl, 2011; Lang et al., 2015; Sapudom et al., 2015; Fischer et al., 2017, 2020). These parameters are eligible to roughly describe the interplay of cancer cell invasion with the microenvironment on a global level. Due to the highly inhomogeneous structure of collagen gels, cancer cells that migrate in confined matrices directly and constantly face soft and stiff areas as well as large and small pores. The diversity of microenvironmental conditions from the perspective of the migrating cell could be seen as inhomogeneity on the cell level. Considering the inhomogeneities of 3D ECM model systems clarify structural dependencies for cancer cell migration.

Observing the stiffness of the collagen networks with conventional AFM approaches could not explain the variations as found in the invasiveness. Thereby a cantilever with an attached bead usually scans the surface of the collagen gels, regardless of the local structural differences present in these gels. In this way, no relevant differences in the elasticity of collagen networks with respect to their composition are found. In fact, this means an assumption of networks as homogeneous by over-simplifying structural conspicuousness. We hypothesized that cells with several μm expansion face inhomogeneities within the surrounding 3D microenvironment in form of less complex areas, such as pores or the fluid phase of the gels and high complex fibril arrangements or node-like structures. It is comprehensible, when indenting into less complex areas (distinguishing between apparent gel and node-like areas), that the elasticity is not the same as when indenting a high complex structure. Although we used simple assumptions of soft and stiff areas distributed at the surface of the collagen matrices, the significant differences confirmed and justified this approach. Subtle distinctions between stiffer and softer areas were constructive and revelatory. Thus, a more comprehensible analysis was feasible. Monitoring stiffer and softer areas, we found for all collagen compositions and all concentrations, significantly differ in their corresponding elasticity. In turn, such a focus depicts mechanical inhomogeneities. In fact, the preeminently inhomogeneous character especially of bovine networks was recognized and provided evidence for the changed invasion characteristics.

The pore size is another crucial parameter to determine structural traits (Fischer et al., 2019). Concerning confined scaffolds with spatial hindrances the pore size is a key value for describing a fibrillary network. Applying advanced 3D pore size analysis represents a solid method to characterize variations of different networks (Molteni et al., 2013; Münster and Fabry, 2013; Fischer et al., 2019; Sauer et al., 2019). The pore size specifies structural differences due to concentration variations within a certain collagen composition. Thus, it is conductive to find a measure for inherent structural factors. According to this, we found a decreased pore size with increasing collagen concentrations for all three collagen compositions. Trying to find an explanation for the different invasion characteristics based on the measured median pore size was not possible. Relying upon the median pore size would promote the expectation that aggressive cancer cells can penetrate all collagen compositions deeply. Furthermore, weakly invasive MCF-7 or intermediary invasive ZR75-1 cells should be hindered to invade bovine collagens in the same manner as found for their invasion into rat and mixed collagens. However, we found an oppositional behavior for all three cell lines, which obviously is caused by structural differences among the collagen compositions. Consequently, the pore size solitary is not able to indicate such structural dependencies. Nevertheless, the pore size is a statistically based parameter and thus blind for the inhomogeneity of the networks to what it is applied. This is especially remarkable for bovine collagen matrices, which have the smallest median pore size compared to the pure rat and rat-cattle mixture compositions. Factual, bovine networks possessed huge node-like entrapments containing a multitude of very small pores. On the contrary, in between the node-like areas very large pores are enclosed. Recapped, bovine collagens form exceedingly inhomogeneous networks. In such considerably inhomogeneous meshwork, the median pore size could not mirror structural details accurately.

The determined collagen networks within this study are all made from collagen type-I. Their differences in network formation, mechanics and matrix scaffold inhomogeneity evidently are connected to the origin of the different connective tissues they were extracted from. Collagen fibers from tendon are described as crimped and more uniform as the even fibers of the skin and thus exhibit different mechanical properties (Meyer, 2019) matched to the tissues they are part of. One major difference in the properties of reconstituted collagen I fibrillary networks from tendon or skin occurs due to the different extraction methods that are used to obtain collagen monomers (Demou et al., 2005; Wolf et al., 2009; Shinsato et al., 2020). More cross-linked skin collagens were additionally pepsinized to cleave telopeptides. This drastically influenced the self-assembly of fibrils to multimeric fibrils that further formed diffuse networks (Demou et al., 2005; Wolf et al., 2009). Early observations (Helseth and Veis, 1981) reported a telopeptide-dependent delayed speed compared with non-pepsinized collagens during the polymerization of telopeptide-poor fibrils which is in line with our turbidity observations (**Supplementary Figure S5**). The combination of telopeptide intact collagen with telopeptide lacking collagens drastically influenced the formation of the network (Helseth and Veis, 1981). The formation of our mixed collagens corresponds to that effect and further they form networks that are more similar to collagens solely made of rat tail collagen than to collagens solely made of bovine skin collagens on the cell level. This similarity between R and RB collagens is reflected in the invasive behavior of the investigated cell lines.

Understanding the influence of the microenvironment on the migration of cancer cells is essential. Here, we introduce a novel parameter that can reflect the matrix scaffold inhomogeneity of networks on the cell level. This parameter describes the inherent changes of the microenvironment among different collagen compositions. In line with this, the novel matrix scaffold inhomogeneity parameter correlates with the composition-related changes in the invasion profiles of all observed cell lines. Thus, this parameter serves as a reliable feature to describe the 3D microenvironment and valorizes elasticity and pore size characteristics.

It is obvious that more inhomogeneous networks force clustered cells to change their migration characteristics to a single cell dominated invasion. Other studies have shown that denser ECMs as well as decreased porosity leads to a change from single to collective cell migration (Haeger et al., 2014). Due to the matrix scaffold inhomogeneity found within bovine networks, which means local disturbance of the ECM density and thus locally increased porosity, we observed a similar effect for the ZR75-1 cells.

Moreover, the inhomogeneity of the microenvironment (mirrored by the novel matrix scaffold inhomogeneity parameter) seems to be crucial for the invasion depth that cancer cells achieved. This finding is in line with other studies concerning the ECM heterogeneity and ECM resistance (Talkenberger et al., 2017). Networks that are more homogeneous could be invaded significantly deeper by highly invasive MDA-MB-231 cancer cells, which predominantly prefer adhesion-based mesenchymal invasion. Mostly highly invasive cancer cells utilize strong adherence dependent mechanisms, which is observable e.g., by pronounced fiber displacements (Fischer et al., 2017), to squeeze through narrow confinements accompanied by several intracellular deforming mechanisms (Krause and Wolf, 2015; Fischer et al., 2020). We hypothesized that these mechanisms could be applied most efficiently to a homogeneous scaffold. Moreover, cells with amoeboid invasion preference were hindered to invade deeply and excessively into these homogeneous networks. For all three cell lines we found the respectively, opposite behavior for invasion into bovine collagen matrices. Consideration of the novel matrix scaffold inhomogeneity parameter directed to the hypothesis that the increased inhomogeneity of the networks, impairs the effects on invasion. In fact, the invasion depth of the highly invasive MDA-MB-231 cells was restricted, although their invasion rate seemed unaffected. However, the invasion of weakly invasive MCF-7 cells into inhomogeneous networks was promoted. As reported by others, the lack of focal adhesions enforces a switch to amoeboid-like migration forms (Friedl and Wolf, 2010; Liu et al., 2015). Local inhomogeneities are

discontinuities in the structure of the networks. It can therefore be assumed that inhomogeneities are places where penetrating cells have no constant adherence option. Thus, a switch of their migration mode from mesenchymal to amoeboid, what means a mesenchymal-amoeboid transition (MAT) (Friedl and Wolf, 2003) appear reasonable. Using amoeboid-like migration as a path-finding (Wolf et al., 2003) migration mode to overcome inhomogeneities, such as collagenous barriers (Sabeh et al., 2004) in networks from pepsinized collagen can explain the almost equal invasion depths and rates of all three cell lines investigated within this study. It is reported as proteinase-independent form of migration (Friedl and Wolf, 2003; Wolf et al., 2003; Sabeh et al., 2004). In the case of MDA-MB-231 cells, this hypothesis is supported by detectable changes of the cell morphology (**Supplementary Figures S6**, **S9**, **Supplementary Table S3**, and **Supplementary Videos S1–S9**). In case of MCF-7 cells (**Supplementary Figure S7**) and ZR75-1 (**Supplementary Figure S8**) cells, the predominant roundish appearance of invaded cells was observed independent from collagen concentration or composition. Nevertheless, future studies might elucidate this matter and thus, explain the change of the invasion profiles for highly invasive MDA-MB-231 cells at bovine networks. For weakly invasive MCF-7 cells, the amoeboid-like invasion seems an advantage to percolate into networks that are more homogeneous. Thus, with increased inhomogeneity they can invade networks at higher rates more efficiently. Anyway, the invasiveness for all observed cell lines adjust to the microenvironment in consequence of changed matrix scaffold inhomogeneity.

Future studies should aim to find a certain shift in stiffness of node-like structures in combination with a correlating pore size that provokes the turnover of cancer cell invasion from weakly to highly invasive and from single to collective migration as well. A sophisticated characterization for stiff and soft network areas describing fibrillary arborization or alignments is promising. When identifying an inhomogeneity barrier that is able to screen inhibited or promoted invasion may provide a more reliable parameter to characterize and compare the migratory and invasive capacity of cancer cells in various ECMs encompassing pure rat, pure bovine and combined rat/bovine gels and may provide a pronounced impact in cancer cell research. Due to a high potential the observations of cancer cell response to an inhomogeneous microenvironment under influence of anti-metastatic and anti-invasion drugs (Gandalovièová et al., 2017) should be enhanced. Subsequent studies focusing on the inhomogeneity of human tissues *in vivo* and ECM models *in vitro* seem to be conducive and help to enlighten the complex metastatic cascade where cell migration and invasion is the central issue.

Finally, observing inhomogeneities on the cell level amplify structural dependencies that directly influence cancer cell invasion. Hence, the characterization of structural inhomogeneities is important to better understand cancer cell invasion. Defined inhomogeneous *in vitro* model systems seem to be more appropriate to mimic *in vivo* ECM and primary tumor microenvironments compared to the commonly employed homogenous ones. The insight to mechanical and structural inhomogeneities can reveal the interplay of cells with the microenvironment and possible explain an altered migration mode.

Key Findings

- Human breast cancer cells MDA-MB-231, MCF-7 and ZR75-1 adjust their invasive capacities into different collagen matrices due to changing environmental conditions.
- Cancer cells are sensitive to local inhomogeneities.
- Mechanical inhomogeneities are present in 3D collagen gels and can be measured by AFM.
- Pore size and elasticity govern cancer cell invasion.
- Local inhomogeneities alter invasion into 3D collagen networks.
- A novel matrix scaffold inhomogeneity parameter serves to explain structural differences in 3D microenvironments on the cell level.

MATERIALS AND METHODS

Cells and Cell Culture

Human breast cancer cell lines (MDA-MB-231, MCF7, and ZR-75-1) were purchased from ATCC-LGC-Promochem (Wesel, Germany). These cell lines were cultured under normal conditions in an incubator (37°C, 5% CO_2, 95% humidity) using 4.5 g/l DMEM culture medium with additional 10% Calf Serum and 1% penicillin streptomycin (Biochrom, Berlin, Germany). At 75–80% confluency cells were harvested.

3D Collagen Matrices

Three types of extracellular matrix models were crafted for this study. Collagens solely comprised of rat tail monomers (4 g/l rat collagen type I, SERVA, Heidelberg, Germany), collagens containing only bovine skin monomers (4 g/l bovine collagen type I, Biochrom, Berlin, Germany) and collagens composed of a mixture of both collagen monomer types (rat tail and bovine skin) in a mass fraction of 1:2 were used for all collagen related experiments (Fischer et al., 2017, 2019, 2020; Kunschmann et al., 2019). For the polymerization of the monomer solution, a 1 M phosphate buffered solution containing disodium hydrogen phosphate (Sigma Aldrich, Cat. No. 71636), sodium dihydrogen phosphate (Sigma Aldrich, Cat. No. 71507) and ultrapure water were mixed keeping stable conditions (pH value 7.4, ionic strength 0.7, final phosphate concentration 200 mM). The components were kept at 0°C for mixing and finally added to 6-well plates for invasion assays, Petri dishes for elasticity measurements, 96-well plates for investigating the polymerization dynamics, or ibidi 24-well µ-plates for studying the pore size characteristics. Due to differences in the polymerization times (**Supplementary Figure S5**) R and RB collagen matrices were incubated for 2 h whereas B collagens were incubated for 5 h under normal conditions.

3D Invasion Assays

To investigate cancer cell invasion into 3D collagen networks we used collagens prepared as described above. As previously described (Fischer et al., 2017, 2020; Mierke et al., 2017; Kunschmann et al., 2019) we used 1.2 ml solution containing collagen and buffer for each well of a 6-well plate. Under normal conditions (95% humidity and 37°C) the collagens polymerized and form around 500 μm thick matrices. Consequently, the gels were treated three times by a rinsing procedure using Dulbecco's phosphate buffered saline (PBS). Afterward 2 ml DMEM were added at each well and incubated over night at normal conditions. We added 50.000 cells per well on top of the collagens, harvested at confluence between 75 and 85% under treatment with 0.125% Trypsin/EDTA solution. The cells invaded the collagen matrices for 72 h (**Figure 1A**). Subsequently, we fixed the assay with 2.5% glutaraldehyde and stained the cell nuclei using 4 μg/ml HOECHST 33342 overnight. Fluorescent image stacks were recorded by a CCD camera (Orca-R2, Hamamatsu-Photonics, Munich, Germany) mounted with a 0.55x c-mount adapter, on an inverted microscope (DMI8000B, Leica, Wetzlar, Germany). A 20x objective and an A4 filter cube (Leica) were used. For each well, we obtained at least 100 image stacks received from a randomly selected 10 × 10 position grid. Focal plane distance (*z*-distance) was 4 μm. We analyzed the image stacks with a method already published (Fischer et al., 2017, 2020). Hereby we used a custom build python application based on elaborated algorithms for 3D image analysis and filtering. We defined cells on the surface of the collagen matrices and in the first two focal planes as non-invasive, in order to counterbalance minimal surface deviations. Cells found 12 μm below the surface and deeper are assumed invasive. Only stacks containing at least 25 cells were evaluated.

Cluster Analysis

Image stacks that served for investigations of the cancer cell invasion were secondary analyzed concerning clustering. Therefore we used a method previously described (Kunschmann et al., 2019). In detail, we used the SciPy (Jones et al., 2001) DBSCAN algorithm that serves for identifying clusters as well as single cells (Ester et al., 1996; Schubert et al., 2017). Detected as a cluster are amassments of at least five cells within a 20 μm nuclei distance.

Analysis of the Pore-Size Characteristics

We analyzed the pore size of the collagen matrices as previously described (Fischer et al., 2020) based on a custom-built python program already published (Fischer et al., 2019). In more detail, polymerized collagen matrices were stained overnight with TAMRA-SE (Sigma-Aldrich, Cat. No.: 21955) and afterward rinsed and stored in PBS. We generated with a confocal laser scanning microscope (Leica TCS SP8, Mannheim, Germany) under usage of a 40x NA/1.10 water immersion objective 3D image stacks in 150 μm cubic dimensions.

Analysis of the Matrix Elasticity

To determine the elasticity of the collagen matrices, we used an AFM method as previously described (Sapudom et al., 2015). To specify, a tip-less cantilever was modified with a 45 μm polystyrene bead. Polymerized collagen matrices were indented using a maximum indentation force of 5 nN (Sapudom et al., 2015). For indentations, we randomly picked areas assumed as node-like or gel areas (**Figure 5B**). For each measurement, we observed a minimum of three different regions. Each region containing at least 10 node-like structures and 10 gel structures. The standard Hertz model was fitted to the retract part of the force distant curves.

Inhomogeneity Analysis

Determining the matrix scaffold inhomogeneity of the examined collagen matrices is crucial to understand the differences in structure, mechanics and cell behavior in these hydrogels. In this study, a novel approach to determine the matrix scaffold inhomogeneity of collagen gels was developed. First, each recorded 3D image stack was divided into smaller parts of 30 μm, which has been considered to be roughly the size of the cell microenvironment. Each part, as well as the whole image cube, were analyzed regarding pore-size, number of pores and collagen volume as shown previously (Fischer et al., 2019), resulting in three key parameters for each part and the whole image cube. The determined parameters of each part were put in relation to the whole image cube as a percentage. Subsequently, the standard deviation of each parameter was calculated, and the Euclidean norm was determined. The resulting number is defined as the matrix scaffold inhomogeneity and is a measure of how much the local structure in the studied collagen matrices varies on the cell level.

Statistical Analysis

All measurements were performed at least in triplicates if not stated otherwise. Statistical analyses were determined by one-way ANOVA and Welch's unequal variance *t*-test analysis. For data not normal distributed, the Kruskal–Wallis and Mann-Whitney *U* test were applied.

DATA AVAILABILITY STATEMENT

The raw data supporting the conclusions of this article will be made available by the authors, without undue reservation.

AUTHOR CONTRIBUTIONS

AH performed the majority of the experiments and data analysis, and wrote the manuscript. TF performed the data analysis, wrote the custom-made programs, and interpreted the data.

CM designed the experiments, analyzed and interpreted the data, and wrote the manuscript. All authors reviewed the manuscript.

FUNDING

This work was supported by the DFG (MI1211/18-1 and INST268/357-1 FUGG), EFRE-SAB infrastructure (No. 100299919), the SAB (No. 100331685), and SMWK TG70 No. 22110853 (MUDIPLEX). The authors acknowledge support from the German Research Foundation (DFG) and Universität Leipzig within the program of Open Access Publishing.

SUPPLEMENTARY MATERIAL

The Supplementary Material for this article can be found online at: https://www.frontiersin.org/articles/10.3389/fcell.2020.593879/full#supplementary-material

REFERENCES

Akhtar, R., Sherratt, M. J., Cruickshank, J. K., and Derby, B. (2011). Characterizing the elastic properties of tissues. *Mater. Today* 14, 96–105. doi: 10.1016/S1369-7021(11)70059-1

Baskaran, J. P., Weldy, A., Guarin, J., Munoz, G., Shpilker, P. H., Kotlik, M., et al. (2020). Cell shape, and not 2D migration, predicts extracellular matrix-driven 3D cell invasion in breast cancer. *APL Bioeng.* 4:26105. doi: 10.1063/1.5143779

Behrens, J., Mareel, M. M., van Roy, F. M., and Birchmeier, W. (1989). Dissecting tumor cell invasion: epithelial cells acquire invasive properties after the loss of uvomorulin-mediated cell-cell adhesion. *J. Cell Biol.* 108, 2435–2447. doi: 10.1083/jcb.108.6.2435

Bersini, S., Jeon, J. S., Moretti, M., and Kamm, R. D. (2014). In vitro models of the metastatic cascade: from local invasion to extravasation. *Drug Discov. Today* 19, 735–742. doi: 10.1016/j.drudis.2013.12.006

Brown, A. F. (1982). Neutrophil granulocytes: adhesion and locomotion on collagen substrata and in collagen matrices. *J. Cell Sci.* 58, 455–467.

Carey, S. P., Goldblatt, Z. E., Martin, K. E., Romero, B., Williams, R. M., and Reinhart-King, C. A. (2016). Local extracellular matrix alignment directs cellular protrusion dynamics and migration through Rac1 and FAK. *Integr. Biol. (Camb.)* 8, 821–835. doi: 10.1039/C6IB00030D

Charras, G., and Sahai, E. (2014). Physical influences of the extracellular environment on cell migration. *Nat. Rev. Mol. Cell Biol.* 15, 813–824. doi: 10.1038/nrm3897

Clark, A. G., and Vignjevic, D. M. (2015). Modes of cancer cell invasion and the role of the microenvironment. *Curr. Opin. Cell Biol.* 36, 13–22. doi: 10.1016/j.ceb.2015.06.004

Demou, Z. N., Awad, M., McKee, T., Perentes, J. Y., Wang, X., Munn, L. L., et al. (2005). Lack of telopeptides in fibrillar collagen I promotes the invasion of a metastatic breast tumor cell line. *Cancer Res.* 65, 5674–5682. doi: 10.1158/0008-5472.CAN-04-1682

Ester, M., Kriegel, H.-P., Sander, J., and Xu, X. (1996). "A density-based algorithm for discovering clusters in large spatial databases with noise," in *Proceedings of the Second International Conference on Knowledge Discovery and Data Mining*, (Palo Alto, CA: AAAI Press), 226–231.

Fischer, T., Hayn, A., and Mierke, C. T. (2019). Fast and reliable advanced two-step pore-size analysis of biomimetic 3D extracellular matrix scaffolds. *Sci. Rep.* 9:8352. doi: 10.1038/s41598-019-44764-5

Fischer, T., Hayn, A., and Mierke, C. T. (2020). Effect of nuclear stiffness on cell mechanics and migration of human breast cancer cells. *Front. Cell Dev. Biol.* 8:167. doi: 10.3389/fcell.2020.00393

Fischer, T., Wilharm, N., Hayn, A., and Mierke, C. T. (2017). Matrix and cellular mechanical properties are the driving factors for facilitating human cancer cell motility into 3D engineered matrices. *Converg. Sci. Phys. Oncol.* 3:44003. doi: 10.1088/2057-1739/aa8bbb

Friedl, P., and Alexander, S. (2011). Cancer invasion and the microenvironment: plasticity and reciprocity. *Cell* 147, 992–1009. doi: 10.1016/j.cell.2011.11.016

Friedl, P., Maaser, K., Klein, C. E., Niggemann, B., Krohne, G., and Zänker, K. S. (1997). Migration of highly aggressive MV3 melanoma cells in 3-dimensional collagen lattices results in local matrix reorganization and shedding of alpha2 and beta1 integrins and CD44. *Cancer Res.* 57, 2061–2070.

Friedl, P., and Wolf, K. (2003). Tumour-cell invasion and migration: diversity and escape mechanisms. *Nat. Rev. Cancer* 3, 362–374. doi: 10.1038/nrc1075

Friedl, P., and Wolf, K. (2010). Plasticity of cell migration: a multiscale tuning model. *J. Cell Biol.* 188, 11–19. doi: 10.1083/jcb.200909003

Gandalovičová, A., Rosel, D., Fernandes, M., Veselý, P., Heneberg, P., Čermák, V., et al. (2017). Migrastatics-anti-metastatic and anti-invasion drugs: promises and challenges. *Trends Cancer* 3, 391–406. doi: 10.1016/j.trecan.2017.04.008

Geiger, B., Spatz, J. P., and Bershadsky, A. D. (2009). Environmental sensing through focal adhesions. *Nat. Rev. Mol. Cell Biol.* 10, 21–33. doi: 10.1038/nrm2593

Gialeli, C., Theocharis, A. D., and Karamanos, N. K. (2011). Roles of matrix metalloproteinases in cancer progression and their pharmacological targeting. *FEBS J.* 278, 16–27. doi: 10.1111/j.1742-4658.2010.07919.x

Gupta, G. P., and Massagué, J. (2006). Cancer metastasis: building a framework. *Cell* 127, 679–695. doi: 10.1016/j.cell.2006.11.001

Haeger, A., Krause, M., Wolf, K., and Friedl, P. (2014). Cell jamming: collective invasion of mesenchymal tumor cells imposed by tissue confinement. *Biochim. Biophys. Acta* 1840, 2386–2395. doi: 10.1016/j.bbagen.2014.03.020

Hakkinen, K. M., Harunaga, J. S., Doyle, A. D., and Yamada, K. M. (2011). Direct comparisons of the morphology, migration, cell adhesions, and actin cytoskeleton of fibroblasts in four different three-dimensional extracellular matrices. *Tissue Eng. Part A* 17, 713–724. doi: 10.1089/ten.tea.2010.0273

Helseth, D. L., and Veis, A. (1981). Collagen self-assembly in vitro. Differentiating specific telopeptide-dependent interactions using selective enzyme modification and the addition of free amino telopeptide. *J. Biol. Chem.* 256, 7118–7128.

Herrmann, D., Conway, J. R. W., Vennin, C., Magenau, A., Hughes, W. E., Morton, J. P., et al. (2014). Three-dimensional cancer models mimic cell-matrix interactions in the tumour microenvironment. *Carcinogenesis* 35, 1671–1679. doi: 10.1093/carcin/bgu108

Holle, A. W., Govindan Kutty Devi, N., Clar, K., Fan, A., Saif, T., Kemkemer, R., et al. (2019). Cancer cells invade confined microchannels via a self-directed mesenchymal-to-amoeboid transition. *Nano Lett.* 19, 2280–2290. doi: 10.1021/acs.nanolett.8b04720

Jones, E., Oliphant, T., and Peterson, P. (2001). *SciPy: Open Source Scientific Tools for Python – ScienceOpen*. https://www.scienceopen.com/document?vid=ab12905a-8a5b-43d8-a2bb-defc771410b9 (accessed July 13, 2020).

Khadpekar, A., Mistry, K., Dwivedi, N., Paspunurwar, A., Tandaiya, P., and Majumder, A. (2019). Asamataxis: a cooperative relayed migration in response to subsurface inhomogeneity leads to long-range self-patterning of cells. *bioRixv* [Preprint]. doi: 10.1101/799437

Koch, T. M., Münster, S., Bonakdar, N., Butler, J. P., and Fabry, B. (2012). 3D Traction forces in cancer cell invasion. *PLoS One* 7:e33476. doi: 10.1371/journal.pone.0033476

Krause, M., and Wolf, K. (2015). Cancer cell migration in 3D tissue: negotiating space by proteolysis and nuclear deformability. *Cell Adh. Migr.* 9, 357–366. doi: 10.1080/19336918.2015.1061173

Krause, M., Yang, F. W., Te Lindert, M., Isermann, P., Schepens, J., Maas, R. J. A., et al. (2019). Cell migration through three-dimensional confining pores: speed accelerations by deformation and recoil of the nucleus. *Philos. Trans. R. Soc. Lond. B Biol. Sci.* 374:20180225. doi: 10.1098/rstb.2018.0225

Kunschmann, T., Puder, S., Fischer, T., Steffen, A., Rottner, K., and Mierke, C. T. (2019). The small GTPase Rac1 increases cell surface stiffness and enhances 3D migration into extracellular matrices. *Sci. Rep.* 9:7675. doi: 10.1038/s41598-019-43975-0

Lang, N. R., Skodzek, K., Hurst, S., Mainka, A., Steinwachs, J., Schneider, J., et al. (2015). Biphasic response of cell invasion to matrix stiffness in three-dimensional biopolymer networks. *Acta Biomater.* 13, 61–67. doi: 10.1016/j.actbio.2014.11.003

Lautscham, L. A., Kämmerer, C., Lange, J. R., Kolb, T., Mark, C., Schilling, A., et al. (2015). Migration in confined 3D environments is determined by a combination of adhesiveness, nuclear volume, contractility, and cell stiffness. *Biophys. J.* 109, 900–913. doi: 10.1016/j.bpj.2015.07.025

Liebersbach, B. F., and Sanderson, R. D. (1994). Expression of syndecan-1 inhibits cell invasion into type I collagen. *J. Biol. Chem.* 269, 20013–20019.

Liu, Y.-J., Le Berre, M., Lautenschlaeger, F., Maiuri, P., Callan-Jones, A., Heuzé, M., et al. (2015). Confinement and low adhesion induce fast amoeboid migration of slow mesenchymal cells. *Cell* 160, 659–672. doi: 10.1016/j.cell.2015.01.007

Lu, P., Weaver, V. M., and Werb, Z. (2012). The extracellular matrix: a dynamic niche in cancer progression. *J. Cell Biol.* 196, 395–406. doi: 10.1083/jcb.201102147

Lyons, S. M., Alizadeh, E., Mannheimer, J., Schuamberg, K., Castle, J., Schroder, B., et al. (2016). Changes in cell shape are correlated with metastatic potential in murine and human osteosarcomas. *Biol. Open* 5, 289–299. doi: 10.1242/bio.013409

Meyer, M. (2019). Processing of collagen based biomaterials and the resulting materials properties. *Biomed. Eng. Online* 18:24. doi: 10.1186/s12938-019-0647-0

Mierke, C. T. (2019a). The matrix environmental and cell mechanical properties regulate cell migration and contribute to the invasive phenotype of cancer cells. *Rep. Prog. Phys.* 82:64602. doi: 10.1088/1361-6633/ab1628

Mierke, C. T. (2019b). The role of the optical stretcher is crucial in the investigation of cell mechanics regulating cell adhesion and motility. *Front. Cell Dev. Biol.* 7:184. doi: 10.3389/fcell.2019.00184

Mierke, C. T., Fischer, T., Puder, S., Kunschmann, T., Soetje, B., and Ziegler, W. H. (2017). Focal adhesion kinase activity is required for actomyosin contractility-based invasion of cells into dense 3D matrices. *Sci. Rep.* 7:42780. doi: 10.1038/srep42780

Mierke, C. T., Puder, S., Aermes, C., Fischer, T., and Kunschmann, T. (2020). Effect of PAK inhibition on cell mechanics depends on Rac1. *Front. Cell Dev. Biol.* 8:13. doi: 10.3389/fcell.2020.00013

Mohammadi, H., Arora, P. D., Simmons, C. A., Janmey, P. A., and McCulloch, C. A. (2015). Inelastic behaviour of collagen networks in cell-matrix interactions and mechanosensation. *J. R. Soc. Interface* 12:20141074. doi: 10.1098/rsif.2014.1074

Molteni, M., Magatti, D., Cardinali, B., Rocco, M., and Ferri, F. (2013). Fast two-dimensional bubble analysis of biopolymer filamentous networks pore size from confocal microscopy thin data stacks. *Biophys. J.* 104, 1160–1169. doi: 10.1016/j.bpj.2013.01.016

Münster, S., and Fabry, B. (2013). A simplified implementation of the bubble analysis of biopolymer network pores. *Biophys. J.* 104, 2774–2775. doi: 10.1016/j.bpj.2013.05.016

Pantel, K., and Brakenhoff, R. H. (2004). Dissecting the metastatic cascade. *Nat. Rev. Cancer* 4, 448–456. doi: 10.1038/nrc1370

Paszek, M. J., Zahir, N., Johnson, K. R., Lakins, J. N., Rozenberg, G. I., Gefen, A., et al. (2005). Tensional homeostasis and the malignant phenotype. *Cancer Cell* 8, 241–254. doi: 10.1016/j.ccr.2005.08.010

Pathak, A., and Kumar, S. (2012). Independent regulation of tumor cell migration by matrix stiffness and confinement. *Proc. Natl. Acad. Sci. U.S.A.* 109, 10334–10339. doi: 10.1073/pnas.1118073109

Paul, C. D., Hung, W.-C., Wirtz, D., and Konstantopoulos, K. (2016). Engineered models of confined cell migration. *Annu. Rev. Biomed. Eng.* 18, 159–180. doi: 10.1146/annurev-bioeng-071114-040654

Paul, C. D., Mistriotis, P., and Konstantopoulos, K. (2017). Cancer cell motility: lessons from migration in confined spaces. *Nat. Rev. Cancer* 17, 131–140. doi: 10.1038/nrc.2016.123

Ridley, A. J., Schwartz, M. A., Burridge, K., Firtel, R. A., Ginsberg, M. H., Borisy, G., et al. (2003). Cell migration: integrating signals from front to back. *Science* 302, 1704–1709. doi: 10.1126/science.1092053

Riedel, S., Hietschold, P., Krömmelbein, C., Kunschmann, T., Konieczny, R., Knolle, W., et al. (2019). Design of biomimetic collagen matrices by reagent-free electron beam induced crosslinking: structure-property relationships and cellular response. *Mater. Des.* 168:107606. doi: 10.1016/j.matdes.2019.107606

Sabeh, F., Ota, I., Holmbeck, K., Birkedal-Hansen, H., Soloway, P., Balbin, M., et al. (2004). Tumor cell traffic through the extracellular matrix is controlled by the membrane-anchored collagenase MT1-MMP. *J. Cell Biol.* 167, 769–781. doi: 10.1083/jcb.200408028

Sapudom, J., Kalbitzer, L., Wu, X., Martin, S., Kroy, K., and Pompe, T. (2019). Fibril bending stiffness of 3D collagen matrices instructs spreading and clustering of invasive and non-invasive breast cancer cells. *Biomaterials* 193, 47–57. doi: 10.1016/j.biomaterials.2018.12.010

Sapudom, J., Rubner, S., Martin, S., Kurth, T., Riedel, S., Mierke, C. T., et al. (2015). The phenotype of cancer cell invasion controlled by fibril diameter and pore size of 3D collagen networks. *Biomaterials* 52, 367–375. doi: 10.1016/j.biomaterials.2015.02.022

Sauer, F., Oswald, L., Ariza de Schellenberger, A., Tzschätzsch, H., Schrank, F., Fischer, T., et al. (2019). Collagen networks determine viscoelastic properties of connective tissues yet do not hinder diffusion of the aqueous solvent. *Soft Matter* 15, 3055–3064. doi: 10.1039/C8SM02264J

Schubert, E., Sander, J., Ester, M., Kriegel, H. P., and Xu, X. (2017). DBSCAN revisited, revisited. *ACM Trans. Database Syst.* 42, 1–21. doi: 10.1145/3068335

Shamir, E. R., and Ewald, A. J. (2014). Three-dimensional organotypic culture: experimental models of mammalian biology and disease. *Nat. Rev. Mol. Cell Biol.* 15, 647–664. doi: 10.1038/nrm3873

Shinsato, Y., Doyle, A. D., Li, W., and Yamada, K. M. (2020). Direct comparison of five different 3D extracellular matrix model systems for characterization of cancer cell migration. *Cancer Rep.* 37:117. doi: 10.1002/cnr2.1257

Stroka, K. M., and Konstantopoulos, K. (2014). Physical biology in cancer. 4. Physical cues guide tumor cell adhesion and migration. *Am. J. Physiol. Cell Physiol.* 306, C98–C109. doi: 10.1152/ajpcell.00289.2013

Talkenberger, K., Cavalcanti-Adam, E. A., Voss-Böhme, A., and Deutsch, A. (2017). Amoeboid-mesenchymal migration plasticity promotes invasion only in complex heterogeneous microenvironments. *Sci. Rep.* 7:9237. doi: 10.1038/s41598-017-09300-3

Um, E., Oh, J. M., Granick, S., and Cho, Y.-K. (2017). Cell migration in microengineered tumor environments. *Lab. Chip* 17, 4171–4185. doi: 10.1039/c7lc00555e

Willis, A. L., Sabeh, F., Li, X.-Y., and Weiss, S. J. (2013). Extracellular matrix determinants and the regulation of cancer cell invasion stratagems. *J. Microsc.* 251, 250–260. doi: 10.1111/jmi.12064

Wisdom, K. M., Adebowale, K., Chang, J., Lee, J. Y., Nam, S., Desai, R., et al. (2018). Matrix mechanical plasticity regulates cancer cell migration through confining microenvironments. *Nat. Commun.* 9:4144. doi: 10.1038/s41467-018-06641-z

Wolf, K., Alexander, S., Schacht, V., Coussens, L. M., von Andrian, U. H., van Rheenen, J., et al. (2009). Collagen-based cell migration models in vitro and in vivo. *Semin. Cell Dev. Biol.* 20, 931–941. doi: 10.1016/j.semcdb.2009.08.005

Wolf, K., and Friedl, P. (2011). Extracellular matrix determinants of proteolytic and non-proteolytic cell migration. *Trends Cell Biol.* 21, 736–744. doi: 10.1016/j.tcb.2011.09.006

Wolf, K., Mazo, I., Leung, H., Engelke, K., von Andrian, U. H., Deryugina, E. I., et al. (2003). Compensation mechanism in tumor cell migration: mesenchymal-amoeboid transition after blocking of pericellular proteolysis. *J. Cell Biol.* 160, 267–277. doi: 10.1083/jcb.200209006

Wolf, K., Te Lindert, M., Krause, M., Alexander, S., Te Riet, J., Willis, A. L., et al. (2013). Physical limits of cell migration: control by ECM space and nuclear deformation and tuning by proteolysis and traction force. *J. Cell Biol.* 201, 1069–1084. doi: 10.1083/jcb.201210152

Conflict of Interest: The authors declare that the research was conducted in the absence of any commercial or financial relationships that could be construed as a potential conflict of interest.

frontiers in Cell and Developmental Biology

METHODS
published: 22 December 2020
doi: 10.3389/fcell.2020.615759

An Integrative and Modular Framework to Recapitulate Emergent Behavior in Cell Migration

Marina B. Cuenca [1,2†], Lucía Canedo [1], Carolina Perez-Castro [1] and Hernan E. Grecco [1,2,3*]*

[1] Instituto de Investigación en Biomedicina de Buenos Aires, Consejo Nacional de Investigaciones Científicas y Técnicas (CONICET), Partner Institute of the Max Planck Society, Buenos Aires, Argentina, [2] Departamento de Física, Facultad de Ciencias Exactas y Naturales (FCEN), Universidad de Buenos Aires and Instituto de Física de Buenos Aires (IFIBA), Consejo Nacional de Investigaciones Científicas y Técnicas (CONICET), Buenos Aires, Argentina, [3] Department of Systemic Cell Biology, Max Planck Institute for Molecular Physiology, Dortmund, Germany

OPEN ACCESS

Edited by:
Chang Y. Chung,
Duke Kunshan University, China

Reviewed by:
Lidija Radenovic,
University of Belgrade, Serbia
Hisham F. Bahmad,
Mount Sinai Medical Center,
United States

***Correspondence:**
Carolina Perez-Castro
cperezcastro@ibioba-mpsp-conicet.gov.ar
Hernan E. Grecco
hgrecco@df.uba.ar;
hernan-edgardo.grecco@mpi-dortmund.mpg.de

†Present address:
Marina B. Cuenca,
Max Planck Institute of Molecular Cell Biology and Genetics, Dresden, Germany

Specialty section:
This article was submitted to Cell Adhesion and Migration, a section of the journal Frontiers in Cell and Developmental Biology

Received: 12 October 2020
Accepted: 30 November 2020
Published: 22 December 2020

Citation:
Cuenca MB, Canedo L, Perez-Castro C and Grecco HE (2020) An Integrative and Modular Framework to Recapitulate Emergent Behavior in Cell Migration. Front. Cell Dev. Biol. 8:615759. doi: 10.3389/fcell.2020.615759

Cell migration has been a subject of study in a broad variety of biological systems, from morphogenetic events during development to cancer progression. In this work, we describe single-cell movement in a modular framework from which we simulate the collective behavior of glioblastoma cells, the most prevalent and malignant primary brain tumor. We used the U87 cell line, which can be grown as a monolayer or spatially closely packed and organized in 3D structures called spheroids. Our integrative model considers the most relevant mechanisms involved in cell migration: chemotaxis of attractant factor, mechanical interactions and random movement. The effect of each mechanism is integrated into the overall probability of the cells to move in a particular direction, in an automaton-like approach. Our simulations fit and reproduced the emergent behavior of the spheroids in a set of migration assays where single-cell trajectories were tracked. We also predicted the effect of migration inhibition on the colonies from simple experimental characterization of single treated cell tracks. The development of tools that allow complementing molecular knowledge in migratory cell behavior is relevant for understanding essential cellular processes, both physiological (such as organ formation, tissue regeneration among others) and pathological perspectives. Overall, this is a versatile tool that has been proven to predict individual and collective behavior in U87 cells, but that can be applied to a broad variety of scenarios.

Keywords: fluorescence microscopy, spheroid, cellular automata, migration, image analysis

1. INTRODUCTION

Collective cell motion is a complex feature in biological systems, crucial for morphogenetic events, where many single-cell level processes are involved. Aberrations in this coordinated behavior is a hallmark of many pathologies including cancer (Gupta et al., 2011; Stieber et al., 2014; Dirkse et al., 2019; Prager et al., 2019). Chemotaxis, mechanical interactions (with other cells and extracellular matrix) and proliferation have been identified as key mechanisms driving cell migration (Kansal et al., 2000; Khain et al., 2005; Rubenstein and Kaufman, 2008; Charteris and Khain, 2014; Li et al., 2017; Manini et al., 2018). How these processes individually contribute to the emergent behavior is not fully understood as we are limited to either observing single cells or the collective behavior at the multicellular level.

Mathematical models are useful in delineating the role and influence of these individual processes, otherwise experimentally inaccessible. Early studies tackle single-cell movement as a

random walker (Fuert, 1920), but this description does not recapitulate the behavior if cell colonies are analyzed or microenvironmental conditions are considered. More complex mathematical frameworks have been developed in continuous models using differential equations. Although such models are computationally inexpensive, the output is a density function that does not reflect single-cell behavior and thus fails to predict subpopulations and patterns in cell colonies (Hatzikirou et al., 2005). On the other hand, in cellular automaton discrete models cells move according to specific rules or probabilities that depend on the neighboring distribution. This approach would allow us to describe the social behavior within cell communities at the single-cell level. However, the rules that drive the automatons are static and do not consider intracellular and molecular mechanisms (Tanaka et al., 2009). To the best of our knowledge, there are no existing models that integrate the broad diversity of biological mechanisms needed to fully predict cell migration.

We developed a simple, fast, powerful and discrete two-dimensional approach that accurately predicts cell migration by considering random movement, proliferation, chemotaxis and mechanical interactions. The algorithm allows for the specification of the initial cell number and colony geometry, as well as the active mechanisms in play. The modular construction of the algorithm allows the user to tune every single aspect of the mechanisms, and make predictions of complex cell arrangements from single-cell characterization. This makes our algorithm a powerful tool that can be adapted to simulate a variety of other complex processes. Wound healing, cell invasion, and morphogenetic events can be addressed even in systems lacking spheroid formation.

2. RESULTS

2.1. Single-Cell Behavior Gives Insights Into Colony-Scale Observations

Glioblastoma (GBM) U87 cells spheroids expressing the nuclei marker pBABE-H2BGFP, placed in Geltrex coated multiwells and covered with fresh stem medium, were imaged for 24 h (**Figure 1A**, see Material and Methods sections 4.1 and 4.2). Different profiles have been observed within the range of spheroid diameters used (60–200 μm). While in smaller colonies most of the cells detached and migrated, in larger colonies they remained clustered as reported previously (**Figure 1B**, **Supplementary Videos 1**, **2**) (Puliafito et al., 2015).

Furthermore, we saw an elongated morphology in cells performing migration, interacting with each other, producing collective migration in a radial protrusion away from the colony. Other cells did not show protrusions but migrated in pairs, which reinforced the existence of mechanical interactions (**Figure 1C**, **Supplementary Video 3**). Finally, some other cells migrated as single cells randomly for the first hours, but then, radial movement and re-clustering were observed (**Figure 1D**, **Supplementary Video 4**).

Taking together these observations, we proposed that random movement was not enough to explain the invasive profile of the colonies. We hypothesized that short-range mechanical interactions between cells might affect motility, and another long-range chemotactic process would radially affect migration direction. Previous studies consider chemotaxis of glucose as an attractant factor driving cell migration in GBM (Khain et al., 2005; Bao et al., 2019). We hypothesized that the cells are dominated by random movement and mechanical interactions during the early hours of the experiment. Later, the chemical diffusion and concentration of a chemo-attractant factor self-generated by the cells would drive re-clustering. This could explain why in large spheroids there are fewer migrating cells, considering that the concentration of chemo-attractant is higher.

Notably, thanks to the nuclei marker visualization, few mitosis events were observed in our time-lapses. We decided to explore within the simulations the influence of proliferation. To keep generality, is a mechanism that cannot be discarded in other cell lines, longer duration of the experiments or higher cell number. Therefore, we added it as a fourth mechanism during cell migration.

2.2. Quantification of Cellular Motility Reveals Time and Colony Size Dependent Behavior

To extract quantitative results that validate our observations, bright field images were segmented to identify the centroid of the spheroid. Then, the trajectories of single-cells expressing the nuclei marker pBABE-H2BGFP were obtained, and for each spheroid, the mean relative radial migration (RRM) was calculated at every time-point (**Figures 2A–F**, see Materials and Methods section 4.3). We chose a nuclear marker because its morphological structure is stable throughout the cell cycle and cellular migration (Cliffe et al., 2017). The mean RRM is a measure of the distribution of cells around the centroid of the spheroid. Thus, a spheroid that remained clustered has a mean RRM of 1, while a spheroid whose cells doubled mean distribution has a mean RRM value of 2.

We observed that for larger spheroids the mean RRM is close to 1, while smaller spheroids could migrate six times their mean initial radius. Analyzing the dynamics after 7.5 h of migration (region of linear increase in RRM), we defined a threshold at 100 μm separating a constant and divergent behavior for large and small spheroids, respectively. From now on, we will show the average data on each side of the threshold (**Figures 2G,H**).

2.3. Single-Cell Model Accurately Predicts Emergent Colony Behavior

In our model, a single isolated cell in a substrate can migrate with a random component, where all directions are equally likely and a diffusion coefficient describes the area covered per unit of time (Fuert, 1920). To estimate this parameter, we analyzed the movement of single cells in a low-density monolayer in the same culture conditions as the spheroids during the migration assays (see Material and Methods section 4.2). Having single cells apart from each other, it is possible to quantify the random motion only without cells interacting mechanically with each other and having a non-significant concentration of self-generated

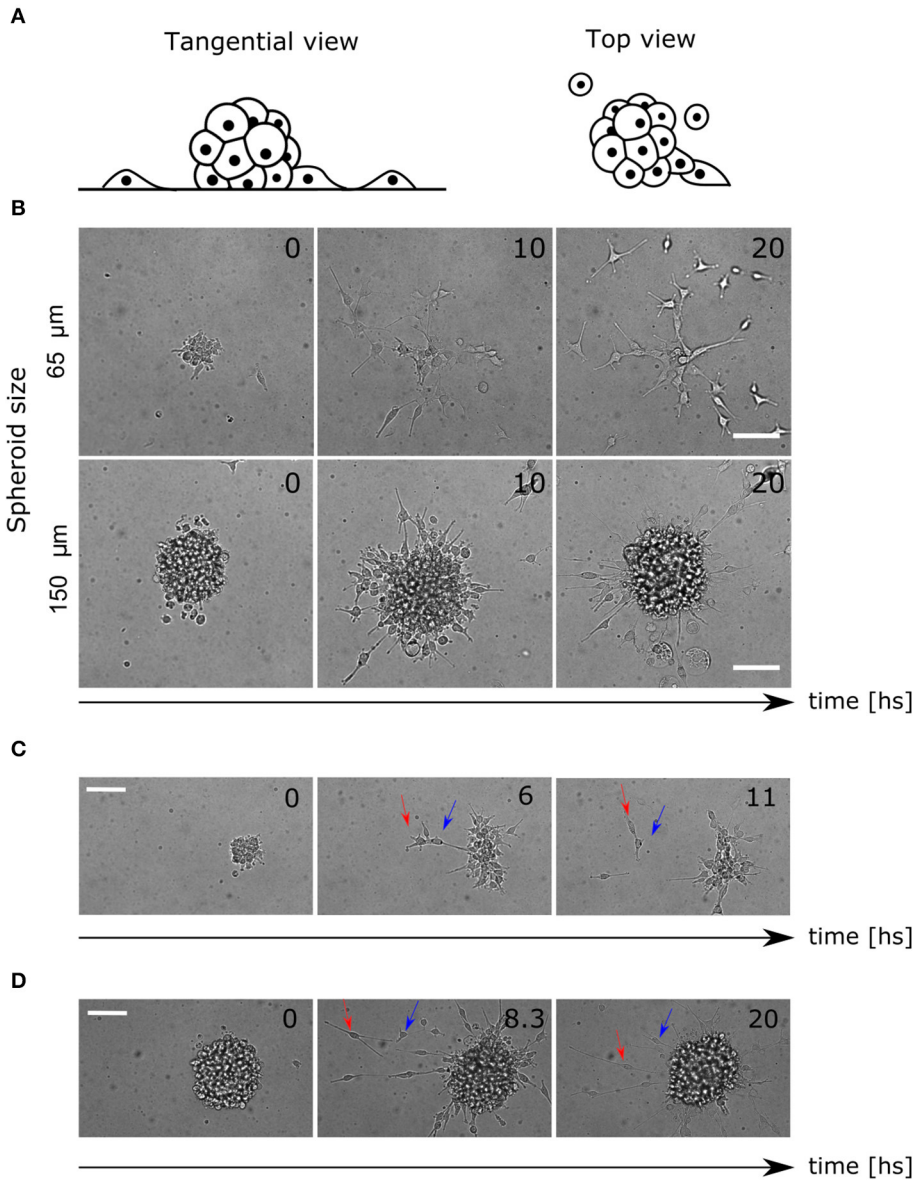

FIGURE 1 | Colony and single cell-level migratory behavior. **(A)** Lateral and top view diagram of cell migration away from the spheroids. The cells are constrained by the Geltrex surface to migrate in 2D trajectories. **(B)** Time-lapse of bright field images where different migration patterns are shown for small and large spheroids. **(C)** Time-lapse of spheroid migration where mechanical interactions between cells are evident. The leading cell (red arrow) migrates away from the colony pulling the second cell (blue arrow). **(D)** Time-lapse of directed radial behavior of two cells (arrows). In the first frame (8.3 hs) they move away and finally (20 hs) they return to the colony again. Scale bar 100 μm.

chemoattractant. We obtained a diffusion coefficient of $D_{cell} = (0.21 \pm 0.04)\ \mu m^2/s$ (mean $\pm$ SEM, see **Supplementary Figure 1**).

Mechanical interactions were included in the model defining a probability q for two cells to interact with each other at first (Charteris and Khain, 2014) and second neighbors (can be extended to further neighbors, see section 4.4.3). Chemotaxis was modeled by assuming an effective chemo-attractant produced and consumed by cells with rates c_1 and c_2, respectively (Keller and Segel, 1971; Hillen and Painter, 2008). It diffuses with a rate $D = D_{chem}/D_{cell}$ times faster than the cells effectively providing a mid-range cell-to-cell interaction. This quantity is delimited by the stability conditions of the chemotaxis equation (see Materials and methods, section 4.4.2). When this chemical gets to the membrane of neighboring cells, some molecules attach to specific receptors and unchain a signaling pathway to produce migration in the direction of the chemical gradient (Kim et al., 2009). The strength of the chemo-attractant to drive cells in a particular direction is given by the quantity c_f. Finally, we also defined α which is the probability of one cell to undergo division during the time step defined previously. As we discussed before, there are

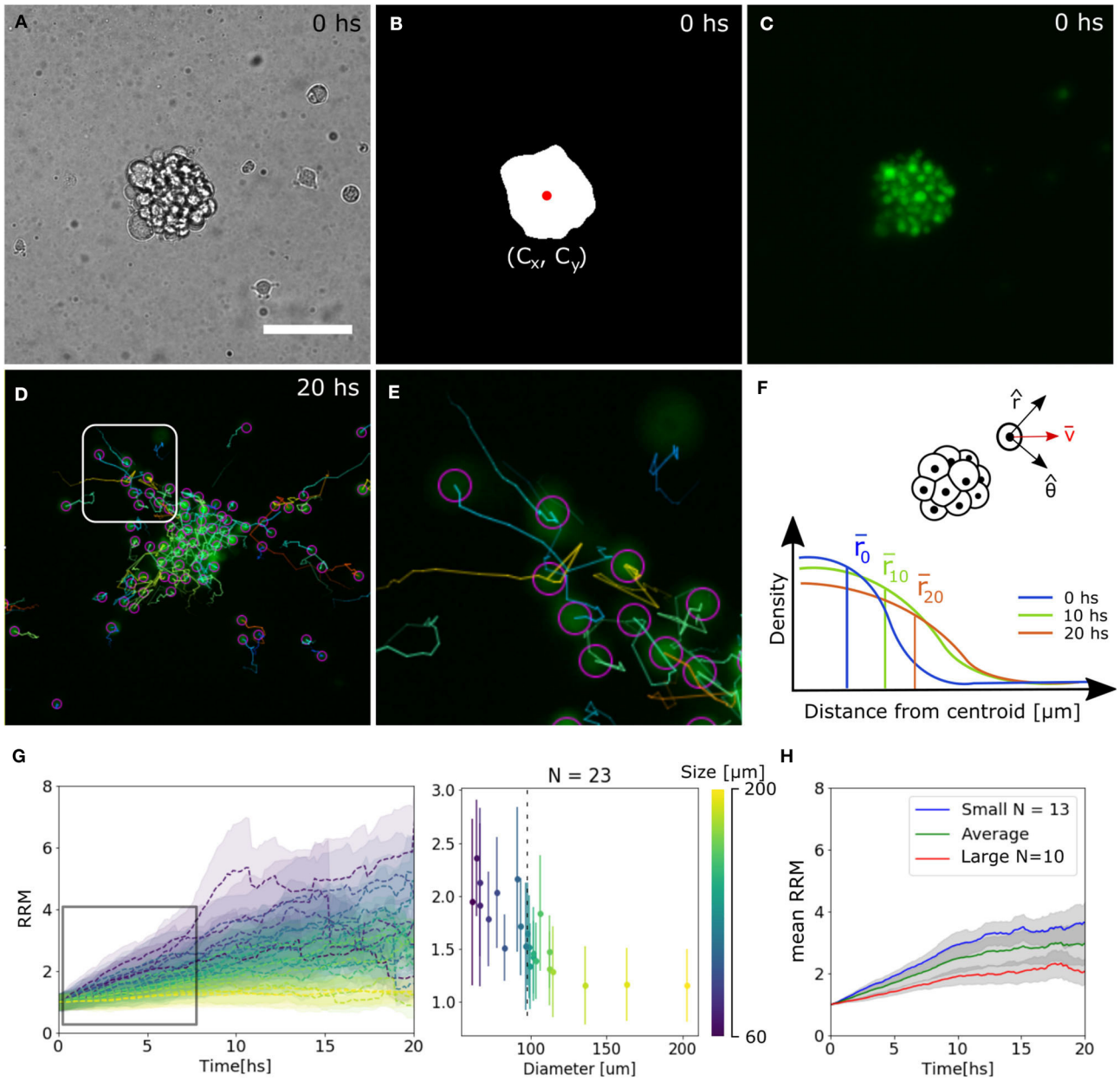

FIGURE 2 | Tracking analysis of individual nuclei. **(A–C)** Bright field, binary mask with centroid and fluorescence channel of spheroid at time 0. **(D,E)** Individual cell tracks and close-up. The track for the last 10 time-points is indicated by a straight line and the final nuclei position with a circle. **(F)** Diagram of polar coordinates calculated from the centroid of the spheroid, distribution of radial distances and mean value. **(G)** Experimental curves of mean RRM for different sizes of spheroids (left) and RRM after 7.5 hs of migration vs. diameter (right). We can define a threshold around 100 μm (dotted line) where the behavior is constant for larger spheroids. **(H)** Average mean RRM for small, large and all sizes of spheroids.

only a few divisions in our migration assays, thus $\alpha = 0$ unless stated otherwise. All the mechanisms considered in addition to random movement are illustrated in **Figure 3A**.

To computationally run the model, we used a discrete lattice (matrix) to describe the cell (N) and chemical (U) distribution. Defining the cell size and time step is sufficient to set the diffusion coefficient D_{cell} in N. Each cell is a square of area 100 μm^2 (average size of 10 μm). Then, in our simulations, we defined a time step of 7 min (205 iterations in total for 24 hs *in silico* experiment). We also defined a probability r for the cells to perform random movement. In this way, we were able to alter D_{cell} in our simulation without changing the geometry of the cells and the number of iterations, which would require to re-scale the other parameters of the model. This might be of interest as we will discuss further ahead. In our simulations, $r = 1$ unless stated otherwise.

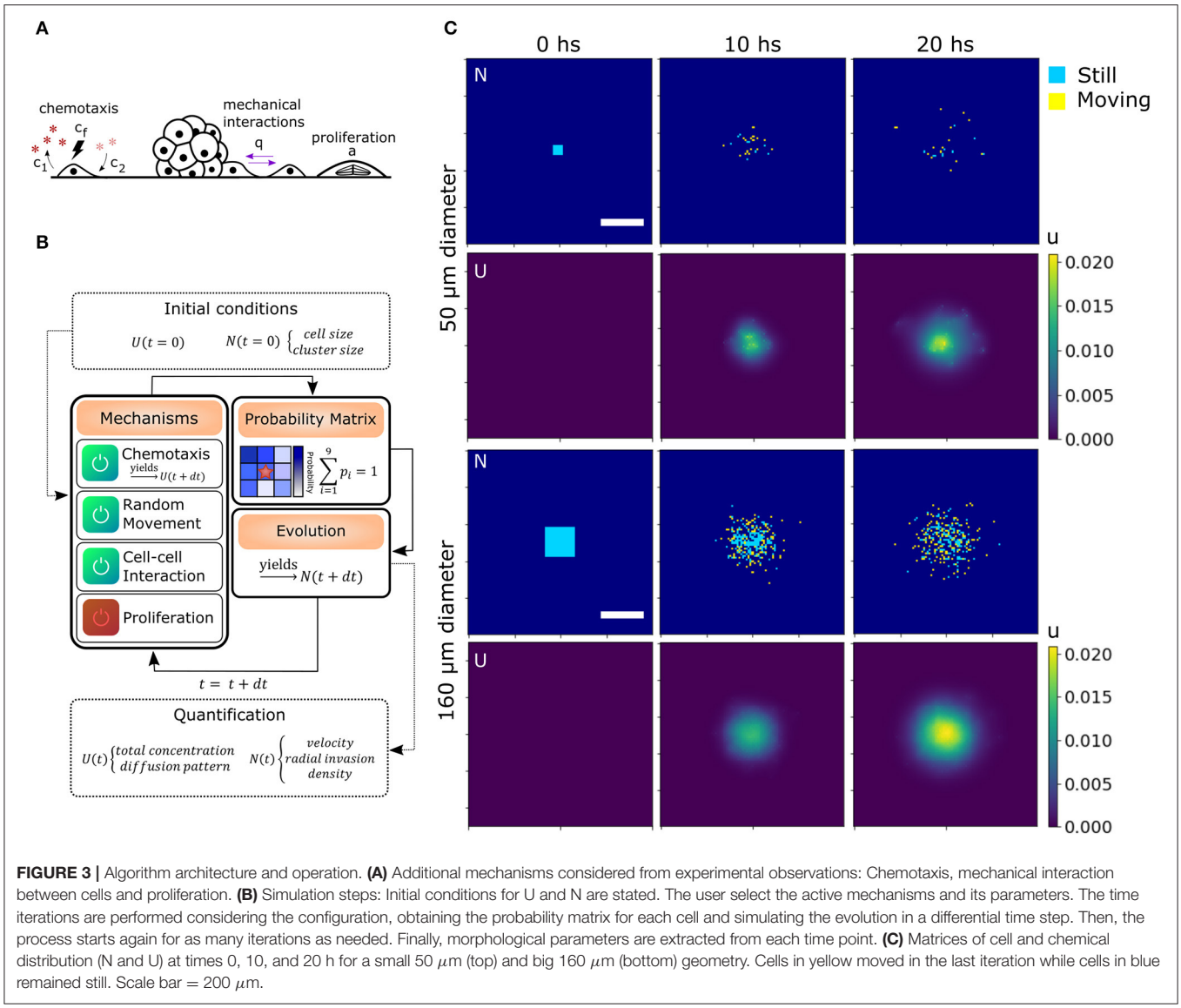

FIGURE 3 | Algorithm architecture and operation. **(A)** Additional mechanisms considered from experimental observations: Chemotaxis, mechanical interaction between cells and proliferation. **(B)** Simulation steps: Initial conditions for U and N are stated. The user select the active mechanisms and its parameters. The time iterations are performed considering the configuration, obtaining the probability matrix for each cell and simulating the evolution in a differential time step. Then, the process starts again for as many iterations as needed. Finally, morphological parameters are extracted from each time point. **(C)** Matrices of cell and chemical distribution (N and U) at times 0, 10, and 20 h for a small 50 μm (top) and big 160 μm (bottom) geometry. Cells in yellow moved in the last iteration while cells in blue remained still. Scale bar = 200 μm.

To perform the simulations, we used a modular approach to combine all the biological processes, translate them into probabilities, and then, consider each cell as an automaton. Cell occupancy N and chemo-attractant distribution U was iteratively evolved according to the described equations (see sections 4.4.2 and 4.4.5). These probabilities change in each iteration (time-point) based on the diffusion of the chemical and cell distribution. The initial conditions, such as cluster (spheroid) size and geometry $N(t = 0)$, and chemical concentration $U(t = 0)$, are given by the user (**Figures 3B,C**). To delimit the possible values of each parameter, we compared the RRM results of the simulations with the random movement *in silico* and the experimental results. Only the parameters with RRMs between the experimental and random curves are candidates (see **Supplementary Figure 2**).

We could assign different behaviors of the curves to different parameters. The mechanical parameter q is strongly associated with the slope or velocity of migration, which makes sense in a scenario where the cells at $t = 0$ are cluster together and the mechanical interactions have a higher impact. While c_1 is associated with the velocity only after ∼2 h, once the chemical has accumulated. On the other hand, c_f changes the final value of the mean RRM (**Figures 4A–C** and **Supplementary Figure 3**). The diffusion coefficient D showed slight differences in the emergent behavior only in large spheroids, where the chemical concentration is higher. In this scenario more diffusion means a lower chemical gradient in the spheroid, and thus, the cells can arrange in a wider distribution with higher mean RRM (**Supplementary Figure 2**). This value of $D = 50$ returned a $D_{chem} = (630 \pm 120)\ \mu m^2/min$ which encloses, for example, the diffusion coefficient of glucose in water ($D_{gluc} = 670$–$700\ \mu m^2/min$) (Øyaas et al., 1995; Andriesse and Hollestelle, 2001). This is not enough to conclude which is/are the molecule(s) involved in the chemotaxis, given the fact that there are probably

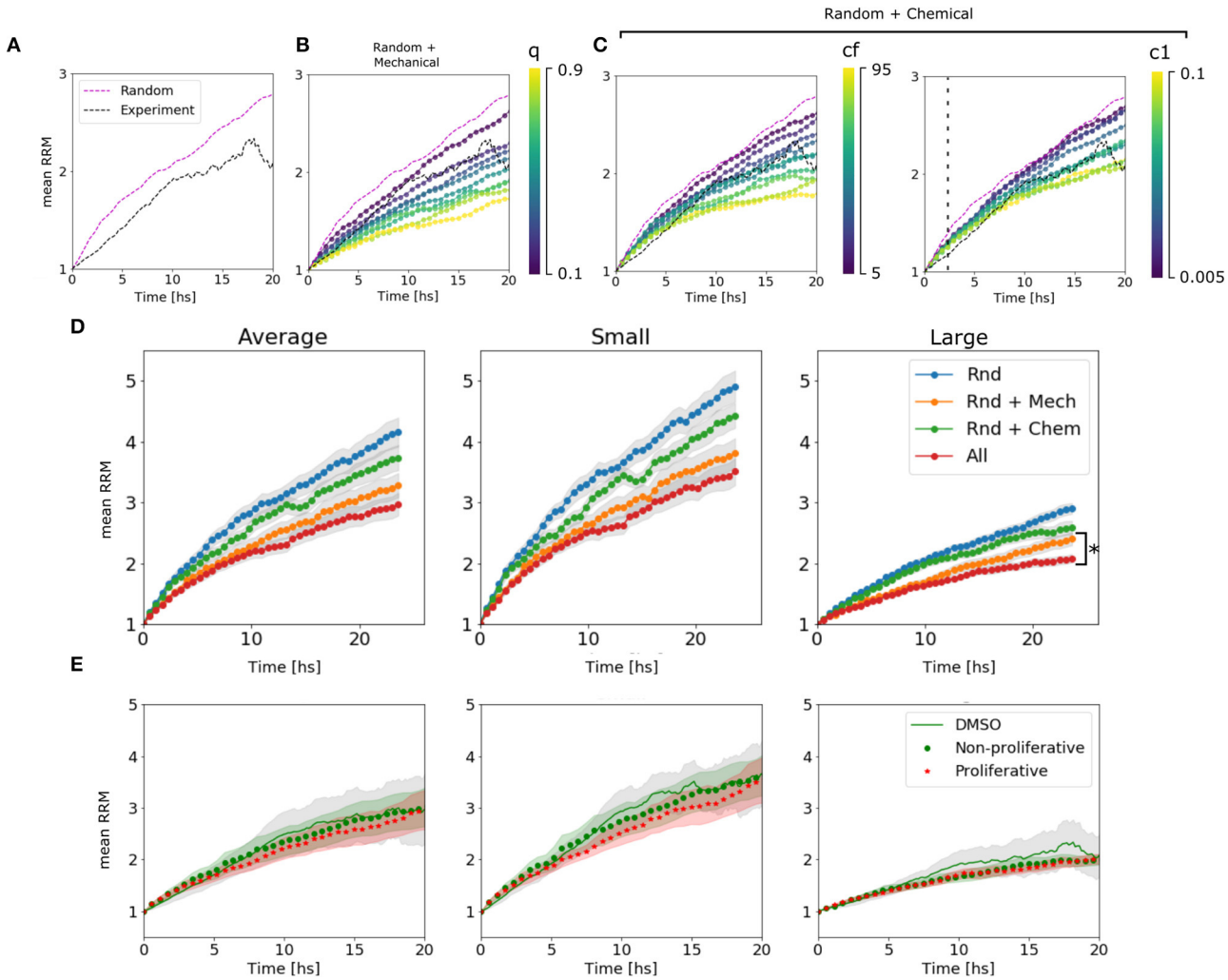

FIGURE 4 | Algorithm behavior and fitting procedure. **(A)** Dynamic range available for the estimation of parameters in the average of large spheroids. We are confined to the region between the random movement simulated curve and the experimental curve. **(B)** Simulated curves for different values of q change their slot. We see that we can move in the range from 0 to 0.3. **(C)** Simulated curves for different values of c_f change the asymptotic value. The range between 5 and 45 is valid. **(D)** Simulated curves for different c_1 change the slot above ∼2 h of migration. All the explored range is, in principle, valid. **(D)** Change in RRM due to the presence/absence of different mechanisms in the average of all, small and large spheroids: In blue, only random movement was taking place; In orange, mechanic interactions were added; In green, it is shown the effect of random movement plus chemotaxis. Finally, all the mechanisms together in red. We can see that the difference between adding chemotactic effects is not significant for small spheroids but remains important for large spheroids (*p-value < 0.05, $N = 24$ spheroids). **(E)** Comparison between experimental curve and simulated curves with and without proliferation.

attractants and repellents. In our model, we are considering an effective chemotaxis that showed to be positive (attractant).

To determine the influence of each mechanism in the simulated results, we turn off one mechanism at a time in the model. Then, we compared the final mean RRM values with the random movement and the complete model simulated curve. As hypothesized, the chemotaxis effect had a significant influence on large spheroids, while it did not change the global behavior on small clusters (see **Figure 4D**). This indicates that the complete model is not only the sum of its components and that the mechanisms at the single-cell level return emergent responses in different size-scales. We also test whether the proliferation affects cell migration pattern setting the probability α to 0.0007–0.0012 [joint probability between the doubling rate of 19–30 h (Charteris and Khain, 2014; Rodríguez-Lozano et al., 2019) and 20% of proliferative cells within the spheroid (Aaberg-Jessen et al., 2013)], concluding that there is no significant difference within 24 h (**Figure 4E**, see Material and Methods section 4.4.4).

Finally, we found a set of parameters that not only fit the experimental results in average, but also replicate the behavior in single spheroids and on each subset of small and large colonies: $D = 50, c_1 = 0.035, c_2 = c_1/2, c_f = 20$, and $q = 0.3$ (**Figures 5A–C**). The algorithm performed each simulation (total number of spheroids = 24) in 10 min (see Materials and Methods section 4.4).

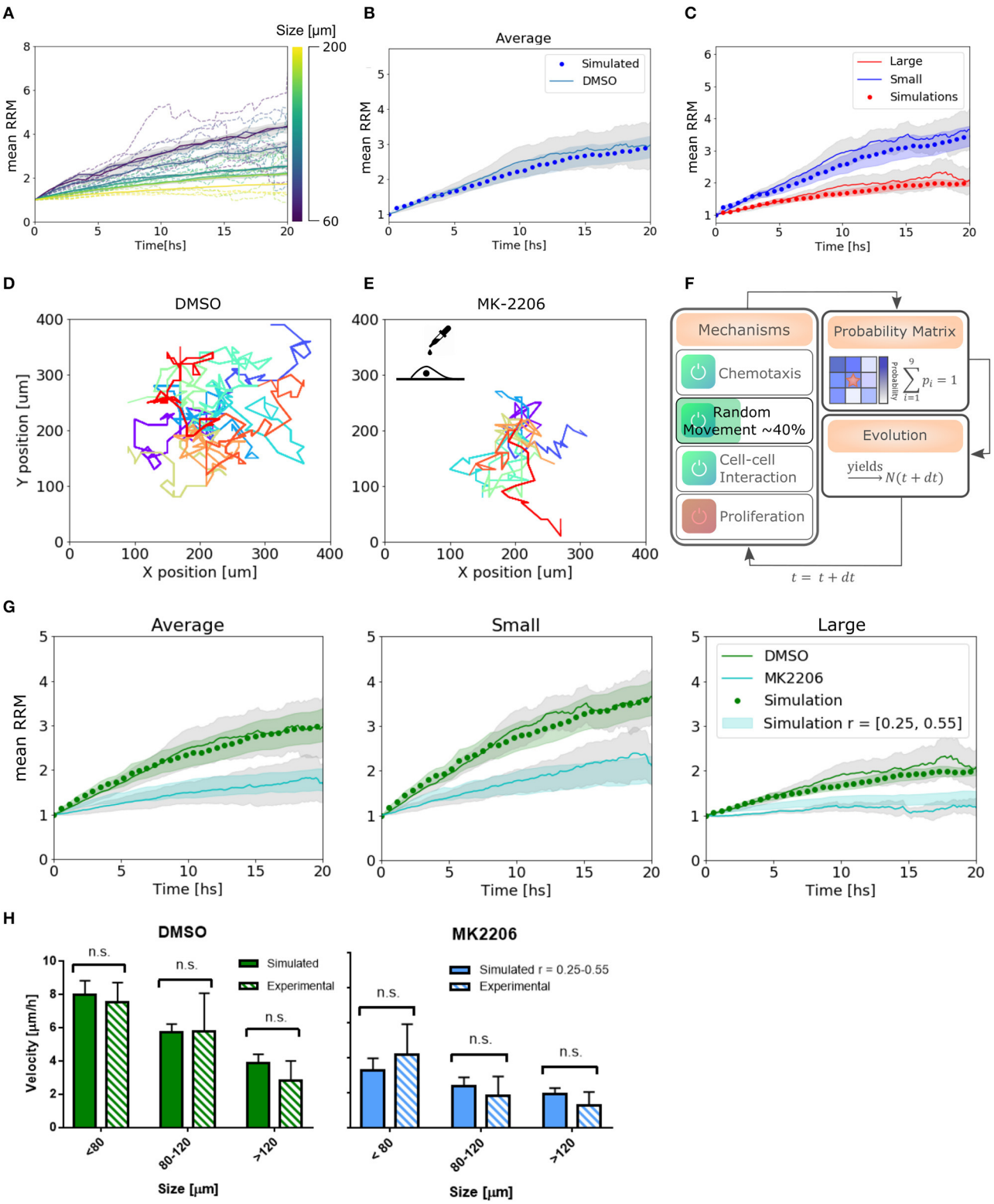

FIGURE 5 | Simulations reproduce migratory behavior and predict drug-assay results. **(A)** Simulated curves of mean relative radial migration for different size of spheroids. **(B)** Average mean RRM for all sizes. Experimental and simulated curve. **(C)** Average mean RRM for small and large spheroids. Experimental and simulated curves. **(D,E)** Single cell trajectories for the diffusion coefficients measured for DMSO and MK-2206 treated cells in monolayer. **(F)** Modification in the model: Only

(Continued)

FIGURE 5 | random movement (diffusion) of the cells was altered in the same range indicated by experimental results. **(G)** Prediction of the model and experimental results with MK-2206 treatment for all spheroids (left). Prediction and experimental results for small ($N = 12$) and large ($N = 11$) spheroids separately. **(H)** Average invasion velocity calculated from linear fit of RRM data for each spheroid during the first 7.5 h of invasion. Non-significant differences have been observed for simulated and experimental data both for MK-2206 treatment and DMSO control. While for DMSO the simulated data corresponds to the optimum set of parameters, for MK-2206 an uniform distribution of the random parameter r between 0.25 and 0.55 was used.

2.4. Experimental Perturbation on Cellular Mobility Impacts the Emergent Behavior, Following the Algorithm Prediction

To test the capability of the model to predict other cell behavior, we created a perturbation in the random motion mechanism experimentally. Single cells in a low-density monolayer were treated with AKT1 allosteric inhibitor MK-2206 (Narayan et al., 2017). Akt is a major signaling molecule that is highly expressed and aberrantly activated in GBM, contributing to the malignant phenotype (Nakada et al., 2013). It is often used in combination with Notch inhibitors and has been proved to be a migration inhibitor, without altering proliferation, in a dose-dependent manner (Jin et al., 2013; Djuzenova et al., 2019).

The diffusion coefficient was quantified from single-cell trajectories as described previously being just 40 ± 15% (mean ± SEM) of the value of cells treated with the vehicle DMSO (**Figures 5D,E**, see **Supplementary Figure 1**). Thus, instead of changing the time step of the iterations to modify D_{cell}, which would have changed also all the set of parameters found, we simply changed the probability to perform random movement. We simulated a set of spheroids *in silico* with r between 0.25 and 0.55 to obtain an effective D_{cell} to match the experimental measurements (**Figure 5F**). Only then, we treated the spheroids with the migration inhibitor and proceeded with the analysis as usual. Modifying only the parameters associated with the altered mechanism, we observe a good agreement between the model predictions and experimental results, both for the average and subsets of data (**Figure 5G**). Moreover, we calculated the mean velocity in the first 7.5 hs of simulated spheroid invasion (linear regime) and obtained non-significant differences compared to the experimental results for three different size subsets (**Figure 5H**). This indicates that not only our model can fit our experimental data correctly, but also predicts dynamic and average quantitative parameters related to collective cell migration.

3. DISCUSSION

The tumor cell migration comprising cell random movement, mechanical interactions, and chemotaxis is extremely complex to interpret. Our data from single-cell and colony behavior analysis allowed us to develop a concise and versatile tool that contributes toward understanding tumor-associated biological processes. Our approach is simple and fast, and can be extended far beyond the GBM model and adapted to other cell lines and scenarios including migration, proliferation, morphogenesis, and wound healing. We have shown how, from a simple determination of the cell diffusion coefficient, our model can replicate a set of migration assays of U87 cellular spheroids. The only experimental requirement would be a nucleus labeling, either by staining or retroviral transfection, to determine each cell position.

We demonstrated the relevance of all the mechanisms proposed in the model and the influence in the migratory process. We found that while random movement and mechanical interactions have a high impact on the mean RRM, they are not sufficient to explain the invasive pattern in large spheroids (>100 μm) where chemotaxis becomes significant. Adjusting random movement of the cells, we were able to make good predictions on the effects of the migration inhibitor MK-2206, obtaining a good agreement between the *in silico* and *in vitro* cell behavior.

No considerations regarding the mechanical properties of the environment have been made. Our model assumes that the rigidity of the substrate is homogeneous and affects the velocity at the single-cell level. Therefore, it is adequate to determine experimentally the diffusion coefficient of isolated cells to encode the mechanical properties. However, the heterogeneous composition of the "real" tumor microenvironment could modify (or affect) the diffusion coefficient of individual cells and alter the emerging behavior of the colonies given by cellular interactions with the surroundings. Since current cancer treatments do not address the dynamic regulation of the tumor microenvironment, primarily responsible for tumor progression and resistance to treatment; future adaptations to this first base model allowing for the presence of microglia and different tumor cell identity states (proliferative, migrating, senescent, etc.) (Tektonidis et al., 2011; Friedmann-Morvinski, 2014) should be considered to evaluate and predict with greater fidelity the cellular behavior *in vivo*.

The traditional therapeutic approach for GBM is surgical resection, where most of the tumor mass is removed. However, some residual cells mostly at the invading edge could persist after treatment (i.e., resection plus chemo and radiation therapy) and have been hypothesized to be responsible for the recurrences observed in patients (Swanson et al., 2000; Stupp et al., 2005). Tumor stem-like cells have been identified as one of the main subpopulation responsible for the tumor recurrence, and though some gene markers and molecular pathways have been recently identified (Wang et al., 2016; Minata et al., 2019), the area is still under investigation. Our finding could contribute to understanding how the different mechanisms considered impact at different colony-size scales and regulate the migratory behavior of tumors. Our results could also be used to integrate with new findings in the area of research and explore the impact of new biomarkers and test future therapeutic interventions.

The cell line used in this study (U87), has been chosen as a model of GBM in over 2000 publications since they reproduce the oncogenic cell signaling in the original tumor (Lenting et al., 2017). Future studies using other GBM and tumor cells

(commercial lines, and cells derived from patients), will be necessary to expand the generality of our observations. The use of these cells will also be useful to better understand the impact and scope of the model, as well as the possibility of proposing new questions, given that patient-derived cells better represent tumor biology and the heterogeneity found daily in the clinic.

The results and the model characterized in two dimensions from spheres culture here are the first approaches to extract the biological parameters, to validate the mechanisms proposed, and to obtain predictions of drug assay experiments *in vitro*. Scaling into the third dimension is an important upcoming step to further predict invasive behavior *in vivo*. Therefore, our contribution will be relevant in the field in order to move forward to try to understand the complex tumor migration and cancer.

4. MATERIALS AND METHODS

The steps involved in producing the experimental and corresponding simulated results were performed in the following order: (i) migration assay experiments with GBM spheroids, (ii) image analysis and data processing, (iii) selection of the biological actuators, (iv) identification of mathematical analogs for the simulations, (v) experimental and *in silico* determination of parameters, (vi) prediction of drug assay response, and (vii) test the predictions experimentally.

4.1. Cell Culture and Viral Infection

Cell line U87MG was acquired from ATCC, kept frozen immediately after receipt or used in culture <2 months and routinely tested negative for mycoplasma. ATCC cells are characterized by Short Tandem Repeat (STR) profiling (Ferreyra-Solari et al., 2016). U87 cells were cultured in DMEM supplemented with 10% fetal bovine serum, Penicillin/Streptomycin, and L-Glutamine to express several of GBM markers as determined previously (Lenting et al., 2017). Cells were kept at 37°C under 5% CO2 humidified air. The plasmid pBABE-H2BGFP was a gift from Fred Dick (Addgene plasmid # 26790; http://n2t.net/addgene:26790; RRMD:Addgene_26790). Retrovirus was created using standard protocols and introduced into U87 cells. Briefly, viruses were harvested at 48 and 72 h, cleared of cell debris. To establish the stable U87-H2GFP cell line, monolayers were subjected to 2 rounds of infection. After retroviral transduction, GFP-positive cells were sorted by FACS, collected for amplification and maintained with puromycin (1 $\mu g/ml$). For neurosphere induction, U87 GBM cells were grown to 90% confluence, trypsinized, and plated in ultra-low adhesion multi-well plates (Corning) in neural stem cell (NSC) medium or DMEM F12 supplemented with B27, N2, 20 ng/ml bFGF, 20 ng/ml EGF, 2 mM L-glutamine, 2 mM non-essential amino acids, 50 U/ml penicillin/streptomycin (Sigma, USA). After 5 days, the number of spheroids was quantified using 10× magnifications under a phase contrast microscope (Carl-Zeiss, AxioObserverZ1), an AxioCam(HRm) camera (Carl-Zeiss, Germany) and Zen pro2011. It is considered a spheroid, a cell cluster bigger than 40 μm in diameter (Sart et al., 2017; Bodgi et al., 2019).

4.2. Migration Assays, Migration Inhibition, and Microscopy

Twelve well plates were coated with 400 μl of LDEV-Free Reduced Growth Factor Geltrex (Invitrogen), adding 1 ml of serum-free fresh medium with spheroids in suspension on top. After half an hour, spheroids were attached to the coating. Bright field images were taken every 10 min for 24 h in a Zeiss AxioObserverZ1 inverted microscope with Live Imaging System.

To inhibit migration the process was the same as described above, but Akt1 inhibitor MK-2206 (Cayman Chemical #11593) was added to the fresh medium. A concentration of 7 μM was used to inhibit migration, without altering proliferation and cell viability as described before (Jin et al., 2013). Control experiments were performed with the vehicle, DMSO in this case. To determine cell's diffusion coefficient a low-density monolayer was cultured in the same conditions as the spheroids, with MK-2206 and the vehicle.

Registration in all cases was performed using 10× magnification under a phase contrast microscope (Carl-Zeiss, AxioObserverZ1) with Live Imaging system, an AxioCam(HRm) camera (Carl-Zeiss, Germany) and Zen pro2011. Bright field and fluorescent images were obtained every 10 min for 24 h.

4.3. Image and Statistical Analysis

Analysis of time-lapses was performed in a custom built Python pipeline and Fiji (Schindelin et al., 2012). First, a binary segmentation based on Otsu's criteria was performed after a Gaussian filtering using the Scikit-Image library (van der Walt et al., 2014) on the bright field images. Morphological parameters, such as the centroid and diameter were extracted from these binary images. Fluorescent nuclei positions were tracked using the Fiji plugin TrackMate (Tinevez et al., 2017). The radial position from the centroid was quantified for each cell in the spheroid, averaged and normalized to obtain the mean relative radial migration

$$meanRRM(t_j) = \frac{\langle\sqrt{(x_i(t_j)-x_c)^2+(y_i(t_j)-y_c)^2}\rangle_i}{\langle\sqrt{(x_i(t_0)-x_c)^2+(y_i(t_0)-y_c)^2}\rangle_i},$$

where $x_i(t), y_i(t)$ is the position of the ith-cell at each time-point and x_c, y_c is the centroid of the spheroid. Note that the average is over the number of cells and not over time.

In single cells, the diffusion coefficient was calculated from single trajectories as

$$d_{cell} = \frac{1}{4T}\sum_{j=1}^{N}[(x(t_j)-x(t_{j-1}))^2+(y(t_j)-y(t_{j-1}))^2],$$

where T is the total duration of the trajectory and N is the total amount of time-points. Then, d_{cell} values for all cells were averaged to obtain D_{Cell}. To analyze the data, Pandas package was used (McKinney, 2010). The statistical test used was the non-parametric Kolmogorov-Smirnov analysis to compare cumulative distributions.

4.4. Mathematical Modeling

A discrete approach was used to simulate the cell clusters. Basically, a squared lattice, represented by a matrix N, was filled with zeros (for empty spaces) and ones (for occupied spaces). The squared lattice has cells of the same size than the actual U87 cells average size, in this case, 10 μm. Consistently, dimensionless quantities were only considered in the matrix. Then, N is a $m \times m$ matrix, being m an appropriate size for the cells to migrate without reaching the borders. In this case, $m = 200$ (which is equal to 2,000 μm) was considered enough. The initial condition for $N(t = 0)$ is a $d \times d$ cluster ($d << m$) of one values centered in the matrix, surrounded by zero values. The value of d will vary from 5 to 15 approximately (50–150 μm), which is the range of the real diameters of the spheroids. The approach is two-dimensional in the vertical and horizontal axes (y and x, respectively), represented by i and j matrix indexes (rows and columns).

The evolution of this matrix will be computed based on four different biological actuators considered of relevance after analyzing the experimental results. The first one is random movement or Brownian motion of the cells. The second one is the chemotaxis generated by some chemo-attractant/repellent factor segregated by the cells. Finally, mechanical interaction between the cells will be considered. With these three processes, a probability matrix $P \in \Re^{3\times3}$ will be calculated for each cell in the grid. That matrix will represent the probability of the cell to remain in the same place ($P_{[2,2]}$) or moving to a neighboring space. After selecting the direction of movement, the cell will move toward that space only if it is free, and will remain in the same space if it is occupied. Cells can also proliferate with a given probability α, and in that case, they will not move. After obtaining the new matrix $N(t = dt)$, the process starts again (see **Figure 4B**).

The time step dt should reflect the time in which one cell is able to move its own diameter. In other words, it is linked with its diffusion coefficient directly. In this case, it was determined to be ∼7 min. To move forward a dimensionless quantity, we defined the total unity of time as 24 h. Then, $dt = 7min/24h \sim 0.0048$. We could have considered a unity of time of 12 h, but it would have an influence on the stability of the chemotaxis equation (see section 4.4.2) restricting the diffusion constant D and it would have doubled the computing time.

Using a processor Intel(R) Core(TM) i7-6500U and 8 GB of RAM, reproducing a complete experiment (a total of 24 spheroids of different sizes) took 10 min.

4.4.1. Random Movement

The random component of the probability matrix for all the cells will be a Gaussian kernel $G \in \Re^{3\times3}$ with standard deviation $\sigma = 2$ spaces. The central value of this matrix $G_{[2,2]}$ was set to zero, so the cell is enhanced to move away, and the rest is re-normalized so

$$\sum_{k,l} G_{[k,l]} = 1.$$

4.4.2. Chemotaxis

The movement of a single cell toward the direction of a chemical gradient is called chemotaxis. If the chemical is an attractant, the cell will move toward the positive gradient. But, if it is a repellent factor, the cell will move toward the negative gradient. Based on the approach used in Charteris and Khain (2014), we also describe the chemical concentration in a discrete squared lattice, represented by the matrix U. The evolution of the chemical concentration in two dimensions is ruled by the differential equation

$$\frac{\partial u}{\partial t} = D\frac{\partial^2 u}{\partial x^2} + D\frac{\partial^2 u}{\partial y^2} + c_1 n - c_2 nu,$$

where u and n are continuous variables describing the chemical and cell concentration, $D = D_{chem}/D_{cell}$ is the dimensionless diffusion coefficient, c_1 is the generation constant, and c_2 is the degradation constant. In this case the production term is proportional to the concentration of cells, because the chemical is being produced by the cells, and the degradation term is proportional to the concentration of the chemical.

The initial condition is $u = 0$ in all the space, and the way to proceed is to solve the differential equation using the initial cell concentration to find $u(t = dt)$. But we have a discrete N so, in order to solve the equation, we performed finite differences to find the discrete chemical concentration U, a matrix with the same size as N. At the end, we obtained

$$U[t + dt] = MU[t] + U[t]M + c_1 dtN[t] - c_2 dtU[t] * N[t]$$

where dt is the discrete time.

M is a tridiagonal matrix given by

$$M = \begin{pmatrix} \frac{1}{2}\Delta & \lambda & 0 & \dots & 0 \\ -\lambda & \frac{1}{2}\Delta & \lambda & \dots & 0 \\ \vdots & \vdots & \vdots & \ddots & \vdots \\ 0 & 0 & 0 & \dots & \frac{1}{2}\Delta \end{pmatrix},$$

where $\Delta = 1 - 4\lambda$, $\lambda = Ddt/h^2$ and h is the discrete step in length ($h = 1$, in this case). The condition for the stability of the solutions is $dt \leq h^2/2D$.

In each iteration, the cell will sense the neighboring chemical concentration in both directions and compute the weighted gradient

$$\mu_x = \frac{U_{[i,j+1]} - U_{[i,j-1]}}{(1 + 3u)^2}$$

$$\mu_y = \frac{U_{[i+1,j]} - U_{[i-1,j]}}{(1 + 3u)^2}.$$

The equation reflects how the chemotaxis effect is lower for higher concentrations of the chemical, which produces a saturation of the cell membrane receptors. Also, we can see how the effect is larger for higher gradients.

In the end, the probability of moving toward the gradient is given by $|\mu|$. And thus, the probability matrix C will be filled with zero values except for the index with maximum gradient modulus.

4.4.3. Mechanical Interaction

Based on observations of the collective behavior of the cells in the spheroids, a mechanical interaction between cells was added. In this case, cells can interact with the first neighbors by performing a convolution between N and a 3×3 matrix O filled with ones. The size of the matrix filled with ones should be changed in order to consider further neighbor interactions. After convolving N and O, we cut the matrix in small 3×3 matrices around each occupied space. To avoid the simulated cells to interact with themselves, we subtract the matrix O and normalize to obtain $I \in \Re^{3\times3}$, a map of forces at first neighbors.

4.4.4. Proliferation

A probability per unit of time α can be assigned to consider proliferation. In this case, for each iteration and cell, the algorithm will decide whether if proliferation will take place or the cell is going to move. If it chooses to proliferate, then a free space must be available. The mother cell will remain still and a daughter cell will be assigned randomly to one of the free neighboring spaces. The proliferation probability is associated with the life cycle (∼19–30 h). Then, the probability per unit of time, considering our time step, is the ratio step/cycle ∼0.004–0.006.

In our scenario, not all the cells are proliferative. Only around 15–20 % of the cells will divide. Then we have to calculate the joint probability of the cells to be proliferative and undergo division per unit of time. In other words, we had to calculate

$$\alpha = P(A \cap B) = P(A|B)P(B)$$

where A represents the process of dividing and B represents a proliferative cell. Then, considering $P(A|B) = 0.004 - 0.006$ and $P(B) = 0.15 - 0.2$, we obtained $\alpha = 0.0007 - 0.001$.

4.4.5. Complete Model

All the interactions and processes described above can be switched on and off. When they act at the same time, the combined probability matrix for each cell is given by $P' = r * G + c_f * C + q * I$. The parameters r and q are numbers between 0 and 1 indicating the proportion of influence of the random motion to the total probabilities and strength of mechanical interactions between cells. While c_f is the chemotaxis coefficient, that indicates the nature ($c_f < 0$ if repellent, > 0 if attractant) and strength of the chemical. In all the simulations $r = 1$ unless specified otherwise. Finally, P' is normalized to obtain P. Be aware that if only random movement is taking place, the last normalization is not needed.

DATA AVAILABILITY STATEMENT

The raw data supporting the conclusions of this article will be made available by the authors, without undue reservation. Code is available at: https://github.com/hgrecco/ca-migration.

AUTHOR CONTRIBUTIONS

MC, CP-C, and HG designed the experiments, discussed the model, and wrote the paper. MC and LC performed the experiments and acquired the data. MC and HG performed the data analysis, implemented the computational code, and run the simulations. All authors reviewed and edited the paper.

FUNDING

This work was supported by Agencia Nacional de Promoción Científica y Técnica, Argentina (ANPCyT), PICT 2016-4201, Consejo Nacional de Investigaciones Científicas y Técnicas (CONICET), for financial support of researchers and students, FOCEM-Mercosur (COF 03/11), and The Pew Latin American Fellows Program for the repatriation award to CP-C.

ACKNOWLEDGMENTS

We thank Alejandra Atorresi and Sergio Senin (IBioBA-MPSP-CONICET, Buenos Aires, Argentina) for their technical assistance. We thank Agustín Corbat, Vasanthanarayan Murugesan, and Luka Jarc for the helpful discussions. We also thank Consejo Nacional de Investigaciones Científicas y Técnicas (CONICET), for financial support of researchers and students, FOCEM-Mercosur (COF 03/11), The Pew Latin American Fellows Program for the repatriation award to CP-C, and MPG Partner Group.

SUPPLEMENTARY MATERIAL

The Supplementary Material for this article can be found online at: https://www.frontiersin.org/articles/10.3389/fcell.2020.615759/full#supplementary-material

Supplementary Video 1 | Smaller spheroids under migration assay show high cell movement away from colony.

Supplementary Video 2 | Larger spheroids remain clustered and few cells detached during migration assay.

Supplementary Video 3 | Some cells show mechanical interactions and migrate collectively, attached to each other.

Supplementary Video 4 | Some cells change their migration direction, re-clustering after several hours of migration.

REFERENCES

Aaberg-Jessen, C., Nørregaard, A., Christensen, K., Pedersen, C., Andersen, C., and Kristensen, B. (2013). Abstract 4305: invasion of primary glioma- and cell line-derived spheroids implanted into corticostriatal slice cultures. *Int. J. Clin. Exp. Pathol.* 6, 546–560. doi: 10.1158/1538-7445.AM2011-4305

Andriesse, C., and Hollestelle, M. (2001). Minimum entropy production in photosynthesis. *Biophys. Chem.* 90, 249–253. doi: 10.1016/S0301-4622(01)00146-6

Bao, Z., Chen, K., Krepel, S., Tang, P., Gong, W., Zhang, M., et al. (2019). High glucose promotes human glioblastoma cell growth by increasing the expression and function of chemoattractant and growth factor receptors. *Transl. Oncol.* 12, 1155–1163. doi: 10.1016/j.tranon.2019.04.016

Bodgi, L., Bahmad, H. F., Araji, T., Al Choboq, J., Bou-Gharios, J., Cheaito, K., et al. (2019). Assessing radiosensitivity of bladder cancer *in vitro*: a 2D vs. 3D approach. *Front. Oncol.* 9:153. doi: 10.3389/fonc.2019.00153

Charteris, N., and Khain, E. (2014). Modeling chemotaxis of adhesive cells: stochastic lattice approach and continuum description. *New J. Phys.* 16:025002. doi: 10.1088/1367-2630/16/2/025002

Cliffe, A., Doupe, D., Sung, H., Lim, I., Ong, K. H., Cheng, L., et al. (2017). Quantitative 3D analysis of complex single border cell behaviors in coordinated collective cell migration. *Nat. Commun.* 8:14905. doi: 10.1038/ncomms14905

Dirkse, A., Golebiewska, A., Buder, T., Nazarov, P., Muller, A., Poovathingal, S., et al. (2019). Stem cell-associated heterogeneity in glioblastoma results from intrinsic tumor plasticity shaped by the microenvironment. *Nat. Commun.* 10:1787. doi: 10.1038/s41467-019-09853-z

Djuzenova, C., Fiedler, V., Memmel, S., Katzer, A., Sisario, D., Brosch, P., et al. (2019). Differential effects of the akt inhibitor mk-2206 on migration and radiation sensitivity of glioblastoma cells. *BMC Cancer* 19:299. doi: 10.1186/s12885-019-5517-4

Ferreyra-Solari, N. E., Belforte, F. S., Canedo, L., Videla-Richardson, G. A., Espinosa, J. M., Rossi, M., et al. (2016). The NSL chromatin-modifying complex subunit Kansl2 regulates cancer stem-like properties in glioblastoma that contribute to tumorigenesis. *Cancer Res.* 76, 5383–5394. doi: 10.1158/0008-5472.CAN-15-3159

Friedmann-Morvinski, D. (2014). Glioblastoma heterogeneity and cancer cell plasticity. *Crit. Rev. Oncog.* 19, 327–336. doi: 10.1615/CritRevOncog.2014011777

Fuert, R. (1920). Die brownsche bewegung bei bercksichtigung einer persistenz der bewegungsrichtung. mit anwendungen auf die bewegung lebender infusorien. *Z. Phys.* 2, 244–256. doi: 10.1007/BF01328731

Gupta, P., Fillmore, C., Jiang, G., Shapira, S., Tao, K., Kuperwasser, C., et al. (2011). Stochastic state transitions give rise to phenotypic equilibrium in populations of cancer cells. *Cell* 146, 633–644. doi: 10.1016/j.cell.2011.07.026

Hatzikirou, H., Deutsch, A., Schaller, C., Simon, M., and Swanson, K. (2005). Mathematical modeling of glioblastoma tumour development: a review. *Math. Models Methods Appl. Sci.* 15, 1779–1794. doi: 10.1142/S0218202505000960

Hillen, T., and Painter, K. J. (2008). A user's guide to pde models for chemotaxis. *J. Math. Biol.* 58:183. doi: 10.1007/s00285-008-0201-3

Jin, R., Nakada, M., Teng, L., Furuta, T., Sabit, H., Hayashi, Y., et al. (2013). Combination therapy using notch and AKT inhibitors is effective for suppressing invasion but not proliferation in glioma cells. *Neurosci. Lett.* 534, 316–321. doi: 10.1016/j.neulet.2012.12.008

Kansal, A., Torquato, S., GR, I., Chiocca, E., and Deisboeck, T. (2000). Simulated bain tumor growth dynamics using a three-dimensional cellular automaton. *J. Theor. Biol.* 203, 367–82. doi: 10.1006/jtbi.2000.2000

Keller, E. F., and Segel, L. A. (1971). Model for chemotaxis. *J. Theor. Biol.* 30, 225–234. doi: 10.1016/0022-5193(71)90050-6

Khain, E., Sander, L., and Stein, A. (2005). A model for glioma growth. *Complexity* 11, 53–57. doi: 10.1002/cplx.20108

Kim, Y., Lawler, S., Nowicki, M. O., Chiocca, E. A., and Friedman, A. (2009). A mathematical model for pattern formation of glioma cells outside the tumor spheroid core. *J. Theor. Biol.* 260, 359–371. doi: 10.1016/j.jtbi.2009.06.025

Lenting, K., Verhaak, R., ter Laan, M., Wesseling, P., and Leenders, W. (2017). Glioma: experimental models and reality. *Acta Neuropathol.* 133, 263–282. doi: 10.1007/s00401-017-1671-4

Li, P., Feng, J., Liu, Y., Liu, Q., Fan, L., Liu, Q., et al. (2017). Novel therapy for glioblastoma multiforme by restoring LRRC4 in tumor cells: LRRC4 inhibits tumor-infitrating regulatory T cells by cytokine and programmed cell death 1-containing exosomes. *Front. Immunol.* 8:1748. doi: 10.3389/fimmu.2017.01748

Manini, I., Caponnetto, F., Bartolini, A., Ius, T., Mariuzzi, L., Di Loreto, C., et al. (2018). Role of microenvironment in glioma invasion: what we learned from *in vitro* models. *Int. J. Mol. Sci.* 19:147. doi: 10.3390/ijms19010147

McKinney, W. (2010). "Data structures for statistical computing in python," in *Proceedings of the 9th Python in Science Conference*, eds S. van der Walt and J. Millman, 51–56. doi: 10.25080/Majora-92bf1922-00a

Minata, M., Audia, A., Shi, J., Lu, S., Bernstock, J., Pavlyukov, M. S., et al. (2019). Phenotypic plasticity of invasive edge glioma stem-like cells in response to ionizing radiation. *Cell Rep.* 26, 1893–1905.e7. doi: 10.1016/j.celrep.2019.01.076

Nakada, M., Kita, D., Teng, L., Pyko, I. V., Watanabe, T., Hayashi, Y., et al. (2013). Receptor tyrosine kinases: principles and functions in glioma invasion. *Adv. Exp. Med. Biol.* 986, 143–170. doi: 10.1007/978-94-007-4719-7_8

Narayan, R. S., Fedrigo, C. A., Brands, E., Dik, R., Stalpers, L. J. A., Baumert, B. G., et al. (2017). The allosteric AKT inhibitor MK2206 shows a synergistic interaction with chemotherapy and radiotherapy in glioblastoma spheroid cultures. *BMC Cancer* 17:204. doi: 10.1186/s12885-017-3193-9

Øyaas, J., Storrø, I., Svendsen, H., and Levine, D. W. (1995). The effective diffusion coefficient and the distribution constant for small molecules in calcium-alginate gel beads. *Biotechnol. Bioeng.* 47, 492–500. doi: 10.1002/bit.260470411

Prager, B. C., Xie, Q., Bao, S., and Rich, J. N. (2019). Cancer stem cells: the architects of the tumor ecosystem. *Cell Stem Cell* 24, 41–53. doi: 10.1016/j.stem.2018.12.009

Puliafito, A., Simone, A. D., Seano, G., Gagliardi, P. A., Blasio, L. D., Chianale, F., et al. (2015). Three-dimensional chemotaxis-driven aggregation of tumor cells. *Sci. Rep.* 5:15205. doi: 10.1038/srep15205

Rodríguez-Lozano, D. C., Piña-Medina, A. G., Hansberg-Pastor, V., Bello-Alvarez, C., and Camacho-Arroyo, I. (2019). Testosterone promotes glioblastoma cell proliferation, migration, and invasion through androgen receptor activation. *Front. Endocrinol.* 10:16. doi: 10.3389/fendo.2019.00016

Rubenstein, B. M., and Kaufman, L. J. (2008). The role of extracellular matrix in glioma invasion : a cellular potts model approach. *Biophys. J.* 95, 5661–5680. doi: 10.1529/biophysj.108.140624

Sart, S., Tomasi, R., Amselem, G., and Baroud, C. (2017). Multiscale cytometry and regulation of 3D cell cultures on a chip. *Nat. Commun.* 8:469. doi: 10.1038/s41467-017-00475-x

Schindelin, J., Arganda-Carreras, I., Frise, E., Kaynig, V., Longair, M., Pietzsch, T., et al. (2012). Fiji: an open-source platform for biological-image analysis. *Nat. Methods* 9, 676–682. doi: 10.1038/nmeth.2019

Stieber, D., Golebiewska, A., Evers, L., Lenkiewicz, E., Brons, N. H. C., Nicot, N., et al. (2014). Glioblastomas are composed of genetically divergent clones with distinct tumourigenic potential and variable stem cell-associated phenotypes. *Acta Neuropathol.* 127, 203–219. doi: 10.1007/s00401-013-1196-4

Stupp et al., R. (2005). Radiotherapy plus concomitant and adjuvant temozolomide for glioblastoma. *N. Engl. J. Med.* 352, 987–996. doi: 10.1056/NEJMoa043330

Swanson, K. R., Jr, E. C. A., and Murray, J. D. (2000). A quantitative model for differential motility of gliomas in grey and white matter. *Cell Prolif.* 33, 317–329. doi: 10.1046/j.1365-2184.2000.00177.x

Tanaka, M. L., Debinski, W., and Puri, I. K. (2009). Hybrid mathematical model of glioma progression. *Cell Prolif.* 42, 637–646. doi: 10.1111/j.1365-2184.2009.00631.x

Tektonidis, M., Hatzikirou, H., Chauvi, A., Simon, M., Schaller, K., and Deutsch, A. (2011). Identification of intrinsic *in vitro* cellular mechanisms for glioma invasion. *J. Theor. Biol.* 287, 131–147. doi: 10.1016/j.jtbi.2011.07.012

Tinevez, J.-Y., Perry, N., Schindelin, J., Hoopes, G. M., Reynolds, G. D., Laplantine, E., et al. (2017). Trackmate: an open and extensible platform for single-particle tracking. *Methods* 115, 80–90. doi: 10.1016/j.ymeth.2016.09.016

van der Walt, S., Schönberger, J. L., Nunez-Iglesias, J., Boulogne, F., Warner, J. D., Yager, N., et al. (2014). Scikit-image: image processing in Python. *PeerJ* 2:e453. doi: 10.7717/peerj.453

Wang, J., Cazzato, E., Ladewig, E., Frattini, V., Rosenbloom, D., Zairis, S., et al. (2016). Clonal evolution of glioblastoma under therapy. *Nat. Genet.* 48, 768–776. doi: 10.1038/ng.3590

Conflict of Interest: The authors declare that the research was conducted in the absence of any commercial or financial relationships that could be construed as a potential conflict of interest.

frontiers in Cell and Developmental Biology

ORIGINAL RESEARCH
published: 14 January 2021
doi: 10.3389/fcell.2020.591011

Cell Proliferation and Collective Cell Migration During Zebrafish Lateral Line System Development Are Regulated by Ncam/Fgf-Receptor Interactions

*Ramona Dries, Annemarie Lange, Sebastian Heiny, Katja I. Berghaus, Martin Bastmeyer and Joachim Bentrop**

Zoological Institute, Cell- and Neurobiology, Karlsruhe Institute of Technology (KIT), Karlsruhe, Germany

The posterior lateral line system (pLLS) of aquatic animals comprises small clustered mechanosensory organs along the side of the animal. They develop from proneuromasts, which are deposited from a migratory primordium on its way to the tip of the tail. We here show, that the Neural Cell Adhesion Molecule Ncam1b is an integral part of the pathways initiating and regulating the development of the pLLS in zebrafish. We find that morpholino-knockdowns of *ncam1b* (i) reduce cell proliferation within the primordium, (ii) reduce the expression of Fgf target gene *erm*, (iii) severely affect proneuromast formation, and (iv) affect primordium migration. Ncam1b directly interacts with Fgf receptor Fgfr1a, and a knockdown of *fgfr1a* causes similar phenotypic changes as observed in *ncam1b*-morphants. We conclude that Ncam1b is involved in activating proliferation by triggering the expression of *erm*. In addition, we demonstrate that Ncam1b is required for the expression of chemokine receptor Cxcr7b, which is crucial for directed primordial migration. Finally, we show that the knockdown of *ncam1b* destabilizes proneuromasts, suggesting a further function of Ncam1b in strengthening the cohesion of proneuromast cells.

Keywords: NCAM, proliferation, zebrafish, lateral line system, developmental biology, FGFR

OPEN ACCESS

Edited by:
Vladimir Sytnyk, University of New South Wales, Australia

Reviewed by:
René-Marc Mège, Centre National de la Recherche Scientifique (CNRS), France
Zhizhan Gu, Albert Einstein College of Medicine, United States

****Correspondence:***
Joachim Bentrop
joachim.bentrop@kit.edu

Specialty section:
This article was submitted to Cell Adhesion and Migration, a section of the journal Frontiers in Cell and Developmental Biology

Received: *03 August 2020*
Accepted: *24 November 2020*
Published: *14 January 2021*

Citation:
Dries R, Lange A, Heiny S, Berghaus KI, Bastmeyer M and Bentrop J (2021) Cell Proliferation and Collective Cell Migration During Zebrafish Lateral Line System Development Are Regulated by Ncam/Fgf-Receptor Interactions. Front. Cell Dev. Biol. 8:591011. doi: 10.3389/fcell.2020.591011

INTRODUCTION

The zebrafish posterior lateral line system (pLLS) is a unique model for studying collective cell migration as well as axonal outgrowth and pathfinding during development of a sensory organ (Metcalfe et al., 1985; Kimmel et al., 1995; Gilmour et al., 2002; Dambly-Chaudière et al., 2007; Aman and Piotrowski, 2008; Lush and Piotrowski, 2014; Romero-Carvajal et al., 2015). Its development starts with the formation of the posterior primary primordium (PrimI), which arises from the disintegration of the posterior primary sensory placode (Gompel et al., 2001; Nikaido et al., 2017). PrimI migrates along the horizontal myoseptum and deposits up to 6 proneuromasts before reaching the tip of the tail at 48 hpf (Gompel et al., 2001; Lecaudey et al., 2008). Deposited proneuromasts differentiate into neuromasts, the sensory organs of the pLLS. Cell-cell interactions in the primordium initiate three major events of PrimI development: (i) Cell proliferation on the one hand takes place in the posterior, leading part (Leading-Zone) where it is driven by expression of the Wnt target gene *lef1* (Aman et al., 2011). On the other hand, Fgfr1a signaling in the anterior,

trailing part (Trailing-Zone) has been identified as a key player for primordial proliferation (Aman et al., 2011). (ii) Directional collective cell migration is a consequence of the polarized expression of Cxcr4b and Cxcr7b in PrimI. These chemokine receptors enable PrimI to generate and sense a gradient of chemokine ligand Cxcl12a/Sdf1 which initially is uniformly expressed along the horizontal myoseptum (Knaut et al., 2003; Valentin et al., 2007; Boldajipour et al., 2008; Donà et al., 2013; Venkiteswaran et al., 2013; Nogare et al., 2014; Lau et al., 2020). Collective migration is mediated by cadherin-dependent adhesion between primordial cells (Colak-Champollion et al., 2019). (iii) Proneuromast formation in the Trailing-Zone is initiated by Fgf signaling. Under the influence of Fgf apically constricted rosettes of cells are established once a group of cells has evaded the influence of Wnt signaling in the Leading-Zone (Aman and Piotrowski, 2008; Lecaudey et al., 2008; Nechiporuk and Raible, 2008). Furthermore, Fgf activation initiates the specification of the centrally located hair cell, the first sensory cell of neuromasts (Lecaudey et al., 2008; Nechiporuk and Raible, 2008).

As we have discovered that Neural Cell Adhesion Molecule 1 (Ncam1) is expressed in the zebrafish pLLS (Langhauser et al., 2012), we intended to investigate its function during pLLS development. NCAM1 is a well-characterized glycoprotein of the immunoglobulin superfamily (IgSF). It is involved in regulating cell adhesion, cell proliferation and cell migration as well as neuritogenesis and plasticity in the adult nervous system (Hinsby et al., 2004). Consisting of five extracellular immunoglobulin-like (Ig) and two fibronectin (FN) domains, the extracellular part of NCAM1 can be involved in numerous homophilic and heterophilic interactions (Cunningham et al., 1987). Besides binding to various members of the IgSF mammalian NCAM1 displays a high binding affinity to Fibroblast Growth Factor Receptor 1 (FGFR1) (Saffell et al., 1994; Williams et al., 1994a,b,c). Interactions between NCAM1 and FGFR1 can occur within the same membrane (*cis*) and/or between two cells (*trans*) (Saffell et al., 1994; Williams et al., 1994a; Kiselyov et al., 2003; Francavilla et al., 2009; Christensen et al., 2011; Zamai et al., 2019). Like NCAM1, FGFR1 comprises three extracellular Ig-like domains with several ligand recognition sites (Johnson and Williams, 1993). The intracellular part of FGFR1 contains two tyrosine kinase domains with up to seven tyrosine residues (Beenken and Mohammadi, 2009).

Binding sites for interactions of NCAM1 and FGFR1 have been identified in the extracellular domains of the molecules (Williams et al., 1994a; Kiselyov et al., 2003; Christensen et al., 2011). Alternative splicing leads to the expression of two isoforms of FGFR1 (FGFR1-IIIb and –IIIc) which vary in the 3rd Ig-domain (Itoh and Ornitz, 2004; Li et al., 2010; Christensen et al., 2011) and bind to NCAM1 with different affinity. Upon binding, FGFR1 can activate various downstream signaling pathways. On the one hand, interaction with NCAM1 triggers the canonical FGFR1 signaling cascades activating PLCγ, PI3-Akt, or Ras-MAPK; it thereby promotes calcium influx and gene expression (Williams et al., 1992; Neiiendam et al., 2004; Anderson et al., 2005; Francavilla et al., 2009; Zamai et al., 2019). On the other hand, NCAM1 can elicit a FGFR1-mediated cellular response remarkably different from that initiated by binding of the FGF ligand. It induces the formation of FGFR1 complexes, which trigger Erk phosphorylation in a Src-dependent manner, whereas FGF binding triggers Erk phosphorylation via Ras (Zamai et al., 2019).

Due to a genome duplication in the teleost lineage, the zebrafish expresses two Ncam1 paralogs: Ncam1a and Ncam1b. These paralogs have subfunctionalized roles in embryonic development, as we have previously shown for the formation of the posterior commissure and for outgrowth, fasciculation and pathfinding of spinal motor axon bundles (Langhauser et al., 2012). In this study, we asked if Ncam1a and Ncam1b are also involved in the development of the zebrafish posterior lateral line system. We find that a knockdown of *ncam1b* severely affects the morphogenesis and the migration of PrimI. Ncam1b directly interacts with Fgfr1a, and a knockdown of *fgfr1a* causes similar phenotypic changes as observed in *ncam1b*-morphants. We identify Ncam1b as a novel factor involved in activating proliferation in the primordium, probably by triggering the expression of the Fgfr1a target gene *erm*. Finally, we show that Ncam1b is required for the expression of *cxcr7b,* which uncovers an as yet unknown function of Ncam1b in the directed migration of PrimI during pLLS development.

MATERIALS AND METHODS

Fish Strains and Animal Care

In all experiments we used the transgenic fish strain *Tg(ClaudinB::lynGFP)*, which was kindly given to us by Darren Gilmour (University of Zürich, CH) (Haas and Gilmour, 2006). Zebrafish were maintained at 28.5°C under standard conditions in a ZebTec system (Tecniplast; Buguggiate, Italy). Embryos were kept in standard embryo medium (E3) at 28.5°C for normal development. To obtain embryos at 36 hpf (hours post fertilization), eggs were incubated for 24 h at 28.5°C and for another 24 h at 25°C. Embryos were manually dechorionated with forceps after 24 hpf. Staging refers to Kimmel et al. (1995).

Morpholino and mRNA Injection

Morpholino or mRNA were pressure-injected into the yolk at the 1-cell stage. Morpholinos (Gene Tools, Oregon, USA) and mRNA (Langhauser et al., 2012) were used in the following concentrations per embryo: *standard control*-Mo (5′-CCTCTT ACCTCAGTTACAATTTATA-3′), same as that of the relevant knockdown-Mo; *ncam1b*-ATG-Mo (5′-AGATTATCGCCTTGG TCGGAAACAT-3′), 3 ng; *ncam1b*-ATG-5 mismatches-Mo (5′-ACATTATGGCCTTCGTCGCAAAGAT-3′), 3 ng; *ncam1b*-5′UTR-Mo (5′-GTTTACTGTTTGTTTTTGCCTTCCG-3′), 3 ng; p53-Mo (5′-GCGCCATTGCTTTGCAAGAATTG-3′), 3 ng; *ncam1a*-5′UTR-Mo (5′-TTCCGTGTAGAATAGGTAGA GTTGG-3′), 3 ng; *erm*-Mo (5′-GAGAAGCAAGCGACATGG ATGGGTT-3′), 5 ng; *fgfr1a*-Mo (5′-GCAGCAGCGTGG TCTTCATTATCAT-3′), 12 ng for 24 hpf and 18 ng for 48 hpf; *ncam1b*-mRNA, 0.3 ng (Langhauser et al., 2012).

Time-Lapse Imaging

Time-lapse imaging was performed beginning at 28 hpf in standard embryo medium (E3). Embryos were dechorionated with forceps, anesthetized in 0.01% MS-222 solution and finally embedded in 1.5% low melt agarose. Agarose was covered with a thin film of embryo medium containing 0.01% MS-222 to avoid evaporation. Images were taken every 15 min for a total duration of 17 h (1,020 min). Imaging was performed on a Zeiss Axiovert 200M with 10× magnification.

Immunostaining Zebrafish

Immunostaining was performed following zebrafish standard procedures as previously described (Marx et al., 2007). Ncam1a and Ncam1b were detected by rabbit anti-NCAM and anti-PCAM kindly provided by Yoshihiro Yoshihara (RIKEN Center for Brain Science, Japan) (both 1:1,000) and Zo-1 was detected by mouse Zo-1 (1:200; Fisher Scientific; Massachusetts, USA). After *in situ* hybridization, GFP intensity in *Tg(ClaudinB::lynGFP)* embryos was enhanced by using rabbit anti-GFP (1:1,000; abcam; Cambridge, GB), as indicated in the figure legends.

Embryos were subsequently placed in secondary antibody for 2 h at room temperature. For secondary antibody staining, Alexa488 (1:1,000; Molecular Probes; Oregon, USA) and cy3 (1:1,000; Dianova; Hamburg, Germany) were used as chromophors. Mounting was performed in Mowiol. Images were taken with ZEISS LSM510 and LSM800.

Whole-Mount *in situ* Hybridization

Whole-mount *in situ* hybridization was performed with DIG-labeled probes as described in Schulte-Merker et al. (1992) and Thisse and Thisse (2008). Probes were synthesized from plasmid DNA. For hybridization 2 ng/µl of each probe were used. Plasmid for *erm* (Scholpp et al., 2004) and *lef1* were kindly provided by Steffen Scholpp (University of Exeter, GB); *cxcr7b* (Dambly-Chaudière et al., 2007); and *cxcl12a* (Li et al., 2004) were kindly given by the lab of Tatjana Piotrowski (Stowers Institute, USA). Probe templates for *cxcr4b* (*forward*: 5′-ATGGAATTTTACGATAGCAT-3′; *reverse*: 5′-CTAACTCGTC AGTGCACTGG-3′) and *fgfr1a* (*forward*: 5′-TCAGATGTAG AGGATCTTTGATA-3′; *reverse*: 5′- ACACACACACTGAGTA AATGAGT-3′) were isolated and cloned from zebrafish cDNA. Afterwards embryos were stained with anti-GFP (1:1,000; abcam; Cambridge, GB) and DAPI (1:1,000; Carl Roth; Karlsruhe, Germany) and were embedded in Mowiol.

Western Blot Analysis

Siblings and morpholino injected embryos were deyolked and lysed in 1× SDS buffer. After heating and sonification cell lysates were cleared by centrifugation at 13,000 g for 5 min. Proteins (five embryos/lane) were resolved by SDS-PAGE and transferred to PVDF membranes. For protein detection antibodies against p53 (mouse; 1:250; abcam; Cambridge, GB), Ncam1b [rabbit; 1:4,000; Yoshihiro Yoshihara (RIKEN Center for Brain Science, Japan)] and acetylated tubulin (mouse; 1:4,000; Sigma-Aldrich; Missouri, USA) were used, followed by specific peroxidase-conjugated secondary antibodies (1:10,000). Super Signal West Pico PLUS Chemiluminescent Substrate (Fisher Scientific; Massachusetts, USA) was used for chemiluminescent visualization.

BrdU Assay

Embryos were chilled on ice in E3 medium for 15 min, followed by incorporation of 10 mM BrdU (Sigma-Aldrich; Missouri, USA) for 20 min on ice. Afterwards embryos were washed several times with pre-warmed E3 medium and were finally fixed with 4% PFA in PBS overnight at 4°C. Fixed embryos were stored in methanol at −20°C overnight. Permeabilization was performed by ProteinaseK treatment (10 µg/ml) for 10 min at room temperature, followed by a PBST wash step. Samples were treated with 2 N HCl for 1 h at 37°C. Finally, embryos were blocked in 1% BSA and incubated overnight with anti-BrdU (mouse; 1:100; abcam; Cambridge, GB) and anti-GFP (rabbit; 1:1,000; abcam; Cambridge, GB) at 4°C. On the next day embryos were washed with PBST and subsequently stained with secondary antibody [Alexa488; 1:1,000; (Molecular Probes; Oregon, USA), cy3; 1:1,000; (Jackson Immunoresearch; Pennsylvania, USA)] and DAPI (1:1,000; Carl Roth; Karlsruhe, Germany). Mounting was performed in Mowiol. For quantification BrdU-DAPI-positive cells within the primordium of all embryos were counted at a ZEISS LSM510.

Isolation of Fgfr1a-Isoforms and Expression Vectors

Fgfr1a isoforms were isolated from total zebrafish mRNA at different developmental stages. RNA was isolated by TriFAST (peqlab; Erlangen, Germany), mRNA was converted into cDNA by reverse transcription (Fisher Scientific; Massachusetts, USA) using Fgfr1a-specific primers (*forward*: 5′-TCAGATGTAGAGGATCTTTGATA-3′; *reverse*: 5′-ACTCATTTACTCAGTGTGTGTGT-3′). After amplification blunt-ended DNA was cloned into pCR-BluntII-TOPO (Thermo Scientific, Pittsburgh, USA).

For the expression of membrane-bound proteins, full coding sequences were cloned into the expression vector pcDNA 3.1 with Myc- and 6× His-Tag (Invitrogen; California, USA). *fgfr1a-w/o exon 7* was synthesized by Fusion-PCR excluding exon 7. The coding sequences for soluble proteins, which comprised only the extracellular parts of Ncam1 or Fgfr1a, were cloned into pcDNA 3.1 with hIgG-Fc-Tag (Rita Gerardy-Schahn, Hannover Medical School, Germany).

Cell Lines, Transfection, and Protein Purification

Overlay assays were performed using *CHO-K1* cells, which were cultured in DMEM with 10% FCS at 37°C in a humidified incubator. Cells were transfected with Lipofectamine2000 (Invitrogen; California, USA) according to the manufacturer′s instructions. Selection occured by antibiotic treatment with geneticin (750 µg/ml).

CHO-2A10 cells were used for expression of soluble proteins. To that end, transfected cells were incubated for 12 days in DMEM with 10% FCS and were selected by adding zeocin (750 µg/ml). After selection, cells were incubated for at least 4 weeks in OPTI-CHO medium containing 4 mM L-Glutamine.

Medium was collected by decanting and centrifugation; the resulting supernatant was stored at 4°C after adding 0.02% Thimerosal (Sigma-Aldrich; Missouri, USA) and Complete Protease Inhibitor (Roche; Basel, Switzerland). Medium was concentrated by Vivaflow2000 (Sartorius; Göttingen, Germany) and Fc-Tagged protein was captured by HiTrap ProteinG HP (GE Healthcare; Illinois, USA). Finally, the eluted protein was concentrated by Amicon Ultra (Merck; Darmstadt, Germany).

Overlay Assay and Immunostaining Cell Culture

CHO-K1 cells were transfected with expression vector pcDNA 3.1 Myc and 6× His-Tag containing complete coding sequence of either *ncam1a*, *ncam1b*, *fgfr1a-IIIb*, *fgfr1a-IIIc,* or *fgfr1a-w/o exon 7*. After antibiotic selection cells were seeded on fibronectin-coated coverslips (10 μg/ml) and cultured overnight. The next day, coverslips were incubated with 20 μg/ml of soluble protein for 1 h at room temperature. Unbound protein was removed by several wash steps. Cells were subsequently fixed with 4% PFA in PBS and treated with sodium borohydride to reduce double bounds. Permeabilization was performed with 0.1% PBST. Incubation with primary antibody anti-His (mouse; 1:400; abcam; Cambridge, GB) and anti-hFcγ (goat; 1:400; Jackson Immunoresearch; Pennsylvania, USA) was performed for 1 h at room temperature. After washing with PBS cells were incubated with secondary antibody [Alexa488 (1:1,000; Molecular Probes; Oregon, USA) and cy3 (1:1,000; Dianova; Hamburg, Germany)], DAPI (2 μg/ml; Carl Roth; Karlsruhe, Germany) and Phalloidin (13 U/ml; Life Technologies; California, USA). Images were taken with ZEISS Axio Imager.Z1 in the Apotome mode. To quantify the difference of Ncam1a/b binding to FGFR-transfected cells vs. the binding to untransfected cells, we first evaluated the efficiency of transfection of membrane-bound, His-tagged Fgfr1a using Fiji by ImageJ. Based on these data we calculated the ratio of the fluorescence intensities resulting from the binding of soluble Fc-tagged Ncam1a/b to transfected vs. non-transfected cells.

Co-immunoprecipitation

Hek293 cells were co-transfected with expression vector pcDNA3.1 Myc and 6× His-Tag containing complete coding sequences of *ncam1a* or *ncam1b*, respectively, and with expression vector pcDNA3.1 FLAG-Tag containing the complete coding sequence of *fgfr1a-IIIb* or *fgfr1a-IIIc*, respectively. Single transfections served as a control; to that end *Hek293* cells were transfected either with expression vector pcDNA3.1 Myc and 6× His-Tag containing the complete coding sequence of *ncam1b* or with expression vector pcDNA3.1 FLAG-Tag containing the complete coding sequence of *fgfr1a-IIIb*. After antibiotic selection cells were lysed in lysis buffer (Cell Signaling Technology, Massachusetts, USA). Cell lysates were incubated with an anti-His-antibody (rabbit; 1:100; abcam; Cambridge, GB) overnight. ProteinA beads (Cell Signaling Technology, Massachusetts, USA) were added at a final dilution of 1:10 and incubated by gently shaking at 4°C for 1.5 h. SDS-PAGE and Western Blot were performed following a modified *Laemmli* protocol (Laemmli, 1970). Each loaded sample contains the material of 100,000 cells. After SDS-PAGE, immunoprecipitates were immunoblotted with biotinylated FLAG-antibody (mouse; 1:800; Sigma-Aldrich; Missouri, USA), followed by HRP-conjugated streptavidin (1:6,000; Sigma-Aldrich; Missouri, USA). Band density (Intensity Density) was measured with Fiji by ImageJ for three independent experiments.

Bead Aggregation Assay

Bead aggregation assays were performed as described (Galuska et al., 2010). Fluorescent beads are pre-coated with ProteinA (Kisker Biotech; Steinfurt, Germany) and then incubated with 10 μg Fc-Tagged soluble protein of either Ncam1a, Ncam1b, Fgfr1a-IIIb, or Fgfr1a-IIIc. Controls were performed with soluble human Fc-fragment (Merck; Darmstadt, Germany). Formation of bead aggregation was observed after 24 h in uncoated γ-slides (ibidi; Gräfelfing, Germany) with ZEISS LSM510.

Sequence Analysis

Zebrafish sequences of Ncam1a, Ncam1b and Fgfr1a were compared with several mammalian and non-mammalian organisms by using CLC Sequence Viewer 8.0 (Qiagen Bioinformatics). For Ncam1 alignment (accession numbers are given in parentheses) the following sequences were used: *H. sapiens* (AAH47244.1), *M. musculus* (XP_006510118.1), *R. norvegicus* (XP_008764414.1), *G. gallus* (XP_015153520.1), *X. laevis* N1A (XP_018082333.1), *X. laevis* N1b (XP_018079824.1), *O. latipes* (XP_023818322.1), *Danio rerio* N1a (HM467818.1) and *Danio rerio* N1b (XP_005157462.1). For Fgfr1 alignment the subsequent sequences were used: *H. sapiens* (XP_006716366.1), *M. musculus* (AAA37620.1), *R. norvegicus* (NP_077060.1), *G. gallus* (XP_015152849.2), *X. laevis* (NP_001090457.1), *O. latipes* (XP_011477376.1), *Danio rerio* (IIIb-exon9(SS)) (MW358033), *Danio rerio* (IIIb-exon9(VT)) (MW358034) and *Danio rerio* (IIIc) (MW358035).

Quantification and Statistical Analysis

For measurements of primordia size and migration distance we used Fiji by ImageJ. For quantification of knockdown phenotypes in **Figure 1**, only those embryos where considered, which did not show expression of the specific protein as judged by immunostaining. For quantification in **Supplementary Figure S1** as well as in **Figure 5** and **Supplementary Figure S8** all embedded embryos were imaged and analyzed. Statistical analysis was done by Origin2019. Boxplots show the 25th and 75th percentiles with median (line inside the box) and mean value (square). The whiskers extend to the minimum and the maximum. Outlier are marked by black diamonds. Bar charts show mean values. For significance calculation we used Students *t*-test or X^2 analysis.

RESULTS

Ncam1 Paralogs Are Expressed in the Posterior Lateral Line System (pLLS)

The posterior lateral line primordium starts its migration around 24 hpf. It follows the horizontal myoseptum for the next 24 hours until it reaches the tip of the embryo′s tail (**Supplementary Videos 1**, **2**). During migration the primordium deposits proneuromasts, clusters of about 30 cells which

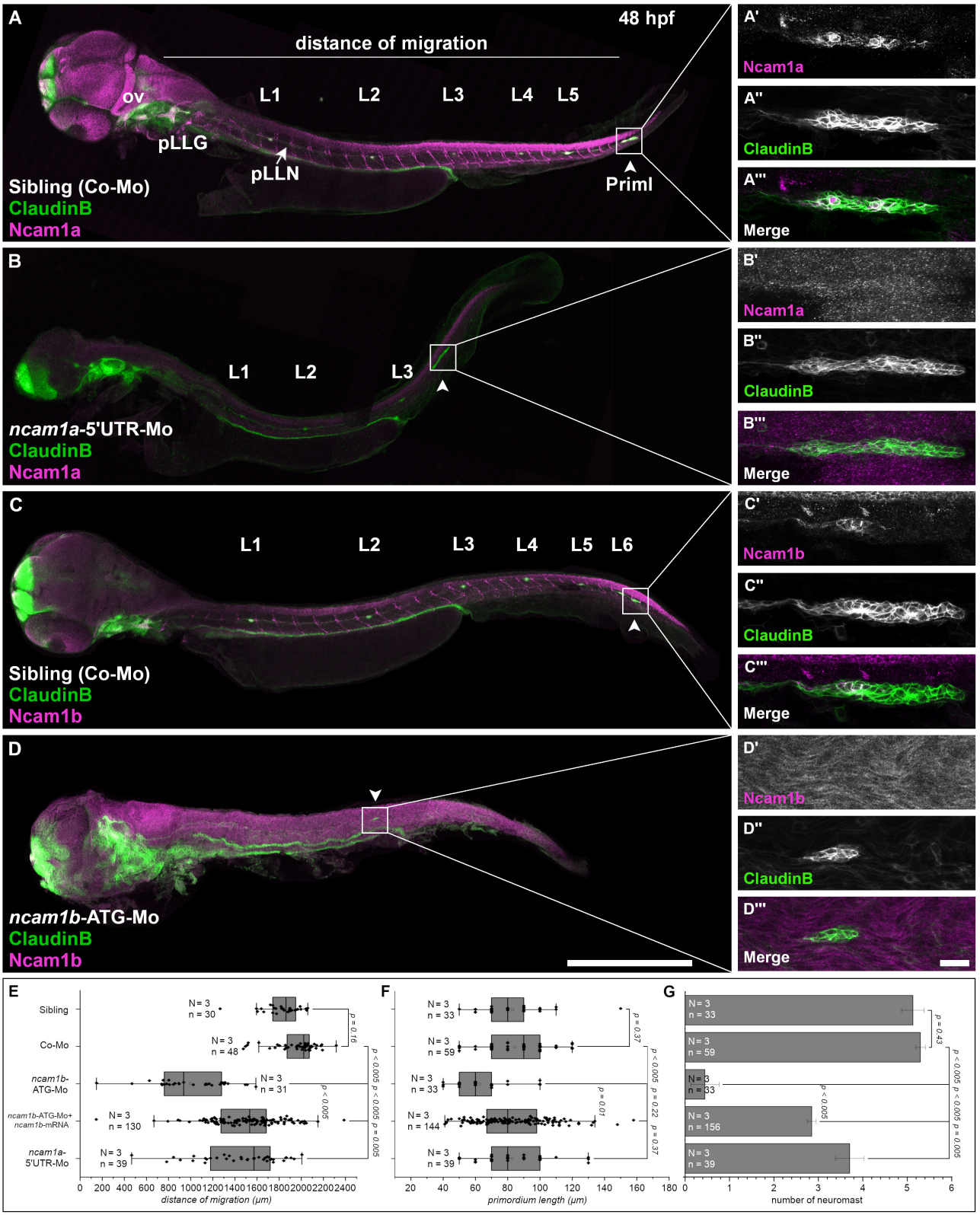

FIGURE 1 | Expression pattern and function of Ncam1 during development of the zebrafish lateral line system. **(A–D)** Lateral views of *Tg(ClaudinB::lynGFP)* (green) embryos (48 hpf) immunostained for Ncam1a or Ncam1b (magenta). **(A,C)** Control-Morpholino (Co-Mo) injected sibling; all structures (excluding interneuromast cells)

(Continued)

FIGURE 1 | of the lateral line system express Ncam1a and Ncam1b. (**A′-A‴,C′-C‴**) Ncam1a is expressed throughout the whole primordium (arrowhead), whereas Ncam1b is found only in the Trailing-Zone. **(B)** *ncam1a*-morphants show only weak migration defects and (**B′-B‴**) primordium length is not affected. (**D**) Morpholino-knockdown of *ncam1b* induces migration defects as well as a reduction in the number of deposited (pro)neuromasts. **(D′-D‴)** *ncam1b*-knockdown also results in a reduced primordium size. (**E,F,G**) Quantification of migration distance, primordium length and number of neuromasts in control and morpholino-injected embryos. Rescue mRNA was co-injected with the morpholino as indicated. Error bars represent standard deviation. Scale bars **(A,D)** 200 μm, **(D‴)** 20 μm. Abbreviations: Co-Mo, Control-Morpholino; L1-6, lateral (pro)neuromast; pLLG, lateral line ganglion; pLLN, lateral line nerve; ov, otic vesicle; PrimI, primary posterior primordium.

subsequently differentiate into mature neuromasts. As cell adhesion and cell communication play crucial roles during the collective and directional cell migration and for proneuromast deposition, we investigated the role of neural cell adhesion molecule Ncam1 in this process. We find, that both zebrafish paralogs of Ncam1, namely Ncam1a and Ncam1b, are expressed during pLLS development (**Figures 1A,C**). Both are detectable in the lateral line ganglion (pLLG), the lateral line nerve (pLLN), neuromasts (L1-L6) as well as in the primordium. Notably, whereas Ncam1a is expressed by all cells of the primordium (**Figures 1A′–A‴**), Ncam1b is expressed only in the Trailing-Zone, but not in the Leading-Zone (**Figures 1C′–C‴**).

Ncam1b Is Necessary for Correct pLLS Development

To study the functions of both paralogs we performed morpholino-knockdowns. We find that a knockdown of *ncam1a* significantly affects pLLS development (**Figures 1B–B‴** and **Supplementary Video 3**) by reducing migration distance of the primordium and the number of deposited proneuromasts. The length of the primordium (PrimI) is not affected (**Figures 1E–G**). Knocking down *ncam1b* by using a morpholino that targets the ATG start codon region (Langhauser et al., 2012) causes significantly stronger phenotypic alterations of the developing pLLS (**Figures 1D–D‴**). Primordium length is drastically reduced (**Figures 1D′–D‴,F**) and the formation and deposition of proneuromasts are rarely observed (**Figure 1G**). Life imaging shows that only in some cases a single proneuromast is formed and deposited which then disintegrates rapidly (**Supplementary Video 4**). Migration of the primordium is also strongly affected (**Figure 1E**). In control-morpholino injected siblings the primordium reaches the tip of the tail at 48 hpf, whereas in *ncam1b*-morphants it reaches the end of the yolk extension at most (**Figure 1D**, **Supplementary Video 4**). In some cases, primordia deviate from their path along the horizontal myoseptum (see below). An increased background staining in immunohistochemistry after morpholino-knockdown of *ncam1b* is an unfortunate feature of the anti-PCAM antibody (see also Langhauser et al., 2012). This staining is unspecific, as the reduction of Ncam1b after morpholino injection is obvious in proven Ncam1b expression domains like the spinal cord, spinal motor axons and the primordium (compare **Figures 1C,D,C′,D′**; see also Western Blots in **Supplementary Figure S1D**). Co-injection of *ncam1b*-mRNA significantly mitigates the knockdown phenotype (**Figures 1E–G**).

Efficacy and paralog specificity of the used *ncam1b*-ATG-morpholino was already demonstrated by Langhauser et al. (2012) and we performed extensive additional control experiments to rule out potential off-target effects and to underpin the effectiveness of the morpholino knockdown. Injection of a second, non-overlapping 5′UTR-morpholino shows the same effects as the start codon morpholino (**Supplementary Figures S1**, **S2**). Phenotypes after injection of an unrelated control-morpholino and a mismatch-morpholino are indistinguishable from those of uninjected siblings (**Supplementary Figures S1A–C**). We rule out, that the reduced primordium size results from increased apoptosis, as co-injection of a p53-morpholino does not rescue the morpholino effect (**Supplementary Figures S1A–C**) and as we do not find an increase of p53 expression following morpholino injections (**Supplementary Figure S1D**). We find Ncam1b protein expression drastically reduced after injection of the start codon and the 5′UTR-morpholino, which is not the case after injection of control morpholinos (**Supplementary Figure S1D**).

Proliferation of Primordial Cells Is Reduced in *ncam1b*-Morphants

A reduction of primordia size and neuromast number in *ncam1b*-morphants could be explained by a reduced cell proliferation rate. Therefore, we performed BrdU incorporation assays. Embryos were treated with BrdU for 20 min and fixed. Cell proliferation in the primordia of 36 hpf uninjected siblings is detected in both Leading- and Trailing-Zones (**Figures 2C–C″**). Proliferation is severely decreased in *ncam1b*-morphants (**Figures 2A–A″**), which show a reduction of the number of BrdU-labeled cells by more than 90% (**Figure 2D**). A knockdown of *ncam1a* has no effect on cell division (**Figures 2B–B″**). These experiments indicate that Ncam1b is involved in primordial cell proliferation. It thereby affects primordium size as well as the formation of proneuromasts.

Ncam1b Drives Expression of Fgfr1a-Target Gene *erm*

It has been shown that primordial cell proliferation is mostly controlled by the Wnt-target gene *lef1* (Lecaudey et al., 2008; Gamba et al., 2010; Valdivia et al., 2011; Breau et al., 2013; Agarwala et al., 2015). We therefore analyzed *lef1* expression in *ncam1a*- and *ncam1b*-morphants by *in situ* hybridization. In 36 hpf uninjected siblings and *ncam1a*-morphants we detect *lef1* in the posterior one third of the primordium, which corresponds to the Leading-Zone (**Figures 3A′,A″**). Surprisingly, in *ncam1b*-knockdowns we observed an expanded *lef1* expression rather than a reduction (**Figure 3A**). While the knockdown primordium is somewhat smaller than its sibling counterpart, *erm* is expressed throughout the complete structure. Thus, Wnt signaling appears not to be suppressed in *ncam1b* morphants,

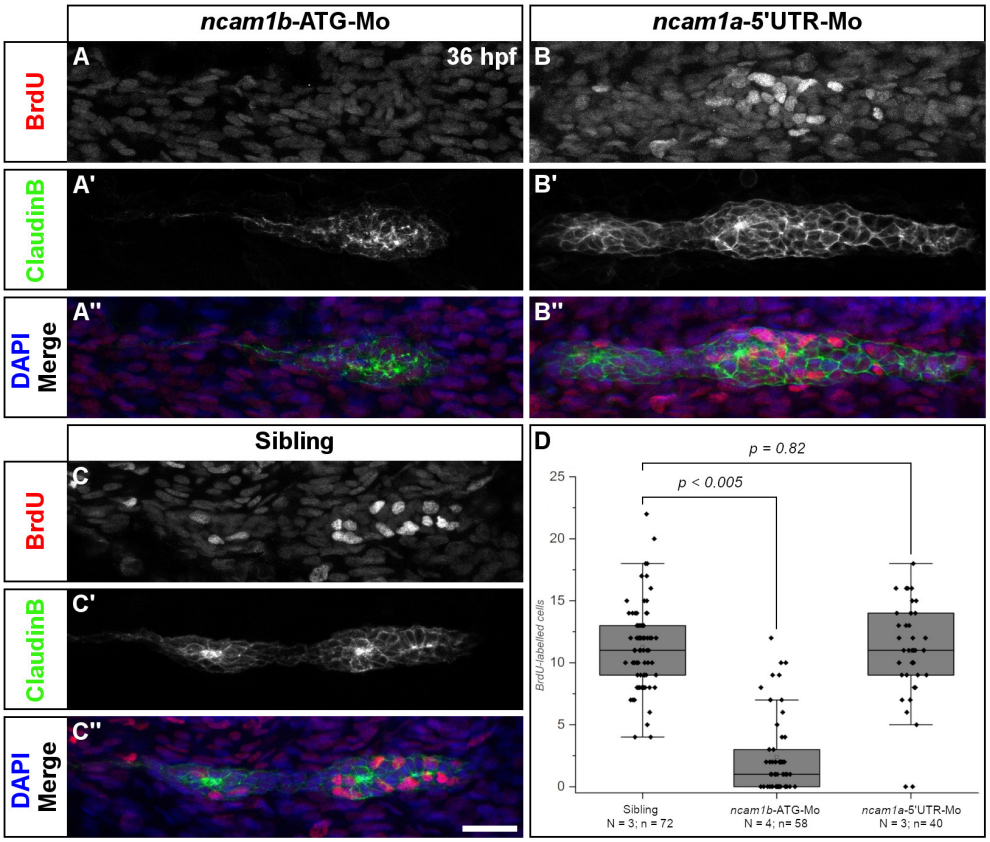

FIGURE 2 | Ncam1b is required for cell proliferation within the primordium. Siblings or morpholino-injected *Tg(ClaudinB::lynGFP)* embryos were treated with BrdU at 36 hpf for 20 min, fixed and immunostained for BrdU (red), GFP (green) and DAPI (blue) as indicated. **(A,A″)** BrdU incorporation is almost absent in *ncam1b*-morphants, but obvious in **(B,B″)** knockdowns of *ncam1a* and **(C,C″)** uninjected siblings. **(D)** Quantification of BrdU-labeled cells within primordia. Scale bar 20 μm.

which indicates that Wnt signaling pathways are not involved in the Ncam1b-dependent regulation of cell division.

Aman et al. (2011) had shown, that Wnt/β-catenin signaling acts in concert with signaling via the Fgf receptor Fgfr1a to promote cell division. Fgfr1a is expressed in the Trailing-Zone and an inhibition leads to a strong reduction in proliferation within the primordium (Aman et al., 2011). The relevant downstream signaling cascade has not yet been identified. We thus investigated Fgfr1a signaling by first analyzing the expression of *fgfr1a* by *in situ* hybridization. We could not detect differences in *fgfr1a* expression between uninjected siblings (**Figure 3B″**) and *ncam1a*-morphants (**Figure 3B′**). In *ncam1b*-morphants, despite an overall reduced primordium size, we still observe robust *fgfr1a* expression in the Trailing-Zone (**Figure 3B**). This implies that Leading- and Trailing-Zones are formed as distinct domains in *ncam1b*-morphants as well. Searching for a downstream target potentially involved in Fgfr1a-dependent proliferation, we next addressed the expression of the transcription factor Erm (Etv5b), which regulates proliferation and differentiation in mouse embryonic stem cells (Akagi et al., 2015). *In situ* hybridizations show *erm* expression within the primordial Trailing-Zone of 36 hpf uninjected siblings (**Figures 3C′,C″**) and *ncam1a*-morphants, where Fgfr1a is also expressed (**Figures 3B′,B″**). In *ncam1b*-morphants, however, we observed a strong reduction of *erm* within the primordia (**Figures 3C,D**). Other reported expression domains of *erm* (Roehl and Nüsslein-Volhard, 2001; Scholpp et al., 2004) like the midbrain-hindbrain boundary and the forebrain were not affected (**Supplementary Figure S3**). To test the role of Erm, we performed BrdU incorporation assays at 36 hpf after knockdown of *erm* (**Supplementary Figure S4**). Cell proliferation within the primordium is decreased, especially in the Trailing-Zone (**Supplementary Figures S4A,C**). These experiments suggest that Ncam1b and Fgfr1a, which are both expressed in the Trailing-Zone, act in the same pathway controlling cell proliferation by regulating the expression of *erm*.

Different Splice Variants of Fgfr1a Are Expressed in the Zebrafish Embryo

A direct interaction of NCAM1 with FGFR1 has already been observed in mammalian cell cultures, where it promotes neurite outgrowth (Williams et al., 1994a,b,c). Mammalian NCAM1 has different affinities for FGFR1 isoforms varying in the 3rd Ig-domain (Li et al., 2010; Christensen et al., 2011). To study an

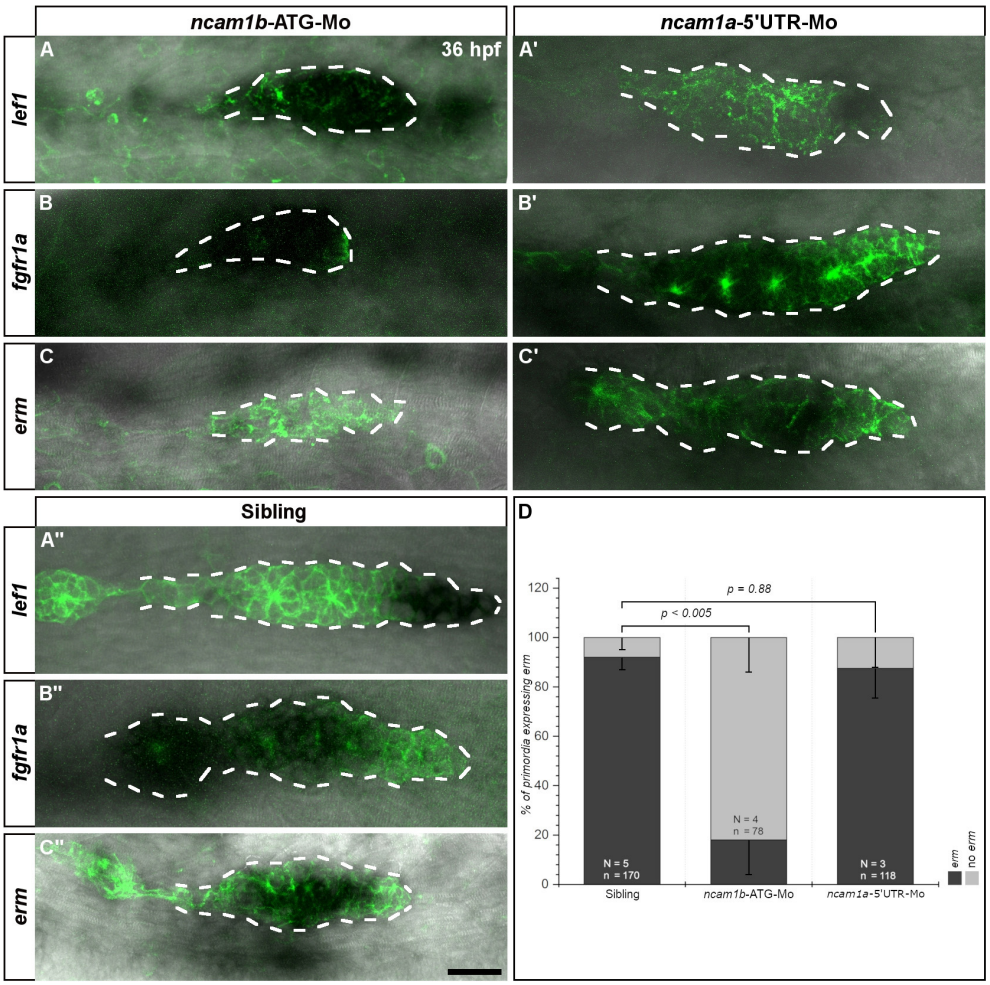

FIGURE 3 | Ncam1b affects the expression of the Fgfr1a-target gene *erm*. *Tg(ClaudinB::lynGFP)* embryos were immunostained labeled for GFP (green). *In situ* hybridizations of probes detecting *lef1* (Leading-Zone), *fgfr1a,* or *erm* (both in the Trailing-Zone) were visualized by NBT/BCIP staining. Primordia outlines are surrounded with a dotted line for better visibility. **(A–C)** Neither expression of *lef1* nor of *fgfr1a* are affected in *ncam1b*-morphants, whereas *erm* expression is markedly reduced. (**A′,C′**) Neither *ncam1a*-morphants nor (**A″,C″**) siblings show alterations for *lef1*, *fgfr1a,* or *erm*. **(D)** Reduced *erm* expression after knockdown of *ncam1b*. Error bars show standard deviation. X^2-test with $ns = p \geq 0.05$. Scale bar 20 μm.

interaction of Ncam1b with Fgfr1a, we first searched for zebrafish isoforms of Fgfr1a that are expressed during pLLS development. From cDNA of 24 to 72 hpf embryos we isolated full length clones representing two isoforms, Fgfr1a-IIIb and –IIIc, which have previously been described by Scholpp et al. (2004). These isoforms differ by usage of different exons 7, which encode the C-terminal part of the 3rd Ig-domain. Whereas, exon 7.1 (blue in **Figures 4F**, **1**) is included in *fgfr1a-IIIc* and has a size of 144 bp (48 aa), exon 7.2 (red in **Figures 4F**, **2**, **3**) is included in *fgfr1a-IIIb* and contains 147 bp (49 aa). Sequence analysis reveals a 47% homology among these alternative domains on the amino acid level. Further isoforms of the extracellular domain (ECD) were not discovered. Within the region encoding the intracellular juxtamembrane domain, *fgfr1a-IIIb* contains either exon 9.1 or exon 9.2, each of which codes for two amino acids (**Figures 4F**, **2**, **3**). Our interaction studies (see below) were performed only with the 9.1 variant of Fgfr1-IIIb since we assume that a two amino acid exchange in the intracellular region will not influence an interaction of Ncam1b and Fgfr1a. A zebrafish homolog of mouse Fgfr1a-IIIa, which lacks an exon 7-coded domain, could not be detected; we thus constructed this isoform artificially as a membrane-bound version (**Figures 4F, 4**).

Ncam1b Interacts Differently With Fgfr1a Isoforms

To test for an interaction of Ncam1b with Fgfr1a, we performed overlay assays. Cells expressing a membrane-tethered, His-tagged version of one protein were incubated with the soluble, Fc-tagged extracellular portion of the potential interaction partner. For a first evaluation of a possible interaction, we calculated a binding coefficient. To that end we determined the percentage of cells expressing the membrane-bound ligand binding partner that were co-labeled by antibodies against the soluble binding partner. Cells expressing membrane-bound Fgfr1a-IIIb also show a strong labeling for soluble Ncam1b (**Figures 4A–A‴**, arrow) and vice versa (**Figures 4B–B‴**, arrow). Around 90% of the transfected cells show a co-localization of the soluble interaction

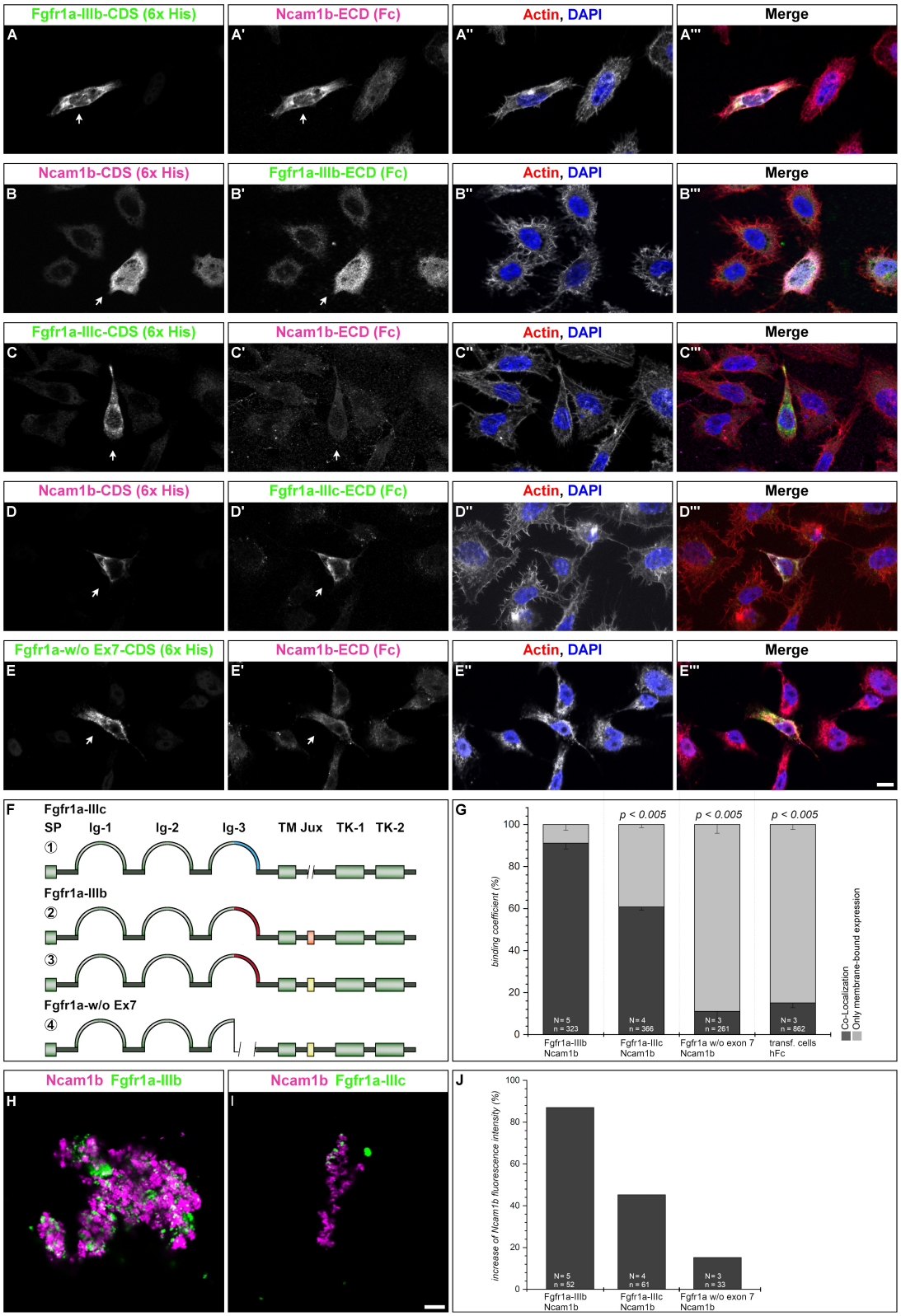

FIGURE 4 | Ncam1b interactions with different isoforms of Fgfr1a. *CHO-K1* cells were transfected with complete coding sequences (CDS) of one of three Fgfr1a-isoforms (green; IIIb, IIIc, or w/o Ex7) or of Ncam1b (magenta). Transfected cells were incubated for 1 hr with either soluble Ncam1b or one of the two

(Continued)

FIGURE 4 | Fgfr1a-isoforms, fixed and immunostained for His-, Fc-Tag, Actin (red), and DAPI (blue). (**A,B‴**) Ncam1b interacts strongly with Fgfr1a-IIIb irrespectively of which of the proteins is membrane-bound. (**C,D‴**) Binding of Ncam1b to Fgfr1a-IIIc is markedly weaker. (**E,E‴**) No interaction occurs if Fgfr1a lacks exon 7. (**F**) Scheme of isolated and cloned Fgfr1a splice variants: ① Fgfr1a-IIIc does not contain any exon 9, ② one splice variant of Fgfr1a-IIIb contains a juxtamembrane region of valine and threonine (orange), ③ another isoform of Fgfr1a-IIIb encodes two serine residues (yellow) within the juxtamembrane domain, ④ Fgfr1a-IIIa, an artificial variant of Fgfr1a, lacks the C-terminal part of Ig-3, which is encoded by exon 7. (**G**) Quantification of the binding of Ncam1b to splice variants of Fgfr1a. Binding coefficient represents the percentage of cells expressing the membrane-bound binding partner that were co-labeled by antibodies against the soluble binding partner. Error bars represent standard deviations (χ^2-test). (**H,I**) Bead aggregation assays reveal a strong homophilic binding of Ncam1b. Ncam1b-coated beads interact with Fgfr1a-IIIb-coated beads and to a lower extend with Fgfr1a-IIIc. **(J)** Measuring the fluorescence intensity of soluble Ncam1b-Fc shows a strong binding to membrane-bound Fgfr1a-IIIb and a weaker to Fgfr1a-IIIc or Fgfr1a without exon 7. Scale bar in (**E‴**) represents 20 μm and in (**I**) 10 μm. Abbreviations: CDS, coding sequence; ECD, extracellular domain; Ig, Immunoglobulin domain; Jux, juxtamembrane domain; SP, Signal peptide; TK, Tyrosine Kinase domain.

partner (**Figure 4G**). The binding coefficient of Ncam1b to Fgfr1a-IIIc is about 60% (**Figures 4C–C‴,D–D‴,G**). The variant of Fgfr1a receptor lacking the exon 7 domain does not exceed binding coefficients above background levels, i.e., coefficients obtained after incubating transfected cells with human Fc only (∼10%, **Figures 4E–E‴,G**). Ncam1a binds weakly to Fgfr1a-IIIb only, its binding coefficient to the other isoforms does not exceed background levels (**Supplementary Figure S5**). The interaction concluded from this analysis was further confirmed by fluorescence intensity measurements. Cells transfected with membrane bound Fgfr1a isoforms showed a fourfold increase in fluorescence intensity compared to untransfected cells (data not shown). When analyzing the fluorescence intensity of soluble Ncam1b bound to the cells, we found that Fgfr1a-IIIb positive cells show 80% higher fluorescence intensities than untransfected cells (**Figure 4J**). Fgfr1a-IIIc transfected cells show a lower fluorescence intensity for Ncam1b, as well as cells expressing a receptor isoform without exon 7. This suggests that Ncam1b has a higher affinity for Fgfr1a-IIIb than for the other splice variants. Ncam1a in general has a lower affinity for all Fgfr1a isoforms (**Supplementary Figure S5J**).

As cell overlay assays do not clearly indicate in which orientation, *cis* or *trans*, a soluble ligand interacts with a membrane-tethered binding partner, we next performed bead aggregation assays. Magenta fluorescent ProteinA beads were coated with either Ncam1a-Fc or Ncam1b-Fc, and green fluorescent ProteinA beads were coated with either Fgfr1a-IIIb-Fc or Fgfr1a–IIIc-Fc. By incubating different combinations of the beads we found large clusters of Ncam1b-coated beads (**Figures 4H,I**) as well as of Ncam1a-coated beads (**Supplementary Figures S5H,I**). Clusters of Ncam1b-coated beads incorporate small clusters of Fgfr1a-IIIb-coupled beads (**Figure 4H** and **Supplementary Figure S6A–A″**) and to a weaker extent small clusters of Fgfr1a-IIIc-coupled beads (**Figure 4I** and **Supplementary Figures S5B–B″**). Clusters of Ncam1a-coupled beads rarely incorporate neither Fgfr1a-IIIb nor Fgfr1-IIIc coupled beads (**Supplementary Figures S5H,I** and **Supplementary Figures S6C–D″**).

Finally, we performed co-immunoprecipitations of Fgfr1a-FLAG and Ncam1-His co-expressed as membrane-bound proteins in *HEK293* cells. Immunoprecipitates of either Ncam1b or Ncam1a contain both receptor splice variants, Fgfr1a-IIIb or Fgfr1a-IIIc, (**Supplementary Figure S5**), supporting the interactions concluded from the experiments described above.

In combination our results indicate that Ncam1b binds to Fgfr1a in *trans in vitro*, with the isoform Fgfr1a-IIIb being a stronger binding partner than Fgfr1a-IIIc. Ncam1a binds Fgfr1a only weakly. This may result from the lack of a CAM Homology Domain (CHD) in Ncam1a (**Supplementary Figure S7**, see also discussion).

A Knockdown of *fgfr1a* Partially Phenocopies the *ncam1b*-Knockdown

Since Ncam1b affects Fgfr1a signaling, as judged by reduced *erm* expression, we expected that knocking down *fgfr1a* should have similar effects on pLLS development as knocking down *ncam1b*. In fact, we observed a reduced migration distance of the primordium after a morpholino-knockdown of *fgfr1a* that targets all isoforms (**Figures 5C,D**). At 48 hpf, *fgfr1a*-knockdown primordia have covered about two thirds of the migration path whereas primordia of uninjected siblings or control-morpholino injected embryos have already reached the tip of the tail. In addition, the size of the primordium is significantly reduced (**Figures 5A′-C‴,E**). A third effect of the *fgfr1a*-knockdown is a reduced number of neuromasts (**Figures 5A–C,F**). As a reduction of neuromast numbers may result from defects in proneuromast development, we studied rosette formation during the initial phase of primordium migration, at 24 hpf. After *fgfr1a*-knockdown we find a strongly reduced Zo-1 staining in the primordium; Zo-1 is a *zonula occludens* protein which marks apical constriction sites in nascent proneuromasts (**Supplementary Figure S8**). Accordingly the knockdown of *fgfr1a* affects proneuromast formation, similar as has been observed in studies using Fgfr inhibitors (Lecaudey et al., 2008; Ernst et al., 2012).

We also measured neuromast spacing at 48 hpf (**Figure 5G**). In uninjected siblings the first proneuromast is deposited after approximately 400 μm of primordium migration, whereas primordia of *fgfr1a*-morphants deposit their first proneuromast after approximately 450 μm. These experiments demonstrate that Fgfr1a signaling is crucial for the formation of proneuromasts and for the timing of their deposition. In general, the knockdown of *fgfr1a* affects pLLS development in a similar way, yet not as strongly as the knockdown of *ncam1b*. It cannot be excluded that this is due to different efficacies of the used morpholinos. *One* may however also assume that the knockdown of *ncam1b*, besides attenuating Fgfr1a signaling, weakens Ncam1b-dependend cell adhesion in the primordium. This could explain the rapid disintegration of rosettes in the morphants (**Supplementary Video 4**).

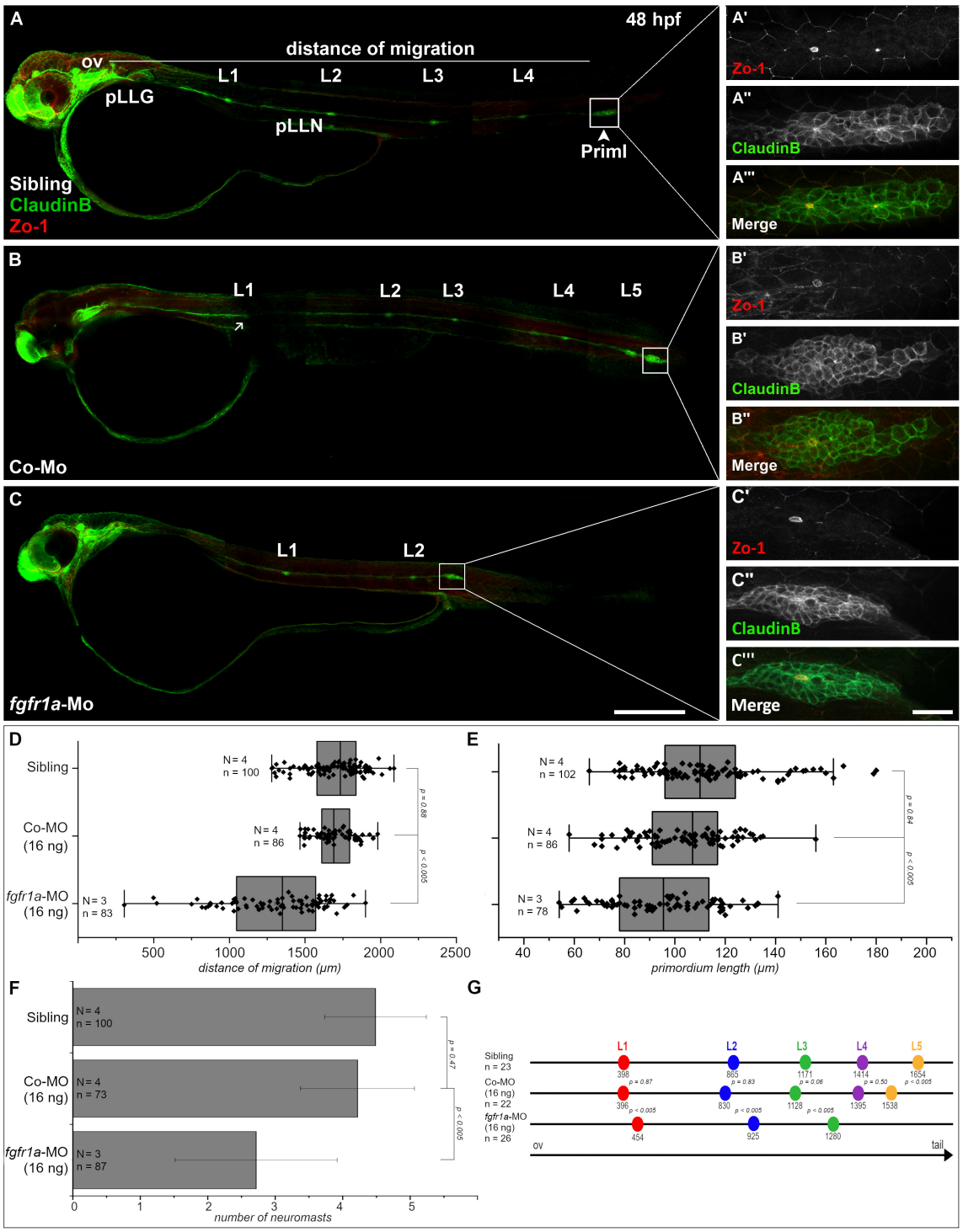

FIGURE 5 | Fgfr1a is important for posterior lateral line development. Lateral views of 48 hpf *Tg(ClaudinB::lynGFP)* (green) embryos. **(A,B)** In siblings and control-morpholino injected embryos Priml has reached the tip of the tail and deposited 5 neuromasts. **(C)** *fgfr1a*-knockdown embryos show a delayed migration of primordia and a reduced number of neuromasts. **(A′-C′)** Apical constriction, visualized by staining of Zo-1, occurs under all conditions. Quantification of **(D)** migration distance, **(E)** primordium length, **(F)** number and **(G)** spacing of neuromasts, respectively. Error bars in bar chart represent standard deviation. Scale bars **(A,B)** 200 µm, **(A′-C″)** 20 µm. Abbreviations: Co-Mo, Control-Morpholino; L1-6, lateral (pro)neuromast; pLLGg, lateral line ganglion; pLLN, lateral line nerve; ov, otic vesicle; Priml, primary posterior primordium.

Ncam1b Impairs Expression of Cxcr7b

In addition to primordial cell proliferation and proneuromast deposition, the knockdown of *ncam1b* affects the migration of the primordium. By the time the primordium of uninjected siblings has reached the tip of the tail, the morphant primordium has only covered about half the distance (**Figure 1E**). In some cases, we also found primordia which leave their path and migrate backward (**Supplementary Figures S9B–E**, **Supplementary Videos 5**, **6**). Other primordia left their path along the horizontal myoseptum, migrated to the yolk border, returned to their original path, and continued migration toward the tail (**Supplementary Video 7**).

The pLLS primordium migrates along the horizontal myoseptum following a path which is delineated by the homogenous expression of chemokine Cxcl12a (Sdf1). Directionality is regulated by polarization of the primordium primarily through asymmetric expression of the chemokine clearance receptor Cxcr7b (Boldajipour et al., 2008; Aman et al., 2011; Donà et al., 2013; Venkiteswaran et al., 2013; Lau et al., 2020). While the expression patterns of the second chemokine receptor, *cxcr4b,* are unaffected by morpholino-knockdown of *ncam1b* (**Figure 6A**, compare to 6C), we found the amount of *cxcr7b* mRNA to be markedly reduced (**Figure 6A′**, compare to 6C′, and 6D). The morpholino-knockdown of *ncam1a* does not affect the expression of *cxcr7b* (**Figure 6B′**); we find a reduction of *cxcr4b*, which we cannot explain (**Figure 6D**). Combining the above results, it is tempting to speculate that Ncam1b directs primordial migration by regulating *cxcr7b* expression.

DISCUSSION

Ncam1b Affects Development of the Zebrafish Lateral Line System

The formation of the posterior lateral line system (pLLS) strongly depends on cell adhesion molecules. So far, calcium-dependent cell adhesion molecules like cadherins have been reported to assure cell type-specific adhesion in the neuromasts (Matsuda and Chitnis, 2010; Colak-Champollion et al., 2019). In the present study we describe the calcium-independent neural cell adhesion molecule Ncam1b as part of the Wnt/Fgfr1 interaction network which controls pLLS development in zebrafish (Aman and Piotrowski, 2008; Lecaudey et al., 2008; Aman et al., 2011; Breau et al., 2012; Ernst et al., 2012; Lush and Piotrowski, 2014; Venero Galanternik et al., 2015). Morpholino-knockdowns of *ncam1b* (i) cause a size reduction of the pLLS primordium, (ii) reduce the number and the stability of deposited proneuromasts, and (iii) affect migration of the primordium (**Figure 1**).

Ncam1b Regulates Cell Proliferation in a Fgfr1a-Dependent Manner

The size of the pLLS primordium depends on cell proliferation which occurs in both, Leading- and Trailing-Zones (**Figure 2**) (Nogare and Chitnis, 2017). In *ncam1b*-morphants, the cell division rate is markedly reduced as our BrdU assays show (**Figure 2**). In principle this could suggest a role of Ncam1b in either or both signaling pathways controlling cell division within the primordium, namely the Wnt and Fgfr1a pathways.

A major regulator of primordial cell proliferation is the Wnt-target gene product Lef1 (Lecaudey et al., 2008; Gamba et al., 2010; Valdivia et al., 2011; Breau et al., 2013; Agarwala et al., 2015). We found, however, that *lef1* expression in the Leading-Zone is unaltered in *ncam1b*-morphants (**Figure 3A**) while proliferation is drastically reduced. Accordingly, Lef1 is not sufficient for inducing primordial cell proliferation. This is supported by studies in *lef1*-mutants, which still show proneuromast formation and deposition, indicating that besides Lef1 other key regulators for primordial cell proliferation must exist (McGraw et al., 2011, 2014). Ncam1b is not expressed in the Leading-Zone, however, it shares expression domains with Fgfr1a in the Trailing-Zone (**Figures 1C′**, **3B″**). In addition, the expression of the Fgfr1 target gene *erm* is inhibited in *ncam1b*-morphants (**Figure 3C**) and a knockdown of *erm* results in a reduced proliferation in the Trailing-Zone (**Supplementary Figure S8**). This suggests that an interaction of Ncam1b with Fgfr1a might be involved in regulating cell proliferation. This is supported by two studies showing that an inhibition of the Fgfr1a receptor strongly reduces primordial cell proliferation in zebrafish (Aman et al., 2011; McGraw et al., 2014). In mature neuromasts proliferation and regenerative cell proliferation are also promoted via FGF signaling and not directly through the Wnt pathway (Tang et al., 2019). A role of Erm (Etv5b) in proliferation was recently shown in murine embryonic stem cells (Akagi et al., 2015).

We here demonstrate a direct interaction between zebrafish Ncam1b and Fgfr1a by cell overlay, bead aggregation and co-immunoprecipitation assays. Binding crucially depends on the C-terminal part of the 3rd Ig-domain of Fgfr1a. We observed a much stronger interaction with isoform Fgfr1a-IIIb (**Figures 4A–B‴,G,H,J**) than with isoform Fgfr1a-IIIc (**Figures 4C–D‴,G,I,J**), which differ in the 3rd Ig-domain as a result of alternative splicing. Fgfr1a-IIIa, which lacks the C-terminal part of the 3rd Ig-domain, does not bind Ncam1b (**Figures 4E–E‴,G,J**).

In contrast to Ncam1b, Ncam1a shows almost no affinity to either Fgfr1a-IIIb or Fgfr1a-IIIc (**Supplementary Figure S5**). To find molecular signatures which account for this difference, we searched the amino acid sequences of both zebrafish Ncam1 paralogs for domains which have been previously identified as putative sites for an interaction with FGFR1 in rats and mice (Saffell et al., 1994; Williams et al., 1994a; Kiselyov et al., 2003; Kochoyan et al., 2008). We found no differences in the *FG Loop* interaction sequences in the FN-domains of zebrafish Ncam1a and Ncam1b; likewise, their counterparts in the 2nd and 3rd Ig-domain of the zebrafish Fgfr1a isoforms are preserved (**Supplementary Figure S7**). Besides these direct NCAM1-FGFR1 interaction sites, the *CAM Homology Domain* (CHD) in the 4th Ig-domain of NCAM1 has been identified as an important binding site. This domain is supposed to be involved in NCAM1 homophilic interactions required for triggering the formation of complexes with FGFR1 (Williams et al., 1994a; Doherty and Walsh, 1996; Anderson et al., 2005; Kochoyan

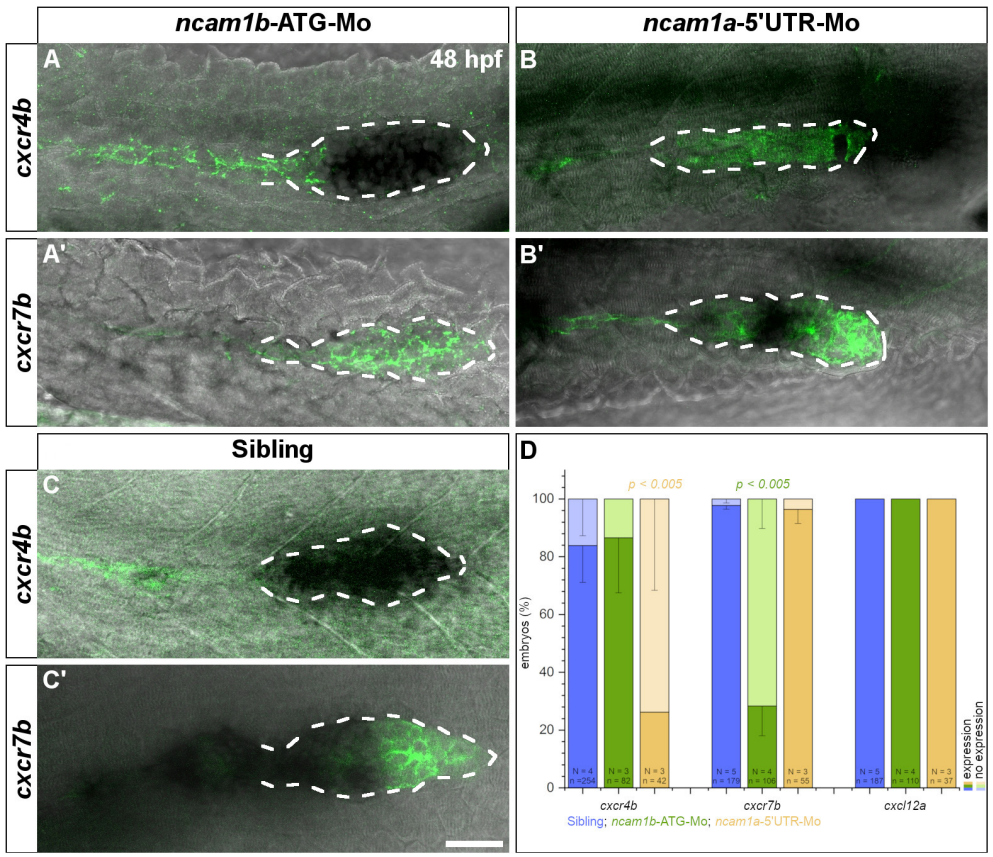

FIGURE 6 | Expression of chemokine receptor *cxcr7b* is affected by knockdown of *ncam1b*. *Tg(ClaudinB::lynGFP)* embryos (48 hpf) were immunostained for GFP (green). *In situ* hybridizations of probes detecting *cxcr4b* (complete Priml) and *cxcr7b* (Trailing-Zone), were visualized by NBT/BCIP staining. Primordia outlines were surrounded with a dotted line for better visibility. (**A,A'**) Expression of *cxcr4b* is not affected in *ncam1b*-morphants, whereas expression of *cxcr7b* is markedly reduced. (**B,B'**) In *ncam1a*-morphants *cxcr7b* is present, whereas *cxcr4b* expression is reduced. (**C,C'**) In siblings, *cxcr7b* is robustly expressed in the Trailing-Zone. (**D**) Drastically reduced *cxcr7b* expression after knockdown of *ncam1b*. Error bars represent standard deviation. X^2-test with *ns* = $p \geq 0.05$. Scale bar 20 μm.

et al., 2008). A removal of this domain inhibits FGFR1 signaling (Williams et al., 1994a). Whereas, zebrafish Ncam1b contains a CHD, Ncam1a lacks this sequence (**Supplementary Figure S7C**). This may account for its severely decreased affinity for Fgfr1a.

We find that a knockdown of *fgfr1a* partially phenocopies the *ncam1b*-knockdown (**Figure 5** and **Supplementary Figure S8**). This finding alone does not directly support a role of Ncam1b in Fgfr1a-mediated signaling. However, the facts that (i) Ncam1b affects expression of the Fgfr1a target gene *erm* and (ii) both knockdowns have similar effects strongly argue for this interaction. We observed that slightly more proneuromasts are formed and deposited in *fgfr1a*-morphants than in *ncam1b*-morphants. This may be attributed to a cell-adhesive role of Ncam1b in stabilizing neuromasts once they are formed (see below).

In conclusion, our data suggest that Ncam1b acts as a non-canonical ligand for Fgfr1a which stimulates primordial cell proliferation by activating the downstream signal Erm (**Figure 7**). It is conceivable that the proposed Ncam1b-Fgfr1a signaling pathway regulates cell proliferation mainly in the Trailing-Zone, where both are expressed. Cell proliferation in the Leading-Zone is activated by the Wnt-Lef1 pathway (Gamba et al., 2010; Aman et al., 2011; Valdivia et al., 2011). Thus, we propose a mechanism in which both, Erm and Lef1, regulate mitosis in the primordium (**Figure 7**). Ncam1b/Fgfr1a/Erm are involved in the generation of cells, which differentiate toward a mechanosensory character, whereas Wnt/Lef1 aids the proliferation of mesenchymal cells.

Ncam1b Is Involved in Proneuromast Formation and Stabilization

Besides cell proliferation and primordium size, proneuromast formation and deposition are affected in *ncam1b*-morphants. We find at most a single proneuromast being formed and deposited (**Figure 1G**). Precursors of proneuromasts are established once a group of cells has evaded the influence of Wnt signaling in the Leading-Zone and reached the Fgf signaling range in the Trailing-Zone. The Trailing-Zone is small in *ncam1b*-morphants due to a reduced overall size of the primordium and an increase of the Wnt signaling domain (**Figure 3A**). Accordingly, the number of proneuromasts is strongly reduced in *ncam1b*-morphants. The proneuromasts formed and deposited in *ncam1b*-morphants

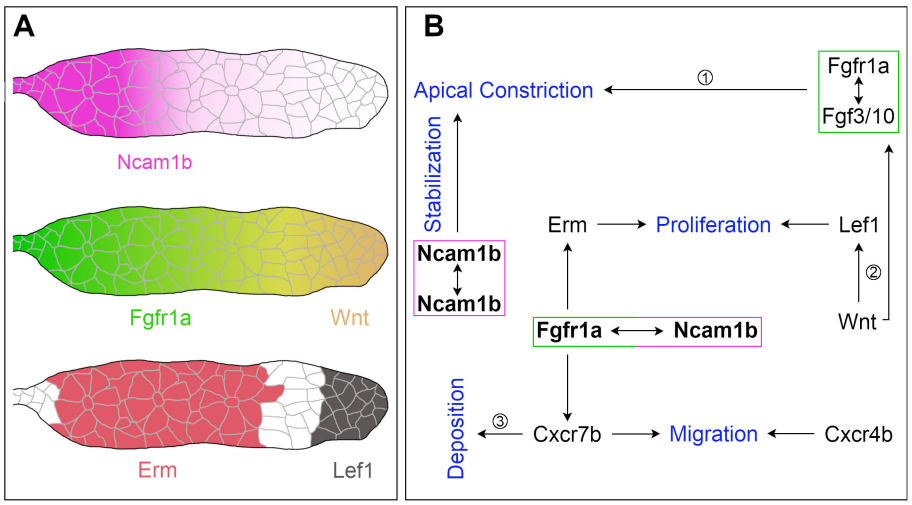

FIGURE 7 | The function of Ncam1b during posterior lateral line development. **(A)** Expression patterns of Ncam1b, Fgfr1a, Wnt, Erm and Lef1 in the pLLS primordium. **(B)** Interaction of Ncam1b with Fgfr1a results in activation of the transcription factor Erm, which is involved in cell proliferation in the Trailing-Zone of PrimI. The Ncam1b/Fgfr1a interaction also initiates the expression of the chemokine receptor Cxcr7b, which is necessary for directional migration of the PrimI and for proneuromast deposition. Wnt signaling controls proliferation in the Leading-Zone via Lef1. In addition, it triggers Fgf signaling in the Trailing-Zone, which initiates apical constriction during formation of proneuromasts. Proneuromasts are stabilized by homophilic Ncam1b binding in *trans*. (Data related to ① Lecaudey et al. (2008) ② Aman et al. (2011) ③ Aman and Piotrowski (2008).

consistently disintegrate shortly after being released from the migrating primordium (**Supplementary Video 4**). A similar fragmentation phenotype has been reported in *notch* mutants, where it was attributed to a loss of cadherin-mediated adhesive interactions between prospective proneuromast cells (Matsuda and Chitnis, 2010). Accordingly, Ncam1b may stabilize the epithelial rosettes by strengthening the apical cohesiveness of the central hair and the surrounding support cells. This could be achieved through homophilic *trans* interactions, which constitute the canonical Ncam1 mode of action.

Ncam1b Is Involved in Primordial Migration

The small primordium of *ncam1b*-morphants eventually stops its migration halfway through the embryo. This is similar to the effect Lecaudey et al. (2008) describe for Fgf signaling-inhibited embryos; primordium migration stops due to an inability to form and deposit proneuromasts.

In addition, some primordia in *ncam1b*-morphants stray from their way along the horizontal myoseptum (**Supplementary Figure S9**). They either later return to their normal path while others "*u-turn*" rostrally. This can be attributed to the reduced expression of *cxcr7b* (**Figure 6A′**). Directionality of primordial migration is a consequence of the polarized expression of Cxcr4b and Cxcr7b. Cxcr7b in the Trailing-Zone degrades the chemokine ligand Cxcl12a resulting in a posterior to anterior gradient of this guidance cue (Donà et al., 2013). The expression of Cxcr7b is restricted to the Trailing-Zone by Wnt-mediated inhibition in the Leading-Zone (Aman and Piotrowski, 2008; Breau et al., 2013) and it is downregulated after inhibiting Fgfr signaling (Aman and Piotrowski, 2008). We have shown here a direct link between Ncam1b and Fgfr1a signaling, which could explain the reduced expression of *cxcr7b* and primordial migration defects in *ncam1b*-morphants. A similar phenotype was described for mutants affecting expression of the chemokine Cxcl12a/Sdf1 (Haas and Gilmour, 2006).

CONCLUSION

Our findings lead us to propose the following model (**Figure 7**): The neural cell adhesion molecule Ncam1b is expressed in the Trailing-Zone of the posterior lateral line primordium. It directly interacts with Fgfr1a to firstly induce expression of transcription factor Erm. Erm in turn activates cell proliferation in the Trailing-Zone. Proliferation in the Leading-Zone is controlled by the Wnt pathway via Lef1. Secondly, Ncam1b induces expression of the chemokine receptor Cxcr7b. This could either be due to direct Fgfr1a signaling (as indicated in **Figure 7**) or result from an Fgfr1a dependent inhibition of Wnt signaling, which in turn inhibits Cxcr7b expression. Besides being involved in generating the Cxcl12a gradient that directs primordial migration, Cxcr7b marks the Trailing-Zone in which proneuromasts slow down to eventually be deposited. Thirdly, homophilic binding of Ncam1b between neighboring cells stabilizes the newly formed proneuromasts. Ncam1a, in contrast, is not crucial for pLLS development. This supports a sub-functionalization of the two Ncam1 paralogs in zebrafish as previously reported by Langhauser et al. (2012). In summary, we here describe Ncam1b as a novel player in the complex feedback network which orchestrates the development of the pLLS; it affects primordial cell proliferation, collective cell migration, and deposition of sensory proneuromasts.

DATA AVAILABILITY STATEMENT

All datasets generated for this study are included in the manuscript. The raw data supporting the conclusions of this article will be made available by the authors after request.

ETHICS STATEMENT

The animal study was reviewed and approved by Animal experimentation: Zebrafish husbandry and experimental work were performed in strict accordance with the recommendations in the German Animal Protection Standards and were approved by the government of Baden-Württemberg, Regierungspräsidium Karlsruhe, Germany (Aktenzeichen: 35-9185.64/BH KIT).

AUTHOR CONTRIBUTIONS

RD carried out the conceptualization and methodology of the study, carried out molecular lab work, validated the results, performed formal analysis, and processed images, drafted, reviewed and edited the manuscript, and funding acquisition. AL participated in validation, formal analysis, molecular lab work, and image processing. SH and KB contributed to molecular lab work and image processing. MB carried out conceptualization, reviewed and edited the manuscript, and acquired funding. JB was part in conceptualization, writing original draft, review, and editing. All authors gave final approval for publication and agree to be held accountable for the work performed therein. All authors contributed to the article and approved the submitted version.

FUNDING

This work was supported by the Landesgraduiertenförderung (Baden-Württemberg) as a State Scholarship to RD and institutional support from the Karlsruhe Institute of Technology (KIT) to RD, AL, SH, KB, MB, and JB.

ACKNOWLEDGMENTS

We are grateful to Dr. Tatjana Piotrowski for the *cxcr4b* and *cxcl12a* plasmid and to Dr. Steffen Scholpp for *lef1* and *erm in situ* probes. We thank Dr. Darren Gilmour for providing the *Tg(ClaudinB::lynGFP)* zebrafish line and Dr. Véronique Orian-Rousseau for sharing *HEK293* cells. We would like to thank Dr. Yoshihiro Yoshihara for kindly providing specific antibodies for Ncam1a and Ncam1b, Dr. Rita Gerardy-Schahn, Dr. Martina Mühlenhoff, and Maike Hartmann for plasmids for the expression of Fc-tagged and FLAG-tagged proteins, for helping with Tag-detection and for *CHO-2A10* cells. We thank Kerstin Weber for excellent technical assistance and Dr. Melanie Langhauser and Dr. Michaela Schober for supplying plasmids for Ncam1a/b-CDS and -ECD. We are grateful to Dr. Franco Weth for helpful comments on the manuscript.

SUPPLEMENTARY MATERIAL

The Supplementary Material for this article can be found online at: https://www.frontiersin.org/articles/10.3389/fcell.2020.591011/full#supplementary-material

Supplementary Figure S1 | Injection of various control morpholinos shows efficacy and paralog specificity of *ncam1b*-ATG Morpholino. **(A–C)** Neither injection of an unrelated standard control (Co-Mo) nor a mismatch-morpholino (partially targeting the ATG-region) alter the migration of the primordium **(A)**, its length **(B)** or the number of neuromasts **(C)**. Co-injection of *ncam1b*-ATG- and *p53*-morpholino does not rescue the *ncam1b*-phenotype, indicating that the observed effects are not caused by increased cell death. Injection of a *ncam1b*-morpholino targeting the 5′UTR phenocopies the knockdown caused by blocking the ATG-region. Error bars in **(C)** show standard deviation. **(D)** Western blot analysis of p53 at 4 hpf indicates that none of the used morpholinos affects expression of the apoptosis marker. Expression of the Ncam1b protein at 48 hpf is drastically reduced following injection of the knockdown morpholinos *ncam1b*-ATG and *ncam1b*-5′UTR. Injections of the unrelated control-morpholino and mismatch-morpholino do not affect Ncam1b expression. Anti-Tubulin stainings were used as loading controls.

Supplementary Figure S2 | Morpholinos targeting different ncam1b-mRNA sites affect posterior lateral line (pLLS) development in the same manner. **(A–F)** Lateral views of *Tg(ClaudinB::lynGFP)* embryos at 48 hpf. **(A)** Lateral line primordium reaches the tip of tail at 48 hpf and deposited several neuromasts. Neither injection of an unrelated control-morpholino (Co-Mo) **(B)** nor of a mismatch morpholino **(C)** affects the development of the pLLS. **(D)** Knockdown of *ncam1b* by blocking the ATG-region results in a delayed migration of the smaller-sized primordium and a reduced number of deposited neuromasts. **(E)** Co-injection of *p53*-Mo does not rescue the phenotype induced by the *ncam1b*-ATG-Mo, indicating the *ncam1b*-ATG-Mo does not act by inducing unspecific p53 side-effects. **(F)** Blocking the 5′UTR of *ncam1b*-mRNA phenocopies the knockdown caused by blocking the ATG-region. Scale bar 200 μm.

Supplementary Figure S3 | *erm* expression is not restricted to the lateral line primordium, but also found in brain structures at 36 hpf. **(A)** Detection of *erm* within the forebrain, eye and the midbrain-hindbrain-boundary (MHB) as well as in Priml. **(B)** *ncam1b*-morphants still express *erm* in the forebrain, eye and MHB but not in Priml.

Supplementary Figure S4 | Erm affects cell proliferation within the Trailing-Zone of primordia. Siblings or morpholino-injected *Tg(ClaudinB::lynGFP)* embryos were treated with BrdU at 36 hpf for 20 min, fixed and immunostained for BrdU (red), GFP (green) and DAPI (blue). **(A,A″)** BrdU incorporation is reduced in *ncam1b*-morphants, but obvious in **(B,B″)** uninjected siblings. **(C,D)** Quantification of BrdU-labeled cells within primordia. Cell proliferation is mainly reduced in the Trailing-Zone. Scale bar 20 μm.

Supplementary Figure S5 | Ncam1a weakly interacts with different isoforms of Fgfr1a. *CHO-K1* cells were transfected either with complete coding sequences (CDS) of one of the three Fgfr1a-isoforms (green; IIIb, IIIc, or w/o Ex7) or with Ncam1a (magenta). Transfected cells were incubated for 1 hr with either soluble Ncam1a or one of the Fgfr1a-isoforms, fixed and immunostained for His-, Fc-Tag, Actin (red) and DAPI (blue). **(A–B‴)** Ncam1a interacts weakly with Fgfr1a-IIIb irrespectively of which of the proteins is membrane-bound. **(C–E‴)** Binding of Ncam1a to Fgfr1a-IIIc or to Fgfr1a which lacks exon 7 could not be detected. **(F) Top**: immunoprecipitates obtained from lysates of cells expressing His-tagged Ncam1a or Ncam1b, respectively, and Flag-tagged Fgfr1a-IIIb or Fgfr1a-IIIc, respectively, as indicated. Both, Flag-tagged Fgfr1a-IIIb and Fgfr1a-IIIc co-precipitate with Ncam1a and Ncam1b (band density (Intensity Density) for untransfected cells: 61,969.7 ± 22,350.7 and for transfected cells: Ncam1b/Fgfr1a-IIIb: 170,493.3 ± 47,282.2; Ncam1b/Fgfr1a-IIIc: 137,674.0 ± 17,380.8; Ncam1a/Fgfr1a-IIIb: 89,512.7 ± 28,322.6; Ncam1a/Fgfr1a-IIIc: 117,447.0 ± 74,743.5). **Bottom**: immunoprecipitates obtained from lysates of cells expressing His-tagged Ncam1b and/or Flag-tagged Fgfr1a-IIIb as indicated. Flag-tagged Fgfr1a-IIIb is contained only in precipitates obtained from lysates of cells expressing both proteins, excluding the possibility of an unspecific background (band density (Intensity Density) for untransfected cells: 31,604 and for transfected cells: Ncam1b: 25,442; Fgfr1a-IIIb: 31,972; Ncam1b/Fgfr1a-IIIb:

202,895). **(G)** Quantification of the binding of Ncam1a to splice variants of Fgfr1a. Binding coefficient represents the percentage of cells expressing the membrane-bound binding partner that were co-labeled by antibodies against the soluble binding partner. Error bars represent standard deviations. (**H,I**) Ncam1a-coated beads have a low affinity for Fgfr1a-IIIb- or –IIIc-coated beads. **(J)** Measuring the fluorescence intensity of soluble Ncam1a-Fc shows a low binding affinity for membrane-bound Fgfr1a-IIIb, Fgfr1a-IIIc, or Fgfr1a without exon 7 in the cell overlay assay. Scale bar in (**E‴**) represents 20 μm and in **(I)** 10 μm. CDS, coding sequence; ECD, extracellular domain.

Supplementary Figure S6 | Ncam1b interacts with clustered Fgfr1a-IIIb. Fluorescently labeled ProteinA-Beads were either coated with Ncam1b, Ncam1a, Fgfr1a-IIIb, Fgfr1a-IIIc or, as a control, with human Fc (hFc). **(A–A″)** Ncam1b and Fgfr1a-IIIb interact in *trans*. Thereby Ncam1b enables clustering of Fgfr1a-IIIb. **(B–B″)** Besides homophilic interactions of Ncam1b, just few Fgfr1a-IIIc-coated beads were incorporated into clusters of Ncam1b-coated beads. **(C–C″)** Ncam1a and Fgfr1a-IIIb rarely interact. **(D–D″)** Ncam1a shows low affinity for Fgfr1a-IIIc. **(E–H″)** Beads coated with Ncam1b, Ncam1a, Fgfr1a-IIIb or Fgfr1a-IIIc do not interact with human Fc-coated beads. Scale bar represents 20 μm.

Supplementary Figure S7 | Ncam1b and Fgfr1a share sequences that code for known protein-protein interaction domains, whereas Ncam1a lacks the CHD-NCAM1 sequence. **(A–C)** Sequences of Ncam1 homologs. **(D)** Sequences of Fgfr1 homologs. **(A)** The *FGF receptor activation motif* (FRM) is located in the 1st FN-domain of Ncam1a and Ncam1b. **(B)** Both Ncam1 paralogs express the highly conserved *FG Loop* (FGL) sequence. **(C)** Ncam1b contains a CAM Homology Domain, which is not found in Ncam1a. **(D)** The CAM Homology Domain in the 2nd Ig-Domain of FGFR1 is found in both zebrafish splice variants.

Supplementary Figure S8 | Knockdown of *fgfr1a* affects the size of PrimI and early formation of proneuromasts. Embryos were immunostained for GFP (green) and Zo-1 (red) **(A)** Lateral view of PrimI which just starts its migration at 24 hpf. It is still connected to the lateral line ganglion (pLLG). **(A–A‴)** Zo-1 staining depicts the formation of two proneuromasts within PrimI. **(B)** Migration initiation of PrimI and **(B–B‴)** proneuromast formation are not affected by injection of the control-morpholino. **(C)** Primordia of *fgfr1a*-morphants are reduced in size but do not show migration defects at this early developmental stage. **(C–C‴)** Formation of proneuromast is reduced as shown by Zo-1 staining. **(D–F)** Quantification of migration distance, primordia size and proneuromast number within PrimI. Error bars in **(F)** represent standard deviation. Scale bar in **(C)** 50 μm and in **(C‴)** 20 μm.

Supplementary Figure S9 | The knockdown of *ncam1b* results in severe abnormalities in primordium shape and migration. Lateral views of *Tg(ClaudinB::lynGFP)* primordia at 48 hpf. **(A)** Primordia of uninjected siblings have an elongated shape and a constant size, they migrate on a direct path to the tip of the tail. **(B–D)** Primordia of *ncam1b*-morphants are reduced in size and lack directional migration. They either stop migration prematurely or they leave the horizontal myoseptum, perform a *u-turn* and migrate backwards. **(E)** *Double*-knockdown of *ncam1a* and *ncam1b* phenocopies the *single*-knockdown of *ncam1b*. Scale bar represents 20 μm.

Supplementary Video 1 | Migration of the primordium in wild type siblings.

Supplementary Video 2 | Control-morpholino injected embryos show no altered phenotype of the pLLS.

Supplementary Video 3 | A knockdown of *ncam1a* has weaker effects on primordium migration and proneuromast formation.

Supplementary Video 4 | The primordium of *ncam1b*-morphants just reaches the end of the yolk extension.

Supplementary Video 5 | Knockdown of *ncam1b* leads primordia to deviate from their path along the horizontal myoseptum.

Supplementary Video 6 | Knockdown of both *ncam1* paralogs phenocopies *ncam1b*-single knockdowns.

Supplementary Video 7 | Primordia of *ncam1b*-morphants can result in different migration abnormalities.

REFERENCES

Agarwala, S., Duquesne, S., Liu, K., Boehm, A., Grimm, L., Link, S., et al. (2015). Amotl2a interacts with the Hippo effector Yap1 and the Wnt/β-catenin effector Lef1 to control tissue size in zebrafish. *Elife* 4:e08201. doi: 10.7554/eLife.08201.044

Akagi, T., Kuure, S., Uranishi, K., Koide, H., Costantini, F., and Yokota, T. (2015). ETS-related transcription factors ETV4 and ETV5 are involved in proliferation and induction of differentiation-associated genes in embryonic stem (ES) cells. *J. Biol. Chem*. 290, 22460–22473. doi: 10.1074/jbc.M115.675595

Aman, A., Nguyen, M., and Piotrowski, T. (2011). Wnt/β-catenin dependent cell proliferation underlies segmented lateral line morphogenesis. *Dev. Biol*. 349, 470–482. doi: 10.1016/j.ydbio.2010.10.022

Aman, A., and Piotrowski, T. (2008). Wnt/beta-catenin and Fgf signaling control collective cell migration by restricting chemokine receptor expression. *Dev. Cell* 15, 749–761. doi: 10.1016/j.devcel.2008.10.002

Anderson, A. A., Kendal, C. E., Garcia-Maya, M., Kenny, A. V., Morris-Triggs, S. A., Wu, T., et al. (2005). A peptide from the first fibronectin domain of NCAM acts as an inverse agonist and stimulates FGF receptor activation, neurite outgrowth and survival. *J. Neurochem*. 95, 570–583. doi: 10.1111/j.1471-4159.2005.03417.x

Beenken, A., and Mohammadi, M. (2009). The FGF family. biology, pathophysiology and therapy. *Nat. Rev. Drug Discov*. 8, 235–253. doi: 10.1038/nrd2792

Boldajipour, B., Mahabaleshwar, H., Kardash, E., Reichman-Fried, M., Blaser, H., Minina, S., et al. (2008). Control of chemokine-guided cell migration by ligand sequestration. *Cell* 132, 463–473. doi: 10.1016/j.cell.2007.12.034

Breau, M. A., Wilson, D., Wilkinson, D. G., and Xu, Q. (2012). Chemokine and Fgf signalling act as opposing guidance cues in formation of the lateral line primordium. *Development* 139, 2246–2253. doi: 10.1242/dev.080275

Breau, M. A.,m Wilkinson, D. G., and Xu, Q. (2013). A Hox gene controls lateral line cell migration by regulating chemokine receptor expression downstream of Wnt signaling. *Proc. Natl. Acad. Sci. U.S.A*. 110, 16892–16897. doi: 10.1073/pnas.1306282110

Christensen, C., Berezin, V., and Bock, E. (2011). Neural cell adhesion molecule differentially interacts with isoforms of the fibroblast growth factor receptor. *Neuroreport* 22, 727–732. doi: 10.1097/WNR.0b013e3283491682

Colak-Champollion, T., Lan, L., Jadhav, A. R., Yamaguchi, N., Venkiteswaran, G., Patel, H., et al. (2019). Cadherin-mediated cell coupling coordinates chemokine sensing across collectively migrating cells. *Curr. Biol*. 29, 2570–2579. doi: 10.1016/j.cub.2019.06.061

Cunningham, B. A., Hemperly, J. J., Murray, B. A., Prediger, E. A., Brackenbury, R., and Edelman, G. M. (1987). Neural cell adhesion molecule. structure, immunoglobulin-like domains, cell surface modulation, and alternative RNA splicing. *Science* 236, 799–806. doi: 10.1126/science.3576199

Dambly-Chaudière, C., Cubedo, N., and Ghysen, A. (2007). Control of cell migration in the development of the posterior lateral line. antagonistic interactions between the chemokine receptors CXCR4 and CXCR7/RDC1. *BMC Dev. Biol*. 7:23. doi: 10.1186/1471-213X-7-23

Doherty, P., and Walsh, F. S. (1996). CAM-FGF receptor interactions. a model for axonal growth. *Mol. Cell. Neurosci*. 8, 99–111. doi: 10.1006/mcne.1996.0049

Donà, E., Barry, J. D., Valentin, G., Quirin, C., Khmelinskii, A., Kunze, A., et al. (2013). Directional tissue migration through a self-generated chemokine gradient. *Nature* 503, 285–289. doi: 10.1038/nature12635

Ernst, S., Liu, K., Agarwala, S., Moratscheck, N., Avci, M. E., Dalle Nogare, D., et al. (2012). Shroom3 is required downstream of FGF signalling to mediate proneuromast assembly in zebrafish. *Development* 139, 4571–4581. doi: 10.1242/dev.083253

Francavilla, C., Cattaneo, P., Berezin, V., Bock, E., Ami, D., De Marco, A., et al. (2009). The binding of NCAM to FGFR1 induces a specific cellular response mediated by receptor trafficking. *J. Cell Biol*. 187, 1101–1116. doi: 10.1083/jcb.200903030

Galuska, S. P., Rollenhagen, M., Kaup, M., Eggers, K., Oltmann-Norden, I., Schiff, M., et al. (2010). Synaptic cell adhesion molecule SynCAM 1 is a target for

polysialylation in postnatal mouse brain. *Proc. Natl. Acad. Sci. U.S.A.* 107, 10250–10255. doi: 10.1073/pnas.0912103107

Gamba, L., Cubedo, N., Lutfalla, G., Ghysen, A., and Dambly-Chaudiere, C. (2010). Lef1 controls patterning and proliferation in the posterior lateral line system of zebrafish. *Dev. Dyn.* 239, 3163–3171. doi: 10.1002/dvdy.22469

Gilmour, D. T., Maischein, H.-M., and Nüsslein-Volhard, C. (2002). Migration and function of a glial subtype in the vertebrate peripheral nervous system. *Neuron* 34, 577–588. doi: 10.1016/S0896-6273(02)00683-9

Gompel, N., Cubedo, N., Thisse, C., Thisse, B., Dambly-Chaudière, C., and Ghysen, A. (2001). Pattern formation in the lateral line of zebrafish. *Mech. Dev.* 105, 69–77. doi: 10.1016/S0925-4773(01)00382-3

Haas, P., and Gilmour, D. (2006). Chemokine signaling mediates self-organizing tissue migration in the zebrafish lateral line. *Dev. Cell* 10, 673–680. doi: 10.1016/j.devcel.2006.02.019

Hinsby, A. M., Berezin, V., and Bock, E. (2004). Molecular mechanisms of NCAM function. *Front. Biosci.* 9, 2227–2244. doi: 10.2741/1393

Itoh, N., and Ornitz, D. M. (2004). Evolution of the Fgf and Fgfr gene families. *Trends Genet.* 20, 563–569. doi: 10.1016/j.tig.2004.08.007

Johnson, D. E., and Williams, L. T. (1993). Structural and functional diversity in the FGF receptor multigene family. *Adv. Cancer Res.* 60, 1–41. doi: 10.1016/S0065-230X(08)60821-0

Kimmel, C. B., Ballard, W. W., Kimmel, S. R., Ullmann, B., and Schilling, T. F. (1995). Stages of embryonic development of the zebrafish. *Dev. Dyn.* 203, 253–310. doi: 10.1002/aja.1002030302

Kiselyov, V. V., Skladchikova, G., Hinsby, A. M., Jensen, P. H., Kulahin, N., Soroka, V., et al. (2003). Structural Basis for a direct interaction between FGFR1 and NCAM and evidence for a regulatory role of ATP. *Structure* 11, 691–701. doi: 10.1016/S0969-2126(03)00096-0

Knaut, H., Werz, C., Geisler, R., and Nüsslein-Volhard, C. (2003). A zebrafish homologue of the chemokine receptor Cxcr4 is a ger-cell guidance receptor. *Nature* 421,279–282. doi: 10.1038/nature01338

Kochoyan, A., Poulsen, F. M., Berezin, V., Bock, E., and Kiselyov, V. V. (2008). Structural basis for the activation of FGFR by NCAM. *Protein Sci.* 17, 1698–1705. doi: 10.1110/ps.035964.108

Laemmli, U. (1970). Cleavage of structural proteins during the assembly of the head of bacteriophage T4. *Nature* 227, 680–685. doi: 10.1038/227680a0

Langhauser, M., Ustinova, J., Rivera-Milla, E., Ivannikov, D., Seidl, C., Slomka, C., et al. (2012). Ncam1a and Ncam1b: two carriers of polysialic acid with different functions in the developing zebrafish nervous system. *Glycobiology* 22, 196–209. doi: 10.1093/glycob/cwr129

Lau, S., Feitzinger, A., Venkiteswaran, G., Wang, J., Lewellis, S. W., Koplinski, C. A., et al. (2020). A negative-feedback loop maintains optimal chemokine concenstrations for directional cell migration. *Nat. Cell Biol.* 22, 266–273. doi: 10.1038/s41556-020-0465-4

Lecaudey, V., Cakan-Akdogan, G., Norton, W. H. J., and Gilmour, D. (2008). Dynamic Fgf signaling couples morphogenesis and migration in the zebrafish lateral line primordium. *Development* 135, 2695–2705. doi: 10.1242/dev.025981

Li, Q., Shirabe, K., and Kuwada, J. Y. (2004). Chemokine signaling regulates sensory cell migration in zebrafish. *Dev. Biol.* 269, 123–136. doi: 10.1016/j.ydbio.2004.01.020

Li, S., Bock, E., and Berezin, V. (2010). Neuritogenic and neuroprotective properties of peptide agonists of the fibroblast growth factor receptor. *Int. J. Mol. Sci.* 11, 2291–2305. doi: 10.3390/ijms11062291

Lush, M. E., and Piotrowski, T. (2014). ErbB expressing Schwann cells control lateral line progenitor cells via non-cell-autonomous regulation of Wnt/β-catenin. *Elife* 3:e10832. doi: 10.7554/eLife.01832

Marx, M., Rivera-Milla, E., Stummeyer, K., Gerardy-Schahn, R., and Bastmeyer, M. (2007). Divergent evolution of the vertebrate polysialyltransferase Stx and Pst genes revealed by fish-to-mammal comparison. *Dev. Biol.* 306, 560–571. doi: 10.1016/j.ydbio.2007.03.032

Matsuda, M., and Chitnis, A. B. (2010). Atoh1a expression must be restricted by Notch signaling for effective morphogenesis of the posterior lateral line primordium in zebrafish. *Development* 137, 3477–3487. doi: 10.1242/dev.052761

McGraw, H. F., Culbertson, M. D., and Nechiporuk, A. V. (2014). Kremen1 restricts Dkk activity during posterior lateral line development in zebrafish. *Development* 141, 3212–3221. doi: 10.1242/dev.102541

McGraw, H. F., Drerup, C. M., Culbertson, M. D., Linbo, T., Raible, D. W., and Nechiporuk, A. V. (2011). Lef1 is required for progenitor cell identity in the zebrafish lateral line primordium. *Development* 138, 3921–3930. doi: 10.1242/dev.062554

Metcalfe, W. K., Kimmel, C. B., and Schabtach, E. (1985). Anatomy of the posterior lateral line system in young larvae of the zebrafish. *J. Comp. Neurol.* 233, 377–389. doi: 10.1002/cne.902330307

Nechiporuk, A., and Raible, D. W. (2008). FGF-dependent mechanosensory organ patterning in zebrafish. *Science* 320, 1774–1777. doi: 10.1126/science.1156547

Neiiendam, J. L., Køhler, L., B., Christensen, C., Li, S., Pedersen, M. V., et al. (2004). An NCAM-derived FGF-receptor agonist, the FGL-peptide, induces neurite outgrowth and neuronal survival in primary rat neurons. *J. Neurochem.* 91, 920–935. doi: 10.1111/j.1471-4159.2004.02779.x

Nikaido, M., Navajas Acedo, J., Hatta, K., and Piotrowski, T. (2017). Retinoic acid is required and Fgf, Wnt, and Bmp signaling inhibit posterior lateral line placode induction in zebrafish. *Dev. Biol.* 431, 215–225. doi: 10.1016/j.ydbio.2017.09.017

Nogare, D. D., and Chitnis, A. B. (2017). A framework for understanding morphogenesis and migration of the zebrafish posterior Lateral Line primordium. *Mech. Dev.* 148, 69–78. doi: 10.1016/j.mod.2017.04.005

Nogare, D. D., Somers, K., Rao, S., Matsuda, M., Reichman-Fried, M., Raz, E., et al. (2014). Leading and trailing cells cooperate in collective migration of the zebrafish posterior lateral line primordium. *Development* 141, 3188–3196. doi: 10.1242/dev.106690

Roehl, H., and Nüsslein-Volhard, C. (2001). Zebrafish pea3 and erm are general targets of FGF8 signaling. *Curr. Biol.* 11, 503–507. doi: 10.1016/S0960-9822(01)00143-9

Romero-Carvajal, A., Navajas Acedo, J., Jiang, L., Kozlovskaja-Gumbrienė, A., Alexander, R., Li, H., et al. (2015). Regeneration of sensory hair cells requires localized interactions between the notch and wnt pathways. *Dev. Cell* 34, 267–282. doi: 10.1016/j.devcel.2015.05.025

Saffell, J. L., Walsh, F. S., and Doherty, P. (1994). Expression of NCAM containing VASE in neurons can account for a developmental loss in their neurite outgrowth response to NCAM in a cellular substratum. *J. Cell Biol.* 125, 427–436. doi: 10.1083/jcb.125.2.427

Scholpp, S., Groth, C., Lohs, C., Lardelli, M., and Brand, M. (2004). Zebrafish fgfr1 is a member of the fgf8 synexpression group and is required for fgf8 signalling at the midbrain-hindbrain boundary. *Dev. Genes Evol.* 214, 285–295. doi: 10.1007/s00427-004-0409-1

Schulte-Merker, S., Ho, R. K., Herrmann, B. G., and Nüsslein-Volhard, C. (1992). The protein product of the zebrafish homologue of the mouse T gene is expressed in nuclei of the germ ring and the notochord of the early embryo. *Development* 116, 1021–1032

Tang, D., He, Y., Li, W., and Li, H. (2019). Wnt/β-catenin interacts with the FGF pathway to promote proliferation and regenerative cell proliferation in the zebrafish lateral line neuromast. *Exp. Mol. Med.* 51, 1–16. doi: 10.1038/s12276-019-0247-x

Thisse, C., and Thisse, B. (2008). High-resolution in situ hybridization to whole-mount zebrafish embryos. *Nat. Protoc.* 3, 59–69. doi: 10.1038/nprot.2007.514

Valdivia, L. E., Young, R. M., Hawkins, T. A., Stickney, H. L., Cavodeassi, F., Schwarz, Q., et al. (2011). Lef1-dependent Wnt/β-catenin signalling drives the proliferative engine that maintains tissue homeostasis during lateral line development. *Development* 138, 3931–3941. doi: 10.1242/dev.062695

Valentin, G., Haas, P., and Gilmour, D. (2007). The chemokine SDF1a coordinates tissue migration through the spatially restricted activation of Cxcr7 and Cxcr4. *Curr. Biol.* 17, 1026–1031. doi: 10.1016/j.cub.2007.05.020

Venero Galanternik, M., Kramer, K. L., and Piotrowski, T. (2015). Heparan sulfate proteoglycans regulate fgf signaling and cell polarity during collective cell migration. *Cell Rep.* 10, 414–428. doi: 10.1016/j.celrep.2014.12.043

Venkiteswaran, G., Lewellis, S. W., Wang, J., Reynolds, E., Nicholson, C., and Knaut, H. (2013). Generation and dynamics of an endogenous, self-generated signaling gradient across a migrating tissue. *Cell* 155,674–687. doi: 10.1016/j.cell.2013.09.046

Williams, E. J., Doherty, P., Turner, G., Reid, R. A., Hemperly, J. J., and Walsh, F. S. (1992). Calcium influx into neurons can solely account for cell contact-dependent neurite outgrowth stimulated by transfected L1. *J. Cell Biol*. 119, 883–892. doi: 10.1083/jcb.119.4.883

Williams, E. J., Furness, J., Walsh, F. S., and Doherty, P. (1994a). Activation of the FGF receptor underlies neurite outgrowth stimulated by L1, N-CAM, and N-cadherin. *Neuron* 13, 583–594. doi: 10.1016/0896-6273(94)90027-2

Williams, E. J., Furness, J., Walsh, F. S., and Doherty, P. (1994b). Characterisation of the second messenger pathway underlying neurite outgrowth stimulated by FGF. *Development* 120, 1685–1693

Williams, E. J., Walsh, F. S., and Doherty, P. (1994c). The production of arachidonic acid can account for calcium channel activation in the second messenger pathway underlying neurite outgrowth stimulated by NCAM, N-cadherin, and L1. *J. Neurochem*. 62, 1231–1234. doi: 10.1046/j.1471-4159.1994.62031231.x

Zamai, M., Trullo, A., Giordano, M., Corti, V., Arza Cuesta, E., Francavilla, C., et al. (2019). *Number and brightness analysis reveals that NCAM and FGF2 elicit different assembly and dynamics of FGFR1 in live cells. J. Cell Sci*. 132:jcs220624. doi: 10.1242/jcs.220624

Conflict of Interest: The authors declare that the research was conducted in the absence of any commercial or financial relationships that could be construed as a potential conflict of interest.

frontiers in Cell and Developmental Biology

ORIGINAL RESEARCH
published: 18 May 2021
doi: 10.3389/fcell.2021.656636

LncRNA Landscape of Coronary Atherosclerosis Reveals Differentially Expressed LncRNAs in Proliferation and Migration of Coronary Artery Smooth Muscle Cells

*Yaqing Zhou†, Sheng Zhang†, Wenfeng Ji, Xiongkang Gan, Lei Hua, Can Hou, Jiaxin Chen, Yanjun Wang, Shu He, Hanxiao Zhou and Enzhi Jia**

Department of Cardiovascular Medicine, The First Affiliated Hospital of Nanjing Medical University, Nanjing, China

OPEN ACCESS

Edited by:
Mitsugu Fujita, Kindai University, Japan

Reviewed by:
Thomas Quertermous, Stanford University, United States
Lidija Radenovic, University of Belgrade, Serbia

***Correspondence:**
Enzhi Jia
enzhijia@njmu.edu.cn

† These authors have contributed equally to this work

Specialty section:
This article was submitted to Cell Adhesion and Migration, a section of the journal Frontiers in Cell and Developmental Biology

Received: *21 January 2021*
Accepted: *15 March 2021*
Published: *18 May 2021*

Citation:
Zhou Y, Zhang S, Ji W, Gan X, Hua L, Hou C, Chen J, Wang Y, He S, Zhou H and Jia E (2021) LncRNA Landscape of Coronary Atherosclerosis Reveals Differentially Expressed LncRNAs in Proliferation and Migration of Coronary Artery Smooth Muscle Cells. Front. Cell Dev. Biol. 9:656636. doi: 10.3389/fcell.2021.656636

We aimed to investigate differentially expressed long non-coding RNAs (lncRNAs) and messenger RNAs (mRNAs) in atherosclerosis and validate the expression of lncRNAs and co-expressed target genes in proliferation and migration models of human coronary artery smooth muscle cells (HCASMCs). Ten coronary artery specimens from a subject who died from a heart attack were employed. The pathological analysis was analyzed by hematoxylin and eosin (H&E) staining, and the lncRNAs and mRNAs were identified by RNA sequencing. Bioinformatic analyses were performed to predict possible mechanisms. The proliferation and migration of HCASMCs were induced with oxidized low-density lipoprotein (ox-LDL). Differentially expressed lncRNAs and mRNAs were validated by quantitative real-time polymerase chain reaction (qRT-PCR). In this study, 68 lncRNAs and 222 mRNAs were identified differentially expressed in atherosclerosis. Gene Ontology (GO) and Kyoto Encyclopedia of Genes and Genomes (KEGG) enrichment analyses showed that the Fanconi anemia pathway may be involved in atherosclerosis. *GON4L* was found to be the co-localized target gene of LNC_000439, and 14 genes had high correlations with the expression of seven lncRNAs. In addition, nine lncRNA–miRNA–mRNA networks were constructed, and 53 co-expressed gene modules were detected with weighted gene co-expression network analysis (WGCNA). LNC_000684, LNC_001046, LNC_001333, LNC_001538, and LNC_002115 were downregulated, while LNC_002936 was upregulated in proliferation and migration models of HCASMCs. In total, six co-expressed mRNAs were upregulated in HCASMCs. This study suggests that the differentially expressed lncRNAs identified by RNA sequencing and validated in smooth muscle cells may be a target for regulating HCASMC proliferation and migration in atherosclerosis, which will provide a new diagnostic basis and therapeutic target for the treatment of cardiovascular diseases.

Keywords: coronary heart disease, coronary artery, RNA sequencing, long non-coding RNA, smooth muscle cell

INTRODUCTION

Coronary heart disease (CHD), also known as coronary artery disease (CAD), is the leading cause of morbidity and mortality globally (Benjamin et al., 2018; Amrein et al., 2020). Traditional risk factors for CAD include diabetes, hyperlipidemia, hypertension, obesity, smoking, and family history. Low-density lipoprotein cholesterol (LDL-C) has been recognized as one of the major risk factors for CAD, which typically develops because of atherosclerotic plaque buildup in the coronary arteries (Case and Waksman, 2020; Jin et al., 2020). According to recent guidelines, it is highly recommended for patients with very high risk to achieve lower levels of LDL-C (Grundy et al., 2019; Mach et al., 2020).

In the pathological processes of atherosclerosis, cholesterol containing oxidized low-density lipoprotein (ox-LDL) accumulates in the arterial wall, which promotes the proliferation and migration of medial vascular smooth muscle cells (VSMCs) in the intima and the formation of foam cells (Orekhov et al., 2020). Aberrant proliferation and migration of VSMCs lead to vascular remodeling during vasculopathy and atherosclerosis (Zhang et al., 2020). Furthermore, VSMCs are exposed to a complex microenvironment, resulting in the mutability of VSMCs. Therefore, the differentially expressed genes and molecular mechanisms of VSMCs participating in atherosclerosis are potential therapeutic targets.

Long non-coding RNAs are over 200 bp single-stranded RNA molecules without protein-coding potential that can function as molecular signals, decoys, guides, scaffolds, or enhancers to regulate gene expression and functions (Robinson et al., 2020). Zhou et al. reported that lncRNA CRNDE regulates the proliferation and migration of VSMCs (Zhou Y. et al., 2019). LncRNA GAS5 was found to regulate vascular smooth muscle cell cycle arrest and apoptosis *via* the p53 pathway (Tang et al., 2019). The phenotypic switch of VSMCs was suppressed by lncRNA CASC2 to inhibit vascular remodeling (Gong et al., 2019). Thus, the vital role of lncRNAs in the pathological processes of atherosclerosis and VSMCs is increasingly important.

In this research, we conducted RNA sequencing analysis to identify differentially expressed lncRNAs and mRNAs of varying degrees of coronary atherosclerosis. Then, proliferation and migration models of human coronary artery smooth muscle cells (HCASMCs) were established with ox-LDL, and the relative expression of differentially expressed lncRNAs was validated using qRT-PCR. This work might provide a novel insight into ox-LDL-induced HCASMC dysfunction in atherosclerosis and may suggest a promising strategy for CAD.

MATERIALS AND METHODS

Study Subjects, Coronary Artery Segment Preparation, Pathological Analysis, and RNA Sequencing

The methods and materials have been described in our previous study (Pan et al., 2019).

Bioinformatic Analysis

Differentially expressed lncRNAs and mRNAs were identified using the R Limma package (version 3.45.9). Kyoto Encyclopedia of Genes and Genomes (KEGG) and Gene Ontology (GO) functional enrichment analyses of these lncRNAs were performed using the clusterprofiler package in R (version 3.17.0). *Cis* target gene prediction involved the identification of mRNA genes located within 100,000 bp upstream or downstream of the lncRNAs as the target genes of the lncRNA. To perform weighted gene coexpression network analysis (WGCNA), we used the R WGCNA package (version 1.69) to build gene coexpression networks. Three databases, miRDB[1], TargetScan[2]), and DIANA-TarBase[3], were used to predict the competing endogenous RNA (ceRNA) network of lncRNA–miRNA–mRNA, and the intersection of the results was analyzed.

Human Coronary Artery Smooth Muscle Cell Culture and Stimulation

Human coronary artery smooth muscle cells were purchased from Sigma. HCASMCs were cultured in a humidified incubator at 37°C supplied with 5% CO_2 using Dulbecco's modified Eagle's medium (DMEM; Gibco, United States) supplemented with 10% fetal bovine serum (FBS; Gibco) and 1% penicillin (100 μ/ml) and streptomycin (100 μg/ml) (Beyotime, Shanghai, China). The cells were divided into two groups. One was cultured with basic DMEM, and the other was administered 0, 25, 50, 75, and 100 mg/L ox-LDL purchased from Yiyuan Biotechnologies (Guangzhou, China) to simulate an abnormal lipid environment and build proliferation and migration models.

Cell Counting Kit 8 Analysis

For the cell viability and proliferation assay, Cell Counting Kit 8 (CCK-8) was conducted using a CCK-8 assay kit (APExBIO, United States). HCASMCs (5,000 cells/well) in 100 μl were plated in a 96-well microplate (Corning, NY, United States). The absorbance was measured at 450 nm every 12 h using a microplate reader (Multiskan FC, Thermo Fisher Scientific, Waltham, MA, United States) according to the manufacturer's instructions.

Cell Cycle Analysis

Two groups of cells were treated with basic DMEM and ox-LDL (50 mg/L) for 24 h. HCASMCs (1 × 106) were detached from six-well plates using 0.25% trypsin–ethylene diamine tetraacetic acid (EDTA) (Beyotime, Shanghai, China) (Corning, NY, United States). Digested cells were collected and washed with phosphate buffered saline (PBS; Beyotime, Shanghai, China), centrifuged twice (2,000 × *g* rpm, 5 min), fixed in 70% ethanol, and kept at 4°C overnight. Next, the cells were centrifuged at 1,000 × *g* rpm for 3 min and washed with PBS to remove residual ethanol. The centrifugation pellet was then resuspended in 500 μl of working fluid containing 10% RNase A and 90% propidium

[1]http://www.mirdb.org/

[2]www.targetscan.org

[3]http://www.microrna.gr/tarbase

iodide (KeyGen BioTECH, Nanjing, China) for 60 min in the dark. The red fluorescence of propidium iodide was analyzed at 488 nm. Cell cycle analysis was conducted with a flow cytometer (Gallios Flow Cytometer; Beckman Coulter, United States), and data were processed with the corresponding software (Kaluza for Gallios; Beckman Coulter, United States).

Wound Healing Assay

Migration of HCASMCs was tested by a wound healing assay. Cells at 95% confluence were plated on six-well plates (Corning, NY, United States) in a monolayer. A sterile 200-μl pipette tip was used to scratch across the monolayer of cells. After 24 h, cells were photographed using an Olympus-CKX53 microscope (Olympus, Tokyo, Japan). The wound area was measured by ImageJ software (version 1.46, NIH, United States). The cell migration rate was calculated as follows: cell migration rate = (wound area at 0 h–wound area at 24 h)/wound area at 0 h × 100%.

Transwell Assay

HCASMCs were plated on six-well plates and stimulated with 50 mg/L ox-LDL for 24 h. Then, 200 μl cells (1×10^5 cells/ml) were seeded into the upper compartment of Transwell chambers (3422, Corning, New York, NY, United States). Then, 500 μl DMEM with 10% FBS was added to the lower chambers, and all of the Transwell chambers were incubated at 37°C in a 5% CO_2 atmosphere for 24 h. After removing the medium, the cells on the upper side of the filter membrane were removed using a cotton swab, and all of the cells that migrated to the lower side were fixed in 4% glutaraldehyde for 30 min. Finally, the fixed cells were stained with 0.1% crystal violet for 30 min and washed with PBS, and then the migratory cells were counted and photographed with an Olympus-CKX53 microscope.

qRT-PCR

Total RNA was extracted using TRIzol (Invitrogen), and cDNA was prepared with TransScript One-Step gDNA Removal (Vazyme, Nanjing, China) and cDNA Synthesis SuperMix (Vazyme) according to the manufacturer's instructions. cDNA was amplified in StepOnePlus (Applied Biosystems) equipment with SYBR qPCR Master Mix (Vazyme). The oligonucleotide sequences of the primers used for qRT-PCR are shown in **Table 1**. glyceraldehyde-3-phosphate dehydrogenase (GAPDH) was used as an internal reference gene to standardize cycle threshold (CT) values to estimate gene expression. Relative lncRNA expression was calculated using the $2^{-\Delta\Delta ct}$ method. Each sample and gene were processed in three parallel holes to ensure quantitative accuracy.

Data Analysis

Statistical analyses were performed with SPSS (version 25.0), GraphPad Prism (version 8.0), and R software (version 3.5.1). Data normality and homogeneity of variance were calculated using SPSS 25.0 software. Statistical analyses were then performed with *t*-tests (parametric unpaired or paired, two groups of analysis) and Mann–Whitney *U* tests (non-parametric unpaired). Multiple-group analysis was performed by ANOVA. Data are represented as the mean ± SD unless otherwise stated. When a p value was less than 0.05, the result was considered to be of statistical significance. All experimental data were presented using GraphPad Prism 8.0 software and R 3.5.1 software.

RESULTS

Global Analysis of Coronary Artery RNA Sequencing Identified lncRNAs and mRNAs

Hematoxylin and eosin (H&E) staining was used to evaluate the natural history and histological classification of coronary atherosclerotic lesions, and the results of H&E staining of histologic characterization were shown in our previous study (Pan et al., 2019). RNA sequencing of coronary artery segments was performed to detect the differentially expressed lncRNAs and mRNAs. After normalization, all the data in these segments are presented in the heatmap (**Figures 1A**, **2A**). A volcano plot showed the highly or lowly expressed (fold change > 2, $p < 0.05$) lncRNAs (**Figures 1B,C**) and mRNAs (**Figures 2B,C**) of stage 1 and stage 2 vs. stage 4 in the data. Taking the intersection, 68 (seven upregulated and 61 downregulated) lncRNAs and 222 (91 upregulated and 131 downregulated) mRNAs were included (**Table 2**; **Figures 1D**, **2D**).

Gene Ontology and Kyoto Encyclopedia of Genes and Genomes Enrichment of the Differentially Expressed Genes

Gene Ontology analyses were performed on three different aspects, including biological process (BP), cellular component (CC), and molecular function (MF), reflecting the dynamic alteration processes during different stages of atherosclerosis (**Figure 3**). According to the functional enrichment results, 78 BP terms, 129 CC terms, and 47 MF terms were enriched in differentially expressed genes (DEGs). The most enriched BP terms included actin filament organization, cell–substrate junction assembly, and cell–substrate junction organization. Focal adhesion, cell-substrate junctions, and clathrin-coated vesicle membranes were the most enriched CC terms. The most enriched MF terms were actin binding, endodeoxyribonuclease activity, producing 3′-phosphomonoesters, and four-way junction DNA binding. Next, a KEGG pathway enrichment analysis was performed to analyze the most significantly enriched pathways for DEGs (**Figure 4**). A total of 178 pathways were enriched in DEGs, and the top 5 enriched pathways were the Fanconi anemia pathway, mechanistic target of rapamycin kinase (mTOR) signaling pathway, homologous recombination, non-small-cell lung cancer, and fatty acid elongation pathway.

Target Genes of lncRNAs and ceRNA Interaction Model

Cis function prediction analysis of the 68 lncRNAs and 222 mRNAs based on positional relations showed that *GON4L*, which is located 72,001 upstream, is the co-localized target gene of LNC_000439. Pearson correlation was applied to analyze the correlation between differentially expressed lncRNAs and mRNA expression in coronary artery samples. The results showed that *GON4L, STMN1, ZNFX1, CD9, HSD17B4, M6PR, PRG4, SNX10,*

TABLE 1 | Summary of the oligonucleotide primer sequences.

Gene/LncRNA	Forward primer	Reverse primer
GAPDH	GTCTCCTCTGACTTCAACAGCG	ACCACCCTGTTGCTGTAGCCAA
LNC_000684	CTGATGCTCCCAACTGTCTACC	CCAACGTGCCCATTTCTTT
LNC_001046	GCTTCTCAACAGCGAAACAA	GGTGGCTCAGCTCCAATCT
LNC_001333	CTTTGAGCCTTTCCTCTGCC	ACCTCCCCGAAGTCTCCTAC
LNC_001538	ATTCTTGGTGAGGTCTTTTGC	CCTGGATTTTACCCCTGTTCT
LNC_002115	ATGTGGGAGATGGGGAAGGC	ATCGGCAAGGTTTGGCTGAC
LNC_002936	GGACCTCATTCCCAAGCAT	GGGTGGCAGCAGGAGTAAA
STMN1	CCTTATCCCAGTTGATTGTGCAGA	TTTGACCGAGGGCTGAGAATC
SNX10	TTCAGAAAGTTCATCCTCTGGGC	GATTCCTGCGGAGCTGTATTTAC
SCAND1	ACGGTGTGTTGTACTTTGTCATCG	AAGTCCTCTCGCTTGGTCAAAC
MSRA	GGAACTGCTCAAGGTCTTCTGG	CTCCATTTGCTTGGCAGAGGTC
M6PR	ACTTGCGACTTGGTAGGAGAAAAG	GGCACACCCTGAAGATGTAGATG
QRICH1	CACCAGTGTTCAGCCACAAACC	GGTTGCTCAGTAGGCTGGTGAA

GAPDH, glyceraldehyde-3-phosphate dehydrogenase; STMN1, stathmin 1; SNX10, sorting nexin 10; SCAND1, SCAN domain containing 1; MSRA, methionine sulfoxide reductase A; M6PR, mannose-6-phosphate receptor; QRICH1, glutamine rich 1.

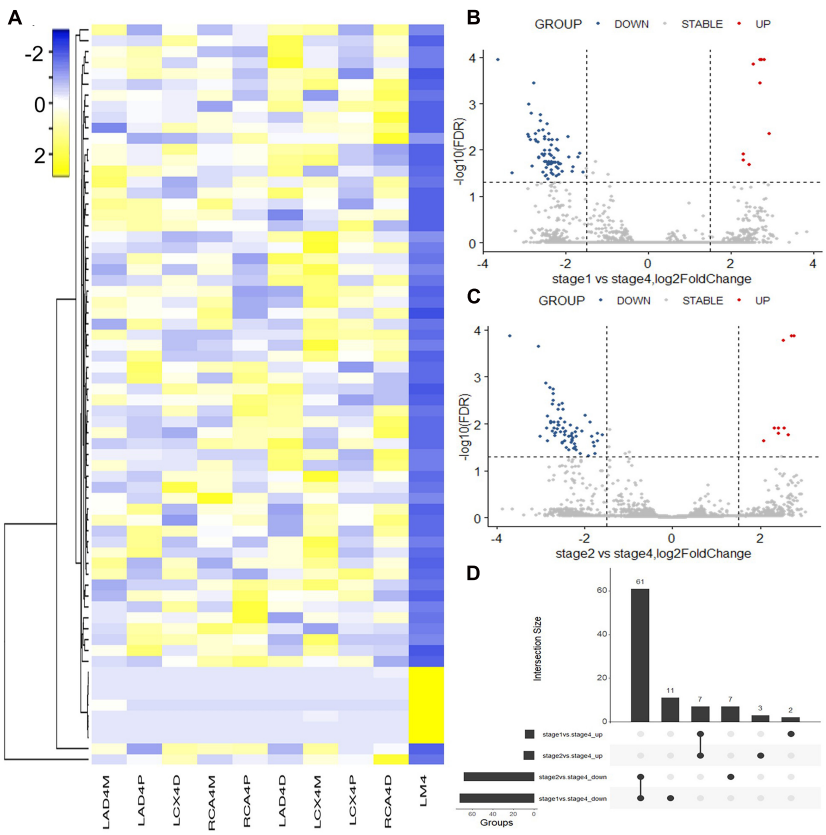

FIGURE 1 | Differentially expressed lncRNAs identified with RNA sequencing. **(A)** Heatmap of the differentially expressed lncRNAs between coronary artery segments. **(B)** Volcano map of differentially expressed lncRNAs between stage 1 and stage 4. **(C)** Volcano map of differentially expressed lncRNAs between stage 2 and stage 4. **(D)** The intersection of differentially expressed lncRNAs in stages 1 and 2 vs. stage 4. Stage: 0, normal tunica intima; 1, fatty streak tunica intima; 2, fibrous plaques tunica intima; 3, atherosclerotic tunica intima; 4, secondary affection tunica intima.

NSDHL, *MSRA*, *SCAND1*, *UBXN6*, *QRICH1*, and *RANBP3* are co-expressed target genes of LNC_002936, LNC_004569, LNC_005730, LNC_004896, LNC_001055, LNC_005605, and LNC_000555. The Pearson correlations of the top 3 correlated genes are presented in **Table 3**, and the regulatory network of lncRNAs and co-expressed genes is shown in **Figure 5A**. Then, using the following three databases, including miRDB, TargetScan, and DIANA-TarBase, as described in the "Materials and Methods" section, and intersected with the RNA sequencing results to predict lncRNA–miRNA–mRNA (ceRNA) networks,

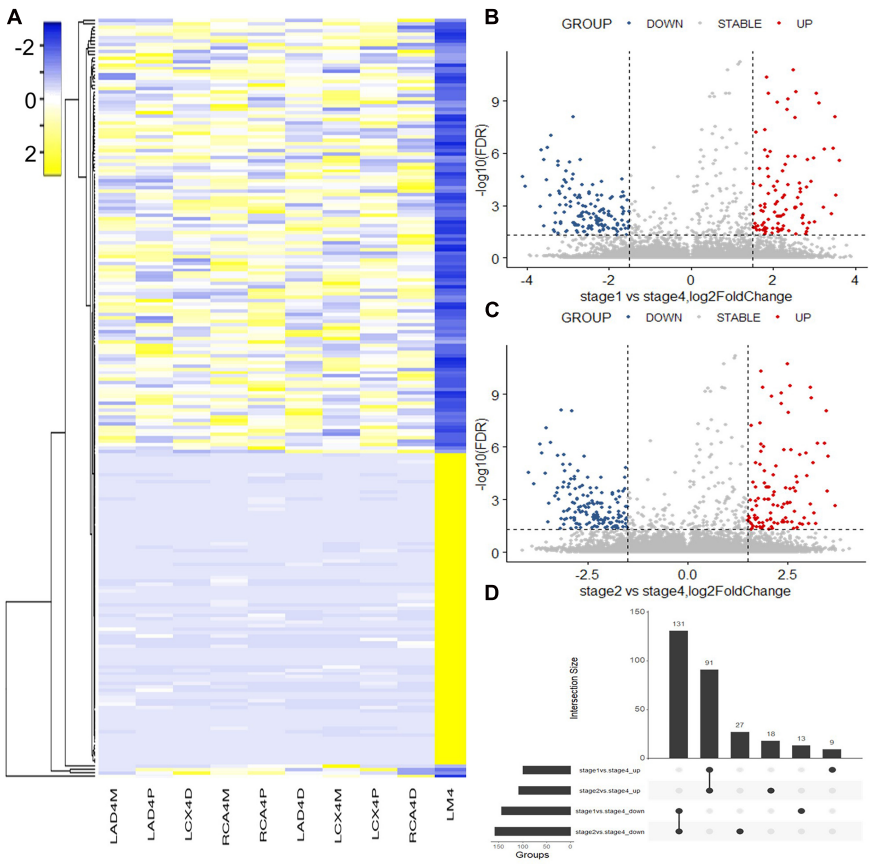

FIGURE 2 | Differentially expressed mRNAs identified with RNA sequencing. **(A)** Heatmap of the differentially expressed mRNAs between coronary artery segments. **(B)** Volcano map of differentially expressed mRNAs between stage 1 and stage 4. **(C)** Volcano map of differentially expressed mRNAs between stage 2 and stage 4. **(D)** The intersection of differentially expressed mRNAs in stages 1 and 2 vs. stage 4. Stage: 0, normal tunica intima; 1, fatty streak tunica intima; 2, fibrous plaques tunica intima; 3, atherosclerotic tunica intima; 4, secondary affection tunica intima.

TABLE 2 | Summary of the comparisons of lncRNA and mRNA expression levels in different stages of atherosclerosis.

Differential analysis	Intersection	Stage 1 vs. Stage 4	Stage 2 vs. Stage 4
Differentially expressed lncRNAs	68	81	78
Upregulated lncRNAs	7	9	10
Downregulated lncRNAs	61	72	68
Differentially expressed mRNAs	222	244	267
Upregulated mRNAs	91	100	109
Downregulated mRNAs	131	144	158

Stage: 0, normal tunica intima; 1, fatty streak tunica intima; 2, fibrous plaques tunica intima; 3, atherosclerotic tunica intima; 4, secondary affection tunica intima.

LNC_000555, LNC_001055, and LNC_005730 can affect the expression of *GON4L, M6PR, MSRA, QRICH1, SNX10, STMN1*, and *ZNFX1* by adsorbing miRNAs, including miR-106a, miR-130a, and miR-221 (**Figure 5B**).

Weighted Gene Co-expression Network Analysis

To identify co-regulated sets of genes, also known as modules participating in the initiation and development of atherosclerosis, we performed a WGCNA of our RNA sequencing data set for atherosclerosis at different developmental stages. A total of 15,501 genes were included, and 53 coexpressed gene modules were detected. The module size ranged from 53 to 2,967 genes. Each module was assigned a different color. Hierarchical clustering of samples to detect outliers used in the analysis is shown in **Figure 6A**. We chose the power of $\beta = 3$ (scale-free $R^2 = 0.9116$, slope $= -1.154$) as the soft thresholding to construct a scale-free network (**Figure 6B**). Next, a cluster dendrogram was generated according to the dissimilarity of the topological overlap matrix, and the different colors correspond to the coexpression modules in atherosclerosis (**Figure 6C**).

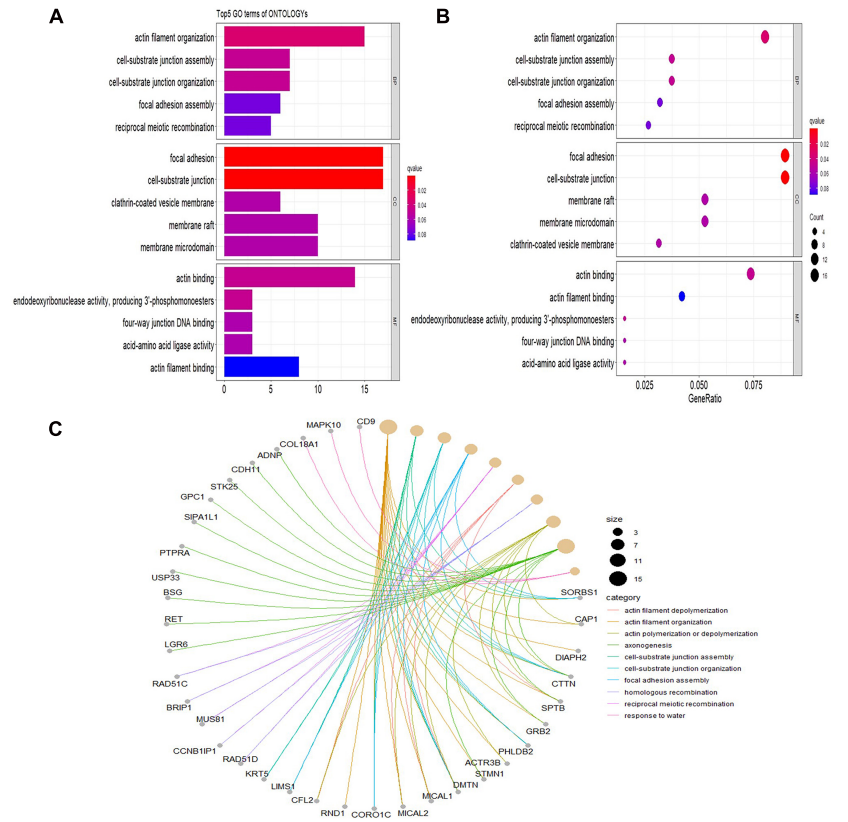

FIGURE 3 | Significantly enriched Gene Ontology (GO) terms of differentially expressed genes based on their functions. **(A)** Bar chart of the top 5 BP, CC, and MF terms in the enrichment analysis. **(B)** Bubble map of the top 5 BP, CC, and MF terms in the enrichment analysis. **(C)** Chord plot of the top 5 BP, CC, and MF terms in the enrichment analysis. BP, biological process; CC, cellular component; MF, molecular function.

Acceptable discriminability was presented between modules in the similarity heatmap plot (**Figure 6D**). The module eigengene (ME) is the first principal component of each module and represents the expression levels of all genes in the module. Gene significance (GS) was used to evaluate the correlation between genes and clinical features with linear regression. The module significance (MS) was calculated by averaging the absolute GS values of all genes in the coexpression module. The most statistically significant module ($p < 0.0001$) was further analyzed. By gathering similarly expressed genes, 53 coexpressed gene modules were detected (**Figure 6E**). The MEs in the yellow module showed a higher correlation with the stage of atherosclerosis ($R^2 = 0.86$, $p = 7.29E\text{-}10$) (**Figure 6F**). Then, a network heatmap plot (**Figure 6G**) was created by WGCNA showing overall module-related gene branches in hierarchical clustering dendrograms.

Proliferation and Migration of Human Coronary Artery Smooth Muscle Cells Induced by ox-LDL

Oxidized low-density lipoprotein was administered to HCASMCs *in vitro* to simulate abnormal lipid metabolism in atherosclerosis. We performed CCK-8 assay and cell cycle analysis to evaluate the proliferation of HCASMCs induced by ox-LDL at 0, 25, 50, 75, and 100 mg/L for different times. The CCK-8 results indicated that the cell proliferation level was significantly increased in the experimental groups (**Supplementary Figure 1A**). Cell cycle analysis showed that the cell population increased in the S and S + G2 phases and decreased in the G1 phase, which confirms the result (**Supplementary Figure 1B**). Wound healing and Transwell assays were performed to validate the migration of HCASMCs exposed to 50 mg/L for 24 h. There was a significant decrease in the wounded area at 24 h post scratch vs. controls (**Supplementary Figure 1C**). In Transwell assays, the intervention group had more cells that migrated to the lower chamber than the control group (**Supplementary Figure 1D**). Therefore, the proliferation and migration of HCASMCs can be induced by ox-LDL at 50 mg/L for 24 h.

Validation of the Differentially Expressed lncRNAs and Coexpressed mRNAs in Human Coronary Artery Smooth Muscle Cells

The relative expression of 68 differentially expressed lncRNAs between the proliferation and migration model of HCASMCs

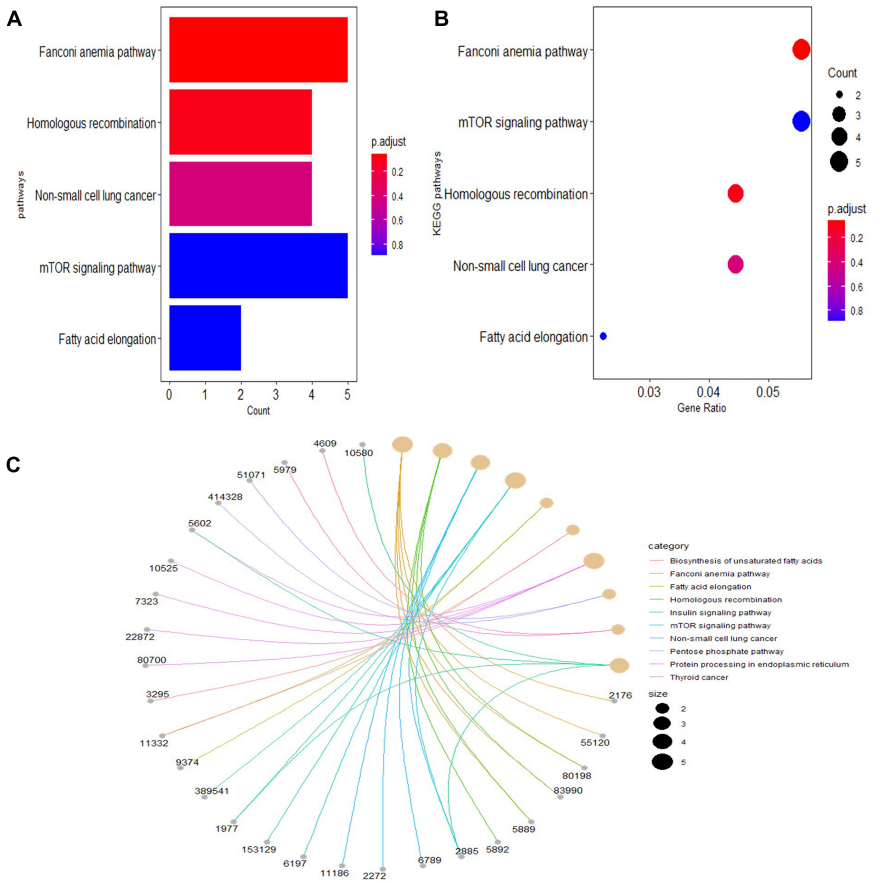

FIGURE 4 | The top 5 enriched Kyoto Encyclopedia of Genes and Genomes (KEGG) pathway terms of differentially expressed genes. **(A)** Bar chart of the top 5 KEGG pathways in the enrichment analysis. **(B)** Bubble map of the top 5 KEGG pathways in the enrichment analysis. **(C)** Chord plot of the top 5 KEGG pathways in the enrichment analysis.

and the control groups was validated using qRT-PCR. The results showed that LNC_000684, LNC_001046, LNC_001333, LNC_001538, and LNC_002115 were downregulated, while LNC_002936 was upregulated in the experimental groups, which was consistent with the RNA sequencing results (**Figure 7A**). In addition, the coexpressed mRNAs of lncRNAs were validated too. Among the 14 coexpressed genes, six of which including *STMN1, SNX10, SCAND1, MSRA, M6PR*, and *QRICH1* were confirmed to be upregulated in the proliferation and migration model of HCASMCs (**Figure 7B**).

DISCUSSION

Cardiovascular diseases are a significant health burden with an ever-increasing prevalence and remain the leading causes of morbidity and mortality worldwide (Shaito et al., 2020). HCASMC proliferation and migration are the pathological basis of atherosclerosis (Catalano et al., 2020; Maguire and Xiao, 2020). The purpose of the present study was to provide a comprehensive survey of lncRNAs and mRNAs in human coronary arteries and identify differentially expressed lncRNAs and mRNAs and possible regulatory pathways according to the histological classification of atherosclerotic lesions. In this study, we identified 68 lncRNAs and 222 mRNAs that were differentially expressed in the 10 coronary artery segment samples by RNA sequencing. GO and KEGG enrichment analyses of the DEGs showed that actin filaments, cell–substrate junctions, and focal adhesion may underlie the occurrence and development of atherosclerosis. *GON4L* was found to be the colocalized target gene of LNC_000439, and 14 genes had high correlations with the expression of seven lncRNAs. In addition, nine lncRNA–miRNA–mRNA networks were constructed, and 53 coexpressed gene modules were detected with WGCNA. The relative expression of six lncRNAs, including downregulated LNC_000684, LNC_001046, LNC_001333, LNC_001538, and LNC_002115 and upregulated LNC_002936, was validated in HCASMCs induced with ox-LDL that proliferate and migrate in the pathological processes of atherosclerosis. In total, six coexpressed target genes, *STMN1, SNX10, SCAND1, MSRA, M6PR*, and *QRICH1*, were upregulated in HCASMCs.

RNA sequencing has become an indispensable tool for transcriptome-wide analysis of differential gene expression,

TABLE 3 | Summary of the top 3 correlated coexpressed genes of lncRNAs.

LncRNA	mRNA gene symbol	Pearson correlation	*p* value
LNC_002936	CD9	0.99966204	5.7×10^{-14}
	NSDHL	0.99958603	1.3×10^{-13}
	ZNFX1	0.99951061	2.5×10^{-13}
LNC_004569	GON4L	0.99341329	8.2×10^{-9}
	MSRA	0.99298806	1.1×10^{-8}
	STMN1	0.99226337	1.6×10^{-8}
LNC_005730	SNX10	0.99862558	1.6×10^{-11}
	SCAND1	0.99825014	4.1×10^{-11}
	PRG4	0.99815934	5.0×10^{-11}
LNC_004896	GON4L	0.99976957	1.2×10^{-14}
	STMN1	0.99972796	2.4×10^{-14}
	UBXN6	0.99967951	4.7×10^{-14}
LNC_001055	ZNFX1	0.99993876	6.2×10^{-17}
	UBXN6	0.99993671	6.5×10^{-17}
	STMN1	0.99993634	7.2×10^{-17}
LNC_005605	UBXN6	0.99904520	3.8×10^{-12}
	ZNFX1	0.99903404	3.8×10^{-12}
	PRG4	0.99902301	4.0×10^{-12}
LNC_000555	GON4L	0.99980242	6.7×10^{-15}
	STMN1	0.99979437	7.8×10^{-15}
	UBXN6	0.99975221	1.7×10^{-14}

CD9, CD9 molecule; NSDHL, NAD(P) dependent steroid dehydrogenase-like; ZNFX1, zinc finger NFX1-type containing 1; GON4L, gon-4 like; MSRA, methionine sulfoxide reductase A; STMN1, stathmin 1; SNX10, sorting nexin 10; SCAND1, SCAN domain containing 1; PRG4, proteoglycan 4; UBXN6, UBX domain protein 6; ZNFX1, zinc finger NFX1-type containing 1.

including non-coding RNAs and differential splicing of mRNAs (Stark et al., 2019). During the study of different cells involved in atherosclerosis, Zhu et al. (2019) performed RNA sequencing to determine miRNA profiles of exosomes derived from control macrophages and nicotine-treated macrophages and found that exosomal miR-21-3p from experimental groups may accelerate the development of atherosclerosis. RNA sequencing was conducted on peripheral blood mononuclear cells (PBMCs) of early onset myocardial infarction (MI) patients, and lncRNA nuclear enriched abundant transcript (NEAT1) was the most highly expressed lncRNA (Gast et al., 2019). In a previous study of specimens of atherosclerosis, the circRNA, miRNA, and mRNA expression profiles of rabbit carotid arteries were analyzed using RNA sequencing, and seven circRNAs were found to be related to atherosclerosis (Zhang et al., 2018). Using RNA sequencing profiling of the aortic intima of lesions, the authors identified a macrophage-specific lncRNA, Macrophage-Associated Atherosclerosis lncRNA Sequence (MAARS), that regulates apoptosis and efferocytosis in atherosclerosis by tethering ELAV like RNA binding protein 1 (ELAVL1) HuR (Simion et al., 2020). Although those RNA sequencing studies of CAD might reflect the pathophysiological changes in CAD, the comprehensive analysis of differentially expressed lncRNAs and mRNAs of human coronary arteries has not been explored with RNA sequencing before. The present study is different from previous studies because it employed the sampling of human coronary artery segments. A large quantity and variety of high-quality lncRNAs and mRNAs were identified. These RNAs were

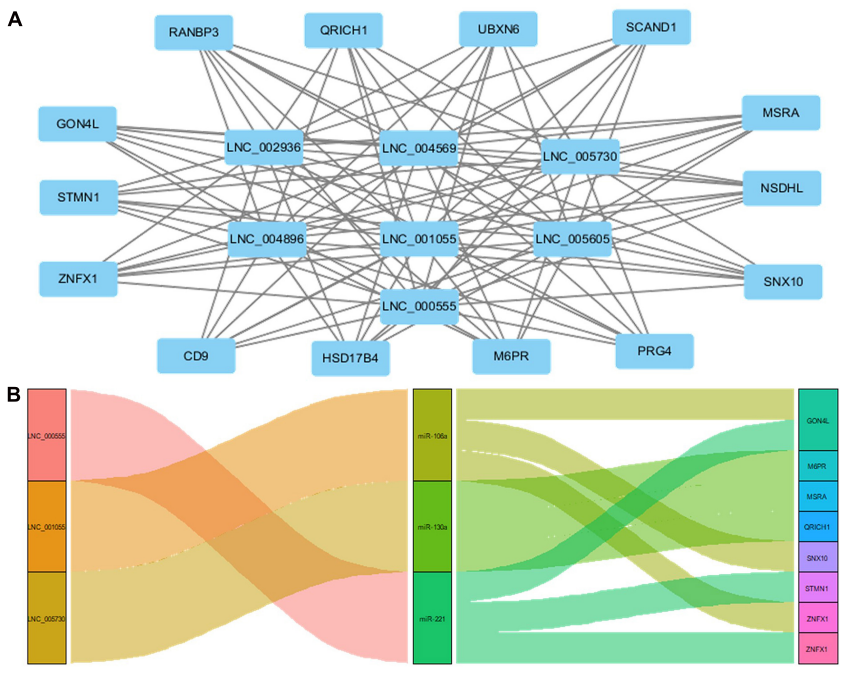

FIGURE 5 | Target genes of lncRNAs and ceRNA interaction model. **(A)** The network of coexpressed target genes of lncRNAs. **(B)** The network of lncRNA–miRNA–mRNA interaction model.

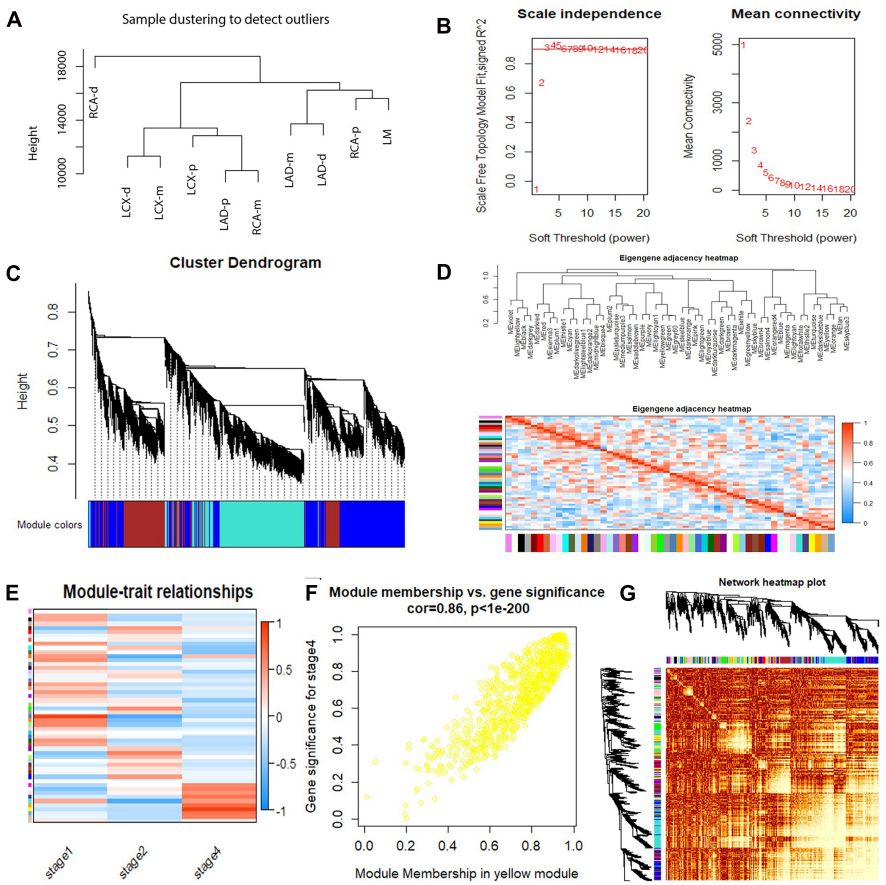

FIGURE 6 | Weighted gene coexpression network analysis (WGCNA) summary. **(A)** Sample clustering to detect outliers. **(B)** Analysis of the scale-free fit index and the mean connectivity for various soft-thresholding powers. **(C)** Cluster dendrogram based on the dissimilarity of the topological overlap matrix. **(D)** The branches of the dendrogram and the eigengene adjacency heatmap. **(E)** Module–trait relationship. **(F)** A scatterplot of gene significance (GS) vs. module membership (MM) in the yellow module. A highly significant correlation between GS and MM in the yellow module (correlation = 0.86; *P* value $< 1^{e-200}$) was detected. **(G)** Network heatmap of the 53 modules.

identified from comprehensive coronary artery tree samples, and histological classification of the atherosclerotic stages was determined by H&E staining. Wide-ranging and deep-going bioinformatic analyses, including GO and KEGG enrichment analyses, target gene prediction, ceRNA interaction models, and WGCNA, were performed to predict possible mechanisms. The top pathway identified in the bioinformatic analysis is the Fanconi anemia pathway, which has been found to regulate important cellular processes such as DNA replication, cell cycle control, and DNA damage repair (Nie et al., 2020). Therefore, the Fanconi anemia pathway might regulate the proliferation and apoptosis of coronary endothelial cells and smooth muscle cells that are associated with atherosclerotic pathology (Wolf and Hunziker, 2020). Previous research indicated that lncRNA can *cis*- or trans-regulate the expression of target genes, which is the main regulation mechanism of lncRNA (Zhou G. F. et al., 2019). The coexpressed target genes in our study are on different chromosomes from the correlated lncRNA, which suggest that these lncRNAs trans-regulate the target genes to affect the occurrence and development of atherosclerosis.

Long non-coding RNAs have emerged as significant players in almost every level of gene function and regulation, and a large number of novel lncRNAs have been uncovered (Qian et al., 2019). A large number of lncRNAs were found to be associated with the proliferation and migration of smooth muscle cells and atherosclerosis. The expression of lncRNA H19 was found to be higher in patients with atherosclerosis, and it promotes atherosclerosis by regulating mitogen-activated protein kinase (MAPK) and nuclear factor (NF)-κ B signaling pathways (Pan, 2017). The lncRNA-FA2H-2-MLKL pathway in atherosclerosis, which regulates autophagic flux and inflammation through the mTOR signaling pathway, was identified by Guo et al. (2019). The lncRNA TUG1 was reported to promote the proliferation of VSMCs and atherosclerosis through the miRNA-21/PTEN axis (Li et al., 2018). Previous studies investigated the functional roles of annotated lncRNAs in cell and animal models; however, no research identified novel differentially expressed lncRNAs and mRNAs from human coronary artery tissues and validated the expression of molecules in HCASMCs. LncRNA can act as a sponge for miRNAs to indirectly regulate miRNA

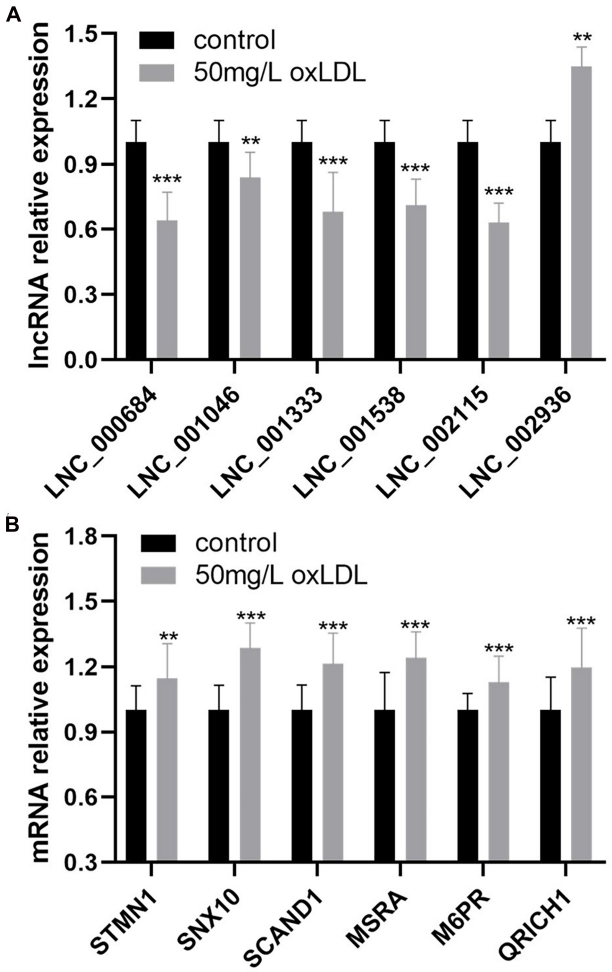

FIGURE 7 | The relative expression of six lncRNAs and coexpressed mRNAs in human coronary artery smooth muscle cells (HCASMCs) induced with oxidized low-density lipoprotein (ox-LDL). **(A)** LNC_000684, LNC_001046, LNC_001333, LNC_001538, and LNC_002115 were downregulated while LNC_002936 was upregulated in the proliferation and migration models of HCASMCs induced with 50 mg/L ox-LDL for 24 h. **(B)** STMN1, SNX10, SCAND1, MSRA, M6PR, and QRICH1 were upregulated in the proliferation and migration models of HCASMCs induced with 50 mg/L ox-LDL for 24 h. $^{**}p < 0.01$, $^{***}p < 0.001$.

downstream target genes, which is defined as the ceRNA regulation model (Han et al., 2020). In our study, through the construction of the ceRNA network, three upregulated lncRNAs including LNC_000555, LNC_001055, and LNC_005730 may act as sponges that absorb miR-106a, miR-130a, and miR-221. Thus, the posttranscriptional inhibition of the three miRNAs on the target genes including *GON4L, M6PR, MSRA, QRICH1, SNX10, STMN1*, and *ZNFX1* was weakened. The target genes are upregulated and affect the occurrence and development of atherosclerosis. CCK-8, cell cycle analysis, Transwell assay, and wound healing assay confirmed the proliferation and migration model of HCASMCs induced with ox-LDL. We identified six novel differentially expressed lncRNAs and six coexpressed target genes from human coronary artery tissues and validated the expression of molecules in HCASMCs. The present study may shed light on the molecular mechanisms underlying the dysfunction of smooth muscle cells in coronary artery atherosclerosis by combining clinical tissues with cells.

There are some limitations in this study. The human coronary artery samples used in the present study were obtained from one case with 10 segments. This sample size was small, and a large-scale study should be conducted in the future to validate the results of this study. In addition, since molecular mechanism and functional experiments were not included in this study, the specific mechanism by which differentially expressed RNAs may participate in the proliferation and migration of HCASMCs, and the development of atherosclerosis was not explored. To increase the potential clinical utility of the identified lncRNAs and mRNAs as CAD biomarkers, the functional roles of the lncRNAs, signaling pathways, and interaction networks identified in the present study should be clarified and validated in further studies.

In the present study, RNA sequencing analysis of coronary arteries identified 68 lncRNAs and 222 mRNAs that were differentially expressed and associated with atherosclerosis. In addition, enrichment analysis, target gene prediction, ceRNA interaction models, and WGCNA were performed to predict possible mechanisms of atherosclerosis. The relative expression of LNC_000684, LNC_001046, LNC_001333, LNC_001538, and LNC_002115 was downregulated, while LNC_002936 was upregulated, which was validated in HCASMCs induced with ox-LDL. In total, six coexpressed target genes were upregulated in the proliferation and migration model of HCASMCs. This study suggests that the differentially expressed lncRNAs may be a target for regulating HCASMC proliferation and migration in atherosclerosis, which will provide a new diagnostic basis and therapeutic target for cardiovascular diseases.

DATA AVAILABILITY STATEMENT

The datasets presented in this study can be found in online repositories. The names of the repository/repositories and accession number(s) can be found below: NCBI SRA; PRJNA705037.

ETHICS STATEMENT

The methods were performed in accordance with the approved guidelines, and all experimental protocols were approved by the Ethics Committee of Nanjing Medical University and The First Affiliated Hospital of Nanjing Medical University.

AUTHOR CONTRIBUTIONS

EJ conceived the study. YZ and SZ drafted the manuscript. YZ, WJ, XG, and LH performed the experiments. CH, JC, and YW analyzed the data. WJ, SH, and HZ edited the manuscript for

intellectual content. All authors read and approved the final manuscript and contributed to the article and approved the submitted version.

FUNDING

This study received support from the National Natural Science Foundation of China (Nos. 81970302, 81170180, 30400173, and 30971257) and the Priority Academic Program Development of Jiangsu Higher Education Institutions.

ACKNOWLEDGMENTS

Dr. En-Zhi Jia is an assistant fellow at the Collaborative Innovation Center for Cardiovascular Disease Translational Medicine. We would like to thank the Core Facility of The First Affiliated Hospital of Nanjing Medical University for its help in the detection of experimental samples.

SUPPLEMENTARY MATERIAL

The Supplementary Material for this article can be found online at: https://www.frontiersin.org/articles/10.3389/fcell.2021.656636/full#supplementary-material

Supplementary Figure 1 | Proliferation and migration of HCASMCs were induced by ox-LDL. **(A)** CCK-8 assay showed the proliferative ability and a marked increase in the viability of HCASMCs after stimulation with ox-LDL at 0, 25, 50, 75, and 100 mg/L. $^{**}p < 0.01$, $^{***}p < 0.001$. **(B)** Cell cycle analysis of HCASMCs stimulated with ox-LDL at 50 mg/L for 24 h. $^{*}p < 0.05$. **(C)** Wound healing assay showing quantification of the residual wounded area at 24 h postscratch vs. controls ($n = 5$). $^{***}p < 0.001$. **(D)** Transwell assays were also used to examine cell migration, and quantitative statistical analysis of cell migration data is presented as the means ± SDs from five samples. $^{***}p < 0.001$.

REFERENCES

Amrein, M. L., Lopez-Ayala, P., Walter, J., Widmer, V., and Mueller, C. (2020). Coronary heart disease and tmao concentrations. *J. Am. Coll. Cardiol.* 75: 3102. doi: 10.1016/j.jacc.2020.03.079

Benjamin, E. J., Virani, S. S., Callaway, C. W., Chamberlain, A. M., Chang, A. R., Cheng, S., et al. (2018). Heart disease and stroke statistics-2018 update: a report from the american heart association. *Circulation* 137, e67–e492. doi: 10.1161/cir.0000000000000558

Case, B. C., and Waksman, R. (2020). Coronary heart disease: have we reached a plateau in primary prevention? *J. Am. Heart Assoc.* 9:e04963. doi: 10.1161/jaha.120.016034

Catalano, A., Bellone, F., Morabito, N., and Corica, F. (2020). Sclerostin and vascular pathophysiology. *Int. J. Mol. Sci.* 21:4779. doi: 10.3390/ijms21134779

Gast, M., Rauch, B. H., Haghikia, A., Nakagawa, S., Haas, J., Stroux, A., et al. (2019). Long noncoding rna neat1 modulates immune cell functions and is suppressed in early onset myocardial infarction patients. *Cardiovasc. Res.* 115, 1886–1906. doi: 10.1093/cvr/cvz085

Gong, J., Chen, Z., Chen, Y., Lv, H., Lu, H., Yan, F., et al. (2019). Long non-coding rna casc2 suppresses pulmonary artery smooth muscle cell proliferation and phenotypic switch in hypoxia-induced pulmonary hypertension. *Respir. Res.* 20:53. doi: 10.1186/s12931-019-1018-x

Grundy, S. M., Stone, N. J., Bailey, A. L., Beam, C., Birtcher, K. K., Blumenthal, R. S., et al. (2019). 2018 aha/acc/aacvpr/aapa/abc/acpm/ada/ags/apha/aspc/nla/pcna guideline on the management of blood cholesterol: a report of the american college of cardiology/american heart association task force on clinical practice guidelines. *Circulation* 139:e1082–e1143. doi: 10.1161/cir.0000000000000625

Guo, F. X., Wu, Q., Li, P., Zheng, L., Ye, S., Dai, X. Y., et al. (2019). The role of the lncrna-fa2h-2-mlkl pathway in atherosclerosis by regulation of autophagy flux and inflammation through mtor-dependent signaling. *Cell Death Differ.* 26, 1670–1687. doi: 10.1038/s41418-018-0235-z

Han, T. S., Hur, K., Cho, H. S., and Ban, H. S. (2020). Epigenetic associations between lncrna/circrna and mirna in hepatocellular carcinoma. *Cancers* 12:2622. doi: 10.3390/cancers12092622

Jin, J. L., Zhang, H. W., Cao, Y. X., Liu, H. H., Hua, Q., Li, Y. F., et al. (2020). Association of small dense low-density lipoprotein with cardiovascular outcome in patients with coronary artery disease and diabetes: a prospective, observational cohort study. *Cardiovasc. Diabetol.* 19:45. doi: 10.1186/s12933-020-01015-6

Li, F. P., Lin, D. Q., and Gao, L. Y. (2018). Lncrna tug1 promotes proliferation of vascular smooth muscle cell and atherosclerosis through regulating mirna-21/pten axis. *Eur. Rev. Med. Pharmacol. Sci.* 22, 7439–7447. doi: 10.26355/eurrev_201811_16284

Mach, F., Baigent, C., Catapano, A. L., Koskinas, K. C., Casula, M., Badimon, L., et al. (2020). 2019 esc/eas guidelines for the management of dyslipidaemias: lipid modification to reduce cardiovascular risk. *Eur. Heart J.* 41, 111–188. doi: 10.1093/eurheartj/ehz455

Maguire, E. M., and Xiao, Q. (2020). Noncoding rnas in vascular smooth muscle cell function and neointimal hyperplasia. *FEBS J.* 287, 5260–5283. doi: 10.1111/febs.15357

Nie, Y., Wilson, A. F., DeFalco, T., Meetei, A. R., Namekawa, S. H., and Pang, Q. (2020). Fancd2 is required for the repression of germline transposable elements. *Reproduction*159, 659–668. doi: 10.1530/rep-19-0436

Orekhov, A. N., Sukhorukov, V. N., Nikiforov, N. G., Kubekina, M. V., Sobenin, I. A., Foxx, K. K., et al. (2020). Signaling pathways potentially responsible for foam cell formation: cholesterol accumulation or inflammatory response-what is first? *Int. J. Mol. Sci.* 21:2716. doi: 10.3390/ijms21082716

Pan, J. X. (2017). Lncrna h19 promotes atherosclerosis by regulating mapk and nf-kb signaling pathway. *Euro. Rev. Med. Pharmacol. Sci.* 21, 322–328.

Pan, R. Y., Zhao, C. H., Yuan, J. X., Zhang, Y. J., Jin, J. L., Gu, M. F., et al. (2019). Circular rna profile in coronary artery disease. *Am. J. Transl. Res.* 11, 7115–7125.

Qian, X., Zhao, J., Yeung, P. Y., Zhang, Q. C., and Kwok, C. K. (2019). Revealing lncrna structures and interactions by sequencing-based approaches. *Trends Biochem. Sci.* 44, 33–52. doi: 10.1016/j.tibs.2018.09.012

Robinson, E. K., Covarrubias, S., and Carpenter, S. (2020). The how and why of lncrna function: an innate immune perspective. *Biochim. Biophys. Acta Gene Regul. Mech.* 1863:194419. doi: 10.1016/j.bbagrm.2019.194419

Shaito, A., Thuan, D. T. B., Phu, H. T., Nguyen, T. H. D., Hasan, H., Halabi, S., et al. (2020). Herbal medicine for cardiovascular diseases: efficacy, mechanisms, and safety. *Front. Pharmacol.* 11:422. doi: 10.3389/fphar.2020.00422

Simion, V., Zhou, H., Haemmig, S., Pierce, J. B., Mendes, S., Tesmenitsky, Y., et al. (2020). A macrophage-specific lncrna regulates apoptosis and atherosclerosis by tethering hur in the nucleus. *Nat. Commun.* 11:6135. doi: 10.1038/s41467-020-19664-2

Stark, R., Grzelak, M., and Hadfield, J. (2019). Rna sequencing: the teenage years. *Nat. Rev. Genet.* 20, 631–656. doi: 10.1038/s41576-019-0150-2

Tang, R., Mei, X., Wang, Y. C., Cui, X. B., Zhang, G., Li, W., et al. (2019). Lncrna gas5 regulates vascular smooth muscle cell cycle arrest and apoptosis via p53 pathway. *Biochim. Biophys. Acta Mol. Basis Dis.* 1865, 2516–2525. doi: 10.1016/j.bbadis.2019.05.022

Wolf, M. P., and Hunziker, P. (2020). Atherosclerosis: insights into vascular pathobiology and outlook to novel treatments. *J. Cardiovasc. Transl. Res.* 13, 744–757. doi: 10.1007/s12265-020-09961-y

Zhang, F., Zhang, R., Zhang, X., Wu, Y., Li, X., Zhang, S., et al. (2018). Comprehensive analysis of circrna expression pattern and circrna-mirna-mrna network in the pathogenesis of atherosclerosis in rabbits. *Aging* 10, 2266–2283. doi: 10.18632/aging.101541

Zhang, X., Bishawi, M., Zhang, G., Prasad, V., Salmon, E., Breithaupt, J. J., et al. (2020). Modeling early stage atherosclerosis in a primary human vascular microphysiological system. *Nat. Commun.* 11:5426. doi: 10.1038/s41467-020-19197-8

Zhou, G. F., Zhang, L. P., Li, B. X., Sheng, O., Wei, Q. J., Yao, F. X., et al. (2019). Genome-wide identification of long non-coding rna in trifoliate orange (poncirus trifoliata (l.) raf) leaves in response to boron deficiency. *Int. J. Mol. Sci.* 20:5419. doi: 10.3390/ijms20215419

Zhou, Y., He, X., Liu, R., Qin, Y., Wang, S., Yao, X., et al. (2019). Lncrna crnde regulates the proliferation and migration of vascular smooth muscle cells. *J. Cell. Physiol.* 234, 16205–16214. doi: 10.1002/jcp.28284

Zhu, J., Liu, B., Wang, Z., Wang, D., Ni, H., Zhang, L., et al. (2019). Exosomes from nicotine-stimulated macrophages accelerate atherosclerosis through mir-21-3p/pten-mediated vsmc migration and proliferation. *Theranostics* 9, 6901–6919. doi: 10.7150/thno.37357

Conflict of Interest: The authors declare that the research was conducted in the absence of any commercial or financial relationships that could be construed as a potential conflict of interest.

frontiers in Cell and Developmental Biology

ORIGINAL RESEARCH
published: 21 May 2021
doi: 10.3389/fcell.2021.660316

Activin A as a Novel Chemokine Induces Migration of L929 Fibroblasts by ERK Signaling in Microfluidic Devices

Lingling Jiang[1,2†], Yan Qi[2†], Xianghan Kong[2], Runnan Wang[3], Jianfei Qi[4], Francis Lin[5], Xueling Cui[3] and Zhonghui Liu[2*]*

[1] Department of Oral Comprehensive Therapy, School and Hospital of Stomatology, Jilin University, Changchun, China, [2] Department of Immunology, College of Basic Medical Sciences, Jilin University, Changchun, China, [3] Department of Genetics, College of Basic Medical Sciences, Jilin University, Changchun, China, [4] Department of Biochemistry and Molecular Biology, School of Medicine, University of Maryland, Baltimore, MD, United States, [5] Department of Physics and Astronomy, University of Manitoba, Winnipeg, MB, Canada

OPEN ACCESS

Edited by:
Dimitra Gkika,
INSERM UMR 1277 Hétérogénéité, Plasticité et Résistance aux Thérapies Anticancéreuses (CANTHER), France

Reviewed by:
Pierre-Olivier Angrand,
Lille University of Science and Technology, France
Samir Jose Bolivar Gonzalez,
University of Atlántico, Colombia

***Correspondence:**
Xueling Cui
cxl@jlu.edu.cn
Zhonghui Liu
liuzh@jlu.edu.cn

† These authors have contributed equally to this work and share first authorship

Specialty section:
This article was submitted to Cell Adhesion and Migration, a section of the journal Frontiers in Cell and Developmental Biology

Received: 02 February 2021
Accepted: 27 April 2021
Published: 21 May 2021

Citation:
Jiang L, Qi Y, Kong X, Wang R, Qi J, Lin F, Cui X and Liu Z (2021) Activin A as a Novel Chemokine Induces Migration of L929 Fibroblasts by ERK Signaling in Microfluidic Devices. Front. Cell Dev. Biol. 9:660316. doi: 10.3389/fcell.2021.660316

Activin A, a member of the transforming growth factor-beta (TGF-β) superfamily, contributes to tissue healing and fibrosis. As the innate tissue cells, fibroblasts also play an important role in wound healing and fibrosis. Herein, this study was aimed to investigate how activin A exhibited regulatory effects on adhesion and migration of fibroblasts. We found that activin A induced the migration of fibroblast cell line L929 cells in transwell chamber and microfluidic device. Activin A also promoted L929 cells adhesion, but did not affect L929 cells viability or proliferation. In addition, activin A induced α-SMA expression and TGF-β1 release, which were factors closely related to tissue fibrosis, but had no effect on IL-6 production, a pro-inflammatory cytokine. Furthermore, activin A elevated calcium levels in L929 cells and increased p-ERK protein levels. Activin A-induced migration of L929 cells was attenuated by ERK inhibitor FR180204. To conclude, these data indicated that activin A as a novel chemokine induced the chemotactic migration of L929 cells via ERK signaling and possessed the pro-fibrosis role. These findings provide a new insight into understanding of activin A in tissue fibrosis.

Keywords: activin A, fibroblasts, migration, ERK, microfluidic device

INTRODUCTION

Fibroblasts are widely distributed in various tissues and actively involved in tissue damage repair, remodeling and fibrosis. Fibroblasts stimulated by degeneration, necrosis or tissue injury are demonstrated to participate in inflammatory response and immune regulation by secreting factors such as nitric oxide (NO), interleukin-1β (IL-1β) and IL-6, and facilitate wound healing by infiltrating to the damaged site, gradually replacing white blood cells (Eming et al., 2014). Fibroblasts are also involved in tissue remodeling in the late stage of inflammation through cell proliferation, adhesion, migration and collagen synthesis (Sun et al., 2014; Burr et al., 2020), while abnormal activation of fibroblasts may result in scar formation and tissue fibrosis (Bai et al., 2015; Nagpal et al., 2016).

As a member of the transforming growth factor-β (TGF-β) superfamily, activin A is widely expressed in a variety of tissues and acts as a multifunctional growth and differentiation factor. Activin A regulates cell proliferation, differentiation, apoptosis and migration in an autocrine/paracrine manner, and plays a critical role in embryonic development, neuroprotection, tissue remodeling and immune response (Aleman-Muench and Soldevila, 2012; van den Ameele et al., 2012; Kaiser et al., 2013; Donovan et al., 2017). As suggested in previous studies, activin A controls the cytokine signaling cascades that drive the inflammatory response (Jones et al., 2007), and regulate the activation of M2 macrophages to affect tissue healing and fibrosis in the late stage of inflammation (Morianos et al., 2019). Furthermore, as an important factor in inducing liver, kidney and lung fibrosis, activin A is reported to be tightly associated with the occurrence and development of numerous fibrotic diseases (Hardy et al., 2015; Hruska et al., 2017; Zhang et al., 2018).

The aberrant overexpression of activin A is frequently detected in the case of inflammation or tissue injury (Sun et al., 2014; Qi et al., 2021). Although our previous study has reported the antagonistic effects of activin A and TNF-α on fibroblast activation (Jiang et al., 2020), the role of activin A in adhesion and migration of fibroblasts is not well characterized. In the present study, the murine fibroblast cell line L929 was utilized to investigate the effects of activin A on adhesion and migration of fibroblasts. We found that activin A promoted L929 cell adhesion, migration and TGF-β1 release in a dose-dependent manner, proving further that activin A was a chemokine for fibroblasts in the process of tissue repair and fibrosis. These findings implicated that activin A may serve as a novel therapeutic target for tissue fibrosis.

MATERIALS AND METHODS

Cell Culture and Treatment

Murine fibroblast cell line L929 (American Type Culture Collection, ATCC, Rockville, MD, United States) was maintained in high glucose DMEM supplemented with 10% fetal bovine serum (FBS) at 37°C in a humidified incubator containing 5% CO_2. L929 cells were seed in 12-well plates and treated with 0, 10, or 20 ng/mL activin A for 2 h, with or without the pretreatment with 1 μmol/L ERK inhibitor (FR180204) for 1 h. Experiments were repeated at least three times with independent cell cultures.

Reagents

Recombinant human/mouse/rat activin A was purchased from R&D systems (Minneapolis, MN, United States). Recombinant murine SDF-1α (CXCL12) were obtained by PeproTech (Rocky Hill, NJ, United States). MTT and Giemsa stain were provided by Sigma-Aldrich (Oakville, ON, Canada). Fluo-4 was bought from Thermo Fisher Scientific (Ottawa, ON, Canada). Enzyme-linked immunosorbent assay (ELISA) kits for TGF-β1 and IL-6 were obtained from eBioscience (San Diego, CA, United States). Selective ERK inhibitor FR180204 was purchased from Absin (Shanghai, China). Rabbit polyclonal antibody against α-SMA was purchased from Abcam (Cambridge, United Kingdom). Rabbit polyclonal antibody against GAPDH was bought from Absin (Shanghai, China). Rabbit polyclonal antibodies against phospho-ERK1/2 (p-ERK) and ERK were obtained from Cell Signaling Technology (Danvers, MA, United States).

Real-Time Cell Analysis

Real-time cell analysis (RTCA) is a technology based on the principle of microelectronic biosensor chip, which can realize the real-time analysis of cells without markers in the process of experiment. The RTCA instrument (xCELLigence RTCA S16; ACEA Biosciences, California, United States) was used to analyze the proliferation and adhesion properties of L929 cells. Initially, 50 μl of cell-free culture medium was added to the well of an E16 xCELLigence microtiter plate, which was then inserted into the RTCA device. After 1 min, the background impedance was measured for each well. Subsequently, L929 cells (2×10^4 cells in 50 μl culture medium) were added to each well and cultured for 3 h, and then treated with different concentrations of activin A for another 67 h in the proliferation assay. In the adhesion assay, cells and activin A were added to each well together and cultured for 4 h. Cells were monitored in 5 or 15 min intervals. Each experiment was performed in duplicate and repeated three times. The impedance of the cell sensor was described and measured as the cell index (CI), which reflected the cell activity.

MTT Assay

L929 cells (2×10^4 cells per well) were seeded into a 96-well plate in triplicate and incubated in 1% FBS-DMEM containing activin A (0, 5, 10, or 20 ng/mL) for 24 h. 10 μl of MTT solution (5 mg/mL) was added to each well and incubated for 3 h at 37°C. Then the medium was removed, and 100 μl DMSO was added to dissolve the formed formazan crystals. Each experiment was carried out in triplicate. The absorbance at 570 nm was measured using a microplate reader.

Transwell Chamber Assay

Chemotactic migration of L929 cells was evaluated by transwell chamber assay as described previously (Yuan et al., 2019). Briefly, L929 cells (2×10^4 cells in 200 μl culture media with 1% FBS) were seeded in the upper chambers (8 μm pore size; Corning, NY, United States). The lower compartments were filled with 500 μl culture media containing activin A (0, 5, 10, and 20 ng/mL) or CXCL12 (100 ng/mL). After incubation for 10 h, the cells on the upper side of chamber were removed with cotton-tipped swabs. Cells that had passed through the insert membranes were fixed with 4% paraformaldehyde for 20 min and stained with Giemsa. Experiments were repeated at least three times. The stained cells were imaged on an inverted microscope and cell numbers were counted in five randomly chosen fields from each chamber.

Microfluidic Cell Migration Assay

A microfluidic triple docking device (D^3-Chip) fabricated by the standard photolithography and soft-lithography technique was used as described previously (Xie et al., 2017; Yang et al., 2017). Briefly, the channel geometries in each layer were defined by patterning the SU-8 photoresist (MicroChem Corporation,

Westborough, MA, United States) through the photomask on a silicon wafer. The SU-8 master was then molded by polydimethylsiloxane (PDMS) (Slugard 184, Dow Corning) by soft lithography to create the negative replica. Inlets and outlets were punched out of the PDMS replica. The PDMS replica was then bonded to a glass slide by air plasma treatment. The microfluidic channels were coated with 0.4% BSA blocking for 40 min at 37°C before cell migration experiments. L929 cells were pretreated with vehicle control [dimethylsulfoxide (DMSO)] or 1 μmol/L FR180204 for 12 h. Then, the unpretreated and pretreated cells were loaded to the three parallel test units of the microfluidic device from the cell inlets and allowed to align in the docking structures. Equal volume of chemoattractant solution and medium were added into the three pairs of source wells to configure different gradient conditions. The conditions included 0, 5, 10, and 20 ng/mL activin A gradients in DMEM with 1% FBS. Each experiment was performed in duplicate and repeated three times. The cell images in the device were captured every 5 h for a total of 20 h. To maintain the gradient, the waste in the outlet was discarded and the appropriate equal volume of chemoattractant solution and medium was supplemented. The device was kept in a 37°C incubator containing 5% CO_2 between the imaging time points.

Wound Healing Assay

A scratch wound healing assay was performed to assess the action of activin A on the wound healing ability of L929 cells. Briefly, L929 cells (8×10^5 cells/well) were seeded on a 12-well plate and allowed to reach 90% confluency overnight. Then, a scratch-wound (400 μm wide) was generated in the surface of monolayer cells using a 10 μl pipette tip, and the free-floating cells and debris were removed by washing twice with 0.1 mol/L PBS. Cells were cultured in 1% FBS-DMEM containing activin A (0, 5, 10, or 20 ng/mL). For each group, the images on an inverted microscope were taken at 0 h and 24 h after wounding, and the degree of wound healing was measured by the cell migratory distance. Independent experiments were repeated three times.

Giemsa Staining

L929 cells were cultured with 1% FBS-DMEM containing activin A (0 or 10 ng/mL) in a 48-well plate. After 24 h, cells were fixed with 4% paraformaldehyde, stained with Giemsa solution, and observed under an optical microscope. Experiments were performed in duplicate.

Western Blotting

Cells were lysed using the protein extraction reagent (Thermo Fisher Scientific, United States) supplemented with the protease and phosphatase inhibitor cocktail (Thermo Scientific, United States) and 0.5 mol/L EDTA solution. Proteins were quantified using the BCA protein assay kit (Thermo Scientific, United States) following the manufacturer's instruction. Twenty microgram of proteins were separated by electrophoresis with 12% SDS-PAGE gel, and transferred onto a polyvinylidene difluoride membrane. Membranes were blocked in 5% BSA-TBS for 2 h at RT, and then incubated with the primary antibodies overnight at 4°C. Membranes were further incubated with secondary antibody conjugated with horseradish peroxidase for 2 h at RT followed by ECL detection (GE Healthcare, United Kingdom). Finally, membranes were scanned with LAS-4000 luminescent image analyzer (Fujifilm, Japan).

Enzyme-Linked Immunosorbent Assay for TGF-β1 and IL-6

The supernatants of cultured L929 cells were collected, and the levels of TGF-β1 and IL-6 were determined by ELISA kits according to the manufacturer's protocol.

Calcium Flux Assay

L929 cells were incubated in 1% FBS-DMEM medium with 4 μmol/L Fluo-4 in dark for 40 min at 37°C. Cells were washed twice using the 1% FBS-DMEM, and Fluo-4-loaded cells were recovered in the incubator for another 30 min in dark. Then the cells were divided into different tubes for analysis by flow cytometry. Fluo-4 signal was first recorded for 1 min to obtain the baseline fluorescence signal (F_0). Cells were stimulated with 0, 5, 10, or 20 ng/mL activin A. The Fluo-4 signal of simulated cells (F) was recorded for another 3 min. The experiment was repeated at least three times. FlowJo software (FlowJo LLC., Ashland, Oregon, United States) was used to analyze the kinetics of Fluo-4 signal intensity. The Fluo-4 intensity was normalized to the baseline for comparison (F/F_0).

Statistical Analysis

All data were presented as mean ± standard deviation (SD). Statistical analysis was performed using Student's *t*-test or one-way ANOVA followed by Tukey's multiple comparisons test. Difference at $P < 0.05$ was considered to be statistically significant.

RESULTS

Effects of Activin A on Adhesion and Proliferation of L929 Cells

As one of the basic cell activities, adhesion is involved in the cell movement and tissue damage repair. Hence, RTCA was conducted to examine the effect of activin A on the adhesion of murine fibroblast cell line L929 cells. The results showed that activin A significantly promoted the adhesion of L929 cells in a dose-dependent manner (**Figure 1A**).

The viability and proliferation of fibroblasts can affect cell adhesion and movement. This study further explored the effect of activin A on viability of L929 cells by MTT method. The results showed that activin A had no significant effect on the viability of L929 cells (**Figure 1B**). In addition, RTCA results showed no significant action of activin A on proliferation of L929 cells (**Figure 1C**). These results indicated that activin A promoted L929 cells adhesion, but had no impact on the viability and proliferation of L929 cells.

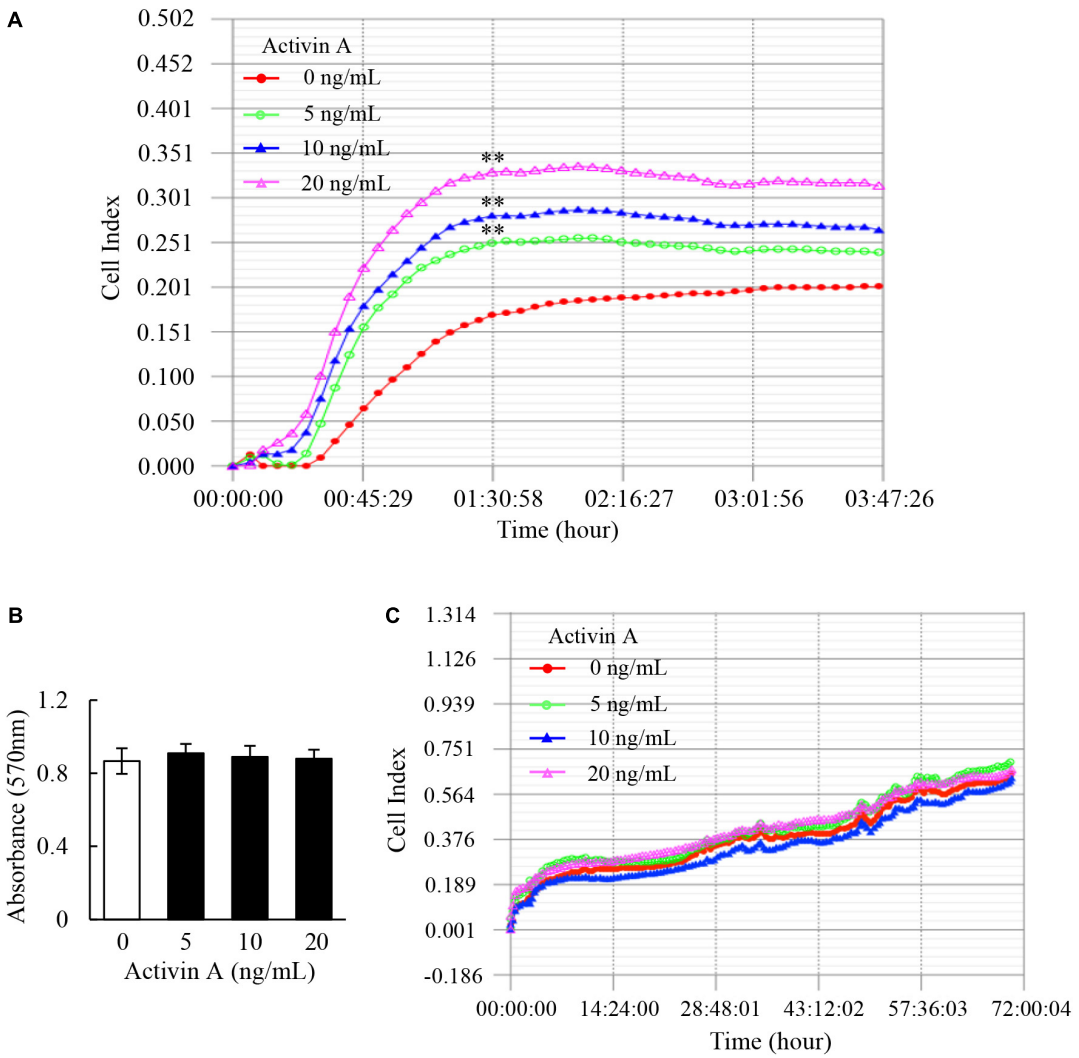

FIGURE 1 | Effects of activin A on adhesion and proliferation of L929 cells. **(A)** Real-time cell adhesion was assessed by RTCA in L929 cells subject to activin A at different concentrations for 4 h. $^{**}P < 0.01$ compared with the 0 ng/ml control group. **(B)** MTT assay was performed to assess the viability of L929 cells treated with activin A at different concentrations for 24 h. Data represent mean ± SD ($n = 6$). **(C)** Real-time cell proliferation of L929 cells was assessed by RTCA in 70 h.

Effects of Activin A on Migration of L929 Cells

The migration of fibroblasts to inflammatory sites is critical for wound healing and tissue fibrosis. In the present study, the transwell chamber assay was first carried out to examine effects of activin A on cell migration. The results showed that activin A significantly induced migration of L929 cells in a dose-dependent manner (**Figure 2A**), in which CXCL12 was used as positive control.

In order to test whether activin A is a chemoattractant to L929 cells, we utilized the D^3-Chip of microfluidic device to determine the motility and chemotactic migration of L929 cells to the activin A gradients. The results revealed that activin A gradients induced the chemotactic migration of L929 cells in both time-dependent and dose-dependent manner (**Figures 2B,C**). Activin A gradients increased not only the number of migrating cells, but also the distance of cell migration by the end-point migration distance analysis (**Figure 2C**). Taken together, the above data indicated that activin A was a chemokine to L929 cells, and suggested that activin A might facilitate tissue repair and fibrosis by inducing the chemotactic migration of fibroblasts to damaged or inflammatory foci.

Effects of Activin A on Wound Healing in L929 Cells

Fibroblasts are the main components involved in wound healing. To examine effects of activin A on wound healing abilities of L929 cell, we performed a scratch wound healing assay in the presence or absence of activin A. As shown in **Figure 3**, activin A exerted no significant effects on the wound healing of L929 cells *in vitro*, suggesting that although activin A induced the chemotactic migration of L929 fibroblasts,

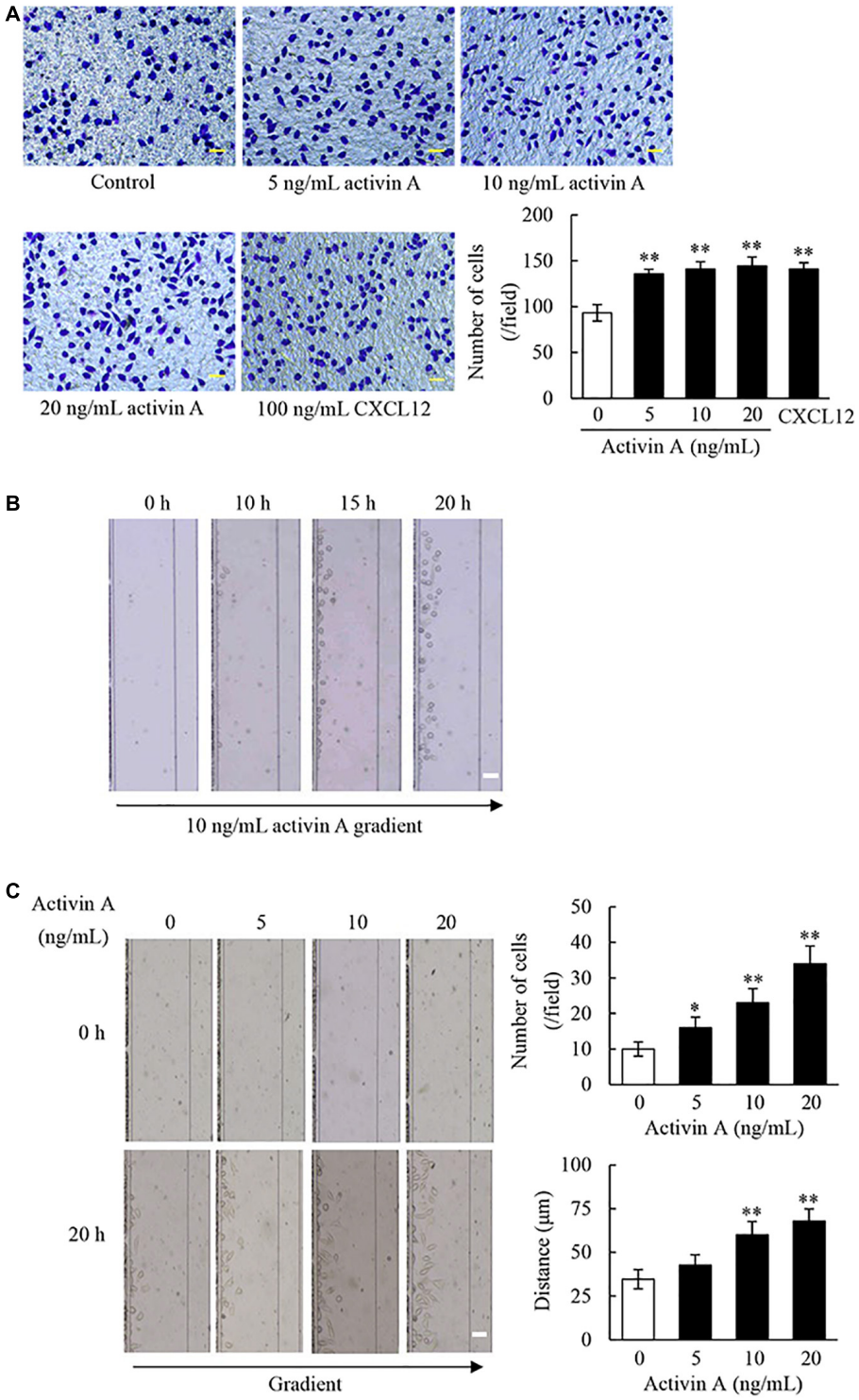

FIGURE 2 | Effect of activin A on migration of L929 cells. **(A)** The chemotactic migration of L929 cells to activin A (0–20 ng/mL) and CXCL12 (100 ng/mL) was analyzed by transwell chamber assay. Cell that passed through porous membrane of the chamber were stained with Giemsa. Scale bar = 50 μm. The graph showed the average number of Giemsa-stained cells in three separate experiments. $^{**}P < 0.01$ compared with 0 ng/mL control group. **(B)** Images of L929 cells migration toward 10 ng/mL activin A gradient at different times were taken in the microfluidic device. Scale bar = 50 μm. **(C)** Images of L929 cells migration toward different concentrations activin A gradient (0–20 ng/mL) were taken in the microfluidic device at 0 and 20 h, respectively. Scale bar = 50 μm. The graph showed the average number and distance of migrating cells in the same size fields of the microfluidic device in three separate experiments. $^{*}P < 0.05$ and $^{**}P < 0.01$ compared with 0 ng/mL control group.

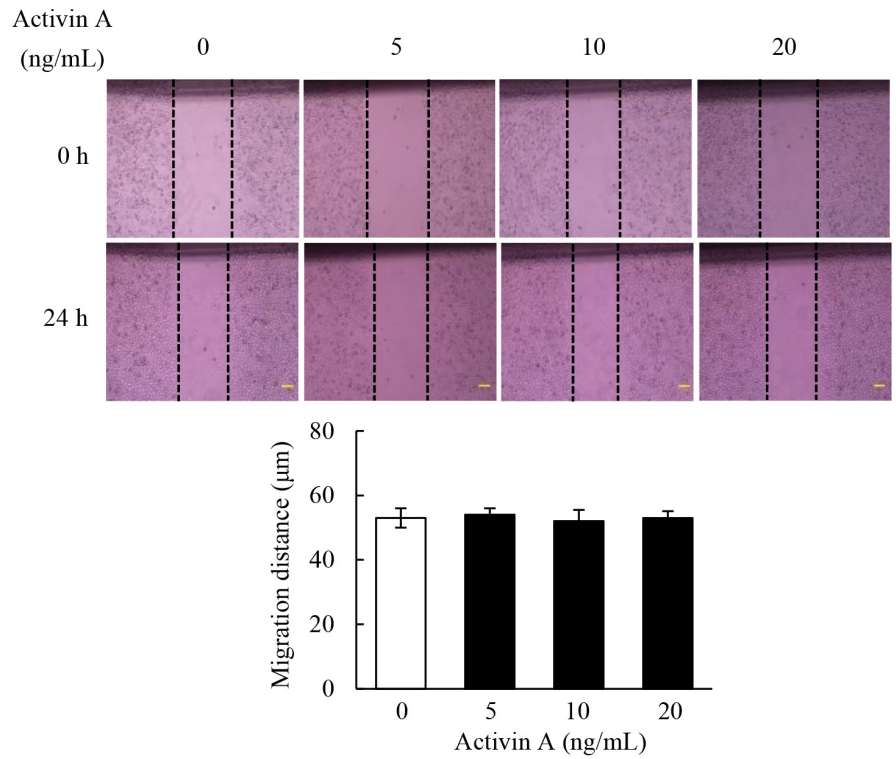

FIGURE 3 | Effects of activin A on wound healing in L929 cells. A scratch-wound was generated in monolayer L929 cells, and then cells were treated with activin A (0–20 ng/mL) for 24 h. The graph showed the degree of wound healing from three separate experiments. Scale bar = 100 μm.

it might not directly affect the horizontal movement of fibroblasts in the wound healing assay that lacks activin A gradients.

Effects of Activin A on Pro-fibrosis in L929 Cells

In the case of tissue repair, fibroblasts can transform to myofibroblasts, that are involved in both fibrogenesis and extracellular matrix (ECM) remodeling stages. To test effects of activin A on pro-fibrosis, we performed Giemsa staining to observe the morphological changes in L929 cells treated with activin A. As shown in **Figure 4A**, the control L929 cells were spindle or polygonal in shape with short cytoplasmic processes. In contrast, L929 cells treated with activin A mainly adopted a spindle shape with longer cytoplasmic processes. Next, α-SMA, a myofibroblast marker, was assessed by Western blotting. The results showed that activin A treatment of L929 cells increased the level of α-SMA in a dose-dependent manner (**Figure 4B**). Finally, we used ELISA to measure levels of TGF-β1, a factor closely related to tissue fibrosis, and IL-6, a pro-inflammatory cytokine. As a result, TGF-β1 levels significantly increased in the supernatant of L929 cells treated with activin A, but IL-6 levels did not change (**Figure 4C**). These results indicated that activin A might not directly trigger the fibroblast-mediated acute inflammation response, but promote fibroblasts-mediated tissue fibrosis.

Effects of Activin A on Calcium Flux in L929 Cells

Calcium signaling has long been well-recognized to be associated with the activation of cells including proliferation, apoptosis and migration (Clapham, 2007; Berridge, 2016). In this regard, the Fluo-4-based calcium assay were performed by flow cytometry to examine the levels of intracellular calcium in L929 cells. The results revealed that activin A increased the calcium levels in L929 cells (**Figure 5**), suggesting that the effects of activin A on L929 cells migration might be associated with calcium signaling.

Effects of Activin A on ERK Signaling in L929 Cells

Previous study has demonstrated that activin A does not antagonize TNF-α-induced activation of L929 cells via classical Smad signaling pathway (Jiang et al., 2020). Therefore, in order to determine the signal transduction mechanism of activin A regulating the migration of L929 cells, levels of ERK and p-ERK proteins were examined by Western blotting. The results showed that the p-ERK protein levels increased in L929 cells treated with activin A (**Figure 6A**). Additionally, pretreatment with FR180204 attenuated activin A-induced increase of p-ERK levels (**Figure 6B**), and decreased activin A-induced migration of L929 cells (**Figure 6C**). Taken together, the above results indicated that activin A might induce the migration of L929 fibroblasts through ERK signaling.

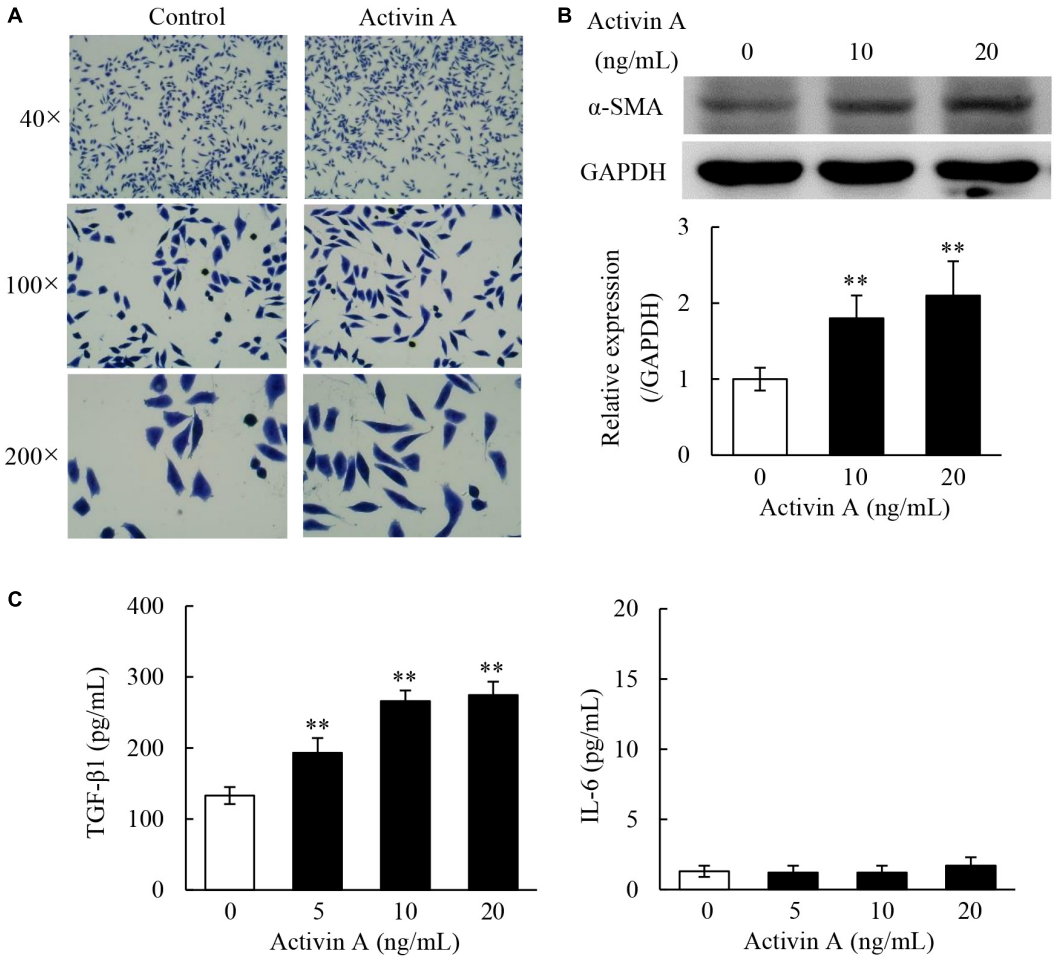

FIGURE 4 | Pro-fibrosis role of activin A in L929 cells. **(A)** Representative images of L929 cells by Giemsa staining. L929 fibroblasts were treated with or without 10 ng/mL activin A for 24 h. **(B)** Western blotting analysis showed that activin A promoted α-SMA expression. The graph represented the relative levels of proteins in three separate experiments. The levels of α-SMA protein were normalized against GAPDH, and the results were shown as the fold-increase of the control. $^{**}P < 0.01$ compared with 0 ng/mL control group. **(C)** L929 cells were incubated containing 0, 5, 10, or 20 ng/mL activin A for 24 h. Levels of TGF-β1 and IL-6 in the supernatant of cultured L929 cells were measured by ELISA. Data represent mean ± SD ($n = 6$). $^{**}P < 0.01$ compared with 0 ng/mL control group.

DISCUSSION

Fibroblasts represent a heterogeneous cell subset differentiated from embryonic mesenchymal cells, which are spindle or polygonal in shape with round or oval nucleus, and lack epithelial and leukocyte lineage markers (Martin and Blaxall, 2012). Traditionally, fibroblasts are suggested to exert a structural role by synthesizing and remodeling ECM in tissues. Additionally, apart from their role in structural support, fibroblasts also secrete and respond to cytokines to be involved in inflammatory and immune response. Thus, fibroblasts maintain the homeostasis of adjacent cells, orchestrate inflammation, and play an important role in tissue development, remodeling and repair. However, in the case of persistent inflammation, fibroblasts will abnormally proliferate and become activated, resulting in excessive production and deposition of ECM to cause tissue fibrosis (Wynn and Ramalingam, 2012). Therefore, the regulation of fibroblast activities is crucial to the inflammatory process and outcome.

Activin, which is originally extracted from porcine follicular fluid, is a double-chain glycoprotein that stimulates the secretion of follicle-stimulating hormone from pituitary extracts and exerts an important effect on reproductive development (Ling et al., 1986; Vale et al., 1986). So far, at least three bioactive forms of activins are identified, including activin A (βA/βA), activin B (βB/βB) and activin AB (βA/βB), among which activin A is the most widely distributed form with the strongest activity (de Kretser et al., 2002). Besides, the amino acid sequence of activin A in mice shared 100% identity to that in humans (Schwall et al., 1988). Activin A is expressed in a variety of tissues and cells, and exerts a critical regulatory function in inflammation, immunity, tumor, tissue repair and fibrosis (Morianos et al., 2019; Roudebush et al., 2019; Zhang et al., 2019). However, it remains unclear whether activin A affects adhesion and migration of fibroblasts.

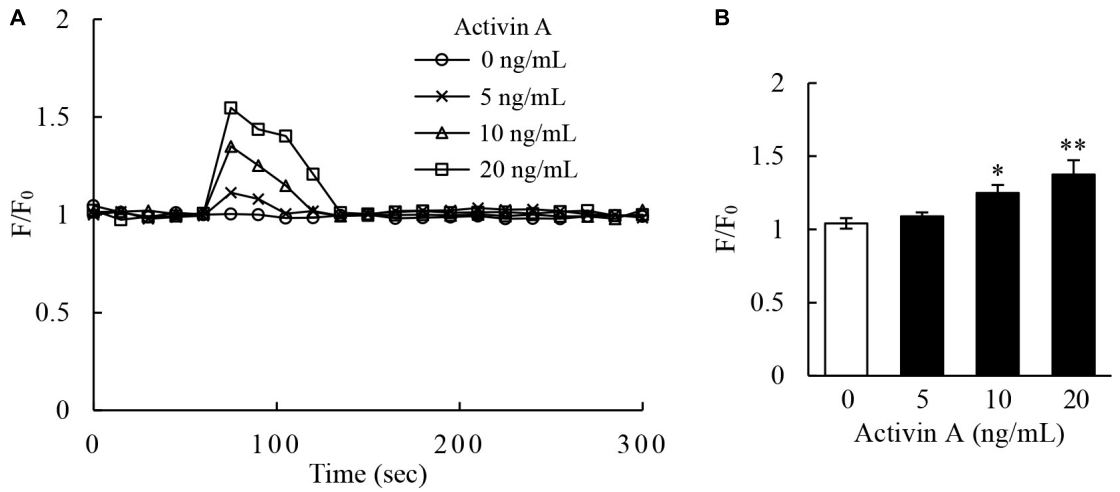

FIGURE 5 | Effect of activin A on calcium signaling of L929 cells. **(A)** Kinetics of calcium signal was measured by the Fluo-4 intensity in L929 cells treated with 0–20 ng/mL activin A. **(B)** The graph showed the peak values of calcium signal upon stimulation under different concentrations activin A. The calcium level was represented by the Fluo-4 signal intensity normalized to the baseline (F/F_0). The graph represented the results from three separate experiments. $^*P < 0.05$ and $^{**}P < 0.01$ compared with 0 ng/mL control group.

Wound repair and tissue fibrosis are related to a series of coordinated processes, such as wound contraction, angiogenesis, cell proliferation and migration, ECM deposition and remodeling. In these processes, various cells are involved, mainly including keratinocytes, fibroblasts and endothelial cells (Gurtner et al., 2008). In the late stage of inflammation or persistent chronic inflammation, the proliferation and adhesion of fibroblasts are the key factors for wound healing and tissue fibrosis (Bainbridge, 2013). Therefore, this study examined effects of activin A on the viability, proliferation and adhesion of fibroblast cell line L929. The results showed that activin A significantly enhanced the adhesion ability of L929 cells, but had no effects on cell viability and proliferation. These findings suggested that activin A profited retention of fibroblasts in the local inflammation tissues.

In the process of tissue repair and fibrosis, fibroblasts can directionally migrate toward the wound sites or inflammation foci. Transwell assay and scratch wound healing assay are the traditional methods to examine cell migration and tissue healing (Tan et al., 2017). Herein, results of scratch wound healing assay showed that activin A had no significant effect on the wound healing of L929 cells *in vitro*, suggesting that activin A might not directly affect the horizontal movement of fibroblasts. However, we found that activin A induced the chemotactic migration of fibroblasts in transwell chamber assay and microfluidic device. The transwell assay evaluates chemotaxis of cells by detecting the number of migrated cells, but it does not determine the migration speed, distance and the specific chemotaxis impact of cytokines on single cells, whereas microfluidic technology is able to detect migration distance and trajectory of single cells (Jia et al., 2019). Indeed, our microfluidic analysis confirmed the chemotactic effect of activin A on L929 cells, including the increased number and distance of migrating cells. Collectively, these data indicated that activin A was a novel chemokine that could induce the directed migration of fibroblasts.

Fibrocytes can be transformed into fibroblasts in the inflammation state. Fibroblasts are spindle or polygonal in shape with abundant cytoplasm and cytoplasmic processes, and they can synthesize and secrete various ECM (Chong et al., 2019). This study found that the number of spindle cells was increased, and the cytoplasmic processes were elongated in L929 cells treated with activin A. These results suggest that activin A may induce the differentiation of fibroblast into myofibroblast, which is the key cellular mediator of fibrosis and can serve as the primary collagen-producing cell when activated (Wynn, 2008). α-SMA is a myofibroblast marker, and over-expressed in the context of organ fibrosis (Duan et al., 2017; Lv et al., 2019). We found that activin A up-regulated the expression of α-SMA in L929 cells, further supporting that activin A might promote the differentiation of fibroblast into myofibroblast. TGF-β1 is not only an important growth and differentiation factor, but also involved in immune response regulation (Delaney et al., 2017). In addition, TGF-β1 plays a key role in the formation of tissue fibrosis in the late stage of inflammation, which is achieved by regulating the phenotype and function of fibroblasts, inducing the differentiation of fibroblasts into myofibroblasts and promoting ECM deposition (Hinz et al., 2012; Kim et al., 2018). This study revealed that activin A promoted the secretion of TGF-β1, but not IL-6 in L929 cells. Typically, IL-6 is an important proinflammatory factor that is mainly produced by the activated T cells, macrophages and fibroblasts. Our findings suggested that activin A might not be involved in the fibroblast-mediated acute inflammatory response, but play a key role in fibroblast-mediated fibrosis.

Activin A, like other members of TGF-β superfamily, can activate Smad signaling pathway to regulate cell activities (Qi et al., 2017). However, previous studies found no significant

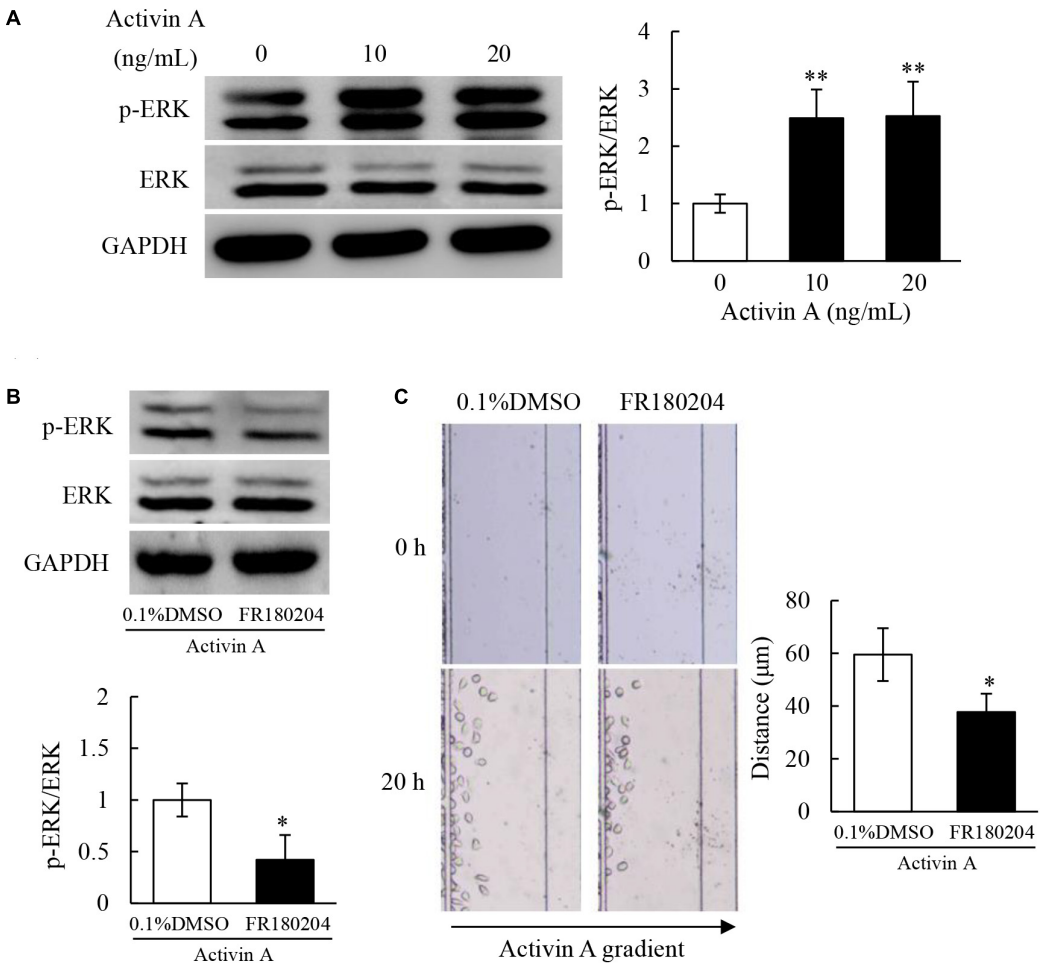

FIGURE 6 | Effects of activin A on ERK signaling in L929 cells. **(A)** Levels of p-ERK and ERK proteins were examined by Western blotting in L929 cells subject to activin A for 2 h. The graph represented the relative levels of proteins in three separate experiments. $^{**}P < 0.01$ compared with 0 ng/mL control group. **(B)** L929 cells were seed in 12-well plates and pretreated for 1 h with 0.1% DMSO or 1 μmol/L FR180204 before treated for 2 h with or without 10 ng/mL activin A. Levels of p-ERK and ERK were examined by Western blotting. The graph represented the relative levels of proteins in three separate experiments. $^{*}P < 0.05$ compared with 0.1% DMSO control group. **(C)** L929 cells were pretreated for 12 h with 0.1% DMSO or 1 μmol/L FR180204 and then cell migration toward 10 ng/mL activin A gradient was examined by microfluidic devices. $^{*}P < 0.05$ compared with 0.1% DMSO control group.

changes of p-Smad3 level in L929 cells stimulated with activin A (Jiang et al., 2020). As an important second messenger in cells, calcium ion extensively exists in the living organisms and participates in a variety of signaling pathways (Varghese et al., 2019). Calcium signaling is involved in the regulation of cell biological activities, such as cell proliferation, differentiation, apoptosis and migration (Pinto et al., 2015; Tiwari et al., 2017). We previously reported that activin A participated in the regulation of neutrophil migration through calcium signaling (Xie et al., 2017). Our present study revealed that activin A significantly increased the calcium flux in L929 cells, indicating that the biological effects of activin A on L929 cells might be related to calcium signaling. MAPK/ERK signaling pathway is also closely related to wound healing and tissue fibrosis (Kim et al., 2019). Aberrant activation of ERK signaling has been confirmed in systemic organ fibrosis, with ERK phosphorylation modulating fibroblast differentiation (Leivonen et al., 2005; Liu et al., 2020). Besides, MAPK/ERK signaling pathway is also involved in the migration of RA-FLSs (Liu et al., 2018). In this study, we found that activin A induced ERK phosphorylation, whereas ERK inhibitor FR180204 corrected the p-ERK excess and inhibited the activin A-induced migration of L929 cells. Thus, these data indicated that activin A regulated fibroblast activities, such as cell migration, through calcium signaling and ERK signaling.

CONCLUSION

In summary, we found that activin A promoted adhesion, induced chemotactic migration of L929 cells by calcium signaling and ERK signaling, and played a pro-fibrosis role by elevating TGF-β1 release. Thus, this study shed new light on understanding the role of activin A in tissue fibrosis.

DATA AVAILABILITY STATEMENT

The original contributions presented in the study are included in the article/Supplementary material, further inquiries can be directed to the corresponding author/s.

AUTHOR CONTRIBUTIONS

ZL and XC designed the experiments. LJ, YQ, and XK performed the experiments. LJ and RW analyzed the data. LJ and ZL drafted the manuscript. JQ, FL, and XC revised the manuscript. All authors read and approved the final manuscript.

FUNDING

This work was supported by the National Basic Research Program of China (2015CB943300), National Natural Science Foundation of China (31871510), Science Foundation of Jilin Province (20200201142JC, 2020J031, and 2019J013), and Department of Finance of Jilin Province (JCSZ2019378-29).

REFERENCES

Aleman-Muench, G. R., and Soldevila, G. (2012). When versatility matters: activins/inhibins as key regulators of immunity. *Immunol. Cell Biol.* 90, 137–148. doi: 10.1038/icb.2011.32

Bai, X., He, T., Liu, J., Wang, Y., Fan, L., Tao, K., et al. (2015). Loureirin B inhibits fibroblast proliferation and extracellular matrix deposition in hypertrophic scar via TGF-β/Smad pathway. *Exp. Dermatol.* 24, 355–360. doi: 10.1111/exd.12665

Bainbridge, P. (2013). Wound healing and the role of fibroblasts. *J. Wound Care 22(8)* 40, 410–412. doi: 10.12968/jowc.2013.22.8.407

Berridge, M. J. (2016). The inositol trisphosphate/calcium signaling pathway in health and disease. *Physiol. Rev.* 96, 1261–1296. doi: 10.1152/physrev.00006.2016

Burr, S. D., Harmon, M. B., and Jr, J. A. S. (2020). The impact of diabetic conditions and AGE/RAGE signaling on cardiac fibroblast migration. *Front. Cell Dev. Biol.* 8:112. doi: 10.3389/fcell.2020.00112

Chong, S. G., Sato, S., Kolb, M., and Gauldie, J. (2019). Fibrocytes and fibroblasts-Where are we now. *Int. J. Biochem. Cell Biol.* 116:105595. doi: 10.1016/j.biocel.2019.105595

Clapham, D. E. (2007). Calcium signaling. *Cell* 131, 1047–1058. doi: 10.1016/j.cell.2007.11.028

de Kretser, D. M., Hedger, M. P., Loveland, K. L., and Phillips, D. J. (2002). Inhibins, activins and follistatin in reproduction. *Hum. Reprod. Update* 8, 529–541. doi: 10.1093/humupd/8.6.529

Delaney, K., Kasprzycka, P., Ciemerych, M. A., and Zimowska, M. (2017). The role of TGF-β1 during skeletal muscle regeneration. *Cell Biol. Int.* 41, 706–715. doi: 10.1002/cbin.10725

Donovan, P., Dubey, O. A., Kallioinen, S., Rogers, K. W., Muehlethaler, K., Muller, P., et al. (2017). Paracrine Activin-A signaling promotes melanoma growth and metastasis through immune evasion. *J. Invest Dermatol.* 137, 2578–2587. doi: 10.1016/j.jid.2017.07.845

Duan, X., Meng, Q., Wang, C., Liu, Z., Liu, Q., Sun, H., et al. (2017). Calycosin attenuates triglyceride accumulation and hepatic fibrosis in murine model of non-alcoholic steatohepatitis via activating farnesoid X receptor. *Phytomedicine* 25, 83–92. doi: 10.1016/j.phymed.2016.12.006

Eming, S. A., Martin, P., and Tomic-Canic, M. (2014). Wound repair and regeneration: mechanisms, signaling, and translation. *Sci. Transl. Med.* 6:265sr6. doi: 10.1126/scitranslmed.3009337

Gurtner, G. C., Werner, S., Barrandon, Y., and Longaker, M. T. (2008). Wound repair and regeneration. *Nature* 453, 314–321. doi: 10.1038/nature07039

Hardy, C. L., King, S. J., Mifsud, N. A., Hedger, M. P., Phillips, D. J., Mackay, F., et al. (2015). The activin A antagonist follistatin inhibits cystic fibrosis-like lung inflammation and pathology. *Immunol. Cell Biol.* 93, 567–574. doi: 10.1038/icb.2015.7

Hinz, B., Phan, S. H., Thannickal, V. J., Prunotto, M., Desmoulière, A., Varga, J., et al. (2012). Recent developments in myofibroblast biology: paradigms for connective tissue remodeling. *Am. J. Pathol.* 180, 1340–1355. doi: 10.1016/j.ajpath.2012.02.004

Hruska, K. A., Sugatani, T., Agapova, O., and Fang, Y. (2017). The chronic kidney disease - Mineral bone disorder (CKD-MBD): advances in pathophysiology. *Bone* 100, 80–86. doi: 10.1016/j.bone.2017.01.023

Jia, L., Zhu, Z., Li, H., and Li, Y. (2019). Shikonin inhibits proliferation, migration, invasion and promotes apoptosis in NCI-N87 cells via inhibition of PI3K/AKT signal pathway. *Artif. Cells Nanomed. Biotechnol.* 47, 2662–2669. doi: 10.1080/21691401.2019.1632870

Jiang, L., Liu, B., Qi, Y., Zhu, L., Cui, X., and Liu, Z. (2020). Antagonistic effects of activin A and TNF-α on the activation of L929 fibroblast cells via Smad3-independent signaling. *Sci. Rep.* 10:20623. doi: 10.1038/s41598-020-77783-8

Jones, K. L., Mansell, A., Patella, S., Scott, B. J., Hedger, M. P., de Kretser, D. M., et al. (2007). Activin A is a critical component of the inflammatory response, and its binding protein, follistatin, reduces mortality in endotoxemia. *Proc. Natl. Acad. Sci. U.S.A.* 104, 16239–16244. doi: 10.1073/pnas.0705971104

Kaiser, O., Paasche, G., Stover, T., Ernst, S., Lenarz, T., Kral, A., et al. (2013). TGF-beta superfamily member activin A acts with BDNF and erythropoietin to improve survival of spiral ganglion neurons in vitro. *Neuropharmacology* 75, 416–425. doi: 10.1016/j.neuropharm.2013.08.008

Kim, J., Kim, B., Kim, S. M., Yang, C. E., Song, S. Y., Lee, W. J., et al. (2019). Hypoxia-induced epithelial-to-mesenchymal transition mediates fibroblast abnormalities via ERK activation in cutaneous wound healing. *Int. J. Mol. Sci.* 20:2546. doi: 10.3390/ijms20102546

Kim, K. K., Sheppard, D., and Chapman, H. A. (2018). TGF-β1 signaling and tissue fibrosis. *Cold Spring Harb. Perspect. Biol.* 10:a022293. doi: 10.1101/cshperspect.a022293

Leivonen, S. K., Häkkinen, L., Liu, D., and Kähäri, V. M. (2005). Smad3 and extracellular signal-regulated kinase 1/2 coordinately mediate transforming growth factor-beta-induced expression of connective tissue growth factor in human fibroblasts. *J. Invest. Dermatol.* 124, 1162–1169. doi: 10.1111/j.0022-202X.2005.23750.x

Ling, N., Ying, S. Y., Ueno, N., Shimasaki, S., Esch, F., Hotta, M., et al. (1986). Pituitary FSH is released by a heterodimer of the beta-subunits from the two forms of inhibin. *Nature* 321, 779–782. doi: 10.1038/321779a0

Liu, F., Feng, X. X., Zhu, S. L., Huang, H. Y., Chen, Y. D., Pan, Y. F., et al. (2018). Sonic hedgehog signaling pathway mediates proliferation and migration of fibroblast-like synoviocytes in rheumatoid arthritis via MAPK/ERK signaling pathway. *Front. Immunol.* 9:2847. doi: 10.3389/fimmu.2018.02847

Liu, J., Zhao, B., Zhu, H., Pan, Q., Cai, M., Bai, X., et al. (2020). Wnt4 negatively regulates the TGF-β1-induced human dermal fibroblast-to-myofibroblast transition via targeting Smad3 and ERK. *Cell Tissue Res.* 379, 537–548. doi: 10.1007/s00441-019-03110-x

Lv, X., Li, J., Hu, Y., Wang, S., Yang, C., Li, C., et al. (2019). Overexpression of miR-27b-3p Targeting Wnt3a regulates the signaling pathway of Wnt/β-catenin and attenuates atrial fibrosis in rats with atrial fibrillation. *Oxid. Med. Cell Longev.* 2019:5703764. doi: 10.1155/2019/5703764

Martin, M. L., and Blaxall, B. C. (2012). Cardiac intercellular communication: are myocytes and fibroblasts fair-weather friends? *J. Cardiovasc. Transl. Res.* 5, 768–782. doi: 10.1007/s12265-012-9404-5

Morianos, I., Papadopoulou, G., Semitekolou, M., and Xanthou, G. (2019). Activin-A in the regulation of immunity in health and disease. *J. Autoimmun.* 104:102314. doi: 10.1016/j.jaut.2019.102314

Nagpal, V., Rai, R., Place, A. T., Murphy, S. B., Verma, S. K., Ghosh, A. K., et al. (2016). MiR-125b is critical for fibroblast-to-myofibroblast transition

and cardiac fibrosis. *Circulation* 133, 291–301. doi: 10.1161/circulationaha.115.018174

Pinto, M. C., Kihara, A. H., Goulart, V. A., Tonelli, F. M., Gomes, K. N., Ulrich, H., et al. (2015). Calcium signaling and cell proliferation. *Cell Signal.* 27, 2139–2149. doi: 10.1016/j.cellsig.2015.08.006

Qi, Y., Ge, J., Ma, C., Wu, N., Cui, X., and Liu, Z. (2017). Activin A regulates activation of mouse neutrophils by Smad3 signalling. *Open Biol.* 7:160342. doi: 10.1098/rsob.160342

Qi, Y., Jiang, L., Wu, C., Li, J., Wang, H., Wang, S., et al. (2021). Activin A impairs ActRIIA(+) neutrophil recruitment into infected skin of mice. *iScience* 24:102080. doi: 10.1016/j.isci.2021.102080

Roudebush, C., Catala-Valentin, A., Andl, T., Le Bras, G. F., and Andl, C. D. (2019). Activin A-mediated epithelial de-differentiation contributes to injury repair in an in vitro gastrointestinal reflux model. *Cytokine* 123:154782. doi: 10.1016/j.cyto.2019.154782

Schwall, R. H., Nikolics, K., Szonyi, E., Gorman, C., and Mason, A. J. (1988). Recombinant expression and characterization of human activin A. *Mol. Endocrinol.* 2, 1237–1242. doi: 10.1210/mend-2-12-1237

Sun, B. K., Siprashvili, Z., and Khavari, P. A. (2014). Advances in skin grafting and treatment of cutaneous wounds. *Science* 346, 941–945. doi: 10.1126/science.1253836

Tan, W., Zhu, S., Cao, J., Zhang, L., Li, W., Liu, K., et al. (2017). Inhibition of MMP-2 expression enhances the antitumor effect of sorafenib in hepatocellular carcinoma by suppressing the PI3K/AKT/mTOR Pathway. *Oncol. Res.* 25, 1543–1553. doi: 10.3727/096504017x14886444100783

Tiwari, M., Prasad, S., Shrivastav, T. G., and Chaube, S. K. (2017). Calcium signaling during meiotic cell cycle regulation and *Apoptosis* in mammalian oocytes. *J. Cell Physiol.* 232, 976–981. doi: 10.1002/jcp.25670

Vale, W., Rivier, J., Vaughan, J., McClintock, R., Corrigan, A., Woo, W., et al. (1986). Purification and characterization of an FSH releasing protein from porcine ovarian follicular fluid. *Nature* 321, 776–779. doi: 10.1038/321776a0

van den Ameele, J., Tiberi, L., Bondue, A., Paulissen, C., Herpoel, A., Iacovino, M., et al. (2012). Eomesodermin induces Mesp1 expression and cardiac differentiation from embryonic stem cells in the absence of Activin. *EMBO Rep.* 13, 355–362. doi: 10.1038/embor.2012.23

Varghese, E., Samuel, S. M., Sadiq, Z., Kubatka, P., Liskova, A., Benacka, J., et al. (2019). Anti-cancer agents in proliferation and cell death: the calcium connection. *Int. J. Mol. Sci.* 20:3017. doi: 10.3390/ijms20123017

Wynn, T. A. (2008). Cellular and molecular mechanisms of fibrosis. *J. Pathol.* 214, 199–210. doi: 10.1002/path.2277

Wynn, T. A., and Ramalingam, T. R. (2012). Mechanisms of fibrosis: therapeutic translation for fibrotic disease. *Nat. Med.* 18, 1028–1040. doi: 10.1038/nm.2807

Xie, D., Liu, Z., Wu, J., Feng, W., Yang, K., Deng, J., et al. (2017). The effects of activin A on the migration of human breast cancer cells and neutrophils and their migratory interaction. *Exp. Cell Res.* 357, 107–115. doi: 10.1016/j.yexcr.2017.05.003

Yang, K., Peretz-Soroka, H., Wu, J., Zhu, L., Cui, X., Zhang, M., et al. (2017). Fibroblast growth factor 23 weakens chemotaxis of human blood neutrophils in microfluidic devices. *Sci. Rep.* 7:3100. doi: 10.1038/s41598-017-03210-0

Yuan, X., Pan, J., Wen, L., Gong, B., Li, J., Gao, H., et al. (2019). MiR-144-3p enhances cardiac fibrosis after myocardial infarction by targeting PTEN. *Front. Cell Dev. Biol.* 7:249. doi: 10.3389/fcell.2019.00249

Zhang, H., Ju, B., Nie, Y., Song, B., Xu, Y., and Gao, P. (2018). Adenovirus-mediated knockdown of activin A receptor type 2A attenuates immune-induced hepatic fibrosis in mice and inhibits interleukin-17-induced activation of primary hepatic stellate cells. *Int. J. Mol. Med.* 42, 279–289. doi: 10.3892/ijmm.2018.3600

Zhang, Z., Wang, J., Chen, Y., Suo, L., Chen, H., Zhu, L., et al. (2019). Activin a promotes myofibroblast differentiation of endometrial mesenchymal stem cells via STAT3-dependent Smad/CTGF pathway. *Cell Commun. Signal.* 17:45. doi: 10.1186/s12964-019-0361-3

Conflict of Interest: The authors declare that the research was conducted in the absence of any commercial or financial relationships that could be construed as a potential conflict of interest.

frontiers in Cell and Developmental Biology

ORIGINAL RESEARCH
published: 18 June 2021
doi: 10.3389/fcell.2021.671233

NudC L279P Mutation Destabilizes Filamin A by Inhibiting the Hsp90 Chaperoning Pathway and Suppresses Cell Migration

Min Liu[1†], Zhangqi Xu[1†], Cheng Zhang[1], Chunxia Yang[1], Jiaxing Feng[1], Yiqing Lu[1], Wen Zhang[1], Wenwen Chen[1], Xiaoyang Xu[1], Xiaoxia Sun[1], Mingyang Yang[1], Wei Liu[1], Tianhua Zhou[1,2,3,4] and Yuehong Yang[1]**

[1] Department of Cell Biology, and Institute of Gastroenterology of the Second Affiliated Hospital, Zhejiang University School of Medicine, Hangzhou, China, [2] The Cancer Center of the Second Affiliated Hospital, Zhejiang University School of Medicine, Hangzhou, China, [3] Collaborative Innovation Center for Diagnosis and Treatment of Infectious Diseases, Hangzhou, China, [4] Department of Molecular Genetics, University of Toronto, Toronto, ON, Canada

OPEN ACCESS

Edited by:
Ben Goult,
University of Kent, United Kingdom

Reviewed by:
Massimiliano Baldassarre,
University of Aberdeen,
United Kingdom
Jari Ylänne,
University of Jyväskylä, Finland

***Correspondence:**
Tianhua Zhou
tzhou@zju.edu.cn
Yuehong Yang
yhyang@zju.edu.cn

† These authors have contributed equally to this work

Specialty section:
This article was submitted to Cell Adhesion and Migration, a section of the journal Frontiers in Cell and Developmental Biology

Received: 23 February 2021
Accepted: 31 May 2021
Published: 18 June 2021

Citation:
Liu M, Xu Z, Zhang C, Yang C, Feng J, Lu Y, Zhang W, Chen W, Xu X, Sun X, Yang M, Liu W, Zhou T and Yang Y (2021) NudC L279P Mutation Destabilizes Filamin A by Inhibiting the Hsp90 Chaperoning Pathway and Suppresses Cell Migration. Front. Cell Dev. Biol. 9:671233. doi: 10.3389/fcell.2021.671233

Filamin A, the first discovered non-muscle actin filament cross-linking protein, plays a crucial role in regulating cell migration that participates in diverse cellular and developmental processes. However, the regulatory mechanism of filamin A stability remains unclear. Here, we find that nuclear distribution gene C (NudC), a cochaperone of heat shock protein 90 (Hsp90), is required to stabilize filamin A in mammalian cells. Immunoprecipitation-mass spectrometry and western blotting analyses reveal that NudC interacts with filamin A. Overexpression of human NudC-L279P (an evolutionarily conserved mutation in NudC that impairs its chaperone activity) not only decreases the protein level of filamin A but also results in actin disorganization and the suppression of cell migration. Ectopic expression of filamin A is able to reverse these defects induced by the overexpression of NudC-L279P. Furthermore, Hsp90 forms a complex with filamin A. The inhibition of Hsp90 ATPase activity by either geldanamycin or radicicol decreases the protein stability of filamin A. In addition, ectopic expression of Hsp90 efficiently restores NudC-L279P overexpression-induced protein stability and functional defects of filamin A. Taken together, these data suggest NudC L279P mutation destabilizes filamin A by inhibiting the Hsp90 chaperoning pathway and suppresses cell migration.

Keywords: cell migration, filamin A, Hsp90, NudC-L279P, protein stability

INTRODUCTION

Cell migration, a highly integrated multistep process, plays a critical role in diverse cellular and developmental processes, including the inflammatory response, tissue repair, embryogenesis, and cancer metastasis (Ridley et al., 2003; George et al., 2013). Accumulating evidence indicates that the dynamic actin cytoskeleton spatially and temporally regulates cell migration

(Tang and Gerlach, 2017). In general, cell migration is initiated by the formation of actin-based plasma membrane protrusions (termed lamellipodia and filopodia) at the leading edge of migrating cells (Lauffenburger and Horwitz, 1996; Small et al., 2002; Ridley et al., 2003; Machesky, 2008). There exists a dynamically remodeling of branched actin filament network in lamellipodia, which is tightly regulated by several actin regulators, including actin-related protein 2/3 (Arp2/3), cofilin, profilin, and filamins (Blanchoin et al., 2000; Cameron et al., 2000; Skau and Waterman, 2015).

Filamin A (also known as Filamin 1 and ABP-280) was the non-muscle actin cross-linking protein, and it is a member of the filamin family that includes filamin A, filamin B, and C (Kesner et al., 2010). Filamin A is widely expressed and plays an important role in cell migration regulation (Stossel et al., 2001; Feng and Walsh, 2004; Razinia et al., 2012; Kircher et al., 2015; Bandaru et al., 2019). Mutations in filamin A are associated with a range of human disorders termed filaminopathies A, including periventricular heterotopia, developmental regression, and West syndrome in males (Fox et al., 1998; Robertson et al., 2003; Zenker et al., 2004; Kyndt et al., 2007; Nurden et al., 2011). Filamin A often forms a non-covalent V-shaped homodimer composed of an N-terminal actin-binding domain (ABD) followed by 24 tandem immunoglobulin-like domains, the last of which mediates its dimerization (Stossel et al., 2001; Zhou et al., 2010). Filamin A crosslinks actin filaments (F-actin) into an isotropic, high-angle orthogonal branching, then sequentially polymerizes F-actin into the tightly organized orthogonal networks (Cukier et al., 2007; Kim and McCulloch, 2011; Kumar et al., 2019). Previous studies have shown that the activity of filamin A is regulated by phosphorylation to cross-link actin (Chen and Stracher, 1989; Schaefer et al., 2012; Hammer et al., 2013; Li et al., 2015; Sato et al., 2016). Recently, a series of studies indicate that Asb2 (ankyrin repeat-containing protein with a suppressor of cytokine signaling box 2), a specific subunit of CRL5 (Cullin 5-RING E3 ubiquitin ligases) is involved in proteasomal degradation of filamin A (Heuze et al., 2008; Razinia et al., 2011, 2013; Lamsoul et al., 2013; Spinner et al., 2015), however, the regulation of filamin A stability remains poorly understood.

Nuclear distribution gene C (NudC) is evolutionally conserved from yeast to human; it was first identified in the filamentous fungus *Aspergillus nidulans* as an upstream factor of NudF (an homolog of human LIS1, a key regulator of dynein) that could regulate nuclear movement (Osmani et al., 1990; Zhu et al., 2010; Fu et al., 2016; Jheng et al., 2018). NudC contains a core domain of p23 (p23 domain) (Zheng et al., 2011; Fu et al., 2016). P23 protein is a main cochaperone of Hsp90 (heat shock protein 90) participating in promoting the folding of various client proteins (Felts and Toft, 2003; Cox and Johnson, 2011). Emerging studies indicate that NudC may enhance the folding of their client proteins by itself chaperoning activity or functioning as an Hsp90 cochaperone by modulating Hsp90 ATPase activity (Zhu et al., 2010; Zheng et al., 2011; Li et al., 2012; Taipale et al., 2014; Zhang et al., 2016; Schopf et al., 2017; Dean and Johnson, 2021). Our recent study has shown that NudC is required to regulate actin dynamics and cell migration by stabilizing cofilin 1 in an Hsp90-independent manner (Zhang et al., 2016). We also found that NudC-L279P (a conserved mutation in human NudC to Leu^{146} in *Aspergillus* that leads to reduced NudF) impairs NudC itself and Hsp90 chaperone function (Zhu et al., 2010). NudC-L279P overexpression leads to reduced LIS1, a key regulator of cell migration, in an Hsp90-dependent manner (Zhu et al., 2010). However, the underlying mechanism of mammalian NudC in cell migration regulation remains unclear.

Here, we provide evidence that NudC stabilizes filamin A. Our data show that NudC interacts with filamin A. Overexpression of NudC L279P destabilizes filamin A and suppresses cell migration. Ectopic expression of Hsp90 reverses the instability of filamin A and phenotype defects caused by NudC-L279P overexpression. Thus, we propose that NudC L279P mutation destabilizes filamin A by inhibiting the Hsp90-mediated chaperoning pathway, providing a previously undescribed mechanism crucial for filamin A stability regulation.

MATERIALS AND METHODS

Plasmids and Oligonucleotides

Human *GFP-NudC*, *GFP-NudC-L279P*, *Flag-NudC* and *Myc-Hsp90* were constructed as described previously (Yang et al., 2010; Zhu et al., 2010; Zhang et al., 2016). *Myc-filamin A* vector was a kind gift from John Blenis. Full-length human *LIS1* cloned by RT-PCR from RPE-1 cells was inserted into pcDNA3.1 (Clontech). All of these constructs were confirmed by DNA sequencing.

All siRNAs were synthesized by GenePharma. The sequences of the sense strands of the siRNA duplexes are as follows:

NudC-1: 5′-GAAGGGATGGCAGAGAAGC-3′ (Zhang et al., 2016);
NudC-2: 5′-AACACCTTCTTCAGCTTCCTT-3′ (Zhang et al., 2016);
Filamin A: 5′-CCAACAAGGUCAAAGUAUATT-3′ (Urra et al., 2018);
LIS1: 5′-CGGACAAGTAGAATAAATG-3′ (Yang et al., 2010).

Cell Culture and Transfections

RPE-1 cells and AGS cells were maintained in Dulbecco's modified Eagle's medium/Ham's F-12 medium (DMEM/F12, Corning) containing 10% fetal bovine serum (FBS, PAA Laboratories) at 37°C in 5% CO_2. HeLa and HEK-293T cells were cultured in Dulbecco's Modified Eagle's Medium (DMEM, Corning) with 10% FBS at 37°C in 5% CO_2. Plasmid transfection was performed using Lipofectamine 2000 (Invitrogen), and the synthetic oligonucleotides were transfected using Lipofectamine RNAiMAX (Invitrogen) according to manufacturer's instructions.

Preparation of Lentivirus and Construction of Stable Cell Lines

Lentiviruses were prepared as previously described (Lu et al., 2017). In brief, HEK-293T cells were transfected with the viral

packaging constructs and the GFP, GFP-NudC or GFP-NudC-L279P vectors. The viral medium was collected 48 h post-transfection, filtered and mixed with fresh culture medium containing 10% FBS to infect the cells for 48 h. Infected cells were treated with 2 μg/ml puromycin for 72 h to select the plasmid-containing cells. Finally, the cell lines stably expressing the indicated proteins were identified by western blotting.

Drug Treatments

Geldanamycin (GA, Tocris) and radicicol (RA, Tocris) were stored in the dark at −20°C as stock solutions at 1.78 mM in dimethylsulfoxide (DMSO, Sangon) and ethanol, respectively. Cells were treated with either GA or RA at the concentrations as described in the text for different times. MG132 (Millipore) was stored at −20°C as a stock solution at 5 mM in DMSO. Cells were treated with MG132 (5 μM) for 2 h. For cycloheximide (CHX, Sigma-Aldrich) chase analysis, 100 μg/ml CHX was used for the indicated times as described in the text.

Antibodies

For western blotting analysis, antibodies against filamin A (1:1,000, 67133-1-Ig, Diagbio), Hsp90 (1:1,000, 13171-1-AP, Proteintech), NudC (1:1,000, 10681-1-AP, Proteintech), LIS1 (1:1,000, a12643, Proteintech), GAPDH (1:2,000, 60004-1-Ig, Proteintech), cofilin 1 (1:1,000, 10960-1-AP, Proteintech), NudCL (1:1,000, 11764-1-AP, Proteintech), Flag (1:1,000, AF519, Beyotime Biotechnology), and c-Myc (1:1,000, sc-40, Santa Cruz) were acquired commercially. Anti-NudCL2 antibody was generated as previously described (Yang et al., 2010). For immunofluorescence, antibody against filamin A (1:200, 67133-1-Ig, Diagbio) was used. The secondary antibodies for immunofluorescence analyses were Alexa Fluor 488-, 568-, and 647-conjugated anti-rabbit or anti-mouse IgG (1:500, Invitrogen). Goat anti-mouse or anti-rabbit secondary antibodies (1:5,000, LI-COR) conjugated with either Alexa Fluor 680 or IRDye 800 were used for western blotting.

Immunoprecipitation and Western Blotting

Immunoprecipitation (IP) was performed as previously described (Li et al., 2019). In brief, cell extracts were generated in TBSN buffer (20 mM Tris [pH 8.0], 150 mM NaCl, 0.5% Non-idet P-40, 5 mM EGTA, 1.5 mM EDTA, 0.5 mM Na_3VO_4, 20 mM p-nitrophenyl phosphate) supplemented with protease inhibitors and subjected to coimmunoprecipitation (Co-IP) analysis with the indicated antibodies. Western blotting analyses were performed with the indicated antibodies and analyzed using the LI-COR Odyssey (LI-COR) system.

Immunofluorescence Staining

Cells were grown on coverslips and fixed for 15 min with 4% paraformaldehyde in phosphate-buffered saline (PBS) at room temperature and incubated with primary antibodies for 2 h and secondary antibodies for 1 h at room temperature. Rhodamine-phalloidin (P1951, SignaGen) and 4,6-diamidino-2-phenylindole (DAPI, Sigma) were used to visualize F-actin and DNA, respectively. The images were acquired using a 63 × oil immersion objective (Zeiss, LSM880).

Quantitative Real-Time RT-PCR

Quantitative RT-PCR analyses for *filamin A* were performed using a Bio-Rad CFX-Touch System with HiScript Q RT SuperMix (Vazyme). All of the reactions were performed at least three times. *GAPDH* was used as an internal control. The primers used to amplify the target *filamin A* were as follows:

Forward: 5′-ATCTTTACGGCAGGAGCTGG-3′;
Reverse: 5′-CTGGTAGCTGCAGCGGTATG-3′.

Cell Tracking

Time-lapse video microscopy was used to track cell migration. The images were captured at 5-s intervals for 700 cycles with an LSM880 confocal microscope (Zeiss). The videos were further analyzed using Imaris 9.1.2 software.

Kymography Analysis

For kymography analysis, phase-contrast time-lapse sequences were obtained using a 63 × oil immersion objective on an LSM880 Zeiss confocal microscope. Movies were recorded for 10-15 min at a rate of one frame every 3 s. Kymographs were produced and analyzed by ImageJ software (NIH). The quantitative analysis of kymographs was performed as previously described (Bear et al., 2002).

Scratch Wound Experiment

Scratch wound assays were performed as described previously (Feng et al., 2017). In brief, cells were plated into 30-mm dishes and incubated at 37°C in 5% CO_2 to establish a confluent monolayer. Then, cells were treated with serum-free medium for 12 h and scratched with a sterile pipette tip. Cellular debris was removed by washing the plate with PBS, and then fresh medium containing 1% FBS was added. Representative images of cells were taken at the indicated time points using a light microscope (Olympus, IX81). For lamellipodia formation assays, the cells were fixed and stained after 3 h of scratching.

Transwell Assays

Transwell assays were performed as described previously (Chen et al., 2020). In brief, transwell inserts (8-μm pore, Corning) were placed into 24-well plates. A 200 μl suspension containing 80, 000 cells in medium with 1% FBS was placed in the upper chamber of a transwell apparatus, and 700 μl medium containing 20% FBS was added in the lower chamber. After 10 h of incubation at 37°C in 5% CO_2, cells were fixed in 4% paraformaldehyde in PBS for 15 min and stained with 0.2% crystal violet for 20 min. Cells on the undersides of the filters were photographed using a microscope (20× magnification). Five random fields were analyzed for each chamber and scored using ImageJ software.

Cell Spreading Assay

Cell spreading assays were performed as described previously (Zhang et al., 2016). Briefly, cells were suspended in serum-free medium after trypsinization and incubated at 37°C in 5% CO_2

for 1 h. Cells were reseeded on fibronectin (10 mg/ml)-coated plates. After 1 h, cells were washed with PBS and fixed with 4% paraformaldehyde in PBS. Photographs were taken using an LSM880 confocal microscope.

Scanning Electron Microscope Analysis

RPE-1 cells grown on fibronectin (10 mg/ml)-coated glass coverslips were treated with extraction buffer (1% Triton X-100, 2% PEG [MW 35 kDa], 100 mM PIPES [free acid, pH 6.9], 1 mM MgCl2 and 1 mM EGTA, 2 μM phalloidin), washed with PBS, and fixed with 2% glutaraldehyde and processed for scanning electron microscope analysis as described previously (Nova NanoSEM 450 scanning electron microscope) (Nakamura, 2001).

LC-MS/MS Analysis and Database Searching

Liquid chromatography/tandem mass spectrometry (LC-MS/MS) analysis was performed as described previously (Zhu et al., 2010). Briefly, HeLa cell lysates were incubated with anti-NudC antibodies. The proteins coimmunoprecipitated by antibodies were subjected to trypsin digestion, and the recovered peptide mixtures were separated by reversed-phase HPLC followed by tandem mass analysis at the Reach Center for Proteome Analysis, Shanghai Institutes of Biological Sciences. The peak lists of all acquired MS/MS spectra were generated by BioWorks software and then automatically searched against the human International Protein Index protein sequence database (version 3.36) using the SEQUEST algorithm (Deng et al., 2010).

Statistics

Data are representative of at least three independent experiments. Means and standard deviations (SD) were calculated and are shown in the graphs. Student's *t*-test was used to determine statistically significant differences between two groups.

RESULTS

Overexpression of NudC-L279P Destabilizes Filamin A

To identify the candidate proteins participating in NudC-mediated cell migration, we performed immunoprecipitation (IP) analysis with endogenous NudC followed by mass spectrometry (MS) in HeLa cells and found that approximately three hundred proteins appeared to associate with NudC (**Supplementary Table 1**, ranked based on relative abundance). When comparing these proteins with our previous interactome data for Flag-NudC (Zhu et al., 2010; **Supplementary Table 2**, ranked based on relative abundance), we found 58 overlapping proteins (**Figure 1A** and **Supplementary Table 3**). Notably, we found that the relative abundance of filamin A is the highest in both interaction datasets (**Supplementary Tables 1, 2**). IP analysis confirmed that filamin A interacted with Flag-NudC in RPE-1 cells (**Figure 1B**). NudC formed a complex with Myc-filamin A (**Figure 1C**). In addition, the results of western blotting following IP and GST pull-down assays verified the interaction of NudC and filamin A in RPE-1 cells (**Figures 1D–F**). To examine whether the direct interaction exists between NudC and filamin A, we analyzed the amino acid sequence of filamin A and constructed 8 truncations according to the protein domains in filamin A. Then we expressed and purified GST-filamin A fragments and His-NudC and carried out GST pull-down analysis. The results showed that F7 and F8 of filamin A appeared to interact with His-NudC (**Figures 1G,H**), suggesting that there is a direct interaction between NudC with both the 20-23 repeats (2132-2516 aa) and with repeat 24 (2517-2648 aa) of filamin A. Furthermore, immunofluorescence results revealed that GFP-NudC appeared to colocalize with filamin A throughout the cytoplasm of RPE-1 cells, especially at the leading edge of motile cells (**Figure 1I**).

Previous data from our laboratory and others suggest that NudC is involved in the regulation of protein stability (Zhu et al., 2010; Zhang et al., 2016). To test whether NudC regulates the stability of filamin A, we used two siRNA oligos targeting two different regions of *NudC* mRNA (NudC RNAi-1 and NudC RNAi-2). The filamin A protein level showed no obvious change in NudC-depleted cells compared to control cells (**Figure 1J** and **Supplementary Figure 1A**). Our previous study demonstrated that the L279P mutation of NudC impairs its chaperone activity to affect protein stability. Thus, we explored whether the L279P mutation of NudC influenced the protein stability of filamin A. We constructed lentiviral vectors containing GFP, GFP-NudC, or GFP-NudC-L279P to establish cell lines stably expressing the above proteins in RPE-1, HeLa and AGS cells. Western blotting revealed that GFP and GFP-fusion proteins were successfully expressed (**Figure 1K**). We found that the protein level of filamin A was substantially decreased in cells stably expressing NudC-L279P compared to the control cells (**Figures 1K,L** and **Supplementary Figure 1B**), whereas its mRNA level was not significantly changed based on RT-PCR analysis (**Figure 1M**). CHX chase analysis revealed that the degradation rate of filamin A was faster in cells stably expressing GFP-NudC-L279P compared to control cells (**Figure 1N**). Moreover, treating cells with the proteasome inhibitor MG132 inhibited the degradation of filamin A in cells stably expressing GFP-NudC-L279P (**Figure 1O**), suggesting that the ubiquitin-proteasome pathway is involved in filamin A degradation. Taken together, these data strongly suggest that the NudC L279P mutation destabilizes filamin A.

Overexpression of NudC-L279P Inhibits Cell Migration

Previous studies have shown that filamin A plays an important role in cell migration regulation (Cunningham et al., 1992; Fox et al., 1998; Sutherland-Smith, 2011; Jacquemet et al., 2013; Bandaru et al., 2019). The downregulation of filamin A inhibits cell migration in mammalian cells (Cunningham et al., 1992; Jacquemet et al., 2013; Bandaru et al., 2019), which is consistent with our data (**Supplementary Figures 2, 3**). Given that NudC-L279P overexpression led to filamin A instability (**Figure 1**), we tested whether the L279P mutation

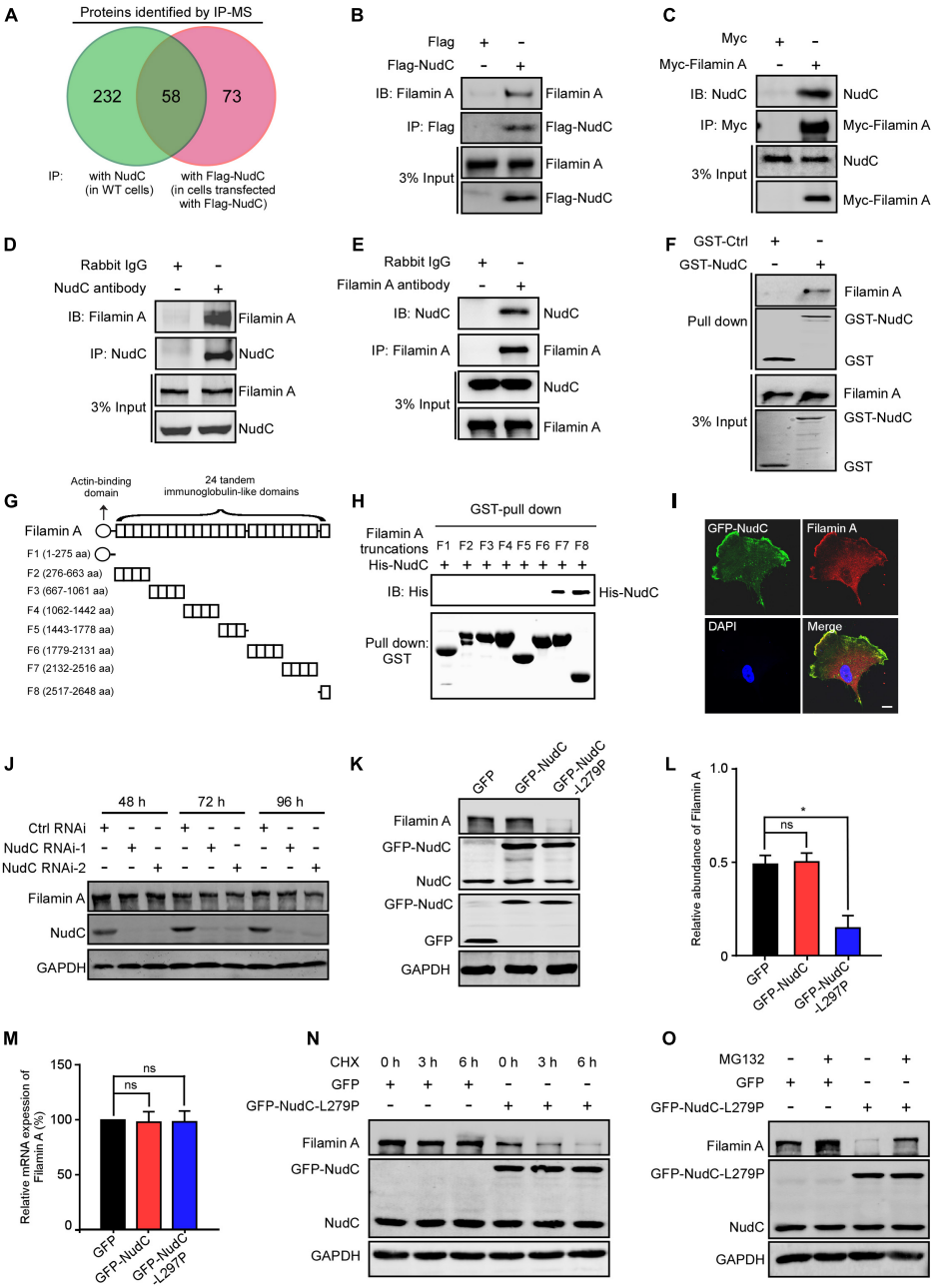

FIGURE 1 | L279P mutation of NudC destabilizes filamin A. **(A)** Venn diagram showing the overlap between two sets of interactors identified by IP (with anti-NudC or anti-Flag antibodies) coupled with mass spectrometry in HeLa cells. **(B,C)** RPE-1 cells transfected with either Flag-NudC or Myc-Filamin A were subjected to IP with anti-Flag or anti-Myc antibodies and western blotting analysis, respectively. 3% of total input is shown. **(D,E)** Total lysates of RPE-1 cells were immunoprecipitated with the indicated antibodies or IgGs and processed for western blotting. 3% of total input is shown. **(F)** Purified GST or GST-NudC protein was incubated with RPE-1 cell lysates and subjected to immunoblotting with anti-filaminA antibody. 3% of total input is shown. GST and GST-NudC input were stained with Coomassie brilliant blue. **(G)** Summary of filamin A truncation mutants. **(H)** The indicated fragments of GST-tagged filamin A and His-NudC proteins were purified. Fragments were incubated with His-NudC and subjected to immunoblotting with the indicated antibodies. **(I)** Cells transfected with GFP-NudC were fixed and stained with anti-filamin A antibody. DNA was visualized with DAPI. Bar, 10 μm. **(J)** RPE-1 cells transfected with *NudC* RNAi-1 or -2 were harvested at various times and subjected to western blotting with anti-NudC and anti-filamin A antibodies. GAPDH, a loading control. **(K)** RPE-1 cells stably expressing GFP, GFP-NudC, or GFP-NudC-L279P were subjected to western blotting analysis by using anti-GFP, -NudC and -filamin A antibodies. GAPDH, a loading control. **(L)** Relative protein levels of filamin A compared to GAPDH in panels **(G)** were measured using ImageJ software. **(M)** Quantitative RT-PCR analysis of filamin A mRNA in RPE-1 cells transfected with the indicated vectors. GAPDH, an internal control. **(N)** Cells transfected with either GFP or GFP-NudC-L279P were treated with 100 μg/ml cycloheximide for different times, harvested, and subjected to western blotting analysis using indicated antibodies. GAPDH, a loading control. **(O)** Cells transfected with either GFP or GFP-NudC-L279P were treated with either 5 μM MG132 or DMSO, lysed, and subjected to western blotting using the indicated antibodies. GAPDH, a loading control. Quantitative data are presented as the means ± SD (at least three independent experiments). $^*P < 0.05$ and ns, not significant ($P > 0.05$). Student's *t*-test.

of NudC has an effect on cell migration. Scratch wound assays revealed that NudC-L279P overexpression significantly suppressed cell migration compared to the control in RPE-1 cells (**Figures 2A–C**). Transwell migration assays also showed that the L279P mutation of NudC decreased RPE-1 cell migration (**Figures 2D,E**). Moreover, tracing the migratory path of live cells by time-lapse microscopy revealed that NudC-L279P overexpression decreased the speed of RPE-1 cell motility (**Figures 2F–H** and **Supplementary Movies 1–3**). Similar results were also found in AGS cells (**Supplementary Figure 4**). Thus, these data suggest that L279P mutation of NudC suppresses cell migration.

Overexpression of NudC-L279P Impairs Actin Dynamics

Given that filamin A regulates cell migration mainly by controlling dynamic actin cytoskeleton remodeling

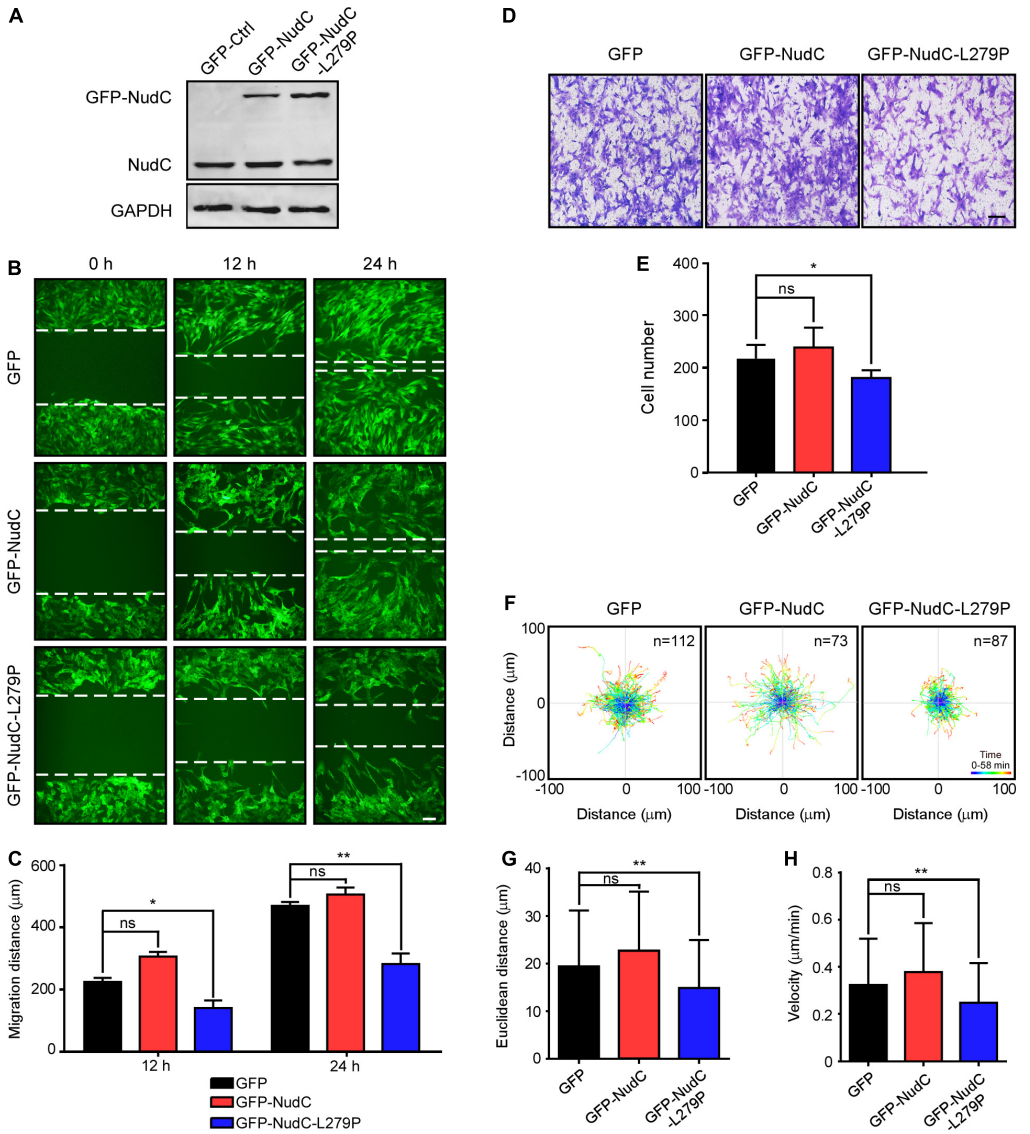

FIGURE 2 | Overexpression of NudC-L279P inhibits cell migration in RPE-1 cells. RPE-1 cells stably expressing GFP, GFP-NudC, or GFP-NudC-L279P were subjected to the following analyses. **(A)** Western blotting analysis of the expression of GFP, GFP-NudC, or GFP-NudC-L279P. GAPDH, a loading control. **(B,C)** Scratch wound assays displayed cell migration at the different time points. Cells expressing GFP signals were monitored with fluorescence microscopy. Dashed lines indicate the approximate line of wound edges. The distance between the two edge lines was measured by ImageJ software. Scale bar, 100 μm. **(D,E)** Transwell migration assays were performed to detect cell motility. Cells that migrated to the undersides of the filters were stained with 0.2% crystal violet and monitored with DIC (differential interference contrast) microscopy. The number of migrated cells per transwell was counted. **(F–H)** The migration track of individual cells was traced using Imaris 9.1.2 software. Representative cell migration tracks are shown. Euclidean distance and migration velocity were analyzed with Imaris 9.1.2 software. Scale bar, 100 μm. Quantitative data are presented as the means ± SD (at least three independent experiments). n, the sample size. $^{*}P < 0.05$; $^{**}P < 0.01$; and ns, not significant ($P > 0.05$). Student's *t*-test.

(Ohta et al., 1999; Nishita et al., 2006; Maceyka et al., 2008; Venkatareddy et al., 2011) and NudC L279P mutation destabilizes filamin A (**Figure 1**), we tested whether overexpression of NudC-L279P would affect the structure and function of the actin cytoskeleton. Immunostaining assay using fluorescent phalloidin-labeled F-actin showed that NudC-L279P overexpression destroyed dynamic actin networks in lamellipodia at the leading edge of cells (**Figures 3A,B**). Scanning electron microscopy also revealed that the L279P mutation impaired cross-linked actin networks and caused an increase in the unbranched actin filaments in lamellipodia (**Figure 3C**). Furthermore, immunostaining data showed that NudC-L279P overexpression significantly decreased lamellipodia formation at the leading edge after scratching (**Figures 3D,E**). Kymographs of lamellipodial protrusion showed that the NudC L279P mutation caused a significant decrease in protrusion velocity with a concomitant increase in protrusion persistence (**Figures 3F–H**). Moreover, phase contrast images showed that NudC L279P suppressed cell spreading (**Figures 3I,J**). Collectively, these data suggest that the NudC L279P mutation impairs actin dynamics.

Enforced Expression of Filamin A Reverses the Phenotypes Induced by NudC-L279P Overexpression

Given that NudC-L279P overexpression destabilizes filamin A and results in defects in actin dynamics and cell migration, we investigated whether filamin A participates in NudC-mediated cell migration. Western blotting revealed that Myc-filamin A was successfully expressed in cells stably overexpressing GFP or GFP-NudC-L279P (**Figure 4A**). Scratch wound, transwell and live cell migration assays showed that ectopic filamin A expression significantly reversed the defects of cell migration in cells that stably expressing NudC-L279P (**Figures 4B–F** and **Supplementary Figure 5**). Furthermore, immunofluorescence results revealed that the disorganization of actin networks in lamellipodia and the decrease in lamellipodia formation in cells stably expressing NudC-L279P were partially reversed by filamin A overexpression (**Figures 4G–I**). Collectively, these data suggest that filamin A is involved in NudC-mediated cell migration regulation.

Hsp90 Binds to and Stabilizes Filamin A

Previous data from our group and others suggest that NudC may be involved in the regulation of protein stability through Hsp90-dependent and Hsp90-independent pathways (Zhu et al., 2010; Fu et al., 2016; Zhang et al., 2016). To test whether Hsp90 is involved in the regulation of filamin A stability, we performed IP experiments in RPE-1 cells transfected with Flag-Hsp90 or Myc-filamin A and found that an interaction between filamin A and Hsp90 (**Figures 5A,B**). In addition, western blotting following IP verified the association of endogenous Hsp90 with filamin A (**Figures 5C,D**). Furthermore, we employed GA and RA, which inhibits Hsp90 ATPase activity and leads to proteasomal degradation of Hsp90 client proteins (Kamal et al., 2004; Pearl and Prodromou, 2006). Western blotting indicated that the inhibition of Hsp90 chaperone activity destabilized filamin A instability in a dose- and time-dependent manner in mammalian cells (**Figures 5E–H** and **Supplementary Figure 6**). Taken together, these data suggest that Hsp90 is involved in the regulation of filamin A protein stability.

Ectopic Expression of Hsp90 Reverses the Defects Induced by NudC-L279P Overexpression

Because both overexpression of L279P and Hsp90 inhibition destabilizes filamin A and the NudC L279P mutation suppresses cell migration, we tested whether Hsp90 is involved in NudC-medicated cell migration via filamin A. We performed a series of rescue experiments and found that ectopic Hsp90 expression reversed the decrease of filamin A protein levels in both RPE-1 and AGS cells stably expressing NudC-L279P (**Figure 6A** and **Supplementary Figure 7A**). Immunofluorescence data showed that the defects in actin networks and lamellipodia formation induced by NudC-L279P overexpression were partially reversed by Hsp90 overexpression (**Figures 6B,C**). Furthermore, scratch wound, transwell, and live cell migration assays revealed that ectopic Hsp90 expression restored the defects induced by NudC-L279P overexpression (**Figures 6D–H** and **Supplementary Figures 7B–G**). Together, these data suggest that Hsp90 is involved in NudC-mediated cell migration via filamin A.

NudCL and NudCL2 Are Involved in the Regulation of Filamin A Stability Coordinating With NudC

Vertebrate NudC has three principal homologs including NudC, NudC-like protein (NudCL), and NudC-like protein 2 (NudCL2) (Zhou et al., 2006; Yang et al., 2010; Zheng et al., 2011; Fu et al., 2016). All members of the NudC family share a conserved p23 domain and may function as Hsp90 cochaperone by modulating Hsp90 ATPase activity to enhance the folding of their client proteins (Zhu et al., 2010; Zheng et al., 2011; Taipale et al., 2014; Yang et al., 2019). In this study, our results displayed that overexpression of NudC L279P, but not overexpression of NudC or single knockdown, causes a decrease in filamin A protein level (**Figure 1**). Interestingly, our recent protein interactome analysis of NudCL2 showed that NudCL2 is able to form a complex with filamin A, but its depletion has no obvious effect on the protein level of filamin A (Chen et al., 2020). These data prompted us to suppose that NudCL2 and/or NudCL may be involved in the regulation of filamin A stability coordinating with NudC. To address this hypothesis, we designed and carried out a series of experiments. Western blotting results showed that depletion of one member of NudC family has no obvious effect on filamin A protein level (**Supplementary Figure 8A**). However, double depletion, especially triple depletion of all NudC family resulted in an obvious decrease in filamin A protein level (**Supplementary Figure 8A**). Furthermore, scratch wound assays revealed that depletion of NudC or NudCL but not NudCL2 suppresses cell migration (**Supplementary Figures 8B,C**), consistenting with our previous studies (Zhang et al., 2016; Chen et al., 2020). It is notable that knockdown of any two or three NudC members led to a significant suppression

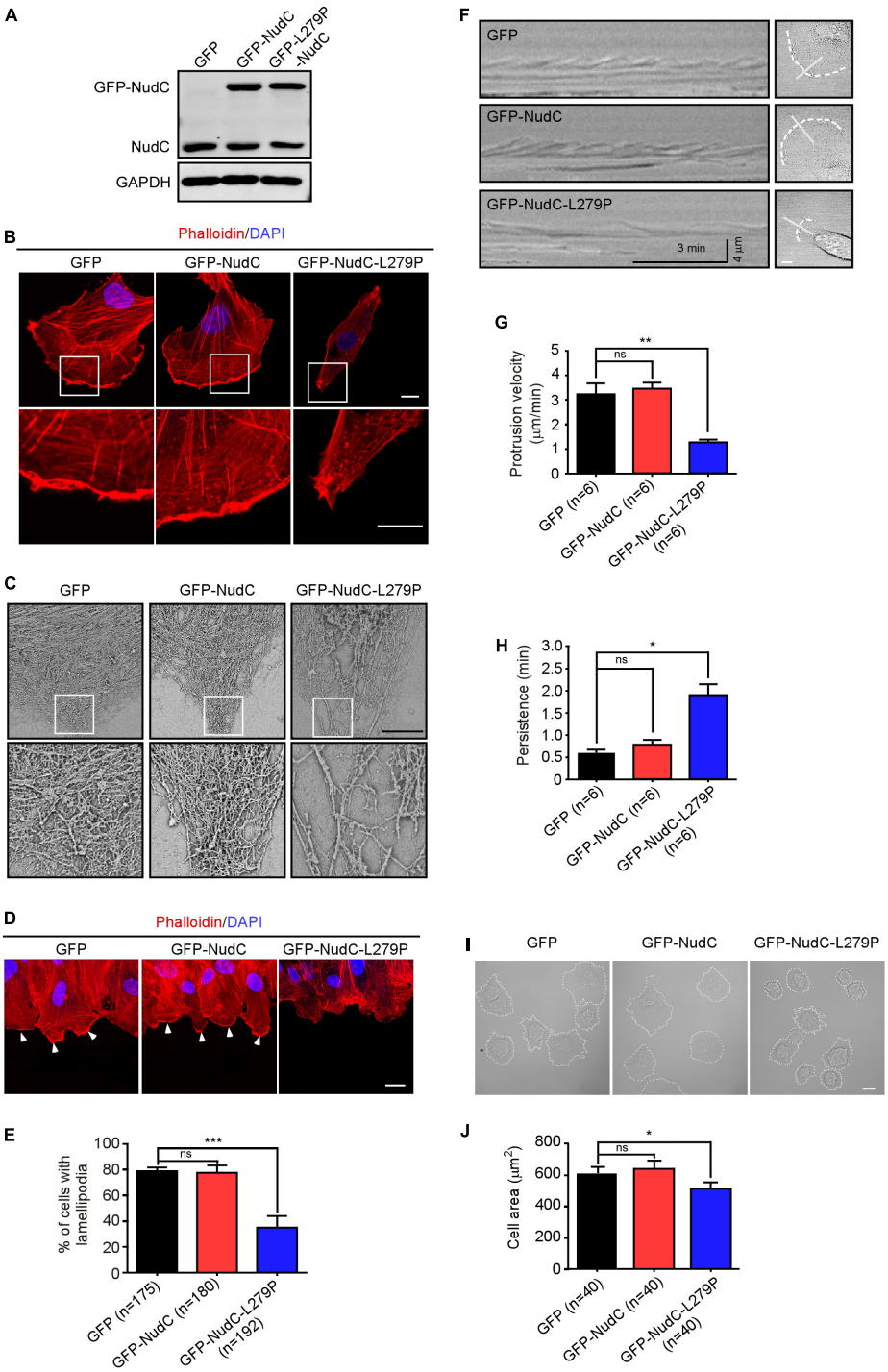

FIGURE 3 | Overexpression of NudC-L279P impairs actin dynamics. RPE-1 cells infected with lentiviruses expressing GFP, GFP-NudC, or GFP-NudC-L279P were subjected to the following analyses. **(A)** Western blotting analysis of the expression of the indicated proteins. GAPDH, a loading control. **(B)** Cells were fixed and stained with phalloidin. DNA was visualized with DAPI. Images were captured using an immunofluorescence microscope. Scale bar, 10 μm. Higher magnifications of the boxed regions are displayed. **(C)** Structural organization of lamellipodia is shown with scanning electron microscopy. Scale bar, 5 μm. Higher magnifications of the boxed regions are displayed. **(D,E)** Cells stably expressing the indicated proteins were fixed and stained with phalloidin after 3 h of scratching. DNA was visualized by DAPI. Scale bar, 20 μm. The lamellipodia at the leading edge of cells are indicated by arrowheads. Cells with lamellipodia were calculated. **(F–H)** A sequence of phase-contrast time-lapse images of the cells was obtained with an LSM880 confocal microscope. Kymographs were analyzed using MetaMorph software. The minimum intensity projection of a 250-frame movie (3 s per frame) is presented on the left. Pixel intensities along a one-pixel-wide line (white) were used to generate the kymograph presented on the right. Cells are outlined with dashed lines. **(I,J)** Cell spreading was detected using a phase contrast microscope. The areas of cell spreading are outlined by dashed lines and measured by ImageJ software (NIH). Scale bar, 10 μm. Quantitative data are presented as the means ± SD (at least three independent experiments). n, the sample size. $^{*}P < 0.05$; $^{**}P < 0.01$; $^{***}P < 0.001$; and ns, not significant ($P > 0.05$). Student's *t*-test.

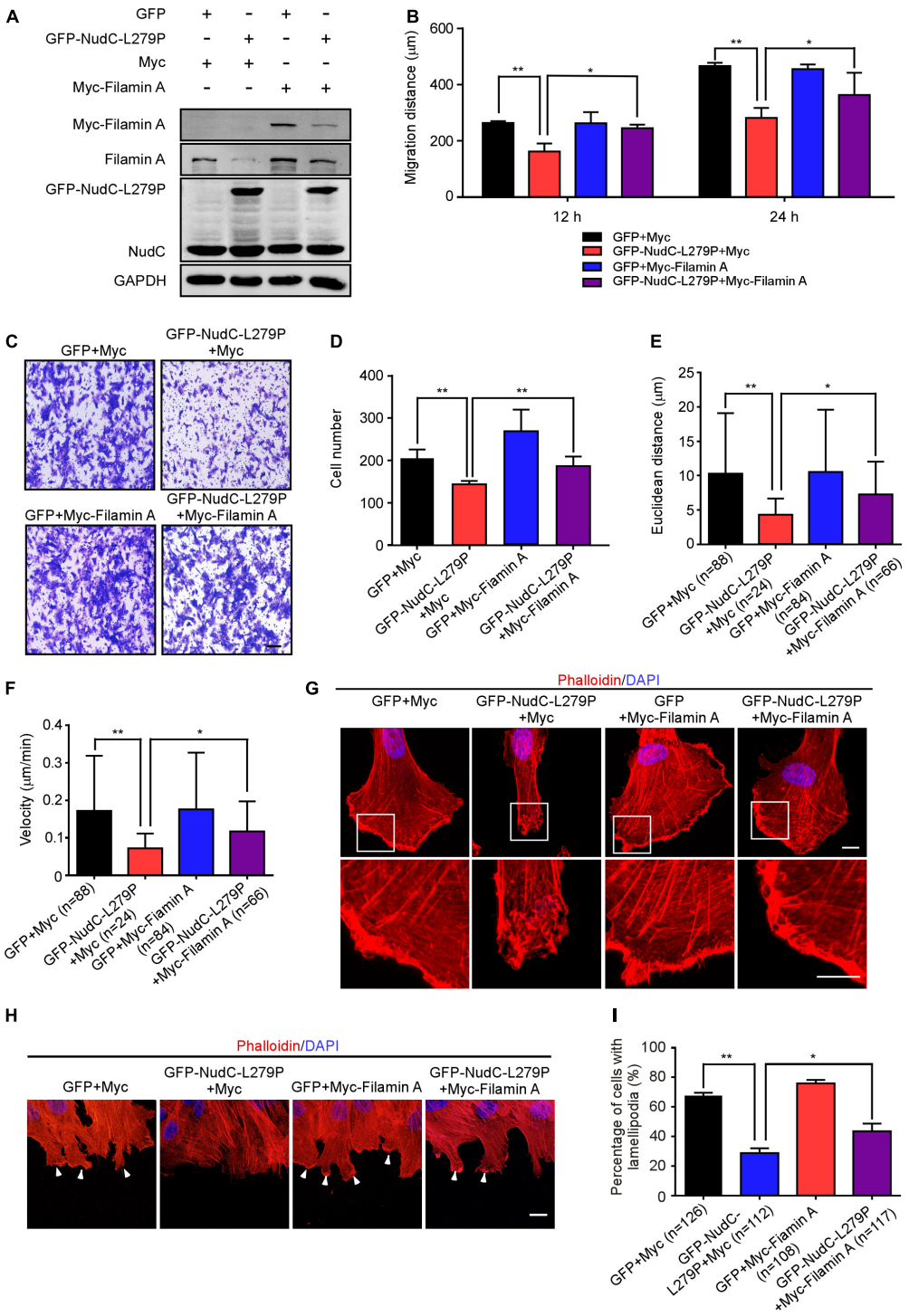

FIGURE 4 | Enforced expression of filamin A reverses the defects caused by NudC-L279P overexpression. RPE-1 cells stably overexpressing GFP or GFP-NudC-L279P were transfected with Myc or Myc-filamin A and then subjected to the following analyses. **(A)** Western blotting analysis of the expression of the indicated proteins. GAPDH, a loading control. **(B)** Scratch wound assays detected cell migration at the different time points. The scratch closure was monitored with fluorescence microscopy. The distance between the two edge lines was measured using ImageJ software. **(C,D)** Transwell migration assays were performed to detect cell migration. Cells that migrated to the undersides of the filters were stained with 0.2% crystal violet and monitored with DIC microscopy. The number of migrated cells per transwell was counted. Scale bar, 100 μm. **(E,F)** The migration tracks of individual cells were traced by Imaris 9.1.2 software. Euclidean distance and migration velocity were analyzed with Imaris 9.1.2 software. **(G)** Cells were fixed and stained with phalloidin. DNA was visualized with DAPI. Images were captured by immunofluorescence microscopy. Scale bar, 10 μm. Higher magnifications of the boxed regions are displayed. **(H,I)** Cells were fixed and stained with phalloidin after 3 h of scratching. DNA was visualized by DAPI. Scale bar, 5 μm. The lamellipodia at the leading edge of cells are pointed by arrowheads. Cells with lamellipodia were counted. Quantitative data are presented as the means ± SD (at least three independent experiments). n, the sample size. $^{*}P < 0.05$ and $^{**}P < 0.01$. Student's *t*-test.

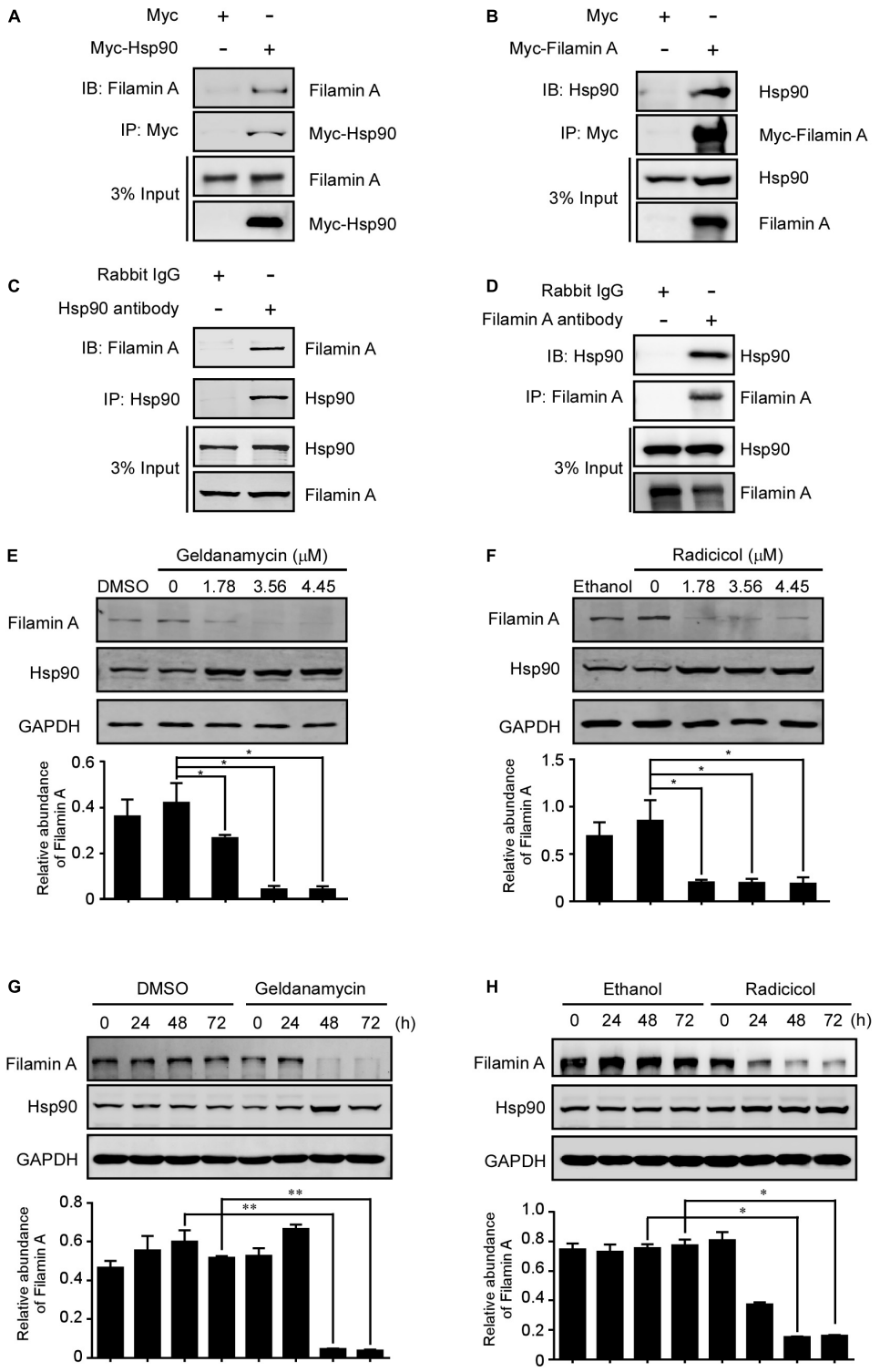

FIGURE 5 | Hsp90 binds to and stabilizes filamin A. **(A,B)** RPE-1 cells transfected with either Myc-Hsp90 or -Filamin A were subjected to IP and western blotting using the indicated antibodies. 3% of total input is shown. **(C,D)** Total lysates of RPE-1 cells were immunoprecipitated with anti-Hsp90, -filamin A, or -IgG antibodies. Then, the samples were subjected to western blotting analysis with the indicated antibodies. 3% of total input is shown. **(E,F)** RPE-1 cells were treated with different concentrations of GA or RA for 48 h and subjected to western blotting analyses with the indicated antibodies as shown. Relative protein levels of filamin A compared to GAPDH were measured using ImageJ software and are shown at the bottom. **(G,H)** RPE-1 cells were treated with 1.78 μM GA or RA for different times and then processed for western blotting analyses with the indicated antibodies. The relative abundances of filamin A compared to GAPDH were measured using ImageJ software and are shown at the bottom. Quantitative data are presented as the means ± SD (at least three independent experiments). $^{*}P < 0.05$ and $^{**}P < 0.01$. Student's *t*-test.

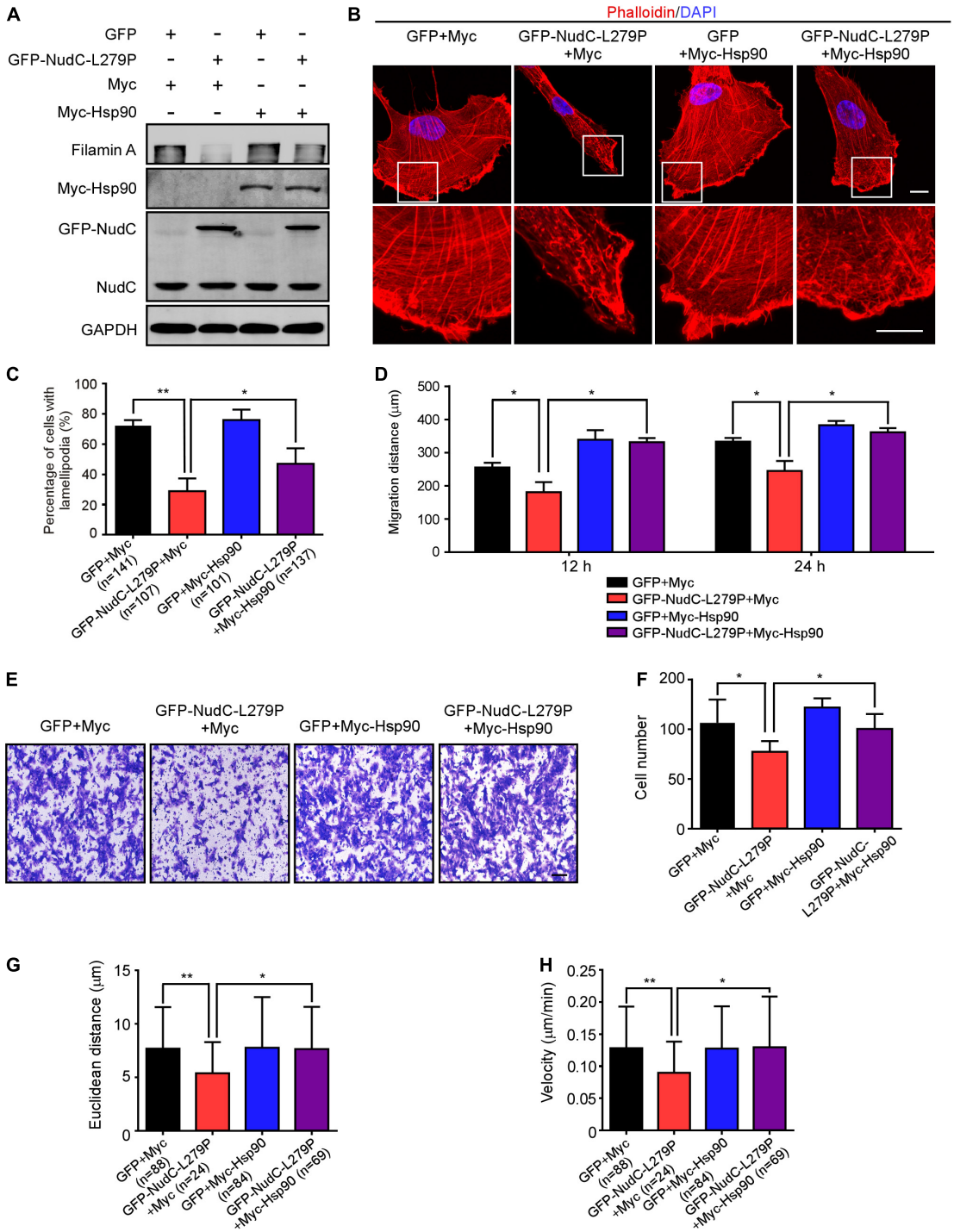

FIGURE 6 | Ectopic expression of Hsp90 reverses the defects induced by NudC-L279P overexpression. RPE-1 cells stably overexpressing GFP or GFP-NudC-L279P were transfected with Myc or Myc-Hsp90 and then subjected to the following analyses. **(A)** Western blotting analysis of the expression of the indicated proteins. GAPDH, a loading control. **(B)** Cells were fixed and stained with phalloidin. DNA was visualized with DAPI. Images were captured by immunofluorescence microscopy. Scale bar, 10 μm. Higher magnifications of the boxed regions are displayed. **(C)** Cells were fixed and stained with phalloidin after 3 h of scratching. Cells with lamellipodia were counted. **(D)** Scratch wound assays detected cell motility. The distance of scratch closure was measured by ImageJ software. **(E,F)** Transwell migration assays were performed to detect cell motility. Cells that migrated to the undersides of the filters were stained with 0.2% crystal violet and monitored with DIC microscopy. The number of migrated cells per transwell was calculated. Scale bar, 100 μm. **(G,H)** The migration tracks of individual cells were traced by Imaris 9.1.2 software. Euclidean distance and migration velocity were analyzed with Imaris 9.1.2 software. Quantitative data are presented as the means ± SD (at least three independent experiments). n, the sample size. $^{*}P < 0.05$ and $^{**}P < 0.01$. Student's *t*-test.

in cell migration (**Supplementary Figures 8B,C**). Furthermore, Co-IP analyses showed that NudC, NudCL or NudCL2 was able to form a complex with filamin A and Hsp90 (**Supplementary Figure 8D**). Taken together, these data suggest that NudC, NudCL, and NudCL2 may synergistically regulate filamin A stability in mammalian cells (**Supplementary Figure 8E**).

Ectopic Expression of LIS1 Is Able to Reverse Cell Migration Defects Caused by NudC-L279P Overexpression

Our previous study showed that the overexpression of human NudC-L279P results in a decrease in the protein level of LIS1 (Zhu et al., 2010). Here, we found that NudC-L279P overexpression destabilizes filamin A and suppresses cell migration. To address whether the suppression of cell migration caused by NudC-L279P overexpression also is mediated by LIS1, we carried out rescue assays in cells overexpressing NudC-L279P. The results showed that ectopic expression of LIS1 in RPE-1 cells was able to reverse the inhibition of cell migration caused by NudC-L279P overexpression (**Supplementary Figure 9**). The further data revealed that LIS1 depletion had no obvious effect on the stability of filamin A, and vice versa (**Supplementary Figure 10**). Together, these data suggest that LIS1 is involved in NudC-mediated the regulation of cell migration with filamin A.

DISCUSSION

Cell migration plays a central role in a wide variety of biological processes (Friedl and Wolf, 2010; Yilmaz and Christofori, 2010), however, the underlying regulatory mechanisms remain incompletely understood. Here, our data show that NudC forms a complex with filamin A. The overexpression of NudC-L279P causes filamin A instability, actin disorganization, and cell migration suppression in mammalian cells. Furthermore, our results show that ectopic Hsp90 expression reverses filamin A degradation and functional defects caused by NudC-L279P overexpression. Together, these data suggest NudC L279P mutation destabilizes filamin A by impairing Hsp90-mediated chaperoning pathway and suppresses cell migration.

Mammalian filamins are a family of actin cross-linking proteins including filamin A, filamin B, and C (Kesner et al., 2010). Previous studies have revealed that filamin A is phosphorylated by several kinases to regulate its ability to cross-link actin (Hammer et al., 2013; Li et al., 2015; Sato et al., 2016). Recent studies also showed that the stability of filamin A is negatively regulated by FILIP (filamin A interacting protein 1) and Asb2α (Nagano et al., 2002, 2004; Sato and Nagano, 2005; Heuze et al., 2008; Razinia et al., 2011, 2013; Lamsoul et al., 2013; Spinner et al., 2015; Métais et al., 2018). Asb2α is able to target filamin A and B for proteasomal degradation (Heuze et al., 2008; Razinia et al., 2011, 2013; Lamsoul et al., 2013; Spinner et al., 2015; Métais et al., 2018). Accumulating studies also indicate that the removal of filamin A and filamin B results in defects in migration and cell spreading (Sheen et al., 2002; Baldassarre et al., 2009, 2012). Here, we provide evidence that overexpression of NudC L279P but not its depletion destabilizes filamin A *via* the ubiquitin-proteasome pathway, which is reversed by exogenous expression of Hsp90 (**Figures 1**, **6**). Furthermore, our results also show that NudCL or NudCL2 forms a complex with filamin A and Hsp90, and participates in the regulation of filamin A stability by coordinating with NudC (**Supplementary Figure 8**). NudC L279P mutant may act as a dominant negative mutation to destabilize filamin A stability. Together, these data suggest a molecular mechanism of the positive regulation of filamin A stability by NudC family.

Cell migration is a highly integrated multistep process, which is regulated by a series of key regulators (Blanchoin et al., 2000; Cameron et al., 2000; Friedl and Wolf, 2010; Yilmaz and Christofori, 2010; Skau and Waterman, 2015). Our previous data showed that depletion of NudC inhibits cell migration by decreasing the protein stability of cofilin 1 via Hsp90-independent pathway (Zhu et al., 2010; Fu et al., 2016). We also found that NudCL2, which is cloned and characterized by our group, is involved in the regulation of cell migration by comodulating the stability of myosin-9 and LIS1 through Hsp90 pathway (Chen et al., 2020). In this report, our data show that NudC is involved in the regulation of cell migration also by positively regulating filamin A stability through the Hsp90 pathway, which is coordinated by NudCL and NudCL2. Meanwhile, our data display that LIS1 also participates in NudC-mediated cell migration regulation. Ectopic expression of LIS1 is able to reverse cell migration defects caused by NudC-L279P overexpression (**Supplementary Figure 9**). Taken together, these studies suggest that NudC family plays an important role in cell migration regulation by stabilizing a series of client proteins.

DATA AVAILABILITY STATEMENT

The original contributions presented in the study are included in the article/**Supplementary Material**, further inquiries can be directed to the corresponding author/s.

AUTHOR CONTRIBUTIONS

ML and ZX designed the study, performed experiments, and wrote the manuscript. CZ designed the study and performed some experiments. CY, JF, YL, and WZ performed some of the experiments. WC, XX, XS, MY, and WL edited the manuscript. TZ and YY conceived the study, participated in its design, and contributed to manuscript writing. All authors contributed to the article and approved the submitted version.

FUNDING

This work was supported by the National Natural Science Foundation of China (31701214, 91740205, 32070709, and 31620103911), the National Key Research and Development

Program of China (2016YFA0100301 and 2019YFA0802202), and the 111 Project (B13026).

ACKNOWLEDGMENTS

We acknowledge Xiangrui Liu for providing advice on the manuscript. We thank John Blenis for providing the myc-filamin A expression vector. We are grateful to Guifeng Xiao and Zhaoxiaonan Lin for confocal imaging assistance. We thank Qin Han for helping with the scanning electron microscope. We also thank the members of the Zhou lab for the helpful comments and suggestions during the work.

SUPPLEMENTARY MATERIAL

The Supplementary Material for this article can be found online at: https://www.frontiersin.org/articles/10.3389/fcell.2021.671233/full#supplementary-material

Supplementary Figure 1 | L279P mutation of NudC destabilizes filamin A in AGS cells. **(A)** Cells transfected with *NudC* RNAi-1, -2 or control were harvested at the indicated times. The cell lysates were subjected to western blotting analysis with anti-NudC and anti-filamin A antibodies. GAPDH, a loading control. **(B)** Cells stably expressing GFP, GFP-NudC or GFP-NudC-L279P were subjected to western blotting analysis using the antibodies as shown. GAPDH, a loading control.

Supplementary Figure 2 | Depletion of filamin A suppresses cell migration in RPE-1 cells. Cells were treated with *filamin A* RNAi or not were subjected to the following analyses. **(A)** Western blotting showed the expression of filamin A. GAPDH, a loading control. **(B,C)** Scratch wound assays revealed cell migration at the different time points. The scratch closure was recorded with DIC microscopy. Dashed lines were used to indicate the approximate line of wound edges. The distance between the two edge lines was measured by ImageJ software. **(D,E)** Transwell migration assays were carried out to detect cell motility. Cells that migrated to the undersides of the filters were stained with 0.2% crystal violet and monitored with DIC microscopy. The number of migrated cells per transwell was counted. **(F-H)** The migration tracks of individual cells were traced by Imaris 9.1.2 software. Representative cell migration tracks are shown. Euclidean distance and migration velocity were analyzed with Imaris 9.1.2 software. Scale bars, 100 μm. Quantitative data are presented as the means ± SD (at least three independent experiments). n, the sample size. $^{*}P < 0.05$ and $^{***}P < 0.001$. Student's *t*-test.

Supplementary Figure 3 | Downregulation of filamin A suppresses cell migration in AGS cells. Cells treated with *filamin A* RNAi or not were subjected to the following analyses. **(A)** Western blotting analysis showed the expression of filamin A. GAPDH, a loading control. **(B,C)** Scratch wound assays revealed cell migration at the different time points. The scratch closure was recorded with DIC microscopy. Dashed lines indicated the approximate line of wound edges. The distance between the two edge lines was measured by ImageJ software. **(D,E)** Transwell migration assays were performed to detect cell motility. Cells that migrated to the undersides of the filters were stained with 0.2% crystal violet and monitored with DIC microscopy. The number of migrated cells per transwell was counted. **(F-H)** The migration tracks of individual cells were traced by Imaris 9.1.2 software. Euclidean distance and migration velocity were analyzed with Imaris 9.1.2 software. Scale bars, 100 μm. Quantitative data are presented as the means ± SD (at least three independent experiments). n, the sample size. $^{*}P < 0.05$ and $^{**}P < 0.01$. Student's *t*-test.

Supplementary Figure 4 | Overexpression of NudC-L279P suppresses cell migration in AGS Cells. AGS cells stably overexpressing GFP, GFP-NudC, or GFP-NudC-L279P were subjected to following analyses. **(A)** Western blotting analysis of the expression levels of the indicated proteins. GAPDH, a loading control. **(B,C)** Scratch wound assays revealed cell migration at the different time points. The scratch closure was recorded with fluorescence microscopy. Dashed lines defined the approximate line of wound edges. The distance between the two edge lines was measured by ImageJ software. **(D,E)** Transwell migration assays were carried out to detect cell motility. Cells that migrated to the undersides of the filters were stained with 0.2% crystal violet and monitored with DIC microscopy. The number of migrated cells per transwell was counted. **(F-H)** The migration tracks of individual cells were traced by Imaris 9.1.2 software. Euclidean distance and migration velocity were analyzed with Imaris 9.1.2 software. Scale bars, 100 μm. Quantitative data are presented as the means ± SD (at least three independent experiments). n, the sample size. $^{*}P < 0.05$; $^{**}P < 0.01$; $^{***}P < 0.001$; and ns, not significant ($P > 0.05$). Student's *t*-test.

Supplementary Figure 5 | Ectopic expression of filamin A reverses the defects of cell migration induced by NudC-L279P overexpression in AGS cells. Cells were transfected with the indicated vectors, and then subjected to the following analyses. **(A)** Western blotting analysis of the expression levels of the indicated proteins. GAPDH, a loading control. **(B,C)** Scratch wound assays revealed cell migration at the different time points. The scratch closure was monitored with fluorescence microscope. Dashed lines defined the approximate line of wound edges. The distance between the two edge lines was measured by ImageJ software. **(D,E)** Transwell migration assays were performed to detect cell motility. Cells that migrated to the undersides of the filters were stained with 0.2% crystal violet and monitored with DIC microscopy. The number of migrated cells per transwell was counted. **(F,G)** The migration tracks of individual cells were traced by Imaris 9.1.2 software. Euclidean distance and migration velocity were analyzed with Imaris 9.1.2 software. Scale bars, 100 μm. Quantitative data are presented as the means ± SD (at least three independent experiments). n, the sample size. $^{*}P < 0.05$; $^{**}P < 0.01$; and $^{***}P < 0.001$. Student's *t*-test.

Supplementary Figure 6 | Inhibition of Hsp90 decreases the protein levels of filamin A in AGS cells. **(A,B)** AGS cells were incubated with different concentrations of GA or RA for 48 h, and then subjected to Western blotting analyses with the indicated antibodies. GAPDH, a loading control. Relative protein levels of filamin A compared to GAPDH were measured using ImageJ software and shown at the bottom. **(C,D)** AGS cells were incubated with 1.78 μM GA or RA for different times, and then processed for western blotting analyses. GAPDH, a loading control. Relative protein levels of filamin A compared to GAPDH are shown at the bottom. Quantitative data are presented as the means ± SD (at least three independent experiments). $^{*}P < 0.05$; $^{**}P < 0.01$; and $^{***}P < 0.001$. Student's *t*-test.

Supplementary Figure 7 | Ectopic expression of Hsp90 reverses the defects in cell migration induced by NudC-L279P overexpression in AGS cells. Cells transfected with indicated vectors were subjected the following analyses. **(A)** Western blotting analysis of the proteins' level with the indicated antibodies. GAPDH, a loading control. **(B,C)** Scratch wound assays indicated cell migration at the different time points. The scratch closure was monitored with fluorescence microscope. Dashed lines defined the approximate line of wound edges. The distance between the two edge lines was measured by ImageJ software. **(D,E)** Transwell migration assays were performed to detect cell motility. Cells that migrated to the underside of the filter were stained with 0.2% crystal violet and monitored with DIC microscopy. The number of migrated cells per transwell was plotted. **(F,G)** The migration tracks of individual cells were traced by Imaris 9.1.2 software. Euclidean distance and migration velocity were analyzed with Imaris 9.1.2 software. Scale bars, 100 μm. Quantitative data are presented as the means ± SD (at least three independent experiments). $^{*}P < 0.05$. Student's *t*-test.

Supplementary Figure 8 | NudCL and NudCL2 are involved in the regulation of filamin A stability coordinating with NudC. **(A)** RPE-1 cells were treated with the indicated siRNAs were subjected to western blotting analysis using the antibodies as shown. GAPDH, the loading control. **(B)** Cells treated with the indicated siRNAs were subjected to scratch wound assays. The scratch closure was monitored with DIC microscopy. The distance between the two edge lines was measured using ImageJ software. Scale bar, 100 μm. **(C)** The distance between the two edge lines of scratch wound assays was measured by ImageJ software. Differences were statistically compared with the control. **(D)** Total lysates of cells were immunoprecipitated with the filamin A antibodies or IgGs and processed for western blotting. 3% of total input is shown. **(E)** Model for the role of NudC family in cell migration regulation. NudC, NudCL, and NudCL2 synergistically regulate filamin A stability and cell migration by the Hsp90 pathway. Scale bar, 100 μm.

Quantitative data are presented as the means ± SD (at least three independent experiments). $^{**}P < 0.01$; $^{***}P < 0.001$; and ns, not significant ($P > 0.05$), Student's *t*-test.

Supplementary Figure 9 | Ectopic expression of LIS1 partially reverses the defects of cell migration induced by NudC-L279P overexpression. RPE-1 cells stably overexpressing GFP, GFP-NudC, or GFP-NudC-L279P were transfected with the indicated vectors, and then subjected to the following analyses. **(A)** Western blotting analysis of the proteins' level with the indicated antibodies. GAPDH, a loading control. **(B,C)** Scratch wound assays revealed cell migration at the different time points. The scratch closure was monitored with fluorescence microscope. Dashed lines indicated the approximate line of wound edges. The distance between the two edge lines was measured by ImageJ software. **(D,E)** Transwell migration assays were performed to analyze cell motility. Cells that migrated to the underside of the filter were stained with 0.2% crystal violet and monitored with DIC microscopy. The number of migrated cells per transwell was counted. **(F,G)** The migration tracks of individual cells were traced by Imaris 9.1.2 software. Euclidean distance and migration velocity were analyzed with Imaris 9.1.2 software. Scale bars, 100 μm. Quantitative data are presented as the means ± SD (at least three independent experiments). $^{*}P < 0.05$ and $^{**}P < 0.01$. Student's *t*-test.

Supplementary Figure 10 | Depletion of LIS1 has no significant effect on the protein level of filamin A, and vice versa. A, RPE-1 cells treated with *LIS1* RNAi were subjected to western blotting analyses using anti-LIS1 and -filamin A antibodies. GAPDH, a loading control. B, RPE-1 cells treated with *filamin A* RNAi were subjected to western blotting analyses using anti-LIS1 and -filamin A antibodies. GAPDH, a loading control.

Supplementary Movie 1 | The migration tracks of RPE-1 cells stably overexpressing GFP-Ctrl.

Supplementary Movie 2 | The migration tracks of RPE-1 cells stably overexpressing GFP-NudC.

Supplementary Movie 3 | The migration tracks of RPE-1 cells stably overexpressing GFP-NudC-L279P.

REFERENCES

Baldassarre, M., Razinia, Z., Brahme, N. N., Buccione, R., and Calderwood, D. A. (2012). Filamin a controls matrix metalloproteinase activity and regulates cell invasion in human fibrosarcoma cells. *J. Cell Sci.* 125, 3858–3869.

Baldassarre, M., Razinia, Z., Burande, C. F., Lamsoul, I., Lutz, P. G., and Calderwood, D. A. (2009). Filamins regulate cell spreading and initiation of cell migration. *PLoS One* 4:e7830. doi: 10.1371/journal.pone.0007830

Bandaru, S., Ala, C., Salimi, R., Akula, M. K., Ekstrand, M., Devarakonda, S., et al. (2019). Targeting filamin a reduces macrophage activity and atherosclerosis. *Circulation* 140, 67–79. doi: 10.1161/circulationaha.119.039697

Bear, J. E., Svitkina, T. M., Krause, M., Schafer, D. A., Loureiro, J. J., Strasser, G. A., et al. (2002). Antagonism between Ena/VASP proteins and actin filament capping regulates fibroblast motility. *Cell* 109, 509–521. doi: 10.1016/s0092-8674(02)00731-6

Blanchoin, L., Pollard, T. D., and Mullins, R. D. (2000). Interactions of ADF/cofilin, Arp2/3 complex, capping protein and profilin in remodeling of branched actin filament networks. *Curr. Biol.* 10, 1273–1282. doi: 10.1016/s0960-9822(00)00749-1

Cameron, L. A., Giardini, P. A., Soo, F. S., and Theriot, J. A. (2000). Secrets of actin-based motility revealed by a bacterial pathogen. *Nat. Rev. Mol. Cell Biol.* 1, 110–119. doi: 10.1038/35040061

Chen, M., and Stracher, A. (1989). In situ phosphorylation of platelet actin-binding protein by cAMP-dependent protein kinase stabilizes it against proteolysis by calpain. *J. Biol. Chem.* 264, 14282–14289. doi: 10.1016/s0021-9258(18)71675-x

Chen, W. W., Wang, W., Sun, X. X., Xie, S. S., Xu, X. Y., Liu, M., et al. (2020). NudCL2 regulates cell migration by stabilizing both myosin-9 and LIS1 with Hsp90. *Cell Death Dis.* 11:534.

Cox, M. B., and Johnson, J. L. (2011). The role of p23, Hop, immunophilins, and other co-chaperones in regulating Hsp90 function. *Methods Mol. Biol.* 787, 45–66. doi: 10.1007/978-1-61779-295-3_4

Cukier, I. H., Li, Y., and Lee, J. M. (2007). Cyclin B1/Cdk1 binds and phosphorylates Filamin a and regulates its ability to cross-link actin. *FEBS Lett.* 581, 1661–1672. doi: 10.1016/j.febslet.2007.03.041

Cunningham, C. C., Gorlin, J. B., Kwiatkowski, D. J., Hartwig, J. H., Janmey, P. A., Byers, H. R., et al. (1992). Actin-binding protein requirement for cortical stability and efficient locomotion. *Science* 255, 325–327. doi: 10.1126/science.1549777

Dean, M. E., and Johnson, J. L. (2021). Human Hsp90 cochaperones: perspectives on tissue-specific expression and identification of cochaperones with similar in vivo functions. *Cell Stress Chaperones* 26, 3–13. doi: 10.1007/s12192-020-01167-0

Deng, W. J., Nie, S., Dai, J., Wu, J. R., and Zeng, R. (2010). Proteome, phosphoproteome, and hydroxyproteome of liver mitochondria in diabetic rats at early pathogenic stages. *Mol. Cell Proteomics* 9, 100–116. doi: 10.1074/mcp.m900020-mcp200

Felts, S. J., and Toft, D. O. (2003). p23, a simple protein with complex activities. *Cell Stress Chaperones* 8, 108–113. doi: 10.1379/1466-1268(2003)008<0108:paspwc>2.0.co;2

Feng, S. J., Song, Y. L., Shen, M. H., Xie, S. S., Li, W. J., Lu, Y., et al. (2017). Microtubule-binding protein FOR20 promotes microtubule depolymerization and cell migration. *Cell Discov.* 3:17032.

Feng, Y., and Walsh, C. A. (2004). The many faces of filamin: a versatile molecular scaffold for cell motility and signaling. *Nat. Cell Biol.* 6, 1034–1038. doi: 10.1038/ncb1104-1034

Fox, J. W., Lamperti, E. D., Eksioglu, Y. Z., Hong, S. E., Feng, Y., Graham, D. A., et al. (1998). Mutations in filamin 1 prevent migration of cerebral cortical neurons in human periventricular heterotopia. *Neuron* 21, 1315–1325. doi: 10.1016/s0896-6273(00)80651-0

Friedl, P., and Wolf, K. (2010). Plasticity of cell migration: a multiscale tuning model. *J. Cell Biol.* 188, 11–19. doi: 10.1083/jcb.200909003

Fu, Q. Q., Wang, W., Zhou, T. H., and Yang, Y. H. (2016). Emerging roles of NudC family: from molecular regulation to clinical implications. *Sci. China Life Sci.* 59, 455–462. doi: 10.1007/s11427-016-5029-2

George, S. P., Chen, H. F., Conrad, J. C., and Khurana, S. (2013). Regulation of directional cell migration by membrane-induced actin bundling. *J. Cell Sci.* 126, 312–326.

Hammer, A., Rider, L., Oladimeji, P., Cook, L., Li, Q., Mattingly, R. R., et al. (2013). Tyrosyl phosphorylated PAK1 regulates breast cancer cell motility in response to prolactin through filamin A. *Mol. Endocrinol.* 27, 455–465. doi: 10.1210/me.2012-1291

Heuze, M. L., Lamsoul, I., Baldassarre, M., Lad, Y., Leveque, S., Razinia, Z., et al. (2008). ASB2 targets filamins A and B to proteasomal degradation. *Blood* 112, 5130–5140. doi: 10.1182/blood-2007-12-128744

Jacquemet, G., Morgan, M. R., Byron, A., Humphries, J. D., Choi, C. K., Chen, C. S., et al. (2013). Rac1 is deactivated at integrin activation sites through an IQGAP1-filamin-A-RacGAP1 pathway. *J. Cell Sci.* 126, 4121–4135.

Jheng, G. W., Hur, S. S., Chang, C. M., Wu, C. C., Cheng, J. S., Lee, H. H., et al. (2018). Lis1 dysfunction leads to traction force reduction and cytoskeletal disorganization during cell migration. *Biochem. Biophys. Res. Commun.* 497, 869–875. doi: 10.1016/j.bbrc.2018.02.151

Kamal, A., Boehm, M. F., and Burrows, F. J. (2004). Therapeutic and diagnostic implications of Hsp90 activation. *Trends Mol. Med.* 10, 283–290. doi: 10.1016/j.molmed.2004.04.006

Kesner, B. A., Milgram, S. L., Temple, B. R., and Dokholyan, N. V. (2010). Isoform divergence of the filamin family of proteins. *Mol. Biol. Evol.* 27, 283–295. doi: 10.1093/molbev/msp236

Kim, H., and McCulloch, C. A. (2011). Filamin A mediates interactions between cytoskeletal proteins that control cell adhesion. *FEBS Lett.* 585, 18–22. doi: 10.1016/j.febslet.2010.11.033

Kircher, P., Hermanns, C., Nossek, M., Drexler, M. K., Grosse, R., Fischer, M., et al. (2015). Filamin A interacts with the coactivator MKL1 to promote the activity of the transcription factor SRF and cell migration. *Sci. Signal.* 8:ra112. doi: 10.1126/scisignal.aad2959

Kumar, A., Shutova, M. S., Tanaka, K., Iwamoto, D. V., Calderwood, D. A., Svitkina, T. M., et al. (2019). Filamin A mediates isotropic distribution of applied force across the actin network. *J. Cell Biol.* 218, 2481–2491. doi: 10.1083/jcb.201901086

Kyndt, F., Gueffet, J. P., Probst, V., Jaafar, P., Legendre, A., Le Bouffant, F., et al. (2007). Mutations in the gene encoding filamin A as a cause for familial cardiac valvular dystrophy. *Circulation* 115, 40–49. doi: 10.1161/circulationaha.106.622621

Lamsoul, I., Metais, A., Gouot, E., Heuze, M. L., Lennon-Dumenil, A. M., MoogLutz, C., et al. (2013). ASB2alpha regulates migration of immature dendritic cells. *Blood* 122, 533–541. doi: 10.1182/blood-2012-11-466649

Lauffenburger, D. A., and Horwitz, A. F. (1996). Cell migration: a physically integrated molecular process. *Cell* 84, 359–369. doi: 10.1016/s0092-8674(00)81280-5

Li, J., Soroka, J., and Buchner, J. (2012). The Hsp90 chaperone machinery: conformational dynamics and regulation by co-chaperones. *Biochim. Biophys. Acta* 1823, 624–635. doi: 10.1016/j.bbamcr.2011.09.003

Li, L., Lu, Y., Stemmer, P. M., and Chen, F. (2015). Filamin A phosphorylation by Akt promotes cell migration in response to arsenic. *Oncotarget* 6, 12009–12019. doi: 10.18632/oncotarget.3617

Li, M., Xu, X. Y., Zhang, J., Liu, M., Wang, W., Gao, Y., et al. (2019). NudC-like protein 2 restrains centriole amplification by stabilizing HERC2. *Cell Death Dis.* 10:628.

Lu, Y., Xie, S. S., Zhang, W., Zhang, C., Gao, C., Sun, Q., et al. (2017). Twa1/Gid8 is a beta-catenin nuclear retention factor in Wnt signaling and colorectal tumorigenesis. *Cell Res.* 27, 1422–1440. doi: 10.1038/cr.2017.107

Maceyka, M., Alvarez, S. E., Milstien, S., and Spiegel, S. (2008). Filamin A links sphingosine kinase 1 and sphingosine-1-phosphate receptor 1 at lamellipodia to orchestrate cell migration. *Mol. Cell Biol.* 28, 5687–5697. doi: 10.1128/mcb.00465-08

Machesky, L. M. (2008). Lamellipodia and filopodia in metastasis and invasion. *FEBS Lett.* 582, 2102–2111. doi: 10.1016/j.febslet.2008.03.039

Métais, A., Lamsoul, L., Melet, A., Uttenweiler-Joseph, S., Poincloux, R., Stefanovic, S., et al. (2018). Asb2α-Filamin A axis is essential for actin cytoskeleton remodeling during heart development. *Circ. Res.* 122, 34–48.

Nagano, T., Morikubo, S., and Sato, M. (2004). Filamin A and FILIP (Filamin A-Interacting Protein) regulate cell polarity and motility in neocortical subventricular and intermediate zones during radial migration. *J. Neurosci.* 24, 9648–9657. doi: 10.1523/jneurosci.2363-04.2004

Nagano, T., Yoneda, T., Hatanaka, Y., Kubota, C., Murakami, F., and Sato, M. (2002). Filamin A-interacting protein (FILIP) regulates cortical cell migration out of the ventricular zone. *Nat. Cell Biol.* 4, 495–501. doi: 10.1038/ncb808

Nakamura, F. (2001). Biochemical, electron microscopic and immunohistological observations of cationic detergent-extracted cells: detection and improved preservation of microextensions and ultramicroextensions. *BMC Cell Biol.* 2:10.

Nishita, M., Yoo, S. K., Nomachi, A., Kani, S., Sougawa, N., Ohta, Y., et al. (2006). Filopodia formation mediated by receptor tyrosine kinase Ror2 is required for Wnt5a-induced cell migration. *J. Cell Biol.* 175, 555–562. doi: 10.1083/jcb.200607127

Nurden, P., Debili, N., Coupry, I., Bryckaert, M., Youlyouz-Marfak, I., Solé, G., et al. (2011). Thrombocytopenia resulting from mutations in filamin A can be expressed as an isolated syndrome. *Blood* 118, 5928–5937. doi: 10.1182/blood-2011-07-365601

Ohta, Y., Suzuki, N., Nakamura, S., Hartwig, J. H., and Stossel, T. P. (1999). The small GTPase RalA targets filamin to induce filopodia. *Proc. Natl. Acad. Sci. U. S. A.* 96, 2122–2128. doi: 10.1073/pnas.96.5.2122

Osmani, A. H., Osmani, S. A., and Morris, N. R. (1990). The molecular cloning and identification of a gene product specifically required for nuclear movement in *Aspergillus nidulans*. *J. Cell Biol.* 111, 543–551. doi: 10.1083/jcb.111.2.543

Pearl, L. H., and Prodromou, C. (2006). Structure and mechanism of the Hsp90 molecular chaperone machinery. *Annu. Rev. Biochem.* 75, 271–294. doi: 10.1146/annurev.biochem.75.103004.142738

Razinia, Z., Baldassarre, M., Bouaouina, M., Lamsoul, I., Lutz, P. G., Calderwood, D. A., et al. (2011). The E3 ubiquitin ligase specificity subunit ASB2alpha targets filamins for proteasomal degradation by interacting with the filamin actin-binding domain. *J. Cell Sci.* 124, 2631–2641. doi: 10.1242/jcs.084343

Razinia, Z., Baldassarre, M., Cantelli, G., and Calderwood, D. A. (2013). ASB2alpha, an E3 ubiquitin ligase specificity subunit, regulates cell spreading and triggers proteasomal degradation of filamins by targeting the filamin calponin homology 1 domain. *J. Biol. Chem.* 288, 32093–30105. doi: 10.1074/jbc.m113.496604

Razinia, Z., Makela, T., Ylanne, J., and Calderwood, D. A. (2012). Filamins in mechanosensing and signaling. *Annu. Rev. Biophys.* 41, 227–246. doi: 10.1146/annurev-biophys-050511-102252

Ridley, A. J., Schwartz, M. A., Burridge, K., Firtel, R. A., Ginsberg, M. H., Borisy, G., et al. (2003). Cell migration: integrating signals from front to back. *Science* 302, 1704–1709. doi: 10.1126/science.1092053

Robertson, S. P., Twigg, S. R., Sutherland-Smith, A. J., Biancalana, V., Gorlin, R. J., Horn, D., et al. (2003). Localized mutations in the gene encoding the cytoskeletal protein filamin A cause diverse malformations in humans. *Nat. Genet.* 33, 487–491. doi: 10.1038/ng1119

Sato, M., and Nagano, T. (2005). Involvement of filamin A and filamin A-interacting protein (FILIP) in controlling the start and cell shape of radially migrating cortical neurons. *Anat. Sci. Int.* 80, 19–29. doi: 10.1111/j.1447-073x.2005.00101.x

Sato, T., Ishii, J., Ota, Y., Sasaki, E., Shibagaki, Y., and Hattori, S. (2016). Mammalian target of rapamycin (mTOR) complex 2 regulates filamin A-dependent focal adhesion dynamics and cell migration. *Genes Cells* 21, 579–593. doi: 10.1111/gtc.12366

Schaefer, A., Nethe, M., and Hordijk, P. L. (2012). Ubiquitin links to cytoskeletal dynamics, cell adhesion and migration. *Biochem. J.* 442, 13–25. doi: 10.1042/bj20111815

Schopf, F. H., Biebl, M. M., and Buchner, J. (2017). The HSP90 chaperone machinery. *Nat. Rev. Mol. Cell Biol.* 18, 345–360.

Sheen, V. L., Feng, Y., Graham, D., Takafuta, T., Shapiro, S. S., and Walsh, C. A. (2002). Filamin A and Filamin B are co-expressed within neurons during periods of neuronal migration and can physically interact. *Hum. Mol. Genet.* 11, 2845–2854. doi: 10.1093/hmg/11.23.2845

Skau, C. T., and Waterman, C. M. (2015). Specification of architecture and function of actin structures by actin nucleation factors. *Annu. Rev. Biophys.* 44, 285–310. doi: 10.1146/annurev-biophys-060414-034308

Small, J. V., Stradal, T., Vignal, E., and Rottner, K. (2002). The lamellipodium: where motility begins. *Trends Cell Biol.* 12, 112–120. doi: 10.1016/s0962-8924(01)02237-1

Spinner, C. A., Uttenweiler-Joseph, S., Metais, A., Stella, A., Burlet-Schiltz, O., Moog-Lutz, C., et al. (2015). Substrates of the ASB2alpha E3 ubiquitin ligase in dendritic cells. *Sci. Rep.* 5:16269.

Stossel, T. P., Condeelis, J., Cooley, L., Hartwig, J. H., Noegel, A., Schleicher, M., et al. (2001). Filamins as integrators of cell mechanics and signaling. *Nat. Rev. Mol. Cell Biol.* 2, 138–145. doi: 10.1038/35052082

Sutherland-Smith, A. J. (2011). Filamin structure, function and mechanics: are altered filamin-mediated force responses associated with human disease? *Biophys. Rev.* 3, 15–23. doi: 10.1007/s12551-011-0042-y

Taipale, M., Tucker, G., Peng, J., Krykbaeva, I., Lin, Z. Y., Larsen, B., et al. (2014). A quantitative chaperone interaction network reveals the architecture of cellular protein homeostasis pathways. *Cell* 158, 434–448. doi: 10.1016/j.cell.2014.05.039

Tang, D. D., and Gerlach, B. D. (2017). The roles and regulation of the actin cytoskeleton, intermediate filaments and microtubules in smooth muscle cell migration. *Respir. Res.* 18, 54–55.

Urra, H., Henriquez, D. R., Canovas, J., Villarroel-Campos, D., Carreras-Sureda, A., Pulgar, E., et al. (2018). IRE1alpha governs cytoskeleton remodelling and cell migration through a direct interaction with filamin A. *Nat. Cell Biol.* 20, 942–953. doi: 10.1038/s41556-018-0141-0

Venkatareddy, M., Cook, L., Abuarquob, K., Verma, R., and Garg, P. (2011). Nephrin regulates lamellipodia formation by assembling a protein complex that includes Ship2, filamin and lamellipodin. *PLoS One* 6:e28710. doi: 10.1371/journal.pone.0028710

Yang, Y. Y., Wang, W., Li, M., Gao, Y., Zhang, W., Huang, Y. L., et al. (2019). NudCL2 is an Hsp90 cochaperone to regulate sister chromatid cohesion by stabilizing cohesin subunits. *Cell Mol. Life Sci.* 76, 381–395. doi: 10.1007/s00018-018-2957-y

Yang, Y. Y., Yan, X. Y., Cai, Y. Q., Lu, Y., Si, J. M., and Zhou, T. H. (2010). NudC-like protein 2 regulates the LIS1/dynein pathway by stabilizing LIS1 with Hsp90. *Proc. Natl. Acad. Sci. U. S. A.* 107, 3499–3504. doi: 10.1073/pnas.0914307107

Yilmaz, M., and Christofori, G. (2010). Mechanisms of motility in metastasizing cells. *Mol. Cancer Res.* 8, 629–642. doi: 10.1158/1541-7786.mcr-10-0139

Zenker, M., Rauch, A., Winterpacht, A., Tagariello, A., Kraus, C., Rupprecht, T., et al. (2004). A dual phenotype of periventricular nodular heterotopia and

frontometaphyseal dysplasia in one patient caused by a single FLNA mutation leading to two functionally different aberrant transcripts. *Am. J. Hum. Genet.* 74, 731–737. doi: 10.1086/383094

Zhang, C., Zhang, W., Lu, Y., Yan, X. Y., and Zhu, X. L. (2016). NudC regulates actin dynamics and ciliogenesis by stabilizing cofilin 1. *Cell Res.* 26, 239–253. doi: 10.1038/cr.2015.152

Zheng, M., Cierpicki, T., Burdette, A. J., Utepbergenov, D., Janczyk, P. Ł, Derewenda, U., et al. (2011). Structural features and chaperone activity of the NudC protein family. *J. Mol. Biol.* 409, 722–741. doi: 10.1016/j.jmb.2011.04.018

Zhou, A. X., Hartwig, J. H., and Akyurek, L. M. (2010). Filamins in cell signaling, transcription and organ development. *Trends Cell Biol.* 20, 113–123. doi: 10.1016/j.tcb.2009.12.001

Zhou, T., Zimmerman, W., Liu, X., and Erikson, R. L. (2006). A mammalian NudC-like protein essential for dynein stability and cell viability. *Proc. Natl. Acad. Sci. U. S. A.* 103, 9039–9044. doi: 10.1073/pnas.0602916103

Zhu, X. J., Liu, X. Y., Jin, Q., Cai, Y. Q., Yang, Y. H., and Zhou, T. H. (2010). The L279P mutation of nuclear distribution gene C (n.d.) influences its chaperone activity and lissencephaly protein 1 (LIS1) stability. *J. Biol. Chem.* 285, 29903–29910. doi: 10.1074/jbc.m110.105494

Conflict of Interest: The authors declare that the research was conducted in the absence of any commercial or financial relationships that could be construed as a potential conflict of interest.

Advantages of publishing in Frontiers

OPEN ACCESS
Articles are free to read for greatest visibility and readership

FAST PUBLICATION
Around 90 days from submission to decision

HIGH QUALITY PEER-REVIEW
Rigorous, collaborative, and constructive peer-review

TRANSPARENT PEER-REVIEW
Editors and reviewers acknowledged by name on published articles

Frontiers
Avenue du Tribunal-Fédéral 34
1005 Lausanne | Switzerland

Visit us: www.frontiersin.org
Contact us: frontiersin.org/about/contact

REPRODUCIBILITY OF RESEARCH
Support open data and methods to enhance research reproducibility

DIGITAL PUBLISHING
Articles designed for optimal readership across devices

FOLLOW US
@frontiersin

IMPACT METRICS
Advanced article metrics track visibility across digital media

EXTENSIVE PROMOTION
Marketing and promotion of impactful research

LOOP RESEARCH NETWORK
Our network increases your article's readership